CARDIAC MODELING: AIMING FOR OPTIMIZATION OF THERAPY

EDITED BY: Javier Saiz and Olaf Doessel
PUBLISHED IN: Frontiers in Physiology

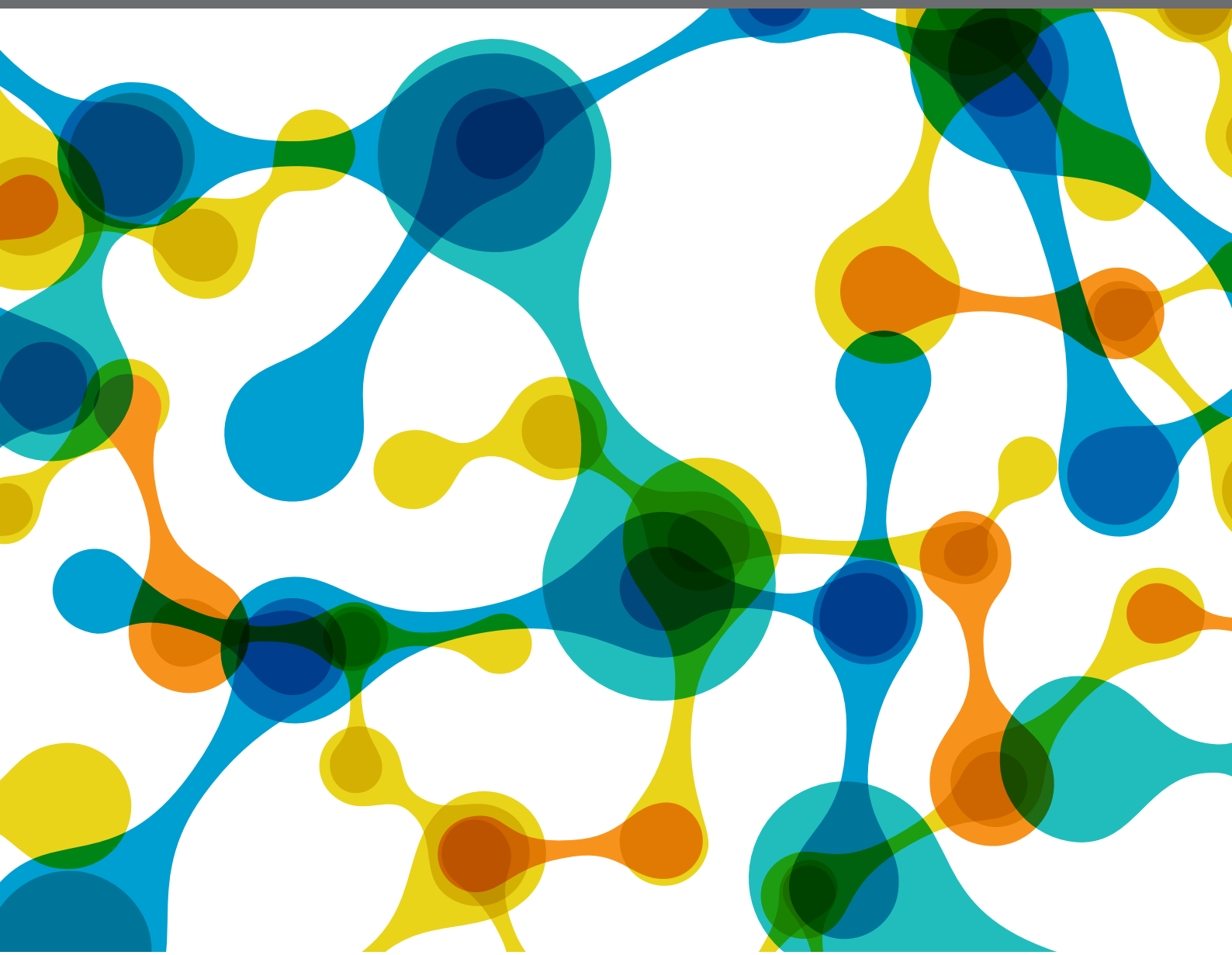

frontiers Research Topics

frontiers

ISSN 1664-8714
ISBN 978-2-88966-219-7
DOI 10.3389/978-2-88966-219-7

About Frontiers

Frontiers is more than just an open-access publisher of scholarly articles: it is a pioneering approach to the world of academia, radically improving the way scholarly research is managed. The grand vision of Frontiers is a world where all people have an equal opportunity to seek, share and generate knowledge. Frontiers provides immediate and permanent online open access to all its publications, but this alone is not enough to realize our grand goals.

Frontiers Journal Series

The Frontiers Journal Series is a multi-tier and interdisciplinary set of open-access, online journals, promising a paradigm shift from the current review, selection and dissemination processes in academic publishing. All Frontiers journals are driven by researchers for researchers; therefore, they constitute a service to the scholarly community. At the same time, the Frontiers Journal Series operates on a revolutionary invention, the tiered publishing system, initially addressing specific communities of scholars, and gradually climbing up to broader public understanding, thus serving the interests of the lay society, too.

Dedication to Quality

Each Frontiers article is a landmark of the highest quality, thanks to genuinely collaborative interactions between authors and review editors, who include some of the world's best academicians. Research must be certified by peers before entering a stream of knowledge that may eventually reach the public - and shape society; therefore, Frontiers only applies the most rigorous and unbiased reviews.
Frontiers revolutionizes research publishing by freely delivering the most outstanding research, evaluated with no bias from both the academic and social point of view. By applying the most advanced information technologies, Frontiers is catapulting scholarly publishing into a new generation.

What are Frontiers Research Topics?

Frontiers Research Topics are very popular trademarks of the Frontiers Journals Series: they are collections of at least ten articles, all centered on a particular subject. With their unique mix of varied contributions from Original Research to Review Articles, Frontiers Research Topics unify the most influential researchers, the latest key findings and historical advances in a hot research area! Find out more on how to host your own Frontiers Research Topic or contribute to one as an author by contacting the Frontiers Editorial Office: researchtopics@frontiersin.org

CARDIAC MODELING: AIMING FOR OPTIMIZATION OF THERAPY

Topic Editors:
Javier Saiz, Universitat Politècnica de València, Spain
Olaf Doessel, Karlsruhe Institute of Technology (KIT), Germany

Citation: Saiz, J., Doessel, O., eds. (2020). Cardiac Modeling: Aiming for Optimization of Therapy. Lausanne: Frontiers Media SA. doi: 10.3389/978-2-88966-219-7

Table of Contents

frontiers in Physiology

ORIGINAL RESEARCH
published: 18 December 2018
doi: 10.3389/fphys.2018.01795

Cellular Mechanisms of Sinus Node Dysfunction in Carriers of the *SCN5A*-E161K Mutation and Role of the H558R Polymorphism

*Ronald Wilders**

Department of Medical Biology, Amsterdam University Medical Centers, Amsterdam, Netherlands

OPEN ACCESS

Edited by:
Javier Saiz,
Universitat Politècnica de València, Spain

Reviewed by:
Yael Yaniv,
Technion – Israel Institute of Technology, Israel
Arun V. Holden,
University of Leeds, United Kingdom

***Correspondence:**
Ronald Wilders
r.wilders@amc.uva.nl

Specialty section:
This article was submitted to Computational Physiology and Medicine, a section of the journal Frontiers in Physiology

Received: *11 September 2018*
Accepted: *29 November 2018*
Published: *18 December 2018*

Citation:
Wilders R (2018) Cellular Mechanisms of Sinus Node Dysfunction in Carriers of the SCN5A-E161K Mutation and Role of the H558R Polymorphism. Front. Physiol. 9:1795. doi: 10.3389/fphys.2018.01795

Background: Carriers of the E161K mutation in the *SCN5A* gene, encoding the $Na_V1.5$ pore-forming α-subunit of the ion channel carrying the fast sodium current (I_{Na}), show sinus bradycardia and occasional exit block. Voltage clamp experiments in mammalian expression systems revealed a mutation-induced 2.5- to 4-fold reduction in I_{Na} peak current density as well as a +19 mV shift and reduced steepness of the steady-state activation curve. The highly common H558R polymorphism in $Na_V1.5$ limits this shift to +13 mV, but also introduces a −10 mV shift in steady-state inactivation.

Aim: We assessed the cellular mechanism by which the E161K mutation causes sinus node dysfunction in heterozygous mutation carriers as well as the potential role of the H558R polymorphism.

Methods: We incorporated the mutation-induced changes in I_{Na} into the Fabbri-Severi model of a single human sinoatrial node cell and the Maleckar et al. human atrial cell model, and carried out simulations under control conditions and over a wide range of acetylcholine levels.

Results: In absence of the H558R polymorphism, the E161K mutation increased the basic cycle length of the sinoatrial node cell from 813 to 866 ms. In the simulated presence of 10 and 25 nM acetylcholine, basic cycle length increased from 1027 to 1131 and from 1448 to 1795 ms, respectively. The increase in cycle length was the result of a significant slowing of diastolic depolarization. The mutation-induced reduction in I_{Na} window current had reduced the contribution of the mutant component of I_{Na} to the net membrane current during diastolic depolarization to effectively zero. Highly similar results were obtained in presence of the H558R polymorphism. Atrial excitability was reduced, both in absence and presence of the H558R polymorphism, as reflected by an increase in threshold stimulus current and a concomitant decrease in capacitive current of the atrial cell.

Conclusion: We conclude that the experimentally identified mutation-induced changes in I_{Na} can explain the clinically observed sinus bradycardia and potentially the occasional exit block. Furthermore, we conclude that the common H558R polymorphism does not significantly alter the effects of the E161K mutation and can thus not explain the reduced penetrance of the E161K mutation.

Keywords: computer simulations, electrophysiology, genetics, human, ion channel, sinus bradycardia, sinus node dysfunction, sodium current

INTRODUCTION

The"fast sodium current" (I_{Na}), which flows through $Na_V1.5$ sodium channels, is a key player in the electrical activity of the human heart (Zimmer et al., 2014), where it is responsible for the fast >150 V/s upstroke of individual atrial and ventricular cardio-myocytes (Workman et al., 2001; O'Hara et al., 2011). The cardiac-specific $Na_V1.5$ protein, encoded by the *SCN5A* gene, is the pore-forming α-subunit of the channel (Remme, 2013). I_{Na} has also been observed in patch-clamp recordings from isolated human sinoatrial (SA) node cells (Verkerk et al., 2009), in line with the observation by Chandler et al. (2009) that $Na_V1.5$ is expressed in human SA nodal tissue. Accordingly, I_{Na} was included in the comprehensive computational model of a single human SA nodal cell that was recently developed by Fabbri et al. (2017) and is known as the Fabbri-Severi model.

Mutations in genes encoding ion channel-related proteins may result in inherited arrhythmia disorders, in particular the long QT syndrome (LQTS) and the Brugada syndrome (BrS). Gain-of-function and loss-of-function mutations in *SCN5A* underlie LQTS type 3 (LQT3) and BrS type 1 (BrS1), respectively (Brugada et al., 2018; Giudicessi et al., 2018; Wilde and Amin, 2018). Mutations in *SCN5A* may also lead to overlapping phenotypes (*SCN5A* overlap syndromes), where clinical characteristics of LQTS, BrS, and other arrhythmia syndromes, e.g., conduction disease and sinus node dysfunction, coexist in a single family or even in a single patient (Remme et al., 2008; Giudicessi et al., 2018). Sinus node dysfunction is a relatively common observation in both LQT3 and BrS1 patients (Hayashi et al., 2018; Wilders and Verkerk, 2018). It should be noted that the "gain of function" in case of LQT3 refers to the persistent I_{Na} that prolongs the ventricular action potential and thus causes QT interval prolongation. If an LQT3 mutation is associated with sinus bradycardia, this mutation shows a concomitant "loss of function" in the voltage range of diastolic depolarization (Wilders and Verkerk, 2018).

In 2005, Smits et al. reported the clinical and biophysical features of a novel sodium channel mutation, E161K, i.e., the replacement of the highly conserved acidic residue glutamic acid (E) with the basic residue lysine (K) at position 161 of the $Na_V1.5$ protein (p.Glu161Lys; c.481G > A) (Smits et al., 2005). This loss-of-function mutation was identified in individuals of two non-related families. Affected patients had a complex clinical phenotype with symptoms of bradycardia, sinus node dysfunction, generalized conduction disease or BrS, or various combinations thereof. Sinus node dysfunction was observed in 8 out of 14 mutation carriers. Twenty-four-hour Holter recordings from 10 mutation carriers revealed that their absolute minimum heart rate, but not their maximum heart rate, was significantly lower compared to controls (39 ± 1 vs. 51 ± 0.6 beats/min, mean ± SEM). Furthermore, the incidence of signs of sinus node dysfunction in E161K mutation carriers was particularly high at night, when vagal tone is dominant.

Smits et al. (2005) assessed the biophysical effects of the E161K mutation by transfecting E161K or wild-type sodium channel α-subunit into tsA201 cells, together with wild-type β_1-subunit. Voltage clamp experiments on the transfected cells revealed a 2.5-fold reduction in peak I_{Na} at −20 mV for E161K sodium channels compared to wild-type channels. Furthermore, the steady-state activation curve of the mutant channels showed a +11.9 mV shift of its half-maximal activation potential ($V_{1/2}$) compared to wild-type (−30.7 ± 0.8 vs. −42.6 ± 1.4 mV, respectively). Also, the steepness of this curve was slightly reduced; its slope factor (k) amounted to 7.9 ± 0.3 vs. 6.7 ± 0.4 mV, respectively. Voltage dependence of steady-state inactivation, recovery from inactivation, and development of slow inactivation were not affected by the E161K mutation. Of note, these data were all obtained in H558 background, i.e., with histidine (H) at position 558 of the $Na_V1.5$ protein.

Iwasa et al. (2000) were the first to report on the c.1673A > G single nucleotide polymorphism ("SNP") in the *SCN5A* gene, which is responsible for the replacement of histidine (H) with arginine (R) at position 558 of the $Na_V1.5$ protein (p.His558Arg or H558R), in relation to familial LQTS. Ackerman et al. (2004) showed that H558R is the most common polymorphism in *SCN5A* and that this variant is present in all four ethnic groups, albeit at a significantly lower prevalence in Asians. In blacks, whites, and Hispanics, the prevalence of R558 instead of H558 amounts to 20–30%, whereas this prevalence is near 10% among Asians (Ackerman et al., 2004). Over the years, it has become clear that the H558R polymorphism can either mitigate or aggravate the effects of specific mutations in *SCN5A*. For example, this polymorphism has mitigating effects on the mutations M1766L (Ye et al., 2003) and P2006A (Shinlapawittayatorn et al., 2011), but aggravating effects on the mutations G400A (Hu et al., 2007) and A572D (Tester et al., 2010).

In 2010, Gui et al. (2010a,b) demonstrated that the H558R polymorphism also affects the E161K mutation. They carried out voltage clamp experiments on HEK-293 cells transfected with E161K mutant or wild-type sodium channel α-subunit. Like

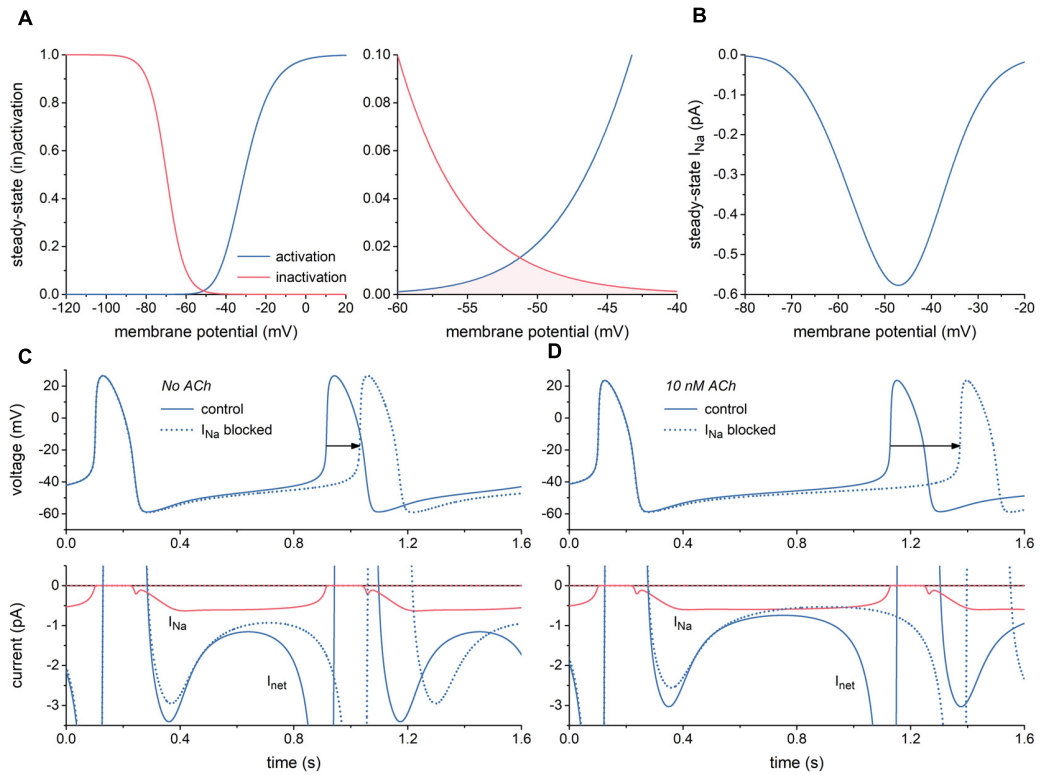

FIGURE 1 | Characteristics of the fast sodium current (I_{Na}) of the Fabbri-Severi model of a human SA nodal pacemaker cell. **(A)** Steady-state activation and inactivation curves (blue and red curves, respectively) of I_{Na} (left) and associated "window" of overlap (shaded area) in the voltage range between −60 and −40 mV (right). **(B)** Current–voltage relationship of steady-state I_{Na}. **(C)** Effect of full block of I_{Na} in the absence of acetylcholine (ACh). Spontaneous action potentials (top) and associated net membrane current (I_{net}) and I_{Na} (bottom). Horizontal arrow indicates increase in cycle length. **(D)** Effect of full block of I_{Na} during simulated administration of 10 nM ACh. Spontaneous action potentials (top) and associated I_{net} and I_{Na} (bottom). Horizontal arrow indicates increase in cycle length.

Smits et al. (2005), they observed a reduction in peak I_{Na} for E161K sodium channels compared to wild-type channels, both in H558 and R558 background. In either case, this reduction was approximately 4-fold, which is more pronounced than the 2.5-fold reduction in the study by Smits et al. (2005). With a value of ≈19 mV, the positive shift in $V_{1/2}$ of the steady-state activation curve in H558 background was also more pronounced. The steepness of this curve showed a reduction similar to that observed by Smits et al. (2005). In R558 background, the reduction in peak I_{Na} and steepness of the steady-state activation curve were both similar to those in H558 background (Gui et al., 2010b). However, the positive shift in $V_{1/2}$ of the steady-state activation curve was less pronounced, with a value of ≈13 mV rather than ≈19 mV. However, the potentially mitigating effects of this less pronounced shift in R558 background was counteracted by a −10 mV shift in $V_{1/2}$ of the steady-state inactivation curve, which was absent in H558 background.

To assess the mechanism by which the E161K mutation causes sinus node dysfunction as well as the potential role of the H558R polymorphism, we incorporated the mutation-induced changes in I_{Na} into the Fabbri-Severi model of a single human SA node cell (Fabbri et al., 2017). Furthermore, we incorporated these changes into the Maleckar et al. human atrial cell model (Maleckar et al., 2008, 2009) to assess the effects of the E161K mutation on atrial excitability, which may also play a role in sinus node dysfunction.

MATERIALS AND METHODS

Implementation of the E161K Mutation and H558R Polymorphism

Effects of the heterozygous E161K mutation in *SCN5A* were implemented in the CellML code (Cuellar et al., 2003) of the Fabbri-Severi human SA nodal cell model (Fabbri et al., 2017) by scaling the fully-activated conductance of I_{Na} (g_{Na}) and shifting the steady-state I_{Na} activation and/or inactivation curves, as detailed below, based on the experimental data from literature described in the Introduction and summarized in **Table 1**. The slight change in steepness of the steady-state activation curve was also included. These modifications were applied to half of the intrinsic I_{Na} channels, thus representing the heterozygous nature of the mutation, taking into account that a functional I_{Na} channel is built with a single $Na_V1.5$ protein.

Identical changes were applied to the Maleckar et al. (2009) human atrial cell model. The latter model, which is also known as the "human atrial myocyte with new repolarization"

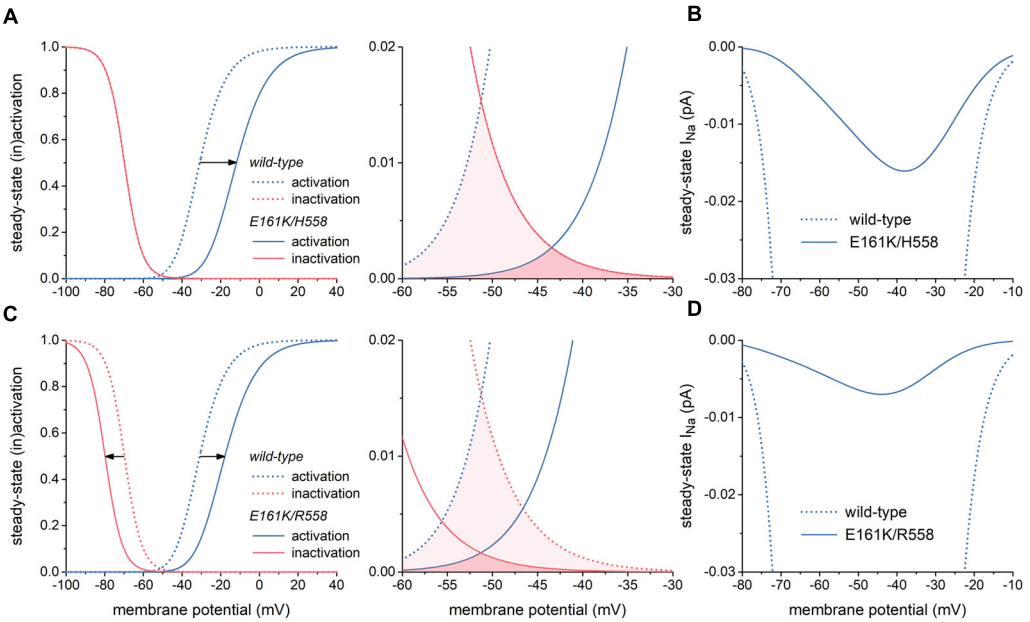

FIGURE 2 | Effects of the E161K mutation in *SCN5A*, either in H558 or R558 background, on biophysical properties of the fast sodium current (I_{Na}) of the Fabbri-Severi model of a human SA nodal pacemaker cell. **(A)** Shift and change in steepness of the steady-state activation curve (left) and effect on "window" (right) in H558 background. Horizontal arrow indicates the +19 mV shift. **(B)** Resulting effect on current–voltage relationship of steady-state I_{Na} in H558 background. **(C)** Shift and change in steepness of the steady-state activation curve and shift of steady-state inactivation curve (left) and effect on "window" (right) in R558 background. Horizontal arrows indicate the +13 and −10 mV shifts. **(D)** Resulting effect on current–voltage relationship of steady-state I_{Na} in R558 background.

(hAMr) model, was selected because it includes well-validated equations for the acetylcholine-activated potassium current $I_{K,ACh}$ (Maleckar et al., 2008), thus allowing simulations over a wide range of acetylcholine levels. Action potentials were elicited with a 1 ms, ≈50% suprathreshold stimulus current at a frequency of 1 Hz. The threshold stimulus current amplitude was determined by increasing the stimulus current amplitude in 0.1 pA/pF steps until a train of 200 action potentials

TABLE 1 | Experimental data on biophysical effects of the E161K mutation in *SCN5A*.

					Steady-state activation			Steady-state inactivation		
Study	**Expression system**	**Background**	**Channel type**	**Peak current density (nA/pF)**	**$V_{1/2}$ (mV)**	**k (mV)**	***n***	**$V_{1/2}$ (mV)**	**k (mV)**	***n***
Experimental Data										
Smits et al., 2005	tsA201 cells	H558	Wild-type	0.71 ± 0.11	−42.6 ± 1.4	6.7 ± 0.4	9	−89.4 ± 1.2	−4.9 ± 0.3	9
			E161K	0.28 ± 0.05*	−30.7 ± 0.8*	7.9 ± 0.3*	13	−88.5 ± 0.9	−4.4 ± 0.1	13
Gui et al., 2010a	HEK-293 cells	H558	Wild-type	0.87 ± 0.08	−34.7 ± 0.7	6.9 ± 0.2	23	−81.4 ± 0.7	−6.4 ± 0.1	24
			E161K	0.20 ± 0.03*	−14.9 ± 0.7*	9.0 ± 0.1*	19	−79.9 ± 0.9	−6.6 ± 0.1	21
Gui et al., 2010b	HEK-293 cells	H558	Wild-type	0.81 ± 0.08	−33.8 ± 0.7	6.7 ± 0.2	11	−80.3 ± 0.9	−6.2 ± 0.1	12
			E161K	0.19 ± 0.03*	−14.7 ± 0.6*	8.9 ± 0.1*	11	−78.4 ± 0.8	−6.5 ± 0.2	12
		R558	Wild-type	0.92 ± 0.17	−35.5 ± 1.3	6.8 ± 0.2	9	−81.8 ± 1.0	−6.5 ± 0.1	10
			E161K	0.15 ± 0.02*	−20.9 ± 1.2*	8.0 ± 0.1*	14	−88.8 ± 1.8*	−6.7 ± 0.2	10
Model Parameters										
Fabbri et al., 2017					−30.5	6.5		−69.8	−4.5	
Maleckar et al., 2009					−15.7	6.4		−63.6	−5.3	

*All experimental data obtained at room temperature and expressed as mean ± SEM. *P < 0.05 vs. wild-type.*

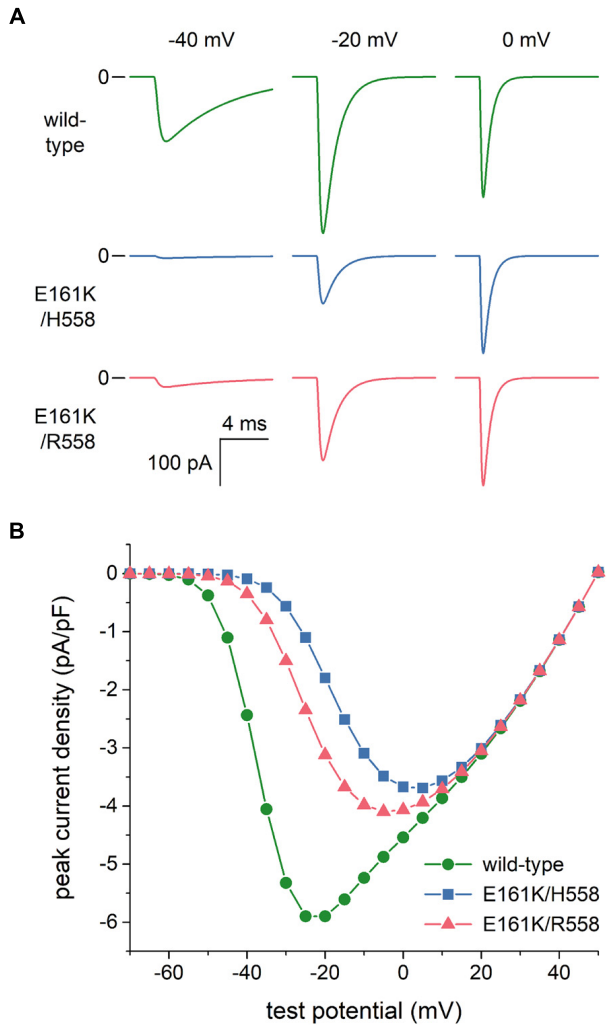

FIGURE 3 | Effects of the E161K mutation in *SCN5A*, either in H558 or R558 background, on the fast sodium current (I_{Na}) of the Fabbri-Severi model of a human SA nodal pacemaker cell during simulated voltage clamp experiments. **(A)** Control ("wild-type") and mutant I_{Na} during voltage clamp steps from a holding potential of −120 mV to test potentials of −40, −20, and 0 mV. **(B)** Current–voltage relationship of peak I_{Na}, as derived from these simulated voltage clamp experiments.

could successfully be elicited. To prevent slow drifts in ion concentrations, the intracellular Na^+ and K^+ concentrations were fixed, as were the cleft ion concentrations.

In H558 background, the E161K mutation was implemented by shifting the steady-state activation curve of the model I_{Na} by +19 mV. In R558 background, this curve was shifted by +13 mV, together with a −10 mV shift in the steady-state inactivation curve. In either background, a 50% decrease in g_{Na} was applied to arrive at an almost 4-fold decrease in peak current density of mutant I_{Na} during voltage clamp simulations. Furthermore, the slope factor of the steady-state activation curve of the model I_{Na} was increased by 20% to account for mutation-induced decrease in steepness of this curve.

Computer Simulations

The CellML code of both models, as available from the CellML Model Repository (Lloyd et al., 2008), was edited and run in version 0.9.31.1409 of the Windows based Cellular Open Resource (COR) environment (Garny et al., 2003b). All simulations were run for a sufficiently long time, i.e., for the duration of a train of 200 action potentials, to reach steady-state behavior. Data from the final ten action potentials were used for analysis.

RESULTS

Characteristics of the SA Nodal Fast Sodium Current

First, we characterized I_{Na} of the Fabbri-Severi model of a single human SA nodal pacemaker cell (Fabbri et al., 2017) and its effect on the spontaneous activity of this cell. **Figure 1A** shows the steady-state activation and inactivation curves of I_{Na} (left) and the associated "window" (area of overlap; right). The window is in the voltage range of diastolic depolarization, between −60 and −40 mV. Because of the relatively slow changes in membrane potential of the SA nodal cell and the relatively fast kinetics of I_{Na}, this window is the major determinant of the course of I_{Na} during the action potential, of course in combination with the fully-activated conductance of I_{Na} (g_{Na}), which amounts to 22.3 nS in the Fabbri-Severi model. The associated steady-state current-voltage relationship of I_{Na} is shown in **Figure 1B**.

With a value near 0.6 pA, the amplitude of I_{Na} during diastolic depolarization is small. However, this amplitude is relatively large in comparison to that of the net membrane current (I_{net}) (**Figure 1C**, solid lines). It is therefore not surprising that full block of I_{Na} results in a 117-ms increase in cycle length from 813 to 930 ms (**Figure 1C**, dotted lines), corresponding with a 13% decrease in beating rate from 74 to 64 beats/min. In the simulated presence of 10 nM acetylcholine (ACh), the amplitude of I_{net} during diastolic depolarization becomes considerably smaller, whereas that of I_{Na} does barely change. Accordingly, full block of I_{Na} now results in a more prominent increase in cycle length, by 245 ms from 1027 to 1272 ms (**Figure 1D**), corresponding with a 19% decrease in beating rate from 58 to 47 beats/min. Of note, I_{Na} hardly affects the cycle length through a change in action potential duration.

Now that the simulations of **Figure 1** had shown that changes in I_{Na} may modify the cycle length of the Fabbri-Severi model cell to a considerable extent, we first assessed the changes in peak and window I_{Na} caused by the E161K mutation in *SCN5A*, either in H558 or R558 background. Next, we tested the effects of these changes on the spontaneous pacemaker activity of the SA nodal model cell.

Effects of the E161K Mutation in SCN5A on Biophysical Properties of I_{Na}

The left panel of **Figure 2A** illustrates the changes in the steady-state I_{Na} activation and inactivation curves due to the E161K mutation in H558 background. These changes

are limited to a +19 mV shift in the steady-state I_{Na} activation curve and a slight decrease in steepness of this curve, which is poorly discernible in **Figure 2A**. As a result, the window of overlap is significantly reduced and shifted to less negative values of membrane potential, now roughly ranging from −50 to −30 mV (**Figure 2A**, right) and thus limiting the contribution of I_{Na} to diastolic depolarization. This is reflected in the current–voltage relationship of steady-state I_{Na} (**Figure 2B**, solid line), which is strongly reduced in comparison with wild-type I_{Na}.

In R558 background, the shift in the steady-state I_{Na} activation curve is less pronounced (+13 vs. +19 mV), but accompanied by a −10 mV shift in the steady-state inactivation curve (**Figure 2C**, left). As a result, the window of overlap is smaller than in H558 background (**Figure 2C**, right). However, it better fits with the voltage range of diastolic depolarization. Yet, the steady-state I_{Na} in this voltage range is even more reduced in comparison with wild-type I_{Na} than in H558 background (**Figure 2D**, solid line).

Effects of the E161K Mutation in SCN5A on I_{Na} in Voltage Clamp Experiments

As set out in the Introduction, voltage clamp experiments on *SCN5A* channels expressed in tsA201 and HEK-293 cells (Smits et al., 2005; Gui et al., 2010a,b) had revealed that the E161K mutation induces a 2.5- to 4-fold decrease in I_{Na} peak current density, both in H558 and R558 background. To assess the extent to which this reduction is due to the changes in the I_{Na} steady-state activation and inactivation curves *per se*, we reconstructed current traces in response to voltage clamp steps from a holding potential of −120 mV to test potentials ranging from −100 to +50 mV. **Figure 3A** shows examples of wild-type and mutant current traces at test potentials of −40, −20, and 0 mV. These already demonstrate that the peak current density of the wild-type channels is higher than that of mutant channels, despite the identical value of g_{Na} used in the voltage clamp simulations. **Figure 3B** summarizes the simulation data. The changes in the steady-state activation and inactivation curves *per se* reduce the peak current density by ≈35%. To arrive at an almost 4-fold decrease in I_{Na} peak current density, in line with the experimental observations, we reduced the mutant g_{Na} by a factor of 2 in our further simulations. Thus we split the original g_{Na} of 22.3 nS of the Fabbri-Severi model cell into 11.15 nS for the wild-type I_{Na} channels and 5.575 nS for the E161K mutant I_{Na} channels, in either background.

Effects of the E161K Mutation on SA Nodal Pacemaker Activity

We applied the mutation-induced changes in I_{Na}, i.e., the shifts in steady-state activation and inactivation curves, the reduction in steepness of the steady-state activation curve, and the reduction in fully-activated conductance, to half of the I_{Na} channels in the Fabbri-Severi model to assess the effects of the heterozygous E161K mutation on the spontaneous pacemaker activity of a human SA nodal cell. **Figures 4A–G**, shows the effects on the action potential (**Figure 4A**), intracellular calcium concentration (**Figure 4B**) and underlying membrane currents (**Figures 4C–G**) under control conditions (no ACh), whereas the corresponding simulation data in the presence of 10 nM ACh are shown in **Figures 4H–N**. The simulated administration of ACh to the Fabbri-Severi model cell does not only activate the acetylcholine-activated potassium current $I_{K,ACh}$, which is zero under control conditions, but also reduces the hyperpolarization-activated "funny current" I_f (through a −4.95 mV shift in its voltage dependence of activation), the L-type calcium current I_{CaL} (through a 3.1% decrease in its maximal conductance), and the rate of Ca^{2+} uptake into the sarcoplasmic reticulum (SR) by the SERCA pump (through a 7.0% decrease in its maximum activity). Of note, the changes in I_{CaL} and Ca^{2+} uptake rate have only marginal effects at this level of ACh (Fabbri et al., 2017).

The main effect of the application of ACh is a prolongation of the basic cycle length from 813 to 1027 ms (**Figures 4A,H**, wild-type traces), which is associated with a decrease in the intracellular calcium concentration $[Ca^{2+}]_i$ (**Figures 4B,I**, wild-type traces), and sodium-calcium exchange current I_{NCX} during diastolic depolarization (**Figures 4E,L**, wild-type traces). I_f is also reduced (**Figures 4F,M**), as a result of the direct effect of ACh on its voltage dependence of activation. The remaining inward currents, i.e., the L-type calcium current I_{CaL} (**Figures 4D,K**), T-type calcium current I_{CaT} (**Figures 4E,L**) and I_{Na} (**Figures 4G,N**), are not largely affected. The total repolarizing current I_{repol} is also hardly affected, with an almost constant value of ≈9 pA during diastolic depolarization (**Figures 4D,K**). This is because it includes the ACh-activated $I_{K,ACh}$, which is also shown separately (**Figures 4F,M**), in addition to the rapid delayed rectifier potassium current I_{Kr}, the slow delayed rectifier potassium current I_{Ks}, the ultrarapid delayed rectifier potassium current I_{Kur}, the transient outward potassium current I_{to}, and the sodium-potassium pump current I_{NaK}, which are not shown separately in **Figure 4**. The reduction in the "pacemaker currents" I_f and I_{NCX} (Lakatta and DiFrancesco, 2009), in combination with the minor changes in other inward currents as well as I_{repol}, result in the reduction in the net membrane current I_{net} (**Figures 4C,J**) that underlies the observed increase in cycle length.

In absence of ACh, the mutation-induced reduction in I_{Na} (**Figure 4G**) causes a reduction in I_{net}, which becomes most prominent during the second half of diastolic depolarization (**Figure 4C**) and in turn results in a prolongation of the cycle length by 53 and 54 ms in H558 and R558 background, respectively (**Figure 4A**, horizontal arrow), from the basic cycle length of 813 ms, corresponding with a 6% decrease in beating rate from 74 to 69 beats/min in either background. Simulations with the wild-type model in which g_{Na} is reduced by 50% (labeled "50% g_{Na}"), thus simply blocking 50% of the channels, result in a cycle length prolongation of 55 ms and traces that are barely distinguishable from the mutant ones, thus demonstrating that the contribution

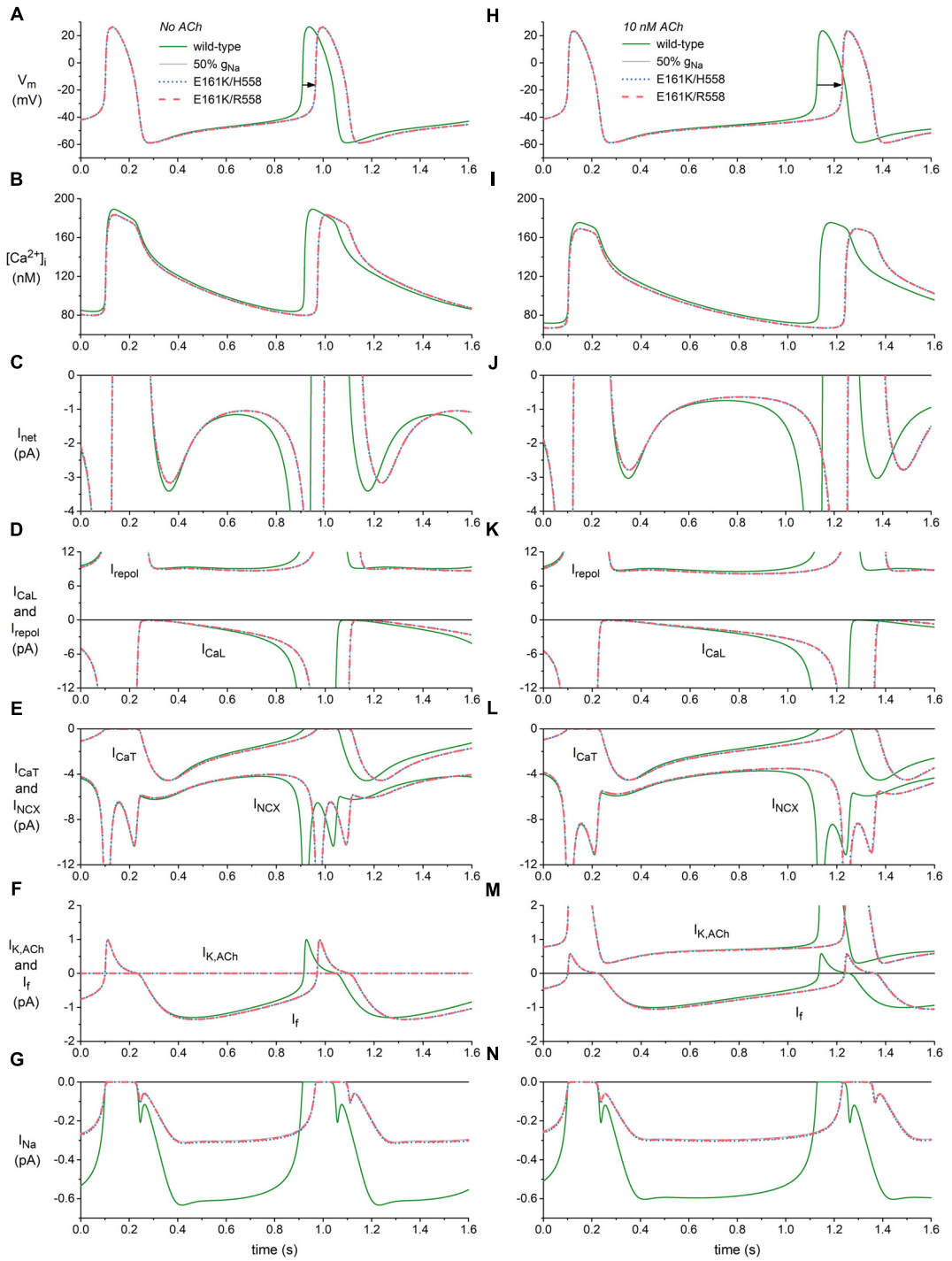

FIGURE 4 | Effects of the E161K mutation in *SCN5A*, either in H558 or R558 background, on the spontaneous activity of the Fabbri-Severi model of a human SA nodal pacemaker cell. **(A)** Membrane potential (V_m), and associated **(B)** intracellular calcium concentration ($[Ca^{2+}]_i$), **(C)** net membrane current (I_{net}), **(D)** L-type calcium current (I_{CaL}) and total repolarizing current (I_{repol}), **(E)** T-type calcium current (I_{CaT}) and sodium-calcium exchange current (I_{NCX}), **(F)** ACh-activated potassium current ($I_{K,ACh}$) and hyperpolarization-activated "funny current" (I_f), and **(G)** fast sodium current (I_{Na}) in the absence of ACh. **(H)** V_m, **(I)** $[Ca^{2+}]_i$, **(J)** I_{net}, **(K)** I_{CaL} and I_{repol}, **(L)** I_{CaT} and I_{NCX}, **(M)** $I_{K,ACh}$, and I_f, and **(N)** I_{Na} during simulated administration of 10 nM ACh. Solid gray lines show the effect of a 50% reduction in fully-activated conductance of I_{Na} (g_{Na}). Horizontal arrows indicate increase in cycle length. I_{repol} consists of $I_{K,ACh}$, the rapid delayed rectifier potassium current I_{Kr}, the slow delayed rectifier potassium current I_{Ks}, the ultrarapid delayed rectifier potassium current I_{Kur}, the transient outward potassium current I_{to}, and the sodium-potassium pump current I_{NaK}.

of the mutant component of I_{Na} to total I_{Na} is almost zero.

In the simulated presence of 10 nM ACh, the effects of the mutation are more pronounced, as reflected by the prolongation of the cycle length by 104 ms in H558 background and 105 ms in R558 background (**Figure 4H**, horizontal arrow), from the basic cycle length of 1027 ms, corresponding with a 9% decrease in beating rate from 58 to 53 beats/min in either background. Again, the contribution of the mutant component of I_{Na} to total I_{Na} is almost zero, as demonstrated by the highly similar prolongation of cycle length, by 107 ms, in case of 50% g_{Na}. The more pronounced effect of the highly similar reduction in I_{Na} in the simulated presence of 10 nM ACh (**Figures 4G,N**) can be explained by its occurrence in the setting of a smaller I_{net} during diastolic depolarization (**Figures 4C,J**).

As illustrated in **Figure 5A**, the mutation-induced increase in cycle length increases with increasing levels of ACh. At 25 nM, this increase amounts to 347 and 355 ms in H558 and R558 background, respectively, from a basic cycle length of 1448 ms, slightly less than the increase of 361 ms in case of 50% g_{Na}. In terms of beating rate (**Figure 5B**), an ACh level of 25 nM results in a rate of 41 beats/min in case of wild-type sodium channels and 33 beats/min in case of the heterozygous E161K mutation, in either background. The percent decrease in beating rate relative to wild type is shown in **Figure 5C**. In absence of ACh (**Figure 5C**, leftmost bars), the E161K mutation results in a 6.1% decrease in beating rate in H558 background and 6.2% decrease in R558 background. This percentage increases with increasing levels of ACh. In the simulated presence of 10 nM ACh, the decrease in beating rate amounts to 9.2 and 9.3%, respectively. At an ACh level of 25 nM (**Figure 5C**, rightmost bars), the mutation-induced decrease in beating rate is almost 20%, with values of 19.3% in H558 background and 19.7% in R558 background.

Effects of the E161K Mutation on Atrial Excitability

Sinus node dysfunction may also be related to changes in atrial excitability, potentially leading to sinus node exit block or atrial conduction block. Therefore, we assessed the effects of the E161K mutation on atrial excitability using the Maleckar et al. human atrial cell model (Maleckar et al., 2009), which we used in combination with its well-validated equations for $I_{K,ACh}$ (Maleckar et al., 2008). Changes in I_{Na}, simulating a heterozygous mutation in *SCN5A*, were implemented as in the Fabbri-Severi model. Of note, the effect of ACh on the Maleckar et al. model cell is limited to the activation of $I_{K,ACh}$.

Figure 6A shows atrial action potentials elicited at 1 Hz with a stimulus current of 1 ms duration under control conditions (no ACh). Both variants of the E161K mutation result in a reduction in the action potential overshoot and a less rapid activation, indicative of a decrease in capacitive current of the atrial cell (**Figure 6A**, inset). The associated I_{Na}, which is shown in **Figure 6B**, is approximately halved or – because the slower activation allows a larger fraction of the channels to inactivate during the activation process – even more than halved. In the simulated presence of 10 nM ACh, the resting membrane potential becomes more negative with a value of −79 mV vs. −74 mV (**Figure 6C**), which results in a larger I_{Na} because less sodium channels are inactivated at this more negative resting potential (**Figure 6D**). This does, however, not imply that action potential generation is facilitated in presence of ACh since the distance to action potential threshold is increased and an additional outward current, i.e., $I_{K,ACh}$, is activated. Again, activation is slowed and the underlying I_{Na} is approximately halved (**Figures 6C,D**, insets).

Atrial excitability was characterized, over a wide range of concentrations of ACh, by determining the threshold stimulus current of the atrial cell as well as its maximum upstroke velocity, as a direct measure of the capacitive current. Threshold stimulus current was determined with 1 ms stimuli of increasing amplitude that were applied at a frequency of 1 Hz. Results are shown in **Figure 7A**. The threshold increases with increasing levels of ACh and is 5–8% higher in case of the E161K mutation. Although barely visible in **Figure 7A**, the threshold in R558 background, with the smaller shift of the steady-state activation curve, is smaller than in H558 background.

Maximum upstroke velocity was determined by eliciting action potentials with a 1 ms, ≈50% suprathreshold stimulus current at a frequency of 1 Hz. As shown in **Figure 7B**, it is not strongly dependent on the level of ACh. Upstroke velocity is approximately halved, or even more than halved, in case of the E161K mutation. As for the threshold stimulus current, the mutation in R558 background is associated with (slightly) less strong effects than in H558 background. In contrast with the SA nodal cell, the mutant component of I_{Na} is not effectively zero, as revealed by the larger I_{Na} (**Figures 6B,D**, insets) and larger maximum upstroke velocity (**Figure 7B**) in comparison with the 50% g_{Na} simulations.

DISCUSSION

General Discussion

Our simulations demonstrate that the E161K mutation in *SCN5A* hampers both impulse generation and impulse propagation through its effects on the electrophysiological properties of human SA nodal and atrial cells. Generation of the SA nodal action potential is hampered by the strong decrease in I_{Na} during diastolic depolarization and the associated decrease in I_{net}, in particular in presence of ACh (**Figures 4**, **5**). Impulse propagation, as comprehensively reviewed by Kléber and Rudy (2004), is hampered by the current-to-load mismatch that results from, on the one hand, the increase in threshold stimulus current and, on the other hand, the decrease in capacitive current of the atrial cell (**Figures 6**, **7**). The highly common H558R polymorphism in *SCN5A* does not have a major effect on the outcome of the simulations, despite its effects on the biophysical properties of the E161K mutant channels (**Figures 2**, **3**).

The E161K mutation has been subject of simulations since its discovery in 2005 (Smits et al., 2005). Smits et al. (2005)

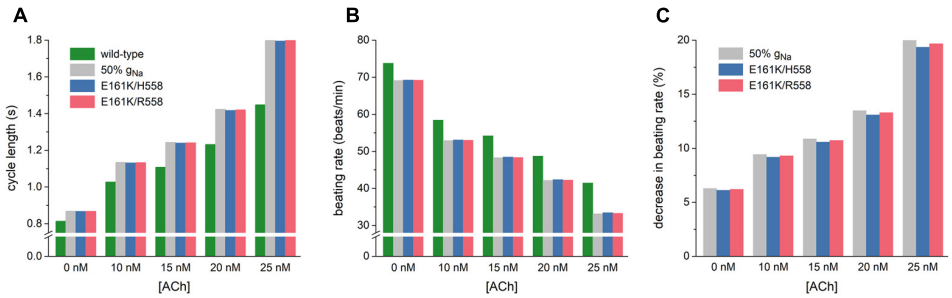

FIGURE 5 | Bradycardic effects of the E161K mutation in *SCN5A*, either in H558 or R558 background, on the Fabbri-Severi model of a human SA nodal pacemaker cell at different levels of ACh (0–25 nM). **(A)** Cycle length. **(B)** Associated beating rate. **(C)** Percent decrease in beating rate relative to wild-type. Solid gray bars show the effect of a 50% reduction in fully-activated conductance of I_{Na} (g_{Na}). Note the breaks in the vertical axes of **(A,B)**.

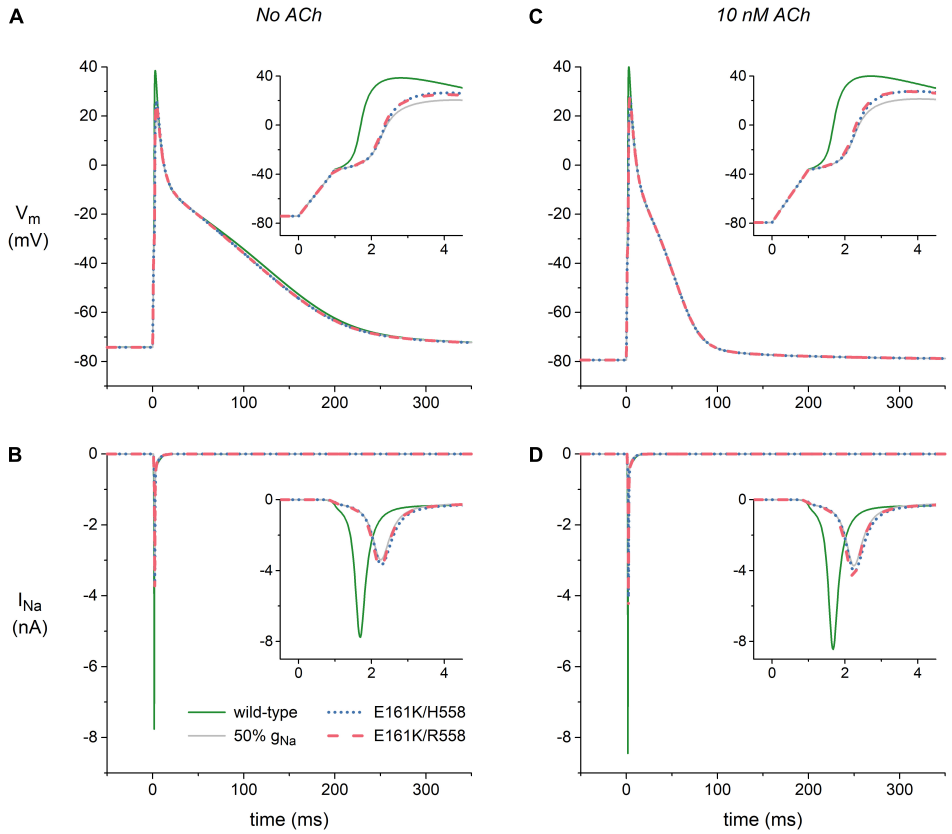

FIGURE 6 | Effects of the E161K mutation in *SCN5A*, either in H558 or R558 background, on the action potential and fast sodium current (I_{Na}) of the Maleckar et al. model of a human atrial myocyte. **(A)** Action potentials elicited at 1 Hz and **(B)** associated fast sodium current (I_{Na}) in the absence of ACh. **(C)** Action potentials elicited at 1 Hz and **(D)** associated I_{Na} during simulated administration of 10 nM ACh. Insets show membrane potential (V_m) and I_{Na} on an expanded time scale. Solid gray lines show the effect of a 50% reduction in fully-activated conductance of I_{Na} (g_{Na}).

showed that the E161K mutation impairs conduction in linear strands of atrial and ventricular cells, using the human atrial and ventricular cell models by Courtemanche et al. (1998) and Priebe and Beuckelmann (1998), respectively. Simulations were based on the observations by Smits et al. (2005) on E161K channels expressed in tsA201 cells. Mutation effects were relatively mild in comparison to later observations by Gui et al. (2010a,b) and obtained in H558 background. Smits et al. (2005) also carried out simulations on SA nodal cells, using the model of a peripheral rabbit SA nodal cell by Zhang et al. (2000), including equations for $I_{K,ACh}$ (Zhang et al., 2002). Despite the largely different time course of the human SA nodal action potential, with a much smaller I_{Na}, a much longer diastolic phase, and a significantly less negative maximum diastolic potential, the main findings of the present study are similar to those of Smits et al. (2005) regarding the SA

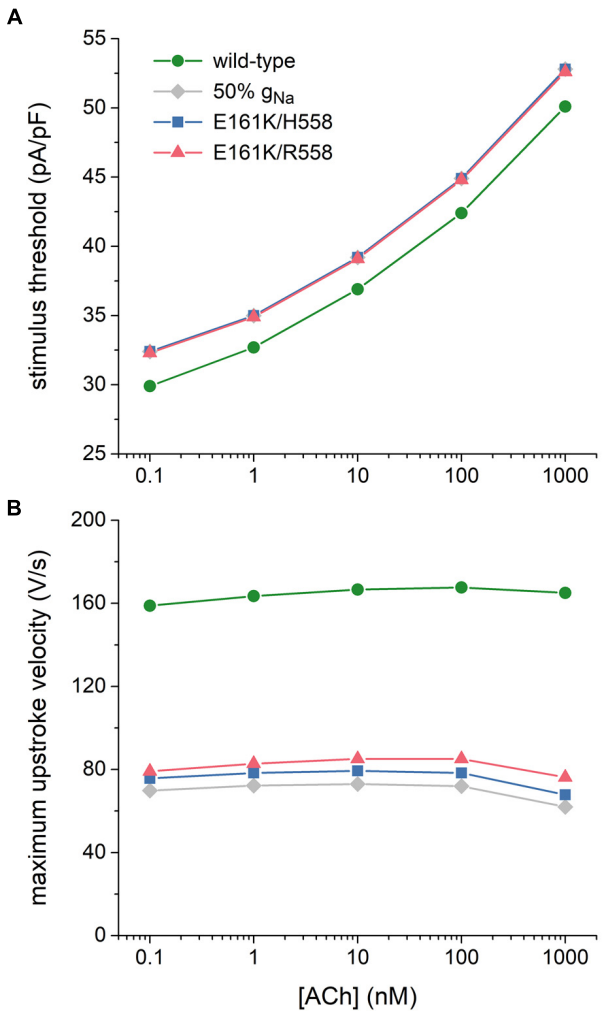

FIGURE 7 | Effects of the E161K mutation in *SCN5A*, either in H558 or R558 background, on the excitability of the Maleckar et al. model of a human atrial myocyte. **(A)** Threshold stimulus current amplitude for a stimulus of 1 ms duration and **(B)** maximum upstroke velocity at ACh concentrations ranging from 0.1 nM to 1 μM. Gray diamonds show the effect of a 50% reduction in fully-activated conductance of I_{Na} (g_{Na}). Note the logarithmic abscissa scale.

nodal action potential: the E161K mutation causes a decrease in diastolic depolarization rate that results in an increase in cycle length, which is much more pronounced in presence of ACh.

Butters et al. (2010) studied the effects of several mutations in *SCN5A*, including E161K, on cardiac pacemaking in a two-dimensional model of sino-atrial tissue based on a reconstruction of a single slice of the rabbit right atrium, using modified versions of the single cell models of rabbit SA nodal and atrial cells by Zhang et al. (2000, 2002) and Lindblad et al. (1996), respectively. Their simulations of the E161K mutation were again based on the observations by Smits et al. (2005). The mutation slowed down pacemaking and this effect was more pronounced in the presence of ACh. Furthermore, a conduction block in the direction toward the atrial septum occurred in the absence of ACh, while conduction in the direction toward the crista terminalis was sustained. With 15 nM ACh, exit block occurred in both directions and the SA node was unable to drive the surrounding atrium.

In the present study, we carried out simulations with the use of comprehensive well-validated human single cell models and implemented effects of the E161K mutation based on the experimental data by Gui et al. (2010a,b). Furthermore, we assessed the role of the highly common H558R polymorphism, also based on the experimental data by Gui et al. (2010a,b). We focused on cellular mechanisms and refrained from using two- or even three-dimensional models of sino-atrial interaction, with their coupling interactions between heterogeneous cells, because results of such simulations are critically dependent on the exact geometry and cell distribution (Garny et al., 2003a), which have not been fully elucidated.

Our simulations show that the effects of the E161K mutation are so large, both in H558 and R558 background, that the contribution of mutant I_{Na} to total I_{Na} of the SA nodal cell is effectively zero. Accordingly, it is not surprising that E161K mutation carriers show sinus node dysfunction as do carriers of several mutations in *SCN5A* that are associated with a complete or almost complete loss of function of the mutant channels, as reviewed by Lei et al. (2007, 2008) and Remme et al. (2008). In many cases, the sinus node dysfunction shows a reduced penetrance, as for the E161K mutation, where 8 out of 14 mutation carriers show the disease. Reduced penetrance is a common finding in primary electrical diseases, including those associated with mutations in *SCN5A* (Remme, 2013; Robyns et al., 2014). Several factors, including co-inherited genetic variants and alternative splicing sites, may play a role. However, our simulations suggest that it is highly unlikely that the common H558R polymorphism can explain the reduced penetrance of the E161K mutation.

Limitations

Unfortunately, experimental data on the effects of the E161K mutation are limited to voltage clamp data from mutant *SCN5A* channels in mammalian expression systems, viz. tsA201 and HEK-293 cells, obtained at room temperature and in the presence (Smits et al., 2005) or absence (Gui et al., 2010a,b) of a wild-type β-subunit. There are some quantitative differences in the experimental data, potentially due to differences in cell type or presence of β-subunit, with a more severe pattern in the data of Gui et al. (2010a,b), with a +19 mV shift of the steady-state activation curve in H558 background vs. the +11.9 mV shift reported by Smits et al. (2005) and a 4-fold vs. 2.5-fold reduction in peak current density. However, the latter difference may partly be explained by the larger shift in the steady-state activation curve. In our simulations, we have assumed that the experimentally observed effects of the mutation in mammalian expression systems at room temperature also hold for cardiac cells at the physiological temperature of 37°C. We cannot rule out that recordings at a more close-to-physiological

temperature would have revealed additional effects of the E161K mutation, as has been the case for several other BrS-related mutations in *SCN5A* expressed in mammalian cell lines, like T1620M and Y1795H (Dumaine et al., 1999; Rivolta et al., 2001). Furthermore, we have to keep in mind that the cardiac sodium channel is part of a macromolecular complex that does not only comprise the α- and β-subunits, but also several other proteins that may regulate channel activity, such as ankyrin, caveolin and syntrophin, and may act differently in case of mutant channels (Ruan et al., 2009). Thus, it is uncertain to which extent the experimental data on the effects of the E161K mutation acquired in mammalian expression systems represent the mutant-induced changes that occur in human cardiac cells.

In our simulations, it is assumed that the Fabbri-Severi model of a human SA nodal cell (Fabbri et al., 2017) and the Maleckar et al. model of a human atrial cell (Maleckar et al., 2009) are fully representative of the biophysical properties of the corresponding real cells. However, experimental data on the biophysical properties of cardiac cells, and human cells in particular, are often incomplete or obtained under non-physiological conditions. Functional data on I_{Na} in human SA nodal cells, for example, are limited to accidental observations by Verkerk et al. (2009) when performing voltage clamp experiments on single human SA nodal pacemaker cells to record I_f. Accordingly, I_{Na} was included in the Fabbri-Severi model, but simply adopted from its parent model, i.e., the model of a rabbit SA nodal cell by Severi et al. (2012), who, in turn, used the equations of the SA nodal cell model by Noble et al. (1989). The latter equations were adopted from the model of SA nodal cell electrical activity by Noble and Noble (1984), who based their equations on the model of cardiac electrical activity by DiFrancesco and Noble (1985). The description of I_{Na} in the latter model is essentially that of Hodgkin and Huxley (1952), but with modifications based on data from experiments on rabbit cardiac Purkinje fibers at 10–26°C (Colatsky, 1980) and from isolated rat ventricular myocytes at 20–22°C (Brown et al., 1981). Activation and inactivation curves were shifted along the voltage axis to account for their observed temperature dependence, whereas rate constants were scaled to arrive at time constant values near the experimentally observed ones. The I_{Na} equations in the Maleckar et al. (2009) model are adopted from the model of an adult human atrial cell by Nygren et al. (1998), who used the voltage clamp data of Sakakibara et al. (1992) on I_{Na} in isolated human atrial myocytes at 17 ± 1°C to construct their model equations. Activation and inactivation curves were shifted in the positive direction along the voltage axis to reach a realistic activation threshold and stable resting potential. The time constants of activation and inactivation are very similar to those of the rabbit atrial cell model of Lindblad et al. (1996), who based their mathematical description of I_{Na} on the voltage clamp data of Wendt et al. (1992), acquired from cultured rabbit atrial myocytes at 17°C, and I_{Na} of the DiFrancesco-Noble model (DiFrancesco and Noble, 1985). Activation kinetics of I_{Na} were modified from those of the DiFrancesco-Noble model with the use of a Q_{10} of 1.7.

In our simulations, it is also assumed that mutation effects are limited to half of the intrinsic I_{Na} channels, thus representing the heterozygous nature of the mutation, taking into account that a functional I_{Na} channel is built with a single $Na_V1.5$ protein. This assumption is challenged by recent experimental findings of Clatot et al. (2018), who demonstrated that wild-type and mutant $Na_V1.5$ proteins can form dimers, enabling coupled gating of wild-type and mutant $Na_V1.5$ sodium channels that can be responsible for a dominant negative effect of the mutation. Thus, the cellular effects of the E161K mutation could be more severe than anticipated.

The action of ACh in the Fabbri-Severi model is, apart from the activation of $I_{K,ACh}$, limited to suppression of I_f, I_{CaL}, and Ca^{2+} uptake into the SR, thus simplifying the intracellular SR-based calcium clock signaling cascade through adenylyl cyclase, cyclic AMP and protein kinase A (Maltsev et al., 2014; Behar et al., 2016). This cascade is important for a detailed understanding of the action of ACh. Yet, in the present study, where the focus is on the effects of the E161K mutation in *SCN5A* and possible effects of the H558R polymorphism, it is sufficient that the suppression by ACh of I_f, I_{CaL}, and Ca^{2+} uptake into the SR, and that of I_{NCX} through the reduced intracellular calcium level, are included, in addition to the activation of $I_{K,ACh}$.

One should be careful in the interpretation of experimental data, not only because of the above considerations, but also because changes in biophysical parameters are not necessarily independent. This is nicely demonstrated by the decrease in peak current density shown in **Figure 3**. Such decrease is often interpreted as a reduction in the number of channels or a reduction in their single conductance. In this case, however, the E161K mutant-induced changes in steady-state activation and inactivation curves *per se* reduce the peak current density by ≈35%. This effect may, at least partly, explain the apparent discrepancy between the ≈30% decrease in cell surface expression of E161K/H558 channels in HEK-293 cells and the > 70% decrease in peak current density reported by Gui et al. (2010a). Similarly, an apparently slower inactivation of E161K/H558 channels at membrane potentials ranging from -40 to 0 mV can, at least partly, be explained by the +19 mV shift in their steady-state activation curve (Gui et al., 2010a). Because experimentally observed changes in time constants of (fast) inactivation or recovery from inactivation, if any, are already small, no attempts were made to include these changes in the simulations of the present study.

CONCLUSION

We conclude that the experimentally identified mutation-induced changes in I_{Na} can explain the clinically observed sinus bradycardia and potentially the occasional exit block. Furthermore, we conclude that the common H558R polymorphism does not significantly alter the effects of the E161K mutation and can thus not explain the reduced penetrance of the E161K mutation.

DATA AVAILABILITY STATEMENT

The raw data supporting the conclusions of this manuscript will be made available by the author, without undue reservation, to any qualified researcher.

AUTHOR CONTRIBUTIONS

RW designed the experiments, acquired, analyzed and interpreted the data, and drafted, edited, and approved the manuscript.

FUNDING

This study was supported by the Amsterdam University Medical Centers, location Academic Medical Center.

ACKNOWLEDGMENTS

I thank the staff of the Departments of Medical Biology and Experimental Cardiology for their valuable contributions.

REFERENCES

Ackerman, M. J., Splawski, I., Makielski, J. C., Tester, D. J., Will, M. L., Timothy, K. W., et al. (2004). Spectrum and prevalence of cardiac sodium channel variants among black, white, Asian, and Hispanic individuals: implications for arrhythmogenic susceptibility and Brugada/long QT syndrome genetic testing. *Heart Rhythm* 1, 600–607. doi: 10.1016/j.hrthm.2004.07.013

Behar, J., Ganesan, A., Zhang, J., and Yaniv, Y. (2016). The autonomic nervous system regulates the heart rate through cAMP-PKA dependent and independent coupled-clock pacemaker cell mechanisms. *Front. Physiol.* 7:419. doi: 10.3389/fphys.2016.00419

Brown, A. M., Lee, K. S., and Powell, T. (1981). Sodium current in single rat heart muscle cells. *J. Physiol.* 318, 479–500. doi: 10.1113/jphysiol.1981.sp013879

Brugada, J., Campuzano, O., Arbelo, E., Sarquella-Brugada, G., and Brugada, R. (2018). Present status of Brugada syndrome: JACC State-of-the-art review. *J. Am. Coll. Cardiol.* 72, 1046–1059. doi: 10.1016/j.jacc.2018.06.037

Butters, T. D., Aslanidi, O. V., Inada, S., Boyett, M. R., Hancox, J. C., Lei, M., et al. (2010). Mechanistic links between Na^+ channel (SCN5A) mutations and impaired cardiac pacemaking in sick sinus syndrome. *Circ. Res.* 107, 126–137. doi: 10.1161/CIRCRESAHA.110.219949

Chandler, N. J., Greener, I. D., Tellez, J. O., Inada, S., Musa, H., Molenaar, P., et al. (2009). Molecular architecture of the human sinus node: insights into the function of the cardiac pacemaker. *Circulation* 119, 1562–1575. doi: 10.1161/CIRCULATIONAHA.108.804369

Clatot, J., Zheng, Y., Girardeau, A., Liu, H., Laurita, K. R., Marionneau, C., et al. (2018). Mutant voltage-gated Na^+ channels can exert a dominant negative effect through coupled gating. *Am. J. Physiol. Heart Circ. Physiol.* 315, H1250–H1257. doi: 10.1152/ajpheart.00721.2017

Colatsky, T. J. (1980). Voltage clamp measurements of sodium channel properties in rabbit cardiac Purkinje fibres. *J. Physiol.* 305, 215–234. doi: 10.1113/jphysiol.1980.sp013359

Courtemanche, M., Ramirez, R. J., and Nattel, S. (1998). Ionic mechanisms underlying human atrial action potential properties: insights from a mathematical model. *Am. J. Physiol.* 275, H301–H321. doi: 10.1152/ajpheart.1998.275.1.H301

Cuellar, A. A., Lloyd, C. M., Nielsen, P. F., Bullivant, D. P., Nickerson, D. P., and Hunter, P. J. (2003). An overview of CellML 1.1, a biological model description language. *Simulation* 79, 740–747. doi: 10.1177/0037549703040939

DiFrancesco, D., and Noble, D. (1985). A model of cardiac electrical activity incorporating ionic pumps and concentration changes. *Philos. Trans. R. Soc. Lond. B Biol. Sci.* 307, 353–398. doi: 10.1098/rstb.1985.0001

Dumaine, R., Towbin, J. A., Brugada, P., Vatta, M., Nesterenko, D. V., Nesterenko, V. V., et al. (1999). Ionic mechanisms responsible for the electrocardiographic phenotype of the Brugada syndrome are temperature dependent. *Circ. Res.* 85, 803–809. doi: 10.1161/01.RES.85.9.803

Fabbri, A., Fantini, M., Wilders, R., and Severi, S. (2017). Computational analysis of the human sinus node action potential: model development and effects of mutations. *J. Physiol.* 595, 2365–2396. doi: 10.1113/JP273259

Garny, A., Hunter, P. J., Noble, D., Boyett, M. R., and Kohl, P. (2003a). "Rabbit sino-atrial node modeling: from single cell to tissue structure," in *Proceedings of the 25th Annual International Conference of the IEEE Engineering in Medicine and Biology Society*, Piscataway, NJ: IEEE, 28–31. doi: 10.1109/IEMBS.2003.1279489

Garny, A., Kohl, P., and Noble, D. (2003b). Cellular Open Resource (COR): a public CellML based environment for modelling biological function. *Int. J. Bifurcat. Chaos* 13, 3579–3590. doi: 10.1142/S021812740300882X

Giudicessi, J. R., Wilde, A. A. M., and Ackerman, M. J. (2018). The genetic architecture of long QT syndrome: a critical reappraisal. *Trends Cardiovasc. Med.* 28, 453–464. doi: 10.1016/j.tcm.2018.03.003

Gui, J., Wang, T., Jones, R. P. O., Trump, D., Zimmer, T., and Lei, M. (2010a). Multiple loss-of-function mechanisms contribute to *SCN5A*-related familial sick sinus syndrome. *PLoS One* 5:e10985. doi: 10.1371/journal.pone.0010985

Gui, J., Wang, T., Trump, D., Zimmer, T., and Lei, M. (2010b). Mutation-specific effects of polymorphism H558R in *SCN5A*-related sick sinus syndrome. *J. Cardiovasc. Electrophysiol.* 21, 564–573. doi: 10.1111/j.1540-8167.2010.01762.x

Hayashi, H., Sumiyoshi, M., Nakazato, Y., and Daida, H. (2018). Brugada syndrome and sinus node dysfunction. *J. Arrhythm* 4, 216–221. doi: 10.1002/joa3.12046

Hodgkin, A. L., and Huxley, A. F. (1952). A quantitative description of membrane current and its application to conduction and excitation in nerve. *J. Physiol.* 117, 500–544. doi: 10.1113/jphysiol.1952.sp004764

Hu, D., Viskin, S., Oliva, A., Carrier, T., Cordeiro, J. M., Barajas-Martinez, H., et al. (2007). Novel mutation in the SCN5A gene associated with arrhythmic storm development during acute myocardial infarction. *Heart Rhythm* 4, 1072–1080. doi: 10.1016/j.hrthm.2007.03.040

Iwasa, H., Itoh, T., Nagai, R., Nakamura, Y., and Tanaka, T. (2000). Twenty single nucleotide polymorphisms (SNPs) and their allelic frequencies in four genes that are responsible for familial long QT syndrome in the Japanese population. *J. Hum. Genet.* 45, 182–183. doi: 10.1007/s100380050207

Kléber, A. G., and Rudy, Y. (2004). Basic mechanisms of cardiac impulse propagation and associated arrhythmias. *Physiol. Rev.* 84, 431–488. doi: 10.1152/physrev.00025.2003

Lakatta, E. G., and DiFrancesco, D. (2009). What keeps us ticking: a funny current, a calcium clock, or both? *J. Mol. Cell. Cardiol.* 47, 157–170. doi: 10.1016/j.yjmcc.2009.03.022

Lei, M., Huang, C. L.-H., and Zhang, Y. (2008). Genetic Na^+ channelopathies and sinus node dysfunction. *Prog. Biophys. Mol. Biol.* 98, 171–178. doi: 10.1016/j.pbiomolbio.2008.10.003

Lei, M., Zhang, H., Grace, A. A., and Huang, C. L.-H. (2007). *SCN5A* and sinoatrial node pacemaker function. *Cardiovasc. Res.* 74, 356–365. doi: 10.1016/j.cardiores.2007.01.009

Lindblad, D. S., Murphey, C. R., Clark, J. W., and Giles, W. R. (1996). A model of the action potential and underlying membrane currents in a rabbit atrial cell. *Am. J. Physiol.* 271, H1666–H1696. doi: 10.1152/ajpheart.1996.271.4.H1666

Lloyd, C. M., Lawson, J. R., Hunter, P. J., and Nielsen, P. F. (2008). The CellML model repository. *Bioinformatics* 24, 2122–2123. doi: 10.1093/bioinformatics/btn390

Maleckar, M. M., Greenstein, J. L., Giles, W. R., and Trayanova, N. A. (2009). K^+ current changes account for the rate dependence of the action potential in the human atrial myocyte. *Am. J. Physiol. Heart Circ. Physiol.* 297, H1398–H1410. doi: 10.1152/ajpheart.00411.2009

Maleckar, M. M., Greenstein, J. L., Trayanova, N. A., and Giles, W. R. (2008). Mathematical simulations of ligand-gated and cell-type specific effects on the action potential of human atrium. *Prog. Biophys. Mol. Biol.* 98, 161–170. doi: 10.1016/j.pbiomolbio.2009.01.010

Maltsev, V. A., Yaniv, Y., Maltsev, A. V., Stern, M. D., and Lakatta, E. G. (2014). Modern perspectives on numerical modeling of cardiac pacemaker cell. *J. Pharmacol. Sci.* 125, 6–38. doi: 10.1254/jphs.13R04CR

Noble, D., DiFrancesco, D., and Denyer, J. C. (1989). "Ionic mechanisms in normal and abnormal cardiac pacemaker activity," in *Neuronal and Cellular Oscillators*, ed. J. W. Jacklet (New York, NY: Marcel Dekker Inc.), 59–85.

Noble, D., and Noble, S. J. (1984). A model of sino-atrial node electrical activity based on a modification of the DiFrancesco-Noble (1984) equations. *Proc. R. Soc. Lond. B Biol. Sci.* 222, 295–304. doi: 10.1098/rspb.1984.0065

Nygren, A., Fiset, C., Firek, L., Clark, J. W., Lindblad, D. S., Clark, R. B., et al. (1998). Mathematical model of an adult human atrial cell: the role of K^+ currents in repolarization. *Circ. Res.* 82, 63–81. doi: 10.1161/01.RES.82.1.63

O'Hara, T., Virág, L., Varró, A., and Rudy, Y. (2011). Simulation of the undiseased human cardiac ventricular action potential: model formulation and experimental validation. *PLoS Comput. Biol.* 7:e1002061. doi: 10.1371/journal.pcbi.1002061

Priebe, L., and Beuckelmann, D. J. (1998). Simulation study of cellular electric properties in heart failure. *Circ. Res.* 82, 1206–1223. doi: 10.1161/01.RES.82.11.1206

Remme, C. A. (2013). Cardiac sodium channelopathy associated with *SCN5A* mutations: electrophysiological, molecular and genetic aspects. *J. Physiol.* 591, 4099–4116. doi: 10.1113/jphysiol.2013.256461

Remme, C. A., Wilde, A. A. M., and Bezzina, C. R. (2008). Cardiac sodium channel overlap syndromes: different faces of *SCN5A* mutations. *Trends Cardiovasc. Med.* 18, 78–87. doi: 10.1016/j.tcm.2008.01.002

Rivolta, I., Abriel, H., Tateyama, M., Liu, H., Memmi, M., Vardas, P., et al. (2001). Inherited Brugada and long QT-3 syndrome mutations of a single residue of the cardiac sodium channel confer distinct channel and clinical phenotypes. *J. Biol. Chem.* 276, 30623–30630. doi: 10.1074/jbc.M104471200

Robyns, T., Nuyens, D., Van Casteren, L., Corveleyn, A., De Ravel, T., Heidbuchel, H., et al. (2014). Reduced penetrance and variable expression of SCN5A mutations and the importance of co-inherited genetic variants: case report and review of the literature. *Indian Pacing Electrophysiol. J.* 14, 133–149. doi: 10.1016/S0972-6292(16)30754-9

Ruan, Y., Liu, N., and Priori, S. G. (2009). Sodium channel mutations and arrhythmias. *Nat. Rev. Cardiol.* 6, 337–348. doi: 10.1038/nrcardio.2009.44

Sakakibara, Y., Wasserstrom, J. A., Furukawa, T., Jia, H., Arentzen, C. E., Hartz, R. S., et al. (1992). Characterization of the sodium current in single human atrial myocytes. *Circ. Res.* 71, 535–546. doi: 10.1161/01.RES.71.3.535

Severi, S., Fantini, M., Charawi, L. A., and DiFrancesco, D. (2012). An updated computational model of rabbit sinoatrial action potential to investigate the mechanisms of heart rate modulation. *J. Physiol.* 590, 4483–4499. doi: 10.1113/jphysiol.2012.229435

Shinlapawittayatorn, K., Du, X. X., Liu, H., Ficker, E., Kaufman, E. S., and Deschênes, I. (2011). A common *SCN5A* polymorphism modulates the biophysical defects of *SCN5A* mutations. *Heart Rhythm* 8, 455–462. doi: 10.1016/j.hrthm.2010.11.034

Smits, J. P. P., Koopmann, T. T., Wilders, R., Veldkamp, M. W., Opthof, T., Bhuiyan, Z. A., et al. (2005). A mutation in the human cardiac sodium channel (E161K) contributes to sick sinus syndrome, conduction disease and Brugada syndrome in two families. *J. Mol. Cell. Cardiol.* 38, 969–981. doi: 10.1016/j.yjmcc.2005.02.024

Tester, D. J., Valdivia, C., Harris-Kerr, C., Alders, M., Salisbury, B. A., Wilde, A. A. M., et al. (2010). Epidemiologic, molecular, and functional evidence suggest A572D-SCN5A should not be considered an independent LQT3-susceptibility mutation. *Heart Rhythm* 7, 912–919. doi: 10.1016/j.hrthm.2010.04.014

Verkerk, A. O., Wilders, R., Van Borren, M. M. G. J., and Tan, H. L. (2009). Is sodium current present in human sinoatrial node cells? *Int. J. Biol. Sci.* 5, 201–204. doi: 10.7150/ijbs.5.201

Wendt, D. J., Starmer, C. F., and Grant, A. O. (1992). Na channel kinetics remain stable during perforated-patch recordings. *Am. J. Physiol.* 263, C1234–C1240. doi: 10.1152/ajpcell.1992.263.6.C1234

Wilde, A. A. M., and Amin, A. S. (2018). Clinical spectrum of *SCN5A* mutations: long QT syndrome, Brugada syndrome, and cardiomyopathy. *JACC Clin. Electrophysiol.* 4, 569–579. doi: 10.1016/j.jacep.2018.03.006

Wilders, R., and Verkerk, A. O. (2018). Long QT syndrome and sinus bradycardia—a mini review. *Front. Cardiovasc. Med.* 5:106. doi: 10.3389/fcvm.2018.00106

Workman, A. J., Kane, K. A., and Rankin, A. C. (2001). The contribution of ionic currents to changes in refractoriness of human atrial myocytes associated with chronic atrial fibrillation. *Cardiovasc. Res.* 52, 226–235. doi: 10.1016/S0008-6363(01)00380-7

Ye, B., Valdivia, C. R., Ackerman, M. J., and Makielski, J. C. (2003). A common human *SCN5A* polymorphism modifies expression of an arrhythmia causing mutation. *Physiol. Genomics* 12, 187–193. doi: 10.1152/physiolgenomics.00117.2002

Zhang, H., Holden, A. V., Kodama, I., Honjo, H., Lei, M., Varghese, T., et al. (2000). Mathematical models of action potentials in the periphery and center of the rabbit sinoatrial node. *Am. J. Physiol. Heart Circ. Physiol.* 279, H397–H421. doi: 10.1152/ajpheart.2000.279.1.H397

Zhang, H., Holden, A. V., Noble, D., and Boyett, M. R. (2002). Analysis of the chronotropic effect of acetylcholine on sinoatrial node cells. *J. Cardiovasc. Electrophysiol.* 13, 465–474. doi: 10.1046/j.1540-8167.2002.00465.x

Zimmer, T., Haufe, V., and Blechschmidt, S. (2014). Voltage-gated sodium channels in the mammalian heart. *Glob. Cardiol. Sci. Pract.* 2014, 449–463. doi: 10.5339/gcsp.2014.58

Conflict of Interest Statement: The author declares that the research was conducted in the absence of any commercial or financial relationships that could be construed as a potential conflict of interest.

frontiers in Physiology

ORIGINAL RESEARCH
published: 19 December 2018
doi: 10.3389/fphys.2018.01832

Fibrosis Microstructure Modulates Reentry in Non-ischemic Dilated Cardiomyopathy: Insights From Imaged Guided 2D Computational Modeling

Gabriel Balaban[1], Brian P. Halliday[2], Caroline Mendonca Costa[1], Wenjia Bai[3], Bradley Porter[1,4], Christopher A. Rinaldi[4], Gernot Plank[5], Daniel Rueckert[3], Sanjay K. Prasad[2,6] and Martin J. Bishop[1]*

[1] School of Biomedical Engineering and Imaging Sciences, King's College London, London, United Kingdom, [2] National Heart and Lung Institute, Imperial College London, London, United Kingdom, [3] Biomedical Image Analysis Group, Department of Computing, Imperial College London, London, United Kingdom, [4] Department of Cardiology, Guy's and St. Thomas Hospital Trust, London, United Kingdom, [5] Institute of Biophysics, Medical University of Graz, Graz, Austria, [6] Cardiovascular Research Centre and Cardiovascular Magnetic Resonance Unit, Royal Brompton Hospital, London, United Kingdom

OPEN ACCESS

Edited by:
Javier Saiz, Universitat Politècnica de València, Spain

Reviewed by:
Olivier Bernus, Université de Bordeaux, France
Bradley John Roth, Oakland University, United States

***Correspondence:**
Gabriel Balaban
gabriel.balaban@kcl.ac.uk

Specialty section:
This article was submitted to Computational Physiology and Medicine, a section of the journal Frontiers in Physiology

Received: *11 September 2018*
Accepted: *06 December 2018*
Published: *19 December 2018*

Citation:
Balaban G, Halliday B, Mendonca Costa C, Bai W, Porter B, Rinaldi CA, Plank G, Rueckert D, Prasad SK and Bishop MJ (2018) Fibrosis Microstructure Modulates Reentry in Non-ischemic Dilated Cardiomyopathy: Insights From Imaged Guided 2D Computational Modeling. Front. Physiol. 9:1832. doi: 10.3389/fphys.2018.01832

Aims: Patients who present with non-ischemic dilated cardiomyopathy (NIDCM) and enhancement on late gadolinium magnetic resonance imaging (LGE-CMR), are at high risk of sudden cardiac death (SCD). Further risk stratification of these patients based on LGE-CMR may be improved through better understanding of fibrosis microstructure. Our aim is to examine variations in fibrosis microstructure based on LGE imaging, and quantify the effect on reentry inducibility and mechanism. Furthermore, we examine the relationship between transmural activation time differences and reentry.

Methods and Results: 2D Computational models were created from a single short axis LGE-CMR image, with 401 variations in fibrosis type (interstitial, replacement) and density, as well as presence or absence of reduced conductivity (RC). Transmural activation times (TAT) were measured, as well as reentry incidence and mechanism. Reentries were inducible above specific density thresholds (0.8, 0.6 for interstitial, replacement fibrosis). RC reduced these thresholds (0.3, 0.4 for interstitial, replacement fibrosis) and increased reentry incidence (48 no RC vs. 133 with RC). Reentries were classified as rotor, micro-reentry, or macro-reentry and depended on fibrosis micro-structure. Differences in TAT at coupling intervals 210 and 500ms predicted reentry in the models (sensitivity 89%, specificity 93%). A sensitivity analysis of TAT and reentry incidence showed that these quantities were robust to small changes in the pacing location.

Conclusion: Computational models of fibrosis micro-structure underlying areas of LGE in NIDCM provide insight into the mechanisms and inducibility of reentry, and their dependence upon the type and density of fibrosis. Transmural activation times, measured at the central extent of the scar, can potentially differentiate microstructures which support reentry.

Keywords: non-ischemic cardiomiopathy, computational modeling, late gadolinium enhanced magnetic resonance imaging, dilated cardiaomypothy, electrophysiology, reentry, arrhythmia (any), ventricular tachycardia (VT)

1. INTRODUCTION

Non-ischemic dilated cardiomyopathy (NIDCM) is characterized by enlarged ventricular cavity size, and impaired ventricular systolic function, which is not a consequence of myocardial ischaemia. Patients who present with NIDCM are known to be at high risk of sudden cardiac death (SCD), with an estimated 20% mortality rate over 5 years (Gulati et al., 2013). Late-gadolinium enhanced cardiovascular magnetic resonance studies (LGE-CMR) of NIDCM have highlighted that approximately one third of NIDCM patients have significant mid-wall fibrosis, corresponding to areas of enhanced image intensity (LGE), which are associated with an approximate 4- to 5-fold increased risk of sudden cardiac death (SCD) (Gulati et al., 2013). Despite this clear association, the specific physiological processes by which the structural remodeling associated with NIDCM underlies such increased arrhythmic burden remains poorly understood.

Further risk stratification in NIDCM based on LGE-CMR is therefore vital, yet is challenged by the lack of knowledge of both the underlying fibrosis micro-structure, as well as its implications for arrhythmogenic mechanisms. This is partially due to the limitations of current clinical scan resolutions, which are an order of magnitude larger than that required to resolve micro-structural fibrosis (Schelbert et al., 2010). Furthermore, detailed quantification of the absolute level of fibrosis in LGE images in non-ischemic patients is not possible, due to the lack of comparison between core scar and remote tissue, as is commonly used in assessing infarct fibrotic density in patients with ischemic cardiomyopathy (Glashan et al., 2018). This greatly confounds the identification of the potential fibrotic arrhythmogenic substrate in non-ischemic disease, and motivates a closer examination of how potential variations in fibrosis micro-structure underlying LGE may relate to differences in arrhythmia susceptibility and the mechanisms responsible for this.

In-light of the limitations of LGE in directly quantifying fibrosis density in non-ischemic disease, it may be possible to enhance risk stratification in NIDCM patients by combining LGE assessment along with functional electrical measurements, such as 12-lead ECG data or invasive electroanatomical mapping recordings (Betensky et al., 2013; Chia and Hsia, 2014), to better understand and assess the potential arrhythmogenic substrate evident on LGE-CMR. Facilitating such an approach first necessitates developing a greater understanding of how the fibrotic make-up of regions of mid-wall fibrosis may cause disruption to electrical wavefronts, under different conditions, which may be interpreted in functional electrical measurements.

Computational modeling provides a useful tool to better understand the mechanistic role of cardiac micro-structural remodeling in the initiation and maintenance of ventricular arrhythmias in the context of mid-wall fibrosis. Recently, detailed computational models have been applied to understand the arrhythmogenic interaction of electrical wavefronts and micro-fibrotic structures in a variety of pathological conditions such as modeling of atrial fibrillation (Roney et al., 2016; Vigmond et al., 2016) as well as micro-reentry (Alonso and Bär, 2013). In this study, we have developed the first computational model of fibrosis in NIDCM based on microstructural discontinuities. Based on a single LGE-CMR image, we explored possible variations in fibrosis micro-structure, and determined the consequences for reentry inducibility and reentry mechanism. Furthermore, we demonstrated the potential of transmural activation times (TAT) as a complementary source of data for the identification of arrhythmogenic substrate.

2. METHODS

2.1. Image Acquisition and Processing

An anonymized LGE-CMR image set of a patient presenting with NIDCM and LGE was acquired from the Royal Brompton Hospital, using a previously described protocol (Gulati et al., 2013), with approval of the UK National Research Ethics Committee [07/H0708/83, 09/H0504/104]. The patient gave written informed consent in accordance with the Declaration of Helsinki. The acquired images had a 0.66 mm^2 in-plane resolution, and an 8 mm out of plane resolution. A single short axis (SA) image, with the largest LGE area (semi-automatic segmentation, 3 std > reference mean), was selected to build 2-D models (see **Figure 1A**).

2.2. Model Geometry

In **Figure 1** the pipeline from LGE-CMR image to computational model is displayed. In this pipeline a triangular mesh (max 250 μm edge length) of the myocardium is made (CGAL), from smoothed (moving average filter) epi, endo, and LGE contours, with local myofiber orientations assigned by a 2-D version of a rule based method (Bayer et al., 2012). The generated fiber orientations were aligned primarily with the local circumferential direction (see **Figure 1G**).

2.3. Fibrosis Microstructures

Interstitial and replacement fibrosis were modeled by modifying mesh edges and triangles, respectively, with a single parameter α controlling the density of fibrosis in LGE. The parameter α was selected from the range $0-1$ in steps of 0.1, which yielded models with varying levels of fibrosis. Additionally, each model's level of fibrosis was related to the normalized image intensity

$$I^* = \frac{I - I_{ref}}{I_{max} - I_{ref}}, \tag{1}$$

with I, I_{max}, I_{ref} denoting the local, maximum, and mean non-LGE reference image intensities respectively, so that higher intensity areas contained more fibrosis. A fibrosis probability was assigned to each mesh triangle or edge, giving a probabilistic distribution of replacement or interstitial fibrosis at each level of α. Concrete realizations of these fibrosis distributions were created by generating a random number for each edge or triangle, and assigning it to be fibrotic if the random number was less than the local fibrosis probability.

For replacement fibrosis, the probability of a mesh triangle being fibrotic was

$$p_{replacement} = \alpha I^*, \tag{2}$$

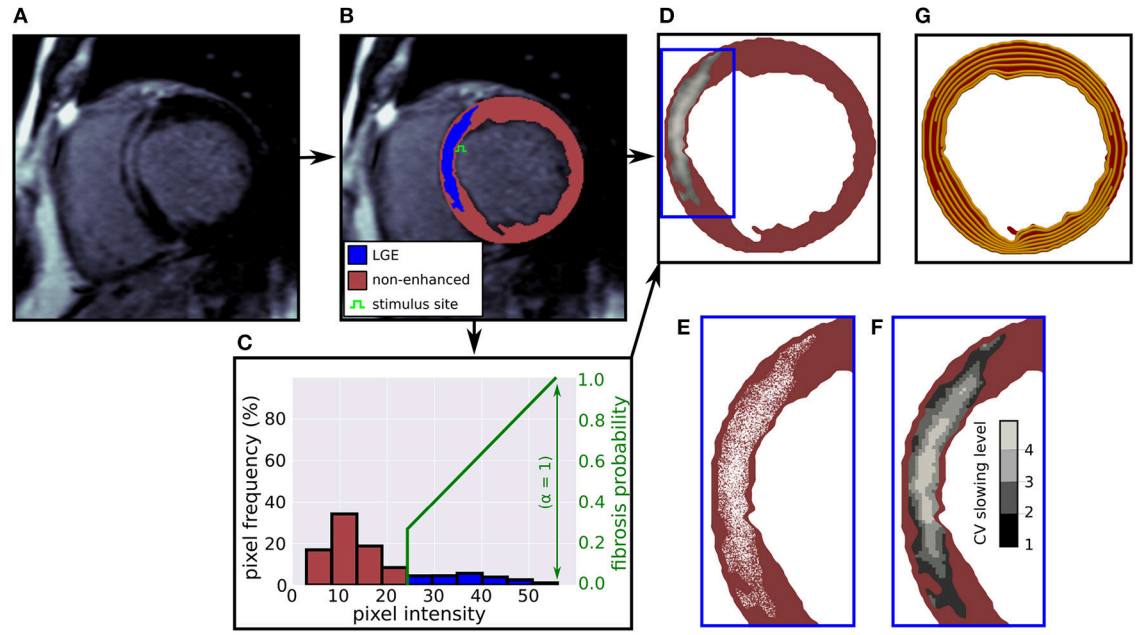

FIGURE 1 | Computational model creation from an LGE-CMR image. **(A)** LGE-CMR image. **(B)** Image segmentation into enhanced and non-enhanced myocardium. **(C)** LV myocardial pixel intensity histogram and example intensity to fibrosis probability mapping. **(D)** Computational model with LGE intensities registered to image. **(E)** Zoomed in view of simulated fibrosis micro-structure. **(F)** Four conduction slowing zones in LGE. **(G)** Rule-based circumferential fibers.

where α is the global fibrosis density. Fibrotic triangles were removed from the mesh, making them electrically inert and non-conducting.

Interstitial fibrosis was represented by a network of random fibrotic clefts (Costa et al., 2014), implemented by doubling mesh vertices across fibrotic edges. Each doubled vertex was assigned to a different neighboring mesh element along the edge, thereby creating a local no-flux boundary condition aligned with the mesh edge. The probability of an edge being fibrotic was

$$p_{interstitial} = \alpha \cos^4(\theta) I^*, \quad (3)$$

where θ is the angle between the triangle edge and the local myocardial fiber direction. The $\cos^4(\theta)$ term in the equation greatly decreases the likelihood of fibrosis not aligned with the myocardial fiber direction. This ensures a highly anisotropic fibrosis distribution, which is what we would expect in the case of interstitial fibrosis.

Model tissues within circuits of interstitial fibrosis were removed, since they were electrically isolated. Example models with both interstitial and replacement fibrosis at various densities are shown in **Figure 2**.

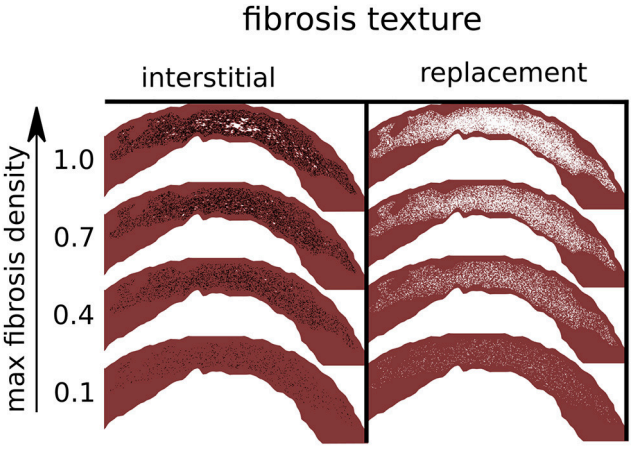

FIGURE 2 | Simulated fibrosis micro-structures with varying type and density. Black lines are separating edges through which current cannot cross, whereas white areas are electrically inactive and non-conducting.

2.4. Conductivities and Conduction Velocities

Conductivity values in non-enhanced areas were tuned to match conduction velocities (CV) from NIDCM (Anderson et al., 1993), 84 and 23 cm/s in the fiber and transverse directions, respectively.

Both normal conduction (NC) and reduced conduction (RC) were considered in LGE. In the case of NC the same conductivity values were used as in non-enhanced areas. In the case of RC, model LGE areas were assigned one of four reduced CVs based on image intensity. Regions in the intensity range 0–25 and 25–50% above threshold had transverse conductivity (CVT) reduced by 25 and 50%, respectively, with normal fiber direction

conductivity (CVF). Finally, regions in the intensity ranges 50–75 and 75–100% above threshold had CVF reduced by 25 and 50%, respectively, and CVT reduced by 50%. These four reduced sets of CV values are consistent with (Anderson et al., 1993), which reported a correlation between fibrosis level and CV slowing, as well as a tendency for preserved longitudinal CV with milder levels of fibrosis.

2.5. Dataset of Fibrosis Microstructures

We constructed a set of model fibrosis micro-structures, consisting of variations in type (replacement, interstitial), conductivity (normal, reduced) and 10 levels of maximum density α (0.1–1.0). Ten random realizations of fibrosis were made for each combination of conductivity, fibrosis type, and fibrosis density, along with a control model with normal conductivity and no fibrosis. This gave a total of 401 models (**Figure 2**).

2.6. Electrophysiology Simulation

Electrical activity was simulated by the standard monodomain formulation, with ionic currents represented by the Ten Tusscher and Panfilov (2006) model of the human ventricular action potential, integrated with step size 20 μs. Due to the lack of experimental evidence for ionic remodeling in NIDCM, the standard ventricular ionic properties for the Ten Tusscher and Panfilov (2006) model were used. Both monodomain solver and cell model are implemented in the Cardiac Arrhythmia Research Package (CARP)(Vigmond et al., 2003).

Models were paced primarily from a site on the LV septal endocardium, approximately halfway down the extent of the LGE (see **Figure 1B**). Two additional endocardial sites were used to perform a sensitivity analysis. These sites were located at three quarters and at the limit of the LGE extent respectively (**Figure 7**). Stimuli had a square shape with 500 μm edge length, strength 500 μA/cm2, and duration 2 ms. Activation times were recorded at the first time that the transmembrane voltage v_m crossed 0 and $\frac{dv_m}{dt} > 0$.

2.7. Pseudo-Electrograms

Pseudo-electrograms were calculated by estimating the extracellular potential (Bishop and Plank, 2011)

$$\phi_e = \frac{1}{4\pi\sigma_b}\int_\Omega \frac{\nabla\cdot(\sigma_i\nabla v_m)}{\|\mathbf{r}\|}d\Omega \tag{4}$$

where Ω is the cardiac domain, $\sigma_i, \sigma_b = 1.0S/m$ the tissue conductivity tensors for the intracellular domain and outside of the heart respectively, and $\|\mathbf{r}\|$ the distance to the electrogram measurement point, which was 4 cm anterior to the computational geometry.

2.8. Stimulation Protocols

Activation patterns and transmural activation times were generated with a fixed stimulation protocol, consisting of 5 beats with coupling intervals (CIs) 500, 340, 250, 210 ms.

Reentry inducibility was tested with a dynamic algorithm, with up to six stimuli with variable CI. The algorithm consists of the components: reentry detection, coupling interval selection, and stimulus capture detection.

2.8.1. Reentry Detection

For each stimulus 600 ms of electrical activity were simulated, and electrical activations were recorded. Reentry was detected if any activations were present after 170 ms in a region of interest (ROI). For all experiments the ROI was defined by a circle with radius 3 mm, centered at the stimulus site, and excluded fibrotic areas.

2.8.2. Coupling Interval Selection

The coupling intervals (CI) between stimuli were determined algorithmically for every stimulus after the first. First the CI of 200 ms was attempted, and if the resulting stimulus generated a new wave, then this CI was kept. Otherwise the effective refractory period (ERP) at the stimulus site was determined, and the CI was set to ERP + 1 ms. This ensured that electrical stimuli were delivered rapidly enough to destabilize the model, and yet slowly enough that each stimulus generated a distinct wave. An effective lower bound of 200 ms was placed on the CI, as pacing rates faster than this can generate reentries under non-pathological conditions (Cao et al., 1999). ERP was calculated to within 1 ms by a binary search when it was required, with an initial bracket of [200, 400 ms].

2.8.3. Stimulus Capture Detection

Knowledge of whether a stimulus generated a new activation wave was required for the coupling interval selection. This was accomplished by tracking a wave of activations for 20 ms after a stimulus was applied, with a stimulus determined as capturing if activations could be tracked up to 20 ms. Initially, all activations inside the reentry detection ROI were found 1 ms after stimulus delivery. For each subsequent millisecond new activations were located inside a set of tracking ROI, which consisted of model tissue that was within the distance that an activation wave could travel in 1 ms, assuming the maximum CV of 84 cm/s.

2.9. Reentry Classification

Reentries were classified by visual inspection of videos of the simulated transmembrane potential. A reentry was classified as a rotor if an organizing center was present, consisting of nearly simultaneous activation and repolarization, as micro-reentry if a narrow conducting channel was involved, and as macro-reentry if activation followed a large circuit. When multiple reentry types were present in a simulation, the reentry type of the earliest circuit was used. Examples of the three reentry types are shown in **Figure 3**, and in the **Supplemental Videos**.

3. RESULTS

3.1. Fibrosis Texture, Density, and Conductivity Modulate Reentry Inducibility

Figure 4 shows the number of reentries per fibrosis texture, density and conductivity. In total 181 reentries were induced: 107 were due to the replacement texture whereas 74 were due to the interstitial texture. The presence of reduced conduction in LGE

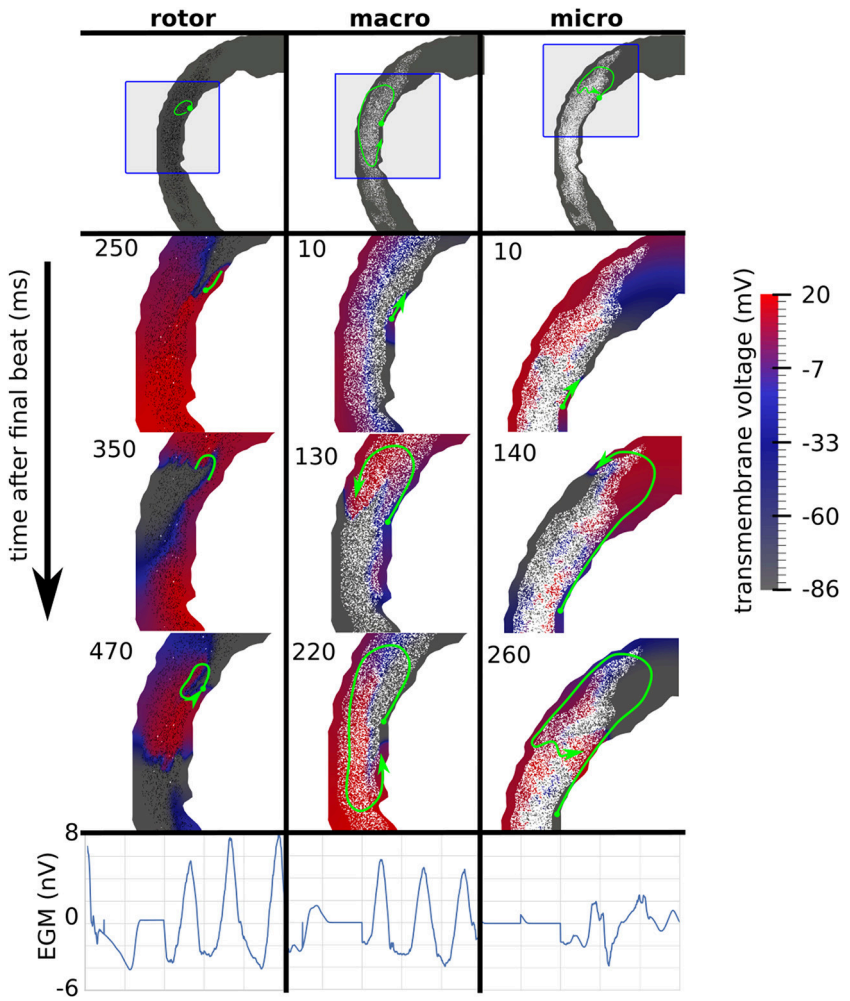

FIGURE 3 | Examples of three canonical reentry mechanisms. **(Top)** Paths of reentrant circuits in green, with blue boxes indicating zoomed-in areas used for the voltage maps below. **(Middle)** Transmembrane voltage maps, with time (ms) after the final stimulus displayed in the top left corner. **(Bottom)** Pseudo-electrograms measured 4 cm anterior to the geometry showing 1s of electrical activity.

was associated with a greater reentry incidence (48 reentries for NC versus 133 with RC), with most of the increase being due to interstitial fibrosis (3 reentries NC vs. 71 with RC). For all fibrosis types there was a minimum level of fibrosis density necessary for reentry. This threshold was lower with reduced conduction, being RC 0.2, 0.4, NC 0.8, 0.6 for interstitial and replacement textures, respectively.

3.2. Reentry Mechanisms Vary With Fibrosis Type and Density

The incidence of each reentry mechanism is shown in **Figure 4**. Rotor reentries mostly occurred with interstitial texture, RC, and lower density, whereas macro-reentries occurred with replacement texture, and for higher densities of interstitial texture with RC. Micro-reentries were prevalent in the maximum density range 0.6–0.9 with RC and replacement texture. The pseudo-electrograms for the example canonical reentries (**Figure 3**) showed differing morphologies, with the rotor and macro-reentry having a signal indicative of monomorphic VT, whereas the micro-reentry showed a more fractionated signal, due to wavefront disorganization. We note the relatively small signal amplitude of the pseudo-electrograms, which we attribute to the small fraction of the total LV mass being represented in our 2-D models.

3.3. Transmural Activation Time Increases With Fibrosis Density and Higher Pacing Rate

We examined the effects of fibrosis type and pacing rate on local activation patterns around the region of LGE. Zoomed in views of the activation maps at CIs, 500, 340, 250, 210 ms, for fibrosis densities 0.5, 0.8, and 1.0, along with the control case, are displayed in **Figure 5**. The activation maps show that both higher fibrosis density and faster pacing rate delayed activation. Furthermore, fibrosis density and pacing rate affected the overall

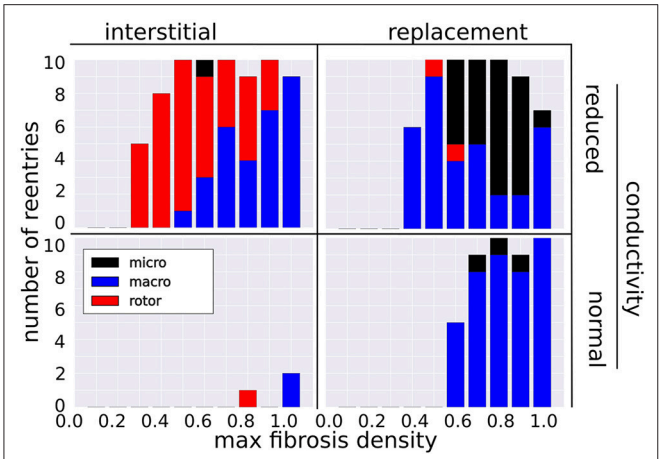

FIGURE 4 | Incidence of reentry mechanisms by fibrosis texture, density, and with normal and reduced conductivity in the LGE.

pattern of activation, which fell into one of two types, direct or compartmentalized (Betensky et al., 2013). The direct pattern was characterized by circumferentially oriented isochrones, and activation times that reached their maximum on the anterior and posterior ends of the fibrosis region (**Figure 5**, control case). In contrast, compartmentalized activation was characterized by the presence of isochrones normal to the region of fibrosis, and a maximum activation time located directly across the pacing site on the right ventricular septum (**Figure 5**, replacement fibrosis, density 1.0). In some cases an increased pacing rate switched the activation pattern from direct to compartmentalized (**Figure 5**, replacement fibrosis, density 0.8), due to functional conduction block, a known precursor to reentry. We sampled the local activation time at a single point opposite the stimulus site, to obtain the trans-mural activation time (TAT). Our results in the top row of **Figure 6** show that TAT always increased with faster pacing rate. Furthermore, TAT tended to increase with higher fibrosis density as well, especially with replacement fibrosis after the reentry threshold had been reached. This was due to large scale conduction block in the areas of fibrosis, which is confirmed by the correlation of the reentry incidence with zones of large TAT in **Figure 6**.

3.4. Transmural Activation Time With Varying Pacing Rate Predicts Reentry Inducibility

We tested the ability of TAT to predict reentry inducibility as a surrogate for knowledge of the fibrosis micro-structure. In particular we considered three metrics, TAT500, TAT210, and ΔTAT. TAT500 and TAT210 refer to TAT at CIs 500 and 210 ms, respectively, whereas ΔTAT refers to the difference between TAT210 and TAT500. Models for which reentry was inducible had significant higher mean values of the three metrics (Mann–Whitney U-test). For the inducible models these were ($\overline{\text{TAT500}}$ = 54.8 ms, $\overline{\text{TAT210}}$ = 115.3 ms, $\overline{\Delta\text{TAT}}$ = 61.1 ms) vs ($\overline{\text{TAT500}}$ = 38.9 ms, $\overline{\text{TAT210}}$ = 74.34 ms, $\overline{\Delta\text{TAT}}$ = 35.42 ms) for the non-inducible models.

Using cut-off values of the TAT metrics, we predicted reentry inducibility using all of the model micro-structures. The results are summarized in **Figure 7** as ROC curves, which show that all three TAT indicies are predictive of reentry. Furthermore, of the three indices, ΔTAT was the most predictive, and TAT500 the least (area under curve = 0.88, 0.92, 0.94 for TAT500, TAT210, ΔTAT respectively). This trend is explained by rate-dependant conduction block, occurring with a CI of 210 ms but not with a CI of 500 ms. As a consequence, TAT210 was a better predictor of reentry than TAT500. We designed ΔTAT to exploit rate-dependant conduction block even further. Such block gives a relatively small TAT500, a relatively large TAT210, and hence a large ΔTAT. Indeed this metric was the best reentry predictor, achieving a 89% sensitivity and 93% specificity at the point of maximum sensitivity and specificity (Youden Index). This compares favorably with the Youden Indicies of TAT500 (sensitivity 85%, specificity 94%) and TAT210 (sensitivity 81%, specificity 89%).

3.5. Reentry Incidence and Activation Delays Are Reduced at Off-Center Pacing Locations

We examined the effects of pacing and measuring TAT from alternate locations (see **Figure 8** top right). Two of these locations (sites 2 and 3) are located very close to the original pacing location (site 1). Site 4 is located halfway between site 1 and the edge of the extent of the scar (site 5). The TAT times and reentry incidence for the alternative sites, with replacement fibrosis and reduced conductivity, are presented in **Figure 8**. For sites 2–3, the results are not very different from those obtained at site 1. At sites 4–5 the transmural activation times no longer correlate as much with the fibrosis density, and the reentry incidence is less. Site 5, which is furthest away from the center of the scar, has the lowest reentry incidence.

4. DISCUSSION

Our study has highlighted the role of fibrosis density and local conduction slowing for the induction of reentry in NIDCM. Furthermore, we identified distinct reentry mechanisms related to the underlying fibrotic substrate, and found that variations in micro-structure density and conductivity had a measurable effect on activation patterns. This allowed for the accurate prediction of reentry inducibility in a wide variety of fibrotic micro-structures with pacing from the endocardium halfway through the extent of the scar.

4.1. A Model of Fibrosis for Non-ischemic Dilated Cardiomyopathy

To the best of our knowledge, our paper is the first to develop a computational model of fibrotic scarring in NIDCM. The main feature of our model is the incorporation of random fibrosis micro-structures. These micro-structures cannot be imaged with

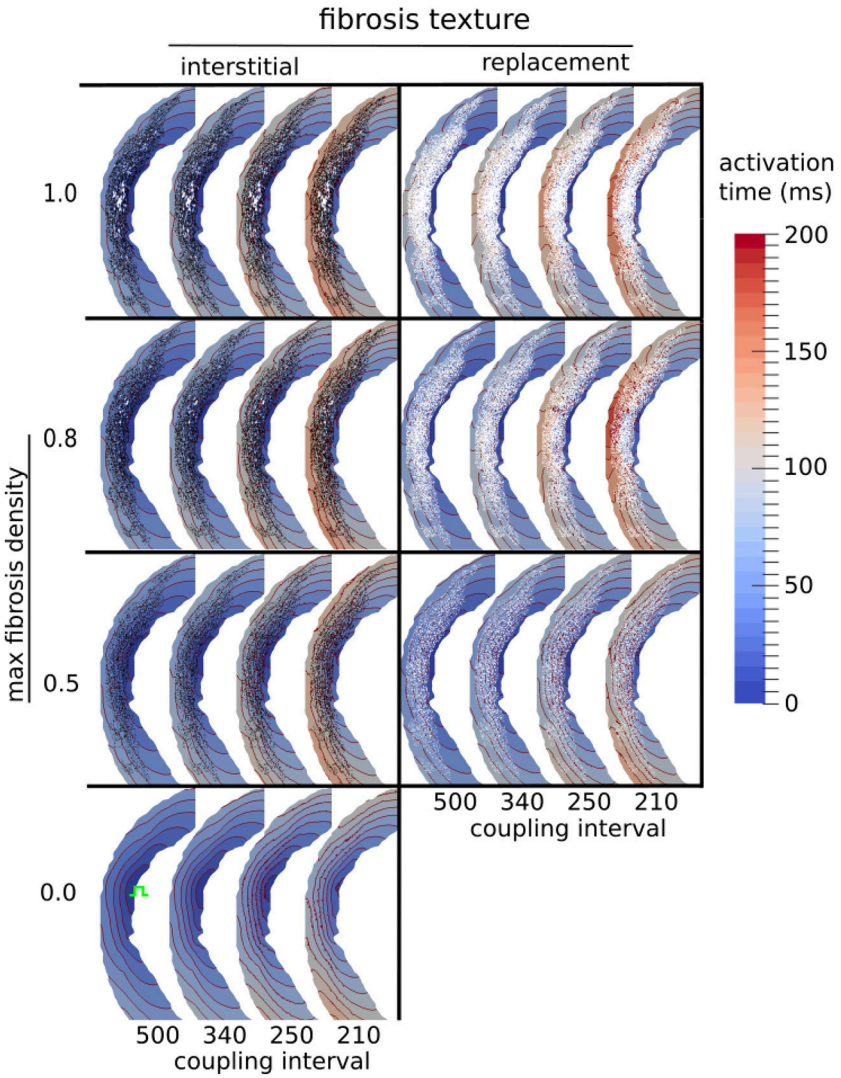

FIGURE 5 | Activation maps around the LGE for three types of fibrosis micro-structure. Red lines are isochrones spaced at 10 ms intervals. The stimulus site is shown in green in the fibrosis-free control model (bottom row).

current clinical modalities, and were therefore approximated by our computational model.

Micro-structures have explained reentry formation in theoretical studies (Alonso and Bär, 2013), and in the context of atrial fibrillation (Roney et al., 2016; Vigmond et al., 2016), and have been shown to cause far-field effects when interacting with external electrical fields, such as those used for defibrillation (Fishler and Vepa, 1998). The densities of our fibrosis micro-structures were guided by LGE-CMR intensity values, which have been shown to reflect the relative volume fraction of fibrosis (Schelbert et al., 2010). A similar approach was also taken in representing fibrosis within the atria (Roney et al., 2016). However, the absolute fibrosis level for any particular non-ischemic LGE-CMR image is difficult to quantify (Glashan et al., 2018), which motivated our approach of systematically varying this parameter in our study.

We modeled reduced passive tissue conductivities within fibrotic areas, based on evidence of reduce gap junction protein expression in the context of fibrosis and dilated cardiomyopathy (Kostin et al., 2003; Glukhov et al., 2012), and showed that such effects greatly influence reentry formation in NIDCM. Similar results have been previously obtained in the context of ventricular infarcted areas (Arevalo et al., 2016) as well as the fibrotic atria (Roney et al., 2016). It is important to note, that any conduction slowing seen in our models is due to either: (a) RC (where present); or, (b) tortuous activation pathways through the micro-fibrosis patterns, which extend path lengths, and cause source-sink mis-matches which slow conduction due to increased electrotonic loading on the wavefront (De Bakker et al., 1993).

We modeled the excitability of fibrotic tissue in NIDCM as normal, which is supported by experimental studies (Anderson

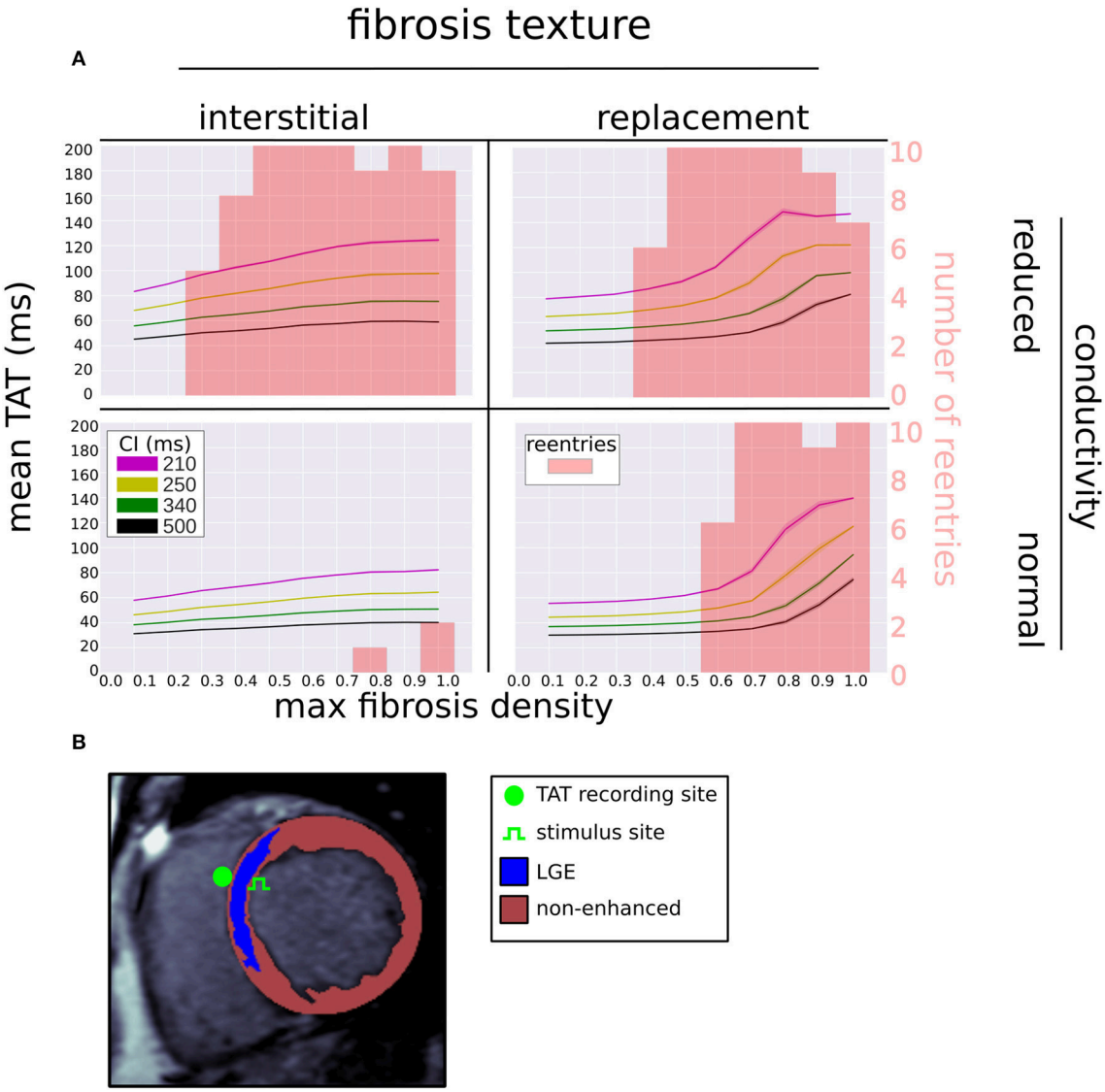

FIGURE 6 | (A) Mean (solid line) and standard deviation (transparent area) of trans-septal activation time (TAT) for four coupling intervals (CI) vs. fibrosis density, fibrosis type, and LGE conductivity. The reentry incidence is overlaid in red. **(B)** Segmented LGE-CMR image with locations of stimulus and TAT recording site.

et al., 1993; Glukhov et al., 2012). This is in contrast to the majority of modeling representations of the infarcted border-zone, which often modulate sodium channel expression (Arevalo et al., 2016). Given the evidence of normal excitability, it is most likely that any ion channel changes in NIDCM would affect the later phases of the action potential and hence the action potential duration (APD). If any local APD effects were included in our NIDCM model, they would likely influence the reentry suspectibility (Clayton and Holden, 2005).

We did not include any models of myocyte-fibroblast coupling (MacCannell et al., 2007), which shorten action potential duration, and reduce excitability. The latter effect is not likely to be present in NIDCM, due to the normal excitability observed experimentally (Anderson et al., 1993; Glukhov et al., 2012). However, we expect that the action potential shortening effect, if included in our NIDCM model, would increase susceptibility to reentries, as was the case with atrial fibrosis (McDowell et al., 2013).

Finally, we did not include the effects of APD prolongation and altered transmural heterogeneity as were observed in Glukhov et al. (2012) for end-stage heart failure patients with NIDCM. This is because such effects are potentially a consequence of heart failure (Nattel et al., 2007). Hence their role in the acute phase of NIDCM is uncertain, which is when our computational model would be ideally used for prospective arrhythmic risk stratification. Further studies are needed to determine the extent to which APD prolongation and altered transmural heterogeneity play a role in acute NIDCM.

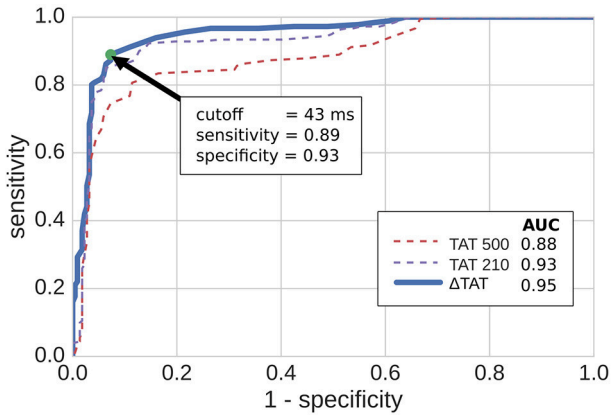

FIGURE 7 | ROC curves for predicting reentry inducibility based on transmural activation times (TAT). TAT500 and TAT210 are the transmural activation times with 500 and 210 ms coupling intervals respectively, while ΔTAT is the difference. The green dot shows the point of maximum sensitivity and specificity. AUC stands for area under curve.

4.2. Mechanisms of Reentry

Previous studies have shown that fibrosis in NIDCM plays a role in both the initiation of block, and in the slowing of propagation (Anderson et al., 1993; Glukhov et al., 2012). Additionally, fibrosis has been associated with suppressed gap junction protein expression (Kostin et al., 2003; Glukhov et al., 2012), which reduces the conductivity of tissue, thereby contributing further to the slowing of conduction and formation of reentry.

By combining the known consequences of fibrosis in NIDCM into a computational model, we were able to simulate three reentry mechanisms, and analyse the relative contributions of fibrosis micro-structure and RC. We observed that macro-reentries involved large areas of functional and anatomical conduction block, which were more likely to form when the fibrosis was sufficiently dense, especially for replacement fibrosis with NC and interstitial fibrosis with RC.

We observed that rotor reentries formed when relatively large wavefronts pivoted and folded back onto an area of transient conduction block. The anisotropic properties of interstitial fibrosis facilitated this. Relatively free conduction in the transverse direction allowed for the preservation of large wavefronts in the fibrotic areas, whereas restricted conduction in the fiber direction caused zones of transient block which could be reentered by the pivoting waves. Indeed, most of the rotor reentries occurred with interstitial fibrosis. RC also played a key role in rotor formation, as only as single rotor was observed with NC.

We observed micro-reentries when propagation was constrained to a narrow pathway, and yet was not completely blocked. This occurred predominantly with replacement fibrosis and RC for the density range 0.6–0.9, at which micro-reentries were more common than macro-reentries. We did not observe micro-reentries with interstitial fibrosis. This was most likely due to the relatively unhindered lateral conduction of interstitial fibrosis which did not support the formation of narrow channels required for micro-reentry.

Previous simulation studies (Alonso and Bär, 2013; Vigmond et al., 2016), based on percolation theory, have also reported micro-reentry at distinct ranges of fibrosis density. These ranges were more narrow than what we observed, which we attribute to the heterogeneous density of our fibrosis micro-structures. This meant that different parts of our fibrotic zone could support micro-reentry, depending on the overall fibrosis density. For both micro-reentry and rotors, our results implicate the role of RC, as the incidence of these reentry types was much greater when the conductivity was reduced.

All reentries were initiated in the presence and absence of RC. The possibility that reentry in NIDCM is possible due to the structural effects of fibrosis alone, without RC, is also supported by previous simulation studies (Kazbanov et al., 2016). However, we show that the additional presence of RC increases the likelihood of reentry initiation. Similarly increased arrhythmic risks due to RC have been noted in the context of myocardial infarction (Cabo et al., 2006), and even in otherwise healthy hearts (Gutstein et al., 2001), which suggests that additional RC may also increase the risk of SCD in NIDCM.

4.3. Transmural Activation Patterns

A comparison of our simulated TAT values to literature provides a preliminary validation of our NIDCM fibrosis model. In particular, for our control case with no fibrosis and NC, we observed a TAT of 25 ms, which is within the range 26 ± 14 ms observed in healthy controls by Vassallo et al. (1986). For our models with fibrosis, we predicted TAT between 25–100 ms at the slow pacing rate. This is within the range 20–150 ms, measured previously in patients with septal scar (Betensky et al., 2013). The fact that we did not observe TAT values above 100 ms was most likely due to the intramural morphology of the scar in our particular patient. We expect that more transmural scars or thicker septal walls would produce higher TAT values.

We found that activation in the fibrotic region followed one of two patterns, direct or compartmentalized. These same patterns were observed by Betensky et al. (2013), with the compartmentalized pattern being attributed to greater scar volume and transmurality. Our simulations indicate the important role of scar density as well. Furthermore, we identified a particularly dangerous situation in which the activation pattern switched from direct to compartmentalized under an increase in pacing rate, reflecting a transient conduction block.

Our ROC analysis indicates that TATs are predictive of reentry. This is supported by Betensky et al. (2013), who reported that clinical VT were more common in patients with delayed TAT, and by Saumarez et al. (2003), who showed an association between SCD and rate dependant pacing delay. All three of our TAT metrics reflect this trend, with ΔTAT being particularly well suited to detecting large scale transient conduction block. Indeed, **Figure 4** shows that, for replacement fibrosis, the difference in average TAT between CI 500 and 210 ms increased from about 90 ms in the reentry-free density regime to 100–200 ms for the densities that supported reentry. These reentries were overwhelmingly of the macro type, which involved large areas of conduction block that greatly increased ΔTAT values. For interstitial fibrosis, the link between ΔTAT and reentry was not

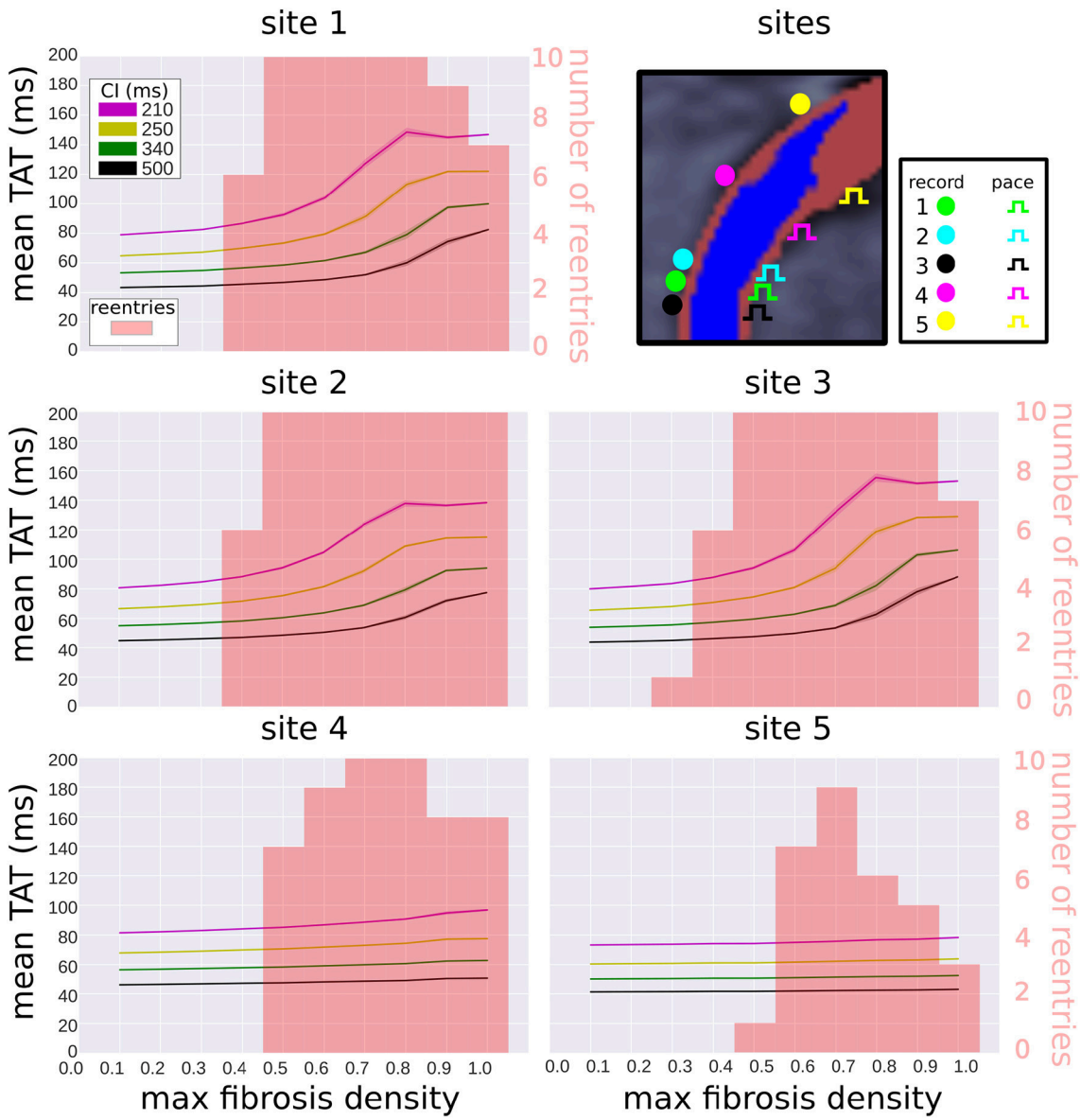

FIGURE 8 | Effect of pacing location on transmural activation times and reentry incidence. Transmural activation times are given as a mean (solid line) and standard deviation (transparent area) for four coupling intervals (CI), taken over 10 random realizations of each fibrosis density. The reentry incidence is overlaid in red for comparison. All results were obtained with replacement fibrosis texture and reduced conductivity. The results for site 1 are the same as in **Figure 6** (top right), whereas sites 2–5 are new locations shown for comparison.

as clear, most likely due to the presence of rotor reentries, which involved relatively small areas of conduction block and were therefore associated with modest ΔTAT values. Nevertheless, all three TAT metrics tended to increase with the interstitial fibrosis density, so that large TAT and ΔTAT values were indicative of being above the minimum density threshold for reentry.

4.4. The Effects of Pacing and TAT Recording Locations

We considered alternative pacing and TAT recording locations and measured the reentry incidence and TAT values at these sites. At the three sites in the center of the scar, the reentry incidence was similar and the TAT values correlated with scar density. At the off-center locations the reentry incidence was lower, with the site furthest away from the center of the scar experiencing the lowest incidence. This is expected since waves approaching the scar from the off-center locations traveled in a vector that was more greatly aligned with the myocardial fiber direction than for waves traveling from the central pacing locations. This meant that the effective CV of waves originating form the off-center locations was higher, and conduction block less likely.

Furthermore, TAT was only weakly correlated with the scar density at the off-center pacing sites. This was due to the effects of waves traveling around the scar, which were more likely to be

the first to reach the TAT recording locations in the off-center setups. Since these waves traveled around the scar rather than through it, they experienced less fibrosis induced delay. For the pacing cite furthest away from the center of the scar, the scar transmurality was also substantially less, which lead to less delay for waves traveling through the scar than from the other pacing sites.

4.5. Clinical Implications

The DANISH trial (Køber et al., 2016) has demonstrated the need to improve the identification of patients with non-ischemic disease who benefit from ICD therapy. LGE-CMR, with its ability to image areas of fibrosis, is a promising tool for SCD risk stratification. Our results show that the type and density of the scar micro-structure underlying LGE play an important role in arrhythmia formation. This motivates the inclusion of data additional to LGE-CMR for the purposes of risk stratification. Our work suggests that electrical measurements, such as transmural activation times are an attractive possibility.

We demonstrated good performance of ΔTAT for predicting simulated reentry induciblity for a single scar macrostructure with a variety of miscrostructures. Further experiments with a variety of macrostructures are warranted. Our results with alternative pacing and TAT recording locations suggest that finding a location central to the scar is crucial for inferring the potential for reentry from TAT measurements. Furthermore, the method is robust to small changes in the pacing/recording locations. This is important for any potential clinical application, where less precision in determining locations can be expected.

Another potential data source complementary to LGE-CMR is T1 mapping, which allows for absolute comparisons to be made, and has been shown to be an independent predictor of arrhythmia (Chen et al., 2015). Future modeling efforts may benefit from the incorporation of both T1 and LGE-CMR.

Computational models of NIDCM, building on the methodology presented here, have the potential to predict SCD in a manner similar to that which has recently been demonstrated for ischemic disease (Arevalo et al., 2016). Future developments should address the *in-vivo* estimation of key fibrosis characteristics, such as density and fibrosis type, as well as the amount of conductivity reduction, as these would greatly improve the predictive capability of computational modeling, and thereby pave the way for personalized *in-silico* prediction of arrhythmic risk in NIDCM.

4.6. Limitations

All models were based on a single image. Consequentially our results do not account for geometric variability, such as wall thickness, scar transmurality, and scar extent. These factors may effect both TAT and reentry inducibility, and therefore the ability to infer reentry susceptibility from TAT measurements. Furthermore, our simulated TAT differences were a consequence of electrical restitution properties, which were governed by the Ten Tusscher and Panfilov (2006) model in our case. This model assumes normal ventricular restitution properties. Whether or not this is appropriate for fibrotic tissue in NIDCM is an open question. Additionally, we did not include any epi-endocardial differences in our cellular model, as the role of such differences in NIDCM is currently unknown.

As shown in section 3.5, the choice of pacing location is critical when making TAT measurements. In the clinical study of Betensky et al. (2013), this issue was handled by first surveying scars via voltage mapping and LGE-CMR, and then choosing an appropriate pacing location. We expect that similar techniques will be of use in future studies of scarring in NIDCM.

Simulations were performed in 2-D, which neglected the 3-D structure of ventricular tissue, myofibers, and interstitial clefts. As a consequence we restricted our study to the generation of reentry and not the sustenance, in which additional electrical pathways in 3-D may be important. Furthermore, micro-structural effects on TAT values could be less pronounced in 3-D at comparable fibrosis levels. This is because the presence of a 3rd dimension would likely increase the degree of connectivity among different paths through the scar, leading to quicker fill-in by multiple propagating activation wavefronts and hence more stable conduction. At the same time source-sink mismatches could be more pronounced in 3D due to the extra electrotonic load on a point in 3-D tissue. This could make conduction block and hence reentries more likely to occur.

Furthermore, the modeled 2-D fiber architecture did not account for the effects of transmural variation in fiber helix angle. Including this effect into a projection of the fibers onto a 2-D short-axis plane would cause the effective conductivity in the in-plane fiber direction to be less at the epicardial and endocardial edges. We expect that including this in our models would act to shorten the electrical wavelength around the scar, potentially increasing the reentry incidence.

Only two levels of conductivity reduction were tested: none and the heterogeneous scheme described in section 2.4. This was due to the lack of experimental data to inform the conductivity values, and to limit the number of model combinations.

Finally heterogeneous blocks of fibrosis corresponding to image pixels were present in our models, which have the potential to affect the probability of reentry (Kazbanov et al., 2016). However, our pixel size of 0.66 mm is well below the threshold of where block size effects were seen in Figure 2b of Kazbanov et al. (2016), which suggests that the fibrosis heterogeneity size was sufficiently resolved in our study.

AUTHOR CONTRIBUTIONS

All authors contributed to the interpretation of the data, drafting, and revising the manuscript, and approved the final version of the manuscript. The original study design was made by GB, MB, SP, BH, and discussed with the other authors. GB ran the simulations and analyzed the resulting data.

FUNDING

This work was supported by the National Institute for Health Research Biomedical Research Center at Guy's and St. Thomas'

Trust and King's College, in addition to the Center of Excellence in Medical Engineering funded by the Welcome Trust and Engineering and Physical Sciences Research Council (EPSRC; WT 088641/Z/09/Z). The views expressed are those of the author(s) and not necessarily those of the National Health Service, and the National Institute for Health Research, or the Department of Health. The authors acknowledge the British Heart Foundation under Project Grant No. PG/14/66/30927. MB is supported by a Medical Research Council New Investigator Grant (MR/ N011007/1).

ACKNOWLEDGMENTS

The authors thank Hermenegild Arevalo for his advice with regards to the design of pacing protocols.

SUPPLEMENTARY MATERIAL

The Supplementary Material for this article can be found online at: https://www.frontiersin.org/articles/10.3389/fphys.2018.01832/full#supplementary-material

REFERENCES

Alonso, S., and Bär, M. (2013). Reentry near the percolation threshold in a heterogeneous discrete model for cardiac tissue. *Phys. Rev. Lett.* 110:158101. doi: 10.1103/PhysRevLett.110.158101

Anderson, K. P., Walker, R., Urie, P., Ershler, P. R., Lux, R. L., and Karwandee, S. V. (1993). Myocardial electrical propagation in patients with idiopathic dilated cardiomyopathy. *J. Clin. Invest.* 92, 122–140. doi: 10.1172/JCI116540

Arevalo, H. J., Vadakkumpadan, F., Guallar, E., Jebb, A., Malamas, P., Wu, K. C., et al. (2016). Arrhythmia risk stratification of patients after myocardial infarction using personalized heart models. *Nat. Commun.* 7:11437. doi: 10.1038/ncomms11437

Bayer, J. D., Blake, R. C., Plank, G., and Trayanova, N. A. (2012). A novel rule-based algorithm for assigning myocardial fiber orientation to computational heart models. *Ann. Biomed. Eng.* 40, 2243–2254. doi: 10.1007/s10439-012-0593-5

Betensky, B. P., Kapa, S., Desjardins, B., Garcia, F. C., Callans, D. J., Dixit, S., et al. (2013). Characterization of trans-septal activation during septal pacing: criteria for identification of intramural ventricular tachycardia substrate in nonischemic cardiomyopathy. *Circulation* 6, 1123–1130. doi: 10.1161/CIRCEP.113.000682

Bishop, M. J., and Plank, G. (2011). Bidomain ECG simulations using an augmented monodomain model for the cardiac source. *IEEE Trans. Biomed. Eng.* 58, 2297–2307. doi: 10.1109/TBME.2011.2148718

Cabo, C., Yao, J., Boyden, P. A., Chen, S., Hussain, W., Duffy, H. S., et al. (2006). Heterogeneous gap junction remodeling in reentrant circuits in the epicardial border zone of the healing canine infarct. *Cardiovasc. Res.* 72, 241–249. doi: 10.1016/j.cardiores.2006.07.005

Cao, J.-M., Qu, Z., Kim, Y.-H., Wu, T.-J., Garfinkel, A., Weiss, J. N., et al. (1999). Spatiotemporal heterogeneity in the induction of ventricular fibrillation by rapid pacing: importance of cardiac restitution properties. *Circul. Res.* 84, 1318–1331. doi: 10.1161/01.RES.84.11.1318

Chen, Z., Sohal, M., Voigt, T., Sammut, E., Tobon-Gomez, C., Child, N., et al. (2015). Myocardial tissue characterization by cardiac magnetic resonance imaging using t1 mapping predicts ventricular arrhythmia in ischemic and non–ischemic cardiomyopathy patients with implantable cardioverter-defibrillators. *Heart Rhythm* 12, 792–801. doi: 10.1016/j.hrthm.2014.12.020

Chia, K. K., and Hsia, H. H. (2014). Ventricular tachycardia in nonischemic dilated cardiomyopathy: electrocardiographic and intracardiac electrogram correlation. *Cardiac Electrophysiol. Clin.* 6, 535–552. doi: 10.1016/j.ccep.2014.05.009

Clayton, R. H., and Holden, A. V. (2005). Dispersion of cardiac action potential duration and the initiation of re-entry: a computational study. *Biomed. Eng. Online* 4:11. doi: 10.1186/1475-925X-4-11

Costa, C. M., Campos, F. O., Prassl, A. J., dos Santos, R. W., Sánchez-Quintana, D., Ahammer, H., et al. (2014). An efficient finite element approach for modeling fibrotic clefts in the heart. *IEEE Trans. Biomed. Eng.* 61, 900–910. doi: 10.1109/TBME.2013.2292320

De Bakker, J. M., Van Capelle, F., Janse, M. J., Tasseron, S., Vermeulen, J. T., De Jonge, N., et al. (1993). Slow conduction in the infarcted human heart.'zigzag'course of activation. *Circulation* 88, 915–926. doi: 10.1161/01.CIR.88.3.915

Fishler, M. G., and Vepa, K. (1998). Spatiotemporal effects of syncytial heterogeneities on cardiac far-field excitations during monophasic and biphasic shocks. *J. Cardiovasc. Electrophysiol.* 9, 1310–1324. doi: 10.1111/j.1540-8167.1998.tb00107.x

Glashan, C. A., Androulakis, A. F., Tao, Q., Glashan, R. N., Wisse, L. J., Ebert, M., et al. (2018). Whole human heart histology to validate electroanatomical voltage mapping in patients with non-ischaemic cardiomyopathy and ventricular tachycardia. *Eur. Heart J.* 39, 2867–2875. doi: 10.1093/eurheartj/ehy168

Glukhov, A. V., Fedorov, V. V., Kalish, P. W., Ravikumar, V. K., Lou, Q., Janks, D., et al. (2012). Conduction remodeling in human end-stage non-ischemic left ventricular cardiomyopathy. *Circulation* 125, 1835–1847. doi: 10.1161/CIRCULATIONAHA.111.047274

Gulati, A., Jabbour, A., Ismail, T. F., Guha, K., Khwaja, J., Raza, S., et al. (2013). Association of fibrosis with mortality and sudden cardiac death in patients with nonischemic dilated cardiomyopathy. *JAMA* 309, 896–908. doi: 10.1001/jama.2013.1363

Gutstein, D. E., Morley, G. E., Tamaddon, H., Vaidya, D., Schneider, M. D., Chen, J., et al. (2001). Conduction slowing and sudden arrhythmic death in mice with cardiac-restricted inactivation of connexin43. *Circul. Res.* 88, 333–339. doi: 10.1161/01.RES.88.3.333

Kazbanov, I. V., Ten Tusscher, K. H., and Panfilov, A. V. (2016). Effects of heterogeneous diffuse fibrosis on arrhythmia dynamics and mechanism. *Sci. Rep.* 6:20835. doi: 10.1038/srep20835

Køber, L., Thune, J. J., Nielsen, J. C., Haarbo, J., Videbæk, L., Korup, E., et al. (2016). Defibrillator implantation in patients with nonischemic systolic heart failure. *New Engl. J. Med.* 375, 1221–1230. doi: 10.1056/NEJMoa1608029

Kostin, S., Rieger, M., Dammer, S., Hein, S., Richter, M., Klövekorn, W.-P., et al. (2003). "Gap junction remodeling and altered connexin43 expression in the failing human heart," in *Cardiac Cell Biology*, eds E. Kardami, L. Hryshko, and N. Mesaelli (Boston, MA: Springer), 135–144.

MacCannell, K. A., Bazzazi, H., Chilton, L., Shibukawa, Y., Clark, R. B., and Giles, W. R. (2007). A mathematical model of electrotonic interactions between ventricular myocytes and fibroblasts. *Biophys. J.* 92, 4121–4132. doi: 10.1529/biophysj.106.101410

McDowell, K. S., Vadakkumpadan, F., Blake, R., Blauer, J., Plank, G., MacLeod, R. S., et al. (2013). Mechanistic inquiry into the role of tissue remodeling in fibrotic lesions in human atrial fibrillation. *Biophys. J.* 104, 2764–2773. doi: 10.1016/j.bpj.2013.05.025

Nattel, S., Maguy, A., Le Bouter, S., and Yeh, Y.-H. (2007). Arrhythmogenic ion-channel remodeling in the heart: heart failure, myocardial infarction, and atrial fibrillation. *Physiol. Rev.* 87, 425–456. doi: 10.1152/physrev.00014.2006

Roney, C. H., Bayer, J. D., Zahid, S., Meo, M., Boyle, P. M., Trayanova, N. A., et al. (2016). Modelling methodology of atrial fibrosis affects rotor dynamics and electrograms. *EP Europace* 18(Suppl. 4), iv146–iv155. doi: 10.1093/europace/euw365

Saumarez, R. C., Chojnowska, L., Derksen, R., Pytkowski, M., Sterlinski, M., Huang, C. L.-H., et al. (2003). Sudden death in noncoronary heart disease is associated with delayed paced ventricular activation. *Circulation* 107, 2595–2600. doi: 10.1161/01.CIR.0000068342.96569.A1

Schelbert, E. B., Hsu, L.-Y., Anderson, S. A., Mohanty, B. D., Karim, S. M., Kellman, P., et al. (2010). Late gadolinium-enhancement cardiac magnetic resonance identifies postinfarction myocardial fibrosis and the border zone at the near cellular level in *ex vivo* rat heart. *Circulation* 3, 743–752. doi: 10.1161/CIRCIMAGING.108.835793

Ten Tusscher, K. H., and Panfilov, A. V. (2006). Alternans and spiral breakup in a human ventricular tissue model. *Am. J. Physiol. Heart Circul. Physiol.* 291, H1088–H1100. doi: 10.1152/ajpheart.00109.2006

Vassallo, J. A., Cassidy, D. M., Miller, J. M., Buxton, A. E., Marchlinski, F. E., and Josephson, M. E. (1986). Left ventricular endocardial activation during right ventricular pacing: effect of underlying heart disease. *J. Am. Coll. Cardiol.* 7, 1228–1233. doi: 10.1016/S0735-1097(86)80140-1

Vigmond, E., Pashaei, A., Amraoui, S., Cochet, H., and Hassaguerre, M. (2016). Percolation as a mechanism to explain atrial fractionated electrograms and reentry in a fibrosis model based on imaging data. *Heart Rhythm* 13, 1536–1543. doi: 10.1016/j.hrthm.2016.03.019

Vigmond, E. J., Hughes, M., Plank, G., and Leon, L. J. (2003). Computational tools for modeling electrical activity in cardiac tissue. *J. Electrocardiol.* 36, 69–74. doi: 10.1016/j.jelectrocard.2003.09.017

Conflict of Interest Statement: The authors declare that the research was conducted in the absence of any commercial or financial relationships that could be construed as a potential conflict of interest.

frontiers in Physiology

ORIGINAL RESEARCH
published: 11 January 2019
doi: 10.3389/fphys.2018.01888

In silico Assessment of Pharmacotherapy for Human Atrial Patho-Electrophysiology Associated With hERG-Linked Short QT Syndrome

Dominic G. Whittaker[1,2], *Jules C. Hancox*[2,3]* *and Henggui Zhang*[2,4,5,6]*

[1] Faculty of Biological Sciences, School of Biomedical Sciences, University of Leeds, Leeds, United Kingdom, [2] Biological Physics Group, School of Physics and Astronomy, The University of Manchester, Manchester, United Kingdom, [3] Cardiovascular Research Laboratories, Department of Physiology, Pharmacology and Neuroscience, School of Medical Sciences, University of Bristol, Bristol, United Kingdom, [4] School of Computer Science and Technology, Harbin Institute of Technology, Harbin, China, [5] Space Institute of Southern China, Shenzhen, China, [6] Key Laboratory of Medical Electrophysiology of Ministry of Education and Medical Electrophysiological Key Laboratory of Sichuan Province, Institute of Cardiovascular Research, Southwest Medical University, Luzhou, China

OPEN ACCESS

Edited by:
Olaf Doessel,
Karlsruhe Institute of Technology (KIT), Germany

Reviewed by:
Richard Gray,
United States Food and Drug Administration, United States
Socrates Dokos,
University of New South Wales, Australia

***Correspondence:**
Jules C. Hancox
jules.hancox@bristol.ac.uk
Henggui Zhang
henggui.zhang@manchester.ac.uk

Specialty section:
This article was submitted to Computational Physiology and Medicine, a section of the journal Frontiers in Physiology

Received: *01 August 2018*
Accepted: *12 December 2018*
Published: *11 January 2019*

Citation:
Whittaker DG, Hancox JC and Zhang H (2019) In silico Assessment of Pharmacotherapy for Human Atrial Patho-Electrophysiology Associated With hERG-Linked Short QT Syndrome. Front. Physiol. 9:1888. doi: 10.3389/fphys.2018.01888

Short QT syndrome variant 1 (SQT1) arises due to gain-of-function mutations to the *human Ether-à-go-go-Related Gene* (*hERG*), which encodes the α subunit of channels carrying rapid delayed rectifier potassium current, I_{Kr}. In addition to QT interval shortening and ventricular arrhythmias, SQT1 is associated with increased risk of atrial fibrillation (AF), which is often the only clinical presentation. However, the underlying basis of AF and its pharmacological treatment remain incompletely understood in the context of SQT1. In this study, computational modeling was used to investigate mechanisms of human atrial arrhythmogenesis consequent to a SQT1 mutation, as well as pharmacotherapeutic effects of selected class I drugs–disopyramide, quinidine, and propafenone. A Markov chain formulation describing wild type (WT) and N588K-hERG mutant I_{Kr} was incorporated into a contemporary human atrial action potential (AP) model, which was integrated into one-dimensional (1D) tissue strands, idealized 2D sheets, and a 3D heterogeneous, anatomical human atria model. Multi-channel pharmacological effects of disopyramide, quinidine, and propafenone, including binding kinetics for I_{Kr}/hERG and sodium current, I_{Na}, were considered. Heterozygous and homozygous formulations of the N588K-hERG mutation shortened the AP duration (APD) by 53 and 86 ms, respectively, which abbreviated the effective refractory period (ERP) and excitation wavelength in tissue, increasing the lifespan and dominant frequency (DF) of scroll waves in the 3D anatomical human atria. At the concentrations tested in this study, quinidine most effectively prolonged the APD and ERP in the setting of SQT1, followed by disopyramide and propafenone. In 2D simulations, disopyramide and quinidine promoted re-entry termination by increasing the re-entry wavelength, whereas propafenone induced secondary waves which destabilized the re-entrant circuit. In 3D simulations, the DF of re-entry was reduced in a dose-dependent manner for disopyramide and quinidine, and propafenone to a lesser extent. All of the anti-arrhythmic

agents promoted pharmacological conversion, most frequently terminating re-entry in the order quinidine > propafenone = disopyramide. Our findings provide further insight into mechanisms of SQT1-related AF and a rational basis for the pursuit of combined I_{Kr} and I_{Na} block based pharmacological strategies in the treatment of SQT1-linked AF.

Keywords: arrhythmia, short QT syndrome, atrial fibrillation, hERG, class I anti-arrhythmics, human atria, potassium channels

INTRODUCTION

The short QT syndrome (SQTS) is characterized primarily by a short QT interval on the ECG, which corresponds to abbreviated ventricular repolarisation. However, symptomatic atrial fibrillation (AF) has also been reported as a common first clinical presentation of the SQTS (Schimpf et al., 2005), suggesting that pathophysiological mechanisms leading to shortening of the QT interval also affect the atria, which can increase susceptibility to AF. The N588K mutation to the *human Ether-à-go-go-Related gene (hERG)*, which encodes the α subunit of channels carrying rapid delayed rectifier potassium current, I_{Kr}, underlies a form of SQTS variant 1 (SQT1) (Brugada et al., 2004), and has been associated with a high incidence of AF in affected probands—as high as 50% (Hu et al., 2017). Whilst ventricular arrhythmia substrates in SQT1 have received much attention (Zhang and Hancox, 2004; Patel and Antzelevitch, 2008; Adeniran et al., 2011), there have been comparatively fewer studies investigating mechanisms by which SQT1 mutations promote AF, which can be an important biomarker of the SQTS. Furthermore, effective management of AF remains a challenge, and is incompletely understood in the context of SQT1 (Enriquez et al., 2016; Hancox et al., 2018).

A previous simulation study (Loewe et al., 2014b) used the Courtemanche-Ramirez-Nattel (CRN) mathematical model of the human atrial action potential (AP) (Courtemanche et al., 1998) to demonstrate shortening of the atrial effective refractory period (ERP) and tissue excitation wavelength (WL) consequent to the N588K-hERG mutation. This was shown to facilitate initiation and sustenance of spiral waves in idealized two-dimensional (2D) sheets of human atrial tissue, which is a likely mechanism for increased susceptibility to AF. However, both the intrinsic electrical heterogeneities and complex anatomy of the human atria have also been suggested to influence arrhythmia vulnerability and dynamics in overall response to K^+ channel mutations (Colman et al., 2017; Whittaker et al., 2017b). Consequently, the first aim of the present study was to assess the arrhythmogenicity of the N588K-hERG mutation in anatomically-detailed models of the human atria with realistic structure and inclusion of regional differences in electrophysiology.

The class Ia anti-arrhythmic drug quinidine is typically used as the frontline therapy for QT interval normalization in SQT1 (Gaita et al., 2004; Giustetto, 2006; Hu et al., 2017), and disopyramide has been suggested as a possible alternative (Dumaine and Antzelevitch, 2006; Schimpf et al., 2007). Regarding management of atrial arrhythmias, the class Ic anti-arrhythmic drug propafenone has been reported to be effective at preventing recurrent episodes of (paroxysmal) AF mediated by the N588K mutation to hERG (Hong et al., 2005; Bjerregaard et al., 2006), maintaining 2 patients free of arrhythmia recurrence for >2 years (Hong et al., 2005). In an experimental setting in which a hERG activator was used to approximate SQT1, quinidine (a blocker of I_{Na} and I_{Kr}) was effective at extending atrial AP duration and ERP and preventing AF (Nof et al., 2010), more so than E-4031 (a selective I_{Kr} blocker) or lidocaine (an I_{Na} blocker) alone, suggesting that K^+ and Na^+ channel blocking effects combine synergistically for improved management of AF in SQT1. Similarly, in our previous study, a multi-scale computational modeling approach was used to investigate ventricular pharmacological effects of disopyramide and quinidine in SQT1 (Whittaker et al., 2017a), where combined I_{Na} and I_{Kr} block by both compounds was shown to prolong ERP to a greater extent than I_{Na} or I_{Kr} block alone. Mechanisms by which Na^+ and K^+-channel blocking agents may provide beneficial effects in the context of SQT1-mediated human atrial pro-arrhythmia remain unclear. A multi-scale cardiac modeling approach is being used increasingly for optimisation of therapy (Yuan et al., 2015). Consequently, the second aim of the present study was to assess the efficacy of the class I drugs disopyramide, quinidine, and propafenone on rate and rhythm control of human atrial arrhythmias mediated by SQT1, from cell to 3D tissue levels, using drug binding models (including reduced potency of drugs against SQT1 mutant I_{Kr}) with multi-channel pharmacology.

METHODS

Modeling Human Atrial Electrophysiology

Human atrial electrophysiology was simulated using the Colman et al. model (Colman et al., 2013), as updated recently (Ni et al., 2017), and is hereinafter referred to as the CNZ (Colman-Ni-Zhang) model. The equations for I_{Kr} in the CNZ model were replaced with previously developed and validated Markov chain formulations of wild type (WT) and N588K mutant I_{Kr}/hERG (Whittaker et al., 2017a). The maximal conductance of I_{Kr} was set to $g_{Kr} = 0.0111375 \cdot \left[K^+\right]_o^{0.59}$, where $\left[K^+\right]_o$ is the extracellular potassium concentration (Adeniran et al., 2011), resulting in an action potential duration (APD) at 90% repolarisation (APD_{90}) of 248.8 ms at 1 Hz in the baseline human atrial cell model, which is well within the experimentally-measured range of APDs in human atrial myocytes (Bosch et al., 1999; Kim et al., 2002; Dobrev and Ravens, 2003; Katoh et al., 2005; Redpath et al., 2006; Pau et al., 2007). A family of regional human atrial cell models was incorporated into the CNZ model, accounting for

distinct differences in electrophysiology of the right and left atrium (RA and LA, respectively), right and left atrial appendages (RAA and LAA, respectively), crista terminalis (CT), pectinate muscles (PM), atrio-ventricular ring (AVR), atrial septum (AS), Bachmann's bundle (BB), and pulmonary veins (PV) (Colman et al., 2013). Changes to maximal ionic conductances relative to the RA model implemented in order to create a family of regional cell models are given in **Table S1**. The homozygous (N588K) form of SQT1 was modeled as consisting of 100% mutant subunits, whereas the heterozygous (WT-N588K) form was assumed to consist of a 1:1 WT:mutant subunit ratio (Whittaker et al., 2017a).

Modeling Pharmacological Actions of Disopyramide and Quinidine

In our previous study (Whittaker et al., 2017a), the actions of the class Ia anti-arrhythmic drugs disopyramide and quinidine on human ventricles were simulated in the setting of SQT1. State-dependent binding of disopyramide and quinidine to hERG channels was simulated through addition of drug-bound open and inactivated states to Markov chain formulations of I_{Kr}, and the guarded receptor model (Starmer et al., 1984) was used to describe use-dependent block of fast sodium current, I_{Na}, by both agents. Furthermore, the blocking actions of disopyramide and quinidine on slow delayed rectifier potassium current, I_{Ks}, L-type calcium current, I_{CaL}, transient outward potassium current, I_{to}, inward rectifier potassium current, I_{K1} (quinidine only), and late sodium current, I_{NaL} (quinidine only), were modeled using a simple "pore block" approach. In the present study, the actions of disopyramide and quinidine on human atrial electrophysiology were represented using the same formulations and IC_{50} (half maximal inhibitory concentration) values presented in Whittaker et al. (2017a). In addition, disopyramide and quinidine have both been reported to block the atrial-specific ultra-rapid delayed rectifier potassium current, I_{Kur}. For disopyramide, the IC_{50} for block of I_{Kur} was taken to be 25.0 μM (Aréchiga et al., 2008), and for quinidine the IC_{50} was taken to be 6.6 μM, as measured in human atrial myocytes (Nenov et al., 1998). As the CNZ model does not include late sodium current, quinidine block of I_{NaL} was not included in simulations. Full details of disopyramide and quinidine models can be found in Whittaker et al. (2017a).

Modeling Pharmacological Actions of Propafenone

Using the same approach as detailed for disopyramide and quinidine in Whittaker et al. (2017a), state-dependent models of drug block by propafenone were developed. Interactions between propafenone and I_{Kr}/hERG were developed based on experimental data obtained at 37°C (Paul et al., 2002; McPate et al., 2008), where estimation of parameters for drug-bound states of the Markov chain formulation of I_{Kr} was performed using the procedure outlined in Moreno et al. (2016). Binding and unbinding rates to activated and inactivated state channels were allowed to vary freely in order to minimize the difference between simulated and experimental dose-dependent steady state block (WT and N588K), mean fractional block of tail currents during a pulse protocol, and voltage-dependence of tail current block (Paul et al., 2002; McPate et al., 2008). The extended drug-free Markov chain model of I_{Kr}/hERG is shown in **Figure 1**, as well as the close concordance between simulated and experimental data regarding propafenone block of I_{hERG}. Parameters and state affinities are given in **Table S2**.

Propafenone is a class Ic sodium channel blocking anti-arrhythmic drug (Roden, 2014). Use-dependent block of sodium channels by propafenone was represented using the guarded receptor hypothesis (Starmer et al., 1984), as described for disopyramide and quinidine. Propafenone is predominantly an open state sodium channel blocker with little to no resting state block (Edrich et al., 2005; Burashnikov et al., 2012), and was thus assumed to bind only to activated and inactivated states. Binding and unbinding parameters were constrained based on the dose-dependent, use-dependent, and steady state block of I_{Na} by propafenone (Harmer et al., 2008), as shown in **Figure 2A**. Binding and unbinding parameters and state affinities are given in **Table S3**.

Whilst propafenone most potently blocks I_{Kr} and I_{Na}, it is a multi-channel blocker, and thus exerts secondary effects on other ion channels, which were modeled using a simple pore block based on IC_{50} values from the literature. Propafenone blocks I_{CaL} with an IC_{50} of 1.5–1.7 μM in mammalian cardiac myocytes (Fei et al., 1993; Hancox and Mitcheson, 1997). In human atrial myocytes, propafenone has been shown to block I_{to} with an IC_{50} of 4.8 μM (Gross and Castle, 1998; Seki et al., 1999) and I_{K1} with an IC_{50} of 16.8 μM (Amorós et al., 2013). Finally, I_{Kur} is blocked with an IC_{50} of 4.4 μM (Franqueza et al., 1998). The therapeutic range of propafenone has been estimated to be between 2 and 6 μM (Paul et al., 2002). Taking into account plasma protein binding, estimates of the most likely unbound concentrations have been given as 0.15–0.7 μM (Slawsky and Castle, 1994), 0.2–0.6 μM (Duan et al., 1993), and 0.33–1 μM (Seki et al., 1999). In this study, the effects of three equally-spaced concentrations which fell within this range were studied—0.2, 0.5, and 0.8 μM propafenone. It should be noted that these concentrations are not intended to be compared directly with those chosen for disopyramide and quinidine (1, 2, and 5 μM), which were taken from Whittaker et al. (2017a) and are not equally-spaced. A comparison of IC_{50} values used for disopyramide, quinidine, and propafenone is given in **Table S4**.

In order to assess whether the combined actions of propafenone in the model induced reasonable rate- and concentration- dependent effects on the AP under control conditions, alterations in the maximum upstroke velocity ($\dot{V}_{max}$) upon application of propafenone were compared with experimental data taken from canine atrial cells (Burashnikov et al., 2012). **Figure 2B** shows changes in $\dot{V}_{max}$ upon application of 0.3 and 1.5 μM propafenone at cycle lengths of 500 and 300 ms, where close concordance can be seen between simulation and experiment (**Figure 2C**). Although experimental data were taken from canine atrial myocytes, the human atrial simulation data nonetheless recapitulated the considerable reduction in $\dot{V}_{max}$ at both concentrations and cycle lengths, which is primarily due to the sodium channel blocking actions of propafenone.

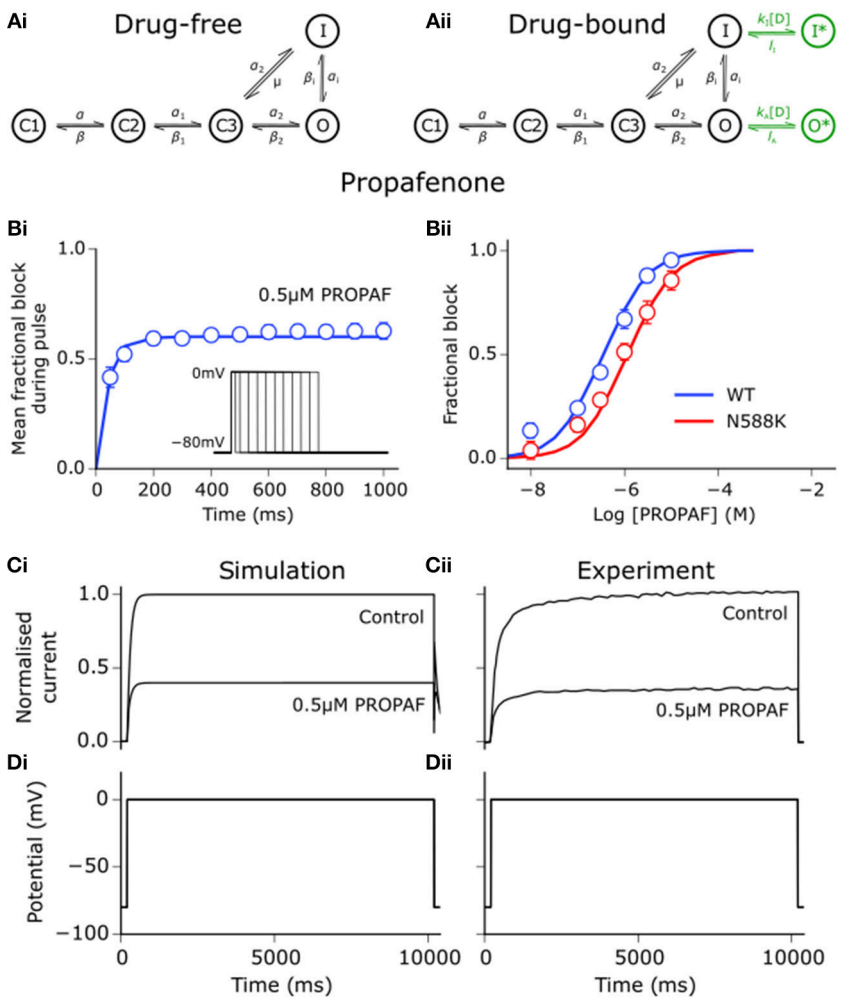

FIGURE 1 | Propafenone interactions with hERG channels. **(Ai)** Drug-free and **(Aii)** drug-bound (additional states shown in green) Markov chain models of I_{Kr}/hERG. Simulated (solid line) and experimental (points) mean fractional block by 0.5 μM propafenone (PROPAF) of I_{hERG} during pulse protocol (shown inset) **(Bi)**, and dose-response curve under WT (blue) and SQT1 mutant N588K (red) conditions **(Bii)**, where IC_{50} values are 390 nM and 936 nM (2.4-fold increase), respectively. **(Ci)** Simulated and **(Cii)** experimental current traces in response to a 10,000 ms depolarising voltage step to 0 mV from a holding potential of −80 mV **(Di,Dii)** under control conditions and with application of 0.5 μM PROPAF – these data were used to validate and not to further train the model. Experimental data at 37°C are taken from Paul et al. (2002) and McPate et al. (2008).

Tissue Simulations

Propagation of excitation waves in tissue was described using the monodomain equation,

$$\frac{\partial V}{\partial t} = \nabla\left(\mathbf{D}\nabla V\right) - \frac{I_{\text{ion}}}{C_{\text{m}}}, \tag{1}$$

where V is the transmembrane voltage, $\mathbf{D}$ is the global conductivity tensor, I_{ion} is the total ionic current, and C_{m} is the membrane capacitance. Equation (1) was solved using a finite difference PDE solver based on the explicit forward Euler method and Strang splitting scheme. Effects of the N588K-hERG mutation on ERP, WL, conduction velocity (CV), and spiral wave dynamics were determined using 1D and 2D models of RA tissue, as described previously (Whittaker et al., 2017b, 2018). Spiral waves were initiated in 2D models using an S1-S2 cross-shock protocol, and spiral wave core trajectories over a 5.0 s simulation period were traced by locating phase singularities (Bray and Wikswo, 2002). The behavior of re-entrant excitations in an anatomically-realistic setting was determined using a 3D human atrial structured grid geometry based on the Visible Female dataset (Seemann et al., 2006; Colman et al., 2013; Whittaker et al., 2017b) with rule-based fiber orientations (Krueger et al., 2011). The transverse value of the diffusion coefficient, $D_{\perp}$, was set to 0.1 mm^2 ms^{-1}, where an anisotropy ratio ($D_{||}$:$D_{\perp}$) of 3:1 in directions longitudinal and transverse to fibers was applied in the atrial working myocardium, and a ratio of 9:1 along the fast conducting bundles of the BB, CT, and PM (Colman et al., 2013; Whittaker et al., 2017b), which gave global and specific regional activation times in close agreement with experimental

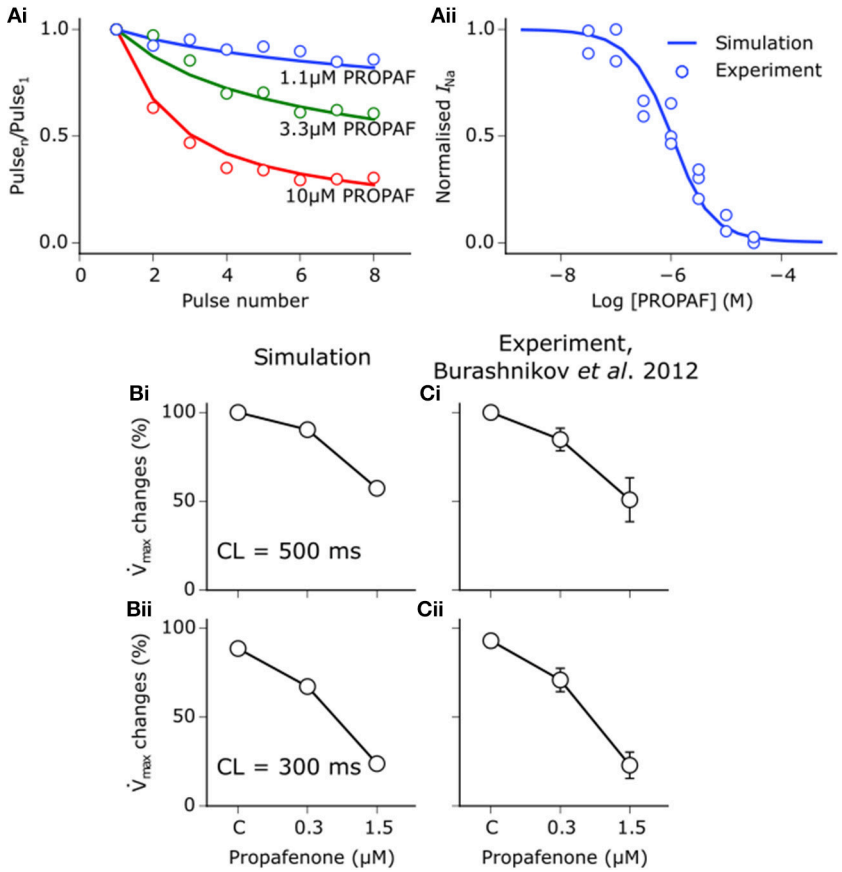

FIGURE 2 | Propafenone interactions with sodium channels. **(Ai)** Simulated (solid lines) and experimental (points) use-dependent block of sodium channels by propafenone (PROPAF) elicited using a series of 8 pulses from −90 mV to 0 mV at 3 Hz for three different test concentrations. **(Aii)** Steady state block of sodium channels using pulses from −90 mV to 0 mV at 3 Hz until a steady state was achieved. Experimental data are taken from Harmer et al. (2008), where the steady state block IC_{50} value is given as 1.4 μM. **(B)** Simulated and **(C)** experimentally-measured PROPAF-induced reduction in maximum upstroke velocity ($\dot{V}_{max}$) upon application of 0.3 and 1.5 μM PROPAF at a cycle length (CL) of (i) 500 ms and (ii) 300 ms. All $\dot{V}_{max}$ reductions are relative to the control (C) value at a CL of 500 ms. Experimental data, recorded from canine atrial myocytes, are taken from Burashnikov et al. (2012).

measurements (Lemery et al., 2007). The activation (ACT) time was defined as the time required for the membrane potential to reach −20 mV at each point in the geometry (Ni et al., 2017). Activation-recovery interval (ARI) was defined as the time interval between membrane potential depolarisation to −20 mV and repolarisation to −70 mV (adjusted to −65 mV in the PV region due to higher resting membrane potential) (Ni et al., 2017).

Re-entry was initiated using the phase distribution method (Biktashev and Holden, 1998; Whittaker et al., 2017a), by initiating either a clockwise or anti-clockwise scroll wave (as seen from a RA posterior wall view). Where sustained re-entrant activity was initiated, a power spectrum was obtained through fast Fourier transform analysis of pseudo ECG (pECG) time series (recorded from within the RA cavity). The dominant frequency (DF) was computed in Matlab from the largest peak in the power spectrum density. For simulating the effects of disopyramide, quinidine, and propafenone on re-entrant excitation, state variables for each node within the 3D anatomical model were saved after 2.5 s of a 10.0 s episode of sustained re-entrant activity in drug-free conditions. These were then used as initial conditions for new 3D simulations of duration 7.5 s (giving 10.0 s activity overall) in which varying concentrations of anti-arrhythmic drugs (1, 2, or 5 μM disopyramide and quinidine; 0.2, 0.5, or 0.8 μM propafenone) were applied immediately. This gave 18 simulations in total; 3 doses for each of the 3 anti-arrhythmic drugs, with 2 scroll wave initial conditions (both clockwise and anti-clockwise).

RESULTS

Effects of SQT1 Mutant I_{Kr} on Human Atrial Action Potentials

Both SQT1 mutant conditions shortened the human atrial APD at a pacing rate of 1 Hz (**Figure 3Ai**), from 248.8 ms in the WT condition to 195.4 and 163.3 ms in heterozygous (WT-N588K) and homozygous (N588K) mutation conditions, respectively. This was due to loss of inactivation associated with the N588K-hERG mutation, which increased I_{Kr} early

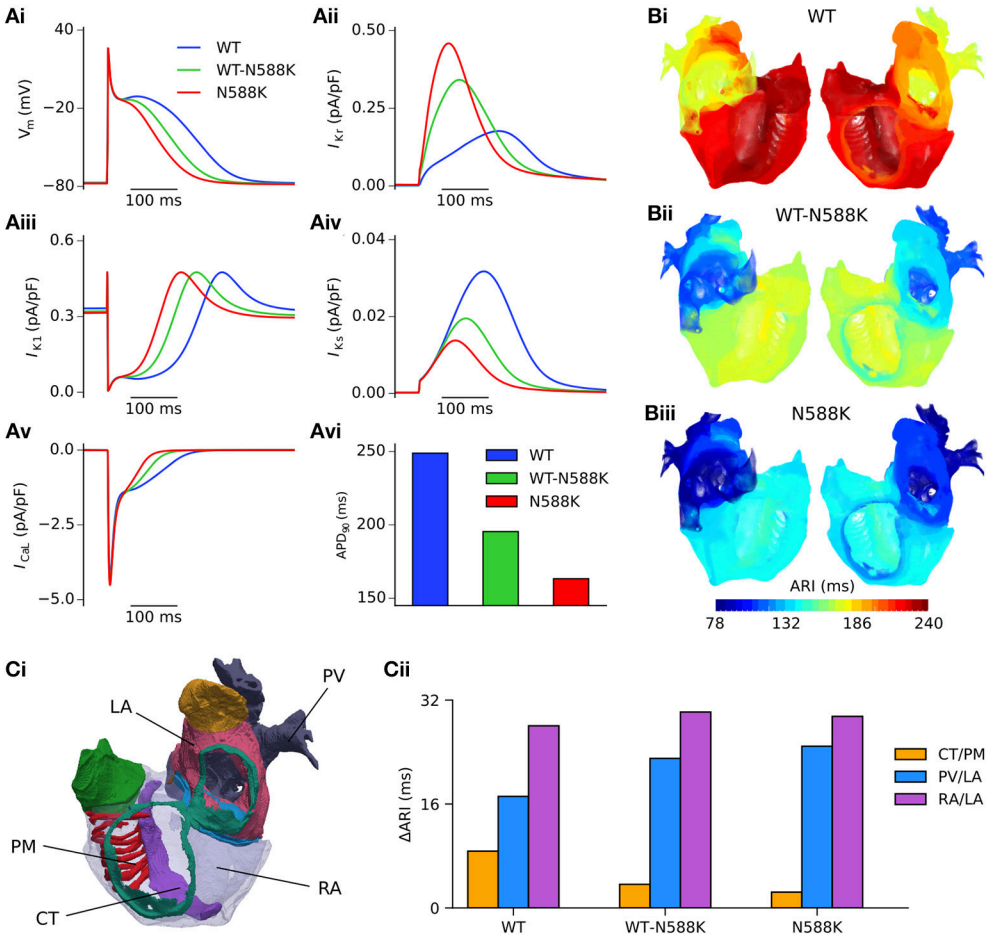

FIGURE 3 | Effects of the N588K-hERG mutation at the single cell and whole human atria level. **(Ai)** Single cell action potential profiles under WT (blue), WT-N588K (green), and N588K (red) conditions at a pacing frequency of 1 Hz, with corresponding current traces for **(Aii)** I_{Kr}, **(Aiii)** I_{K1}, **(Aiv)** I_{Ks}, and **(Av)** I_{CaL}, and **(Avi)** a summary of the measured APD_{90}. **(B)** Activation-recovery interval (ARI) maps under (i) WT, (ii) WT-N588K, and (iii) N588K conditions. **(Ci)** View looking into the cavities of the 3D anatomical human atria model, with the following regions highlighted: crista terminalis (CT), left atrium (LA), pectinate muscles (PM), pulmonary veins (PV), and right atrium (RA). **(Cii)** Measured dispersion of activation-recovery interval, ΔARI, between different atrial regions under WT and SQT1 mutation conditions.

during the AP and served to accelerate the repolarisation process (**Figure 3Aii**). Action potential abbreviation reduced considerably the duration of the plateau phase, causing I_{K1} to contribute to terminal repolarisation earlier during the AP (**Figure 3Aiii**), and lesser activation and reduced contribution of I_{Ks} (**Figure 3Aiv**). The SQT1 mutation also decreased net I_{CaL} due to the abbreviated plateau phase (**Figure 3Av**), shortening the APD_{90} under heterozygous and homozygous conditions (**Figure 3Avi**). In tissue, accelerated repolarisation under SQT1 conditions shortened the ERP and consequently the excitation WL. At the organ scale (in the 3D anatomical human atria model), both heterozygous and homozygous forms of the N588K-hERG mutation decreased global ARI (**Figure 3B**), whilst preserving the global dispersion of ARI. Furthermore, whereas ΔARI was decreased between CT/PM regions, it was increased between PV/LA and RA/LA regions under SQT1 conditions (**Figure 3C**). A summary of the effects of the N588K-hERG mutation on multi-scale human atrial AP biomarkers is given in **Table 1**.

Scroll Wave Dynamics in 3D Anatomical Human Atria Geometry

A summary of 3D scroll wave simulations in the anatomical human atria model under WT and SQT1 mutation conditions (in a clockwise configuration from a RA posterior wall aspect) is given in **Figure 4**. In the WT condition, scroll waves followed 2 transient, fragmented circuits around the RA, before self-terminating at ∼0.7 s (**Video S1**), which precluded accurate measurement of the DF. In the WT-N588K condition, re-entrant wave activity sustained for the entire 10.0 s with a DF of 4.99 Hz, and was driven mostly by a macro re-entrant circuit around the right AVR, whilst also showing CT/isthmus driven activity in the RA (**Video S2**). Under homozygous N588K mutation conditions, scroll wave activity was also driven

TABLE 1 | A summary of multi-scale simulation results.

	Single cell		1D		3D	
	APD_{90} (ms)	APD_{50} (ms)	ERP (ms)	WL (ms)	ΔARI (ms)	DF (Hz)
WT	248.8	144.6	273	198.9	77	4.19*
WT-N588K	195.4	100.3	218	158.4	77	4.99
N588K	163.3	75.3	187	135.7	71	5.59

*Analysis biomarkers at the single cell, 1D, and 3D levels under WT, WT-N588K, and N588K conditions at a pacing rate of 1 Hz. ΔARI refers to global dispersion of ARI. DF was measured from the first 5.0 s of activity. APD_{90} and APD_{50}, Action Potential Duration at 90% and 50% repolarisation respectively; ERP, Effective Refractory Period; WL, Excitation Wavelength; ARI, Activation-Recovery Interval; DF, Dominant Frequency. The DF is an average computed from two simulations with clockwise and anti-clockwise initial conditions, except in the case marked with *, in which only one value was used.*

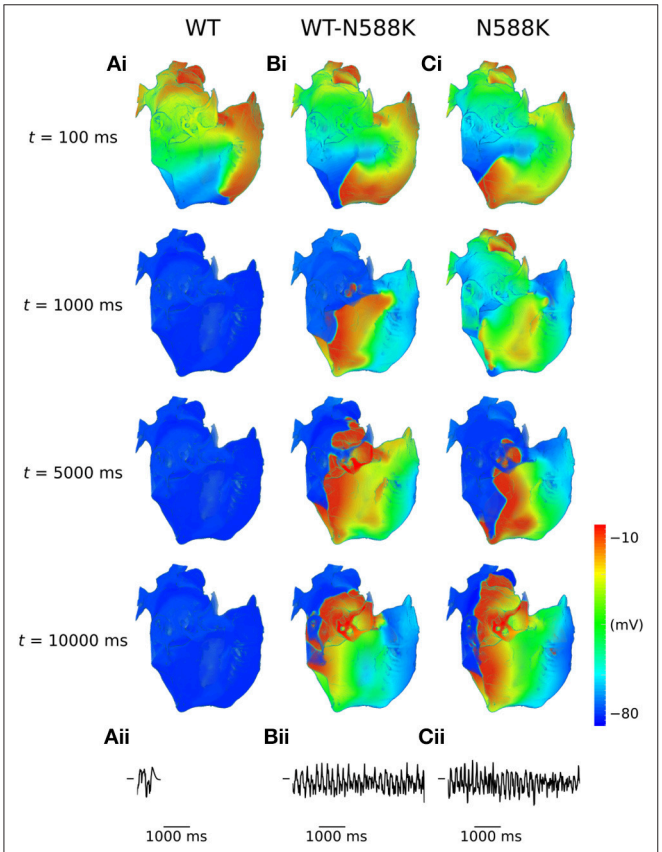

FIGURE 4 | Scroll waves under WT and SQT1 mutation conditions in the 3D anatomical human atria model. (i) Evolution of scroll waves following initiation of re-entry in a clockwise configuration (from a RA posterior wall aspect) at times $t = 100$ ms, $t = 1{,}000$ ms, $t = 5{,}000$ ms, and $t = 10{,}000$ ms under **(A)** WT, **(B)** WT-N588K, and **(C)** N588K conditions, with (ii) corresponding pseudo ECGs taken from the first 5.0 s of re-entry simulations.

predominantly by a re-entrant circuit around the AVR, with occasional existence of multiple waves on the RA free wall (**Video S3**), and a DF of 5.59 Hz. A summary of simulations using anti-clockwise scroll wave initial conditions is shown in **Figure S1**, and an average of the DF from both simulations (where applicable) measured from the first 5.0 s of activity is given in **Table 1**.

Effects of Class I Drugs on Human Atrial Action Potentials

In order to assess the actions of class I anti-arrhythmic drugs on the human atria at the cellular level, the effects of applying various concentrations of disopyramide, quinidine, and propafenone were investigated on the single cell AP under heterozygous WT-N588K (hereinafter referred to simply as SQT1) conditions. **Figure 5** shows AP profiles under drug-free SQT1 conditions and upon application of different concentrations of each drug at a pacing frequency of 1 Hz, with corresponding fractional block of I_{Kr} and I_{Na}. Application of all concentrations of disopyramide and propafenone produced only modest prolongation of the APD, failing to restore it to that of the WT condition. Quinidine, on the other hand, was more effective at prolonging the APD due to extensive I_{Kr} block, with the highest concentration (5 μM) prolonging the APD beyond that of the WT level. In contrast, all three agents prolonged the ERP effectively, restoring it to (or exceeding) that of the WT level at the highest respective concentrations tested, due to additional ERP-prolonging effects of I_{Na} block.

Conduction slowing due to sodium channel block by the three drugs caused an increase in activation time in the 3D anatomical human atria model (**Figure 5D**), which was most prominent for quinidine and least prominent for propafenone at the concentrations tested. A summary of the effects of pharmacological modulation across multiple scales is given in **Table 2**. In addition, in the 1D tissue model, the rate-dependent effects of disopyramide, quinidine, and propafenone on the ERP, CV, and WL are shown in **Figure S2**. Quinidine was shown to produce the most potent effects on CV and ERP at all pacing rates. Propafenone exerted the weakest effects on ERP at fast pacing rates, but had the greatest propensity to promote beat-to-beat alternans.

Pharmacological Effects of Class I Drugs on Re-entry Dynamics

In 2D simulations, under drug-free WT conditions the initiated spiral wave failed to re-enter the tissue (not shown). Under drug-free SQT1 conditions, the initiated spiral wave sustained for the 5.0 s duration of the simulation, eventually settling into a stationary, epicycloidal trajectory (**Figure 6Ai**). Application of 5 μM disopyramide was sufficient to terminate re-entry, as the re-entry wavelength was increased to such an extent that

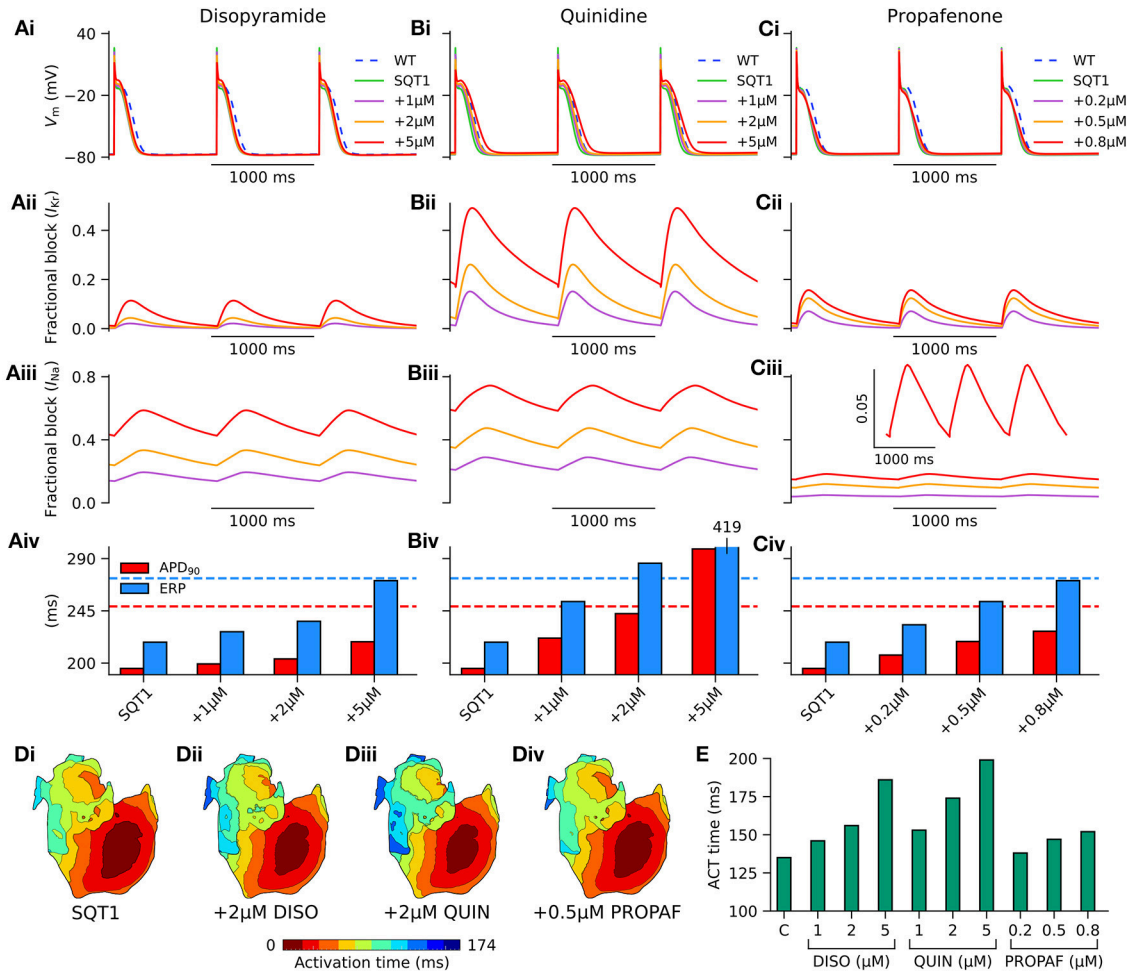

FIGURE 5 | Effects of class I drugs on human atrial electrophysiology in SQT1. Effects of **(A)** disopyramide (DISO), **(B)** quinidine (QUIN), and **(C)** propafenone (PROPAF) on (i) single human atrial cell action potentials (APs) under wild type (WT) conditions (blue, dashed line), drug-free WT-N588K (SQT1) conditions (green, solid line), and SQT1 + varying drug concentrations (purple, orange, and red solid lines). Corresponding fractional block of (ii) I_{Kr} and (iii) I_{Na}, and (iv) increase in APD_{90} (red) and effective refractory period (ERP; blue). **(D)** Activation sequences in the 3D anatomical human atria model under (i) drug-free SQT1 (control – C), (ii) SQT1 + 2 μM DISO, (iii) SQT1 + 2 μM QUIN, and (iv) SQT1 + 0.5 μM PROPAF conditions, with corresponding **(E)** activation (ACT) time summarized as a barchart. All simulations performed at a basic cycle length of 1,000 ms.

the spiral wave meandered out of the tissue (**Figure 6Aii**). On the other hand, both 1 and 2 μM disopyramide did not terminate re-entrant activity, but did increase the area over which spiral waves meandered (from 0.35 mm^2 ms^{-1} in the WT condition to 0.40 and 0.47 mm^2 ms^{-1}, respectively '(**Figure 6B**). Similarly, 1 μM quinidine increased the area of meander to 0.44 mm^2 ms^{-1} without terminating re-entry, whereas 2 and 5 μM quinidine terminated re-entry without inducing wave break (**Figure 6C**). Application of 0.2 and 0.5 μM propafenone resulted in termination of re-entry by decreasing both the stationarity and stability of spiral waves (**Figure 6D**), whereas 0.8 μM propafenone did not terminate re-entry but did destabilize the re-entrant circuit and substantially increase the area of meander (to 0.75 mm^2 ms^{-1}).

In 3D simulations using clockwise scroll wave initial conditions, quinidine terminated re-entry at all concentrations, and disopyramide terminated re-entry at concentrations of 1 and 5 μM (arrhythmia termination by 5 μM disopyramide and 2 μM quinidine are shown in **Videos S4**, **S5**, respectively). At a concentration of 2 μM disopyramide, the DF was reduced from 4.79 to 3.99 Hz (measured from the final 5.0 s of activity). Propafenone, on the other hand, was comparatively ineffective at reducing the DF at the concentrations tested, but terminated re-entry at a concentration of 0.5 μM (**Video S6**). Representative examples of arrhythmia termination by disopyramide, propafenone, and quinidine are shown in **Figure 7**. Disopyramide and quinidine produced a dose-dependent decrease in the DF which was greater than for propafenone (**Figure 7C**). In an anti-clockwise scroll wave configuration, the efficacy of anti-arrhythmic drugs was less favorable, with pharmacological conversion of re-entrant waves occurring only for 0.5 μM propafenone and 5 μM quinidine. A quantitative summary of all 2D and 3D re-entry simulations is given in **Table S5**.

TABLE 2 | A summary of multi-scale pharmacological simulation results.

		Single cell	1D			3D
		APD_{90} (ms)	ERP (ms)	CV (cm/s)	WL (mm)	ACT time (ms)
Drug-free	**SQT1**	195.4	218	72.7	158.4	135
DISO (μM)	**1**	199.3	227	68.7	155.9	146
	2	203.6	236	65.4	154.3	156
	5	218.4	271	57.8	156.5	186
QUIN (μM)	**1**	221.5	253	66.6	168.4	153
	2	242.6	286	61.6	176.1	174
	5	298.3	419	49.4	207.2	199
PROPAF (μM)	**0.2**	206.9	233	72.0	167.8	138
	0.5	218.6	253	70.6	178.7	147
	0.8	227.4	271	69.1	187.4	152

Analysis biomarkers at the single cell, 1D, and 3D levels at a pacing rate of 1 Hz under drug-free SQT1 conditions, and upon application of various concentrations of disopyramide (DISO), quinidine (QUIN), and propafenone (PROPAF). APD_{90}, Action Potential Duration at 90% repolarisation ; ERP, Effective Refractory Period; CV, Conduction Velocity; ACT time, Activation Time.

DISCUSSION

In this study, pathophysiological effects of the SQT1-related N588K-hERG mutation on human atrial electrophysiology were assessed, investigating mechanisms of increased susceptibility to the development of atrial arrhythmias in multi-scale cellular and tissue models incorporating electrical and anatomical heterogeneities. Furthermore, the actions of the class I anti-arrhythmic drugs disopyramide, quinidine, and propafenone were assessed in the context of sustained atrial arrhythmic excitations mediated by the SQT1 N588K mutation using drug simulations including binding kinetics, altered potency of I_{Kr}/hERG block in SQT1, and multiple ion channel block. Both quinidine and disopyramide have demonstrated efficacy in QT interval prolongation in the setting of SQT1 (Gaita et al., 2004; Schimpf et al., 2007; Mizobuchi et al., 2008; Giustetto et al., 2011; Hu et al., 2017), whereas propafenone has been used in 3 patients for management of episodes of paroxysmal AF mediated by SQT1, which prevented recurrence of arrhythmias but did not prolong the QT interval (Hong et al., 2005; Bjerregaard et al., 2006). This study provides clinically-relevant insights into pharmacology of SQT1 by evaluating and comparing the actions of all three drugs in the context of accelerated atrial repolarisation and arrhythmias mediated by SQT1, offering an important step toward *in silico* optimisation of pharmacological therapy in this context.

Main Findings

The major findings presented in this study are as follows. (1) Heterozygous and homozygous forms of the SQT1-linked N588K-hERG mutation shortened significantly the APD of human atrial cells, whilst preserving global dispersion of ARI, and increasing ΔARI between certain regions of the human atria. (2) The dominant frequency and lifespan of re-entry in 3D arrhythmia simulations was increased by heterozygous and homozygous forms of the N588K mutation. (3) Disopyramide, quinidine, and propafenone all produced ERP prolongation in the setting of SQT1, the extent of which was greatest for quinidine. (4) In 2D simulations, disopyramide and quinidine terminated re-entry at high concentrations due to increased re-entry wavelength, whereas propafenone terminated re-entry in a non-dose-dependent manner, by inducing secondary waves. (5) In 3D simulations, the DF of re-entry was reduced in a dose-dependent manner for clinically-relevant doses of disopyramide and quinidine, and propafenone to a lesser extent. (6) All three anti-arrhythmic agents demonstrated some efficacy in pharmacological rhythm control, most frequently terminating re-entry in the order quinidine > propafenone = disopyramide. A summary of findings regarding pro-arrhythmic mechanisms of the N588K-hERG mutation in human atria and anti-arrhythmic actions of selected class I drugs is given in **Figure 8**.

SQT1 Mutant I_{Kr} Promotes Human Atrial Arrhythmogenesis

The fact that the N588K-hERG mutation is associated with both a short QT interval and reports of AF (Hong et al., 2005) suggests that pathophysiological mechanisms leading to QT interval shortening in SQT1 also affect the atria and may promote AF. In an experimental model of SQT1, application of 20 μM of the I_{Kr} agonist PD-118057 shortened the APD in both CT and PM cell types of canine atrial tissue (Nof et al., 2010), as well as increasing APD dispersion between them. In the present study, at the cellular level heterozygous and homozygous forms of the N588K-hERG mutation produced a shortening of the human right atrial APD of 53.4 and 85.5 ms, respectively–values which are consistent with a previous simulation study (Loewe et al., 2014b). At the tissue level, global ΔARI was unaffected by the WT-N588K mutation condition, and was slightly decreased by the homozygous form. The model predicted an increase in ΔARI between PV/LA and RA/LA regions for both heterozygous and homozygous forms of the N588K mutation (**Figure 3C**), but not between CT/PM regions. This may be due to the fact that the effects of the hERG activator PD-118057 and of the N588K mutation on I_{Kr}/hERG are different: the former

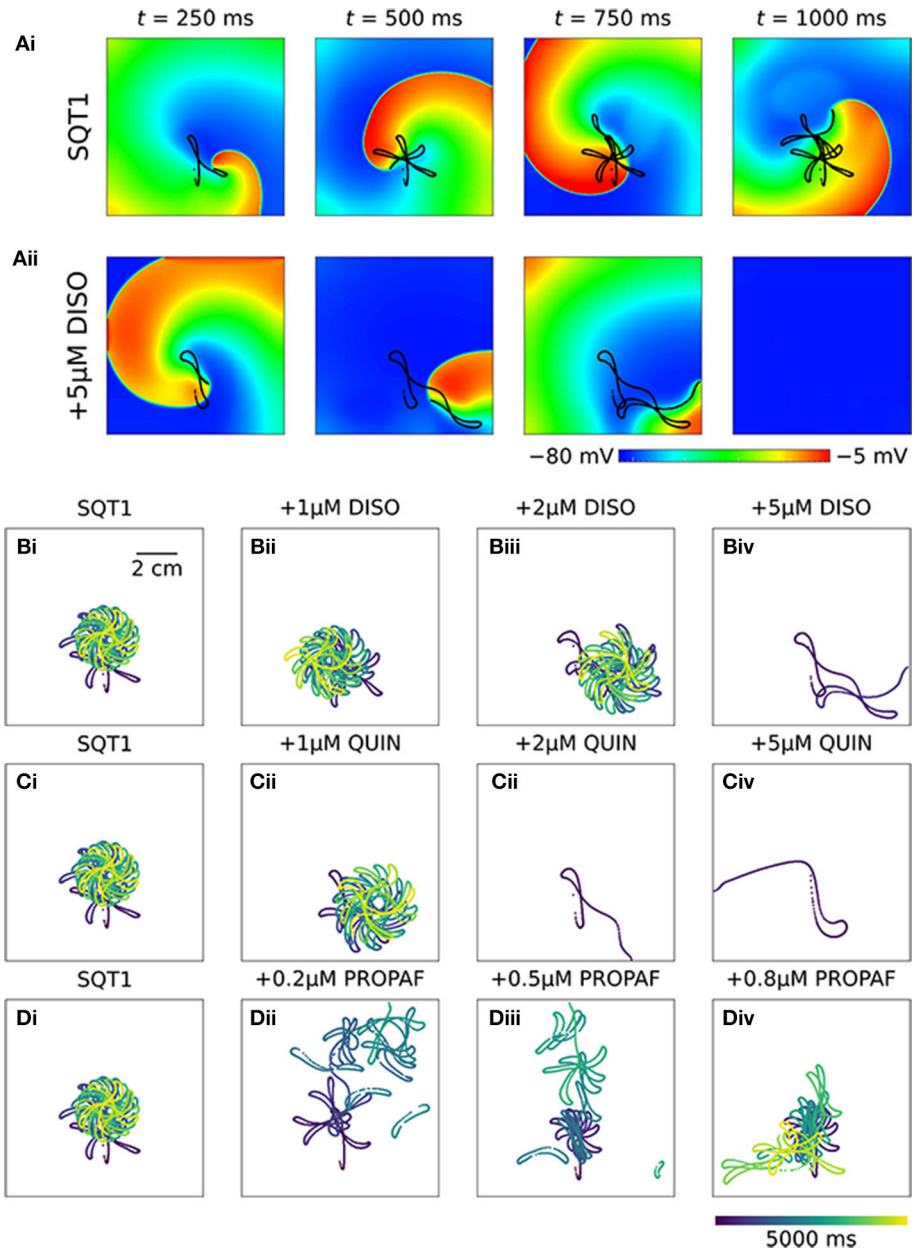

FIGURE 6 | Re-entry dynamics in homogeneous 2D sheets upon application of disopyramide, propafenone, and quinidine in SQT1 mutation conditions. **(A)** Representative snapshots of re-entrant spiral waves under (i) drug-free SQT1 and (ii) SQT1 + 5 μM disopyramide (DISO) conditions at times, $t = 250$, 500, 750, and 1,000 ms following re-entry initiation, with spiral wave core trajectories superimposed onto membrane potentials in black. Spiral wave core trajectories over a 5,000 ms period under **(Bi, Ci, Di)** drug-free SQT1 conditions, and upon application of **(Bii)** 1 μM, **(Biii)** 2 μM, and **(Biv)** 5 μM DISO, **(Cii)** 1 μM, **(Ciii)** 2 μM, and **(Civ)** 5 μM quinidine (QUIN), and **(Dii)** 0.2 μM, **(Diii)** 0.5 μM, and **(Div)** 0.8 μM propafenone (PROPAF).

increases I_{Kr}/hERG channel open probability without altering gating kinetics (Zhou et al., 2005), whereas the latter alters kinetics through profound attenuation of inactivation (Cordeiro et al., 2005; McPate et al., 2005).

Interestingly, there is clinical evidence of a LA-RA gradient in the DF in paroxysmal AF (Lazar et al., 2004), which may be underlain by APD differences between the RA and LA in pathological conditions which promote AF (Voigt et al., 2010). Furthermore, regional differences in APD between PV/LA regions have been identified previously as high frequency excitation or microreentrant sources underlying AF (Mandapati et al., 2000; Arora et al., 2003; Kumagai et al., 2004)–this suggests that localized increases in the spatial dispersion of repolarisation could be a mechanism by which atrial arrhythmogenesis is promoted in SQT1, as suggested in the previous experimental study (Nof et al., 2010).

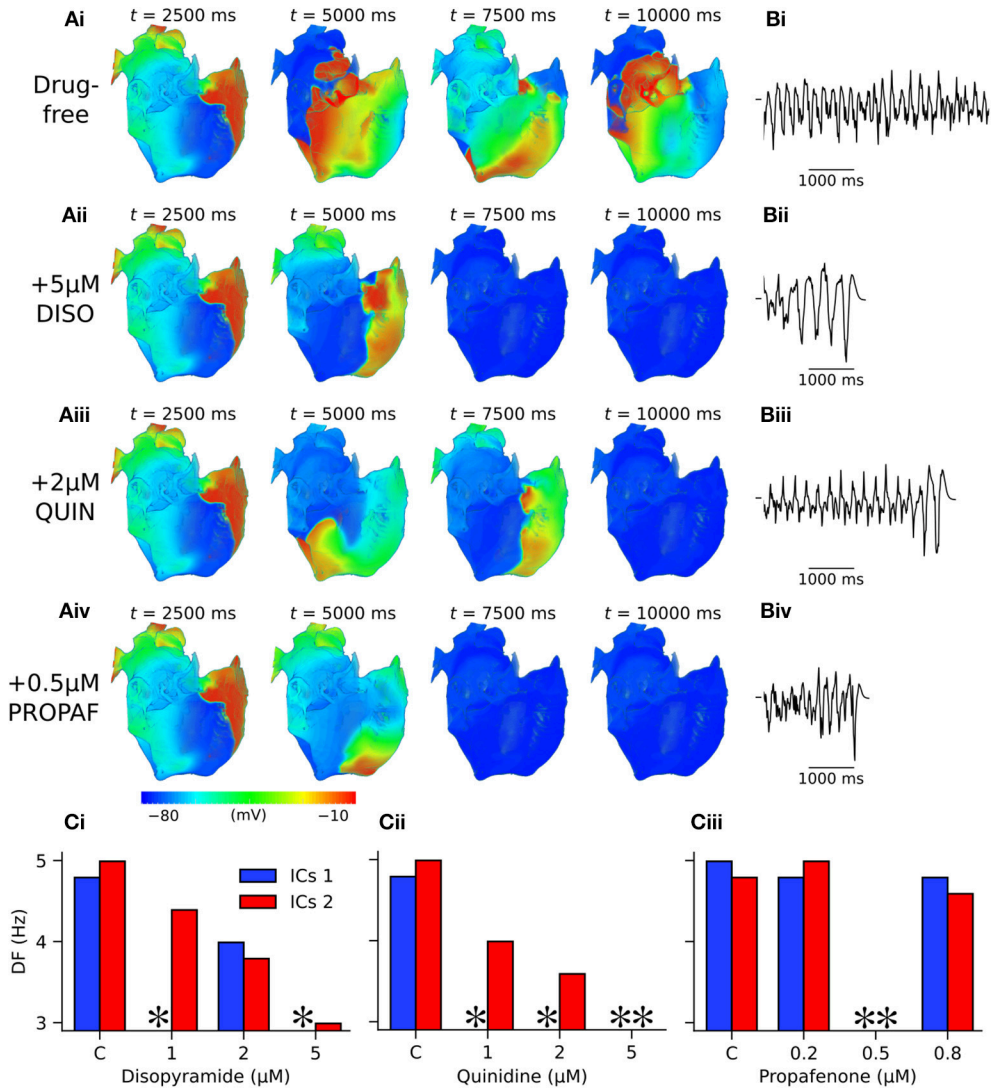

FIGURE 7 | Arrhythmia termination in 3D anatomical human atria by representative concentrations of disopyramide, propafenone, and quinidine under SQT1 mutation conditions. **(A)** Snapshots of re-entrant scroll waves in a clockwise configuration (viewed from RA posterior wall) at various time points after initiation of a scroll wave in the 3D anatomical human atrial model under (i) drug-free WT-N588K conditions, and upon application of (ii) 5 μM disopyramide (DISO), (iii) 0.5 μM propafenone (PROPAF), and (iv) 2 μM quinidine (QUIN) conditions, with **(B)** corresponding pseudo ECG recorded during the final 5.0 s. In pharmacological simulation drugs were applied at $t = 2{,}500$ ms. **(C)** Barcharts summarizing DF upon application of various concentrations of (i) DISO, (ii) PROPAF, and (iii) QUIN for clockwise and anti-clockwise initial conditions (ICs 1 and ICs 2, respectively). * denotes simulations in which DF was not calculated due to occurrence of re-entry termination.

In a previous simulation study (Loewe et al., 2014b), the N588K-hERG mutation in a 1:1 mutant to WT ratio was shown to increase inducibility and lifespan of rotors in idealized 2D sheets of human atrial tissue, but did not permit sustained re-entry. By contrast, in the present study, the heterozygous WT-N588K (SQT1) condition permitted the sustenance of spiral waves in 2D simulations. This may be due to several differences in the modeling, one of which is that the CRN model used in that study (Loewe et al., 2014b) produces an ERP restitution curve which is around 50 ms higher than available experimental data (Wilhelms et al., 2013), making re-entry more difficult to sustain, whereas the CNZ model ERP restitution curve lies mostly within the experimental range (**Figure S3**). In this study, the presence of realistic structure and heterogeneous electrophysiology, in addition to the cellular electrophysiological substrate induced by the N588K-hERG mutation, also favored the sustenance of re-entrant scroll waves in the 3D anatomical human atria model (using both clockwise and anti-clockwise scroll wave initial conditions), and could both prolong or shorten the lifespan of re-entrant excitations under pharmacological modulation conditions when compared directly to observations in 2D homogeneous sheets. This highlights the value of including both approaches in probing the arrhythmia substrate associated with genetic mutations in human atria, as behavior in heterogeneous

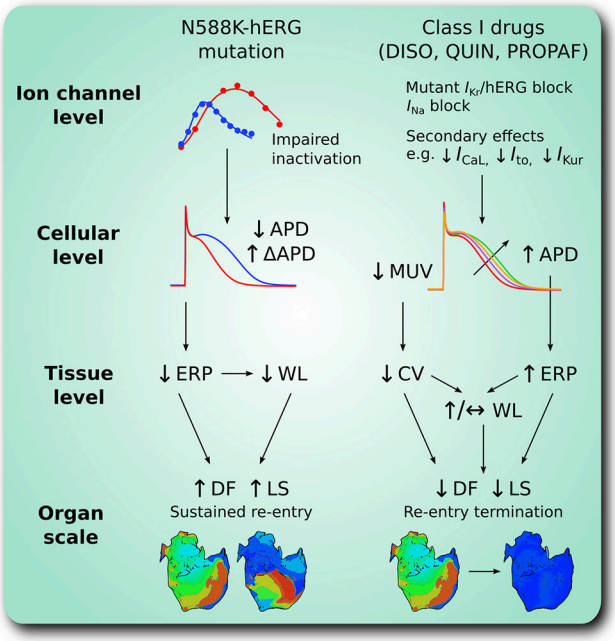

FIGURE 8 | A schematic summary of pro-arrhythmic effects of the N588K-hERG mutation in human atria and anti-arrhythmic effects of class I drugs. At the ion channel level, the N588K mutation impairs hERG channel inactivation, increasing I_{Kr} which shortens the action potential duration (APD) at the cellular level, and increases its dispersion, ΔAPD, between certain regions of the human atria. In tissue, shortened APD corresponds to shortened effective refractory period (ERP) and excitation wavelength (WL), promoting sustenance of arrhythmias at the organ scale through higher dominant frequency (DF) and lifespan (LS) of re-entry. Class I drugs disopyramide (DISO), quinidine (QUIN), and propafenone (PROPAF) exert effects at the ion channel level by blocking I_{Kr} and I_{Na}, in addition to secondary actions. This prolongs APD and ERP, and reduces maximum upstroke velocity (MUV) and conduction velocity (CV) at the cellular and tissue levels, respectively. At the organ scale these pharmacological actions promote arrhythmia rate and rhythm control through reduced DF and LS of re-entry.

3D anatomical models cannot necessarily be predicted from homogeneous 2D simulations, and vice versa. It should be noted nonetheless that electrical activity observed in 3D re-entry simulations in this study remained relatively organized and generally not driven by multiple wavelets. This lack of complex, chaotic behavior which is observed in persistent AF is consistent with reports of paroxysmal AF in some patients with the N588K-hERG mutation (Hong et al., 2005) – addition of electrical and intracellular gap junction remodeling or fibrosis in patients may be required to promote degeneration of paroxysmal AF into persistent AF.

Class I Drugs May Represent Useful SQT1-Specific Pharmacotherapy for AF

Despite the prevalence of AF and decades of research, anti-arrhythmic therapies for AF continue to have limited efficacy and safety (Workman et al., 2011). In this study, the class I anti-arrhythmic drugs disopyramide, quinidine, and propafenone were shown to be only moderately effective in the management of atrial arrhythmias mediated by the SQT1-linked N588K-hERG mutation, although it should be noted that the 7.5 s duration of 3D drug simulations is much shorter than clinical time scales. Pharmacological rhythm control occurred under application of both disopyramide and quinidine, but in an unpredictable, non-dose-dependent way, as observed in our previous *in silico* study (Whittaker et al., 2017a). One mechanism of re-entry termination involving reduction of the excitable gap under application of 5 μM quinidine is shown in **Figure S4**.

Both disopyramide and quinidine reduced consistently the DF of re-entry in a dose-dependent manner, although as in (Whittaker et al., 2017a) quinidine was more effective than disopyramide at rate control in the setting of SQT1, likely due to its more potent block of I_{Kr} (McPate et al., 2008) and I_{Na} (Koumi et al., 1992). Propafenone was comparatively ineffective at controlling the rate of atrial arrhythmias under the WT-N588K mutation condition, although did demonstrate some efficacy in re-entry termination. **Figure S5** shows a mechanism of pharmacological rhythm control by 0.5 μM propafenone, in which secondary waves induced by propafenone extinguished all re-entrant pathways. This is consistent with the use of propafenone to manage paroxysmal AF in SQT1 patients (Hong et al., 2005; Bjerregaard et al., 2006), which maintained 3 patients free of arrhythmia recurrence during follow up. However, as propafenone has been reported to have no prolonging effect on the QT interval in the setting of SQT1 (Hong et al., 2005)— an effect which was demonstrated with variable success using two leading human ventricle models (ten Tusscher and Panfilov, 2006; O'Hara et al., 2011) in **Figure S6**—it is likely that quinidine and disopyramide will remain more suitable pharmacotherapies.

In this study, cellular and tissue level simulations (in a 1D model) alone did not serve as good predictors of the overall effects of anti-arrhythmic drugs in the electrically-heterogeneous, 3D anatomical whole atria model, consistent with previous modeling studies (Varela et al., 2016; Whittaker et al., 2017b). For example, disopyramide was shown not to strongly affect the excitation WL in RA tissue (**Table 2**; **Figure S2**), and yet it decreased reliably the DF of re-entrant excitations under heterozygous N588K mutation conditions in 3D simulations. This is likely due to the fact that scroll waves were largely anatomically driven by a typical macro re-entrant atrial flutter/tachycardia circuit (Lee et al., 2012) which was larger than the functional WL; effects of disopyramide on CV were thus more important. In contrast, propafenone produced only modest changes to the CV and was thus less effective at rate control in the model, but did terminate re-entry under conditions in which the re-entrant circuit was abolished by interaction with secondary waves (**Figure S5**).

Insights Into the Efficacy of Class I Drugs in SQT1

Further support for quinidine as a useful pharmacotherapy for AF in the setting of SQT1 comes from the experimental use

of the I_{Kr} agonist PD-118057 model (Nof et al., 2010). That study suggested that the combined blocking actions on I_{Kr} and I_{Na} are what made quinidine effective at preventing sustained AF in canine right atrial tissue preparations, as neither I_{Kr} nor I_{Na} block alone (by E-4031 or lidocaine, respectively) was effective at terminating AF. Similarly, in our previous simulation study of ventricular pharmacotherapy for SQT1 we showed that combined block of I_{Na} and I_{Kr} by disopyramide and quinidine prolonged the ERP to a greater extent than block of I_{Na} or I_{Kr} alone (Whittaker et al., 2017a). In this study, we sought to determine whether the greater ERP prolongation associated with the synergistic combination of I_{Na} and I_{Kr} block by class I drugs would also translate to greater efficacy in terminating re-entry in a 2D sheet of SQT1 mutant human atrial tissue. **Figure S7** shows that the actions of 5 μM of a hypothetical drug with disopyramide kinetics for I_{Na} and I_{Kr} block were able to terminate re-entry, whereas I_{Na} or I_{Kr} block alone did not, as combined block produced the greatest prolongation of the ERP. The spiral wave trajectories highlight the fact that I_{Na} block in particular destabilized the re-entrant circuit, which, when combined with I_{Kr} block, caused the spiral wave to meander out of the tissue boundaries (**Video S7**). The findings from *in silico* and *in vitro* experiments thus suggest that the combination of prolonged APD and refractoriness arising from K^+ and Na^+ channel inhibition is likely to be valuable in the setting of SQT1. Though selective blockers of I_{Ks} and I_{K1} are not yet clinically-available, this combination may also warrant investigation as a pharmacotherapeutic strategy for other forms of K^+-linked SQTS (SQT2 and SQT3).

LIMITATIONS

There are a number of limitations of the simulations presented in this study. The 3D anatomical human atria model which was employed for simulations in this study incorporated rule-based fiber orientations (Krueger et al., 2011), which may not capture sufficiently the complex cardiac microstructure of the human atria (Stephenson et al., 2017) which could contribute to the arrhythmia substrate. Whilst several hERG mutations have now been identified in SQT1 (Hancox et al., 2018), the present study focused only on the N588K-hERG mutation (which produces a more marked effect on hERG kinetics than some other mutations, Hancox et al., 2018), so the results here may not apply to all forms of SQT1. However, recently the S631A-hERG mutation (previously engineered for hERG structure-function studies), which produces a similar extent of attenuation of inactivation to N588K-hERG (McPate et al., 2008) has been reported in an SQT1 family (Akdis et al., 2018), and thus the findings of this study are likely also to be relevant to that form of SQT1. An additional potential limitation arises from the fact that mechanical contraction was not considered, which has been reported previously to be impaired in the setting of SQT1 in single human atrial cell simulations (Whittaker et al., 2015) as well as in organ-scale ventricle simulations (Adeniran et al., 2013), and based on clinical measurements (Frea et al., 2015).

The models of disopyramide and quinidine used in this study were adopted from (Whittaker et al., 2017a), in which the effects of anti-arrhythmic drugs were assessed in the setting of SQT1 in the human ventricles. However, both agents also exhibit modest anti-cholinergic effects in the atria (Nakajima et al., 1989) which were not accounted for, due to the absence of a formulation for acetylcholine-activated potassium current, $I_{K,ACh}$, in the CNZ model. Similarly, the β-adrenergic receptor blocking effects of propafenone were not considered (McLeod et al., 1984). Inclusion of these factors could give some insight into the response of the SQT1 phenotype to anti-arrhythmic drugs in the presence of autonomic modulation, and could give more favorable results in terms of arrhythmia prevention, especially for propafenone, which may be particularly effective against AF triggered by increased vagal tone. In addition, dynamic effects of agents due to the influence of circadian variations in drug concentration and heart rate on bioavailability were not investigated, which can give further insights into differing clinical efficacies of drugs (Loewe et al., 2014a). In relation to this, a further, more general limitation is that translation of drug concentrations from experiments and computer simulations to meaningful clinical concentrations is potentially problematic. Finally, whilst the 1:1 mutant to WT ratio, which was intended to represent the heterozygous state of the proband, may represent an oversimplification of the real hERG channel population in SQT1, the approach adopted in this and our previous studies (Adeniran et al., 2011, 2017; Whittaker et al., 2017a) reproduced quantitatively QT interval shortening and T wave morphology in SQTS conditions which was concordant with clinical observations.

CONCLUSIONS

The simulations performed in this study further substantiate a causative link between the SQTS-related N588K mutation and APD/ERP shortening in human atria, as well as increased spatial dispersion of repolarisation, which promotes development of AF. In 3D human atria simulations which included heterogeneous anatomy and electrophysiology, the N588K mutation was shown to increase the dominant frequency and lifespan of re-entrant excitation beyond that observed in WT conditions. Pharmacological simulations demonstrated that disopyramide and quinidine were more effective at rate control than propafenone in the setting of SQT1, and quinidine was most effective at rhythm control. Combined block of I_{Na} and I_{Kr} by a hypothetical drug was shown to be more beneficial in terms of re-entry termination in a 2D sheet of human atrial tissue than I_{Kr} or I_{Na} block alone in this context, suggesting useful targets for future pharmacotherapies. The multi-scale integrative cardiac modeling approach adopted in this study serves as a useful paradigm for optimisation of pharmacological therapy, allowing investigation of how genetic defects at the ion channel level influence organ scale propagation, arrhythmogenesis, and response to pharmacotherapies.

AUTHOR CONTRIBUTIONS

DW, JH, and HZ conceived the experiments and wrote the manuscript. DW developed and validated computer models and performed numerical experiments and analysis.

FUNDING

DW was supported by the British Heart Foundation (FS/14/5/30533–HZ and JH) and is now supported by a Wellcome Trust ISSF fellowship (204825/Z/16/Z). This work was also supported by grants from EPSRC (UK) (EP/J00958X/1; EP/I029826/1), MC-IRSES CORDIS3D (317766), NSFC (61179009), Shenzhen Science and Technology Innovation Committee (JCYJ20151029173639477; JSGG20160229125049615. The funders had no role in study design, data collection and analysis, decision to publish, or preparation of the manuscript.

ACKNOWLEDGMENTS

JH gratefully acknowledges receipt of a University of Bristol research fellowship.

SUPPLEMENTARY MATERIAL

The Supplementary Material for this article can be found online at: https://www.frontiersin.org/articles/10.3389/fphys.2018.01888/full#supplementary-material

REFERENCES

Adeniran, I., Hancox, J. C., and Zhang, H. (2013). *In silico* investigation of the short QT syndrome, using human ventricle models incorporating electromechanical coupling. *Front. Physiol.* 4:166. doi: 10.3389/fphys.2013.00166

Adeniran, I., McPate, M. J., Witchel, H. J., Hancox, J. C., and Zhang, H. (2011). Increased vulnerability of human ventricle to re-entrant excitation in hERG-linked variant 1 short QT syndrome. *PLoS Comput. Biol.* 7:e1002313. doi: 10.1371/journal.pcbi.1002313

Adeniran, I., Whittaker, D. G., Harchi, A. E., Hancox, J. C., and Zhang, H. (2017). *In silico* investigation of a KCNQ1 mutation associated with short QT syndrome. *Sci. Rep.* 7:8469. doi: 10.1038/s41598-017-08367-2

Akdis, D., Saguner, A. M., Medeiros-Domingo, A., Schaller, A., Balmer, C., Steffel, J., et al. (2018). Multiple clinical profiles of families with the short QT syndrome. *EP Eur.* 20, f113–f121. doi: 10.1093/europace/eux186

Amorós, I., Dolz-Gaitón, P., Gómez, R., Matamoros, M., Barana, A., de la Fuente, M. G., et al. (2013). Propafenone blocks human cardiac Kir2.x channels by decreasing the negative electrostatic charge in the cytoplasmic pore. *Biochem. Pharmacol.* 86, 267–278. doi: 10.1016/j.bcp.2013.04.023

Aréchiga, I. A., Barrio-Echavarria, G. F., Rodríguez-Menchaca, A. A., Moreno-Galindo, E. G., Decher, N., Tristani-Firouzi, M., et al. (2008). Kv1.5 open channel block by the antiarrhythmic drug disopyramide: molecular determinants of block. *J. Pharmacol. Sci.* 108, 49–55. doi: 10.1254/jphs.08084FP

Arora, R., Verheule, S., Scott, L., Navarrete, A., Katari, V., Wilson, E., et al. (2003). Arrhythmogenic substrate of the pulmonary veins assessed by high-resolution optical mapping. *Circulation* 107, 1816–1821. doi: 10.1161/01.CIR.0000058461.86339.7E

Biktashev, V. N., and Holden, A. V. (1998). Reentrant waves and their elimination in a model of mammalian ventricular tissue. *Chaos. Interdiscip. J. Nonlinear Sci.* 8, 48–56. doi: 10.1063/1.166307

Bjerregaard, P., Jahangir, A., and Gussak, I. (2006). Targeted therapy for short QT syndrome. *Expert Opin. Ther. Targets* 10, 393–400. doi: 10.1517/14728222.10.3.393

Bosch, R. F., Zeng, X., Grammer, J. B., Popovic, K., Mewis, C., and Kühlkamp, V. (1999). Ionic mechanisms of electrical remodeling in human atrial fibrillation. *Cardiovasc. Res.* 44, 121–131. doi: 10.1016/S0008-6363(99)00178-9

Bray, M.-A., and Wikswo, J. P. (2002). Use of topological charge to determine filament location and dynamics in a numerical model of scroll wave activity. *IEEE Trans. Biomed. Eng.* 49, 1086–1093. doi: 10.1109/TBME.2002.803516

Brugada, R., Hong, K., Dumaine, R., Cordeiro, J., Gaita, F., Borggrefe, M., et al. (2004). Sudden death associated with Short-QT syndrome linked to mutations in HERG. *Circulation* 109, 30–35. doi: 10.1161/01.CIR.0000109482.92774.3A

Burashnikov, A., Belardinelli, L., and Antzelevitch, C. (2012). Atrial-selective sodium channel block strategy to suppress atrial fibrillation: ranolazine versus propafenone. *J. Pharmacol. Exp. Ther.* 340, 161–168. doi: 10.1124/jpet.111.186395

Colman, M. A., Aslanidi, O. V., Kharche, S., Boyett, M. R., Garratt, C., Hancox, J. C., et al. (2013). Pro-arrhythmogenic effects of atrial fibrillation-induced electrical remodelling: insights from the three-dimensional virtual human atria. *J. Physiol.* 591, 4249–4272. doi: 10.1113/jphysiol.2013.254987

Colman, M. A., Ni, H., Liang, B., Schmitt, N., and Zhang, H. (2017). *In silico* assessment of genetic variation in KCNA5 reveals multiple mechanisms of human atrial arrhythmogenesis. *PLOS. Comput. Biol.* 13:e1005587. doi: 10.1371/journal.pcbi.1005587

Cordeiro, J. M., Brugada, R., Wu, Y. S., Hong, K., and Dumaine, R. (2005). Modulation of IKr inactivation by mutation N588K in KCNH2: A link to arrhythmogenesis in short QT syndrome. *Cardiovasc. Res.* 67, 498–509. doi: 10.1016/j.cardiores.2005.02.018

Courtemanche, M., Ramirez, R. J., and Nattel, S. (1998). Ionic mechanisms underlying human atrial action potential properties: insights from a mathematical model. *Am. J. Physiol. Heart Circ. Physiol.* 275, H301–H321.

Dobrev, D., and Ravens, U. (2003). Remodeling of cardiomyocyte ion channels in human atrial fibrillation. *Basic Res. Cardiol.* 98, 137–148. doi: 10.1007/s00395-003-0409-8

Duan, D., Fermini, B., and Nattel, S. (1993). Potassium channel blocking properties of propafenone in rabbit atrial myocytes. *J. Pharmacol. Exp. Ther.* 264, 1113–1123.

Dumaine, R., and Antzelevitch, C. (2006). Disopyramide: although potentially life-threatening in the setting of long QT, could it be life-saving in short QT syndrome? *J. Mol. Cell. Cardiol.* 41, 421–423. doi: 10.1016/j.yjmcc.2006.06.070

Edrich, T., Wang, S.-Y., and Wang, G. K. (2005). State-dependent block of human cardiac hNav1.5 sodium channels by propafenone. *J. Membr. Biol.* 207, 35–43. doi: 10.1007/s00232-005-0801-4

Enriquez, A., Antzelevitch, C., Bismah, V., and Baranchuk, A. (2016). Atrial fibrillation in inherited cardiac channelopathies: from mechanisms to management. *Heart Rhythm.* 13, 1878–1884. doi: 10.1016/j.hrthm.2016.06.008

Fei, L., Gill, J. S., McKenna, W. J., and Camm, A. J. (1993). Effects of propafenone on calcium currents in single ventricular myocytes of guinea-pig. *Br. J. Pharmacol.* 109, 178–182. doi: 10.1111/j.1476-5381.1993.tb13550.x

Franqueza, L., Valenzuela, C., Delpón, E., Longobardo, M., Caballero, R., and Tamargo, J. (1998). Effects of propafenone and 5-hydroxy-propafenone on hKv1.5 channels. *Br. J. Pharmacol.* 125, 969–978. doi: 10.1038/sj.bjp.0702129

Frea, S., Giustetto, C., Capriolo, M., Scrocco, C., Fornengo, C., Benedetto, S., et al. (2015). New echocardiographic insights in short QT syndrome: more than a channelopathy? *Heart Rhythm.* 12, 2096–2105. doi: 10.1016/j.hrthm.2015.05.024

Gaita, F., Giustetto, C., Bianchi, F., Schimpf, R., Haissaguerre, M., Cal,ò, L., et al. (2004). Short QT syndrome: pharmacological treatment. *J. Am. Coll. Cardiol.* 43, 1494–1499. doi: 10.1016/j.jacc.2004.02.034

Giustetto, C. (2006). "Quinidine to treat short QT syndrome: a real alternative to ICD?," in *Cardiac Arrhythmias 2005*, ed. A. R. MD (Milan: Springer), 333–335.

Giustetto, C., Schimpf, R., Mazzanti, A., Scrocco, C., Maury, P., Anttonen, O., et al. (2011). Long-term follow-Up of patients with short QT syndrome. *J. Am. Coll. Cardiol.* 58, 587–595. doi: 10.1016/j.jacc.2011.03.038

Gross, G. J., and Castle, N. A. (1998). Propafenone inhibition of human atrial myocyte repolarizing currents. *J. Mol. Cell. Cardiol.* 30, 783–793. doi: 10.1006/jmcc.1998.0643

Hancox, J. C., and Mitcheson, J. S. (1997). Inhibition of L-type calcium current by propafenone in single myocytes isolated from the rabbit atrioventricular node. *Br. J. Pharmacol.* 121, 7–14. doi: 10.1038/sj.bjp.0701086

Hancox, J. C., Whittaker, D. G., Du, C., Stuart, A. G., and Zhang, H. (2018). Emerging therapeutic targets in the short QT syndrome. *Expert Opin. Ther. Targets* 22:439–51. doi: 10.1080/14728222.2018.1470621

Harmer, A. R., Abi-Gerges, N., Easter, A., Woods, A., Lawrence, C. L., Small, B. G., et al. (2008). Optimisation and validation of a medium-throughput electrophysiology-based hNav1.5 assay using IonWorks^{TM}. *J. Pharmacol. Toxicol. Methods* 57, 30–41. doi: 10.1016/j.vascn.2007.09.002

Hong, K., Bjerregaard, P., Gussak, I., and Brugada, R. (2005). Short QT syndrome and atrial fibrillation caused by mutation in KCNH2. *J. Cardiovasc. Electrophysiol.* 16, 394–396. doi: 10.1046/j.1540-8167.2005.40621.x

Hu, D., Li, Y., Zhang, J., Pfeiffer, R., Gollob, M. H., Healey, J., et al. (2017). The phenotypic spectrum of a mutation hotspot responsible for the short QT syndrome. *JACC. Clin. Electrophysiol.* 3, 727–43. doi: 10.1016/j.jacep.2016.11.013

Katoh, H., Shinozaki, T., Baba, S., Satoh, S., Kagaya, Y., Watanabe, J., et al. (2005). Monophasic action potential duration at the crista terminalis in patients with sinus node disease. *Circ. J.* 69, 1361–1367. doi: 10.1253/circj.69.1361

Kim, B.-S., Kim, Y.-H., Hwang, G.-S., Pak, H.-N., Lee, S. C., Shim, W. J., et al. (2002). Action potential duration restitution kinetics in human atrial fibrillation. *J. Am. Coll. Cardiol.* 39, 1329–1336. doi: 10.1016/S0735-1097(02)01760-6

Koumi, S., Sato, R., Katori, R., Hisatome, I., Nagasawa, K., and Hayakawa, H. (1992). Sodium channel states control binding and unbinding behaviour of antiarrhythmic drugs in cardiac myocytes from the guinea pig. *Cardiovasc. Res.* 26, 1199–1205. doi: 10.1093/cvr/26.12.1199

Krueger, M. W., Schmidt, V., Tobón, C., Weber, F. M., Lorenz, C., Keller, D. U. J., et al. (eds.). (2011). "Modeling atrial fiber orientation in patient-specific geometries: a semi-automatic rule-based approach," in *Functional Imaging and Modeling of the Heart Lecture Notes in Computer Science*. (Springer, Berlin, Heidelberg), 223–232.

Kumagai, K., Ogawa, M., Noguchi, H., Yasuda, T., Nakashima, H., and Saku, K. (2004). Electrophysiologic properties of pulmonary veins assessed using a multielectrode basket catheter. *J. Am. Coll. Cardiol.* 43, 2281–2289. doi: 10.1016/j.jacc.2004.01.051

Lazar, S., Dixit, S., Marchlinski, F. E., Callans, D. J., and Gerstenfeld, E. P. (2004). Presence of left-to-right atrial frequency gradient in paroxysmal but not persistent atrial fibrillation in humans. *Circulation* 110, 3181–3186. doi: 10.1161/01.CIR.0000147279.91094.5E

Lee, G., Sanders, P., and Kalman, J. M. (2012). Catheter ablation of atrial arrhythmias: state of the art. *Lancet* 380, 1509–1519. doi: 10.1016/S0140-6736(12)61463-9

Lemery, R., Birnie, D., Tang, A. S., l., Green, M., Gollob, M., Hendry, M., et al. (2007). Normal atrial activation and voltage during sinus rhythm in the human heart: an endocardial and epicardial mapping study in patients with a history of atrial fibrillation. *J. Cardiovasc. Electrophysiol.* 18, 402–408. doi: 10.1111/j.1540-8167.2007.00762.x

Loewe, A., Lutz, Y., Wilhelms, M., Sinnecker, D., Barthel, P., Scholz, E. P., et al. (2014a). *In-silico* assessment of the dynamic effects of amiodarone and dronedarone on human atrial patho-electrophysiology. *Europace* 16, iv30–iv38. doi: 10.1093/europace/euu230

Loewe, A., Wilhelms, M., Fischer, F., Scholz, E. P., Dössel, O., and Seemann, G. (2014b). Arrhythmic potency of human ether-à-go-go-related gene mutations L532P and N588K in a computational model of human atrial myocytes. *Europace* 16, 435–443. doi: 10.1093/europace/eut375

Mandapati, R., Skanes, A., Chen, J., Berenfeld, O., and Jalife, J. (2000). Stable microreentrant sources as a mechanism of atrial fibrillation in the isolated sheep heart. *Circulation* 101, 194–199. doi: 10.1161/01.CIR.101.2.194

McLeod, A. A., Stiles, G. L., and Shand, D. G. (1984). Demonstration of beta adrenoceptor blockade by propafenone hydrochloride: clinical pharmacologic, radioligand binding and adenylate cyclase activation studies. *J. Pharmacol. Exp. Ther.* 228, 461–466.

McPate, M. J., Duncan, R. S., Hancox, J. C., and Witchel, H. J. (2008). Pharmacology of the short QT syndrome N588K-hERG K+ channel mutation: differential impact on selected class I and class III antiarrhythmic drugs. *Br. J. Pharmacol.* 155, 957–966. doi: 10.1038/bjp.2008.325

McPate, M. J., Duncan, R. S., Milnes, J. T., Witchel, H. J., and Hancox, J. C. (2005). The N588K-HERG K^+ channel mutation in the 'short QT syndrome': mechanism of gain-in-function determined at 37 °C. *Biochem. Biophys. Res. Commun.* 334, 441–449. doi: 10.1016/j.bbrc.2005.06.112

Mizobuchi, M., Enjoji, Y., Yamamoto, R., Ono, T., Funatsu, A., Kambayashi, D., et al. (2008). Nifekalant and disopyramide in a patient with short QT syndrome: evaluation of pharmacological effects and electrophysiological properties. *Pacing Clin. Electrophysiol.* 31, 1229–1232. doi: 10.1111/j.1540-8159.2008.01169.x

Moreno, J. D., Lewis, T. J., and Clancy, C. E. (2016). Parameterization for *in-silico* modeling of ion channel interactions with drugs. *PLoS ONE* 11:e0150761. doi: 10.1371/journal.pone.0150761

Nakajima, T., Kurachi, Y., Ito, H., Takikawa, R., and Sugimoto, T. (1989). Anticholinergic effects of quinidine, disopyramide, and procainamide in isolated atrial myocytes: mediation by different molecular mechanisms. *Circ. Res.* 64, 297–303. doi: 10.1161/01.RES.64.2.297

Nenov, N. I., Crumb, W. J., Pigott, J. D., Harrison, L. H., and Clarkson, C. W. (1998). Quinidine interactions with human atrial potassium channels. *Circ. Res.* 83, 1224–1231. doi: 10.1161/01.RES.83.12.1224.

Ni, H., Whittaker, D. G., Wang, W., Giles, W. R., Narayan, S. M., and Zhang, H. (2017). Synergistic anti-arrhythmic effects in human atria with combined use of sodium blockers and acacetin. *Front. Physiol.* 8:946. doi: 10.3389/fphys.2017.00946

Nof, E., Burashnikov, A., and Antzelevitch, C. (2010). Cellular basis for atrial fibrillation in an experimental model of short QT1: Implications for a pharmacological approach to therapy. *Heart Rhythm* 7, 251–257. doi: 10.1016/j.hrthm.2009.10.017

O'Hara, T., Virág, L., Varr,ó, A., and Rudy, Y. (2011). Simulation of the undiseased human cardiac ventricular action potential: model formulation and experimental validation. *PLoS Comput. Biol.* 7:e1002061. doi: 10.1371/journal.pcbi.1002061

Patel, C., and Antzelevitch, C. (2008). Cellular basis for arrhythmogenesis in an experimental model of the SQT1 form of the short QT syndrome. *Heart Rhythm* 5, 585–590. doi: 10.1016/j.hrthm.2008.01.022

Pau, D., Workman, A. J., Kane, K. A., and Rankin, A. C. (2007). Electrophysiological and arrhythmogenic effects of 5-hydroxytryptamine on human atrial cells are reduced in atrial fibrillation. *J. Mol. Cell. Cardiol.* 42, 54–62. doi: 10.1016/j.yjmcc.2006.08.007

Paul, A. A., Witchel, H. J., and Hancox, J. C. (2002). Inhibition of the current of heterologously expressed HERG potassium channels by flecainide and comparison with quinidine, propafenone and lignocaine. *Br. J. Pharmacol.* 136, 717–729. doi: 10.1038/sj.bjp.0704784

Redpath, C. J., Rankin, A. C., Kane, K. A., and Workman, A. J. (2006). Anti-adrenergic effects of endothelin on human atrial action potentials are potentially anti-arrhythmic. *J. Mol. Cell. Cardiol.* 40, 717–724. doi: 10.1016/j.yjmcc.2006.01.012

Roden, D. M. (2014). Pharmacology and toxicology of Nav1.5-class 1 anti-arrhythmic drugs. *Card. Electrophysiol. Clin.* 6, 695–704. doi: 10.1016/j.ccep.2014.07.003

Schimpf, R., Veltmann, C., Giustetto, C., Gaita, F., Borggrefe, M., and Wolpert, C. (2007). *In vivo* effects of mutant HERG K+ channel inhibition by disopyramide in patients with a short QT-1 syndrome: a pilot study. *J. Cardiovasc. Electrophysiol.* 18, 1157–1160. doi: 10.1111/j.1540-8167.2007.00925.x

Schimpf, R., Wolpert, C., Gaita, F., Giustetto, C., and Borggrefe, M. (2005). Short QT syndrome. *Cardiovasc. Res.* 67, 357–366. doi: 10.1016/j.cardiores.2005.03.026

Seemann, G., Höper, C., Sachse, F. B., Dössel, O., Holden, A. V., and Zhang, H. (2006). Heterogeneous three-dimensional anatomical and electrophysiological model of human atria. *Philos. Trans. R. Soc. Lond. Math. Phys. Eng. Sci.* 364, 1465–1481. doi: 10.1098/rsta.2006.1781

Seki, A., Hagiwara, N., and Kasanuki, H. (1999). Effects of propafenone on K currents in human atrial myocytes. *Br. J. Pharmacol.* 126, 1153–1162. doi: 10.1038/sj.bjp.0702428

Slawsky, M. T., and Castle, N. A. (1994). K+ channel blocking actions of flecainide compared with those of propafenone and quinidine in adult rat ventricular myocytes. *J. Pharmacol. Exp. Ther.* 269, 66–74.

Starmer, C. F., Grant, A. O., and Strauss, H. C. (1984). Mechanisms of use-dependent block of sodium channels in excitable membranes by local anesthetics. *Biophys. J.* 46, 15–27. doi: 10.1016/S0006-3495(84)83994-6

Stephenson, R. S., Atkinson, A., Kottas, P., Perde, F., Jafarzadeh, F., Bateman, M., et al. (2017). High resolution 3-Dimensional imaging of the human cardiac conduction system from microanatomy to mathematical modeling. *Sci. Rep.* 7:7188. doi: 10.1038/s41598-017-07694-8

ten Tusscher, K. H., and Panfilov, A. V. (2006). Alternans and spiral breakup in a human ventricular tissue model. *Am. J. Physiol. - Heart Circ. Physiol.* 291, H1088–H1100. doi: 10.1152/ajpheart.00109.2006

Varela, M., Colman, M. A., Hancox, J. C., and Aslanidi, O. V. (2016). Atrial heterogeneity generates re-entrant substrate during atrial fibrillation and anti-arrhythmic drug action: mechanistic insights from canine atrial models. *PLOS. Comput. Biol.* 12:e1005245. doi: 10.1371/journal.pcbi.1005245.

Voigt, N., Trausch, A., Knaut, M., Matschke, K., Varró, A., Wagoner, D. R. V., et al. (2010). Left-to-right atrial inward rectifier potassium current gradients in patients with paroxysmal versus chronic atrial fibrillationclinical perspective. *Circ. Arrhythm. Electrophysiol.* 3, 472–480. doi: 10.1161/CIRCEP.110.954636

Whittaker, D. G., Colman, M. A., Ni, H., Hancox, J. C., and Zhang, H. (2015). *In silico* investigation of short QT syndrome-linked potassium channel mutations on electro-mechanical function of human atrial cells. *Comput. Cardiol. Conference* 2015, 853–856. doi: 10.1109/CIC.2015.7411045.

Whittaker, D. G., Colman, M. A., Ni, H., Hancox, J. C., and Zhang, H. (2018). Human atrial arrhythmogenesis and sinus bradycardia in KCNQ1-linked short QT syndrome: insights from computational modelling. *Front. Physiol.* 9:1402. doi: 10.3389/fphys.2018.01402

Whittaker, D. G., Ni, H., Benson, A. P., Hancox, J. C., and Zhang, H. (2017a). Computational analysis of the mode of action of disopyramide and quinidine on hERG-linked short QT syndrome in human ventricles. *Front. Physiol.* 8:759. doi: 10.3389/fphys.2017.00759

Whittaker, D. G., Ni, H., Harchi, A. E., Hancox, J. C., and Zhang, H. (2017b). Atrial arrhythmogenicity of KCNJ2 mutations in short QT syndrome: insights from virtual human atria. *PLOS. Comput. Biol.* 13:e1005593. doi: 10.1371/journal.pcbi.1005593

Wilhelms, M., Hettmann, H., Maleckar, M. M., Koivumäki, J. T., Dössel, O., and Seemann, G. (2013). Benchmarking electrophysiological models of human atrial myocytes. *Front. Physiol.* 3:487. doi: 10.3389/fphys.2012.00487

Workman, A. J., Smith, G. L., and Rankin, A. C. (2011). Mechanisms of termination and prevention of atrial fibrillation by drug therapy. *Pharmacol. Ther.* 131, 221–241. doi: 10.1016/j.pharmthera.2011.02.002

Yuan, Y., Bai, X., Luo, C., Wang, K., and Zhang, H. (2015). The virtual heart as a platform for screening drug cardiotoxicity. *Br. J. Pharmacol.* 172, 5531–5547. doi: 10.1111/bph.12996

Zhang, H., and Hancox, J. C. (2004). *In silico* study of action potential and QT interval shortening due to loss of inactivation of the cardiac rapid delayed rectifier potassium current. *Biochem. Biophys. Res. Commun.* 322, 693–699. doi: 10.1016/j.bbrc.2004.07.176

Zhou, J., Augelli-Szafran, C. E., Bradley, J. A., Chen, X., Koci, B. J., Volberg, W. A., et al. (2005). Novel potent human ether-à-Go-Go-related gene (hERG) potassium channel enhancers and their *in vitro* antiarrhythmic activity. *Mol. Pharmacol.* 68, 876–884. doi: 10.1124/mol.105.014035

Conflict of Interest Statement: The authors declare that the research was conducted in the absence of any commercial or financial relationships that could be construed as a potential conflict of interest.

frontiers in Physiology

ORIGINAL RESEARCH
published: 14 January 2019
doi: 10.3389/fphys.2018.01910

Patient-Specific Identification of Atrial Flutter Vulnerability–A Computational Approach to Reveal Latent Reentry Pathways

Axel Loewe[1]*, *Emanuel Poremba*[1], *Tobias Oesterlein*[1], *Armin Luik*[2], *Claus Schmitt*[2], *Gunnar Seemann*[1,3,4] *and Olaf Dössel*[1]

[1] *Institute of Biomedical Engineering, Karlsruhe Institute of Technology (KIT), Karlsruhe, Germany,* [2] *Medizinische Klinik IV, Städtisches Klinikum Karlsruhe, Karlsruhe, Germany,* [3] *Institute for Experimental Cardiovascular Medicine, University Heart Center Freiburg Bad Krozingen, Freiburg, Germany,* [4] *Faculty of Medicine, Albert-Ludwigs University, Freiburg, Germany*

Atypical atrial flutter (AFlut) is a reentrant arrhythmia which patients frequently develop after ablation for atrial fibrillation (AF). Indeed, substrate modifications during AF ablation can increase the likelihood to develop AFlut and it is clinically not feasible to reliably and sensitively test if a patient is vulnerable to AFlut. Here, we present a novel method based on personalized computational models to identify pathways along which AFlut can be sustained in an individual patient. We build a personalized model of atrial excitation propagation considering the anatomy as well as the spatial distribution of anisotropic conduction velocity and repolarization characteristics based on a combination of a priori knowledge on the population level and information derived from measurements performed in the individual patient. The fast marching scheme is employed to compute activation times for stimuli from all parts of the atria. Potential flutter pathways are then identified by tracing loops from wave front collision sites and constricting them using a geometric snake approach under consideration of the heterogeneous wavelength condition. In this way, all pathways along which AFlut can be sustained are identified. Flutter pathways can be instantiated by using an eikonal-diffusion phase extrapolation approach and a dynamic multifront fast marching simulation. In these dynamic simulations, the initial pattern eventually turns into the one driven by the dominant pathway, which is the only pathway that can be observed clinically. We assessed the sensitivity of the flutter pathway maps with respect to conduction velocity and its anisotropy. Moreover, we demonstrate the application of tailored models considering disease-specific repolarization properties (healthy, AF-remodeled, potassium channel mutations) as well as applicabiltiy on a clinical dataset. Finally, we tested how AFlut vulnerability of these substrates is modulated by exemplary antiarrhythmic drugs (amiodarone, dronedarone). Our novel method allows to assess the vulnerability of an individual patient to develop AFlut based on the personal anatomical, electrophysiological, and pharmacological characteristics. In contrast to clinical electrophysiological studies, our computational approach provides the means to identify all possible AFlut pathways and not just the currently dominant one. This allows to consider all relevant AFlut pathways when tailoring clinical ablation therapy in order to reduce the development and recurrence of AFlut.

Keywords: atrial flutter, ablation, vulnerability, computational modeling, personalized model

OPEN ACCESS

Edited by:
Patrick M. Boyle,
University of Washington,
United States

Reviewed by:
Jichao Zhao,
The University of Auckland,
New Zealand
Jason D. Bayer,
Université de Bordeaux, France

***Correspondence:**
Axel Loewe
publications@ibt.kit.edu

Specialty section:
This article was submitted to Computational Physiology and Medicine, a section of the journal Frontiers in Physiology

Received: *15 September 2018*
Accepted: *18 December 2018*
Published: *14 January 2019*

Citation:
Loewe A, Poremba E, Oesterlein T, Luik A, Schmitt C, Seemann G and Dössel O (2019) Patient-Specific Identification of Atrial Flutter Vulnerability–A Computational Approach to Reveal Latent Reentry Pathways. Front. Physiol. 9:1910. doi: 10.3389/fphys.2018.01910

1. INTRODUCTION

The long-term success rate of atrial fibrillation (AF) ablation is unsatisfactory low, particularly in patients suffering from persistent AF. Besides AF recurrence, the development of post-ablational atrial flutter (AFlut) represents a major problem (Villacastín et al., 2003; Kobza et al., 2004; Chugh et al., 2005; Patel et al., 2008; Yamada and Kay, 2013; Biviano et al., 2015). In more than half of the patients, sustained AF is reinitiated within 5 years after ablation or AFlut develops (Bunch et al., 2016). 20% of recurrences after AF ablation in elderly are due to AFlut (Dong et al., 2015). In the general AF population, 18.5% of patients were diagnosed with AFlut during a median follow-up time of 421 day post ablation (Gucuk Ipek et al., 2016). Liang et al. (2015) observed AF or organized atrial tachycardia in 53% of 300 patients within the first 6 weeks after pulmonary vein (PV) isolation. AF and AFlut are often even combined endpoints in studies evaluating the success of AF ablation (Bunch et al., 2016). Waldo and Feld (2008) highlighted the inter-relationship between AF and AFlut. AF precedes AFlut in most cases forming the required line of block by fibrillatory conduction. Moreover, ablation of atrial tissue can lead to a substrate for AFlut. Particularly gaps in linear lesions forming isthmuses or revitalized tissue areas forming zones of slow conduction render the atria vulnerable. Also PV isolation has been associated with a substantial risk to develop AFlut (Mesas et al., 2004; Deisenhofer et al., 2006; Jaïs et al., 2006). Castrejón-Castrejón et al. (2011) reviewed the occurrence of organized atrial tachycardia such as AFlut after AF ablation and emphasize that more extensive left atrium (LA) ablation renders the patient more vulnerable to AFlut. However, the exact origin of the pathologic substrate is not understood. Therefore, we present a method to assess the vulnerability to AFlut in personalized computational models. Besides an identification of possibly AFlut sustaining pathways in the observed state of the patient (*baseline*), the approach allows to assess the effect of different therapeutic strategies such as ablation patterns, pharmacological compounds, or other anatomical and electrophysiological interventions *in silico* before actually performing them *in vivo*.

A common approach to simulate complex excitation patterns is the monodomain reaction-diffusion model which is based on the transport of ions within the domains and across the cell membrane (Niederer et al., 2011). As such, it considers electrotonic effects and source-sink relations resulting in e.g., convex or concave wavefronts. On the one hand, the monodomain approach provides the means to study complex and chaotic patterns such as fibrillation including wave breaks. On the other hand, the monodomain model is computationally expensive even using optimized implementations (Labarthe et al., 2014; Pezzuto et al., 2017). Hence, a thorough exploration of the parameter space regarding effects on the three-dimensional whole organ level, as e.g., the vulnerability to arrhythmia caused by ectopic stimuli from a multitude of locations and at varying time instants, is infeasible. Eikonal approximations of the continuous dynamics of the reaction-diffusion system allow to simulate excitation propagation in terms of activation times with significantly reduced computational load by several orders of magnitude (Wallman et al., 2012; Labarthe et al., 2014; Loewe, 2016; Neic et al., 2017; Pezzuto et al., 2017) as only one static, non-linear partial differential equation derived from the monodomain model has to be solved, which makes it interesting for simulations of cardiac activation (Keener, 1991; Franzone and Guerri, 1993). In contrast to level set methods in general, shortest pathway (van Dam and van Oosterom, 2003) and fast marching methods assume monotonously expanding wavefronts. Thus, a specific approach considering multiple fronts, reentry, and anisotropic conduction was developed for cardiac electrophysiology (Sermesant et al., 2007; Pernod et al., 2011) based on the fast marching method on structured grids (Sethian, 1996, 1999; Sermesant et al., 2005). Several extensions provide the means to consider wavefront curvature and the mesh structure if that is needed for the specific application (Sethian and Vladimirsky, 2000, 2003). Ablation of ventricular tissue in order to prevent scar-related ventricular tachycardia was presented as a potential application for this method (Pernod et al., 2011). However, one should keep in mind that while current multifront fast marching methods faithfully represent macro-reentrant arrhythmias like AFlut, they are not well suited to study more complex reentries like spiral wave or multiple wavelet reentry where local source-sink mismatch plays a crucial role (Loewe, 2016).

The aim of this work is to develop a method that allows to comprehensively assess the vulnerability to AFlut in personalized models considering both anatomical and electrophysiological properties allowing to evaluate therapeutic approaches such as ablation and drug treatment *in silico*.

2. MATERIALS AND METHODS

A simulation pipeline consisting of several steps (**Figure 1**) was developed in order to assess the vulnerability to AFlut. In this section, the different building blocks of the workflow are presented.

2.1. Fast Marching Simulation of Excitation Propagation

The eikonal equation governs the spread of an activation wave in a possibly anisotropic medium resulting in a scalar field $t_a(x_i)$ – the activation map:

$$c\sqrt{\nabla t_a \vec{G} \nabla t_a} = 1, \tag{1}$$

with $c(x_i)$ being the speed function defined for each node x_i, $t_a(x_i)$ being the activation time, and $\vec{G}$ being a tensor enabling anisotropy to account for faster conduction along the principal axis of myocytes than perpendicular to it (Loewe, 2016):

$$\vec{G} = R(\phi,\theta)\begin{pmatrix} k & 0 & 0 \\ 0 & 1 & 0 \\ 0 & 0 & 1 \end{pmatrix} R(\phi,\theta)^T, \tag{2}$$

with $R(\phi,\theta)$ rotating the coordinate system to align the positive x-axis with the prinicipal myocyte orientation. The multifront fast marching scheme for the eikonal-based simulation of

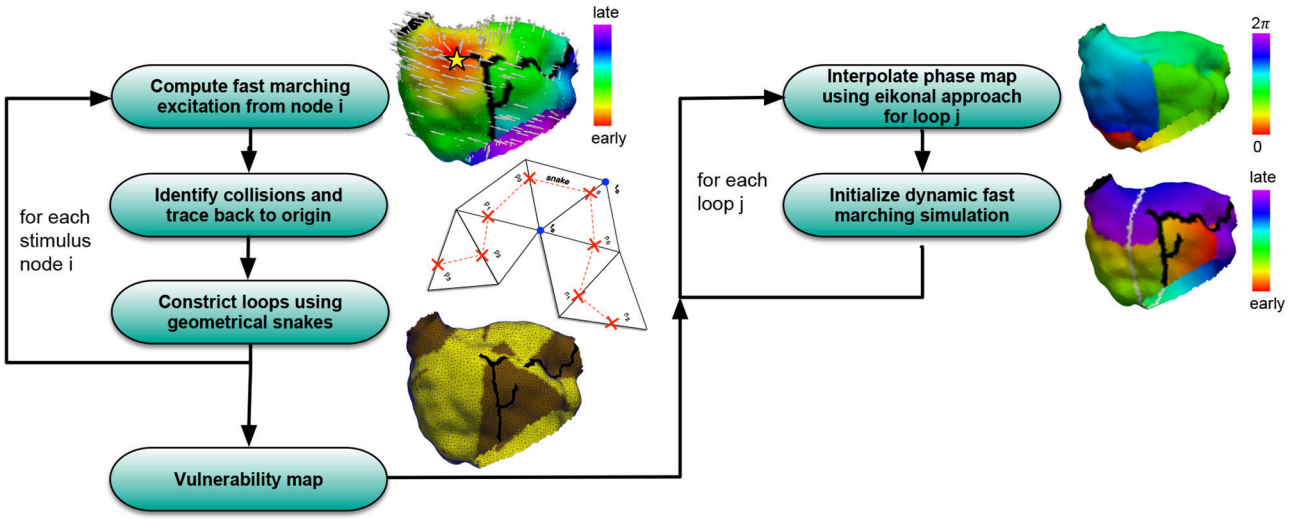

FIGURE 1 | Overview of the algorithm to compute vulnerability maps considering all possible AFlut loops (left) and transfer the AFlut scenarios to dynamic simulations (right).

excitation propagation introduced by Sermesant et al. (2007) (**Supplementary Algorithm 1**) was extended to consider restitution of conduction velocity (CV) and effective refractory period (ERP). Restitution of both parameters with respect to basic cycle length (BCL) was determined by pacing in a one-dimensional tissue strand using the Courtemanche et al. cell model (Courtemanche et al., 1998) coupled in a monodomain approach as detailed in Wilhelms et al. (2013). These restitution curves provide opportunities for functional model personalization in the future as further discussed below. The resulting curves for CV were approximated by fitting to exponential decays:

$$CV\,(BCL) = A - B \cdot \exp\left(-\frac{BCL}{C}\right). \tag{3}$$

The BCL was defined as the time passed since the last activation of the respective node and initialized with a user-defined value either globally or for each node individually. The restitution of the ERP was described the same way.

2.2. Identification of Flutter Loop Candidates

The fast marching approach was used to trigger excitations from a multitude of locations sequentially. For each stimulus location, activation times were computed and stored together with information regarding the spread of excitation in terms of a vector pointing from the activating to the activated node. Wavefront collision sites were defined as points of latest activation on circular pathways composed of two traces originating from the stimulus site to opposite sides, i.e., at an angle of approximately π. On the one hand, these pathways are the shortest in the sense of wave propagation, i.e., they are not artificially prolonged by zig-zag patterns but determined as the shortest connection by the fast marching algorithm. On the other hand, they are locally the longest as two independent waves collided on the loop. A wavefront collision for node i was identified if the following condition was fulfilled for any neighboring node j:

$$\frac{\vec{a}_i}{\|\vec{a}_i\|_2} + \frac{\vec{a}_j}{\|\vec{a}_j\|_2} < 0.99\,, \tag{4}$$

with $\vec{a}_i/\vec{a}_j$ being the vector pointing from the node that activated node i/j to node i/j itself. The condition identifies all points at which the vectors meet at an angle $\in (\pi/2,3\pi/2)$, thus pointing in opposite directions. From the sites of collisions, loops were defined by the two traces along the steepest negative activation time gradient leading back to the stimulus location. A loop was thus composed of a circular, ordered series of nodes. Along the loop, the round trip time (RTT) was calculated considering the heterogeneous and anisotropic tissue properties in terms of CV. If a loop did not fulfill the wavelength (WL) condition

$$\max_i \left(ERP_i(RTT)\right) < RTT, \tag{5}$$

it was disregarded. Here, ERP_i is the ERP of node i considering a BCL equal to the RTT according to Equation (3). i iterates over all nodes spanning the loop candidate.

2.3. Constriction of Flutter Loop Candidates

The fact that the loops were traced back all the way to the initial stimulus site introduced artifacts as a dynamic wave would cut short between the two traces from the site of collision to the stimulus site in many cases. In the easier case, both half loops share a part of the loop. Under such circumstances, all common nodes can be neglected, thus shrinking the loop (**Supplementary Figure 1A**). In most

cases, however, artifacts of other types were present as well. In **Supplementary Figure 1B**, a shortcut of the two half loops running adjacent on the posterior LA wall can be anticipated between the posterior interatrial connections and the connection via the coronary sinus. Therefore, a geometric snake approach (**Supplementary Figures 2, 3**) considering anisotropy was implemented in order to constrict the loops like a rubber band by minimizing the spline energy. Evolving snakes on triangular meshes were proposed before for mesh scissoring operations and constriction detection (Lee and Lee, 2002; Hétroy and Attali, 2003; Bischoff and Kobbelt, 2004; Lee et al., 2004) and were adapted to the requirements of the specific application in this work as further detailed in the **Supplementary Methods**.

2.4. Eikonal-Diffusion Phase Extrapolation

The methods introduced above allow to identify pathways in an atrial model that can potentially sustain AFlut. However, the pathways are not necessarily dominant and might thus not be expressed in dynamic scenarios. An example is shown in **Figure 2** where several pathways run from the septal side of the tricuspid valve to the right atrial appendage and to the coronary sinus region. Each pathway is locally the shortest and long enough to sustain AFlut according to the WL condition. However, according to Huygen's principle, only one pathway will dominate the excitation pattern distal to the constriction at the tricuspid valve where all pathways narrow. Thus, the remaining pathways will be suppressed. In order to identify the dominant pathway, i.e., to distinguish between theoretically vulnerable pathways and practically inducible pathways, the initial state for a dynamic simulation can be extrapolated from a single loop to the entire simulation domain as detailed in the **Supplementary Methods**.

Figure 1 summarizes the pipeline used to generate AFlut vulnerability maps and transfer the results to dynamic simulations.

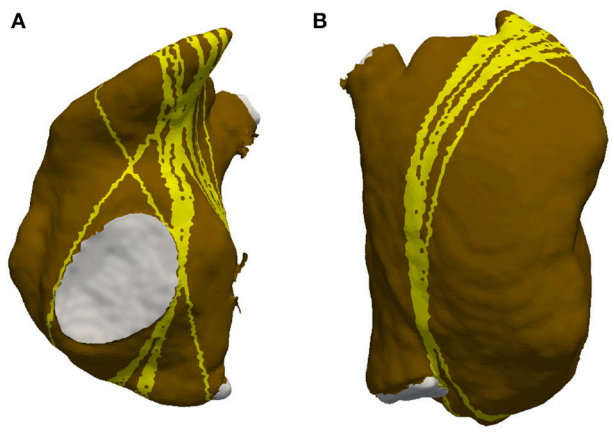

FIGURE 2 | Example of an AFlut vulnerability map for the right atrium (anterior aspect in **A**, posterior aspect in **B**). The vulnerable pathways are marked in yellow on the substrate of the right atrium (brown); the blood pool is indicated in gray. Several pathways run from the septal side of the tricuspid valve to the right atrial appendage.

2.5. Heterogeneous Tissue Properties, Disease-Specific Substrates, and Drug Effects

The restitution of CV and ERP was determined through monodomain simulations in a one-dimensional tissue strand as detailed in Wilhelms et al. (2013). CV and ERP were determined for 50 BCLs between 200 and 1,000 ms distributed linearly in frequency domain. Regional heterogeneity between different anatomical areas within the atria was accounted for as described previously in terms of both electrophysiological properties (Krueger et al., 2013) and monodomain conductivities (Loewe et al., 2015) in a heterogeneous setup. Furthermore, four different atrial substrates were analyzed in homogeneous setups: (i) a control substrate representing healthy myocardium modeled by the original Courtemanche et al. (1998) cellular model, (ii) a substrate which has undergone remodeling due to chronic atrial fibrillation (cAF) (Loewe et al., 2014b), (iii) a substrate with the N588K mutation in the human ether-à-go-go-related gene (hERG) (Loewe et al., 2014c), and (iv) a substrate with hERG mutation L532P (Loewe et al., 2014c). The latter two substrates have been associated with familial AF and are used here to demonstrate how patient-specific information like genotype-specific repolarization properties can be included in the overall workflow. All four substrates were investigated with and without the influence of two exemplary antiarrhythmic drugs to demonstrate how not only ablation but also drug therapy can be considered and evaluated using our method. Based on a previous study (Loewe et al., 2014a), the class III antiarrhythmic compounds amiodarone and dronedarone where chosen and modeled as detailed there. **Figure 3** shows the exponential fit of the restitution curves based on the coefficients in **Supplementary Table 1**. The CV for the homgeneous control model was reduced compared to the RA/LA tissue in the heterogeneous setup to obtain a similar total activation time.

The ERP for long BCLs ranged between 256 ms for the tricuspid and mitral valve rings to 332 ms for the crista terminalis. Crista terminalis, Bachmann's bundle, and the working myocardium showed a steeper decrease toward shorter BCLs compared to the remaining regions (**Figure 3C**). Regarding AFlut vulnerability, the WL is the decisive factor. Both, different regions and different substrates, exhibited distinct behavior at different BCLs. For example, at short BCLs, crista terminalis was the region with the shortest WL opposed to long BCLs where it was the region with the longest WL together with Bachmann's bundle (**Figure 3E**).

2.6. Clinical Example

The proposed method was applied to a clinical example from a 70 year-old female patient who underwent electroanatomical mapping due to atypical AFlut after previous ablation for AF. The previous AF ablation comprised PV isolation, ablation of a mitral isthmus line and the cavotricuspid isthmus. The patient presented with atypical AFlut with a cycle length of 420 ms. Mapping was performed using the Rhythmia system (Boston Scientific, Marlborough, MA, USA). The PVs were still isolated, electrogram voltage along the mitral isthmus line was reduced

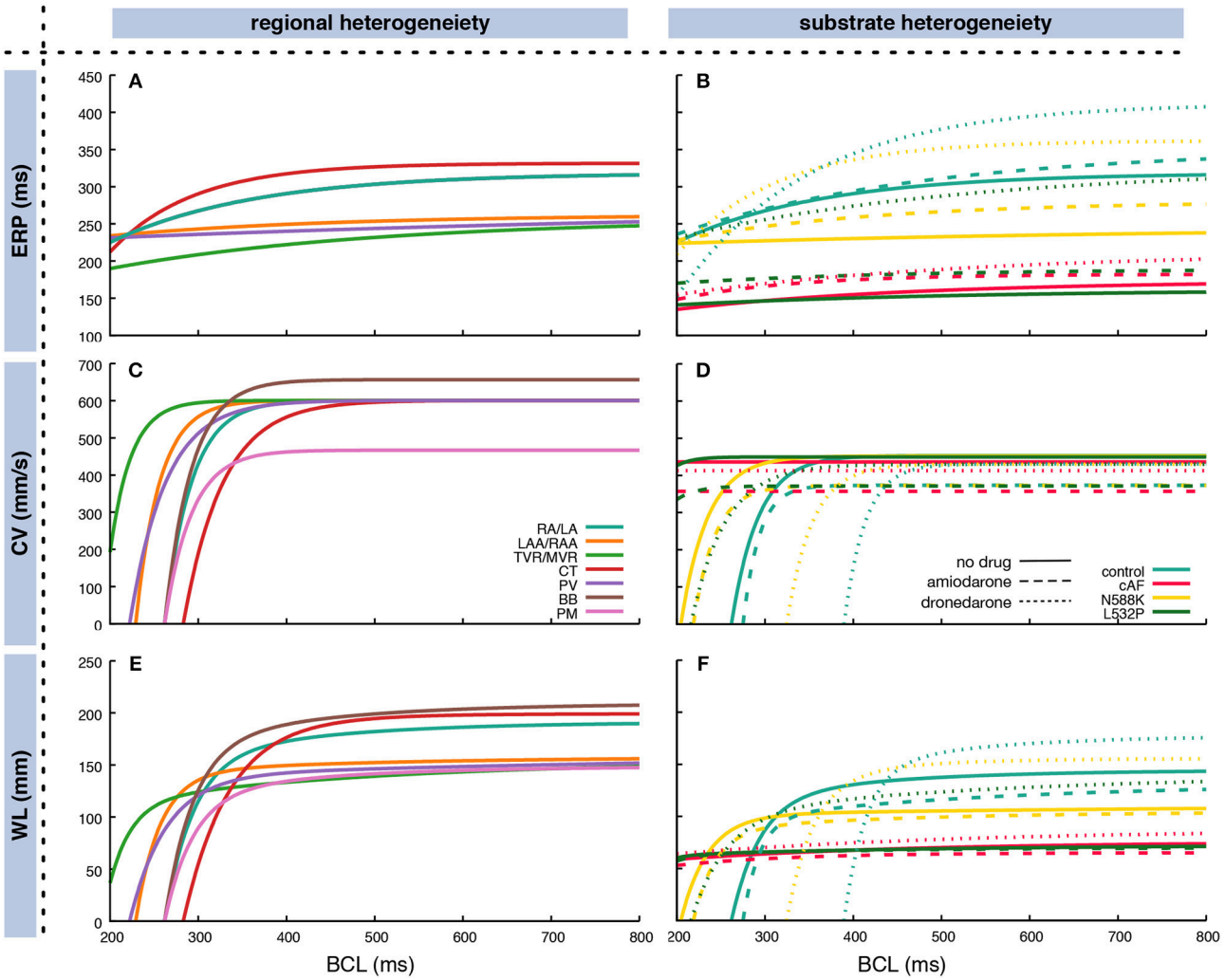

FIGURE 3 | Fitted exponential restitution curves of ERP **(A,B)** and CV **(C,D)**, as well as the WL as the product of the former measures **(E,F)** for different anatomical regions in the atria **(A,C,E)** and different substrates **(B,D,F)**. In **(B,D,F)**, the dashed lines represent the respective substrates under the influence of 2.3 μM amiodarone whereas the dotted lines represent the influence of 0.21 μM dronedarone. Exponential curves according to Equation (3) were used to fit the output of monodomain tissue strand simulations. The CV for the homgeneous control model in **(D)** was reduced compared to the RA/LA tissue in the heterogeneous setup in **(C)** to obtain a similar total atrial activation time. In **(A)**, BB and PM curves are covered by the RA/LA curve. Coefficients are listed in **Supplementary Table 1**. RA, right atrium; LA, left atrium; CT, crista terminalis; PM, pectinate muscles; BB, Bachmann's bundle; II, inferior isthmus; PV, pulmonary veins; RAA, right atrial appendage; LAA, left atrial appendage; TVR, tricuspid valve ring; MVR, mitral valve ring.

but the line was not blocked. A zone of slow conduction was identified on the left anterior wall close to the left PVs. Five different AFlut types with cycle lengths between 280 and 470 ms could be induced clinically. The arrhythmia terminated to sinus rhythm upon the first ablation in the zone of slow conduction. Further ablation points were placed in the area of the anterior line and connected to the mitral valve. Afterwards, tachycardia could not be induced anymore by burst pacing from the coronary sinus with cycle lengths down to 200 ms. The LA geometry aquired during the procedure comprising 7,471 nodes was retrospectively exported from the clinical system and transferred to the fast marching simulation environment. The previous ablations were manually annotated in the patient LA geometry (**Figure 10A**). To reproduce the clinical reentry pattern and activation map qualitatively, the CV was homogeneously set to 650 mm/s and the ERP to 250 ms. The protocol was approved by the ethics committee of the University of Freiburg. The subject gave written informed consent in accordance with the Declaration of Helsinki.

3. RESULTS

3.1. Flutter Loops and Geometric Snakes

Excitation propagation was calculated from several stimulus locations and sites of collision were detected using the activation vectors as shown in **Figures 4A,B**. From the sites of wavefront collision, the activation front was traced back

to the stimulus site along the gradient of the activation time field. Combining the traces obtained by following the activation waves of both colliding waves yielded a set of initial loops for each stimulus node (**Figure 4C**). The WL condition Equation (5) was not fulfilled by several loops that could thus be neglected during the following steps (lighter colored loops in **Figure 4C**).

A geometrical snake was initialized for each valid loop candidate. **Figure 5** shows a geometrical snake initialized along a flutter loop candidate in the LA. The stimulus leading to

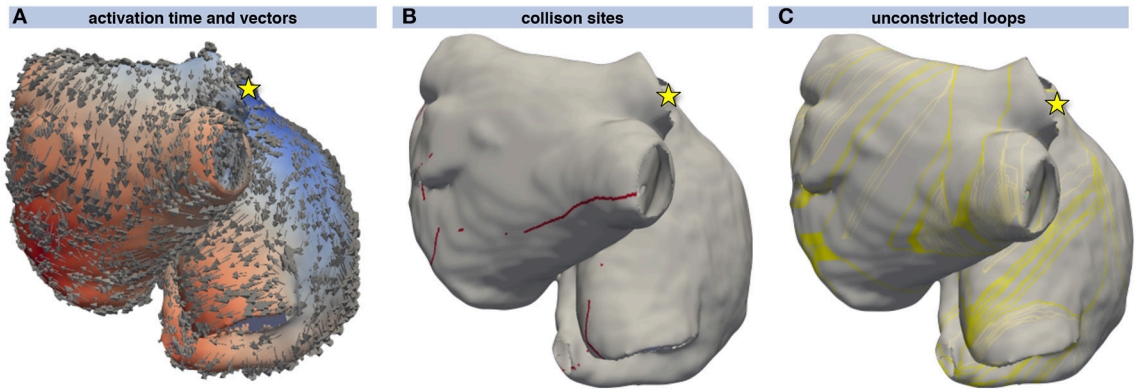

FIGURE 4 | Loop candidate finding. Activation time resulting from a stimulus at the junction of the superior vena cava with the right atrial appendage (yellow star) ranging from early (blue) to late (red). The direction of activation is indicated by arrows **(A)**. Points of wavefront collisions were detected and are indicated by red dots in **(B)**. **(C)** shows the loops composed of the two traces leading from the collision site to the stimulus site (yellow star). The yellow loops fulfill the WL condition Equation (5) whereas the light gray loops do not and were thus not considered for further steps.

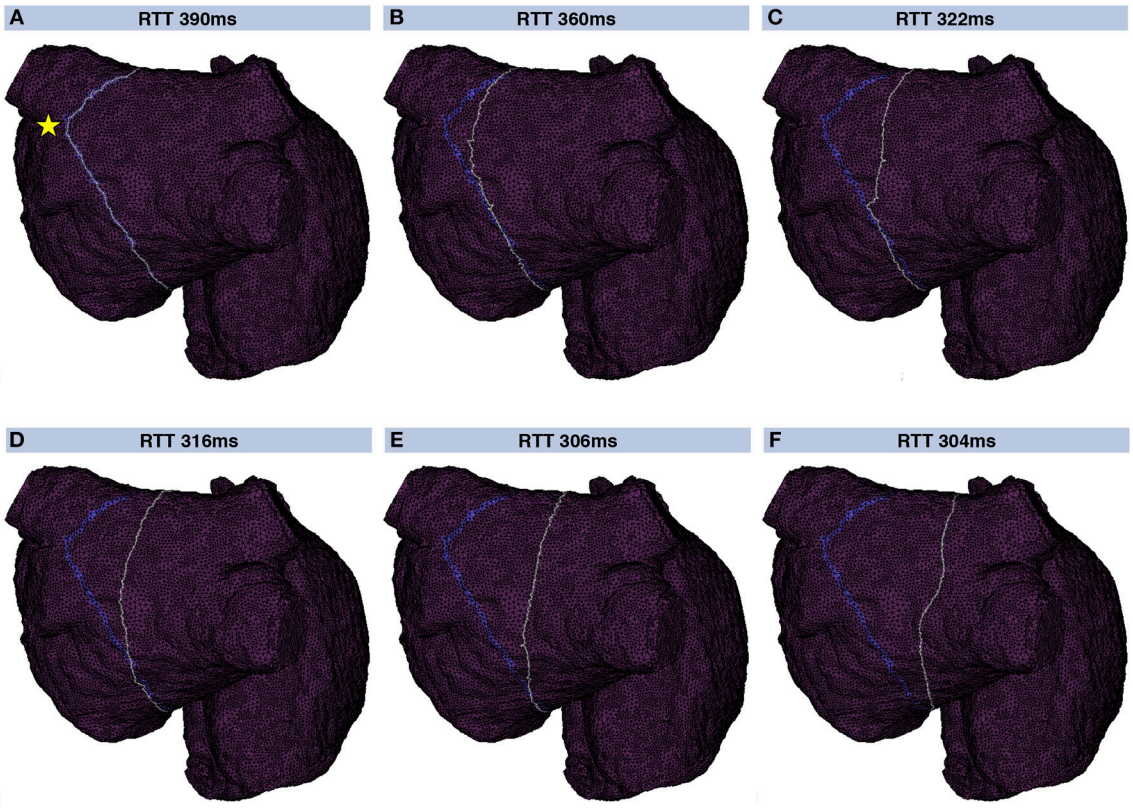

FIGURE 5 | Evolution of a geometric snake covering the LA. Initially, the snake (gray) covered the loop found by the collision tracing algorithm (blue band) corresponding to a RTT of 390 ms **(A)**. By iteratively constricting the snake **(B–F)**, the shortest RTT of 304 ms considering heterogeneous CV and anisotropy was found. In this way, the influence of the particular choice of the stimulus site (yellow star in **A**) was reduced.

that loop was applied between the two left PVs (yellow star in **Figure 5A**). The segment connecting the loop candidate with the stimulus location was shared by both half loops and disregarded before the snake was initialized. The initial RTT of 390 ms was reduced to 304 ms by iterating the snake according to **Supplementary Equation (4)**. The converged snake reflects myocyte orientation and CV heterogeneity (**Figure 5F**).

3.2. Vulnerability Maps

By triggering stimulation from different points, identifying loop candidates, and constricting them using geometrical snakes, AFlut vulnerability maps were generated as outlined in **Figure 1**. In a first step, an MRI-derived triangular mesh of the RA comprising 19,296 nodes augmented with rule-based tissue labels and myocyte orientation (Wachter et al., 2015) was used. The triangular surface model is a lumped representation of the atrial wall with a single myocyte orientation in each element. As detailed in Wachter et al. (2015) and Loewe (2016), crista terminals and the pectinate muscles were integrated within the RA wall. The vulnerability maps were sensitive to tissue anisotropy as indicated by the lower number of flutter pathways in the isotropic models (**Figures 6A,C**) compared to the anisotropic cases (**Figures 6B,D**). While the heterogeneous A and B values defining the CV according to Equation (3) were scaled in the isotropic and homogeneous cases to match the sinus rhythm activation time of the last element in the heterogeneous anisotropic simulation, both anisotropy and heterogeneity increased the number of vulnerable pathways. In the homogeneous isotropic setup (**Figure 6A**), only 12.7% of all elements were covered by vulnerable pathways. Adding anisotropy (**Figure 6B**) increased the coverage to 20.8% whereas adding heterogeneity (**Figure 6C**) lead to 15.9% coverage. 51.7% of the fully heterogenous and anisotropic model (**Figure 6D**) were covered by vulnerable pathways.

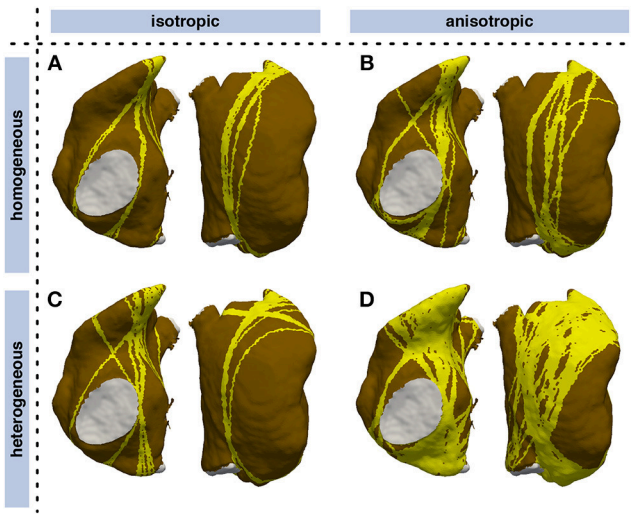

FIGURE 6 | Influence of heterogeneity and anisotropic conduction on vulnerability maps of the RA. Vulnerable pathways are marked in yellow on the RA myocardium (brown); the blood pool is indicated in gray. While CV was tuned such that the latest sinus rhythm activation coincided in all models, both anisotropy and heterogeneity lead to a higher number of vulnerable pathways. **(A)** isotropic homogeneous; **(B)** anisotropic homogeneous; **(C)** isotropic heterogeneous; **(D)** anisotropic heterogeneous.

The number of vulnerable pathways and the share of RA myocardium covered by them was highly dependent on the CV. In a homogeneous anisotropic setup (ERP 318 ms at long BCLs), the coverage increased from 0% at a CV of 475 mm/s to over 90% for CVs of 360 mm/s and lower (**Figure 7A**). When interpreting these findings, one should keep in mind the homogeneous ERP restitution used in this experiment (solid green line in **Figure 3B**). The degree of coverage also depends on the number of different stimulus locations evaluated (**Figure 7B**). Considering all 19,296 RA nodes yielded a coverage of 54.5% for a fixed CV of 425 mm/s. Requiring a minimum distance of 1 mm between stimulus points reduced their number to 8,254 without affecting the coverage result markedly (50.9%). Considering less points yielded lower coverage rates (39.4% for 2 mm $\widehat{=}$ 2,136 nodes, 3.8% for 20 mm $\widehat{=}$ 19 nodes).

The degree of coverage was highly dependent on the substrate as detailed in **Table 1**. 8,254 stimulus points with a minimum distance of 1 mm were considered using the CV and ERP values fitted from the monodomain model output using the biophysically detailed cell models given in **Supplementary Table 1**. While the fitted exponential restitution of ERP and CV was modeled homogeneously across the RA, its region-dependent heterogeneous anisotropy (k in **Supplementary Table 1**) was kept. To operate in an interesting range of vulnerability (**Figure 7A**), CV at long BCLs (A in **Supplementary Table 1**) was set to 454 mm/s in the following yielding a total RA activation time of 194 ms in the *control* model without any drug applied.

Both the cAF substrate and the two hERG mutations were more vulnerable to AFlut than the control model representing healthy myocytes. The higher degree of coverage under the influence of amiodarone observed for all substrates can be explained by the WL restitution (**Figure 3F**). The WL was shortened by the administration of amiodarone due to conduction slowing caused by the sodium channel inhibition. This effect was most pronounced in the control substrate and was reflected in the vulnerability maps as well (**Figure 8**).

In order to separate the effects of the different substrates and compounds on CV and ERP, the total activation time of the RA was matched with the activation of the last element in the control model and no drug (192 ms) in a second set of simulations (**Supplementary Figure 4**), i.e., the A and B parameters determining the CV according to Equation (3) were scaled while keeping the anisotropy ratio k constant. In this way, only the effect on repolarization (ERP) was considered leading to a reduction of vulnerable pathways under the influence of amiodarone in all substrates and a more pronounced reduction under the influence of dronedarone compared to **Figure 8**.

Besides evaluating different substrates, distinct spatial heterogeneities were introduced in the RA model. The normal RA myocardium was parametrized with an isotropic CV of 700 mm/s and an ERP of 250 ms for all BCLs. A circular zone of slow conduction on the posterior wall was modeled

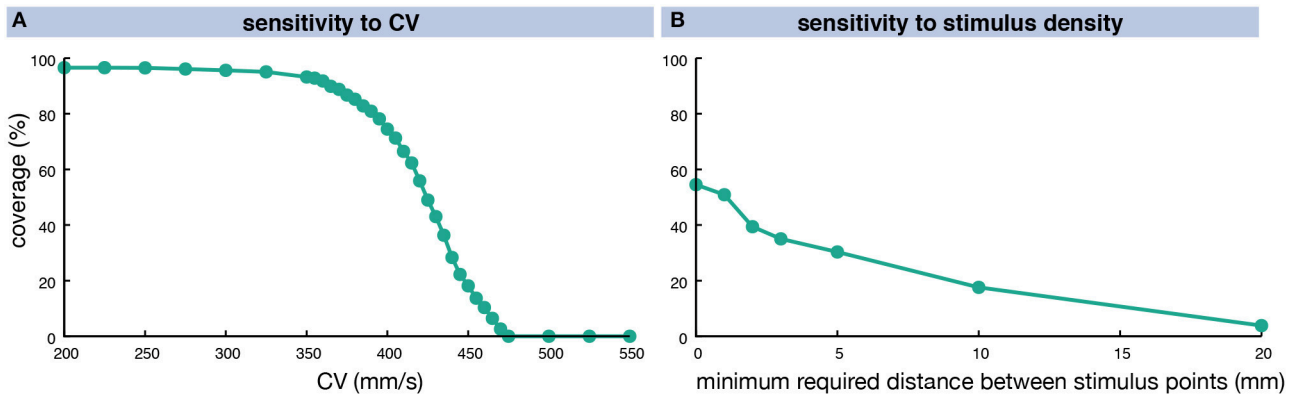

FIGURE 7 | Sensitivity of vulnerable pathway coverage to changes in homogeneous, anisotropic CV **(A)** and the stimulus point density **(B)**. The CV was altered in a homogeneous, anisotropic setup causing different degrees of RA coverage by vulnerable pathways for a fixed stimulus density of 1 mm. In **(B)**, the distance between stimulus points was varied for a fixed CV of 425 mm/s.

TABLE 1 | Degree of coverage of RA elements with pathways vulnerable to AFlut for different substrates and antiarrhythmic drugs amiodarone (*amio*) and dronedarone (*drone*).

	Degree of coverage					
	Original CV			Total activation time matched		
	no drug	amio	drone	no drug	amio	drone
Control	18.1%	70.5%	0.0%	18.1%	0.0%	0.0%
cAF	96.0%	96.3%	95.6%	96.2%	96.1%	94.9%
N588K	93.2%	94.1%	0.0%	93.0%	77.8%	0.0%
L532P	96.2%	96.5%	34.5%	96.3%	96.0%	11.1%

In the right three columns, the A and B values determining the CV according to Equation (3) were scaled to match the activation time of the last element during sinus rhythm in the control substrate with no drug applied.

(**Figures 9B,C**). Depending on the CVs inside and outside this zone, the wave might be faster bypassing the zone than propagating through it. Comparing the time the wave takes to bypass the circle with the time it takes to propagate through the zone of slow conduction yields a critical CV_{slow}/CV_{normal} ratio of $2/\pi \approx 0.63$. If the ratio is higher, the dominant pathway is through the zone of slow conduction. If it is lower, the bypassing wave is faster. Therefore, the zone of slow conduction within the surrounding tissue conducting at 700 mm/s was parametrized with a CV of 500 mm/s resulting in a ratio of 0.71 (**Figure 9B**), and 250 mm/s ($\widehat{=}$ 0.36, **Figure 9C**). In contrast to the control model (**Figure 9A**), the zones of slow conduction yielded additional flutter pathways. For the CV of 500 mm/s in the zone of slow conduction, 24.1% of the RA were covered by vulnerable pathways (**Figure 9B**) in contrast to 14.1% in the control case (**Figure 9A**). Additional flutter pathways crossed the periphery of the zone of slow conduction and thereby prolonged the RTT. For the slower CV of 250 mm/s, the entire zone of slow conduction was covered by vulnerable pathways yielding a total RA coverage of 47.8% (**Figure 9C**). The pathways were not constricted to the faster route outside the zone as the route through the zone of slow conduction was optimal considering the field of view of the geometrical snake. When computing an inducability map (see Discussion), the driving pathway would be running around the zone of slow conduction, though.

The second spatial substrate modification was an ablation lesion which encircled the RA completely (**Figure 9D**). Rather than being a clinically used ablation pattern, this scenario serves as an example separating the RA into two electrically isolated regions. The lesion was modeled as non-conductive, thus no flutter pathways could cross it. In additional scenarios, a gap in the ablation lesion of varying extent was assumed at the central posterior wall (**Figures 9E,F**). In case of the complete lesion, no flutter pathways were identified (**Figure 9D**) as the WL condition could not be fulfilled on any of the two separated, smaller substrates. The gap in the ablation lesion yielded numerous vulnerable pathways running through the gap at various angles (**Figure 9E**). The flutter pathways covered 42.9% of the RA in contrast to 14.1% in the control case, thus the ablation increased AFlut vulnerability markedly. In case of a smaller gap (**Figure 9F**), the number of loops was smaller than for the wider gap as the narrow gap served as a funnel. Nevertheless, the coverage (23.3%) was still markedly higher than for the control case.

The time to compute a complete vulnerability map depends on the mesh resolution as well as the number of stimulus points considered and the number of loop candidates fulfilling the WL condition over time. The computation is faster, the fewer loop candidates there are and the earlier the constricted loops are disregarded because they no longer fulfill the WL

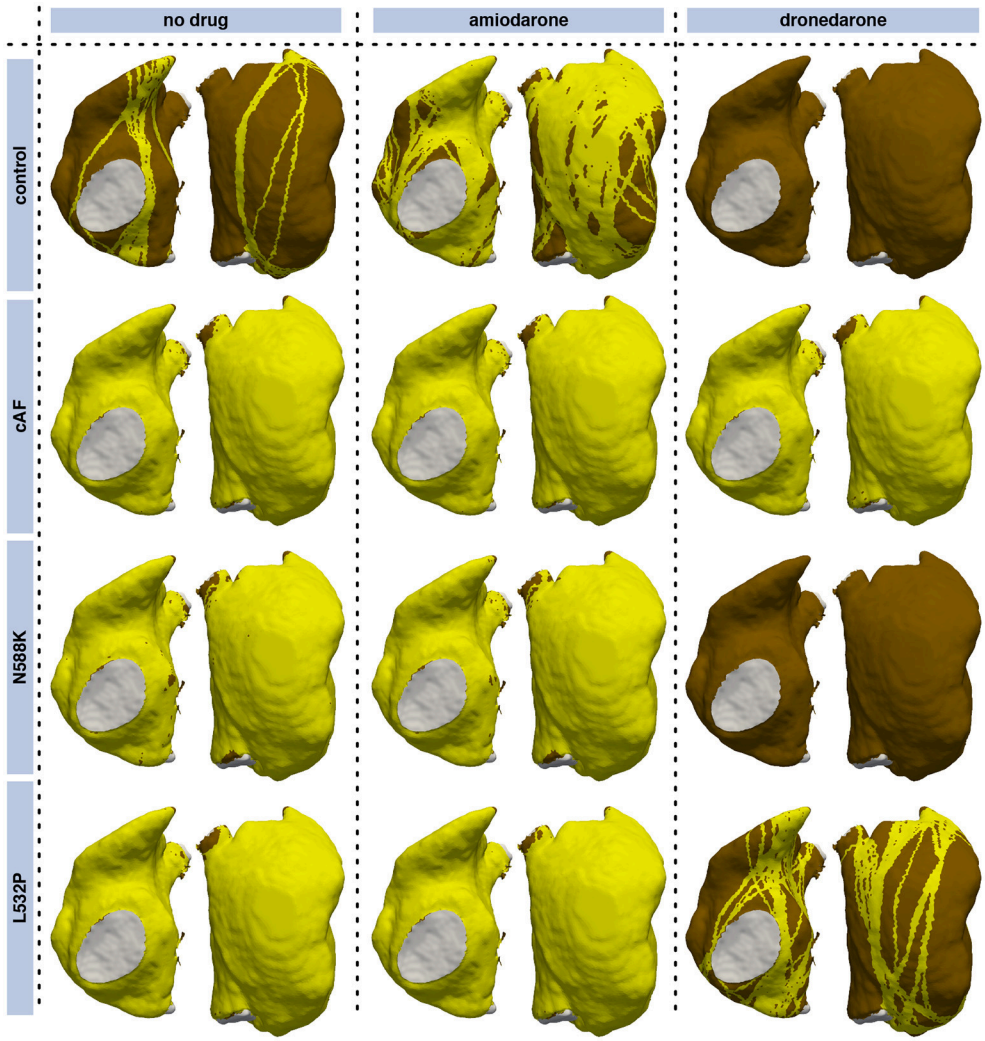

FIGURE 8 | Vulnerability maps of the RA for combinations of different substrates and pharmacological agents. Besides a control substrate representing healthy myocytes, a cAF remodeled substrate (neglecting changes of cell-to-cell coupling), and the two hERG mutations N588K and L532P were evaluated. Standard concentrations of the antiarrhythmic agents amiodarone (2.3 μM) and dronedarone (0.21 μM) were administered in the center and right columns, respectively. Vulnerable pathways are marked in yellow on the RA myocardium (brown); the blood pool is indicated in gray. **Supplementary Figure 4** shows the results for a matched total sinus rhythm activation time in all setups.

condition (data not shown). For the RA mesh consisting of 19,296 nodes, computation was timed on an *Intel Xeon E5-2697V2* machine with twelve cores at a base clock rate of 2.7 GHz. The control vulnerability map in **Figure 9A** with a coverage of 14.1% was computed within 4.0 min whereas it took 5.5 min to compute the vulnerability map for the RA including the zone of slow conduction yielding a coverage of 47.8% (**Figure 9C**).

3.3. Phase Extrapolation

The vulnerable pathways represented in the vulnerability maps and identified using the methods described above were extrapolated on the whole RA in terms of phase using the methods described in section 2.4. Each vulnerable pathway was extrapolated in phase space individually. The eikonal-diffusion approach converged within 16 to 18 iterations and was robust against variations of the CV [**Supplementary Equation (7)**] and the RTT [**Supplementary Equation (9)**], i.e., the cycle length of the reentry. CV was varied between 0.1× and 2× the ground truth value used in the fast marching simulation and assumed RTTs between 0.3× and 3× the ground truth value. The phase map was then used to determine the initial state of a dynamic fast marching simulation as exemplified in the next section for a clinical dataset.

3.4. Clinical Example

The inital vulnerability map representing the state with which the patient presented for the redo procedure (compare section 2.6) covered most parts of the LA (**Figure 10A**). AFlut pathways

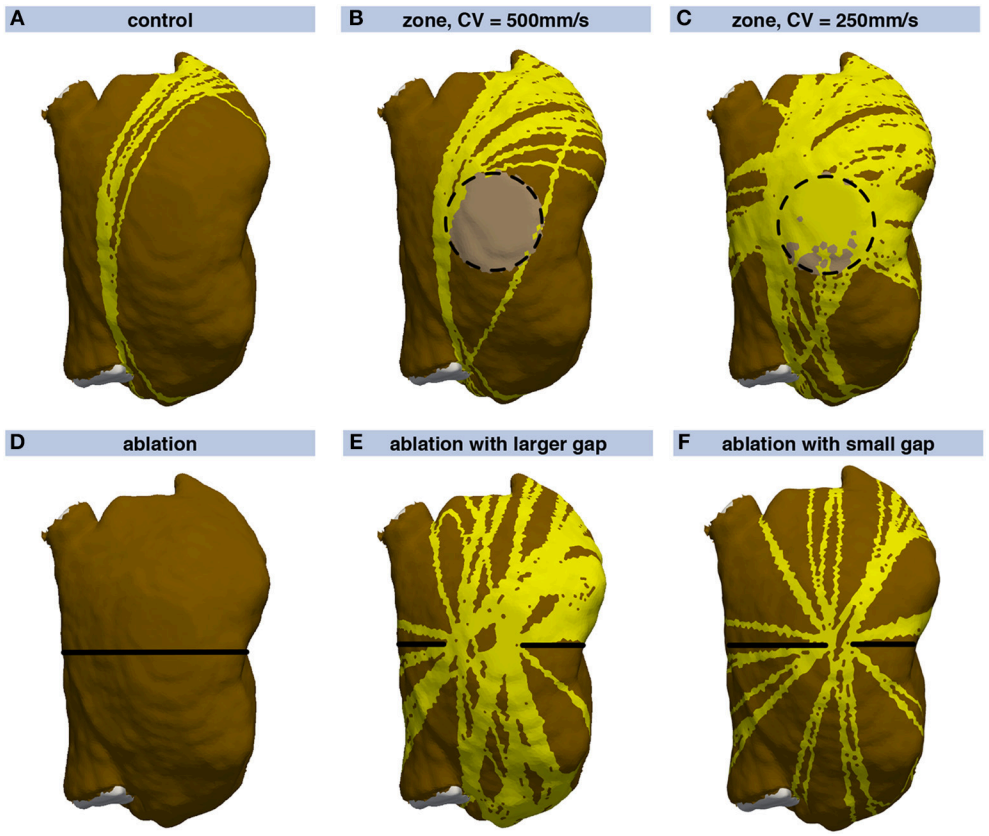

FIGURE 9 | Vulnerability maps of the RA for different substrate modifications. Compared, to **(A)**, a zone of slow conduction was introduced in **(B,C)** (light brown area enclosed by dashed circle). A circular ablation lesion (black line) was introduced in **(D)**. In **(E,F)**, a gap in the ablation lesion with varying extent was modeled on the central posterior wall.

running through the gap in the anterior line were present. After closing this gap, the left part of the anterior wall became free from AFlut pathways and they were restricted to the central part of the posterior wall (**Figure 10B**). However, there were still numerous AFlut pathways remaining. These pathways (the gray line in **Figure 10D** shows one example) were used to extrapolate a phase map on the whole domain (**Figure 10C**) and intialize a dynamic fast marching flutter simulation (**Figure 10D**). Reentry was stable for the entire simulation duration of 100 reentrant cycles. After connecting the line on the anterior wall to the RSPV by additional ablation, no more vulnerable pathways could be identified (**Figure 10E**).

4. DISCUSSION

4.1. Main Findings

In this study, a simulation workflow to identify vulnerable pathways potentially sustaining AFlut was presented. The approach builds on personalized fast marching simulations of excitation propagation and geometric snakes to constrict pathways identified on the basis of wavefront collision sites. Throughout the whole pipeline, heterogeneous, anisotropic, and heart rate-dependent tissue properties are considered in terms of CV and ERP.

The geometrical snake approach presented by Bischoff and Kobbelt (2004) was adapted to the excitation propagation application scenario considering the tissue property heterogeneities mentioned above. Applying the geometric snake approach to loop candidates identified as circular pathways from an initial stimulus point via a site of wavefront collision back to the initial stimulus yielded AFlut vulnerability maps. The number and the location of the identified vulnerable flutter pathways were sensitive to (i) anisotropy (**Figure 6**), (ii) the substrate properties regarding CV and repolarization, as well as modification of these parameters due to pharmacological compounds (**Figure 8** and **Supplementary Figure 4**), (iii) zones of slow conduction or ablation lesions (**Figure 9**), and most importantly (iv) the assumed CV (**Figure 7**). Anisotropic substrates were more vulnerable than isotropic tissue when matching the total sinus rhythm activation time of the RA. The WL is a crucial parameter as can be seen by the higher number of vulnerable pathways identified for the cAF and hERG mutated substrates compared to control. While dronedarone reduced the AFlut vulnerability, amiodarone rendered the substrate more vulnerable due to the reduced WL caused by

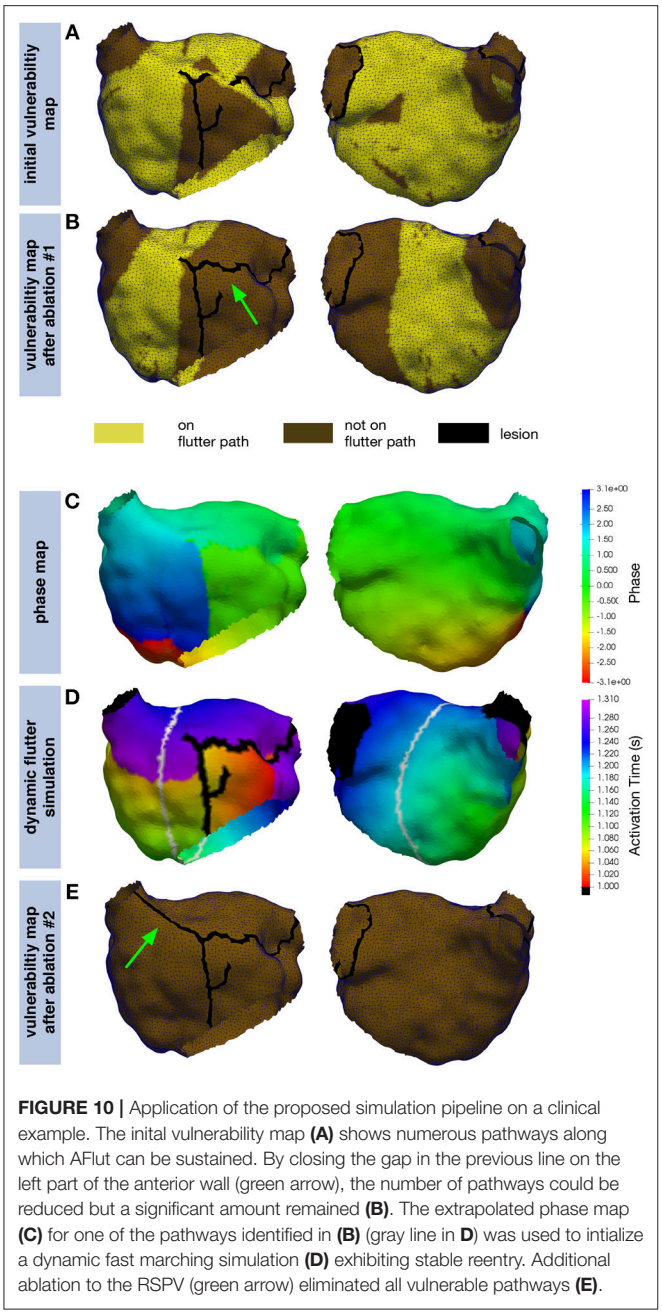

FIGURE 10 | Application of the proposed simulation pipeline on a clinical example. The inital vulnerability map **(A)** shows numerous pathways along which AFlut can be sustained. By closing the gap in the previous line on the left part of the anterior wall (green arrow), the number of pathways could be reduced but a significant amount remained **(B)**. The extrapolated phase map **(C)** for one of the pathways identified in **(B)** (gray line in **D**) was used to intialize a dynamic fast marching simulation **(D)** exhibiting stable reentry. Additional ablation to the RSPV (green arrow) eliminated all vulnerable pathways **(E)**.

the slowed CV (**Figure 3**). When only considering the effect on repolarization, thus altering ERP to represent the influence of the drug, amiodarone exhibited antiarrhythmic properties as well. The effect was less pronounced than for dronedarone, though. Zones of slow conduction increased the number and the density of vulnerable pathways as the cycle length increases both by conducting through the slow zone and by bypassing it. Ablation lesions isolating different regions completely rendered the RA invulnerable to AFlut. However, even a small gap in the lesion increased the number of vulnerable pathways markedly compared to control. This effect can be explained by the narrow isthmus formed by the gap in the lesion and highlights the importance of lesion durability. When linear lesions are partly revitalizing, they form ideal pathways for AFlut. In particular, shortcuts leading to wavefront collision and ceasing the reentrant activation are cut off by the lesion, thus stabilizing the reentry. The assumed CV had the biggest effect on the number of vulnerable pathways and the degree of RA coverage by them. A CV slowing by 25% rendered an invulnerable RA model highly vulnerable with a flutter pathway coverage of over 90%. This finding highlights the importance of a reliable CV estimation to draw relevant conclusions from personalized models using the method presented here. The CV of the individual patient has to be measured in a spatially resolved, and preferably heart rate-dependent, manner. Weber et al. (2010, 2011) proposed a method to estimate local CV and its restitution based on a cosine fit method. The advent of new electro-anatomical mapping systems and catheters with improved signal quality as well as sophisticated signal processing approaches gives rise to hope for such CV mapping in the near future (Latcu and Saoudi, 2014; Cantwell et al., 2015; Verma et al., 2018).

The application to a clinical example can be considered a proof of concept. We built on the individual anatomy exported from the mapping system and tailored the substrate to the clinically observed activation pattern. The model prediction and the clinical observations show good qualitative agreement. However, it has to be considered that the substrate was modeled homogeneously apart from the lesions and restitution properties were not taken into account. Therefore the lack of exact quantitative match is not surprising.

The computation of a single activation sequence was faster than real-time, a complete vulnerability map took several minutes. Most of the computational cost was due to the constriction of the loop candidates using the geometrical snake approach. While the time spent to calculate excitation propagation accounted for only a minor share, less complex alternatives to the fast marching algorithm exist. Graph-based approaches, such as the A* algorithm (Hart et al., 1968; Wallman et al., 2012) or the fastest route algorithm (van Dam et al., 2009) are however only faster if the activation time at only a subset of nodes is needed. Cellular automata on the other hand do not consider quadratic approximation of activation times. The computational complexity of the geometrical snake implementation could be reduced by optimizing the number of neighbors considered for the calculation of the snaxel velocity [**Supplementary Equation (4)**] and the convergence criteria. Indeed, the approach considering $N = 30$ neighbors with decreasing weight could be approximated by a spatial multi-grid approach starting with distant neighbors in early iterations and focussing on closer nodes at later iterations. When aiming at an interactive modification of the substrate, e.g., by introducing virtual ablation lesions, results from previous evaluations can be reused for regions not affected by the last modification. Moreover, intermediate results could be precomputed, thus trading memory footprint in for reduced computation time. This potential for optimizations together with parallel computing approaches make interactive assessment of ablation therapy in almost real-time appear achievable.

4.2. Relation to Previous Work

Dang et al. (2005) and Reumann et al. (2008) compared different standard ablation patterns for AF using idealized computational models and suggest that PV isolation together with linear lesions is the most effective treatment for AF. However, they did not investigate the vulnerability to AFlut post AF ablation systematically. Hwang et al. (2014) proposed a method to test AF ablation patterns *in silico* using a monodomain approach on anatomically, but not electrophysiologically personalized models. Thus, no substrate information regarding fibrosis, zones of slow conduction or the degree of electrophysiological remodeling is considered. Recently, Alessandrini et al. (2018) presented an *in silico* framework to holistically consider the entire cycle from excitation propagation, catheter deformation, electrogram acquisition and processing to virtual ablation. McDowell et al. (2015) published a proof-of-concept how computational modeling can predict ablation sites terminating rotors driving AF in personalized models including fibrosis distribution. Bayer et al. (2016) evaluated the potency of PV isolation, mitral and roof lines, ablation guided by rotor mapping, and lesions streamlining sinus activation regarding the termination of AF *in silico*. The potential of clinically-derived computational models to optimize catheter ablation of AF was recently reviewed by Zhao et al. (2015). They conclude that high-resolution three-dimensional models of functionally and structurally mapped atria of the exact patient are imperative to provide clinically relevant insights on a personalized level.

Lines et al. (2009) presented a method to parametrize a monodomain simulation in a standard bi-atrial model aiming to incorporate electrograms acquired during electroanatomic mapping studies in order to replicate clinically mapped AFlut *in silico*. The extracellular potentials at 32 computational nodes served as a boundary condition for the solution of the monodomain system. While the algorithm synchronized the simulation to the synthetic reference simulation, the algorithm is computationally expensive and only allows to study clinically observed cases *in silico* but cannot provide information on the vulnerability to AFlut.

While those previous studies assessed ablation patterns regarding the prevention or termination of AF, this is the first work to assess the vulnerability to AFlut based on an individualized anatomical model besides a recent work by Zahid et al. (2016) to the best of our knowledge (see also reviews by Jacquemet, 2016; Boyle et al., 2017). Zahid et al. employed the minimum cut algorithm to predict optimal ablation sites for AFlut in the LA with substantially increased computational effort. Child et al. (2015) introduced the reentry vulnerability index (RVI) as a quantitative metric based on the difference between activation and repolarization intervals at pairs of spatial locations. The RVI correlates with exit sites of scar-related reentrant arrhythmia as commonly observed in the ventricles (Hill et al., 2016). However, it aims at predicting functional lines of block rather than providing a comprehensive map of vulnerable pathways based on the individual geometrical properties. The same holds for a study by Wallman et al. (2013) quantifying the arrhythmogeneity of scar and left-to-right heterogeneity in the ventricles.

Trächtler et al. (2015) used the fast marching implementation presented here for a similar *in silico* reproduction of clinical cases. While both methods allow to test ablation strategies regarding the termination of the specific reentry, they do not allow to draw conclusions regarding the vulnerability to AFlut along other pathways. Thus, these approaches do not provide the means to optimize AF ablation aiming at the prevention of post-ablational AFlut.

4.3. Outlook

The method presented here could be further developed regarding two aspects. First, the extrapolated phase map obtained by the eikonal-diffusion approach could not only be used to initialize a fast marching simulation but also to replicate the flutter pathway in a monodomain simulation. Matene and Jacquemet (2012) proposed a suitable approach, which they used to initiate AF by extrapolating phase singularities (Jacquemet, 2010; Herlin and Jacquemet, 2011). By initiating the same flutter loop in both the fast marching and the monodomain environment, the fast marching approach could be further validated with respect to macro-reentry. Second, the dominant flutter pathways sustaining reentry in the dynamic simulations could be tracked and compared to the pathways used to extrapolate the initial state. In this way, not only a map of vulnerable flutter pathways but also a map of inducible flutter pathways could be computed.

Moving forward, the complete simulation pipeline should be validated in the clinical setting once tools for a spatially resolved CV and ERP estimation become available. The anatomical model of the individual patient built from MRI data could be augmented with a priori knowledge (Wachter et al., 2015). CV and ERP would be parametrized using intracardiac measurements (Unger et al., 2017; Verma et al., 2018) and complemented with rule-based assumptions. Preferably, the subjects should be recruited from patients undergoing ablation of AFlut that developed after AF ablation. Ideal validation cases would be formed by patients in which a gap in the intial ablation lesion set is identified during the second procedure. The lesions placed during the initial AF ablation procedure as well as the gap in it would be included in the suggested pipeline as further a priori knowledge. The clinically observed flutter pathway should then be found in the vulnerability and inducability map. Moreover, the ablation terminating the flutter in the clinical setting should also remove the specific vulnerable pathway from the map. In this way, the concepts and methodologies for both vulnerabiltiy and inducability maps could be clinically validated.

4.4. Limitations

The implementation of the fast marching algorithm used in this work does consider anisotropic CV but does not consider recursive anisotropic correction as proposed by (Sermesant et al., 2007). In Pernod et al. (2011), the authors of Sermesant et al. (2007) show that the computation time is higher by a factor of $\approx$1.6 when considering anisoptropic correction. While the influence of the anisotropic correction has never been evaluated systematically, it should not be too relevant for moderate

anisotropy values. For the application presented in this work, subtle differences of the activation sequence do not play a major role for the final result as fast marching activation times serve only as the input for subsequent processing.

Another limitation of the presented method is its restriction to monoatrial flutter pathways. The reason for this can be seen in **Supplementary Figure 5** in which a biatrial loop candidate was constricted using the geometrical snakes approach. While a shortcut within the LA exists, it cannot be resolved by the snake as it is constrained by the interatrial connections and can thus not cross the septum. However, the method could be extended to identify shortcuts within the two atria by also considering monoatrial loops in addition. The final constricted biatrial loop could be used to initialize additional monoatrial loops comprising the segment of the biatrial loop and shortest connection between the two open ends at the interatrial connections. When computing inducability maps instead of vulnerability maps, this limitation is not relevant since reentry along a loop as in **Supplementary Figure 5** could not be induced if this would not be the case for a comparable monoatrial loop as well. Regarding the dynamic simulation of AFlut, the missing representation of electrotonic coupling is a limitation.

The biggest hurdle is the sparsity of the available clinical data to characterize an individual's substrate and the associated uncertainty. The importance of a reliable CV estimation is highlighted by the fact that a CV uncertainty of Δc corresponds to scaling of the atrium by a factor of $\sqrt{\Delta c}$ (Jacquemet, 2016). Considering that the minimal WL needed to sustain reentry is defined by the product of CV and ERP, uncertainty of ERP plays an important role as well (Jacquemet et al., 2005; Krogh-Madsen and Christini, 2012; Deng et al., 2017). Improved electro-anatomic mapping systems providing better signal quality and simultaneous mapping using a multitude of electrodes, as well as advanced signal processing methods (Cantwell et al., 2015; Unger et al., 2017; Verma et al., 2018) make it seem probable to have suitable data available in the near future. Moreover, the uncertainty in the data could be taken into account by probabilistic modeling using Bayesian inference and compressed sensing methods (Konukoglu et al., 2011).

4.5. Conclusion

We presented a comprehensive method to analyze the vulnerability to AFlut in a personalized way and demonstrated its applicability for clinical data. The individual anatomy as well as electrophysiology in terms of CV, ERP, and their heart rate dependence is taken into account. This tool provides the means to evaluate potential ablation strategies *in silico* regarding their arrhythmic potential for AFlut before actually applying them in the electrophysiology lab. In this way, this work can be one piece in the puzzle to overcome the *learning by burning* paradigm and eventually reduce the number of patients suffering from post-ablational AFlut.

DISCLOSURE

Part of this study was published before as a thesis (Loewe, 2016).

AUTHOR CONTRIBUTIONS

ALo, TO, GS, and OD concepted the study. ALo, EP, and TO implemented the algorithms and performed the *in silico* experiments. ALo, EP, TO, GS, and OD analyzed and interpreted the data. ALu and CS performed the clinical procedure. ALo drafted the manuscript. EP, TO, ALu, CS, GS, and OD revised the manuscript critically. All authors approved the final version of the manuscript.

FUNDING

This work was supported by Deutsche Forschungsgemeinschaft under grant DFG DO637/22-3, SE1758/3-3, and through CRC 1173. We acknowledge support by Open Access Publishing Fund of Karlsruhe Institute of Technology.

SUPPLEMENTARY MATERIAL

The Supplementary Material for this article can be found online at: https://www.frontiersin.org/articles/10.3389/fphys.2018.01910/full#supplementary-material

REFERENCES

Alessandrini, M., Valinoti, M., Unger, L., Oesterlein, T., Doessel, O., Corsi, C., et al. (2018). A computational framework to benchmark basket catheter guided ablation in atrial fibrillation. *Front. Physiol.* 9:1251. doi: 10.3389/fphys.2018.01251

Bayer, J. D., Roney, C. H., Pashaei, A., Jaïs, P., and Vigmond, E. J. (2016). Novel radiofrequency ablation strategies for terminating atrial fibrillation in the left atrium: a simulation study. *Front. Physiol.* 7:108. doi: 10.3389/fphys.2016.00108

Bischoff, S., and Kobbelt, L. P. (2004). Parameterization-free active contour models with topology control. *Vis. Comput.* 20, 217–228. doi: 10.1007/s00371-003-0228-9

Biviano, A. B., Ciaccio, E. J., Fleitman, J., Knotts, R., Lawrence, J., Haynes, N., et al. (2015). Atrial tachycardias after atrial fibrillation ablation manifest different waveform characteristics: implications for characterizing tachycardias. *J. Cardiovasc. Electrophysiol.* 26, 1187–1195. doi: 10.1111/jce.12770

Boyle, P. M., Zahid, S., and Trayanova, N. A. (2017). Using personalized computer models to custom-tailor ablation procedures for atrial fibrillation patients: are we there yet? *Expert Rev. Cardiovasc. Ther.* 15, 339–341. doi: 10.1080/14779072.2017.1317593

Bunch, T. J., May, H. T., Bair, T. L., Jacobs, V., Crandall, B. G., Cutler, M., et al. (2016). The impact of age on 5-year outcomes after atrial fibrillation catheter ablation. *J. Cardiovasc. Electrophysiol.* 27, 141–146. doi: 10.1111/jce.12849

Cantwell, C. D., Roney, C. H., Ng, F. S., Siggers, J. H., Sherwin, S. J., and Peters, N. S. (2015). Techniques for automated local activation time annotation and conduction velocity estimation in cardiac mapping. *Comput. Biol. Med.* 65, 229–242. doi: 10.1016/j.compbiomed.2015.04.027

Castrejón-Castrejón, S., Ortega, M., Perez-Silva, A., Doiny, D., Estrada, A., Filgueiras, D., et al. (2011). Organized atrial tachycardias after atrial fibrillation ablation. *Cardiol Res. Pract.* 2011:957538. doi: 10.4061/2011/957538

Child, N., Bishop, M. J., Hanson, B., Coronel, R., Opthof, T., Boukens, B. J., et al. (2015). An activation-repolarization time metric to predict localized regions of high susceptibility to reentry. *Heart Rhythm* 12, 1644–1653. doi: 10.1016/j.hrthm.2015.04.013

Chugh, A., Oral, H., Lemola, K., Hall, B., Cheung, P., Good, E., et al. (2005). Prevalence, mechanisms, and clinical significance of macroreentrant atrial

tachycardia during and following left atrial ablation for atrial fibrillation. *Heart Rhythm* 2, 464–471. doi: 10.1016/j.hrthm.2005.01.027

Courtemanche, M., Ramirez, R. J., and Nattel, S. (1998). Ionic mechanisms underlying human atrial action potential properties: Insights from a mathematical model. *Am. J. Physiol. Heart Circ. Physiol.* 275(1 Pt 2), H301–H321.

Dang, L., Virag, N., Ihara, Z., Jacquemet, V., Vesin, J. M., Schlaepfer, J., et al. (2005). Evaluation of ablation patterns using a biophysical model of atrial fibrillation. *Ann. Biomed. Eng.* 33, 465–474. doi: 10.1007/s10439-005-2502-7

Deisenhofer, I., Estner, H., Zrenner, B., Schreieck, J., Weyerbrock, S., Hessling, G., et al. (2006). Left atrial tachycardia after circumferential pulmonary vein ablation for atrial fibrillation: incidence, electrophysiological characteristics, and results of radiofrequency ablation. *Europace* 8, 573–582. doi: 10.1093/europace/eul077

Deng, D., Murphy, M. J., Hakim, J. B., Franceschi, W. H., Zahid, S., Pashakhanloo, F., et al. (2017). Sensitivity of reentrant driver localization to electrophysiological parameter variability in image-based computational models of persistent atrial fibrillation sustained by a fibrotic substrate. *Chaos* 27:093932. doi: 10.1063/1.5003340

Dong, L., Bie, Z., Sun, L., Pan, X., and Guo, L. (2015). Long-term clinical outcome and risk of catheter ablation in elderly with non-paroxysmal atrial fibrillation. *Int. J. Clin. Exp. Med.* 8, 16050–16056.

Franzone, P. C., and Guerri, L. (1993). Spreading of excitation in 3-d models of the anisotropc cardiac tissue. I. Validation of the eikonal model. *Math Biosci.* 113, 145–209.

Gucuk Ipek, E., Marine, J. E., Habibi, M., Chrispin, J., Lima, J., Rickard, J., et al. (2016). Association of left atrial function with incident atypical atrial flutter after atrial fibrillation ablation. *Heart Rhythm* 13, 391–398. doi: 10.1016/j.hrthm.2015.09.028

Hart, P. E., Nilsson, N. J., and Raphael, B. (1968). A formal basis for the heuristic determination of minimum cost paths. *IEEE Trans. Syst. Sci. Cybern.* 4, 100–107. doi: 10.1109/TSSC.1968.300136

Herlin, A., and Jacquemet, V. (2011). Eikonal-based initiation of fibrillatory activity in thin-walled cardiac propagation models. *Chaos* 21:043136. doi: 10.1063/1.3670060

Hétroy, F., and Attali, D. (2003). "From a closed piecewise geodesic to a constriction on a closed triangulated surface," in *11th Pacific Conference on Computer Graphics and Applications* (Canmore, AB), 394–398.

Hill, Y. R., Child, N., Hanson, B., Wallman, M., Coronel, R., Plank, G., et al. (2016). Investigating a novel activation-repolarisation time metric to predict localised vulnerability to reentry using computational modelling. *PLoS ONE* 11:e0149342. doi: 10.1371/journal.pone.0149342

Hwang, M., Kwon, S.-S., Wi, J., Park, M., Lee, H.-S., Park, J.-S., et al. (2014). Virtual ablation for atrial fibrillation in personalized *in-silico* three-dimensional left atrial modeling: comparison with clinical catheter ablation. *Prog. Biophys. Mol. Biol.* 116, 40–47. doi: 10.1016/j.pbiomolbio.2014.09.006

Jacquemet, V. (2010). The inverse problem of phase singularity distribution: an eikonal approach. *Comput. Cardiol.* 37, 863–866. doi: 10.1109/TBME.2010.2051156

Jacquemet, V. (2016). Lessons from computer simulations of ablation of atrial fibrillation. *J. Physiol.* 594, 2417–2430. doi: 10.1113/JP271660

Jacquemet, V., Virag, N., and Kappenberger, L. (2005). Wavelength and vulnerability to atrial fibrillation: Insights from a computer model of human atria. *Europace* 7(Suppl. 2), 83–92. doi: 10.1016/j.eupc.2005.03.017

Jaïs, P., Sanders, P., Hsu, L.-F., Hocini, M., Sacher, F., Takahashi, Y., et al. (2006). Flutter localized to the anterior left atrium after catheter ablation of atrial fibrillation. *J. Cardiovasc. Electrophysiol.* 17, 279–285. doi: 10.1111/j.1540-8167.2005.00292.x

Keener, J. P. (1991). An eikonal-curvature equation for action potential propagation in myocardium. *J. Math. Biol.* 29, 629–651.

Kobza, R., Hindricks, G., Tanner, H., Schirdewahn, P., Dorszewski, A., Piorkowski, C., et al. (2004). Late recurrent arrhythmias after ablation of atrial fibrillation: incidence, mechanisms, and treatment. *Heart Rhythm* 1, 676–683. doi: 10.1016/j.hrthm.2004.08.009

Konukoglu, E., Relan, J., Cilingir, U., Menze, B. H., Chinchapatnam, P., Jadidi, A., et al. (2011). Efficient probabilistic model personalization integrating uncertainty on data and parameters: application to eikonal-diffusion models in cardiac electrophysiology. *Prog. Biophys. Mol. Biol.* 107, 134–146. doi: 10.1016/j.pbiomolbio.2011.07.002

Krogh-Madsen, T., and Christini, D. J. (2012). Nonlinear dynamics in cardiology. *Annu. Rev. Biomed. Eng.* 14, 179–203. doi: 10.1146/annurev-bioeng-071811-150106

Krueger, M. W., Dorn, A., Keller, D. U. J., Holmqvist, F., Carlson, J., Platonov, P. G., et al. (2013). *In-silico* modeling of atrial repolarization in normal and atrial fibrillation remodeled state. *Med. Biol. Eng. Comput.* 51, 1105–1119. doi: 10.1007/s11517-013-1090-1

Labarthe, S., Bayer, J., Coudière, Y., Henry, J., Cochet, H., Jaïs, P., et al. (2014). A bilayer model of human atria: mathematical background, construction, and assessment. *EP Europace* 16(Suppl_4), iv21–iv29. doi: 10.1093/europace/euu256

Latcu, D. G., and Saoudi, N. (2014). How fast does the electrical impulse travel within the myocardium? the need for a new clinical electrophysiology tool: the conduction velocity mapping. *J. Cardiovasc. Electrophysiol.* 25, 395–397. doi: 10.1111/jce.12350

Lee, Y., and Lee, S. (2002). Geometric snakes for triangular meshes. *Comput. Graphics Forum* 21, 229–238. doi: 10.1111/1467-8659.t01-1-00582

Lee, Y., Lee, S., Shamir, A., Cohen-Or, D., and Seidel, H.-P. (2004). "Intelligent mesh scissoring using 3D snakes," in *12th Pacific Conference on Computer Graphics and Applications* (Seoul), 279–287.

Liang, J. J., Elafros, M. A., Chik, W. W., Santangeli, P., Zado, E. S., Frankel, D. S., et al. (2015). Early recurrence of atrial arrhythmias following pulmonary vein antral isolation: timing and frequency of early recurrences predicts long-term ablation success. *Heart Rhythm* 12, 2461–2468. doi: 10.1016/j.hrthm.2015.07.015

Lines, G. T., MacLachlan, M. C., Linge, S., and Tveito, A. (2009). Synchronizing computer simulations with measurement data for a case of atrial flutter. *Ann. Biomed. Eng.* 37, 1287–1293. doi: 10.1007/s10439-009-9692-3

Loewe, A. (2016). *Modeling Human Atrial Patho-electrophysiology From Ion Channels to ECG: Substrates, Pharmacology, Vulnerability, and P-waves*. PhD thesis, Karlsruhe Institute of Technology (KIT).

Loewe, A., Krueger, M. W., Platonov, P. G., Holmqvist, F., Dössel, O., and Seemann, G. (2015). "Left and right atrial contribution to the p-wave in realistic computational models," in *Functional Imaging and Modeling of the Heart 2015, Lecture Notes in Computer Science*, Vol. 9126 (Berlin; Heidelberg), 439–447.

Loewe, A., Lutz, Y., Wilhelms, M., Sinnecker, D., Barthel, P., Scholz, E. P., Dossel, O., Schmidt, G., and Seemann, G. (2014a). *In-silico* assessment of the dynamic effects of amiodarone and dronedarone on human atrial patho-electrophysiology. *Europace* 16(Suppl. 4), iv30–iv38. doi: 10.1093/europace/euu230

Loewe, A., Wilhelms, M., Dössel, O., and Seemann, G. (2014b). Influence of chronic atrial fibrillation induced remodeling in a computational electrophysiological model. *Biomed. Tech.* 59, S929–S932. doi: 10.1515/bmt-2014-5012

Loewe, A., Wilhelms, M., Fischer, F., Scholz, E. P., Dössel, O., and Seemann, G. (2014c). Arrhythmic potency of human ether-a-go-go-related gene mutations L532P and N588K in a computational model of human atrial myocytes. *Europace* 16, 435–443. doi: 10.1093/europace/eut375

Matene, E., and Jacquemet, V. (2012). Fully automated initiation of simulated episodes of atrial arrhythmias. *Europace* 14(Suppl. 5), v17–v24. doi: 10.1093/europace/eus271

McDowell, K. S., Zahid, S., Vadakkumpadan, F., Blauer, J., MacLeod, R. S., and Trayanova, N. A. (2015). Virtual electrophysiological study of atrial fibrillation in fibrotic remodeling. *PLoS ONE* 10:e0117110. doi: 10.1371/journal.pone.0117110

Mesas, C. E., Pappone, C., Lang, C. C., Gugliotta, F., Tomita, T., Vicedomini, G., et al. (2004). Left atrial tachycardia after circumferential pulmonary vein ablation for atrial fibrillation: electroanatomic characterization and treatment. *J. Am. Coll. Cardiol.* 44, 1071–1079. doi: 10.1016/j.jacc.2004.05.072

Neic, A., Campos, F. O., Prassl, A. J., Niederer, S. A., Bishop, M. J., Vigmond, E. J., et al. (2017). Efficient computation of electrograms and ECGs in human whole heart simulations using a reaction-eikonal model. *J. Comput. Phys.* 346, 191–211. doi: 10.1016/j.jcp.2017.06.020

Niederer, S. A., Kerfoot, E., Benson, A. P., Bernabeu, M. O., Bernus, O., Bradley, C., et al. (2011). Verification of cardiac tissue electrophysiology simulators using

an n-version benchmark. *Philos. Trans. R. Soc. A Math. Phys. Eng. Sci.* 369, 4331–4351. doi: 10.1098/rsta.2011.0139

Patel, A. M., d'Avila, A., Neuzil, P., Kim, S. J., Mela, T., Singh, J. P., et al. (2008). Atrial tachycardia after ablation of persistent atrial fibrillation: identification of the critical isthmus with a combination of multielectrode activation mapping and targeted entrainment mapping. *Circ. Arrhythm. Electrophysiol.* 1, 14–22. doi: 10.1161/CIRCEP.107.748160.

Pernod, E., Sermesant, M., Konukoglu, E., Relan, J., Delingette, H., and Ayache, N. (2011). A multi-front eikonal model of cardiac electrophysiology for interactive simulation of radio-frequency ablation. *Comput. Graph.* 35, 431–440. doi: 10.1016/j.cag.2011.01.008

Pezzuto, S., Kal'avský, P., Potse, M., Prinzen, F. W., Auricchio, A., and Krause, R. (2017). Evaluation of a rapid anisotropic model for ecg simulation. *Front. Physiol.* 8:265. doi: 10.3389/fphys.2017.00265

Reumann, M., Bohnert, J., Seemann, G., Osswald, B., and Dössel, O. (2008). Preventive ablation strategies in a biophysical model of atrial fibrillation based on realistic anatomical data. *IEEE Trans. Biomed. Eng.* 55, 399–406. doi: 10.1109/TBME.2007.912672

Sermesant, M., Coudiere, Y., Moreau-Villeger, V., Rhode, K. S., Hill, D. L. G., and Razavi, R. S. (2005). "A fast-marching approach to cardiac electrophysiology simulation for XMR interventional imaging," in *MICCAI International Conference on Medical Image Computing and Computer-Assisted Intervention* (Berlin; Heidelberg), 607–615.

Sermesant, M., Konukoglu, E., Delingette, H., Coudiere, Y., Chinchapatnam, P., Rhode, K., et al. (2007). "An anisotropic multi-front fast marching method for real-time simulation of cardiac electrophysiology," in *Functional Imaging and Modeling of the Heart 2015, Lecture Notes in Computer Science*, volume 4466, pages 160–169.

Sethian, J. A. (1996). A fast marching level set method for monotonically advancing fronts. *Proc. Natl. Acad. Sci. U.S.A.* 93, 1591–1595.

Sethian, J. A. (1999). *Level Set Methods and Fast Marching Methods*. Cambridge, UK: Cambridge University Press.

Sethian, J. A., and Vladimirsky, A. (2000). Fast methods for the Eikonal and related Hamilton-Jacobi equations on unstructured meshes. *Proc. Natl. Acad. Sci. U.S.A.* 97, 5699–5703. doi: 10.1073/pnas.090060097

Sethian, J. A., and Vladimirsky, A. (2003). Ordered upwind methods for static Hamilton-Jacobi equations: Theory and algorithms. *SIAM J. Numer. Anal.* 41, 325–363. doi: 10.1137/S0036142901392742

Trächtler, J., T., O., Loewe, A., Poremba, E., Luik, A., Schmitt, C., and Dössel, O. (2015). Virtualizing clinical cases of atrial flutter in a fast marching simulation including conduction velocity and ablation scars. *Curr. Dir. Biomed. Eng.* 1, 405–408. doi: 10.1515/cdbme-2015-0098

Unger, L., Oesterlein, T., Seemann, G., Dössel, O., Spector, P., and Loewe, A. (2017). Estimating refractory periods during atrial fibrillation based on electrogram cycle lengths in a heterogeneous simulation setup. *Curr. Dir. Biomed. Eng.* 3, 317–320. doi: 10.1515/cdbme-2017-0181

van Dam, P. M., Oostendorp, T. F., and van Oosterom, A. (2009). Application of the fastest route algorithm in the interactive simulation of the effect of local ischemia on the ECG. *Med. Biol. Eng. Comput.* 47, 11–20. doi: 10.1007/s11517-008-0391-2

van Dam, P. M., and van Oosterom, A. (2003). Atrial excitation assuming uniform propagation. *J. Cardiovasc. Electrophysiol.* 14(10 Suppl.), S166–S171. doi: 10.1046/j.1540.8167.90307.x

Verma, B., Oesterlein, T., Loewe, A., Luik, A., Schmitt, C., and Dössel, O. (2018). Regional conduction velocity calculation from clinical multichannel electrograms in human atria. *Comput. Biol. Med.* 92, 188–196. doi: 10.1016/j.compbiomed.2017.11.017

Villacastín, J., Perez-Castellano, N., Moreno, J., and Gonzalez, R. (2003). Left atrial flutter after radiofrequency catheter ablation of focal atrial fibrillation. *J. Cardiovasc. Electrophysiol.* 14, 417–421. doi: 10.1046/j.1540-8167.2003.02418.x

Wachter, A., Loewe, A., Krueger, M. W., Dössel, O., and Seemann, G. (2015). Mesh structure-independent modeling of patient-specific atrial fiber orientation. *Curr. Dir. Biomed. Eng.* 1, 409–412. doi: 10.1515/cdbme-2015-0099

Waldo, A. L., and Feld, G. K. (2008). Inter-relationships of atrial fibrillation and atrial flutter: mechanisms and clinical implications. *J. Am. Coll. Cardiol.* 51, 779–786. doi: 10.1016/j.jacc.2007.08.066

Wallman, M., Bueno-Orovio, A., and Rodriguez, B. (2013). "Computational probabilistic quantification of pro-arrhythmic risk from scar and left-to-right heterogeneity in the human ventricles," in *Computing in Cardiology Conference (CinC)* (Zaragoza), 711–714.

Wallman, M., Smith, N. P., and Rodriguez, B. (2012). A comparative study of graph-based, eikonal, and monodomain simulations for the estimation of cardiac activation times. *IEEE Trans. Biomed. Eng.* 59, 1739–1748. doi: 10.1109/TBME.2012.2193398

Weber, F. M., Luik, A., Schilling, C., Seemann, G., Krueger, M. W., Lorenz, C., et al. (2011). Conduction velocity restitution of the human atrium–an efficient measurement protocol for clinical electrophysiological studies. *IEEE Trans. Biomed. Eng.* 58, 2648–2655. doi: 10.1109/TBME.2011.2160453

Weber, F. M., Schilling, C., Seemann, G., Luik, A., Schmitt, C., Lorenz, C., et al. (2010). Wave-direction and conduction-velocity analysis from intracardiac electrograms–a single-shot technique. *IEEE Trans. Biomed. Eng.* 57, 2394–2401. doi: 10.1109/TBME.2010.2055056

Wilhelms, M., Hettmann, H., Maleckar, M. M. C., Koivumäki, J. T., Dössel, O., and Seemann, G. (2013). Benchmarking electrophysiological models of human atrial myocytes. *Front. Physiol.* 3:487. doi: 10.3389/fphys.2012.00487

Yamada, T., and Kay, G. N. (2013). Atrial flutter following pulmonary vein isolation: what is the mechanism? *J. Cardiovasc. Electrophysiol.* 24, 1186–1188. doi: 10.1111/jce.12167

Zahid, S., Whyte, K. N., Schwarz, E. L., Blake, R. C., Boyle, P. M., Chrispin, J., et al. (2016). Feasibility of using patient-specific models and the "minimum cut" algorithm to predict optimal ablation targets for left atrial flutter. *Heart Rhythm* 13, 1687–1698. doi: 10.1016/j.hrthm.2016.04.009

Zhao, J., Kharche, S. R., Hansen, B. J., Csepe, T. A., Wang, Y., Stiles, M. K., et al. (2015). Optimization of catheter ablation of atrial fibrillation: insights gained from clinically-derived computer models. *Int. J. Mol. Sci.* 16, 10834–10854. doi: 10.3390/ijms160510834

Conflict of Interest Statement: The authors declare that the research was conducted in the absence of any commercial or financial relationships that could be construed as a potential conflict of interest.

frontiers in Physiology

ORIGINAL RESEARCH
published: 22 January 2019
doi: 10.3389/fphys.2018.01938

The Impact of Left Atrium Appendage Morphology on Stroke Risk Assessment in Atrial Fibrillation: A Computational Fluid Dynamics Study

Alessandro Masci[1], Lorenzo Barone[1], Luca Dedè[2], Marco Fedele[2], Corrado Tomasi[3], Alfio Quarteroni[2] and Cristiana Corsi[1]**

[1] DEI, University of Bologna, Bologna, Italy, [2] MOX, Mathematics Department, Politecnico di Milano, Milan, Italy, [3] Department of Cardiology, Santa Maria delle Croci Hospital, AUSL della Romagna, Ravenna, Italy

Atrial fibrillation (AF) carries out a 5-fold increase in stroke risk, related to embolization of thrombi clotting in left atrium (LA). Left atrial appendage (LAA) is the site with the highest blood stasis which causes thrombus formation. About 90 % of the intracardiac thrombi in patients with cardioembolic events originally develop in the LAA. Recent studies have been focused on the association between LAA anatomical features and stroke risk and provided conflicting results. Haemodynamic and fluid dynamic information on the LA and mostly on the LAA may improve stroke risk stratification. Therefore, the aim of this study was the design and development of a workflow to quantitatively define the influence of the LAA morphology on LA hemodynamics. Five 3D LA anatomical models, obtained from real clinical data, which were clearly different as regard to LAA morphology were used. For each LAA we identified and computed several parameters describing its geometry. Then, one LA chamber model was chosen and a framework was developed to connect the different LAAs belonging to the other four patients to this model. These new anatomical models represented the computational domain for the computational fluid dynamics (CFD) study; simulations of the hemodynamics within the LA and LAA were performed in order to evaluate the interplay of the LAA shape on the blood flow characteristics in AF condition. CFD simulations were carried out for five cardiac cycles. Blood velocity, vorticity, LAA orifice velocity, residence time computed in the five models were compared and correlated with LAA morphologies. Results showed that not only complex morphologies were characterized by low velocities, low vorticity and consequently could carry a higher thrombogenic risk; even qualitatively simple morphologies showed a thrombogenic risk equal, or even higher, than more complex auricles. CFD results supported the hypothesis that LAA geometric characteristics plays a key-role in defining thromboembolic risk. LAA geometric parameters could be considered, coupled with the morphological characteristics, for a comprehensive evaluation of the regional blood stasis. The proposed procedure might address the development of a tool for patient-specific stroke risk assessment and preventive treatment in AF patients, relying on morpho-functional defintion of each LAA type.

Keywords: left atrial appendage, computational fluid dynamics, thrombogenicity, atrial fibrillation, stroke risk assessment

OPEN ACCESS

Edited by:
Javier Saiz, Universitat Politécnica de Valéncia, Spain

Reviewed by:
Mariano Vàzquez, Barcelona Supercomputing Center, Spain
Chris Patrick Bradley, The University of Auckland, New Zealand

****Correspondence:***
Alessandro Masci
alessandro.masci4@unibo.it
Cristiana Corsi
cristiana.corsi3@unibo.it

Specialty section:
This article was submitted to Computational Physiology and Medicine, a section of the journal Frontiers in Physiology

Received: *02 August 2018*
Accepted: *21 December 2018*
Published: *22 January 2019*

Citation:
Masci A, Barone L, Dedè L, Fedele M, Tomasi C, Quarteroni A and Corsi C (2019) The Impact of Left Atrium Appendage Morphology on Stroke Risk Assessment in Atrial Fibrillation: A Computational Fluid Dynamics Study. Front. Physiol. 9:1938. doi: 10.3389/fphys.2018.01938

1. INTRODUCTION

Atrial Fibrillation (AF) is the most common type of arrhythmia. It was demonstrated that the lifetime risk of developing AF after 40 years of age is 26% for men and 23% for women of European descent (Briceno et al., 2015; Zakeri et al., 2017). Over 6 million Europeans suffer from AF and its prevalence is estimated to at least at least double in the next 50 years as the population ages. of stroke 5-fold (January et al., 2014). LAA is the remnant of the embryonic left atrium where the smooth-walled LA originates from the primordial pulmonary vein and its branches (Reddy et al., 2014). Because of its hooked morphology, the LAA is the left atrial site of the highest blood stasis risk, increasing the incidence of thrombus formation and stroke. In fact, 90 % of the intracardiac thrombi in patients with cardioembolic stroke/TIA are considered as originating in the LAA (Yaghi et al., 2015). Oral anticoagulation therapy was the only option available until recently. However, it increases bleeding risk and interpheres with other drugs and multiorgan functioning, and its risk can overtake the otherwise remakable benefits on thromboembolic events. (Hankey and Eikelboom, 2011).

For these reasons, different strategies have been developed such as the use of interventional treatments, i.e., LAA percutaneous closure, which seems to better reduce the risk of thromboembolism compared to warfarin anticoagulation therapy (Reddy et al., 2013). These treatments are restricted to small subgroups of patients, due to the procedural risks and costs which may overcome the preventive antiembolic efficacy.

Therefore, morphological and quantitative features of LAA have been increasingly studied in the past few years. Di Biase et al. (2012) presented a classification of LAA morphology into four different classes (chicken wing, cauliflower, windsock, and cactus) based on their morphological complexity. They studied the correlation between this characteristic and the patient-specific stroke history. Results demonstrated that chicken wing LAA morphology, which is the most prevalent, was less likely to have an embolic event compared to the other LAA types.

Jeong et al. (2016) investigated whether the morphometric or volumetric parameters of LAA would be related to the development of cardioembolism in subjects with AF. They found that LAA orifice diameter and LAA volume were larger in patients with a history of cardioembolic stroke with respect to the control group. AF determines alterations in the LAA wall and surrounding structures and this could explain why elevated LAA volumes are found in stroke patients. Despite these attempts, the association between the aforementioned LAA anatomical features and stroke risk does not seem straightforward, and conflicting results have been published. Moreover, it is still uncertain what is the best strategy for stroke prevention in AF. To this purpose, several clinical studies suggested that stroke risk stratification could be improved by using hemodynamic information on the left atrium (LA) and mainly on the left atrial appendage (LAA) (Gupta et al., 2013; Markl et al., 2016). Computational fluid dynamics (CFD) represents a valuable non-invasive tool to determine and assess meaningful biophysical indicators in a complex fluid dynamics systems, such as velocity, pressure fields, cardiac blood flowrates, vorticity, turbulent kinetic energy, etc. To date, few contributions are based on the CFD modeling of the LAA (Koizumi et al., 2015; Otani et al., 2016; Olivares et al., 2017; Bosi et al., 2018). These studies are more focused on the correlation between LAA hemodynamic characteristics and morphology type in order to compare the results obtained with the observations by Di Biase et al. (2012).

To the best of our knowledge, the interplay of the geometric parameters such as LAA length, tortuosity, surface area and volume with the fluid dynamics parameters have not been investigated. This analysis might highlight new insights into the effects of atrial fibrillation on the LAA haemodynamics, thus providing a better understanding of the thrombi formation risk. Moreover, previous studies considered not only different LAA morphologies for the CFD simulation but also different LA shapes which varied for each patient analyzed. Therefore, considerations regarding the LAA fluid dynamics and mainly its thrombogenicity could be affected also by the variation of the other LA anatomical structures.

The aim of this study was the design and development of a workflow to quantify the influence of LAA morphology alone on the LA hemodynamics. Five 3D LA (including LAA) anatomical models, obtained from real clinical data (CT (CT and MRI), which were all different in regards to the LAA each LAA we computed several parameters describing its geometry. Then, one LA chamber model was chosen and a framework was developed to connect the different LAAs belonging to the other four patients to this model. These anatomical models represented the computational domain for the CFD model described in Masci et al. (2017). Simulations of the haemodynamics within the LA and LAA in AF conditions were performed. In this paper we discuss the details of the developed pipeline. A quantitative analysis for each LAA was performed before the CFD simulations by evaluating the most significant geometrical parameters. Afterwards, the association between geometrical and fluid dynamics indexes were computed in order to evaluate, for each LAA, the correlation with the blood stasis risk and thrombi formation.

2. METHODS

A schematic workflow of the project is shown in **Figure 1**.

2.1. Patients Data

The data-set consisted of five LA 3D anatomical models. These models were extracted from CT (one) and MRI (four) data, in patients affected by AF. The study was approved by the Ethics IRST, IRCCS AVR Committee (CEIIAV n. 1456 prot. 6076/2015 I.5/220). All subjects gave written informed consent in accordance with the Declaration of Helsinki.

Data were processed with specifically designed in-house image segmentation algorithms, described in Valinoti et al. (2018); Masci et al. (2017). From the 3D LA binary masks, we generated the surface meshes by using the MATLAB iso2mesh toolbox (Fang and Boas, 2010).

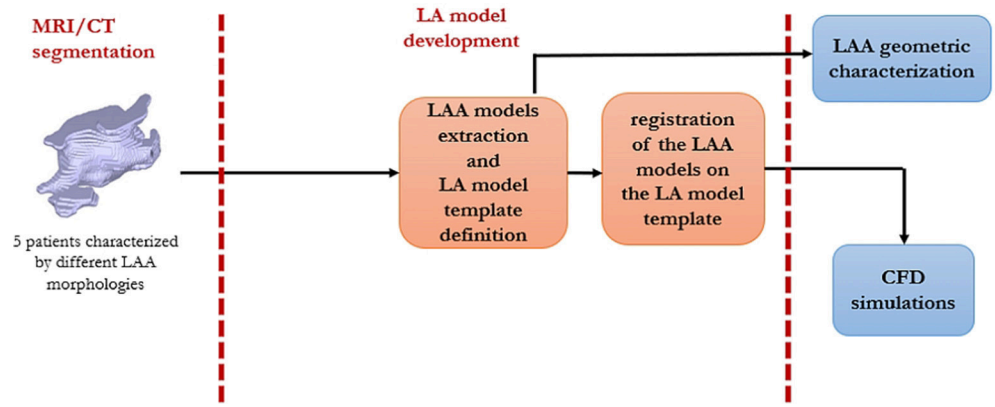

FIGURE 1 | A schematic description of the workflow of this study.

2.2. LAA Extraction

The next step was focused on the implementation of an algorithm which automatically recognized and isolated the LAA from the data-set of left atrial anatomical models. To this purpose, the shape diameter function (SDF) proposed by Shapira et al. (2008) was employed. SDF defines a scalar function on the mesh surface M ($f_s : M \rightarrow \mathbb{R}$) that measures the local object diameter. From a point p, a cone of rays was sent toward the interior of the mesh in the opposite direction to the normal at p and the distance between p and the intersection of each ray with the mesh was computed. In order to remove false intersections, the intersections with normals at the point of intersection in the same direction as p, were removed. Furthermore, only the rays whose length fell within one standard deviation from the median of all lengths were considered. The final SDF value at the point p was defined as the weighted average of the remaining lengths, where the weight values were the inverse of the angle between ray and the center of the cone. In this study, the SDF was calculated for each 3D surface using the CGAL software (Fabri and Teillaud, 2011). An example of the SDF values computation for one LA anatomical model is depicted in **Figure 2**.

The SDF values created iso-contours on the mesh which were used to separate regions with different SDF values. Based on this idea, we obtained a semantic clusterization of our 3D models where each cluster had a different id number. The output of this procedure was a vector that contained a label for each facet. This step allowed the identification of pulmonary veins (PVs), LA chamber and LAA for each mesh. In order to identify the LAA, we detected the atrial chamber identificator by calculating the mode (statistics) of the label vector; afterwards we assigned to the PVs the same identificator of the LA chamber. Based on the anatomical position of the LAA we were able to select this region of interest in order to automatically identify it and isolate from the LA surface mesh. An example of the result of this step is shown in **Figure 3**.

Applying this approach, we obtained five LAA surface meshes. Once the LAA was removed, the LA mesh shown in **Figure 2** was used as template for the definition of the new LA anatomical models, each one was characterized by a particular LAA morphology.

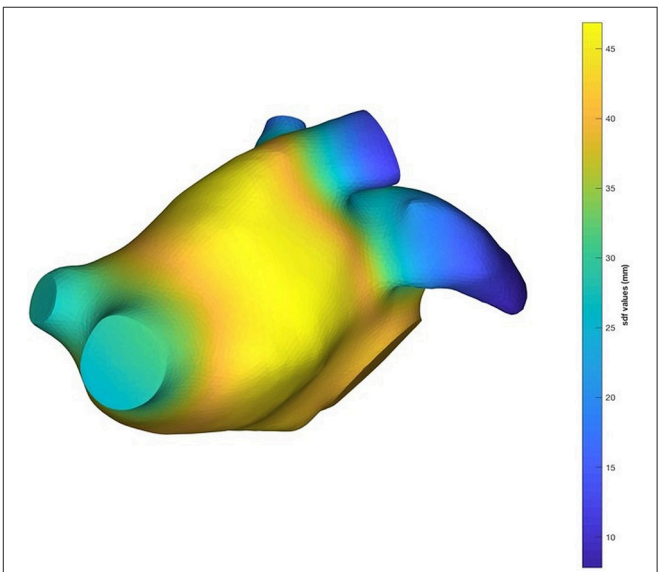

FIGURE 2 | An example of the SDF result on a LA mesh.

2.3. LAA Alignment and Definition of the New LA Models

Once the previous steps were performed, in order to accomplish the alignment between the LA template and the LAA meshes, we identified the vertices which belong to LAA ostia and the LA ostium template. The output was a vector that contained the detected vertex coordinates. The local correspondence between LAA and LA template ostium vertices was achieved by using the iterative closest point (ICP) algorithm (Besl and McKay, 1992). The ICP algorithm matched closest points between two point data sets: one was used as a fixed data set and the other as a

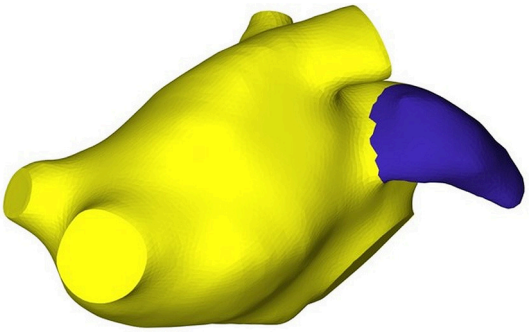

FIGURE 3 | LAA vertices and faces detection.

floating data set. In our case, the fixed one was composed by vertices of the LA ostium and the floating one by the LAA ostium vertices.

The ICP algorithm iteratively performed the following steps:

1. Matching: for each vertex of the floating data set, the nearest neighbor vertex of the fixed data set was found;
2. Minimization: the error metric was minimized between these two set of vertices;
3. Transformation: floating data points were then mapped in the new space using the computed transformation.

Once this procedure was employed, a set of five LA anatomical models, presenting the same atrial chamber but different LAA geometries, was created.

Finally, in order to refine the anatomical models and to comply with the requirement of providing a smooth geometrical representation of the computational domain for the CFD simulation, a Laplacian smoothing filtering and Poisson surface reconstruction were applied by using MeshLab (Cignoni et al., 2008).

2.4. LAA Geometrical Parameters

The five anatomical models created by the framework described above are illustrated in **Figure 4**. The shape and the geometry of the LAAs were different and, in order to quantify the differences between the LAAs and their impact on the haemodynamic characteristics, we performed a specific analysis by quantifying LAA volume, LAA surface area, length, tortuosity, and LAA orifice perimeter and area. Length was evaluated by the LAA centerlines computation. Tortuosity was defined as (Piccinelli et al., 2009):

$$\mathcal{X} = \frac{L}{D} - 1; \tag{1}$$

where L is the centerline length and D is the Euclidean distance between the centerline endpoints. Tortuosity values much higher than 0 reflect the complexity of the LAA shapes, whereas values near to 0 describe more orderly the LAA geometries.

In order to compute the LAA volumes and orifice (i.e., LAA ostium) areas, LAA volume meshes were generated. For this step, the VMTK library was employed (Antiga and Steinman, 2012). The finite element count for each LA mesh is reported in **Table 1**. The LA volume meshes represented the computational domain of the CFD model.

2.5. CFD Model

The CFD model used for the simulation of the haemodynamics of each anatomical model was the one presented by Masci et al. (2017) and based on the $\mathbb{P}1 - \mathbb{P}1$ finite element method with SUPG-VMS stabilization of the Navier-Stokes equations described in Forti and Dedè (2015). In particular, the blood flow was modeled as a fluid governed by the incompressible Navier-Stokes equations written in the ALE frame of reference (Khurram and Masud, 2006; Reymond et al., 2013; Quarteroni et al., 2017).

Regarding the imposition of the boundary conditions, we considered a mitral valve (MV) flowrate Q^0 from Koizumi et al. (2015). This flowrate was suitably modified for our application: indeed, we removed the atrial contraction wave (A wave) because this is strongly reduced during AF (Gautam and John, 2011). Afterwards, the flowrate at each pulmonary vein (PV) was computed by enforcing mass balance conservation for all $t \in (0, T]$:

$$Q_1^{pv} + Q_2^{pv} + Q_3^{pv} + Q_4^{pv} + Q^O + \frac{dV}{dt} = 0 \tag{2}$$

where $Q_i^{pv}, (i = 1, 2, 3, 4)$ were the flowrates of each pulmonary veins, Q^O was the flowrate at the MV section and $\frac{dV}{dt}$ is the LA volume variation. From Equation 2, we defined Q_{tot}^{pv}, the total flux at the PVs:

$$Q_{tot}^{pv} = Q_1^{pv} + Q_2^{pv} + Q_3^{pv} + Q_4^{pv}. \tag{3}$$

The total flux Q_{tot}^{pv} through the four pulmonary veins was split with a criterion based on proportionality with their sectional area:

$$Q_l^{pv} = \frac{A_l}{A_t} Q_{tot}^{pv} - Q_l^w \qquad l = 1, 2, 3, 4, \tag{4}$$

where A_l is the sectional area of each PV and A_t is the sum of PVs sectional areas. Q_l^w represents the term related to each PV section velocity during the cardiac cycle. This term is not null in our application since we applied a random displacement function to our computational domain throughout the cardiac cycle. Therefore, PVs sections are allowed to displace along the heartbeat. In this way, for each $t \in (0, T]$, we were able to evaluate the flowrate at each PV to be applied at the computational model.

In order to limit the presence of unphysical backflows which may give rise to numerical instabilities at the outflow boundary (i.e., MV), we considered the natural-type boundary condition reported in Bazilevs et al. (2009) with backflow penalization.

The numerical discretization of the CFD model was implemented in LifeV, a state-of-art library for the CFD simulations in the parallel setting [1]. Twenty cores (Intel Xeon processor E5, 2.5 GHz) were used for each LA CFD simulation.

[1] www.lifev.org

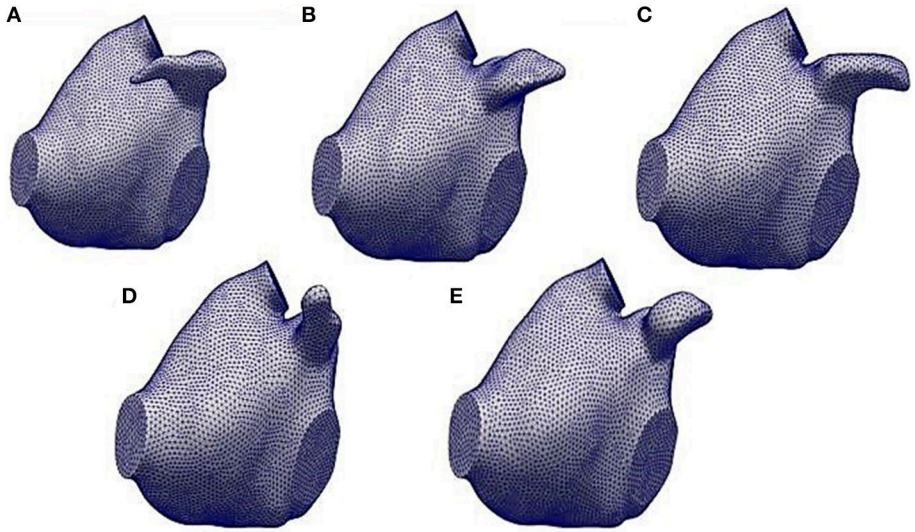

FIGURE 4 | The five LA anatomical models obtained by the automatic framework described in sections 2.2 and 2.3. **(A)** refers to the LA model with the LAA1, **(B)** the one with the LAA2, **(C)** with the LAA3, **(D)** with the LAA4 and **(E)** with the LAA5.

TABLE 1 | Mesh size of each analyzed model.

	Mesh size (# of finite elements)
LA model with LAA1	1,878,564
LA model with LAA2	1,767,432
LA model with LAA3	1,923,543
LA model with LAA4	1,698,675
LA model with LAA5	1,716,897

2.6. Numerical Simulation and Fluid Dynamics Parameter Computation

For each LA anatomical model, we performed a simulation in AF condition. Unfortunately, due to the requirement of ECG triggering, no imaging technique is available to acquire data during AF episodes from which a realistic and patient-specific deformation model might be derived. Since LA motion in AF is qualitatively defined as an irregular, disorganized, very rapid and strongly reduced contraction, we modeled atrial contraction by employing a random displacement applied independently to each vertex of the anatomical LA model and consisting in a sinusoidal function at a frequency of 4 Hz multiplied by a random factor from an uniform probability density function from 0 to 1. Moreover, the sinusoidal wave was modulated by a small amplitude (0.1 mm) in order to mimic the strongly reduced contraction and avoid numerical issues arising from an excessive worsening of the mesh quality. Simulations were run for five cardiac cycles to avoid the influence of the unphysiological initial condition on fluid velocity. We report the results of the fifth simulated cardiac cycle.

Regarding the parameters of the fluid dynamics model, the time step was set to 0.005 s, dynamic viscosity was 0.035 *poise* and the density was set to 1.06 g/cm^3.

The most significant parameters able to describe LAA fluid dynamics including velocity and vortex structures, LAA orifice velocity and mainly the residence time were computed. For the computation of the vortex structures the Q-criterion was employed. It is defined as in the following:

$$Q = \frac{1}{2}(\mathbf{W}_{ij}\mathbf{W}_{ij} - \mathbf{S}_{ij}\mathbf{S}_{ij}); \tag{5}$$

being $\mathbf{S}_{ij} = \left(\frac{\partial \mathbf{u}_{fi}}{\partial \mathbf{x}_j} + \frac{\partial \mathbf{u}_{fj}}{\partial \mathbf{x}_i}\right)$ and $\mathbf{W}_{ij} = \left(\frac{\partial \mathbf{u}_{fi}}{\partial \mathbf{x}_j} - \frac{\partial \mathbf{u}_{fj}}{\partial \mathbf{x}_i}\right)$ the symmetric and antisymmetric parts of the velocity-gradient tensor $\frac{\partial \mathbf{u}_{fi}}{\partial \mathbf{x}_j}$. Through this quantity, we identified and visualized some connected regions where $Q > 0$ and the pressure was lower than the ambient value at the vortexes core.

3. RESULTS

3.1. LAA Shape Descriptors

The values of the computed geometric parameters for each LAA are reported in **Table 2**.

Results showed a relevant variability in the LAA characteristics: for example, volume varied between 2.04 and 2.60 cm^3, length from 2.26 to 3.54 cm and tortuosity values are between 0.03 and 0.46. Comparing these quantities with a qualitative analysis of each LAA from **Figure 4**, we notice how the geometric indexes reflected the LAA geometric and morphological features. Considering LAA4, we observed, from a purely qualitative point of view, that it presented a very simple geometry and a linear morphology. Indeed, looking at the computation of its geometric indexes, tortuosity was the lowest

TABLE 2 | LAA geometrical parameters: V, volume; A_S, surface area; A_O, orifice area; P_O, orifice perimeter; L, length; χ, tortuosity.

LAA	V (cm^3)	A_S (cm^2)	A_O (cm^2)	P_O (cm)	L (cm)	χ
1	2.04	8.94	1.86	4.98	3.54	0.46
2	2.57	9.25	2.13	5.65	2.26	0.05
3	2.60	10.10	1.87	5.06	2.80	0.08
4	2.21	9.11	1.62	4.90	2.52	0.03
5	2.12	8.31	1.15	3.88	2.36	0.26

(0.03) with respect to the other LAAs. As expected, LAA3 showed the highest volume and surface area, as we can see from **Figure 4**. Moreover, LAA2 had the lowest length despite the major values of LAA orifice perimeter and area. Finally, LAA1 presented the highest tortuosity and length even though its volume was small. Therefore, these results confirmed the high variability of the geometric characteristics of the LAA and it could be relevant quantifying their implications in the appendage fluid dynamics mainly during AF in order to evaluate their impact on the probability of thrombi formation.

3.2. Velocity analysis

The computed velocity from the CFD simulations for the five LAAs is depicted in **Figure 5**.

Looking at the LAA1, we noticed that the blood flow started to enter into the auricle during the ventricular systole (first row, see **Supplemental Video1.mp4**) with velocity values between 7 and 9 cm/s. After the end of the ventricular systole the mitral valve opened (second row) and the blood flow exited from the LAA. Velocity was very low in this phase (2–3 cm/s) and these values could be associated with the morphology of the LAA1. Finally, looking at the end diastole phase (third row), blood flow continued to exit from the LAA1, reaching the maximum velocity (10 cm/s). Regarding the LAA2, the shape of this auricle was different with respect to the LAA1 and these differences were reflected by the velocity analysis. These two LAAs had comparable surface areas, orifice perimeters and areas; however volume (V), length (L) and tortuosity (χ) were very different (26 %, 56.6 % and one order of magnitude variations, respectively) and their values helped to elucidate the differences in the hemodynamic parameters. Blood flow entered and came out with a higher velocity than LAA1 (range:15–20 cm/s, see **Supplemental Video3.mp4**) and a more copious quantity of the blood flow within the LAA2 was noticed. Having a volume higher than LAA1 and a less compexity and length, LAA2 held a great quantity of blood flow which reached also its distal part. Regarding the LAA3, we supposed that, giving its qualitative similarity with the LAA1, also the velocity characteristics should not expect great variability between these two auricles. However, changes in the velocity profile were observed and they could be related to the different geometric parameters with respect to the LAA1. LAA3 presented a higher length than LAA2 but less than LAA1 and χ was one order of magnitude less than LAA1 and double with respect to the LAA2. Therefore, blood flow entered (first row **Figure 5**, see **Supplemental Video5.mp4**) and exited (third row **Figure 5**) from this appendage with intermediate values between LAA1 and LAA2 (6-7 cm/s). Moreover, the different orientation with respect to LAA1 allowed the blood flow to get into the auricle more easily. These observations indicated that blood washout for LAAs geometries similar to the LAA3 was not strongly reduced; however it was limited by the complexity of this morphology and also by its non-linear geometry. LAA4 was the most "linear" geometry. Indeed, looking at the **Table 2**, tortuosity was the smallest with respect to the other auricles. Therefore, we expected that this type of LAA would have a blood flow washout similar to the LAA2. However, even though its simple morphology, we noticed that blood flow, differently from the LAA2, did not reach, throughout the cardiac cycle, the distal parts of this LAA. In order to better understand these findings, we studied the differences in the other geometric parameters. We found that LAA4 was characterized by a particular geometry: it presented a high orifice perimeter and, as we can see from **Figure 4**, shrinked toward its distal part. Indeed the volume was not very high (2.21 cm^3). This particular geometry allowed the blood to easily enter in the LAA, giving the large orifice, but it did not penetrate in the more shrinked part of the auricle and it was forced to exit with high velocities (10–12 cm/s, see third row of **Figure 5**, **Supplemental Video7.mp4**). LAA5 velocity values were much lower than the other appendages and they did not exceed 7 cm/s (see **Supplemental Video9.mp4**). LAA5 had the smallest values of A_o, V, A_s, P_o coupled with a high value of the tortuosity (0.26). These characteristics probably explain the difficulty of the blood flow to enter in this type of LAA because of its reduced orifice, despite its length was not very high (2.52 cm). Therefore, only a small quantity of the blood flow entered in LAA5 with low velocity, implying a reduced washout of this auricle comparable to LAA1 and LAA3 but much lower than LAA2.

3.3. Vortex Structures Analysis

Vortex structures in each LAA are reported in **Figure 6**. In general, the presence of vortex structures within the LAA may be indicative of a better blood flow washout, thus avoiding the risk of blood stasis. Our considerations focused on the velocity of each LAA were confirmed by the vorticity analysis. LAA1 vortex structures in three different phases of the cardiac cycle are depicted in the first column of **Figure 6** (see also **Supplemental Video2.mp4**). We noticed that most of the vortices were localized in proximity of the LAA orifice, where we found the highest velocity. After the MV opening (second row **Figure 6**), vortex structures were characterized by low velocities. Moreover, throughout the cardiac cycle, vortices did not reach the distal part of the LAA, thus implying a scarce blood washout in AF. Different findings were observed on the LAA2. Indeed, given its simple morphology, vortex structures with higher velocity values than LAA1 occurred. Moreover, these vortices were not concentrated only in proximity to the LAA ostium and they reached all the anatomical parts of the LAA. (see **Supplemental Video4.mp4**) Results obtained on the LAA3 (third column, **Figure 6**, **Supplemental Video6.mp4**) were similar to the LAA1. Indeed, vortex structures were localized near to the orifice. However, it seemed that these

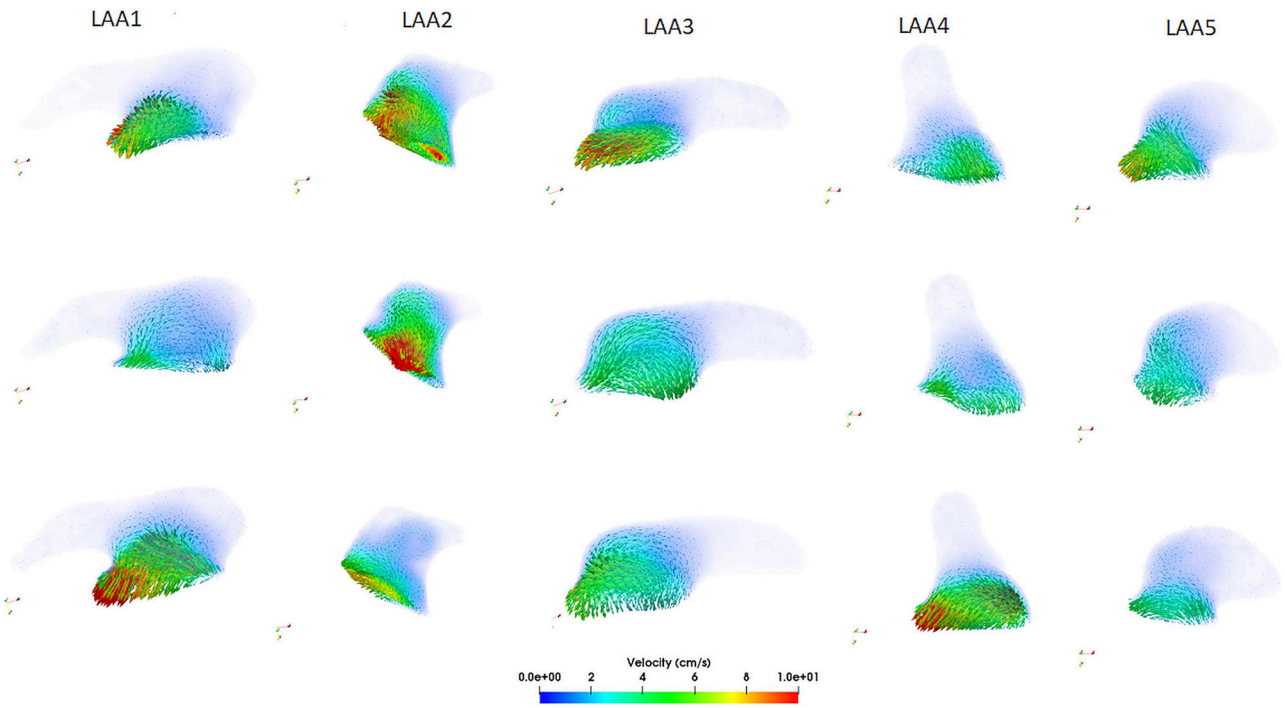

FIGURE 5 | Computed velocity within each LAA during the ventricular systole (first row), at the beginning of the ventricular diastole (second row), and at the end diastole (third row).

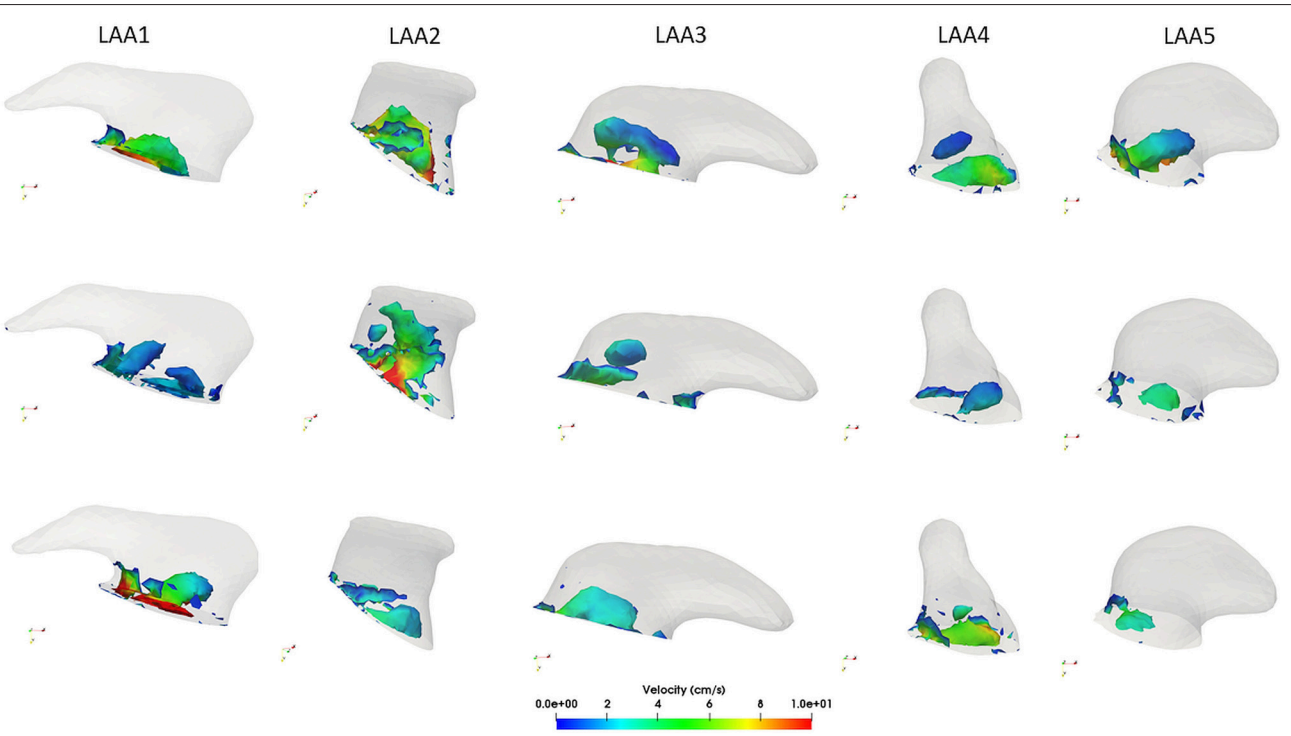

FIGURE 6 | Computed vortex structures with the Q-criterion within each LAA during the ventricular systole (first row), at the beginning of the ventricular diastole (second row) and at the end diastole (third row).

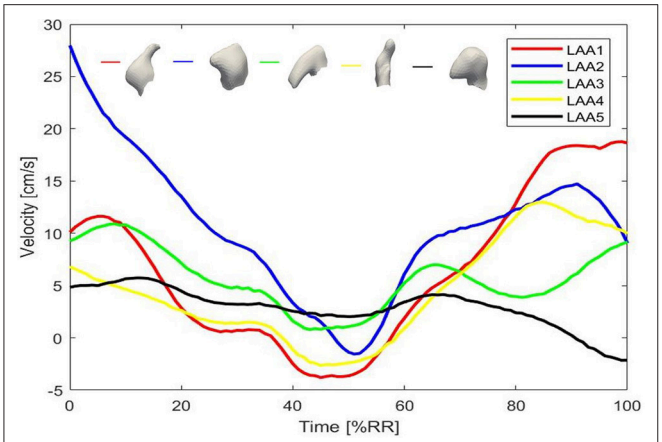

FIGURE 7 | Computed velocity at the LAA ostia for the five LAAs.

vortices got closer to the LAA tip, favoring a better blood flow washout with respect to the LAA1.

As discussed in the LAA4 velocity profile analysis, we expected that most of the vortex structures are localized in proximity of its orifice. Our hypothesis was confirmed, as shown in the fourth column of **Figure 6** (see also **Supplemental Video8.mp4**). In all the phases of the cardiac cycle vortex structures remained near to the ostium with low velocities. Looking at the LAA5 (see **Supplemental Video10.mp4**), giving its low velocities throughout the cardiac cycle, also the number of vortex structures was scarce and characterized by small velocities. Moreover, as for the LAA4, they were localized most in proximity of the orifice.

3.4. Blood Velocity at the LAA Orifice

The profile of the LAA ostium velocity was evaluated and the results are reported in **Figure 7**. We considered the last cardiac cycle for each LAA and negative values of the velocity indicated a filling of the LAA, whereas positive values meant LAA emptying. As highlighted in **Figure 7**, all the auricles were characterized by low values of filling velocity (values between 0 and −5 cm/s). The most relevant result on this analysis was the evaluation of the emptying velocity since it could provide a measure of the washout. We noticed an oscillatory trend in all the appendages and this was probably due to the lack of the atrial contraction imposed in our simulation in order to represent AF condition, which implied a passive LAA emptying and filling. The lack of the contraction of the LA and of the LAA led the orifice velocity not to exceed, except for LAA2, the threshold of 20 cm/s. This data, in agreement with literature (Beigel et al., 2014), implied a confined/circumscribed washout and consequently a possible increase of the thrombogenicity.

Looking at the LAA1, orifice velocity after an initial increase, decreased and reached the lowest value with respect to the other LAAs. This phase was followed by a new increase characterized by a velocity peak of 18.8 cm/s, which was closed to the threshold and could indicate a good washout. However, in the earlier stage the filling occurred with high velocity (absolute value 5 cm/s) and this meant that that part of blood flow could remain in part within the LAA. LAA2 peak velocity was 29 cm/s. Therefore, this evaluation confirmed that within the LAA2 geometry blood flow entered and exited with higher velocity and reached also the tip of the auricle, providing a significant washout. Regarding LAA3 and LAA4, their peak orifice velocity were 10.9 and 13 cm/s, respectively.

LAA5 ostium velocity strengthened our previous findings, indeed it showed a peak value at the ostium of 6 cm/s.

TABLE 3 | Number of fluid particles which remained in the LAA at the end of the third, fourth and last cardiac cycle for the five LAAs in AF.

Cardiac Cycle	LAA1	LAA2	LAA3	LAA4	LAA5
0	500	500	500	500	500
3	204	186	266	437	310
4	182	124	133	379	178
5	168	58	103	312	126

Cardiac cycle = 0 indicates the beginning of the simulation.

3.5. LAA Blood Stasis Quantification

In order to quantify blood stasis in the LAA, we performed a specific study. Each LAA was populated by 500 fluid particles at the beginning of the CFD simulation. The The fluid particles were distributed as a sphere around the center c, the midpoint of the LAA centerline. Paraview software was employed for this analysis (Ahrens et al., 2005). Then, we evaluated how many fluid particles remained within the LAA at the end of the third, fourth and fifth cardiac cycle. The number of residual particles at different timesteps of the cardiac cycle could provide a direct measure of LAA blood stasis: more particles remain in the LAA, higher is the probability of the clot formation within the LAA. Results of this computation are reported in **Table 3**.

At the end of the fifth cardiac cycle, 33.6 % of fluid particles remained in the LAA1. LAA2 results showed important differences with respect to the LAA1: only the 11.6 % of the fluid particles remained within the auricle. LAA3, as expected, presented a better washout with respect to the LAA1. Indeed, 20.6 % of fluid particles did not exit from the LAA. Despite their similarity in shape, the difference between LAA1 and LAA3 could be caused by the opposite orientation and the different value of tortuosity.

62.4 % of fluid particles remained within the LAA4 because the blood flow pushed the particles to the tip and velocities in this part were very low.

The blood washout of the LAA5 was not strongly reduced: 25.2 % of particles remained within the appendage.

4. DISCUSSION AND CONCLUSION

In this study, we assessed the influence of the LAA morphology on the LA hemodynamics. The framework developed and described in this study is fully automatic and fast. In our experience this procedure is very robust since it worked correctly for all our data; it requires < 1 min to generate one models and most of this time is required to import the mesh and compute

the shape diameter function. Several geomeric parameters were computed and correlated with blood velocities, vorticity, LAA ostium velocity and residence time for each anatomical model. We found the LAA geometric characteristics impact on the hemodyamic pattern within the LAA highlighting that not only the appendage morphology types should be considered for the stroke risk assessment in patients affected by AF (Di Biase et al., 2012). Our results on the velocity and vorticity within the LAA, LAA orifice velocity and on the residence time demonstrated and confirmed that not only complex LAA morphologies were characterized by low velocities, low vorticity and consequently a higher thrombogenic risk. Simple morphologies can have a thrombogenic risk equal, or even higher, than more complex auricles and their geometric features could play a key role in defining thromboembolic risk. Indeed, in our opinion, LAA geometric parameters should be considered, coupled with the morphological characteristics, for a comprehensive evaluation of the blood stasis and stroke risk. These geometric characteristics were not investigated in the previous works, neither correlated with hemodynamic parameters.

LAA1 presented the highest length (3.54 cm) and tortuosity (0.46), thus representing a complex shape. Indeed, the quantity of the blood flow which reached the distal part of the LAA1 throughout the cardiac cycle was strongly reduced due to the complex morphology of this LAA, as explained in section 3.2. Moreover, vortex structures within this appendage were limited in number and did not reach its distal part. Since Beigel et al. (2014), observed that the stroke risk is 2.6 fold higher in AF patients in which the velocity at the ostium throughout the cardiac cycle is <20 cm/s and these findings were confirmed in the CFD studies on the LAA in AF by Zhang and Gay (2008); Olivares et al. (2017), we also evaluated the LAA orifice velocity. LAA1 ostium velocity was lower than 20 cm/s, indicating a high trombogenicity. LAA1 blood stasis quantification confirmed this result, showing 33.6 % of fluid particles remained within the LAA1. Fluid particles were pushed toward the appendage tip and the low blood flow velocity hampered an effective washout. Therefore, we expect that LAA geometries similar to LAA1 may have an high thromembolic risk.

Study of LAA2 fluid dynamics indicators proved that linear structures, coupled with a small length, had a better washout, thus implying a reduction of the blood stasis and thrombi formation risk. Moreover, the positioning of the LAA2 could have a key role for the stroke risk assessment. As highlighted in **Figure 4**, LAA1 had an opposite positioning with respect to the others. This characteristic could explain the scarce washout, mainly in the distal part, thus increasing the probability of thrombi formation risk. The LAA2 blood stasis analysis confirmed this consideration: indeed the simple geometry allowed and helped the blood flow to reach the tip of the LAA and therefore to fill the appendage volume. We concluded that the probability of clot formation for the auricles which present a morphology similar to the LAA2 is low.

LAA3, despite its qualitative similarity with the LAA1, presented relevant differences in the hemodynamic parameters. Velocities were slightly higher than LAA1 and blood flow entered within this auricle more easily and consequently vortex structures were deeper. Moreover, looking at the number of fluid particles which remained in the LAA3 at the end of the fifth cardiac cycle, we found that LAA3 had a better washout than LAA1. Hemodynamic differences between these two auricles could be related to the different orientation and tortuosity, as explained in section 3.2. Therefore, the thrombogenicity risk of this type of LAA could be classified as medium.

LAA4 velocity profile highlighted that for the assessment of left atrial appendage thrombogenicity, geometric and morphological features should be take into account. Indeed, as reported in the velocity field analysis, even qualitatively simple LAAs (i.e., LAA4) could show a high probability of blood stasis and therefore thrombi formation. LAA4 vortex structures were localized in proximity of its orifice implying that blood washout in the distal parts of this auricle was scarce, thus increasing the probability of clot formation with respect to the other LAAs. Yet, we found low velocity values at the ostium in the LAA3 and LAA4, thus indicating a moderate clot formation risk for this particular LAA shape. In order to confirm our previous findings, we quantified the LAA4 blood stasis. The fluid did not reach the auricle tip because of the shrinking toward the distal part. These characteristics led to a scarce washout of the LAA4 (see **Table 3**), moreover the vortex structures were absent, thus implying a blood stasis in proximity of the LAA4 tip. This result was very relevant because it proved that the LAA4 showed the highest probability of blood stasis and consequently of thrombi formation with respect to the other appendages, despite its simple and linear geometry, where a low thrombogenicity was expected. Regarding the LAA5, velocity within the auricle and at the orifice showed low values that could imply a relevant risk of blood stasis and thrombi formation. Also, vortex structures were localized only in proximity of the LAA orifice. However, even though the velocities and the number of vortex structures were very small, the blood washout of the LAA5 was not strongly reduced. LAA5 limited extension could compensate the high tortuosity, allowing the blood flow to entirely cover its volume, thus providing a good washout.

The few CFD studies available on this topic (Koizumi et al., 2015; Otani et al., 2016; Olivares et al., 2017; Bosi et al., 2018) focused on the correlation between the four type of the LAA morphologies proposed by Di Biase et al. (2012) and the thrombogenicity. However, they did not analyze other characteristics of the auricles that might have a crucial role in pathological conditions. With respect to the other works, we designed and developed a procedure which allowed to consider the same LA shape for each LAA. To perform this task, the SDF was employed. Most of previous segmentation approaches were based on local surface properties, such as curvature or geodesic distance, that often depend on the topology and on the pose of the object. SDF overcame these problems and provided a link between the surface mesh and the object's volume, thus allowing the extraction a specific part of the mesh. We chose this option because the variability of the left atrial chamber could affect the validity of the hemodynamics changes when different types of LAA were compared, since these variations could be caused also by the LA geometric features (dimensions, structure, and pulmonary vein attachments and

morphology). Obviously the clinical problem we are facing is very complex and we think there may be an interchangeable conditioning effect between the LA and the LAA shapes and both effects should be considered. However, we also think the comprehension of each single effect may help in clarifying the interplay between them. In this study we focused on better understanding the influence of each specific LAA shape on blood hemodynamics and, to this aim, we were forced to eliminate the dependence from the LA shape and from other patient-specific factors. Our results, based on a simplification of the real phenomenon, showed that the complexity of the LAA shape alone does not correlate with clot formation and additional parameters should be considered for a clear comprehension of the link between LAA shape and the risk of stroke.

Our approach can be further improved because a limitation consists in the number of the available left atrial data-set. Future developments will be focused on considering a larger number of patient-specific LAAs in order to fully its wide anatomical variability. Results on a larger dataset would also allow to link the modeling results to thrombogenic risk potentially identifying clinically measurable parameters that may inform as to which treatment option would be best for a particular patient. Unfortunately, for the patients analyzed in this study this information was not available. In addition, the results of this study could benefit from the application of a patient-specific motion field of the LA in AF. Unfortunately, up to date, quantification of such a motion field is not possible using the standard 3D acquisition, MRI or CT. Since AF is described by a disorganized and reduced motion of the LA, in this study we applied a random displacement field with small amplitudes in order to avoid mesh degeneration during simulations. Once the patient-specific motion in AF has become available, our pipeline would strongly benefit from such information. Another possibility is to build a FSI model in which the control of the motion of the computational domain throughout the cardiac cycle could be more realistic than using a random displacement function as the one employed in this study.

To conclude, the presented framework might represent a step toward the development of a better tool for the patient-specific cardioembolic risk assessment and preventive treatment in AF patients.

AUTHOR CONTRIBUTIONS

AM: Conception of the study, software development, simulations, analysis of the results, manuscript drafting, figure, and video preparation, revision of manuscript. LB: Software development, simulations. LD: Analysis of the results, revision of manuscript. CT: Image acquisition. MF: Simulator set up. AQ: Simulator design, analysis of the results, revision of manuscript. CC: Conception of the study, analysis of the results, manuscript drafting, revision of manuscript, supervision of the study.

ACKNOWLEDGMENTS

AQ, LD, and MF acknowledge the support of the European Research Council (ERC) under the European Union's Horizon 2020 research and innovation programme (grant agreement No. 740132). We would like to thank Dr. Francesca Mazzotti for her valuable inputs on this study during the initial phase of research.

SUPPLEMENTARY MATERIAL

The Supplementary Material for this article can be found online at: https://www.frontiersin.org/articles/10.3389/fphys.2018.01938/full#supplementary-material

REFERENCES

Ahrens, J., Geveci, B., and Law, C. (2005). *Paraview: an end-user tool for large data visualization*. The visualization handbook, 717.

Antiga, L., and Steinman, D. A. (2012). VMTK: vascular modeling toolkit. Available online at: http://www.vmtk.org

Bazilevs, Y., Gohean, J., Hughes, T., Moser, R., and Zhang, Y. (2009). Patient-specific isogeometric fluid–structure interaction analysis of thoracic aortic blood flow due to implantation of the Jarvik 2000 left ventricular assist device. *Comput. Methods Appl. Mechan. Eng.* 198, 3534–3550. doi: 10.1016/j.cma.2009.04.015

Beigel, R., Wunderlich, N. C., Ho, S. Y., Arsanjani, R., and Siegel, R. J. (2014). The left atrial appendage: anatomy, function, and noninvasive evaluation. *JACC Cardiovasc. Imaging* 7, 1251–1265. doi: 10.1016/j.jcmg.2014.08.009

Besl, P. J. and McKay, N. D. (1992). Method for registration of 3-d shapes. In *Sensor Fusion IV: Control Paradigms and Data Structures*, Vol 1611. International Society for Optics and Photonics (Boston, MA), 586–607.

Bosi, G. M., Cook, A., Rai, R., Menezes, L. J., Schievano, S., Torii, R., et al. (2018). Computational fluid dynamic analysis of the left atrial appendage to predict thrombosis risk. *Front. Cardiovasc. Med.* 5:34. doi: 10.3389/fcvm.2018.00034

Briceno, D. F., Spinetto, P. V., Cyrille, N., Massera, D., Bader, E., Manheimer, E., et al. (2015). Left atrial appendage occlusion device and novel oral anticoagulants versus warfarin for stroke prevention in non-valvular atrial fibrillation: a systematic review and meta-analysis of randomized control trials. *Circ. Arrhythm. Electrophysiol.* 8, 1057–1064. doi: 10.1161/CIRCEP.115.002993

Cignoni, P., Callieri, M., Corsini, M., Dellepiane, M., Ganovelli, F., and Ranzuglia, G. (2008). "Meshlab: an open-source mesh processing tool," in *Eurographics Italian Chapter Conference*, Vol 2008 (Salerno), 129–136.

Di Biase, L., Santangeli, P., Anselmino, M., Mohanty, P., Salvetti, I., Gili, S., et al. (2012). Does the left atrial appendage morphology correlate with the risk of stroke in patients with atrial fibrillation? results from a multicenter study. *J. Am. College Cardiol* 60, 531–538. doi: 10.1016/j.jacc.2012.04.032

Fabri, A. and Teillaud, M. (2011). "Cgal-the computational geometry algorithms library," in *10e Colloque National En calcul des Structures* (Giens), 6.

Fang, Q. and Boas, D. (2010). iso2mesh: a 3d surface and volumetric mesh generator for matlab/octave. Available online at: http://www.iso2mesh.sourceforge.net

Forti, D. and Dedè, L. (2015). Semi-implicit BDF time discretization of the Navier–Stokes equations with VMS-LES modeling in a high performance computing framework. *Comput. Fluids* 117, 168–182. doi: 10.1016/j.compfluid.2015.05.011

Gautam, S. and John, R. M. (2011). Interatrial electrical dissociation after catheter-based ablation for atrial fibrillation and flutter. *Circ. Arrhyth. Electrophysiol.* 4, e26–e28. doi: 10.1161/CIRCEP.111.961920

Gupta, D. K., Shah, A. M., Giugliano, R. P., Ruff, C. T., Antman, E. M., Grip, L. T., et al. (2013). Left atrial structure and function in atrial fibrillation: Engage af-timi 48. *Eur. Heart J.* 35, 1457–1465. doi: 10.1093/eurheartj/eht500

Hankey, G. J. and Eikelboom, J. W. (2011). Dabigatran etexilate: a new oral thrombin inhibitor. *Circulation* 123, 1436–1450. doi: 10.1161/CIRCULATIONAHA.110.004424

January, C. T., Wann, L. S., Alpert, J. S., Calkins, H., Cigarroa, J. E., Conti, J. B., et al. (2014). 2014 aha/acc/hrs guideline for the management of patients with

atrial fibrillation: a report of the american college of cardiology/american heart association task force on practice guidelines and the heart rhythm society. *J. Am. College Cardiol.* 64, e1–e76. doi: 10.1016/j.jacc.2014.03.022

Jeong, W. K., Choi, J.-H., Son, J. P., Lee, S., Lee, M. J., Choe, Y. H., et al. (2016). Volume and morphology of left atrial appendage as determinants of stroke subtype in patients with atrial fibrillation. *Heart Rhythm* 13, 820–827. doi: 10.1016/j.hrthm.2015.12.026

Khurram, R. A. and Masud, A. (2006). A multiscale/stabilized formulation of the incompressible Navier–Stokes equations for moving boundary flows and fluid–structure interaction. *Comput. Mech.* 38, 403–416. doi: 10.1007/s00466-006-0059-4

Koizumi, R., Funamoto, K., Hayase, T., Kanke, Y., Shibata, M., Shiraishi, Y., et al. (2015). Numerical analysis of hemodynamic changes in the left atrium due to atrial fibrillation. *J. Biomecha.* 48, 472–478. doi: 10.1016/j.jbiomech.2014.12.025

Markl, M., Lee, D. C., Ng, J., Carr, M., Carr, J., and Goldberger, J. J. (2016). Left atrial 4d flow mri: stasis and velocity mapping in patients with atrial fibrillation. *Invest. Radiol.* 51, 147–154. doi: 10.1097/RLI.0000000000000219

Masci, A., Alessandrini, M., Forti, D., Menghini, F., Dedé, L., Tommasi, C., et al. (2017). "A patient-specific computational fluid dynamics model of the left atrium in atrial fibrillation: Development and initial evaluation," in *International Conference on Functional Imaging and Modeling of the Heart* (Toronto, ON: Springer), 392–400. doi: 10.1007/978-3-319-59448-4_37

Olivares, A. L., Silva, E., Nuñez-Garcia, M., Butakoff, C., Sánchez-Quintana, D., Freixa, X., et al. (2017). "*In silico* analysis of haemodynamics in patient-specific left atria with different appendage morphologies," in *International Conference on Functional Imaging and Modeling of the Heart* (Toronto, ON: Springer), 412–420.

Otani, T., Al-Issa, A., Pourmorteza, A., McVeigh, E. R., Wada, S., and Ashikaga, H. (2016). A computational framework for personalized blood flow analysis in the human left atrium. *Ann. Biomed. Eng.* 44, 3284–3294. doi: 10.1007/s10439-016-1590-x

Piccinelli, M., Veneziani, A., Steinman, D. A., Remuzzi, A., and Antiga, L. (2009). A framework for geometric analysis of vascular structures: application to cerebral aneurysms. *IEEE Trans. Med. Imaging* 28, 1141–1155. doi: 10.1109/TMI.2009.2021652

Quarteroni, A., Manzoni, A., and Vergara, C. (2017). The cardiovascular system: mathematical modelling, numerical algorithms and clinical applications. *Acta Numer.* 26, 365–590. doi: 10.1017/S0962492917000046

Reddy, V. Y., Möbius-Winkler, S., Miller, M. A., Neuzil, P., Schuler, G., Wiebe, J., et al. (2013). Left atrial appendage closure with the watchman device in patients with a contraindication for oral anticoagulation: the asap study (asa plavix feasibility study with watchman left atrial appendage closure technology). *J. Am. College Cardiol.* 61, 2551–2556. doi: 10.1016/j.jacc.2013.03.035

Reddy, V. Y., Sievert, H., Halperin, J., Doshi, S. K., Buchbinder, M., Neuzil, P., et al. (2014). Percutaneous left atrial appendage closure vs warfarin for atrial fibrillation: a randomized clinical trial. *Jama* 312, 1988–1998. . doi: 10.1001/jama.2014.15192

Reymond, P., Crosetto, P., Deparis, S., Quarteroni, A., and Stergiopulos, N. (2013). Physiological simulation of blood flow in the aorta: comparison of hemodynamic indices as predicted by 3-d fsi, 3-d rigid wall and 1-d models. *Med. Eng. Phys.* 35, 784–791. doi: 10.1016/j.medengphy.2012.08.009

Shapira, L., Shamir, A., and Cohen-Or, D. (2008). Consistent mesh partitioning and skeletonisation using the shape diameter function. *Visual Comput.* 24:249. doi: 10.1007/s00371-007-0197-5

Valinoti, M., Fabbri, C., Turco, D., Mantovan, R., Pasini, A., and Corsi, C. (2018). 3d patient-specific models for left atrium characterization to support ablation in atrial fibrillation patients. *Mag. Res. Imaging* 45, 51–57. doi: 10.1016/j.mri.2017.09.012

Yaghi, S., Song, C., Gray, W. A., Furie, K. L., Elkind, M. S., and Kamel, H. (2015). Left atrial appendage function and stroke risk. *Stroke* 46, 3554–3559. doi: 10.1161/STROKEAHA.115.011273

Zakeri, R., Van Wagoner, D. R., Calkins, H., Wong, T., Ross, H. M., Heist, E. K., et al. (2017). The burden of proof: the current state of atrial fibrillation prevention and treatment trials. *Heart Rhythm* 14, 763–782. doi: 10.1016/j.hrthm.2017.01.032

Zhang, L. T. and Gay, M. (2008). Characterizing left atrial appendage functions in sinus rhythm and atrial fibrillation using computational models. *J. Biomechan.* 41, 2515–2523. doi: 10.1016/j.jbiomech.2008.05.012

Conflict of Interest Statement: The authors declare that the research was conducted in the absence of any commercial or financial relationships that could be construed as a potential conflict of interest.

frontiers in Physiology

ORIGINAL RESEARCH
published: 01 February 2019
doi: 10.3389/fphys.2019.00017

The Left and Right Ventricles Respond Differently to Variation of Pacing Delays in Cardiac Resynchronization Therapy: A Combined Experimental-Computational Approach

Erik Willemen[1], Rick Schreurs[1], Peter R. Huntjens[1,2], Marc Strik[3], Gernot Plank[4], Edward Vigmond[5], John Walmsley[1], Kevin Vernooy[3], Tammo Delhaas[1], Frits W. Prinzen[1] and Joost Lumens[1,2]*

[1] Cardiovascular Research Institute Maastricht (CARIM), Maastricht University, Maastricht, Netherlands, [2] IHU-LIRYC Electrophysiology and Heart Modeling Institute, Pessac, France, [3] Department of Cardiology, Maastricht University Medical Center, Maastricht, Netherlands, [4] Institute of Biophysics, Medical University of Graz, Graz, Austria, [5] Univeristy of Bordeaux, IMB UMR 5251, Talence, France

OPEN ACCESS

Edited by:
Olaf Doessel,
Karlsruhe Institute of Technology (KIT), Germany

Reviewed by:
Bradley John Roth,
Oakland University, United States
Joakim Sundnes,
Simula Research Laboratory, Norway

***Correspondence:**
Erik Willemen
e.willemen@maastrichtuniversity.nl

Specialty section:
This article was submitted to Computational Physiology and Medicine, a section of the journal Frontiers in Physiology

Received: 09 October 2018
Accepted: 10 January 2019
Published: 01 February 2019

Citation:
Willemen E, Schreurs R, Huntjens PR, Strik M, Plank G, Vigmond E, Walmsley J, Vernooy K, Delhaas T, Prinzen FW and Lumens J (2019) The Left and Right Ventricles Respond Differently to Variation of Pacing Delays in Cardiac Resynchronization Therapy: A Combined Experimental-Computational Approach. Front. Physiol. 10:17. doi: 10.3389/fphys.2019.00017

Introduction: Timing of atrial, right (RV), and left ventricular (LV) stimulation in cardiac resynchronization therapy (CRT) is known to affect electrical activation and pump function of the LV. In this study, we used computer simulations, with input from animal experiments, to investigate the effect of varying pacing delays on both LV and RV electrical dyssynchrony and contractile function.

Methods: A pacing protocol was performed in dogs with atrioventricular block ($N = 6$), using 100 different combinations of atrial (A)-LV and A-RV pacing delays. Regional LV and RV electrical activation times were measured using 112 electrodes and LV and RV pressures were measured with catheter-tip micromanometers. Contractile response to a pacing delay was defined as relative change of the maximum rate of LV and RV pressure rise (dP/dt_{max}) compared to RV pacing with an A-RV delay of 125 ms. The pacing protocol was simulated in the CircAdapt model of cardiovascular system dynamics, using the experimentally acquired electrical mapping data as input.

Results: Ventricular electrical activation changed with changes in the amount of LV or RV pre-excitation. The resulting changes in dP/dt_{max} differed markedly between the LV and RV. Pacing the LV 10–50 ms before the RV led to the largest increases in LV dP/dt_{max}. In contrast, RV dP/dt_{max} was highest with RV pre-excitation and decreased up to 33% with LV pre-excitation. These opposite patterns of changes in RV and LV dP/dt_{max} were reproduced by the simulations. The simulations extended these observations by showing that changes in steady-state biventricular cardiac output differed from changes in both LV and RV dP/dt_{max}. The model allowed to explain the discrepant changes in dP/dt_{max} and cardiac output by coupling between atria and ventricles as well as between the ventricles.

Conclusion: The LV and the RV respond in a opposite manner to variation in the amount of LV or RV pre-excitation. Computer simulations capture LV and RV behavior during pacing delay variation and may be used in the design of new CRT optimization studies.

Keywords: cardiac resynchronization therapy, right ventricle, optimization, computer simulation, therapy optimization studies, CircAdapt, hemodynamics, dyssynchrony

INTRODUCTION

Cardiac resynchronization therapy (CRT) is an established therapy for heart failure patients with a reduced left ventricular (LV) ejection fraction (EF), and left bundle branch block (LBBB) (Brignole et al., 2013). Through biventricular pacing, CRT aims to establish a more synchronous electrical activation of the ventricles and thereby improves cardiac pump function (Vernooy et al., 2007) and clinical outcome (Brignole et al., 2013). However, approximately one-third of the patients that receive CRT do not benefit from this therapy (Abraham et al., 2002; Cleland et al., 2005; Auricchio and Prinzen, 2011; Prinzen et al., 2013).

Programming of both atrioventricular (AV) and ventriculoventricular (VV) pacing delays strongly influences the contractile response to CRT, as determined by both ultrasound and maximum rate of LV pressure rise (LV dP/dt_{max}) (Bogaard et al., 2012; Auger et al., 2013; Strik et al., 2013b). However, meta-analyses of multiple optimization methods showed that pacing delay optimization fails to provide long-term improvement in clinical outcome (Auger et al., 2013). Suggested reasons for the absence of long-term benefits of such optimization are that the default "out-of-the-box" delays are already fairly good and that the optimization methods employed are not accurate or robust enough. An alternative explanation could be that most pacing delay optimization strategies that have been developed solely take LV function into account. Right ventricular (RV) function is often overlooked, although several studies show that RV failure is an independent predictor of mortality in patients with LV failure with and without CRT (Groote et al., 1998; Ricci et al., 2017). Two clinical studies indicated that there was a poor correlation between the pacing delay settings providing the highest LV dP/dt_{max} and RV dP/dt_{max} values (Sciaraffia et al., 2009; Hyde et al., 2016).

In recent years, computational models of cardiac electrophysiology, mechanics of the heart and cardiovascular system have increased our understanding of dyssynchronous heart failure and its treatment with CRT (Lee et al., 2018). Right ventricular function and its effect on CRT has, however, not been studied extensively using a computer modeling approach. Our group has been using the CircAdapt model of the heart and closed-loop circulatory system. While using a simplified cardiac anatomy, the advantages of this model are the inclusion of the entire (systemic and pulmonary) circulation and its high calculation speed (almost real time). In combination with experimental and clinical measurements, CircAdapt has shown to be able to identify and mechanistically understand the electromechanical substrates of the heart that are most responsive to CRT (Lumens et al., 2013, 2015; Huntjens et al., 2018).

A vast majority of the studies on the heart, also our aforementioned studies, are related largely to the LV. In the present study, we aim to study the changes in both LV and RV contractile response to variations of pacing delay settings in CRT, and to evaluate whether the CircAdapt computer model reliably simulates LV and RV pump function during these interventions. Subsequently we aim to use the computer modeling results to investigate how cardiac output is affected by differences between LV and RV contractile changes.

MATERIALS AND METHODS

Animal Experiments

Animal handling was performed according to the Dutch Law on Animal Experimentation and the European Directive for the Protection of Vertebrate Animals Used for Experimental and Other Scientific Purpose. The protocol was approved by the Animal Experimental Committee of Maastricht University. The animal experiments have been conducted in 2010–2011 and the methodology used has partially been described in a previous publication (Strik et al., 2013b), reporting on the LV pressure data. In the current study we analyzed both RV and LV pressure data and related them to the electrical conduction measurements. In short, 6 adult mongrel dogs were anesthetized using midazolam (0,25 mg/kg/h) and sufentanil (3 μg/kg/h) and a complete AV-block was induced by radiofrequency ablation. The dogs received pacing electrodes in the right atrium (A), RV apex and epicardially on the basal posterolateral wall via a left-sided thoracotomy.

Measurements were performed 12–21 weeks after inducing the AV-block using an external custom-built pacing system. RV-only pacing with an A to RV (A-RV) pacing delay of 125 ms was used as the baseline pacing setting, mimicking the activation pattern as seen in LBBB. The A-RV and A to LV (A-LV) delays were then programmed individually, ranging from 50 to 230 ms in steps of 20 ms, resulting in 100 possible combinations (**Figure 1A**). Pacing delay settings were assigned in a random order and baseline recordings were repeated after every 5th setting. During each setting, continuous, invasive hemodynamic and electrocardiographic measurements were performed (**Figure 1B**). 7F catheter-tip manometers were used for LV and RV pressure measurement. Epicardial electrograms of the LV free wall (LVFW) and RV free wall (RVFW) were recorded from 2 multielectrode custom-made bands holding 102 contact electrodes. Septal endocardial electrograms were recorded from

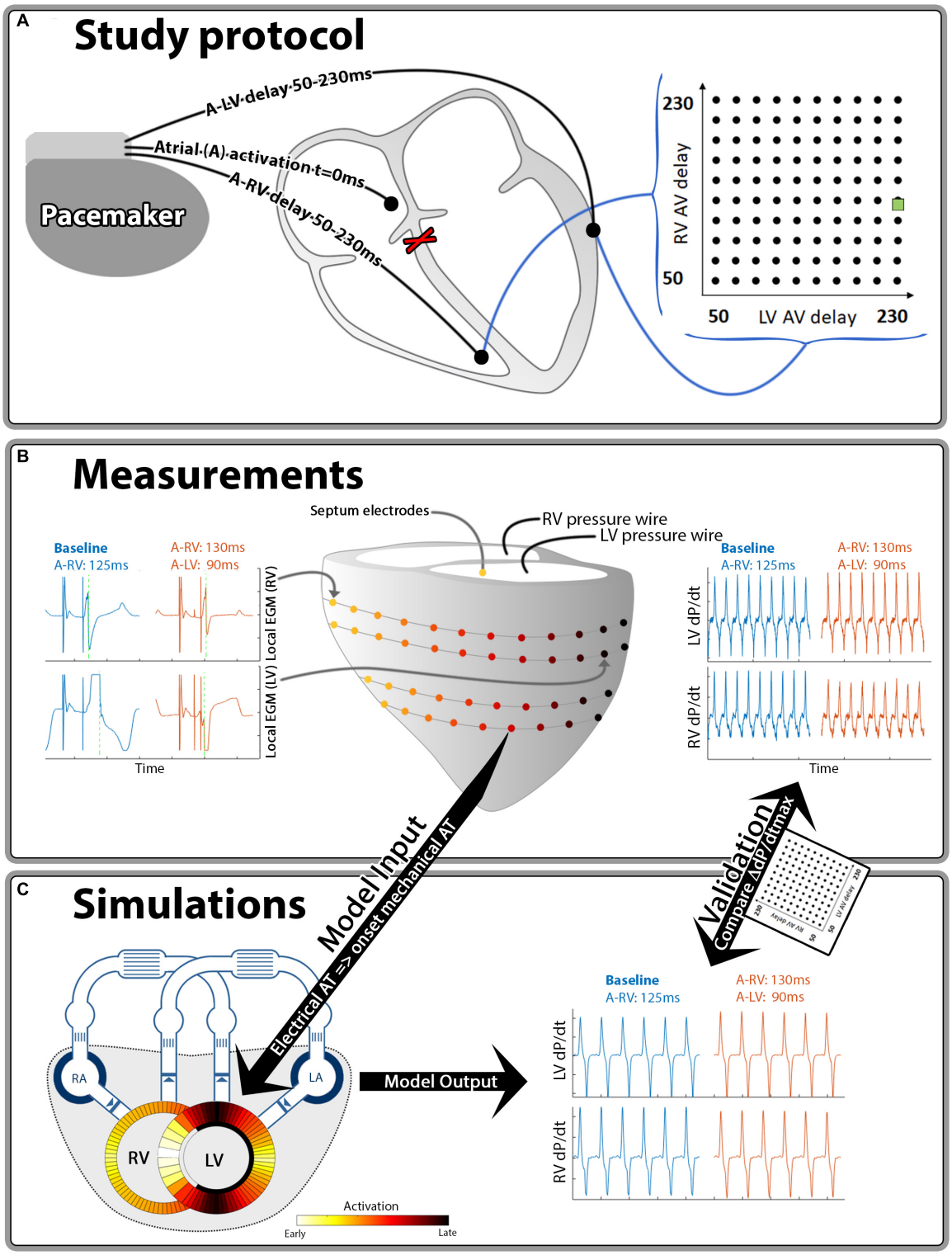

FIGURE 1 | Schematic representation of the methods used in this study. Hundred different A-LV/A-RV pacing delay combinations were programmed **(A)** while pressures and local electrical activation were measured **(B)**. Generic activation maps, derived from local electrograms, were used as onset of mechanical activation in the computer simulations **(C)**. The resulting output of the simulations and measurements was compared for validation purposes. The green square in the heat maps indicates the baseline pacing setting.

two multielectrode catheters with 7 contact electrodes on the RV septum and 3 on the LV septum. Measurements were recorded for a minimum of two respiratory cycles at each pacing delay setting.

Data Analysis

Local electrical activation times were determined as the duration between the atrial pace and the timepoint of steepest negative deflection of the electrogram using custom software (**Figure 1B**, green line in local EGM's). For quantification of intraventricular electrical dyssynchrony we calculated total activation time as the difference between earliest and latest activation time of the RVFW (RV TAT) and of the whole LV (LV TAT). The latter was calculated from the combination of epicardial LVFW and endocardial septal electrodes. To quantify electrical interventricular dyssynchrony we used the ventricular electrical uncoupling (VEU) index. VEU was defined as the difference between mean LVFW and mean RVFW activation times (Ploux et al., 2013).

For both the LV and the RV, response to pacing was defined as the relative change in dP/dt_{max} compared to the baseline setting. We applied quadratic LOESS fitting to account for measurement variability within each dog (Cleveland, 1979). Furthermore, in order to quantify a generic canine response to changes in pacing delay, we created a single representative canine dataset by taking the mean values of the dogs for each setting. We also applied linear 2D interpolation between the measurements in the heat map visualizations of all pacing delay settings. All these calculations were performed in Matlab 2016A (The Mathworks Inc., Natick, MA, United States).

Computer Simulations

The CircAdapt model of the entire heart and circulation (Arts et al., 2005; Lumens et al., 2009; Walmsley et al., 2015a), which can be downloaded from www.circadapt.org, was used to simulate cardiovascular mechanics and hemodynamics during pacing delay variations as applied in the animal experiments (**Figure 1C**). Previous experimental and clinical studies have shown that the CircAdapt model realistically relates local ventricular myofiber mechanics to global cardiovascular hemodynamics in dyssynchronous and paced hearts (Leenders et al., 2012; Huntjens et al., 2014; Lumens et al., 2015; Walmsley et al., 2015a,b).

The source code of the CircAdapt model used for all simulations as well as the Matlab® (The MathWorks, Natick, MA, United States) scripts to perform all simulations and analysis thereof are provided as an online supplement **(Supplementary Data Sheet S1**). In summary, the CircAdapt model is a reduced order model of the human four-chamber heart connected to a closed-loop cardiovascular system, with lumped pulmonary and systemic circulations. It uses a simplified ventricular geometry, where cardiac walls are represented by thick spherical shells consisting of contractile myocardium. The MultiPatch module enables cardiac walls to be subdivided into an arbitrary number of wall segments (patches). Tissue properties and activation time can differ between patches, but all patches within a wall share a common wall tension and curvature. Since wall tension is the same in all patches within a wall, spatial location within a wall is not required to calculate deformation in a patch.

In CircAdapt wall tension and curvature determine cavity pressure through Laplace's law (Lumens et al., 2009; Walmsley et al., 2015a) Fiber stress in a patch is the sum of an active component, representing myofiber contraction, and a passive component. The active stress component incorporates length-dependence of the force generated and the duration of contraction. The passive component provides a non-linear relationship between myofiber stress and strain. More details on the phenomenological model of myocardial contraction and the validation of the MultiPatch module are previously published by Walmsley et al. (2015a).

Simulating a Healthy Human Reference Heart and Circulation

Cardiac adaptation implemented in the CircAdapt model was used to obtain a reference parameterization that represents a healthy human cardiovascular system (Arts et al., 1994, 2005, 2012). The tissue volumes and areas in the cardiac walls and large blood vessels were adapted as described previously (Arts et al., 2005, 2012). A resting cardiac output of 5.1 l/min and heart rate of 70 bpm were assumed. Cardiac output was tripled and the heart rate was doubled during the stress-state of the adaptation process. Mean arterial pressure (MAP) was maintained at 92 mmHg during the adaptation process. The resulting reference simulation was used as the basis for subsequent pacing simulations.

Using Electrical Activation to Simulate the Pacing Delay Optimization Protocol

We divided the ventricular wall in the same amount of segments as the number of available electrodes (52 LV free wall, 50 RV free wall and 10 septal segments). Time of onset of activation was assigned based on the electrical activation times measured in the animal experiments. As previously stated, in the current MultiPatch module the segments were considered to be mechanically coupled in series, meaning that the order in which patches were placed was not significant (Walmsley et al., 2015a). This allowed sorting of the activation times per wall in each measurement, before taking the median of the dogs, to get a generic activation pattern. The benefit of this generic activation pattern is that it was less affected by differences in band placement, heart size and electrodes with insufficient contact in the dogs.

A representative baseline simulation was obtained by imposing the ventricular activation pattern measured during the experimental baseline condition, i.e., RV-only pacing with an A-RV delay of 125 ms. Systemic vascular resistance was adapted to obtain a MAP of 60 mmHg and heart rate was set to 80 bpm, both similar to the animal experiments. Furthermore, total circulating blood volume was adjusted so that cardiac output was maintained at 5.1 L/min. The resulting baseline simulation was used as the starting point for the pacing setting simulations. For each of the 100 pacing delay simulations, the pattern of ventricular activation was changed to the activation pattern

measured in the canine experiments and the resulting beat-to-beat changes in ventricular mechanics and hemodynamics were stored until a new hemodynamic steady state was reached. During all pacing simulations, systemic vascular resistance and total circulating blood volume were kept constant in order to quantify the acute effect of pacing-induced changes of ventricular pump mechanics and cardiac hemodynamics. Simulated steady-state dP/dt_{max} values are compared with the experimental measurements. In addition, the simulations extended the animal experiments by providing quantitative insight in the beat-to-beat and steady-state changes of ventricular volumes and cardiac output.

RESULTS

Baseline characteristics for the AV-blocked dogs are described in **Table 1**.

Electrical Effects of Altering Pacing Delay Settings

Figure 2 shows the typical examples of electrical activation patterns acquired using contact mapping in a dog with AV block during LV pre-excitation, simultaneous RV and LV pacing and RV pre-excitation. In case of extreme pre-excitation, capture in the last paced ventricle was lost due to activation via the contralateral ventricle (indicated by the gray line). RV pre-excitation led to the largest LV TAT while LV pre-excitation resulted in an increase of RV TAT. During simultaneous pacing, two wave fronts originating from the RV and LV pacing electrodes fused and resynchronized the heart as indicated by a decrease in LV TAT.

Figure 3 shows the changes in electrical dyssynchrony indexes in dogs with variation of pacing delay settings. There was no change in LV and RV TAT and VEU when changing the AV delay during simultaneous activation of the LV and RV (left column). Both LV and RV TAT (first 2 rows of **Figure 3**) were lowest during simultaneous RV + LV pacing. The RV showed the largest TAT during LV pre-excitation or LV-only pacing (upper left corners in the heat maps). LV TAT showed a relatively large increase with large RV pre-excitation (right side of middle panels and lower right corners in heat maps), while RV TAT did not increase much. As indicated by the VEU (bottom row **Figure 3**), during LV-only pacing the LVFW was activated more than 40 ms before the RVFW. During RV-only pacing the LVFW was, on average, activated more than 20 ms later than the RVFW. The LVFW and RVFW were activated simultaneously with very slight LV pre-excitation (**Figure 3** bottom right, VEU = 0).

TABLE 1 | Baseline characteristics in median (range) of dogs during baseline (RV-only, A-RV 125 ms pacing).

	During baseline RV-only pacing
Weight (kg)	19.8 (19.4–21.4)
MAP (mmHg)	55 (42–71)
Systolic arterial pressure (mmHg)	70 (62–81)
Diastolic arterial pressure (mmHg)	45 (31–53)
LV dP/dt_{max} (mmHg/s)	1205 (1183–1646)
RV dP/dt_{max} (mmHg/s)	520 (345–700)
Weeks between AVB and Sacrifice (weeks)	13 (12–21)

Hemodynamic Effects of Altering Pacing Delay Settings

The changes in LV and RV dP/dt_{max} in response to changes in pacing delay settings are presented in **Figure 4** (top and bottom, respectively). Increasing AV delay during simultaneous RV and LV pacing (left column and identity line in the heat maps) hardly affected LV and RV dP/dt_{max} in both measurements and simulations. The relative effect of changing VV delay (green, second column from left) was largest in RV dP/dt_{max}. Changing pacing settings from RV to LV pre-excitation decreased RV dP/dt_{max} with more than 30% in the experiment. The decrease in RV dP/dt_{max} was less pronounced in the simulations but followed the same pattern. LV dP/dt_{max} was highest with LV pre-excitation and simultaneous pacing in both the experiment and simulations.

The heat maps of both the animal experiments and computer simulations (right side of **Figure 4**) show a qualitatively similar pattern where the largest changes in both LV and RV dP/dt_{max} are observed when changing the VV delay. The largest increase in LV dP/dt_{max} in the measurements was reached with a short A-LV (50 ms) and A-RV (90 ms). LV pre-excitation led to a larger increase in LV dP/dt_{max} than RV pre-excitation during all measurements and simulation, with an optimal LV pre-excitation range of 10–50 ms. For RV dP/dt_{max}, all LV pre-excitation pacing settings led to a decrease up to 33% in the experiment and 18% in the simulations, while RV pre-excitation caused little change compared to baseline (RV-only) pacing.

Changes in Simulated Cardiac Output at Different Pacing Delays

While dP/dt_{max} values are regarded as a measure of ventricular contractility, cardiac output may be more closely related to pump function of the entire heart. Note that due to the closed loop circulation, in a steady state situation cardiac output of the RV and LV are the same. Cardiac output was not determined in the experiments, but it was calculated in the model simulations. In these simulations the changes in cardiac output following a switch in pacing delay differed from the changes in both LV and RV dP/dt_{max} (**Figure 5**). Cardiac output was more sensitive to changes in AV-delay than to changes in VV-delay. AV-delays of 50 and 70ms led to the largest increases in cardiac output, amounting up to 9%.

In order to find an explanation for the differences in behavior between cardiac output and RV and LV dP/dt_{max} we compared the time course of these parameters as well as EDV during the first beats after start of a certain setting, in this case LV pre-excitation (**Figure 6**). In the first beat after the change in pacing setting and therefore also activation sequence (see above), both LV stroke volume and dP/dt_{max} increased while RV stroke volume and dP/dt_{max} decreased. In

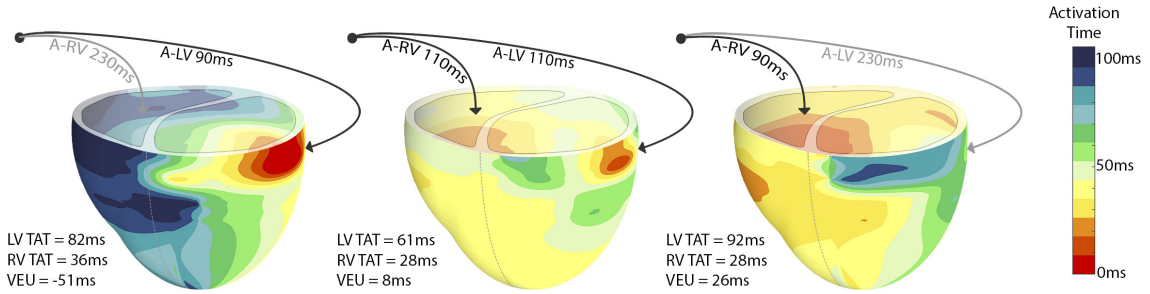

FIGURE 2 | Epicardial electric activation maps in a paced dog heart with complete AV block during LV pre-excitation **(left)**, simultaneous pacing **(middle)**, and RV pre-excitation **(right)**. Black arrows indicate capture, whereas gray arrows indicate loss of capture.

the subsequent beat RV EDV increased, due to the smaller SV of the previous beat, whereas LVEDV decreased. As a consequence of these EDV changes, RV SV recovered and LV SV decreased to some extent and in the third and subsequent beats an steady state (SS) was reached, with SV in both ventricles (and therefore cardiac output) increasing by about 3%. This example, representative for the other conditions, illustrates that dP/dt_{max} was largely independent of preload, whereas SV depended on it, most likely due to the length dependent activation, implemented in the CircAdapt model (see section "Materials and Methods").

Figure 7 shows the response of stroke volume of the LV and RV after simulated programming of nine different pacing settings. In the first beat RV SV remained either unchanged or decreased as compared to baseline, indicating little direct mechanical benefit of the change in pacing delay for the RV. However, similar to the example in **Figure 6**, copied into the left upper panel of **Figure 7**, RV stroke volume changed considerably in subsequent beats. While changes in LV SV initially differed from RV SV, a steady state was reached after several simulated beats. Note that the largest benefit in SV, and therefore cardiac output, was primarily dependent on AV-delay. For example, in the bottom row (A-RV 70 ms) the optimized RV filling improved stroke volume to such a degree that, through the serial coupling, LV preload increased, leading to a further increase in LV stroke volume after the second cycle. On the other hand, at longer AV-delays this atrial-ventricular coupling decreases, resulting in a lower steady-state cardiac output.

DISCUSSION

In this study we investigated the influence of LV and RV pacing delay settings on LV and RV electrical activation and contractility in animal studies and computer simulations. Both studies showed that LV TAT is smallest during synchronous RV and LV stimulation and increases when VV delays increase. RV TAT becomes larger in particular during LV pre-excitation. LV and RV contractility vary most, and in opposite direction, with changes in VV delay settings. After demonstrating the realistic simulations in the model, we used the model to calculate cardiac output changes and to explain why changes cardiac output differed from both RV and LV contractility. The latter findings demonstrate how a model like CircAdapt can extend mechanistic understanding of circulatory changes due to a device therapy.

LV and RV Contractility Respond in Opposite Manner to Variations in VV Pacing Delays

A key finding in the present study is that LV and RV dP/dt_{max} change in opposite direction when changing the VV pacing delay. Sciaraffia et al. (2009) previously demonstrated that RV and LV dP/dt_{max} identify different "optimal" VV delays in most of the patients included in their study. Furthermore, Houston et al. (2018) recently showed that in patients with dyssynchronous heart failure, RV-only pacing leads to higher RV dP/dt_{max} than LV-only or simultaneous LV + RV pacing. In an experimental study in pigs, different VV delays were tested at different pacing locations (Quinn et al., 2006). Similar to our study, these investigators found that RV pre-excitation led to a higher RV dP/dt_{max} than LV pre-excitation. The fact that findings were consistent in patients, animals and a computer model implies that the opposing changes in hemodynamics, caused by varying VV pacing delays, are caused by a universal mechanism.

Another key finding is that ventricular specific pre-excitation is required for a good contractile function in both the LV and RV. This is illustrated by LV pre-excitation increasing LV dP/dt_{max} and RV pre-excitation leading to the largest RV dP/dt_{max} values. In contrast, changes in AV delay have less effect on measured and simulated LV and RV dP/dt_{max}. In a previous study, in which we evaluated the relative importance of interventricular and intraventricular dyssynchrony for contractile response to CRT (change in LV dP/dt_{max}), it was demonstrated that interventricular dyssynchrony during intrinsic rhythm is the dominant electrical substrate driving response to CRT (Huntjens et al., 2018). In contrast, intraventricular dyssynchrony showed little effect on LV dP/dt_{max}, which is in line with experimental observations that reducing LV TAT by multipoint pacing does not improve LV dP/dt_{max} (Ploux et al., 2014). However, results

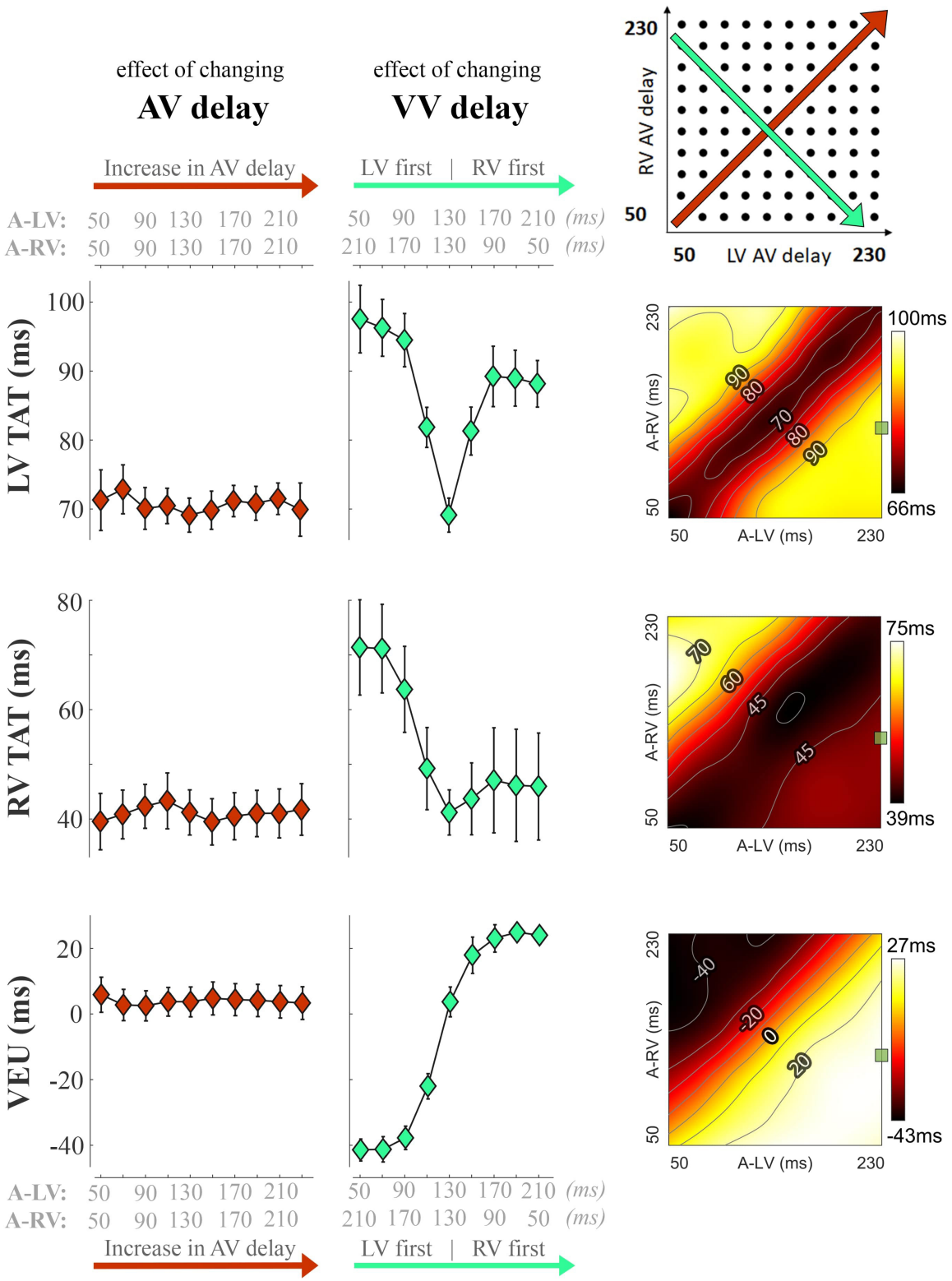

FIGURE 3 | Changes in electrical dyssynchrony indices during variation in pacing delay in the animal experiments. The left column shows the effect of increasing AV delay during simultaneous RV + LV pacing; the middle column shows changes in VV delay (green, from LV pre-excitation to RV pre-excitation) and the heat maps on the right are the results for all pacing setting (mean of six dogs, bars represent standard errors of the mean). From top to bottom: Total activation time (TAT) of the total LV (free wall and septum), RV free wall (RVFW), and VEU (Ventricular Electrical Uncoupling). The green square in each heat map indicate the baseline pacing setting.

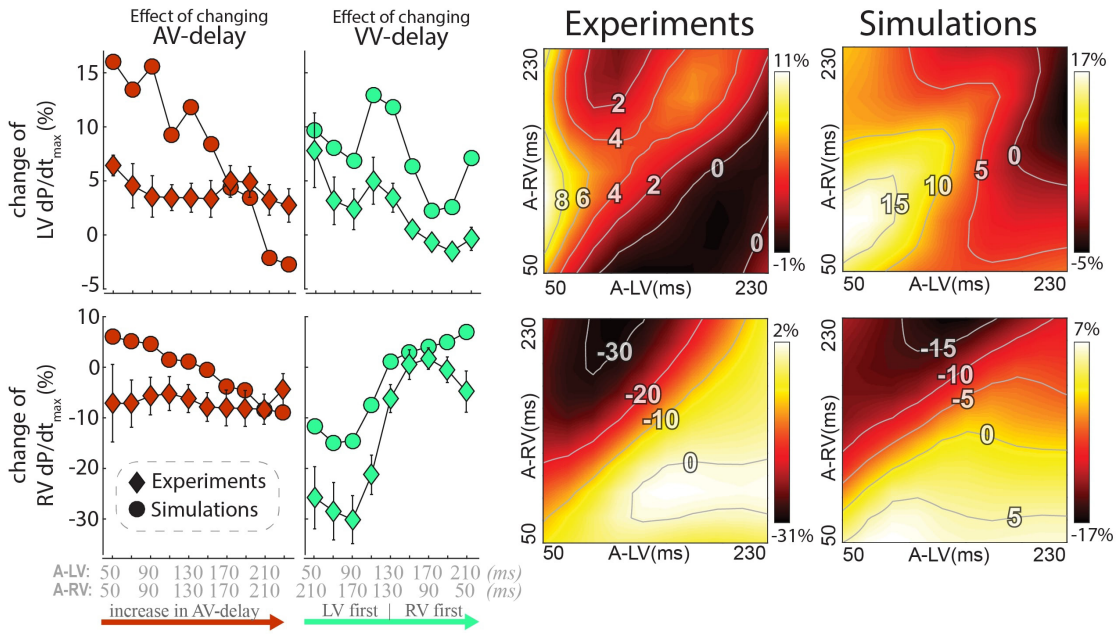

FIGURE 4 | Changes in contractile response as a result of changes in pacing delays in experiments and simulations. Percentile change from baseline of LV dP/dt_{max} (top) and RV dP/dt_{max} (bottom). The left rows depict the same AV and VV delay settings as in **Figure 3** are shown. Heat maps for both the experiment (3rd column) and simulations (4th column). Diamonds: Canine measurements (Mean (standard error of the mean) of six dogs; Circles: Simulation output.

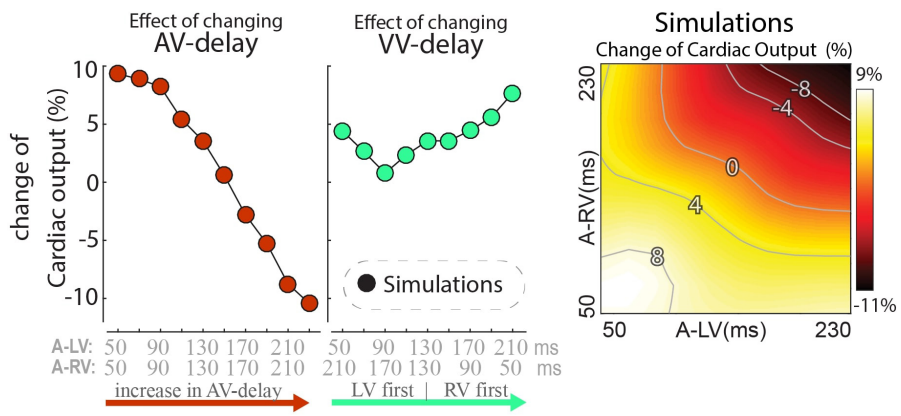

FIGURE 5 | Relative change in simulated steady-state cardiac output with a change in pacing delay settings. Depicted are the changes relative to baseline (see text).

in this study suggest that intraventricular dyssynchrony might still play a modulating role since increase in LV TAT, with large LV pre-excitation, led to a decrease in LV dP/dt_{max} compared to slight LV pre-excitation. Because RV TAT increases concurrently with decreases in VEU we cannot distinguish if either intra- or interventricular dyssynchrony has a larger effect on RV contractility.

In agreement with our observations, other studies in patients have shown that the lowest electrical dyssynchrony does not necessarily lead to the highest LV contractility or better clinical outcome (Thibault et al., 2011; Lumens et al., 2013). Optimization based on minimization of electrical dyssynchrony alone might therefore not be sufficient. Even if the optimal electrical activation for LV contractility is known, further clinical studies are required to investigate whether the gain in LV contractility outweighs the loss of RV contractility, especially since cardiac output might not match either or both but be a combination/compromise.

CircAdapt Simulations Capture Both LV and RV Contractile Response to Pacing Delay Changes

The present study demonstrates that the CircAdapt model can capture pacing-induced changes to both LV and RV contractile function. It is especially the response of the RV to pacing that has been less well studied, both by our group and by others.

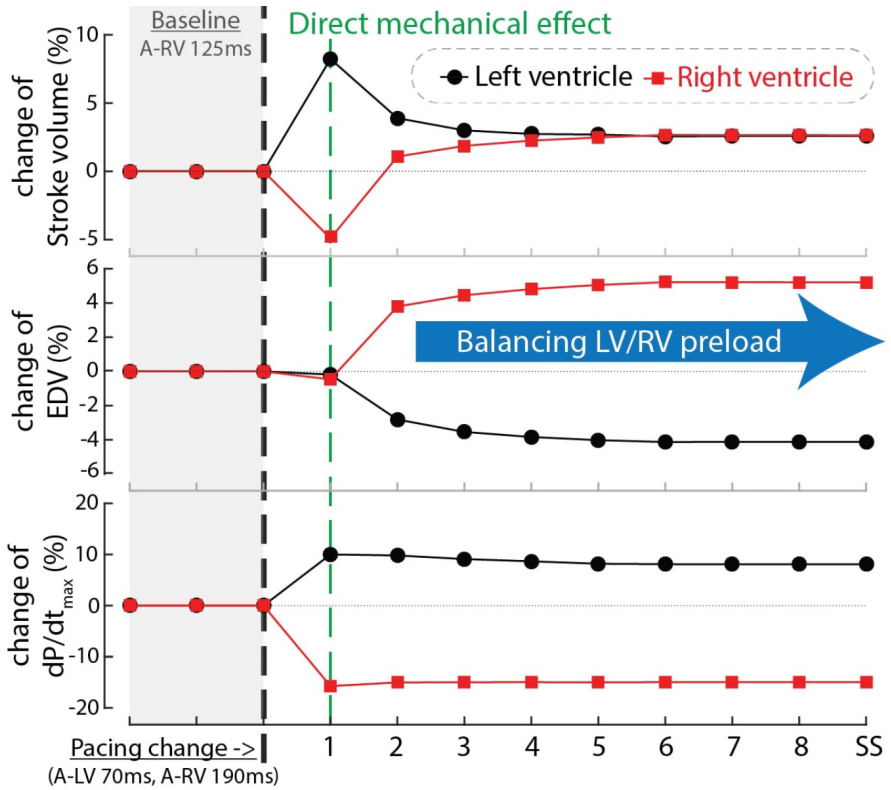

FIGURE 6 | Time courses of the relative change of stroke volume (top), end-diastolic volume (EDV, mid) and dP/dt_{max} of the LV (black circles) and RV (red squares) after changing pacing delay from baseline (A-RV 125 ms) to LV pre-excitation (A-LV 70 ms, A-RV 190 ms) in computer simulations. The black dashed line indicates the start of the change in pacing delay. The numbers in the blue bar indicate the number of simulated cardiac cycles. SS, steady state.

The use of experimental measurements electrical activation of the paced dog heart, derived from canine experiments, coupled to the simulation of the entire circulation, resulted in changes in RV and LV dP/dt_{max} that closely mimicked values measured in dog experiments.

Earlier studies have shown that CircAdapt enables realistic simulation of cardiac response to CRT, mostly focusing on LV function (Lumens et al., 2013, 2015; Huntjens et al., 2018). In one of those studies, it was demonstrated that the RV plays an important role in the improvement of LV function during LV-only pacing (Lumens et al., 2013). The present study extends the mechanistic insight in the working action of CRT in the context of pacing delay optimization, where the complex mechanical and hemodynamic interactions between the four cardiac cavities and the surrounding circulations are found to be important.

As demonstrated in this study, the CircAdapt model can capture the complexity of different LV and RV responses to CRT by incorporating several relevant components of cardiovascular interaction. Firstly, it realistically incorporates direct mechanical interaction between the three ventricular walls (Lumens et al., 2009). Secondly, it allows realistic simulation of regional myocardial mechanics in the ventricular walls of the asynchronously activated heart (Leenders et al., 2012; Walmsley et al., 2015a), thereby enabling experimentally measured activation times to be imposed and the related intraventricular heterogeneities in mechanical myofiber behavior to be simulated. Thirdly, it is a closed-loop system allowing for indirect (serial) hemodynamic interaction between the left and right side of the heart through the systemic and pulmonary circulations (Arts et al., 2005; Lumens et al., 2010). Fourthly, its four-chamber heart captures the dynamics of hemodynamic atrioventricular interactions (Jones et al., 2017). Lastly, it includes the mechanical interaction through pericardial constraint, with an increase in the volume of a chamber altering the pressure in the other chambers and, hence, diastolic filling and septal position (Palau-Caballero et al., 2017).

Simulation-Derived Mechanistic Insights

The ability of CircAdapt to realistically simulate both LV and RV hemodynamics during pacing allowed us to further study the impact of differences between both chambers on cardiac output. In particular, the model showed a difference in response between dP/dt_{max} and SV/CO. Similar differences have been observed in a clinical study where LV dP/dt_{max} responses differed from responses in stroke work (van Everdingen et al., 2018).

Our simulations provided a plausible explanation for this paradoxical observation. While LV and RV stroke volume

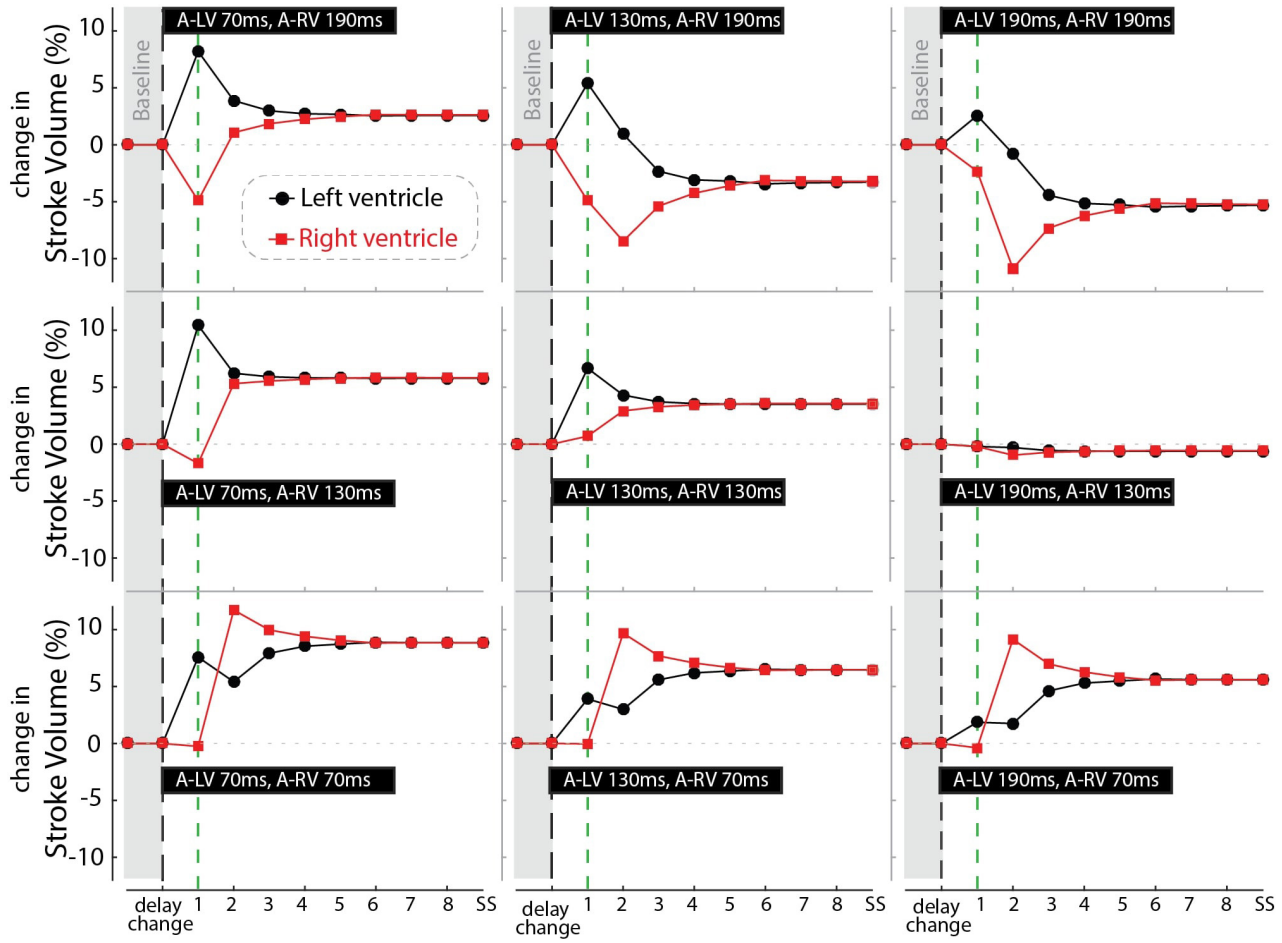

FIGURE 7 | Relative change in stroke volume of the left (black circles) and right (red squares) ventricle over a number of simulated cycles until steady-state (SS) after changing pacing delay (the nine settings shown in the black bars). Black dashed line indicates the moment of changing the pacing delays while the green line marks the first beat.

of the first beat after a change of pacing delay can differ substantially, a common steady-state stroke volume and thereby cardiac output is reached due to balancing ventricular preload conditions during the next few beats. There are three main determinants of the newly achieved steady-state preload condition. First, the changes in stroke volumes directly change the end-systolic volumes and thereby the end-diastolic volumes in the next beat. Second, the pacing-induced changes in effective left and right AV delays change the efficiency of atrial and ventricular diastolic filling and subsequent systolic contraction. Thirdly, changes in stroke volume affect the filling of the other ventricle through the systemic and pulmonary circulations.

While dP/dt_{max} changes congruently with first-beat stroke volume in the same ventricle, it is less affected by changes in preload. As a result, LV and RV dP/dt_{max} are much more sensitive to changes of VV-delay and, hence, asynchrony of electrical activation than to changes of AV-delay. On the other hand, changes of AV-delay affect cardiac output more than LV and RV dP/dt_{max}.

Computer Modeling in Therapy Optimization

Other cardiac computer modeling studies have been conducted to investigate other factors in the optimization of CRT therapy. For example, in a cohort of 648 virtual patients it was found that the location of the LV pacing site is an important factor in response to CRT (Crozier et al., 2016). Electrophysical cardiac computer modeling studies also demonstrated the importance of LV pacing site and the potential of simulations to predict the electrical optimal pacing location and setting (Reumann et al., 2007; Miri et al., 2009; Niederer et al., 2011). Our study shows, however, that an electrical optimum (lowest electrical dyssynchrony) might not necessarily be optimal for overall pump function.

The CircAdapt simulations performed for this study can run on a single core in real time. CircAdapt requires activation time as input and lacks the cardiac electrophysiological model necessary to extract this information from standard clinical data. This input could, however, potentially be generated by other models, for example the ones referred to in the previous

paragraph. This would also allow for testing of alternative pacing sites, which would result in different activation patterns, which subsequently can be used as input for CircAdapt simulations. A workflow where fast and anatomically realistic cardiac electrophysiological simulations are combined with cardiac mechanical and circulatory CircAdapt simulations might further increase the clinical applicability of cardiac computer models.

Study Limitations

In this study the pacing experiments were performed in relatively healthy canine hearts. Previous work from our group showed that chronic total AV-block leads to structural changes (hypertrophy) and electrical remodeling (QT-time prolongation), but normal contractility (Peschar et al., 2003). On the other hand, patients treated with CRT have different levels of myocardial remodeling and heart failure, which may affect the response to pacing (Strik et al., 2013a, Nguyên et al., 2018). Results of this study might differ from patient data since long-term structural remodeling was not included in both the animal and computational experiments. On the other hand, differences in RV and LV response observed in this study could mean that different pacing settings might affect the positive and/or negative remodeling of the LV and RV.

A major difference between this animal experiment and patients in day-to-day life is that the animals were anesthetized. To allow comparison between the experiments and simulations, the model's LV afterload in the baseline situation was adapted to fit the measured mean arterial pressure in the dogs. After the change in activation delays regulation was disabled, which is likely similar to the anesthetic condition were regulation is slow. Caution should, however, be taken when translating results of this study toward the clinical setting considering that loading conditions potentially affect the effect of pacing delay changes (Quinn et al., 2009). Future studies are needed to investigate how load-dependent the observed effects of pacing delay optimization are and how homeostatic regulation interacts with changes in LV and RV contractility. A final limitation of the CircAdapt (and most other computer models in this field) is that changes in function of the autonomic nervous system are not taken into account.

Clinical Perspective

The results of this study raise the question what outcome measure is best to use for optimization of pacing delay. Current clinical practice focusses almost exclusively on the LV, using parameters like LV dP/dt_{max}, aortic outflow integral, and LV systolic (or aortic) pressure. This study demonstrates that improving LV function can reduce RV function. Furthermore, cardiac output is not necessarily increasing when LV dP/dt_{max} increases. Hence, An exclusive focus on the LV might not lead to the best overall outcome. Therefore, future studies on optimization of therapy should not exclusively focus on the LV but also include measures of RV and/or whole heart function. In our analysis of cardiac output we also demonstrated that the moment of measurement affects what physiological phenomenon is actually observed. Contractile function alone might better be observed in the first beats while longer lasting measurements, that allow reaching a steady state, will provide more information about the loading of the heart and its interaction with homeostatic regulation. Insights acquired in the present opens the way for designing better optimization protocols, possibly even including computer modeling.

CONCLUSION

The LV and the RV respond in an opposite manner to LV or RV pre-excitation. LV pre-excitation improved LV contractility and decreased RV contractility, while RV pre-excitation had the opposite effects. The CircAdapt computer model realistically captures these opposite responses of LV and RV contractile function. Computer simulations extend animal experimental findings by revealing that improving ventricular contractility does not necessarily lead to an improvement of cardiac output. This study demonstrates the potential of CircAdapt to provide a valuable and efficient *in silico* platform for further optimization studies for device therapy.

AUTHOR CONTRIBUTIONS

EW, PH, MS, JW, FP, and JL conceived and designed the experiments. EW, RS, and MS performed the experiments. EW, RS, PH, MS, GP, EV, FP, and JL analyzed and interpreted the data. MS, JW, FP, and JL contributed to materials and analysis tools. EW, RS, PH, MS, GP, EV, JW, KV, TD, FP, and JL wrote or provided the critical revision on the manuscript.

FUNDING

This work was funded through the EraCoSysMed PUSHCART project. Dr. Lumens was funded through a grant within the framework of the Dr. E. Dekker program of the Dutch Heart Foundation (NHS-2015T082). JL has received funding from Medtronic Bakken Research Center for consulting services. FWP received research grants from Medtronic, Abbott, LivaNova, Biosense Webster, MSD, and Biotronik. KV received research grants from Medtronic and Abbott. GP and EV are co-owners of CardioSolv LLC and Numericor.

SUPPLEMENTARY MATERIAL

The Supplementary Material for this article can be found online at: https://www.frontiersin.org/articles/10.3389/fphys.2019.00017/full#supplementary-material

REFERENCES

Abraham, W. W. T., Fisher, W. G. W., Smith, A. L., Delurgio, D. B., Leon, A. R., Loh, E., et al. (2002). Cardiac resynchronization in chronic heart failure. *N. Engl. J. Med.* 346, 1845–1853. doi: 10.1056/NEJMoa013168

Arts, T., Delhaas, T., Bovendeerd, P., Verbeek, X., and Prinzen, F. (2005). Adaptation to mechanical load determines shape and properties of heart and circulation: the CircAdapt model. *Am. J. Physiol. Heart Circ. Physiol.* 288, 1943–1954. doi: 10.1152/ajpheart.00444.2004

Arts, T., Lumens, J., Kroon, W., and Delhaas, T. (2012). Control of whole heart geometry by intramyocardial mechano-feedback: a model study. *PLoS Comput. Biol.* 8:e1002369. doi: 10.1371/journal.pcbi.1002369

Arts, T., Prinzen, F. W., Snoeckx, L. H. E., Rijcken, J. M., and Reneman, R. S. (1994). Adaption of cardiac structure by mechanical feedback in the environment of the cell: a model study. *Biophys. J.* 66, 953–961. doi: 10.1016/S0006-3495(94)80876-8

Auger, D., Hoke, U., Bax, J. J., Boersma, E., and Delgado, V. (2013). Effect of atrioventricular and ventriculoventricular delay optimization on clinical and echocardiographic outcomes of patients treated with cardiac resynchronization therapy: a meta-analysis. *Am. Heart J.* 166, 20–29. doi: 10.1016/j.ahj.2013.03.021

Auricchio, A., and Prinzen, F. W. (2011). Non-responders to cardiac resynchronization therapy. *Circ. J.* 75, 521–527. doi: 10.1253/circj.CJ-10-1268

Bogaard, M. D., Meine, M., Tuinenburg, A. E., Maskara, B., Loh, P., and Doevendans, P. A. (2012). Cardiac resynchronization therapy beyond nominal settings: who needs individual programming of the atrioventricular and interventricular delay? *Europace* 14, 1746–1753. doi: 10.1093/europace/eus170

Brignole, M., Auricchio, A., Baron-Esquivias, G., Bordachar, P., Boriani, G., Breithardt, O.-A., et al. (2013). 2013 ESC guidelines on cardiac pacing and cardiac resynchronization therapy: the task force on cardiac pacing and resynchronization therapy of the European society of cardiology (ESC). Developed in collaboration with the European Heart Rhythm Association. *Eur. Heart J.* 34, 2281–2329. doi: 10.1093/eurheartj/eht150

Cleland, J. G., Daubert, J. C., Erdmann, E., Freemantle, N., Gras, D., Kappenberger, L., et al. (2005). The effect of cardiac resynchronization on morbidity and mortality in heart failure. *N. Engl. J. Med.* 352, 1539–1549.

Cleveland, W. S. (1979). Robust locally weighted regression and smoothing scatterplots. *J. Am. Stat. Assoc.* 74, 829–836. doi: 10.1080/01621459.1979.10481038

Crozier, A., Blazevic, B., Lamata, P., Plank, G., Ginks, M., Duckett, S., et al. (2016). The relative role of patient physiology and device optimisation in cardiac resynchronisation therapy: a computational modelling study. *J. Mol. Cell. Cardiol.* 96, 93–100. doi: 10.1016/j.yjmcc.2015.10.026

Groote, P. D. E., Millaire, A., Foucher-hossein, C., de Groote, P., Millaire, A., Foucher-hossein, C., et al. (1998). Right ventricular ejection fraction is an independent predictor of survival in patients with moderate heart failure. *J. Am. Coll. Cardiol.* 32, 948–954.

Houston, B. A., Sturdivant, J. L., Yu, Y., and Gold, M. R. (2018). Acute biventricular hemodynamic effects of cardiac resynchronization therapy in right bundle branch block. *Heart Rhythm* 15, 1525–1532. doi: 10.1016/j.hrthm.2018.05.017

Huntjens, P. R., Ploux, S., Strik, M., Walmsley, J., Ritter, P., Haissaguerre, M., et al. (2018). Electrical substrates driving response to cardiac resynchronization therapy. *Circ. Arrhythm. Electrophysiol.* 11:e005647. doi: 10.1161/CIRCEP.117.005647

Huntjens, P. R., Walmsley, J., Ploux, S., Bordachar, P., Prinzen, F. W., Delhaas, T., et al. (2014). Influence of left ventricular lead position relative to scar location on response to cardiac resynchronization therapy: a model study. *Europace* 16(Suppl. 4), iv62–iv68. doi: 10.1093/europace/euu231

Hyde, E. R., Behar, J. M., Crozier, A., Claridge, S., Jackson, T., Sohal, M., et al. (2016). Improvement of right ventricular hemodynamics with left ventricular endocardial pacing during cardiac resynchronization therapy. *Pacing Clin. Electrophysiol.* 39, 531–541. doi: 10.1111/pace.12854

Jones, S., Lumens, J., Sohaib, S. M. A., Finegold, J. A., Kanagaratnam, P., Tanner, M., et al. (2017). Cardiac resynchronization therapy: mechanisms of action and scope for further improvement in cardiac function. *Europace* 19, 1178–1186. doi: 10.1093/europace/euw136

Lee, A. W. C., Costa, C. M., Strocchi, M., Rinaldi, C. A., and Niederer, S. A. (2018). Computational modeling for cardiac resynchronization therapy. *J. Cardiovasc. Transl. Res.* 11, 92–108. doi: 10.1007/s12265-017-9779-4

Leenders, G. E., Lumens, J., Cramer, M. J., De Boeck, B. W. L., Doevendans, P. A., Delhaas, T., et al. (2012). Septal deformation patterns delineate mechanical dyssynchrony and regional differences in contractility: analysis of patient data using a computer model. *Circ. Heart Fail.* 5, 87–96. doi: 10.1161/CIRCHEARTFAILURE.111.962704

Lumens, J., Blanchard, D. G., Arts, T., Mahmud, E., and Delhaas, T. (2010). Left ventricular underfilling and not septal bulging dominates abnormal left ventricular filling hemodynamics in chronic thromboembolic pulmonary hypertension. *AJP Heart Circ. Physiol.* 299, H1083–H1091. doi: 10.1152/ajpheart.00607.2010

Lumens, J., Delhaas, T., Kirn, B., and Arts, T. (2009). Three-wall segment (TriSeg) model describing mechanics and hemodynamics of ventricular interaction. *Ann. Biomed. Eng.* 37, 2234–2255. doi: 10.1007/s10439-009-9774-2

Lumens, J., Ploux, S., Strik, M., Gorcsan, J., Cochet, H., Derval, N., et al. (2013). Comparative electromechanical and hemodynamic effects of left ventricular and biventricular pacing in dyssynchronous heart failure: electrical resynchronization versus left-right ventricular interaction. *J. Am. Coll. Cardiol.* 62, 2395–2403. doi: 10.1016/j.jacc.2013.08.715

Lumens, J., Tayal, B., Walmsley, J., Delgado-Montero, A., Huntjens, P. R., Schwartzman, D., et al. (2015). Differentiating electromechanical from non-electrical substrates of mechanical discoordination to identify responders to cardiac resynchronization therapy. *Circ. Cardiovasc. Imaging* 8:e003744. doi: 10.1161/CIRCIMAGING.115.003744

Miri, R., Graf, I. M., and DÖssel, O. (2009). Efficiency of timing delays and electrode positions in optimization of biventricular pacing: a simulation study. *IEEE Trans. Biomed. Eng.* 56, 2573–2582. doi: 10.1109/TBME.2009.2027692

Nguyên, U. C., Verzaal, N. J., van Nieuwenhoven, F. A., Vernooy, K., and Prinzen, F. W. (2018). Pathobiology of cardiac dyssynchrony and resynchronization therapy. *Europace* 6, 1660–1665. doi: 10.1093/europace/euy035

Niederer, S., Mitchell, L., Smith, N., and Plank, G. (2011). Simulating human cardiac electrophysiology on clinical time-scales. *Front. Physiol.* 2:14. doi: 10.3389/fphys.2011.00014

Palau-Caballero, G., Walmsley, J., Van Empel, V., Lumens, J., and Delhaas, T. (2017). Why septal motion is a marker of right ventricular failure in pulmonary arterial hypertension: mechanistic analysis using a computer model. *Am. J. Physiol. Heart Circ. Physiol.* 312, H691–H700. doi: 10.1152/ajpheart.00596.2016

Peschar, M., Vernooy, K., Vanagt, W. Y. R., Reneman, R. S., Vos, M. A., and Prinzen, F. W. (2003). Absence of reverse electrical remodeling during regression of volume overload hypertrophy in canine ventricles. *Cardiovasc. Res.* 58, 510–517. doi: 10.1016/S0008-6363(03)00331-6

Ploux, S., Lumens, J., Whinnett, Z., Montaudon, M., Strom, M., Ramanathan, C., et al. (2013). Noninvasive electrocardiographic mapping to improve patient selection for cardiac resynchronization therapy: beyond QRS duration and left bundle branch block morphology. *J. Am. Coll. Cardiol.* 61, 2435–2443. doi: 10.1016/j.jacc.2013.01.093

Ploux, S., Strik, M., Van Hunnik, A., Van Middendorp, L., Kuiper, M., and Prinzen, F. W. (2014). Acute electrical and hemodynamic effects of multisite left ventricular pacing for cardiac resynchronization therapy in the dyssynchronous canine heart. *Heart Rhythm* 11, 119–125. doi: 10.1016/j.hrthm.2013.10.018

Prinzen, F. W., Vernooy, K., and Auricchio, A. (2013). Cardiac resynchronization therapy: state-of-the-art of current applications, guidelines, ongoing trials, and areas of controversy. *Circulation* 128, 2407–2418. doi: 10.1161/CIRCULATIONAHA.112.000112

Quinn, T. A., Berberian, G., Cabreriza, S. E., Maskin, L. J., Weinberg, A. D., Holmes, J. W., et al. (2006). Effects of sequential biventricular pacing during acute right ventricular pressure overload. *Am. J. Physiol.*

Heart Circ. Physiol. 291, H2380–H2387. doi: 10.1152/ajpheart.00446.2006

Quinn, T. A., Cabreriza, S. E., Richmond, M. E., Weinberg, A. D., Holmes, J. W., and Spotnitz, H. M. (2009). Simultaneous variation of ventricular pacing site and timing with biventricular pacing in acute ventricular failure improves function by interventricular assist. *Am. J. Physiol. Heart Circ. Physiol.* 297, H2220–H2226. doi: 10.1152/ajpheart.00802.2009

Reumann, M., Farina, D., Miri, R., Lurz, S., Osswald, B., and Dössel, O. (2007). Computer model for the optimization of AV and VV delay in cardiac resynchronization therapy. *Med. Biol. Eng. Comput.* 45, 845–854. doi: 10.1007/s11517-007-0230-x

Ricci, F., Mele, D., Bianco, F., Bucciarelli, V., De Caterina, R., and Gallina, S. (2017). Right heart-pulmonary circulation unit and cardiac resynchronization therapy. *Am. Heart J.* 185, 1–16. doi: 10.1016/j.ahj.2016.11.005

Sciaraffia, E., Malmborg, H., Lönnerholm, S., Blomström, P., and Blomström Lundqvist, C. (2009). Right ventricular contractility as a measure of optimal interventricular pacing setting in cardiac resynchronization therapy. *Europace* 11, 1496–1500. doi: 10.1093/europace/eup288

Strik, M., Van Deursen, C. J. M., Van Middendorp, L. B., Van Hunnik, A., Kuiper, M., Auricchio, A., et al. (2013a). Transseptal conduction as an important determinant for cardiac resynchronization therapy, as revealed by extensive electrical mapping in the dyssynchronous canine heart. *Circ. Arrhythm. Electrophysiol.* 6, 682–689. doi: 10.1161/CIRCEP.111.000028

Strik, M., Van Middendorp, L. B., Houthuizen, P., Ploux, S., Van Hunnik, A., Kuiper, M., et al. (2013b). Interplay of electrical wavefronts as determinant of the response to cardiac resynchronization therapy in dyssynchronous canine hearts. *Circ. Arrhythm. Electrophysiol.* 6, 924–931. doi: 10.1161/CIRCEP.113.000753

Thibault, B., Ducharme, A., Harel, F., White, M., Omeara, E., Guertin, M. C., et al. (2011). Left ventricular versus simultaneous biventricular pacing in patients with heart failure and a qrs complex =120 milliseconds. *Circulation* 124, 2874–2881. doi: 10.1161/CIRCULATIONAHA.111.032904

van Everdingen, W. M., Zweerink, A., Salden, O. A. E., Cramer, M. J., Doevendans, P. A., van Rossum, A. C., et al. (2018). Atrioventricular optimization in cardiac resynchronization therapy with quadripolar leads: should we optimize every pacing configuration including multi-point pacing? *Europace* 21, e11–e19. doi: 10.1093/europace/euy138

Vernooy, K., Cornelussen, R. N. M., Verbeek, X. A., Vanagt, W. Y., Van Hunnik, A., Kuiper, M., et al. (2007). Cardiac resynchronization therapy cures dyssynchronopathy in canine left bundle-branch block hearts. *Eur. Heart J.* 28, 2148–2155. doi: 10.1093/eurheartj/ehm207

Walmsley, J., Arts, T., Derval, N., Bordachar, P., Cochet, H., Ploux, S., et al. (2015a). Fast simulation of mechanical heterogeneity in the electrically asynchronous heart using the multipatch module. *PLoS Comput. Biol.* 11:e1004284. doi: 10.1371/journal.pcbi.1004284

Walmsley, J., Huntjens, P. R., Prinzen, F. W., Delhaas, T., and Lumens, J. (2015b). Septal flash and septal rebound stretch have different underlying mechanisms. *Am. J. Physiol. Heart Circ. Physiol.* 310, H394–H403. doi: 10.1152/ajpheart.00639.2015

Conflict of Interest Statement: The authors declare that the research was conducted in the absence of any commercial or financial relationships that could be construed as a potential conflict of interest.

frontiers in Physiology

ORIGINAL RESEARCH
published: 11 February 2019
doi: 10.3389/fphys.2019.00074

Optimization of Lead Placement in the Right Ventricle During Cardiac Resynchronization Therapy. A Simulation Study

*Edison F. Carpio[1], Juan F. Gomez[1], Rafael Sebastian[2], Alejandro Lopez-Perez[1], Eduardo Castellanos[3], Jesus Almendral[3], Jose M. Ferrero[1] and Beatriz Trenor[1]**

[1] Centre for Research and Innovation in Bioengineering (Ci2B), Universitat Politècnica de València, Valencia, Spain, [2] Computational Multiscale Simulation Lab (CoMMLab), Department of Computer Science, Universitat de València, Valencia, Spain, [3] Electrophysiology Laboratory and Arrhythmia Unit, Grupo HM Hospitales, Hospital Monteprincipe, University CEU-San Pablo, Madrid, Spain

Patients suffering from heart failure and left bundle branch block show electrical ventricular dyssynchrony causing an abnormal blood pumping. Cardiac resynchronization therapy (CRT) is recommended for these patients. Patients with positive therapy response normally present QRS shortening and an increased left ventricle (LV) ejection fraction. However, around one third do not respond favorably. Therefore, optimal location of pacing leads, timing delays between leads and/or choosing related biomarkers is crucial to achieve the best possible degree of ventricular synchrony during CRT application. In this study, computational modeling is used to predict the optimal location and delay of pacing leads to improve CRT response. We use a 3D electrophysiological computational model of the heart and torso to get insight into the changes in the activation patterns obtained when the heart is paced from different regions and for different atrioventricular and interventricular delays. The model represents a heart with left bundle branch block and heart failure, and allows a detailed and accurate analysis of the electrical changes observed simultaneously in the myocardium and in the QRS complex computed in the precordial leads. Computational simulations were performed using a modified version of the O'Hara et al. action potential model, the most recent mathematical model developed for human ventricular electrophysiology. The optimal location for the pacing leads was determined by QRS maximal reduction. Additionally, the influence of Purkinje system on CRT response was assessed and correlation analysis between several parameters of the QRS was made. Simulation results showed that the right ventricle (RV) upper septum near the outflow tract is an alternative location to the RV apical lead. Furthermore, LV endocardial pacing provided better results as compared to epicardial stimulation. Finally, the time to reach the 90% of the QRS area was a good predictor of the instant at which 90% of the ventricular tissue was activated. Thus, the time to reach the 90% of the QRS area is suggested as an additional index to assess CRT effectiveness to improve biventricular synchrony.

Keywords: cardiac resynchronization therapy, heart failure, LBBB, computational modeling, QRS duration, optimization

OPEN ACCESS

Edited by:
Olaf Doessel, Karlsruhe Institute of Technology (KIT), Germany

Reviewed by:
Joakim Sundnes, Simula Research Laboratory, Norway
Sanjay Ram Kharche, University of Western Ontario, Canada

***Correspondence:**
Beatriz Trenor
btrenor@eln.upv.es

Specialty section:
This article was submitted to Computational Physiology and Medicine, a section of the journal Frontiers in Physiology

Received: *10 October 2018*
Accepted: *22 January 2019*
Published: *11 February 2019*

Citation:
Carpio EF, Gomez JF, Sebastian R, Lopez-Perez A, Castellanos E, Almendral J, Ferrero JM and Trenor B (2019) Optimization of Lead Placement in the Right Ventricle During Cardiac Resynchronization Therapy. A Simulation Study. Front. Physiol. 10:74. doi: 10.3389/fphys.2019.00074

INTRODUCTION

Heart failure (HF) constitutes a major public health problem worldwide and much attention has been paid to the understanding of the arrhythmogenic mechanisms in the failing heart induced by the structural, electrical, and metabolic remodeling. Heart failure is also characterized by a compromised ventricular contraction, which is fundamental for an optimal cardiac function. Lack of synchrony in heart contraction is worsened when the failing heart is also affected by left bundle branch block (LBBB). These patients present electrical and mechanical ventricular dyssynchrony causing pump dysfunction, reduced functional capacity, and myocardial remodeling. In particular, LBBB is associated with delayed contraction of the left ventricle (LV), reduced ventricular performance and widening of the QRS complex.

The relative QRS duration (QRSd) provides a powerful prognostic value for patients with HF and is a primary indicator of eligibility for cardiac resynchronization therapy (CRT). CRT helps to reduce mortality and morbidity associated with HF (Abraham et al., 2002; Cleland et al., 2005). Recent studies have also concluded that patients with LBBB are more likely to respond to CRT than those with right bundle branch block (RBBB) or nonspecific interventricular conduction delays (IVCDs) (Zareba et al., 2011).

During CRT, two synchronized electrical stimuli are usually delivered to reduce ventricular dyssynchrony. One stimulation lead is usually placed on the apex of the right ventricle (RV), and the other one on the epicardium of the LV lateral wall. Patients with positive therapy response present QRS shortening and an increased LV ejection fraction (LVEF) (Bonakdar et al., 2009; Zhang et al., 2015; Coppola et al., 2016). However, around one third of the patients do not respond favorably to this therapy (Linde et al., 2012; Bertaglia et al., 2017) and implantation issues, such as perforation of the RV apex, have been observed.

Optimal location of pacing leads is crucial to achieve the best degree of ventricular synchrony. LV lead position has been recognized as an important determinant for response to CRT since the initial development of this therapy (Singh et al., 2011; Crozier et al., 2016; Lee et al., 2017). Experimental studies and computational models (Lopez-Perez et al., 2015) have been used to optimize LV lead location. In current guidelines (Brignole et al., 2013), the LV posterior-lateral wall is the recommended LV region for CRT application. Several studies have reported the beneficial results of pacing from the lateral region of the LV (Rossillo et al., 2004). However, there are still several open questions.

Abbreviations: AV, atrioventricular; AVD, atrioventricular delay; BiV, biventricular; CRT, cardiac resynchronization therapy; CV, conduction velocity; dV/dt_{max}, maximum upstroke velocity; FEM, finite element method; HF, heart failure; LBBB, left bundle branch block; LV, left ventricle; LV dP/dt_{max}, LV pressure rise; LVEF, LV ejection fraction; LVLED, LV lead electrical delay; PMJ, Purkinje myocardial junction; PS, Purkinje system; QRSa, QRS area; QRSd, QRS duration; RV, right ventricle; TAT, total ventricular activation time; t_{90}, time to 90% of the ventricular activation; t_{90}QRSa, time to 90% of the QRS area; VVD, interventricular delay.

First, as suggested by Zanon et al. the ideal LV lead placement should be the latest electrical intrinsic activated region (Zanon et al., 2014), typically the postero-lateral wall (Sipal et al., 2018). This location provided the maximum increase in contractility, expressed as the highest value of the first derivative of LV pressure over time (LV dP/dt_{max}). However, the electromechanical modeling study by Pluijmert et al. (2016) determined that in fascicular block conditions the latest activated area did not provide the maximum response in contractility. A different criterion suggested in the literature is to place the LV lead in the site corresponding to the shortest QRS registered. Nevertheless, simulation studies that apply this last non-invasive criterion (Miri et al., 2009a,b) estimated QRSd through calculation of the total ventricular activation time (TAT), a parameter not easily accessible in clinical or even experimental settings. In addition, studies such as Potse et al. (2012) have observed that biventricular pacing did not change QRS duration but reduced total ventricular activation time when the stimulation was applied in one point of the LV free wall.

Second, there is controversy about whether a higher degree of synchrony can be achieved by stimulating from points in the RV other than the apex (Da Costa et al., 2013; Pastore et al., 2013). Third, individualized programming of the atrioventricular delay (AVD) and interventricular delay (VVD) intervals is not typically performed in most patients in the normal clinical practice, and it has been primarily reserved for non CRT responders (Gras et al., 2009). The largest trials studying CRT used various methods to optimize these intervals, most frequently based on echocardiography and intracardiac electrogram interval measurements, but unequivocal proof of the benefit brought by optimization is still lacking (Abraham et al., 2010; Krum et al., 2012; Brugada et al., 2014). Echocardiography presents inherent variability of results and is highly operator dependent. Optimization based on intracardiac electrogram intervals has not proved yet to be of clear benefit above arbitrary atrioventricular interval (Ulč and Vančura, 2013). Another optimization method based on the surface ECG uses fusion with intrinsic conduction and avoids echocardiographic atrioventricular and biventricular optimization (Arbelo et al., 2014). Applying this method Arbelo et al. determined that electrocardiographic optimization improved invasive LV dP/dt_{max}. Similarly, randomized studies demonstrated that electrocardiographic optimization had superior LV remodeling at 6-month follow up although survival was not different, compared with optimization by echocardiography (Bertini et al., 2008; Tamborero et al., 2011). All these results suggest that minimizing QRSd could be used as a non-invasive method to optimize CRT.

In this study, we used a 3D biophysical model of the heart and torso to optimize pacing leads location, AVD, and VVD settings during CRT procedure, based on the shortest QRS duration measured on the torso surface. Results were compared with other optimization criteria. This analysis was used to define an electrical biomarker that relates the optimal lead configuration with the observed surface electrocardiogram signals.

METHODS

Anatomical Model

A 3D biventricular model of the heart was built from segmentation of a DE-MRI images stack. The cardiac DE-MRI was acquired from the Hospital Clinic Universitari de Valencia (Valencia, Spain). Regarding the ethical considerations, the protocol was approved by the Ethics Committee for Clinical Research of the Hospital Clinic Universitari de Valencia, which certifies that the present study was conducted in accordance with the recommendations gathered in the Declaration of Helsinki, originally adopted by the General Assembly of the World Medical Association in 1964, and in its subsequent revisions. Furthermore, the patient, who underwent the standard clinical protocol, gave written informed consent for the use of his anonymized clinical data in this study.

Manual image segmentation was performed using Seg3D software (Scientific Computing and Imaging Institute, University of Utah, USA) (Seg3D, 2013), including papillary muscles and main endocardial trabeculations (**Figure 1A**). From the segmented DE-MRI stack, a surface model of the ventricles was generated and subsequently meshed using MeshGems-Hexa (Distene S.A.S., Bruyeres-le-Chatel, France), obtaining a hexahedra-based volume mesh comprised of 4 million nodes (vertices) and 3.71 million elements, with an average edge length of 0.4 mm (see **Supplementary Material** for further detailed information). Transmural heterogeneity (**Figure 1B**) was defined by three different transmural layers for endocardial (blue), midmyocardial (green), and epicardial (red) cells within the volume mesh of our ventricular model, spanning 17, 41, and 42% of ventricular wall thickness, respectively (Sicouri and Antzelevitch, 1991; Sicouri et al., 1994; Desk et al., 1998).

To include the anisotropy of the cardiac muscle through fibers orientation (**Figure 1C**), we implemented Streeter's rule-based method (Streeter, 1979) modeled by the set of equations described in Sebastian et al. (2009) defining the helix (α_h) and transmural (α_t) angles. In papillary muscles and endocardial trabeculations, fibers are known to be aligned parallel to the longitudinal axis of those anatomical structures (Greenbaum et al., 1981). In order to reproduce such configuration, we performed the topological skeletonization of the volume mesh to extract the medial axes of each one of those structures, what enabled to properly assign the fiber orientation. Finally, we performed a Gaussian smoothing with a 3D kernel to soften abrupt transitions in fibers direction between the myocardial wall and the papillary muscles and trabeculations.

A Purkinje system (PS) network (**Figures 1D,E**) was developed based on a stochastic grown method (Sebastian et al., 2013) formed by linear elements. The RV section was composed of two main branches, one descending to the apex, and another extending to the surroundings of the moderator band, with several subdivisions. The LV section was formed by three main branches with several subdivisions: one descending to the apex toward the papillary muscles of the lateral wall, another one to the anterior wall, and the last one to the posterior wall. The location of the PMJs that start the endocardial activation from the main PS branches was optimized to obtain a typical ECG wave morphology in the precordial leads. Purkinje-Myocardial junctions (PMJs) conductivity were adjusted to allow retrograde and anterograde electrical propagation. A total of 1391 PMJ were distributed across the RV and LV.

The biventricular mesh was fit into a human torso mesh (Ferrer et al., 2015) to be able to properly solve the forward problem in electrophysiology and simulate the electrocardiogram (ECG) (**Figure 1F**). The torso dataset was obtained from the online open repository at the Center for Integrative Biomedical Computing (CBIC) from University of Utah (MacLeod et al., 1991). The torso volume mesh was made of tetrahedral elements of 0.5 mm spatial resolution. Note that the problem of passive propagation of extracellular potentials, i.e., only diffusion without reaction component, does not require such a fine spatial resolution outside the heart domain (Prassl et al., 2009); for this reason, the torso mesh is highly refined only in the region where it intersects with the ventricles (see **Supplementary Material** for complementary description).

Electrophysiological Model

O'Hara et al. (2011) model is the most recent action potential model developed for human ventricular electrophysiology. Our simulations were conducted using a modified version of this model to achieve realistic conduction velocity and electrical propagation in 3D ventricular tissue. For this reason, the original fast sodium current (I_{Na}) formulation was modified. Firstly, the steady state inactivation (h_{ss} and j_{ss}) and activation (m_{ss}) gates were changed as in Passini et al. (2016) and Mora et al. (2017), respectively. Secondly, the time constant of the inactivation gates was modified as in Dutta et al. (2017). Finally, the sodium conductance (G_{Na}) was decreased to 23% of its original value to obtain approximately a maximum upstroke velocity (dV/dt_{max}) of 260 V/ms as in the original O'Hara et al. (2011) model. Furthermore, the late sodium current (I_{NaL}) conductance (G_{NaL}) was duplicated to maintain the relationship between I_{NaL} and peak I_{Na} observed in voltage-clamp experiments as described in Mora et al. (2017). All these changes are detailed in the **Supplementary Material** together with the action potential (**Figure S1**) obtained with the original and modified O'Hara et al. models. The action potential model for Purkinje cells developed by Stewart et al. (2009) was used in the cardiac conduction system.

The electrical propagation through the ventricles was calculated by solving the monodomain equation (Equation 1) using ELVIRA FEM software (Heidenreich et al., 2010),

$$\nabla \cdot (\mathbf{D}\nabla V_m) = C_m \frac{\partial V_m}{\partial t} + I_{ion} + I_{stim} \tag{1}$$

where $\mathbf{D}$ is the equivalent conductivity tensor, V_m the transmembrane potential field, C_m the cell membrane capacitance, I_{ion} the transmembrane ionic current and I_{stim} the transmembrane stimulation current.

The ECG was simulated by solving the extracellular potential φ_e from the equation

$$\nabla \cdot ([D_i + D_e]\nabla \varphi_e) = -\nabla \cdot (D_i \nabla V_m) \tag{2}$$

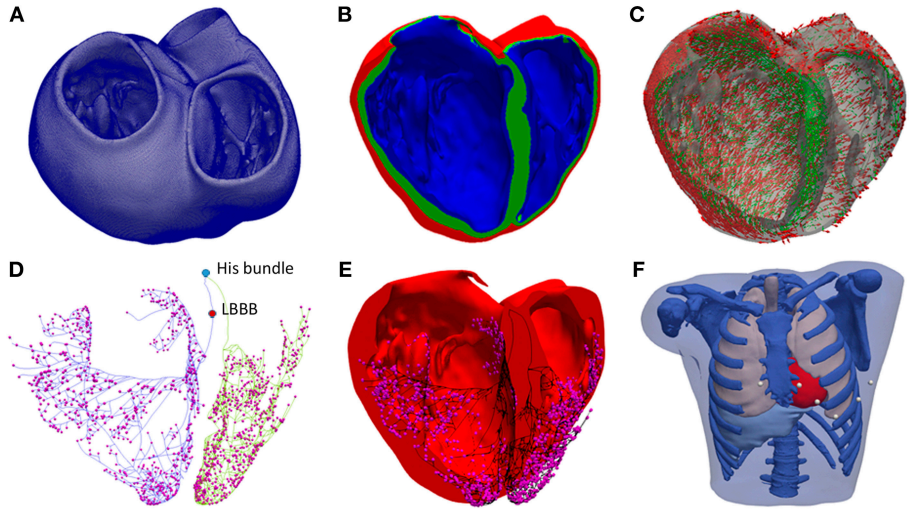

FIGURE 1 | Anatomical model. **(A)** Biventricular hexahedral mesh of a segmented human heart. **(B)** Model color-coded to show the assignment of the elements to the different cellular model in order to model the transmural heterogeneity: endocardial cells (blue), midmyocardial cells (green) and epicardial cells (red). **(C)** Arrows indicating the principal myofiber orientation of epicardial (red) and midmyocardial (green) cells. **(D)** Purkinje System (PS), including three main LV branches (posterior, septal, anterior) and RV main brunches (septal and anterior). Purkinje-Junctions are represented as magenta spheres. His Bundle, and the location of the LBBB are labeled in the model. **(E)** PS (black) coupled to the biventricular model. **(F)** Torso model with the biventricular mesh embedded (red) and precordial leads location (white).

where D_i and D_e are the volume-average conductivity tensors of the intra and extracellular domains, respectively (Potse et al., 2006). The reaction-diffusion simulation was run on the biventricular mesh. The right-hand side of Equation (2) was evaluated on this fine mesh and then interpolated on the coarser torso mesh. The extracellular potential φ_e was solved on the coarser mesh. The precordial ECG leads were then computed by extracting the extracellular potential at the electrode locations taking into account the Wilson terminal, as in clinical practice (see **Supplementary Material**).

In order to establish the conductivities that will define the conduction velocities (CV) in the heart domain, we performed a set of test simulations on a 3D slab model (20 × 20 × 6 mm) composed of regular hexahedral elements (voxels) with an edge length of 0.4 mm, matching the average length in the ventricular model. As a result, we set the conductivity values to 0.5 S/m and 0.1 S/m for longitudinal (σ_L) and transversal (σ_T) conductivity, respectively. This resulted in a CV of 0.61 m/s along the fiber direction and of 0.29 m/s in transverse direction. These values are consistent with experimental measurements in human ventricles (Taggart et al., 2000).

CV in the PS was adjusted to 2.5 m/s (Durrer et al., 1970; Dux-santoy et al., 2012). The electrical propagation in the torso mesh was considered isotropic and specific conductivities were assigned to each organ: (i) myocardium (4.589 mS/cm), (ii) bones (0.200 mS/cm), (iii) liver (0.277 mS/cm), (iv) lungs (0.389 mS/cm), (v) muscle (2.390 mS/cm), and (vi) blood (7.0 mS/cm) based on several experimental studies (Roth, 1992; Bradley et al., 1997; Keller et al., 2010).

Pathological Model

To simulate LBBB, an electrical block was generated on the left section of the PS before the bifurcation into three sub-branches by imposing null conductivity in two linear elements (see **Figure 1D**). HF condition was modeled by a reduction of 50% in CV, in accordance with protein connexin43 (Cx43) reduction observed in failing tissue (Coronel et al., 2013). The decrease and lateralization of this protein is associated with reduced longitudinal conduction velocity (Ai and Pogwizd, 2005; Akar et al., 2007; Wang and Hill, 2010).

Stimulation Protocols

For the present study a 3D anatomical model of the ventricles was generated, which does not include the geometry of the atria. Therefore, the intrinsic activation from the sinoatrial node was simulated by applying an electrical stimulus to the His bundle, either in healthy or HF + LBBB conditions (see **Figure 1D**). CRT leads were modeled as 0.5 mm^3 cubes injecting a transmembrane current of 400 $\mu A/\mu F$ in amplitude (see Equation 1). Four scenarios of CRT pacing were defined for HF + LBBB conditions with different combinations of atrioventricular delay (AVD) and interventricular delay (VVD) for each lead location configuration (AVD = 100 ms, VVD = 0 ms; AVD = 100 ms, VVD = 30 ms; AVD = 140 ms, VVD = 0 ms; AVD = 140 ms, VVD = 30 ms).

AVD is the time delay between the instant of initial activation of the sinoatrial node (external or intrinsic stimulation) and the instant of time of external CRT stimulation of the ventricles. To set the value of AVD in our simulations, several considerations were taken into account. Firstly, the typical duration of PR interval observed in LBBB patients is 200 ms (Rickard et al., 2017), which is the time that takes the initial atrial stimulation

to spread through the atria (100 ms), plus the time delay in the atrioventricular (AV) node (80 ms) (Prinzen et al., 2017), plus the propagation time from the His bundle through Purkinje system to finally reach the first activation site of the ventricles (20 ms approximately). Secondly, our model does not include the atria or the AV node as mentioned before, so that the intrinsic activation was simulated by stimulating His bundle, which is included in our 3D model.

In our simulations, different AVDs could be simulated by changing the stimulation time of the His bundle (coming from the intrinsic activation of the atria). Thus, an AVD of 100 ms was modeled by applying an electrical stimulus to the His bundle of 80 ms after ventricular leads activation. Indeed, when we applied the external CRT ventricular stimulation, 100 ms after initial activation of the sinoatrial node (AVD of 100 ms), this intrinsic activation had reached the atrial side of the AV node (this takes 100 ms) and needed still 80 ms to reach His bundle (delay needed in the AV node). In the case of an AVD of 140 ms, the electrical stimulus in the His bundle was applied 40 ms after ventricular leads activation. Indeed, when we applied the external CRT ventricular stimulation, 140 ms after initial activation of the sinoatrial node, this intrinsic activation had reached the AV node in 100 and 40 ms of delay in the AV have also elapsed, the stimulus needed 40 ms more to reach the His bundle, and this is why we stimulated the His bundle 40 ms after the ventricles. Additionally, VVD was set to 0 ms (stimulation in both ventricles simultaneously) and 30 ms (the RV was stimulated 30 ms after the LV), according to the time ranges used in clinical practice (Brignole et al., 2013; Urbanek et al., 2017).

Leads Location

The RV septal wall is an alternative location for the RV pacing lead in CRT. In this study, three different locations for the RV pacing lead were tested based on medical protocols and research works (Da Costa et al., 2013; Pastore et al., 2013). The RV septal electrode was placed in the apex (RVapex), middle septal region (RVmid) or upper region near the outflow tract (RVupper) (**Figure 2A**).

For the LV pacing lead location, the LV free wall was divided into three different regions (Singh et al., 2011; Dou et al., 2012): anterior, lateral, and posterior (**Figure 2B**). In addition, each region was divided into three segments: apical, mid-cavity, and basal, leading to a set of nine segments for the LV free wall as illustrated in **Figure 2C** as in Singh et al. (2011). The LV pacing lead was placed in the middle of each segment, both in the epicardial (**Figure 2C**) and endocardial wall (**Figure 2D**) to represent and simplify the different possible positions of the electrode within the same region, due to variety of veins configurations observed in CRT patients.

To summarize, we have a total of 54 lead location configurations obtained by combination of the three RV lead locations with 18 LV lead locations (9 epicardial and 9 endocardial) for the application of the CRT protocol.

QRS Measurements

QRS complex was computed in the precordial leads location on the torso surface for each CRT configuration and QRSd was measured using an algorithm implemented in Matlab software (Mathworks Inc., Natick, MA, USA). This algorithm determines the beginning and end of the QRS complex based on the first and second derivate of the electrocardiographic signal (see **Figure S2**). The QRS onset was calculated applying a threshold in the first derivate to determine a change in the slope. To estimate the end of QRS complex, additional signal processing was required as baseline was not reached in most CRT configurations. A time interval after the QRS complex was set based on the 95% of the accumulated area under the curve of the second derivate, and the end of the signal. To set the end of the QRS, the lowest value of the first derivate was used within this interval (see **Supplementary Material** for details). Once the beginning and end of QRS complex were determined for each precordial lead, the QRSd was calculated as the time interval between the onset beginning and the latest end of the QRS among all leads (Surawicz et al., 2009). This is the recommended criterion by the American Heart Association, the American College of Cardiology Foundation, and the Heart Rhythm Society (AHA/ACC/HRS). The total activation time (TAT) of the ventricular mesh was estimated as the time interval between the first and last depolarized node mesh above a threshold of −10 mV.

Correlation Analysis

Shortest QRSd was the criterion applied to evaluate the optimal location of the LV lead for different positions of the pacing lead in the RV. However, the total activation time (TAT), QRS area (QRSa) and the time to 90% of activated tissue (t_{90}) are other important parameters that have been used to evaluate CRT response. For this reason, three linear correlations between these parameters were performed using Pearson correlation method. Values of $p < 0.05$ were considered statistically significant. Values for the analysis are shown in **Tables S1–S5**.

RESULTS

Model Validation

Simulated ventricular activation maps for non-pathological and HF conditions with LBBB (HF + LBBB) are shown in **Figure 3A**. In healthy conditions, the electrical impulse traveled from the bundle of His to the first activation point in the LV endocardium in approximately 20 ms. RV activation started 10 ms after the onset of LV activation (Durrer et al., 1970). The computed time until all the ventricular tissue was depolarized (total activation time or TAT) was approximately 103 ms, in accordance with human data (Boukens et al., 2014). The outflow tract and the posterobasal area were the last activated regions in the RV, while the latest areas depolarized in the LV were the anterior mid and basal regions.

Under HF + LBBB conditions, activation began in the RV endocardium and reached the LV endocardium in the apical septal region after 46 ms from the onset of the RV depolarization. This is in agreement with the data recorded experimentally by Auricchio et al. (2004). The last activated region in the LV was the lateral wall in accordance with the study of Mafi Rad et al.

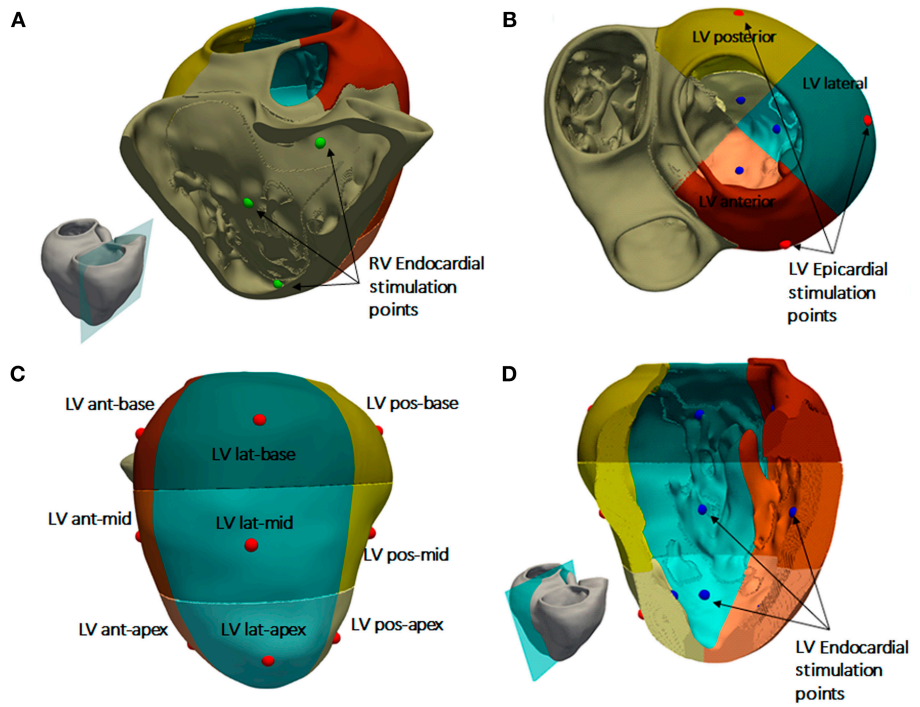

FIGURE 2 | Heart subdivisions and stimulation points for CRT protocol. **(A)** RV septal endocardial stimulation points tested (green). **(B)** Left ventricular (LV) free wall region divided into three regions: posterior (yellow), anterior (brown), and lateral (green). **(C)** Subdivisions of the three LV free wall regions into nine segments. Epicardial stimulation points tested in the middle of each segment (red dots). **(D)** Endocardial stimulation points tested in the LV free wall (blue dots).

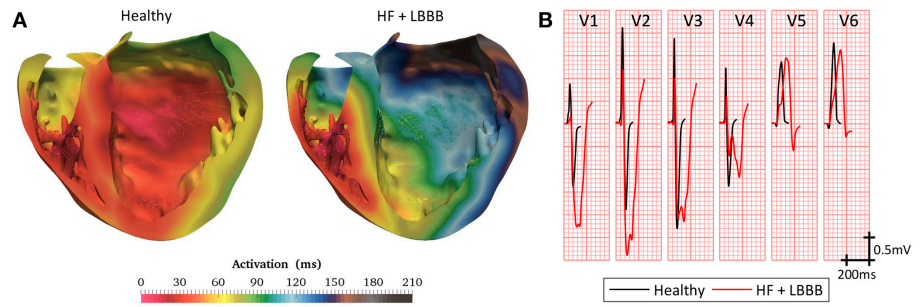

FIGURE 3 | Model validation. **(A)** Cross section of biventricular model showing color coded local activation maps of a healthy (left) and pathological heartbeat (right). **(B)** Precordial leads signals recorded on torso surface.

(2014). Additionally, the TAT was increased in 104% compared to a healthy heart.

Figure 3B shows the computed QRS complexes in the precordial leads for simulations in a healthy heart and under HF + LBBB conditions. For non-pathological conditions, QRS duration (QRSd) was 93 ms, while in HF + LBBB QRSd was increased to 190 ms. Both values are within experimental ranges (Spragg et al., 2010; Tian et al., 2017). Additionally, QRS complexes in HF + LBBB simulations present an rS pattern (small R wave followed by a bigger S wave) (Sweeney et al., 2014) in leads V1 and V2 and a mid-QRS notching in several leads. These observations are in agreement with the criteria proposed by Strauss et al. (2011) to define complete LBBB.

QRS Duration During CRT

A total of 54 electrode placement configurations with four different delays (two AVD and two VVD configurations) settings were tested for the CRT simulations. QRSd values are shown in **Table S1**.

Figure 4 compares the simulated QRS complexes in a scenario with HF + LBBB before (red traces) and after (green traces) the application of the CRT protocol. The optimal configurations in terms of shortest QRSd for the RV lead placement tested (apex, mid septum, and upper septum) are shown in the different rows. Epicardial vs. endocardial LV lead stimulation for those configurations are shown in columns.

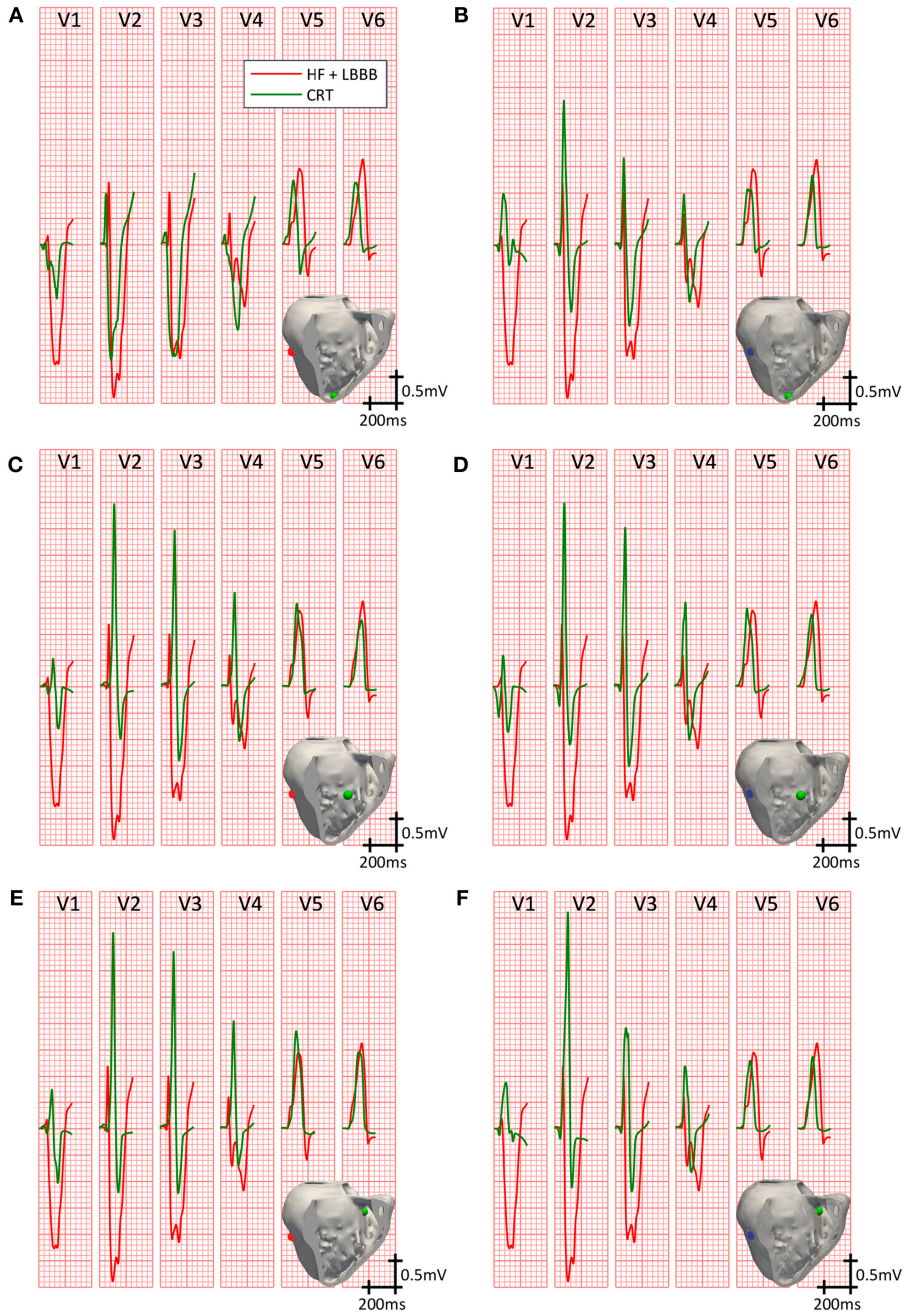

FIGURE 4 | Precordial leads signals on CRT. QRS complexes in the precordial leads under HF + LBBB conditions, before (red trace) and after (green trace) the application of the best CRT configurations (shorter QRSd). Three different locations for the RV pacing lead were tested: RV apex with epicardial **(A)** and endocardial **(B)** LV lead stimulation; RV mid septum with epicardial **(C)** and endocardial **(D)** LV lead stimulation; and RV upper septum with epicardial **(E)** and endocardial **(F)** LV lead stimulation. Stimulation points are shown in light green inside the insets for the RV lead, and in blue and red for the LV endocardial and epicardial lead, respectively.

Firstly, we analyzed the optimal lead placement. The shortest QRSd among all configurations tested was obtained when the RV lead was placed in the upper septum near the outflow track (third row). Furthermore, for all RV lead placement the optimal location of the LV lead, both in the epicardium and endocardium, was the LV mid posterior wall.

Secondly, we analyzed the effect of the delay between pacing leads and intrinsic activation in a fixed location. The best configurations for the RV lead placed in the apex are depicted in the first row. QRSd was reduced from 172 ms (**Figure 4A**) to 157 ms (**Figure 4B**), but bigger reductions were obtained for different intrinsic and pacing delays (AVD = 140 ms, VVD = 0 ms; AVD = 100 ms, VVD = 30 ms, respectively).

When the RV lead was located in the middle of the septum (second row), the QRSd was reduced from 161 ms (**Figure 4C**) to 146 ms (**Figure 4D**) for optimal configurations. In this case, these results were obtained for different pacing delays between leads but the same AVD (AVD = 140 ms and VVD = 30 ms vs. AVD = 140 ms and VVD = 0 ms, respectively).

If the RV lead was placed in the upper septum, the QRSd was reduced from 149 ms (**Figure 4E**) to 143 ms (**Figure 4F**). However, in this case both configurations were achieved with the same intrinsic and biventricular delay (AVD = 140 ms, VVD = 30 ms).

Finally, the influence of LV epicardial vs. endocardial pacing was assessed. QRSd was decreased in all cases after CRT application, but the reduction was greater for LV leads placed in the endocardium (column 2) compared to epicardium (column 1).

Summarizing, the optimal location in terms of shortest QRSd was obtained when the RV lead was placed in the upper septum and the LV lead was located in the mid posterior wall region. Once the optimal lead location was selected for both RV and LV leads, the shortest QRSd was measured for different intrinsic and biventricular delays, without highlighting a particular optimal setting. Finally, the shortest QRSd was obtained in all configurations when the LV lead was placed in the endocardium compared with those in the epicardium.

Ventricular Activation Time During CRT

Another helpful parameter to assess CRT outcome is the total activation time (TAT) of the ventricles. This parameter is not directly accessible in clinical practice during CRT procedures, but simulations can provide additional information to achieve the ideal configuration. Ideally, within normal physiological ranges, the shorter the QRS the shorter TAT, leading to an increase in ventricular synchrony. In **Figure 5**, the percentage of activated ventricular tissue is shown as a function of time for the healthy heart, under HF + LBBB conditions, and for the optimal CRT configurations (as a function of RV location), which are shown in **Figure 4**. Under HF + LBBB conditions (red trace), the electrical impulse spreads throughout the ventricles much slower (gradual slope) than in the healthy heart (black trace) or in CRT (green trace) configurations, completing ventricular activation after 210 ms. For CRT simulations, the rate of activated tissue was initially low, but increased rapidly to reach rates similar to those observed in healthy cases. This was especially noticeable when the LV lead was located in the epicardium (first column) and the RV lead was located in the mid and upper septum (**Figures 4C,E**, respectively). These results can be explained because of several factors. Firstly, the configuration of the PS and the PMJ distribution strongly affects the initial spread of the wavefront. Given the PS RV morphology, i.e., two main branches, one descending to the apex and another growing around the moderator band (**Figure 1D**), when the RV lead was located in the apex, the electrical stimulus entered fast in the PS (around 5 ms) and propagated to remote areas faster than through the myocardium (see **Video 1**, CRT). However, it took around 40 ms to retrogradely enter in the PS when the RV lead was located in the mid septal region, and around 90 ms when the RV lead was in the upper septum. For this reason, it took 75 ms to activate initially only 10% of the myocardium. Secondly, stimulation in the epicardial layer took longer to reach PMJ locations. Thirdly, the stimulation delay between both ventricles (VVD) also affected the initial slope of cardiac activation. Nevertheless, after 70 ms for the endocardial configurations (second column) and 125 ms for the epicardial ones the percentage of activated tissue during CRT application was higher than the percentage of HF + LBBB conditions. Moreover, during the final phase of ventricular activation, the rising rate was considerably reduced. Indeed, the electrical impulse took between 26 and 54 ms (15% to 26% of the TAT) to activate the last 10% of the ventricular tissue.

Finally, after applying the CRT protocol, the TAT was decreased by 15, 14, 12, 15, 19, 22%, with respect to HF + LBBB conditions, as shown in **Figures 5A–F**, respectively. The locations of the pacing leads for the shorter QRS complexes coincided with the locations of the electrodes for the shorter TAT. However, when VVD and AVD were modified, the shortest QRS did not match the shortest TAT, which means that QRSd and TAT are not totally correlated. In addition, the difficulty in QRS measurement at the beginning and end of the signals has to be considered.

In clinical practice, a shorter QRSd is one of the standard criteria used to evaluate CRT response. However, both non-responder and responder patients show a reduction in QRSd after CRT application (Molhoek et al., 2004; Elhakam Elzoghby et al., 2017). Therefore, an additional indicator would be useful for a better perception of CRT benefit. As shown in **Figure 5**, TAT could be strongly modified by the initial rate of activation, as well as by the last activation interval. To avoid this, we analyzed the time elapsed to 90% of ventricular activation (t_{90}), (**Figure 6**). This parameter allows us to determine which configuration leads to a faster activation of most of the ventricular tissue, thus decreasing electrical dyssynchrony.

Figure 6 shows t_{90} values for a configuration with the RV lead placed in the apex, mid septum, and upper septum, and the LV lead located in the epicardium (**Figures 6A–C**), and the same RV configurations with the LV located in the endocardium (**Figures 6D–F**). The different delays applied between the His Bundle and CRT leads (AVD) and between the RV and LV leads (VVD) are shown in columns.

The optimal location of the LV pacing lead, both in the epicardium and endocardium, changed during CRT application for each of the pacing lead locations in the RV. However, the optimal AVD and VVD were the same in all cases, 140 and 0 ms (third column), respectively.

On the one hand, when AVD was modified (column 1 vs. column 3 and column 2 vs. column 4) similar results were obtained, except when the RV lead was located in the upper septum area. The electrical propagation of the intrinsic stimulus contributed to decrease t_{90} (7% reduction) for an AVD of 140 ms. On the other hand, when VVD was increased (column 1 vs. column 2 and column 3 vs. column 4) t_{90} increased up to 19% for all the RV lead locations.

When the RV lead was located in the apex, the optimal location of the LV lead in the epicardium was the LV anterior wall at basal level (**Figure 6A**). For the same RV lead location,

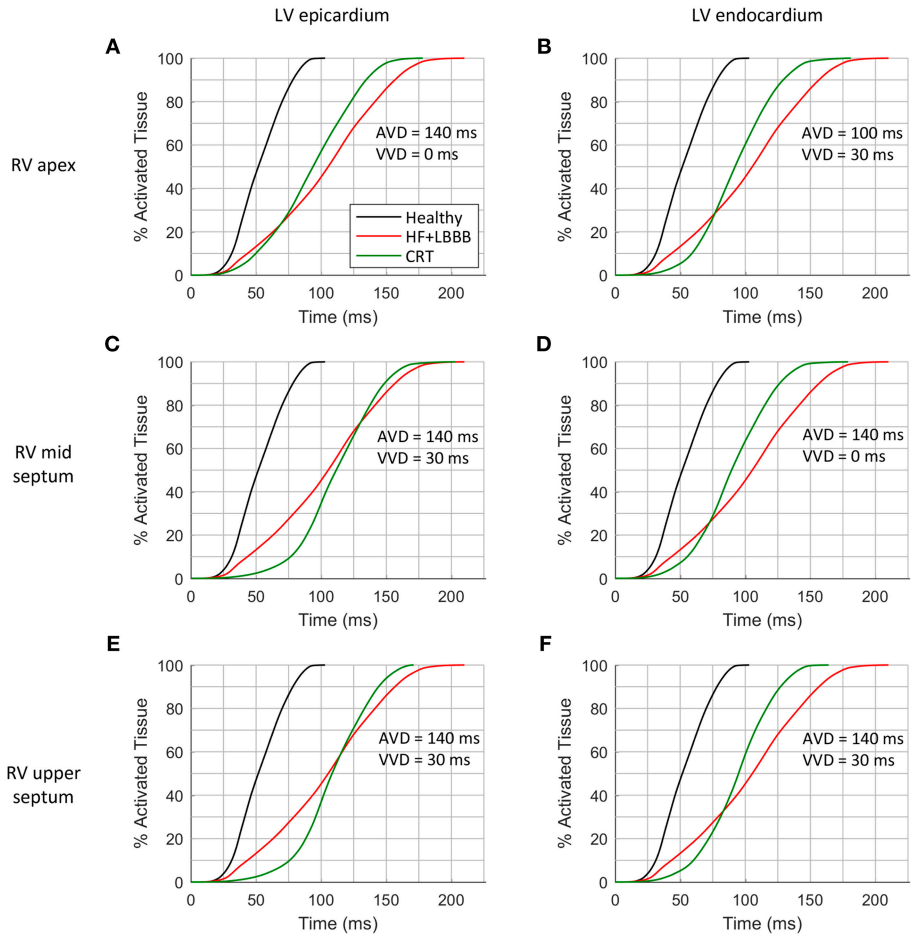

FIGURE 5 | Cumulative frequency histograms of the normalized percentage of activated tissue. The curves correspond to healthy (black), HF + LBBB (red) and CRT (green) scenarios. The best CRT configurations (shortest QRSd) for the three locations of the RV lead were tested: RV apex with epicardial **(A)** and endocardial **(B)** LV lead stimulation; RV mid septum with epicardial **(C)** and endocardial **(D)** LV lead stimulation; and RV upper septum with epicardial **(E)** and endocardial **(F)** LV lead stimulation.

the optimal LV lead location in the endocardium was the LV posterior wall at mid-cavity level (**Figure 6D**). Changing the RV lead location to mid septum, the optimal LV lead location in the epicardium was the LV mid lateral wall, while the optimal LV lead location in the endocardium was the LV mid posterior wall (**Figures 6B,E**, respectively).

Finally, for the RV lead location in the upper septum, the optimal placement of the LV pacing lead in the epicardium was in the LV mid lateral wall, while the optimal placement of the LV lead in the endocardium was the apex of the LV lateral wall (**Figures 6C,F**, respectively). **Table 1** summarizes the optimal placement of the LV lead for a faster activation of 90% of the ventricular tissue. The optimal locations calculated are not in agreement with the optimal RV lead location determined based on a shorter QRSd in most cases. This result suggests the hypothesis that the shortest QRSd does not necessarily imply the fastest ventricular activation of 90% of the ventricular muscle.

Correlation Between Ventricular Activation and QRS

To better highlight the relationship between QRSd and TAT, a correlation analysis was carried out (**Figure 7A**). Results showed an elliptical distribution of data with a moderate positive linear relationship, statistically significant ($R = 0.78$ and $p < 0.05$). This moderate correlation could justify the difference between the optimal AVD and VVD values for the simulations with a shortest QRSd and with a shortest TAT.

A similar correlation analysis was made between area of the QRS (QRSa) and TAT (**Figure 7B**). We first calculated the QRSa for the average signal of the six precordial leads, between the beginning and end values determined during the measurement of the QRSd. The results of the correlation show a scattering distribution of data with a statistically non-significant p-value ($R = -0.12$ and $p = 0.076$). Thus, a linear relationship between QRSa and TAT was not observed in this study.

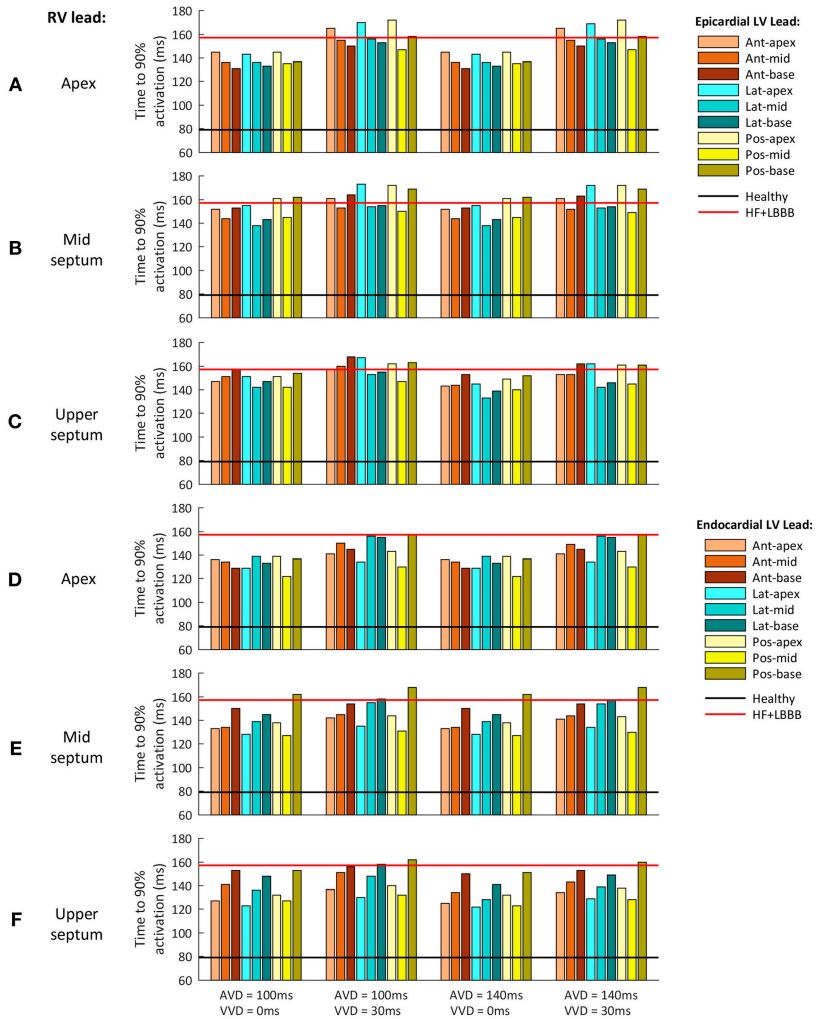

FIGURE 6 | Time to 90% of ventricular activation for the different CRT configuration delays assessed. **(A–C)** Epicardial LV lead stimulation for the three RV lead location tested: **(A)** RV apex, **(B)** RV mid septum and **(C)** RV upper septum. **(D–F)** Endocardial LV lead stimulation for the three RV lead location tested: **(D)** RV apex, **(E)** RV mid septum and **(F)** RV upper septum. The three LV regions (anterior, lateral and posterior walls) are shown in different color brightness (red, blue and yellow). The values for healthy and HF + LBBB configurations are depicted in black and red lines respectively.

Finally, when correlating the curves of percentage of activated tissue and percentage of QRS area as a function of time, a direct relationship between both variables was observed. **Figure 7C** shows the correlation between time to 90% of QRSa (t_{90}QRSa) and time to 90% of the ventricular activation (t_{90}) for each CRT simulations. A significant correlation with a high linear dependence was observed ($R = 0.94$ and $P < 0.05$). Simulations with shorter t_{90}QRSa correspond to the simulations with shorter t_{90}. Therefore, a new biomarker based on time up to 90% of the QRS area can be used as an indicator of electrical synchrony.

DISCUSSION

In this study, biophysical 3D multiscale simulations were conducted to assess alternative locations of the RV lead for a better CRT response in LBBB HF patients. The major findings of this study can be summarized as follows: (i) the optimal leads location based on shortest QRS criterion was the RV upper septum and the LV mid posterior region minimizing also TAT; (ii) for the optimal lead location, the delay configuration leading to the shortest QRSd was AVD = 140 ms, VVD = 30 ms. However, the AVD and VVD setting leading to the shortest TAT was different, suggesting that minimizing QRSd is a good criterion to select leads location but not to select the pacing delay; iii) the time to 90% of the QRS area (t_{90}QRSa) was a good predictor of the instant at which 90% of the ventricular tissue had been activated (t_{90}). This indicator could be used in clinical trials to complement QRSd criterion to select the optimal delay of the pacing leads to obtain a faster ventricular activation of most of the ventricular muscle.

Optimal Lead Location

The location of the optimal pacing site varies significantly between patients, so that a strategy of individualized LV lead placement is required to maximize the benefit of CRT (Derval

TABLE 1 | Optimal placement of the LV lead on CRT.

Criterion	RV lead	LV lead	AVD (ms)	VVD (ms)
LV EPICARDIAL STIMULATION				
Shortest QRS duration	Apex	Posterior - mid	140	0
	Mid septum	Posterior - mid	140	30
	Upper septum	Posterior - mid	140	30
Shortest TAT	Apex	Posterior - mid	140	0
	Mid septum	Posterior - mid	140	0
	Upper septum	Posterior - mid	140	0
Faster activation of 90% of the ventricular tissue	Apex	Anterior - base	140	0
	Mid septum	Lateral - mid	140	0
	Upper septum	Lateral - mid	140	0
LV ENDOCARDIAL STIMULATION				
Shortest QRS duration	Apex	Posterior - mid	100	30
	Mid septum	Posterior - mid	140	0
	Upper septum	Posterior - mid	140	30
Shortest TAT	Apex	Posterior - mid	140	0
	Mid septum	Posterior - mid	140	0
	Upper septum	Posterior - mid	140	0
Faster activation of 90% of the ventricular tissue	Apex	Posterior - mid	140	0
	Mid septum	Posterior - mid	140	0
	Upper septum	Lateral - apex	140	0

TAT, total activation time; AVD, atrioventricular delay; VVD, interventricular delay.

et al., 2010; Spragg et al., 2010). The apex for permanent LV pacing should be avoided, as this location has been associated with poor outcomes in studies such as MADIT-CRT (Yoshikawa et al., 2010; Singh et al., 2011). The experimental study PATH-CHF I suggested that the mid lateral left ventricular site for the LV lead may show greater acute benefit in patients with LBBB (Auricchio et al., 1999). In general, a lateral or posterior vein is the desired location for achieving optimal hemodynamic support as this is usually the site of most delayed activation of the left ventricular wall in patients with LBBB (Stellbrink et al., 2000; Singh et al., 2006).

Our simulation results suggested the upper area of the RV septum as the optimal position for the RV lead, in agreement with some experimental (Muto et al., 2007; Flevari et al., 2009; Cano et al., 2010; Da Costa et al., 2013) and simulation (Miri et al., 2009a) studies. The study of Leclerq and coworkers (Leclercq et al., 2016) demonstrates that septal and apical RV pacing in CRT have a similar clinical outcome and similar LV reverse remodeling after 6 months of therapy. However, other studies (Victor et al., 2006) reported the shortest QRSd for RV septum pacing but not a better CRT response (similar LVEF at 6 months). This highlights the need of additional indicators to determine the optimal placement of the pacing leads.

In the present simulation study the most delayed activation area was located in the anterior basal LV region in the HF + LBBB configuration under intrinsic activation. We also assessed the latest activated area of the LV, when only RV stimulation was applied. If the RV lead was placed in the apex, the anterior basal LV area was activated the latest. However, the LV lateral wall was the latest activated area when the RV lead was located either in the middle or upper septal regions (see **Figure S3**).

The study of Zanon et al. (2014) determined that the LV lead location in the latest activated site was predictive of the maximum increase in contractility (LV dP/dt_{max}). On the other hand, in the recent study of Sipal and coworkers (Sipal et al., 2018), comparing the clinical benefits of LV lead implantation guided by the shortest BiV-paced QRSd using surface ECG and with the standard unguided CRT, there was a significantly higher rate (85 vs. 50%, $p = 0.02$) of response (>15% reduction in LV end-systolic volume) to CRT as well as a shorter QRSd ($p < 0.001$) and a greater QRS shortening for the surface ECG guided group. Furthermore, the optimal site for LV lead placement was the posterior and posterolateral region, in agreement with our simulations. For all RV lead locations tested in our study, when the LV lead was placed in the latest activated area of the LV, none of those configurations led to the shortest QRSd.

In our study, we also showed that when pacing in the latest electrically activated area of the LV, that area did not provide the shortest TAT. Similar results were observed in the simulation study by Pluijmert et al. (2016). In that work, the authors found that the LV pacing region that provided the maximum acute hemodynamic response, located near the latest activated area, did not lead to the largest reduction of TAT during biventricular stimulation. Even stimulating regions leading to the largest reduction of TAT showed poor increase of hemodynamic response. However, other studies have found a positive correlation between acute hemodynamic response and TAT reduction (Crozier et al., 2016). The optimal method to place the LV pacing lead is thus object of controversy: while several studies support that pacing in the latest activated area leads to better hemodynamic response, others consider the criterion of maximal reduction in QRSd as the best choice.

Optimal Delay Between Pacing Leads

Optimization of AVD and VVD is crucial during CRT application. A longer inter-lead electrical delay was associated with more pronounced LV reverse remodeling in CRT patients with a presumed optimal LV lead position concordant or adjacent to the latest mechanically activated non-scarred segment (Sommer et al., 2018).

In clinical practice this value should be specifically set for each patient, although optimization is rarely performed in the real practice. The largest trials studying CRT used various methods to optimize these intervals, most frequently based on echocardiography and intracardiac electrogram interval measurement, but unequivocal proof of the benefit brought by optimization is still lacking (Abraham et al., 2010; Krum et al., 2012; Brugada et al., 2014). Echocardiography presents inherent variability of results and is highly operator dependent (Gras et al., 2009). Optimization based on intracardiac electrogram intervals has not proved yet to be of clear benefit above arbitrary AV interval (Ulč and Vančura, 2013). Multisite pacing has shown favorable results, although it is technically complex (Cazeau et al., 2001). A less time-consuming and easier optimization method

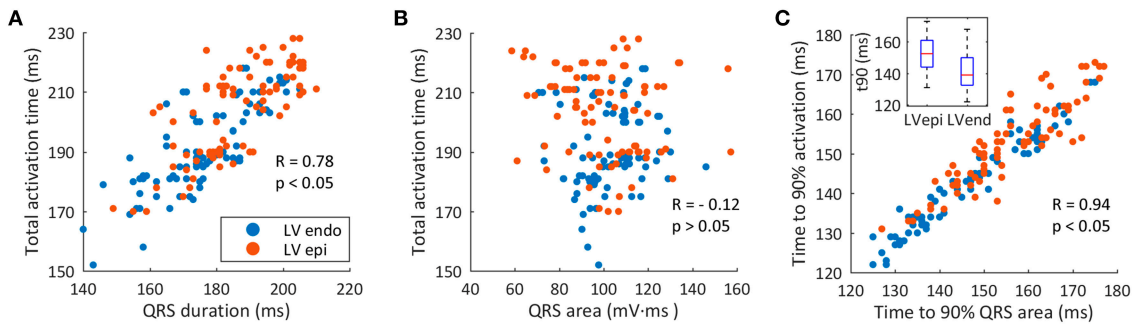

FIGURE 7 | Correlation between ventricular activation and QRS. **(A)** Correlation between QRS duration and TAT (red circles show LV epicardial leads, blue circles show LV endocardial leads). **(B)** Correlation between the QRS area and TAT. **(C)** Correlation between t_{90}QRSa and t_{90}.

might enable a more systematic optimization of the AVD and VVD at routine follow-up visits in all recipients of CRT systems.

The morphology of the PS clearly determined in our study the influence of AVD. When the RV lead was placed in the apex, the intrinsic activation of the His bundle found the majority of the Purkinje network already depolarized via retrograde conduction. However, if the RV lead was placed in the middle septum or closer to the outflow tract, further from any possible entrance to the cardiac conduction system, the intrinsic depolarization wavefront spread faster to the myocardium than the wavefront generated through the CRT leads, leading to a reduction in TAT. Some experimental studies (Prinzen and Peschar, 2002) support the idea that PS may not allow retrograde conduction in LBBB patients due to structural damage, or if allowed, reduced conduction velocity would be observed in LV PS sections, neglecting the influence of PS. Whether the rest of the LV branches are able to conduct retrogradely (Huang et al., 2017) or other areas of the Purkinje network deteriorate, as HF evolves, remains unknown. Experimental studies have measured a strong reduction in septal conduction velocity during LBBB when HF was advanced compare to acute LBBB (Strik et al., 2013). In that case, the simulation results of this study should be considered with caution. Although new methodologies are arising to better describe the PS (Lee et al., 2014; Barber et al., 2018). The lack of technology to characterize the PS in a patient specific manner, limits the optimal configuration for CRT.

Traditional CRT pacing mode does not promote ventricular activation through conduction system from the sinoatrial node. The lack of enough information on the chronic effects of the fusion leads (intrinsic stimulation combined with external pacing) and this method is avoided, setting the shortest AVD based on echocardiography (Barold et al., 2008). In our study, a fusion between the intrinsic activation and biventricular (BiV) pacing for the optimal CRT configuration (pacing lead location and delays) was assessed. Several experimental works support this procedure (Van Gelder et al., 2005; Vatasescu et al., 2009; Arbelo et al., 2014; Guo et al., 2015). Guo et al. determined that congestive heart failure patients with BiV pacing + intrinsic activation presented improvement in cardiac function and quality of life (Guo et al., 2015). Meanwhile, Vatasescu and coworkers observed that BiV pacing fused with intrinsic activation might increase the rate of structural responders (Vatasescu et al., 2009).

Biophysical models of the heart have been used to optimize AVD, VVD and lead location during CRT simulation (Miri et al., 2008, 2009a,b; Pluijmert et al., 2016; Lee et al., 2017). QRSd, estimated as the difference between the time of the first and last activated cardiac cell (or TAT), have been used as one optimization criterion by Miri and coworkers. In our study, the optimal LV lead location based on the shortest QRSd (calculated in the ECG signal) was similar to the region with shortest TAT (see **Table 1**). However, VVD value that produced the shortest QRSd did not match with the VVD that produced the shortest TAT, which means that QRSd and TAT are not totally correlated. A simulation study by Potse et al. (2012) support this result. The authors observed that biventricular pacing did not change QRS duration but reduced total ventricular activation time when the LV stimulation was applied in one point of the LV free wall.

Indicators to Evaluate CRT Outcome

The Echocardiography Guided Cardiac Resynchronization Therapy (EchoCRT) study further reinforced the importance of QRSd over mechanical dyssynchrony as the most important indicator for CRT responses (Ruschitzka et al., 2013). Other studies have proposed indexes based on QRS measurements. Van Gelder et al. (2009) showed a relation between the Q-LV interval (the interval from Q wave to intrinsic deflection on the LV EGM) and the acute hemodynamic effect on optimized biventricular stimulation. A longer Q-LV interval predicted a greater increase in LV pressure rise ($LVdP/dt_{max}$) and vice versa. Normalizing the QLV by QRS duration, termed LV lead electrical delay (LVLED), was also shown to correlate with Doppler-derived dP/dt values. LVLED greater than or equal to 50 % was associated with significantly greater reductions in all-cause death or HF hospitalization at 12 months of follow-up in patients with non-ischemic cardiomyopathy (Singh et al., 2006).

Our simulations show that the difference in QRSd was significant when the LV was paced in different sites and for a fixed placement of RV. However, these differences in QRSd were decreased when adjusting the delay between leads in a fixed location for both leads (see **Table S1**). Thus, the shortest QRSd predicted precisely the region in the LV subdomains that

produced the shortest TAT for the three locations of the RV lead tested, leading to an increase in ventricular synchrony. However, this index could not determine the pacing delay configuration between leads that allows to obtain the shortest TAT. There is no consensus on how QRS should be accurately measured, and therefore small differences are expected between methods (De Pooter et al., 2016). In our study, the optimal QRSd obtained after CRT application supposed a 20% reduction of the QRSd. This result is in agreement with the study of Elhakam Elzoghby et al. (2017), where 180 patients under heart failure conditions and LBBB were studied, and similar reductions were obtained. Other studies obtained lower QRS reduction values, namely 17 and 12%, for CRT responders in Molhoek et al. (2004) and Pitzalis et al. (2002) studies, respectively.

The assessment of interventricular dyssynchrony was done analyzing the TAT. Our results showed that a shorter duration of the QRS complex is moderately correlated with a shorter TAT (**Figure 7A**). The narrowest QRS complex predicted the optimal location of the stimulation leads but not the optimal value of the VVD. In this way, the t_{90} index selected correctly the best delay configuration to provide the fastest activation of the majority of the heart. In several configurations, TAT value was exactly the same (see **Table S2**), but t_{90} discerned the shortest order of activation. Thus, the shortest QRSd predicted the location for the optimal leads placement, but t_{90} predicted the best pacing delay with the shortest TAT. We hypothesized that setting the pacing delay properly with this new index could improve CRT non-responders rate.

Other simulation studies have assessed the evolution of TAT during CRT (Romero et al., 2010; Potse et al., 2012) focused on the assessment of the LV intraventricular delay. The recent study of Tomassoni (2016) showed how CRT response assessment is highly variable depending on the criteria used to define the response. QRS width has been shown to correlate well with interventricular dyssynchrony but unfortunately this has poor accuracy for detecting intraventricular dyssynchrony. As a result, it is estimated that only 70% of patients with LBBB have echocardiographic evidence of mechanical dyssynchrony (Bleeker et al., 2004). The role of mechanical dyssynchrony for improving patient selection for CRT remains controversial. The multicenter, nonrandomized Predictors of Response to CRT (PROSPECT) study evaluated the ability of 12 echocardiographic indices of dyssynchrony to predict CRT responses at 6 months (Chung et al., 2008). These indices provided only modest sensitivity and specificity, and researchers reported large variability in quantification of dyssynchrony. Mechanical dyssynchrony has also been used to select CRT candidates with a narrow QRS duration $\leq$ 120 ms, with limited success in randomized multicenter studies. In this line, mechanical response generated by electrical excitation (excitation-contraction coupling) could be different depending on the heart region (Gurev et al., 2010). Multiple simulation studies have addressed CRT from different perspectives. The recent work of Lee et al. (2018) organized and summarized the state of the art of computational modeling for CRT.

To our knowledge, and given the benefits of using a model where all variables are accessible, our study is the first to systematically explore the correlation between the activated portion of tissue (less accessible in clinical practice) and the QRS complex in the torso surface. Thus, we found that an index based on time to 90% of the QRS area (t_{90}QRSa) is a good predictor of the instant at which 90% of the ventricular tissue has been activated (t_{90}). This indicator could be used in clinical trials to complement QRSd measurements in defining the optimal location and delay of the pacing leads to produce faster ventricular activation of most of the ventricular muscle.

Epicardial vs. Endocardial Pacing

Although LV epicardial stimulation decreased QRS width in most cases, a greater reduction was observed for endocardial pacing. The study conducted by Spragg et al. (2010) showed that CRT administered at the optimal site of the LV endocardium was more effective than stimulation through an electrode in the coronary sinus. There is evidence to suggest that endocardial stimulation yields to more natural transmural activation patterns and a better response for CRT patients (Prinzen et al., 2009; Bordachar et al., 2010; Behar et al., 2016). In this line, new devices that allow endocardial pacing and single lead stimulation (Sperzel et al., 2015) coordinated with intrinsic activation will provide new possibilities.

The better results obtained with endocardial pacing are strongly influenced by PS. As PMJs are located in the endocardial surface, the wavefront generated for the LV lead gets into the Purkinje conduction system retrogradely and spreads faster to other inactivated areas (see **Video 2**, RETROGRADE). Thus, knowing the distribution and location of PMJ, as well as the conduction system morphology is a determinant factor for CRT improvement.

Limitations

CRT was analyzed only from an electrical point of view in our study. Mechanical behavior based on echocardiography is a common alternative to assess hemodynamic response, although this method is time-consuming and the optimal measurements remain unclear. Simulation studies including the mechanical behavior would be certainly enlightening.

In this study, a particular heart geometry and PS were assessed. The inclusion or not of the moderator band (which may be very patient-specific) may affect QRSd and TAT measurements, especially when pacing on the RV upper septal area. Although our results have been compared to other related studies, the specific findings observed in this study should be carefully validated against clinical studies and complemented with a set of computational models of different patients. In addition, two isolated stimuli were employed to assess CRT efficiency. The development of strategies that allow multi-site pacing should be taken into account in future studies. Additionally, the incorporation of levels of HF in different ventricular areas could modify simulation results.

CONCLUSION

In conclusion, our study showed that the optimal location for the RV lead in CRT site as an alternative to RV apex, is the upper septum close to the outflow tract, based on the shortest QRSd criterion. Furthermore, LV endocardial pacing leads improve CRT outcome, with respect to epicardial stimulation, and areas with a higher density of PMJ are suggested for better CRT response.

CRT optimization based only on the shortest QRSd criterion may not be totally effective to reach the maximum TAT reduction, or to optimize biventricular pacing delay. However, a biomarker based on minimizing the value of t_{90} (time elapsed to 90% of ventricular activation) could be used to determine the optimal VVD value. The time to reach the 90% of the QRS area (t_{90}QRSa) is related to the time at which 90% of the ventricles are already activated (t_{90}). Thus, t_{90}QRSa is suggested as an additional index to assess CRT effectiveness to improve biventricular synchrony.

AUTHOR CONTRIBUTIONS

EFC, EC, JA, JF, and BT contributed to the conception and design of study. AL-P created the anatomical model and Purkinje system was developed by RS and JG. Computational simulations were performed by EFC and JG. The analysis/interpretation of results was performed by EFC, JG, RS, and BT. All authors contributed to draft the manuscript and all authors revised and approved the submitted version.

FUNDING

This work was supported by the Secretaría de Educación Superior, Ciencia, Tecnología e Innovación (SENESCYT) of Ecuador CIBAE-023-2014, the Plan Estatal de Investigación Científica y Técnica y de Innovación 2013–2016 from the Ministerio de Economía, Industria y Competitividad of Spain and Fondo Europeo de Desarrollo Regional (FEDER) DPI2016-75799-R (AEI/FEDER, UE), and by Dirección General de Política Científica de la Generalitat Valenciana (PROMETEU 2016/088).

SUPPLEMENTARY MATERIAL

The Supplementary Material for this article can be found online at: https://www.frontiersin.org/articles/10.3389/fphys.2019.00074/full#supplementary-material

REFERENCES

Abraham, W. T., Fisher, W. G., Smith, A. L., Delurgio, D. B., Leon, A. R., Loh, E., et al. (2002). Cardiac resynchronization in chronic heart failure. *N. Engl. J. Med.* 346, 1845–1853. doi: 10.1056/NEJMoa013168

Abraham, W. T., Gras, D., Yu, C. M., Guzzo, L., and Gupta, M. S. (2010). Rationale and design of a randomized clinical trial to assess the safety and efficacy of frequent optimization of cardiac resynchronization therapy: the Frequent Optimization Study Using the QuickOpt Method (FREEDOM) trial. *Am. Heart J.* 159, 944–948.e1. doi: 10.1016/j.ahj.2010.02.034

Ai, X., and Pogwizd, S. M. (2005). Connexin 43 downregulation and dephosphorylation in nonischemic heart failure is associated with enhanced colocalized protein phosphatase type 2A. *Circ. Res.* 96, 54–63 doi: 10.1161/01.RES.0000152325.07495.5a

Akar, F. G., Nass, R. D., Hahn, S., Cingolani, E., Shah, M., Hesketh, G. G., et al. (2007). Dynamic changes in conduction velocity and gap junction properties during development of pacing-induced heart failure. *Am. J. Physiol. Hear. Circ. Physiol.* 293, H1223–H1230. doi: 10.1152/ajpheart.00079.2007

Arbelo, E., Jos', J., Josémar', J., Tolosana, J., Penela, D., Borr'as, R., et al. (2014). Cardiac resynchronization therapy, electrocardiogram, fusion, optimization. *J. Cardiovasc. Electrophysiol.* 25, 283–292. doi: 10.1111/jce.12322

Auricchio, A., Fantoni, C., Regoli, F., Carbucicchio, C., Goette, A., Geller, C., et al. (2004). Characterization of left ventricular activation in patients with heart failure and left bundle-branch block. *Circulation* 109, 1133–1139. doi: 10.1161/01.CIR.0000118502.91105.F6

Auricchio, A., Klein, H., Tockman, B., Sack, S., Stellbrink, C., Neuzner, J., et al. (1999). Transvenous biventricular pacing for heart failure: can the obstacles be overcome. *Am. J. Cardiol.* 83, 136D−142D. doi: 10.1016/S0002-9149(98)01015-7

Barber, F., García-Fernández, I., Lozano, M., and Sebastian, R. (2018). Automatic estimation of Purkinje-Myocardial junction hot-spots from noisy endocardial samples: a simulation study. *Int. J. Numer. Method. Biomed. Eng.* 34, 1–15. doi: 10.1002/cnm.2988

Barold, S. S., Ilercil, A., and Herweg, B. (2008). Echocardiographic optimization of the atrioventricular and interventricular intervals during cardiac resynchronization. *Europace* 10 (Suppl. 3), iii88–iii95. doi: 10.1093/europace/eun220

Behar, J. M., Jackson, T., Hyde, E., Claridge, S., Gill, J., Bostock, J., et al. (2016). optimized left ventricular endocardial stimulation is superior to optimized epicardial stimulation in ischemic patients with poor response to cardiac resynchronization therapy: a combined magnetic resonance imaging, electroanatomic contact mapping, and hemodynamic study to target endocardial lead placement. *JACC Clin. Electrophysiol.* 2, 799–809. doi: 10.1016/j.jacep.2016.04.006.

Bertaglia, E., Migliore, F., Baritussio, A., De Simone, A., Reggiani, A., Pecora, D., et al. (2017). Stricter criteria for left bundle branch block diagnosis do not improve response to CRT. *PACE - Pacing Clin. Electrophysiol.* 40, 850–856. doi: 10.1111/pace.13104

Bertini, M., Ziacchi, M., Biffi, M., Martignani, C., Saporito, D., Valzania, C., et al. (2008). Interventricular delay interval optimization in cardiac resynchronization therapy guided by echocardiography versus guided by electrocardiographic QRS interval width. *Am. J. Cardiol.* 102, 1373–1377. doi: 10.1016/j.amjcard.2008.07.015

Bleeker, G. B., Schalij, M. J., Molhoek, S. G., Verwey, H. F., Holman, E. R., Boersma, E., et al. (2004). Relationship between QRS duration and left ventricular dyssynchrony in patients with end-stage heart failure. *J. Cardiovasc. Electrophysiol.* 102, 1373–1377. 15, 544–549. doi: 10.1046/j.1540-8167.2004.03604.x

Bonakdar, H. R., Jorat, M. V., Fazelifar, A. F., Alizadeh, A., Givtaj, N., Sameie, N., et al. (2009). Prediction of response to cardiac resynchronization therapy using simple electrocardiographic and echocardiographic tools. *Europace* 11, 1330–1337. doi: 10.1093/europace/eup258

Bordachar, P., Derval, N., Ploux, S., Garrigue, S., Ritter, P., Haissaguerre, M., et al. (2010). Left ventricular endocardial stimulation for severe heart failure. *J. Am. Coll. Cardiol.* 56, 747–753. doi: 10.1016/j.jacc.2010.04.038

Boukens, B. J., Rivaud, M. R., Rentschler, S., and Coronel, R. (2014). Misinterpretation of the mouse ECG: "Musing the waves of Mus musculus." *J. Physiol.* 592, 4613–26. doi: 10.1113/jphysiol.2014.279380

Bradley, C. P., Pullan, A. J., and Hunter, P. J. (1997). Geometric modeling of the human torso using cubic hermite elements. *Ann. Biomed. Eng.* 25, 96–11. doi: 10.1007/BF02738542

Brignole, M., Auricchio, A., Baron-Esquivias, G., Bordachar, P., Boriani, G., Breithardt, O.-A., et al. (2013). 2013 ESC Guidelines on cardiac pacing and cardiac resynchronization therapy: the task force on cardiac pacing and resynchronization therapy of the European Society of Cardiology (ESC). Developed in collaboration with the european heart rhythm association. *Eur. Heart J.* 34, 2281–2329. doi: 10.1093/eurheartj/eht150

Brugada, J., Brachmann, J., Delnoy, P. P., Padeletti, L., Reynolds, D., Ritter, P., et al. (2014). Automatic optimization of cardiac resynchronization therapy using SonR - rationale and design of the clinical trial of the sonrtip lead and automatic AV-VV optimization algorithm in the paradym RF SonR CRT-D (RESPOND CRT) trial. *Am. Heart J.* 167, 429–436. doi: 10.1016/j.ahj.2013.12.007

Cano, O., Osca, J., Sancho-Tello, M. J., Sánchez, J. M., Ortiz, V., Castro, J. E., et al. (2010). Comparison of effectiveness of right ventricular septal pacing versus right ventricular apical pacing. *Am. J. Cardiol.* 105, 1426–1432. doi: 10.1016/j.amjcard.2010.01.004

Cazeau, S., Leclercq, C., Lavergne, T., Walker, S., Varma, C., Linde, C., et al. (2001). Effects of multisite biventricular pacing in patients with heart failure and intraventricular conduction delay. *N. Engl. J. Med.* 344, 873–880. doi: 10.1056/NEJM200103223441202

Chung, E. S., Leon, A. R., Tavazzi, L., Sun, J. P., Nihoyannopoulos, P., Merlino, J., et al. (2008). Results of the predictors of response to crt (prospect) trial. *Circulation* 117, 2608–2616. doi: 10.1161/CIRCULATIONAHA.107.743120

Cleland, J. G. F., Daubert, J.-C., Erdmann, E., Freemantle, N., Gras, D., Kappenberger, L., et al. (2005). *The Effect of Cardiac Resynchronization on Morbidity and Mortality in Heart Failure*. Available online at: www.nejm

Coppola, G., Ciaramitaro, G., Stabile, G., DOnofrio, A., Palmisano, P., Carità, P., et al. (2016). Magnitude of QRS duration reduction after biventricular pacing identifies responders to cardiac resynchronization therapy. *Int. J. Cardiol.* 221, 450–455. doi: 10.1016/j.ijcard.2016.06.203

Coronel, R., Wilders, R., Verkerk, A. O., Wiegerinck, R. F., Benoist, D., and Bernus, O. (2013). Electrophysiological changes in heart failure and their implications for arrhythmogenesis. *Biochim. Biophys. Acta* 1832, 2432–2441. doi: 10.1016/j.bbadis.2013.04.002

Crozier, A., Blazevic, B., Lamata, P., Plank, G., Ginks, M., Duckett, S., et al. (2016). The relative role of patient physiology and device optimisation in cardiac resynchronisation therapy: a computational modelling study. *J. Mol. Cell. Cardiol.* 96, 93–100. doi: 10.1016/j.yjmcc.2015.10.026

Da Costa, A., Gabriel, L., Romeyer-Bouchard, C., Géraldine, B., Gate-Martinet, A., Laurence, B., et al. (2013). Focus on right ventricular outflow tract septal pacing. *Arch. Cardiovasc. Dis.* 106, 394–403. doi: 10.1016/j.acvd.2012.08.005

De Pooter, J., El Haddad, M., Timmers, L., Van Heuverswyn, F., Jordaens, L., Duytschaever, M., et al. (2016). Different methods to measure QRS duration in CRT patients: impact on the predictive value of QRS duration parameters. *Ann. Noninvasive Electrocardiol.* 21, 305–315. doi: 10.1111/anec.12313

Derval, N., Steendijk, P., Gula, L. J., Deplagne, A., Laborderie, J., Sacher, F., et al. (2010). Optimizing hemodynamics in heart failure patients by systematic screening of left ventricular pacing sites. The lateral left ventricular wall and the coronary sinus are rarely the best sites. *J. Am. Coll. Cardiol.* 55, 566–575. doi: 10.1016/j.jacc.2009.08.045

Desk, R., Williams, L., and Health, K. (1998). *Characteristics and Distribution of M Cells in Arterially*. Available online at: http://ahajournals.org

Dou, J., Xia, L., Deng, D., Zang, Y., Shou, G., Bustos, C., et al. (2012). A study of mechanical optimization strategy for cardiac resynchronization therapy based on an electromechanical model. *Comput. Math. Methods Med.* 2012:948781. doi: 10.1155/2012/948781

Durrer, D., van Dam, R. T., Freud, G. E., Janse, M. J., Meijler, F. L., and Arzbaecher, R. C. (1970). Total excitation of the isolated human heart. *Circulation* 41, 899–912. doi: 10.1161/01.CIR.41.6.899

Dutta, S., Mincholé, A., Quinn, T. A., and Rodriguez, B. (2017). Electrophysiological properties of computational human ventricular cell action potential models under acute ischemic conditions. *Prog. Biophys. Mol. Biol.* 129, 40–52. doi: 10.1016/j.pbiomolbio.2017.02.007

Dux-santoy, L., Rodriguez, J. F., Sebastian, R., Saiz, J., Ferrero, J. M., Val, D., et al. (2012). "Biophysical modelling of bundle branch reentry initiation and maintenance," in *2012 Computing in Cardiology* (Krakow), 221–224.

Elhakam Elzoghby, I. A., Attia, I., Azab, A., Hammouda, M. E. A. (2017). Impact of cardiac resynchronization therapy on heart failure patients: experience from one center. *Arch. Med.* 9, 1–7. doi: 10.21767/1989-5216.1000232

Ferrer, A., Sebastián, R., Sánchez-Quintana, D., Rodríguez, J. F., Godoy, E. J., Martínez, L., et al. (2015). Detailed anatomical and electrophysiological models of human atria and torso for the simulation of atrial activation. *PLoS ONE* 10:e0141573. doi: 10.1371/journal.pone.0141573

Flevari, P., Leftheriotis, D., Fountoulaki, K., Panou, F., Rigopoulos, A. G., Paraskevaidis, I., et al. (2009). Long-term nonoutflow septal versus apical right ventricular pacing: Relation to left ventricular dyssynchrony. *PACE - Pacing Clin. Electrophysiol.* 32, 354–362. doi: 10.1111/j.1540-8159.2008.02244.x

Gras, D., Gupta, M. S., Boulogne, E., Guzzo, L., and Abraham, W. T. (2009). Optimization of AV and VV delays in the real-world CRT patient population: an international survey on current clinical practice. *PACE - Pacing Clin. Electrophysiol.* 32 (Suppl. 1), S236–S239. doi: 10.1111/j.1540-8159.2008.02294.x

Greenbaum, R. A., Ho, S. Y., Gibson, D. G., Becker, A. E., and Anderson, R. H. (1981). Left ventricular fibre architecture in man. *Heart* 45, 248–263. doi: 10.1136/hrt.45.3.248

Guo, T., Li, R., Zhang, L., Luo, Z., Zhao, L., Yang, J., et al. (2015). Biventricular pacing with ventricular fusion by intrinsic activation in cardiac resynchronization therapy. *Int. Heart J.* 56, 293–297. doi: 10.1536/ihj.14-260

Gurev, V., Constantino, J., Rice, J. J., and Trayanova, N. A. (2010). Distribution of electromechanical delay in the heart: insights from a three-dimensional electromechanical model. *Biophys. J.* 99, 745–754. doi: 10.1016/j.bpj.2010.05.028

Heidenreich, E. A, Ferrero, J. M., Doblaré, M., and Rodríguez, J. F. (2010). Adaptive macro finite elements for the numerical solution of monodomain equations in cardiac electrophysiology. *Ann. Biomed. Eng.* 38, 2331–2345. doi: 10.1007/s10439-010-9997-2

Huang, W., Su, L., Wu, S., Xu, L., and Xiao, F. (2017). Case report a novel pacing strategy with low and stable output : pacing the left bundle branch immediately beyond the conduction block. *Can. J. Cardiol.* 33, 1736.e1–1736.e3. doi: 10.1016/j.cjca.2017.09.013

Keller, D. U., Weber, F. M., Seemann, G., and Dössel, O. (2010). Ranking the influence of tissue conductivities on forward-calculated ecgs. *IEEE Trans. Biomed. Eng.* 57, 1568–1576. doi: 10.1109/TBME.2010.2046485

Krum, H., Lemke, B., Birnie, D., Lee, K. L. F., Aonuma, K., Starling, R. C., et al. (2012). A novel algorithm for individualized cardiac resynchronization therapy: rationale and design of the adaptive cardiac resynchronization therapy trial. *Am. Heart J.* 163, 747–752.e1. doi: 10.1016/j.ahj.2012.02.007

Leclercq, C., Sadoul, N., Mont, L., Defaye, P., Osca, J., Mouton, E., et al. (2016). Comparison of right ventricular septal pacing and right ventricular apical pacing in patients receiving cardiac resynchronization therapy defibrillators: the SEPTAL CRT study. *Eur. Heart J.* 37, 473–483. doi: 10.1093/eurheartj/ehv422

Lee, A. W., Crozier, A., Hyde, E. R., Lamata, P., Truong, M., Sohal, M., et al. (2017). Biophysical modeling to determine the optimization of left ventricular pacing site and AV/VV delays in the acute and chronic phase of cardiac resynchronization therapy. *J. Cardiovasc. Electrophysiol.* 28, 208–215. doi: 10.1111/jce.13134

Lee, A. W. C., Costa, C. M., Strocchi, M., Rinaldi, C. A., and Niederer, S. A. (2018). Computational modeling for cardiac resynchronization therapy. *J. Cardiovasc. Transl. Res.* 11, 92–108. doi: 10.1007/s12265-017-9779-4

Lee, H., Park, J. H., Seo, I., Park, S. H., and Kim, S. (2014). Improved application of the electrophoretic tissue clearing technology, CLARITY, to intact solid organs including brain, pancreas, liver, kidney, lung, and intestine. *BMC Dev. Biol.* 14:48. doi: 10.1186/s12861-014-0048-3

Linde, C., Ellenbogen, K., and McAlister, F. A. (2012). Cardiac resynchronization therapy (CRT): Clinical trials, guidelines, and target populations. *Hear. Rhythm.* 9(8 Suppl), S3–S13. doi: 10.1016/j.hrthm.2012.04.026

Lopez-Perez, A., Sebastian, R., and Ferrero, J. M. (2015). Three-dimensional cardiac computational modelling: methods, features and applications. *Biomed. Eng. Online* 14:35. doi: 10.1186/s12938-015-0033-5

MacLeod, R. S., Johnson, C. R., and Ershler, P. R. (1991). Construction of an inhomogeneous model of the human torso for use in computational electrocardiography. *Proc. Annu. Conf. Eng. Med. Biol.* 13, 688–689.

Mafi Rad, M., Blaauw, Y., Dinh, T., Pison, L., Crijns, H. J., Prinzen, F. W., et al. (2014). Different regions of latest electrical activation during left bundle-branch block and right ventricular pacing in cardiac resynchronization therapy patients determined by coronary venous electro-anatomic mapping. *Eur. J. Heart Fail.* 16, 1214–1222. doi: 10.1002/ejhf.178

Miri, R., Graf, I. M., and DÖssel, O. (2009a). Efficiency of timing delays and electrode positions in optimization of biventricular pacing: a simulation study. *IEEE Trans. Biomed. Eng.* 56, 2573–2582. doi: 10.1109/TBME.2009.2027692

Miri, R., Reumann, M., Farina, D., and Dössel, O. (2009b). Concurrent optimization of timing delays and electrode positioning in biventricular pacing based on a computer heart model assuming 17 left ventricular segments. *Biomed. Tech.* 54, 55–65. doi: 10.1515/BMT.2009.013

Miri, R., Reumann, M., Keller, D. U. J., Farina, D., and Dossel, O. (2008). "Comparison of the electrophysiologically based optimization methods with different pacing parameters in patient undergoing resynchronization treatment," in *2008 30th Annual International Conference of the IEEE Engineering in Medicine and Biology Society* (Vancouver, BC).

Molhoek, S. G., VAN Erven, L., Bootsma, M., Steendijk, P., Van Der Wall, E. E., et al. (2004). QRS duration and shortening to predict clinical response to cardiac resynchronization therapy in patients with end-stage heart failure. *Pacing Clin. Electrophysiol.* 27, 308–313. doi: 10.1111/j.1540-8159.2004.00433.x

Mora, M. T., Ferrero, J. M., Romero, L., and Trenor, B. (2017). Sensitivity analysis revealing the effect of modulating ionic mechanisms on calcium dynamics in simulated human heart failure. *PLoS ONE* 12:e0187739. doi: 10.1371/journal.pone.0187739

Muto, C., Ottaviano, L., Canciello, M., Carreras, G., Calvanese, R., Ascione, L., et al. (2007). Effect of pacing the right ventricular mid-septum tract in patients with permanent atrial fibrillation and low ejection fraction. *J. Cardiovasc. Electrophysiol.* 18, 1032–1036. doi: 10.1111/j.1540-8167.2007.00914.x

O'Hara, T., Virág, L., Varró, A., and Rudy, Y. (2011). Simulation of the undiseased human cardiac ventricular action potential: model formulation and experimental validation. *PLoS Comput. Biol.* 7:e1002061. doi: 10.1371/journal.pcbi.1002061

Passini, E., Mincholé, A., Coppini, R., Cerbai, E., Rodriguez, B., Severi, S., et al. (2016). Mechanisms of pro-arrhythmic abnormalities in ventricular repolarisation and anti-arrhythmic therapies in human hypertrophic cardiomyopathy. *J. Mol. Cell. Cardiol.* 96, 72–81. doi: 10.1016/j.yjmcc.2015.09.003

Pastore, G., Zanon, F., Baracca, E., Rigatelli, G., Corbucci, G., Mazza, A., et al. (2013). How can we identify the optimal pacing site in the right ventricular septum? A simplified method applicable during the standard implanting procedure. *Am. J. Cardiovasc. Dis.* 3, 264–272.

Pitzalis, M. V., Iacoviello, M., Romito, R., Massari, F., Rizzon, B., Luzzi, G., et al. (2002). Cardiac resynchronization therapy tailored by echocardiographic evaluation of ventricular asynchrony. *J. Am. Coll. Cardiol.* 40, 1615–1622. doi: 10.1016/S0735-1097(02)02337-9

Pluijmert, M., Bovendeerd, P. H. M., Lumens, J., Vernooy, K., Prinzen, F. W., and Delhaas, T. (2016). New insights from a computational model on the relation between pacing site and CRT response. *Europace* 18, iv94–iv103. doi: 10.1093/europace/euw355

Potse, M., Dubé, B., Richer, J., Vinet, A., and Gulrajani, R. M. (2006). A comparison of monodomain and bidomain reaction-diffusion models for action potential propagation in the human heart. *IEEE Trans. Biomed. Eng.* 53(12 Pt. 1), 2425–2435. doi: 10.1109/TBME.2006.880875

Potse, M., Krause, D., Bacharova, L., Krause, R., Prinzen, F. W., and Auricchio, A. (2012). Similarities and differences between electrocardiogram signs of left bundle-branch block and left-ventricular uncoupling. *Europace* 14(Suppl. 5), v33–v39. doi: 10.1093/europace/eus272

Prassl, A. J., Kickinger, F., Ahammer, H., Grau, V., Schneider, J. E., Hofer, E., et al. (2009). Automatically generated, anatomically accurate meshes for cardiac electrophysiology problems. *IEEE Trans. Biomed. Eng.* 56, 1318–1330. doi: 10.1109/TBME.2009.2014243

Prinzen, F. W., and Peschar, M. (2002). Relation between the pacing induced sequence of activation and left ventricular pump function in animals. *PACE - Pacing Clin. Electrophysiol.* 25, 484–498. doi: 10.1046/j.1460-9592.2002.00484.x

Prinzen, F. W., Van Deursen, C., Van Geldorp, I. E., Rademakers, L. M., Van Hunnik, A., Kuiper, M., et al. (2009). Left ventricular endocardial pacing improves resynchronization therapy in canine left bundle-branch hearts. *Circ. Arrhythmia Electrophysiol.* 2, 580–587. doi: 10.1161/CIRCEP.108.846022

Prinzen, F. W., Vernooy, K., Lumens, J., and Auricchio, A. (2017). "Physiology of cardiac pacing and resynchronization," in *Clinical Cardiac Pacing, Defibrillation and Resynchronization Therapy*, eds K. A. Ellenbogen, B. L. Wilkoff, G. N. Kay, C.-P. Lau, and A. Auricchio (Philadelphia, PA: Elsevier), 213–248. doi: 10.1016/B978-0-323-37804-8.00007-9

Rickard, J., Karim, M., Baranowski, B., Cantillon, D., Spragg, D., Tang, W. H. W., et al. (2017). Effect of PR interval prolongation on long-term outcomes in patients with left bundle branch block vs non–left bundle branch block morphologies undergoing cardiac resynchronization therapy. *Hear. Rhythm.* 14, 1523–1528. doi: 10.1016/j.hrthm.2017.05.028

Romero, D., Sebastian, R., Bijnens, B. H., Zimmerman, V., Boyle, P. M., Vigmond, E. J., et al. (2010). Effects of the purkinje system and cardiac geometry on biventricular pacing: a model study. *Ann. Biomed. Eng.* 38, 1388–1398. doi: 10.1007/s10439-010-9926-4

Rossillo, A., Verma, A., Saad, E. B., Corrado, A., Gasparini, G., Marrouche, N. F., et al. (2004). Impact of coronary sinus lead position on biventricular pacing: mortality and echocardiographic evaluation during long-term follow-up. *J. Cardiovasc. Electrophysiol.* 15, 1120–1125. doi: 10.1046/j.1540-8167.2004.04089.x

Roth, B. J. (1992). How the anisotropy of the intracellular and extracellular conductivities influences stimulation of cardiac muscle. *J. Math. Biol.* 30, 633–646. doi: 10.1007/BF00175610

Ruschitzka, F., Abraham, W. T., Singh, J. P., Bax, J. J., Borer, J. S., Brugada, J., et al. (2013). Cardiac-resynchronization therapy in heart failure with a narrow QRS complex. *N. Engl. J. Med.* 369, 1395–1405. doi: 10.1056/NEJMoa1306687

Sebastian, R., Zimmerman, V., Romero, D., Sanchez-Quintana, D., and Frangi, A. F. (2013). Characterization and modeling of the peripheral cardiac conduction system. *IEEE Trans. Med. Imaging.* 32, 45–55. doi: 10.1109/TMI.2012.2221474

Sebastian, R., Zimmerman, V., Sukno, F., Bijnens, B. B., and Frangi, A. F. (2009). Cardiac modelling for pathophysiology research and clinical applications. The need for an automated pipeline. *IFMBE Proc.* 25, 2207–2210. doi: 10.1007/978-3-642-03882-2_586

Sicouri, S., and Antzelevitch, C. (1991). A subpopulation of cells with unique electrophysiological properties in the deep subepicardium of the canine ventricle. *M cell. Circ. Res.* 68, 1729–1741. doi: 10.1161/01.RES.68.6.1729

Sicouri, S., Fish, J., and Antzelevitch, C. (1994). Distribution of m-cells in the canine ventricle. *J Cardiovasc.* 5, 824–837. doi: 10.1111/j.1540-8167.1994.tb01121.x

Singh, J. P., Fan, D., Heist, E. K., Alabiad, C. R., Taub, C., Reddy, V., et al. (2006). Left ventricular lead electrical delay predicts response to cardiac resynchronization therapy. *Hear. Rhythm* 3, 1285–1292. doi: 10.1016/j.hrthm.2006.07.034

Singh, J. P., Klein, H. U., Huang, D. T., Reek, S., Kuniss, M., Quesada, A., et al. (2011). Left ventricular lead position and clinical outcome in the multicenter automatic defibrillator implantation trial-cardiac resynchronization therapy (MADIT-CRT) trial. *Circulation* 123, 1159–1166. doi: 10.1161/CIRCULATIONAHA.110.000646

Sipal, A., Bozyel, S., Aktaş, M., and Akbulut, T., Argan, O., Çelikyurt, U., et al. (2018). Surface electrogram-guided left ventricular lead placement improves response to cardiac resynchronization therapy. *Anatol. J. Cardiol.* 19, 184–191. doi: 10.14744/AnatolJCardiol.2018.09216

Sommer, A., Kronborg, M. B., Nørgaard, B. L., Stephansen, C., Poulsen, S. H., Kristensen, J., et al. (2018). Longer inter-lead electrical delay is associated with response to cardiac resynchronization therapy in patients with presumed optimal left ventricular lead position. *Eurospace* 20, 1–8. doi: 10.1093/europace/eux384

Sperzel, J., Burri, H., Gras, D., Tjong, F. V. Y., Knops, R. E., Hindricks, G., et al. (2015). State of the art of leadless pacing. *Europace* 17, 1508–1513. doi: 10.1093/europace/euv096

Spragg, D. D., Dong, J., Fetics, B. J., Helm, R., Marine, J. E., Cheng, A., et al. (2010). Optimal left ventricular endocardial pacing sites for cardiac resynchronization therapy in patients with ischemic cardiomyopathy. *J. Am. Coll. Cardiol.* 56, 774–781. doi: 10.1016/j.jacc.2010.06.014

Stellbrink, C., Auricchio, A., Butter, C., Sack, S., Vogt, J., Böcker, D., et al. (2000). Pacing therapies in congestive heart failure II study. *Am. J. Cardiol.* 86, K138–K143. doi: 10.1016/S0002-9149(00)01298-4

Stewart, P., Aslanidi, O. V., Noble, D., Noble, P. J., Boyett, M. R., and Zhang, H. (2009). Mathematical models of the electrical action potential of Purkinje fibre cells. *Philos. Trans. A Math. Phys. Eng. Sci.* 367, 2225–2255. doi: 10.1098/rsta.2008.0283

Strauss, D. G., Selvester, R. H., and Wagner, G. S. (2011). Defining left bundle branch block in the era of cardiac resynchronization therapy. *Am. J. Cardiol.* 107, 927–934. doi: 10.1016/j.amjcard.2010.11.010

Streeter, D. G. (1979). "Morphology and fiber geometry of the heart," in *The Cardiovascular System*, Vol. 1, ed R. Berne (Bethesda, USA: American Physiological Society). 61–112.

Strik, M., Van Deursen, C. J. M., Van Middendorp, L. B., Van Hunnik, A., Kuiper, M., Auricchio, A., et al. (2013). Transseptal conduction as an important determinant for cardiac resynchronization therapy, as revealed by extensive electrical mapping in the dyssynchronous canine heart. *Circ. Arrhythmia Electrophysiol.* 6, 682–689. doi: 10.1161/CIRCEP.111.000028

Surawicz, B., Childers, R., Deal, B. J., and Gettes, L. S. (2009). AHA/ACCF/HRS recommendations for the standardization and interpretation of the electrocardiogram. Part III: intraventricular conduction disturbances a scientific statement from the american heart association electrocardiography and arrhythmias committee, council on clinical cardiology; the american college of cardiology foundation; and the heart rhythm society. *J. Am. Coll. Cardiol.* 53, 976–981. doi: 10.1016/j.jacc.2008.12.013

Sweeney, M. O., Hellkamp, A. S., Van Bommel, R. J., Schalij, M. J., Jan Willem Borleffs, C., and Bax, J. J. (2014). QRS fusion complex analysis using wave interference to predict reverse remodeling during cardiac resynchronization therapy. *Hear. Rhythm*. 11, 806-813. doi: 10.1016/j.hrthm.2014.01.021

Taggart, P., Sutton, P. M., Opthof, T., Coronel, R., Trimlett, R., Pugsley, W., et al. (2000). Inhomogeneous transmural conduction during early ischaemia in patients with coronary artery disease. *J. Mol. Cell. Cardiol.* 32, 621–630. doi: 10.1006/jmcc.2000.1105

Tamborero, D., Vidal, B., Tolosana, J. M., Sitges, M., Berruezo, A., Silva, E., et al. (2011). Electrocardiographic versus echocardiographic optimization of the interventricular pacing delay in patients undergoing cardiac resynchronization therapy. *J. Cardiovasc. Electrophysiol.* 22, 1129–1134. doi: 10.1111/j.1540-8167.2011.02085.x

Tian, Y., Zhang, Y., Yan, Q., Mao, J., Dong, J., Ma, C., et al. (2017). Fragmented QRS complex in healthy adults: prevalence, characteristics, mechanisms, and clinical implications. *Int. J. Hear. Rhythm* 2, 34–39. doi: 10.4103/2352-4197.208459

Tomassoni, G. (2016). How to define cardiac resynchronization therapy response. *J. Innov. Card. Rhythm Manag.* 35, 777–780. doi: 10.1002/clc.22043

Ulč, I., and Vančura, V. (2013). Optimization of pacing intervals in cardiac resynchronization therapy. *Cor Vasa* 55, e403–e410. doi: 10.1016/j.crvasa.2013.06.001

Urbanek, B., Kaczmarek, K., Klimczak, A., Ruta, J., Chudzik, M., Piestrzeniewicz, K., et al. (2017). Potential benefit of optimizing atrioventricular and interventricular delays in patients with cardiac resynchronization therapy. *Indian J. Med. Res.* 146, 71–77. doi: 10.4103/ijmr.IJMR_1560_14

Van Gelder, B. M., Bracke, F. A., Meijer, A., and Pijls, N. H. J. (2005). The hemodynamic effect of intrinsic conduction during left ventricular pacing as compared to biventricular pacing. *J. Am. Coll. Cardiol.* 46, 2305–2310. doi: 10.1016/j.jacc.2005.02.098

Van Gelder, B. M., Meijer, A., and Bracke, F. A. (2009). Timing of the left ventricular electrogram and acute hemodynamic changes during implant of cardiac resynchronization therapy devices. *PACE - Pacing Clin. Electrophysiol.* 32 (Suppl. 1), S94–S97. doi: 10.1111/j.1540-8159.2008.02262.x

Vatasescu, R., Berruezo, A., Mont, L., Tamborero, D., Sitges, M., Silva, E., et al. (2009). Midterm "super-response" to cardiac resynchronization therapy by biventricular pacing with fusion: insights from electro-anatomical mapping. *Europace* 11, 1675–1682. doi: 10.1093/europace/eup333

Victor, F., Mabo, P., Mansour, H., Pavin, D., Kabalu, G., Place, C., et al. (2006). A randomized comparison of permanent septal versus apical right ventricular pacing: short-term results. *J. Cardiovasc. Electrophysiol.* 17, 238–242. doi: 10.1111/j.1540-8167.2006.00358.x

Wang, Y., and Hill, J. A. (2010). Electrophysiological remodeling in heart failure. *J. Mol. Cell. Cardiol.* 48, 619–632. doi: 10.1016/j.yjmcc.2010.01.009

Yoshikawa, H., Suzuki, M., Tezuka, N., Otsuka, T., and Sugi, K. (2010). Differences in left ventricular dyssynchrony between high septal pacing and apical pacing in patients with normal left ventricular systolic function. *J. Cardiol.* 56, 44–50. doi: 10.1016/j.jjcc.2010.02.002

Zanon, F., Baracca, E., Pastore, G., Fraccaro, C., Roncon, L., Aggio, S., et al. (2014). Determination of the longest intrapatient left ventricular electrical delay may predict acute hemodynamic improvement in patients after cardiac resynchronization therapy. *Circ. Arrhythmia Electrophysiol.* 7, 377–383. doi: 10.1161/CIRCEP.113.000850

Zareba, W., Klein, H., Cygankiewicz, I., Hall, W. J., McNitt, S., Brown, M., et al. (2011). Effectiveness of cardiac resynchronization therapy by QRS morphology in the multicenter automatic defibrillator implantation trial-cardiac resynchronization therapy (MADIT-CRT). *Circulation* 123, 1061–1072. doi: 10.1161/CIRCULATIONAHA.110.960898

Zhang, J., Zhang, Y., Zhou, X., Li, J., Li, Y., Zhang, Y., et al. (2015). QRS duration shortening predicts left ventricular reverse remodelling in patients with dilated cardiomyopathy after cardiac resynchronization therapy. *Acta Cardiol.* 70, 307–313. doi: 10.1080/AC.70.3.3080635

Conflict of Interest Statement: The authors declare that the research was conducted in the absence of any commercial or financial relationships that could be construed as a potential conflict of interest.

frontiers in Physiology

ORIGINAL RESEARCH
published: 18 March 2019
doi: 10.3389/fphys.2019.00259

Investigating the Complex Arrhythmic Phenotype Caused by the Gain-of-Function Mutation KCNQ1-G229D

Xin Zhou[1], Alfonso Bueno-Orovio[1], Richard J. Schilling[2], Claire Kirkby[2], Chris Denning[3], Divya Rajamohan[3], Kevin Burrage[1,4,5], Andrew Tinker[6], Blanca Rodriguez[1] and Stephen C. Harmer[6]*†*

[1] Department of Computer Science, British Heart Foundation Centre of Research Excellence, University of Oxford, Oxford, United Kingdom, [2] St Bartholomew's Hospital, London, United Kingdom, [3] Department of Stem Cell Biology, Centre for Biomolecular Sciences, University of Nottingham, Nottingham, United Kingdom, [4] Australian Research Council Centre of Excellence for Mathematical and Statistical Frontiers, Queensland University of Technology, Brisbane, QLD, Australia, [5] School of Mathematical Sciences, Queensland University of Technology, Brisbane, QLD, Australia, [6] The William Harvey Research Institute, Barts and The London School of Medicine and Dentistry, Queen Mary University of London, London, United Kingdom

OPEN ACCESS

Edited by:
Javier Saiz,
Universitat Politècnica de València, Spain

Reviewed by:
Arun V. Holden,
University of Leeds, United Kingdom
Jieyun Bai,
The University of Auckland, New Zealand

***Correspondence:**
Blanca Rodriguez
blanca.rodriguez@cs.ox.ac.uk
Stephen C. Harmer
s.c.harmer@bristol.ac.uk

†Present address:
Stephen C. Harmer,
School of Physiology, Pharmacology and Neuroscience, University of Bristol, Bristol, United Kingdom

Specialty section:
This article was submitted to Computational Physiology and Medicine, a section of the journal Frontiers in Physiology

Received: 18 December 2018
Accepted: 28 February 2019
Published: 18 March 2019

Citation:
Zhou X, Bueno-Orovio A, Schilling RJ, Kirkby C, Denning C, Rajamohan D, Burrage K, Tinker A, Rodriguez B and Harmer SC (2019) Investigating the Complex Arrhythmic Phenotype Caused by the Gain-of-Function Mutation KCNQ1-G229D. Front. Physiol. 10:259. doi: 10.3389/fphys.2019.00259

The congenital long QT syndrome (LQTS) is a cardiac electrophysiological disorder that can cause sudden cardiac death. LQT1 is a subtype of LQTS caused by mutations in KCNQ1, affecting the slow delayed-rectifier potassium current (I_{Ks}), which is essential for cardiac repolarization. Paradoxically, gain-of-function mutations in KCNQ1 have been reported to cause borderline QT prolongation, atrial fibrillation (AF), sinus bradycardia, and sudden death, however, the mechanisms are not well understood. The goal of the study is to investigate the ionic, cellular and tissue mechanisms underlying the complex phenotype of a gain-of-function mutation in KCNQ1, c.686G > A (p.G229D) using computer modeling and simulations informed by *in vitro* measurements. Previous studies have shown this mutation to cause AF and borderline QT prolongation. We report a clinical description of a family that carry this mutation and that a member of the family died suddenly during sleep at 21 years old. Using patch-clamp experiments, we confirm that KCNQ1-G229D causes a significant gain in channel function. We introduce the effect of the mutation in populations of atrial, ventricular and sinus node (SN) cell models to investigate mechanisms underlying phenotypic variability. In a population of human atrial and ventricular cell models and tissue, the presence of KCNQ1-G229D predominantly shortens atrial action potential duration (APD). However, in a subset of models, KCNQ1-G229D can act to prolong ventricular APD by up to 7% (19 ms) and underlie depolarization abnormalities, which could promote QT prolongation and conduction delays. Interestingly, APD prolongations were predominantly seen at slow pacing cycle lengths (CL > 1,000 ms), which suggests a greater arrhythmic risk during bradycardia, and is consistent with the observed sudden death during sleep. In a population of human SN cell models, the KCNQ1-G229D mutation results in slow/abnormal sinus rhythm, and we identify that a stronger L-type

calcium current enables the SN to be more robust to the mutation. In conclusion, our computational modeling experiments provide novel mechanistic explanations for the observed borderline QT prolongation, and predict that KCNQ1-G229D could underlie SN dysfunction and conduction delays. The mechanisms revealed in the study can potentially inform management and treatment of KCNQ1 gain-of-function mutation carriers.

Keywords: KCNQ1, long QT syndrome, gain-of-function, arrhythmia, sinus node, computational biology

INTRODUCTION

Long QT Syndrome (LQTS) is a type of cardiac disorder that is often related to syncope and sudden cardiac death. LQT1, which is the most common form of LQTS, is caused by mutations in the KCNQ1 gene, affecting the slow delayed-rectifier repolarizing current (I_{Ks}) (Barhanin et al., 1996; Sanguinetti et al., 1996). Loss-of-function mutations in KCNQ1 can reduce I_{Ks} and underlie the inherited form of long QT syndrome (LQT1) (Wang et al., 1996), while gain-of-function mutations in KCNQ1 can act to increase channel opening, resulting in enhanced I_{Ks} (Chen et al., 2003; Hong et al., 2005; Lundby et al., 2007; Das et al., 2009; Bartos et al., 2011, 2013; Ki et al., 2014; Moreno et al., 2015).

Gain-of-function mutations in KCNQ1 associate with complex phenotypes. To date, eight gain-of-function mutations in KCNQ1 have been identified that underlie persistent familial atrial fibrillation (AF) (Hancox et al., 2014; Hasegawa et al., 2014), and four have been reported to cause short QT syndrome type 2 (SQT2) (Bellocq et al., 2004; Hong et al., 2005; Moreno et al., 2015; Wu et al., 2015). Some of these gain-of-function mutations are additionally associated with sinus bradycardia [S140G (Chen et al., 2003), V141M (Hong et al., 2005), R231C (Henrion et al., 2012), V241F (Ki et al., 2014), and F279I (Moreno et al., 2015)], and paradoxically, some KCNQ1 gain-of-function mutations have been linked to QT prolongation (borderline LQT) [S140G (Chen et al., 2003), Q147R (Lundby et al., 2007), R231C (Bartos et al., 2011; Henrion et al., 2012) and R231H (Bartos et al., 2013)]. The mechanisms underlying how certain KCNQ1 gain-of-function mutations cause AF and SQT2 have been revealed by *in silico* studies. In general, the gain in I_{Ks} function acts to shorten the refractory period and stabilize re-entrant waves, therefore promoting AF and ventricular arrhythmia (Kharche et al., 2012; Zulfa et al., 2016; Adeniran et al., 2017). In addition, the effects of several gain-of-function KCNQ1 mutations (V141M, R231C, and V241F) on sinus bradycardia have recently been explored using human *in silico* models of the sinus node (SN) (Fabbri et al., 2017; Whittaker et al., 2018). However, the mechanisms that underlie why certain KCNQ1 gain-of-function mutations are associated with borderline LQT and the factors that may explain phenotypic variability remain unclear.

The goal of this study is to investigate the ionic, cellular and tissue mechanisms underlying the complex phenotype of a gain-of-function mutation in KCNQ1, p.G229D (c.686G > A), (KCNQ1-G229D) using human atrial, ventricular and SN models informed by *in vitro* patch-clamp measurements. This mutation was first reported in 2014 in a 16-year-old boy with AF (Hasegawa et al., 2014). Interestingly, after radiofrequency catheter ablation therapy sinus rhythm was maintained, but the boy represented with borderline LQT (Hasegawa et al., 2014). Here, we report the clinical features of members of a British family affected by the same mutation. In addition to AF and borderline LQT, sudden death also happened in this family. By using a population of models approach, we investigate how natural variations in ionic current density could underlie variability in the phenotype of mutation carriers. In particular, we focus on the mechanisms that underlie the associated borderline LQT, which has also been reported for other KCNQ1 gain-of-function mutations but has not been explored. In addition, we investigate potential effects on the SN, based on the SN dysfunction caused by other KCNQ1 gain-of-function mutations.

MATERIALS AND METHODS

Clinical Data and QT Interval Duration Assessment

The clinical characterisation of the family carrying the G229D mutation was carried out in accordance with the recommendations of the National Health Service (NHS) Health Research Authority. The protocol was approved by the National Research Ethics Service (NRES Committee) East Midlands - Nottingham 2 [Research Ethics Committee (REC) reference: 09/H0508/74]. All subjects gave written informed consent in accordance with the Declaration of Helsinki. QT interval duration was measured on resting electrocardiograms (ECGs) using lead V5 or II (**Figure 1**). In patients in sinus rhythm an average of three consecutive beats was calculated. In patients with AF an average of six consecutive beats was calculated. The Bazett formula (Bazett, 1920) was used to correct QT according to heart rate (QTc).

Molecular Biology and Cell Culture

We characterized the effects of the G229D mutation on KCNQ1/KCNE1 (I_{Ks}) channel function by whole-cell patch-clamp in a heterologous expression system [Chinese Hamster Ovary-K1 (CHO-K1) cells]. KCNQ1 (GenBank® accession number AF000571) and KCNE1 are as described in Harmer et al. (2014). pEGFP-N1 was from Clontech. The patient-identified G229D mutation (c.686G > A) was introduced into KCNQ1 using site-directed mutagenesis [Quikchange II XL (Agilent Technologies)].

CHO-K1 cells (Sigma-Aldrich, 85051005) were cultured as described in Harmer et al. (2014). To analyze the effects of G229D, cells were transfected with 250 ng of wild-type (WT) KCNQ1 or LQT1 mutant cDNA and 500 ng of KCNE1 (+50 ng pEGFP-N1) (I_{Ks}-WT or I_{Ks}-G229D, respectively). To mimic the heterozygous patient phenotype (I_{Ks}-HET), cells were transfected with 125 ng of wild-type channel + 125 ng of mutant channel and 500 ng KCNE1 (+50 ng pEGFP-N1). Transfections were performed as described in Harmer et al. (2014). After transfection, cells were split at low density onto 10 mm glass coverslips and transfected cells (identified by fluorescence) were patched 48 h later.

Patch-Clamp Electrophysiological Recording and Analysis

Whole-cell currents were recorded using an Axopatch 200B amplifier (Axon Instruments/Molecular Devices). Data acquisition was performed using pCLAMP10 software through a Digidata 1440A (Axon Instruments/Molecular Devices). Data digitization (sampling) rates were 0.5 kHz and recordings were lowpass Bessel filtered at 1 kHz.

Whole-Cell Patch-Clamp

For the experiments detailed in **Figure 2** whole-cell patch-clamp recording was performed at room temperature (22°C) as described in Thomas et al. (2011). The intracellular (pipette) solution contained: (mmol/L) 150 KCl, 10 HEPES, 5 EGTA, 2 $MgCl_2$, 1 $CaCl_2$ and 5 $(Na)_2ATP$ (pH 7.2 with KOH). The extracellular (bath) solution contained: (mmol/L) 150 NaCl, 5 KCl, 10 HEPES, 2 $MgCl_2$, and 1 $CaCl_2$ (pH 7.4 with NaOH). Pipette resistances were, once filled with intracellular solution, between 2 and 3 mega-ohms (MΩ). Pipette capacitance was reduced by coating the pipette tip with SigmaCote (SL2, Sigma). Once the whole-cell configuration had been achieved cells were dialyzed for 2 min before recording. Series resistance (R_{series}) was compensated by at least 70% using the amplifier circuitry. The liquid junction potential [calculated using the Junction Potential tool in pCLAMP (Axon Instruments/Molecular Devices)] was relatively small (+4.3 mV) and therefore post-recording adjustments of membrane potential were not performed. The voltage protocol used is outlined in **Figure 2** and the cycle length for this protocol was 0.1 Hz.

Patch-Clamp Recording Analysis

Data were analyzed using Clampfit (Molecular Devices) and GraphPad Prism. As previously described in Thomas et al. (2011) current-voltage relationships were generated by normalizing the maximal current densities at the end of each pulse-potential to cell capacitance. Peak-tail current density (PTCD) was analyzed by normalizing the peak tail currents (in response to the prior test potential) to cell capacitance. The voltage-dependence of channel activation (or steady-state of activation) was determined by fitting the normalized peak tail current amplitudes (y/y_{max}) versus a test potential (V_t) with a Boltzmann function [$y/y_{max} = 1/(1 + \exp[(V_{0.5} - V_t)/k])$] ($k$ indicates the slope factor). The $V_{0.5}$ value indicates the potential at which channel activation is half-maximal.

Computational Modeling of the Effects of the G229D Mutation on KCNQ1/KCNE1 Channel Function

The I_{Ks} formulation from the human ventricular O'Hara-Rudy dynamic model (ORd) model (O'Hara et al., 2011) was used to replicate the patch-clamp data (**Supplementary Material**). Least square curve fitting (lsqcurvefit) was combined with the Multi-Start algorithm in Matlab to find the parameters with optimized fitting results for the mutated I_{Ks}. Additional fitting details including model formulation are presented in the **Supplementary Material**. The optimized fitting results for I_{Ks}-HET (KCNQ1 + G229D + KCNE1) and I_{Ks}-G229D (G229D + KCNE1) were inserted into the I_{Ks} current formulation of the ORd model, the human atrial (Grandi et al., 2011) and (Maleckar et al., 2009) and Fabbri human SN models (Fabbri et al., 2017).

To test whether the effects of our I_{Ks}-HET formulation on action potential duration (APD) and SN were stable, we also used the I_{Ks}/I_{Ks}-HET formulations of Hasegawa et al. (2014) to check the robustness of our results. Action Potential (AP) clamp simulations using three AP traces with different plateau levels were used to examine whether the effect of AP plateau on rapid delayed rectifier potassium current (I_{Kr}) was model specific by comparing the ORd, Maleckar, and Grandi models.

In silico Populations of Human Ventricular Cell and One-Dimensional (1D) Tissue Fibers Models

A population of 2326 ORd-derived models calibrated with human *in vivo* data was used to account for the effect of human electrophysiological variability as in Zhou et al. (2016). An initial population of 10,000 models was constructed by varying the main ionic conductances by up to ±100% using Latin Hypercube Sampling, including fast sodium current conductance (G_{Na}), late sodium current conductance (G_{NaL}), transient outward potassium current conductance (G_{to}), L-type calcium current conductance (G_{CaL}), rapid delayed rectifier potassium current conductance (G_{Kr}), slow delayed rectifier potassium current conductance (G_{Ks}), inward rectifier potassium current conductance (G_{K1}), sodium-potassium pump current conductance (G_{NaK}), sodium-calcium exchange current conductance (G_{NaCa}), sarcoplasmic reticulum (SR) calcium release permeability (P_{Jrel}) and SR calcium re-uptake permeability (P_{Jup}). The initial population of 10,000 models was calibrated using the human *in vivo* measurements described in Zhou et al. (2016). The advantage of using a population of models rather than just a standard baseline model is that it provides scenarios of natural variability (Muszkiewicz et al., 2016), in particular for investigations on multiple disease phenotypes and variable penetrance (Passini et al., 2016).

In the ORd model, the level of G_{Ks} is greatest in epicardial cells. Therefore, in order to evaluate the strongest possible effects in ventricles, we simulated the effect of the KCNQ1-G229D mutation in epicardial fibers. A population of monodomain homogeneous epicardial 1D fibers of 2 cm was derived from the

ORd single cell population. Pseudo-ECG signals were computed as the integral of spatial gradient of transmembrane potentials from all the points in the fibers (Gima and Rudy, 2002). The tissue simulations and pseudo-ECG calculations were conducted in the open-source software CHASTE (Pitt-Francis et al., 2009) for 50 beats with a conductivity of 3.92 mS/cm to obtain a conduction velocity of 69 cm/s in the baseline ORd epicardial fiber. Transmural fibers consisting of 80% of endocardial cells and 20% of epicardial cells were also simulated for some representative cases with a conductivity of 1.19 mS/cm to obtain a transmural conduction velocity of 40 cm/s in the baseline ORd model.

Construction and Calibration of Human Atrial Cell Population of Models

Using a similar methodology as in Britton et al. (2013), the nine current conductances of the Grandi atrial cell models (Grandi et al., 2011) were varied by up to ±100% using Latin Hypercube Sampling to generate an initial candidate population of 5,000 models: G_{Na}, G_{NaL}, G_{to}, G_{CaL}, G_{Kr}, G_{Ks}, G_{K1}, ultrarapid delayed rectifier potassium current conductance (G_{Kur}), G_{NaK}, and G_{NaCa}. These currents were chosen based on their direct contributions to the regulation of APDs, and intracellular calcium fluxes were not varied due to their relatively small effects on APD (Muszkiewicz et al., 2018). After pacing each model under CL = 1,000 ms for 500 beats, the experimental biomarker ranges from human atrial cells were used to select the models in range with the experimental data reported in Sanchez et al. (2014). The models accepted under cycle length (CL) = 1,000 ms were then paced under CL = 2,000 ms and CL = 500 ms. The 917 models that did not display delayed afterdepolarizations, early afterdepolarizations or depolarization failure under all three CLs were accepted for further analysis.

Construction and Calibration of Human Sinus Node Cell Population of Models

An initial population of 5,000 models was generated from the baseline Fabbri model (Fabbri et al., 2017) by using Latin hypercube sampling to introduce up to ±100% variations to 12 current conductances and ion flux magnitudes: funny current conductance (G_f), G_{CaL}, T-type calcium current conductance (G_{CaT}), G_{Kr}, G_{Ks}, G_{to}, G_{Na}, G_{NaK}, G_{NaCa}, G_{Kur}, P_{Jrel}, and P_{Jup}. These currents were chosen because both sarcolemmal currents and calcium handling affect spontaneous depolarization. After simulating each model for 1,000 s, 1046 models with a basic cycle length between 600 and 1,000 ms (heart rate between 60 and 100 bpm) and a positive overshoot membrane potential were accepted for further analysis. The effects of I_{Ks}-HET in human SN models were classified into three categories: Robust (heart rate between 60 and 100 bpm and a positive overshoot potential), Bradycardia (a positive overshoot potential and heart rate slower than 60 bpm), and Pacemaking failure (a negative maximum potential or a loss of spontaneous activity).

Statistical Analysis

Patch-clamp experimental data was compared/analyzed using a one-way ANOVA with Bonferroni *post hoc* test for multiple comparisons. Patch-clamp data was considered significantly different if $P < 0.05$. Statistical analysis of *in silico* modeling was conducted with Wilcoxon rank-sum test using Matlab, using a standard $P < 0.05$, and differences in current conductances are reported in the figures and visualized as the differences of the medians of the distributions.

RESULTS

Clinical Description of KCNQ1-G229D Mutation Carriers

Patient A was seen after her daughter (Patient C) died unexpectedly whilst sleeping at 21 years of age (**Figure 1A**). Patient A reported that as a teenager she had occasional periods of fainting but no reported exertional syncope. Her ECG was in sinus rhythm at 68 bpm (**Figures 1B,C**) and her QTc was 465 ms. It was noted following an ectopic beat that her QTc prolonged to 490 ms.

On the basis of the borderline QT prolongation and the death of her daughter she was genetically tested. Genetic testing found a previously reported pathogenic variant in *KCNQ1* c.686G > A (p.G229D) (Hasegawa et al., 2014). Based on this finding, other members of the family were genetically screened. Screening revealed that her mother (Patient B) and granddaughter (Patient D) are carriers of the *KCNQ1* c.686G > A (p.G229D) mutation. Genetic testing for Patient C was not performed during autopsy but her relationship in the family proves that she was an obligate carrier. Clinical details for Patient D are unavailable. Patient B was first diagnosed with AF at 60 years of age and does not have a history of syncope. Her QTc values, measured in the presence of AF, were 440–446 ms (**Figure 1C**). Our clinical data, and that reported by (Hasegawa et al., 2014) and (Moreton et al., 2013), indicate that *KCNQ1* c.686G > A (p.G229D) has high penetrance and that it is associated with AF, borderline LQT and sudden cardiac death.

Effect of the G229D Mutation on I_{Ks} Channel Function *in vitro* and *in silico*

Patch clamp measurements show that G229D co-expression with KCNE1 (I_{Ks}-G229D) produced currents with marked instantaneous activation and tail currents that failed to deactivate (**Figure 2A**). To mimic the patient phenotype KCNQ1 and G229D were co-expressed (with KCNE1) in heterozygous form (I_{Ks}-HET). The currents produced by I_{Ks}-HET possessed both instantaneous and slow activation components reflecting a combined phenotype (**Figure 2A**) and the presence of G229D acted to shift the voltage-dependence of channel activation ($V_{0.5}$) by approximately −35 mV (**Figure 2D**).

Overall, our observed effects of G229D on channel function correlate well with the gain-of-function effect first reported by (Hasegawa et al., 2014). Using the electrophysiological data from the patch-clamp studies, we then modeled *in silico* the effects of the G229D mutation on channel function. The fitting details for I_{Ks}-G229D and I_{Ks}-HET are shown in **Supplementary Figures S1–S3**. The resulting I_{Ks}-G229D and I_{Ks}-HET models

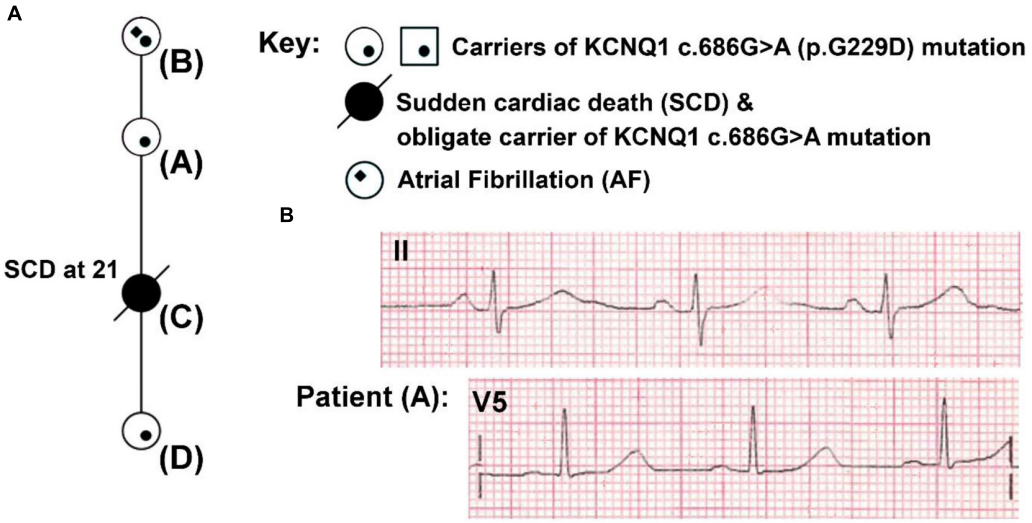

C

Patient	Age at last clinic visit	Mutation carrier	Atrial fibrillation	Sinus node dysfunction	QT interval (ms)	Heart rate (bpm) (resting ECG)
(A)	61	Yes	No	No	QTc 460-465	68
(B)	81	Yes	Yes	NK	QTc 440-446	78
(C)	Sudden death age 21	Yes*	NK	NK	NA	NA
(D)	8	Yes	NK	NK	NA	NA

FIGURE 1 | Partial pedigree and clinical information for members of a family carrying the KCNQ1 mutation G229D (c.686G>A). **(A)** Partial mini pedigree of a British family that present with a complex arrhythmic phenotype that includes sudden cardiac death (SCD), atrial fibrillation (AF), and borderline QT prolongation. Circles indicate female family members. **(B)** Lead II and V5 electrocardiograms (ECGs) from Patient (A) with borderline QT prolongation but not AF. **(C)** Clinical characteristics of carriers of the KCNQ1-G229D mutation. * = Not genetically tested but obligate carrier of the KCNQ1-G229D mutation (c.686G>A) based on position in the family. Please refer to **(A)** for the location of each patient in the pedigree. NK, not known; NA, not available.

were then incorporated into the populations of human atrial, ventricular and sino-atrial cell models to investigate the complex electrophysiological consequences of the mutation.

The Predominant Effect of I_{Ks} Gain-of-Function G229D Mutation Is APD Shortening in Both the Atria and Ventricle

In the baseline human atrial Grandi model, I_{Ks}-HET caused significant reductions in APD (14.22%) and weakened the AP upstroke (**Figure 3A**), in agreement with (Hasegawa et al., 2014). Similarly, in the baseline ventricular ORd model, the presence of I_{Ks}-HET also weakened the AP upstroke and led to AP shortening by 9.83%. Both APD shortenings occurred because I_{Ks}-HET produced a much stronger current during the whole AP, and therefore repolarization proceeded more quickly. The degree of shortening in the Grandi atrial model was greater than in the ventricular model (**Figures 3A,B**), and even greater shortening of APD was seen in the Maleckar human atrial model (33.23% reduction, **Supplementary Figure S4**). Therefore, the more significant APD shortening observed in human atrial models is not model-dependent.

We investigated potential variability in the effect of I_{Ks}-HET formulations when inserted in populations of human ventricular and atrial models with variable ionic profiles. As an accumulation of I_{Ks} during increases in heart rate may be important for repolarization (Viswanathan et al., 1999), we applied both slow and fast pacing CLs (2,000, 1,000, 500, and 333 ms). For both populations of models, the most common effect of the mutation was APD shortening (**Supplementary Figure S5** and **Figures 3C,D**). Under CL = 1,000 ms, the median APD shortening in the human ventricular cell population was 22 ms, while in the human atrial cell population, the median shortening was 29 ms (**Figures 3C,D**). Thus, when considering ionic variability in the population, the G229D mutation induced greater APD shortening in human atria than in the ventricular models. Since the baseline Maleckar atrial model already showed an even greater APD shortening than the Grandi atrial model under the mutation, we did not construct a population of Maleckar atrial models to verify this phenomenon. Further analysis showed that the conductances of I_{Kr}, I_{Ks}, and I_{CaL} were the main determinants for the extent of ventricular APD shortening caused by I_{Ks}-HET (**Figure 3E**). Models with weak G_{CaL} and G_{Kr} and strong G_{Ks} tended to present with more significant APD shortening under I_{Ks}-HET (**Figure 3F**). In the atrial population of models, a greater number of currents played roles in the regulation of APD shortening, and the most important factor was G_{Ks} (**Figure 3E**). Stronger G_{Ks},

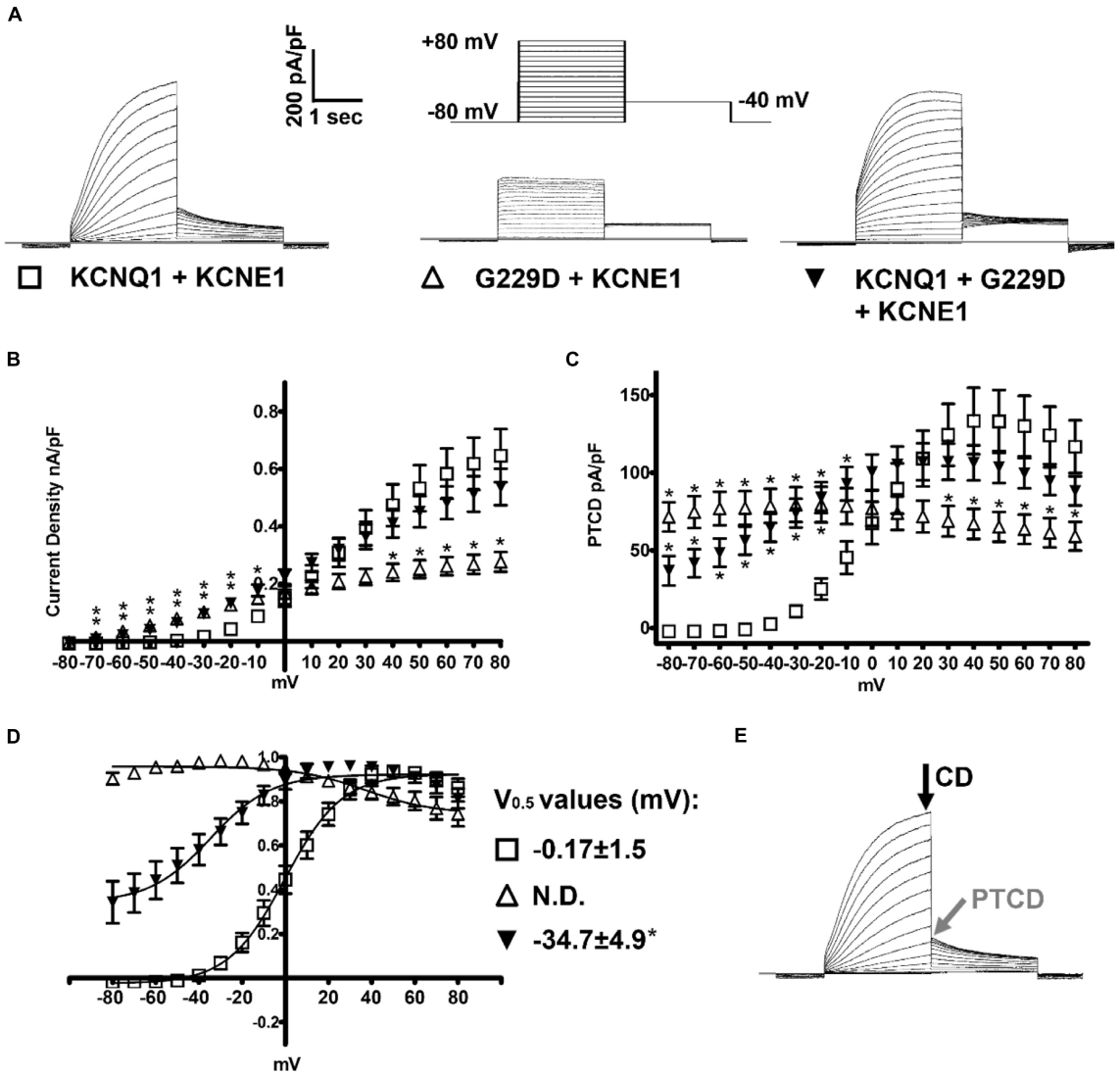

FIGURE 2 | KCNQ1-G229D dramatically alters the biophysical properties of the KCNQ1/KCNE1 (I_{Ks}) channel. **(A)** Representative traces of the currents produced by wild-type (WT) KCNQ1 (KCNQ1 + KCNE1: I_{Ks}-WT) or G229D when expressed homozygously (G229D + KCNE1: I_{Ks}-G229D) or in heterozygous fashion (KCNQ1 + G229D + KCNE1: I_{Ks}-HET). The effect of the G229D mutation on channel function, in CHO-K1 cells, was analyzed by whole-cell patch-clamp. In all cases, to recapitulate the I_{Ks} current, KCNE1 was co-expressed. The zero-current level (0 pA) is indicated by the gray line. The voltage protocol used to elicit these currents is inset in **(A)**. **(B)** Mean current-voltage relationships (current density). **(C)** Peak-tail current density (PTCD). **(D)** Normalized voltage-dependent activation curves ($V_{0.5}$) (in mV). The activation curves are fit with Boltzmann functions (solid lines). **(E)** Black and gray arrows indicate the points where the current density signals [current density (CD)] and PTCD were used to calculate the corresponding biomarkers for analysis and fitting. Data are presented as mean ± SEM. (n = 8–12). N.D., not determined. * indicates significantly different from WT control value ($P < 0.05$) (One-way ANOVA analysis with Bonferroni *post hoc* test).

G_{NaK}, and G_{CaL}, and weaker G_{K1}, G_{to}, G_{Kur}, and G_{Kr} were associated with more significant APD shortening in the atrial cells (**Figure 3E**).

Borderline APD Prolongation May Occur Due to the Interplay Between I_{Kr} and I_{Ks}-HET

Although APD shortening was consistently observed under four pacing CLs (**Supplementary Figure S5**), some human ventricular models in the population resulted in APD prolongation in the presence of I_{Ks}-HET, especially at slower pacing rates (**Figure 4A**). Furthermore, the number of ventricular cell models that showed obvious APD prolongation (>5 ms) was also increased as pacing rates became slower (no models under CL = 500/333 ms, 5 models under CL = 1,000 ms and 25 models under CL = 2,000 ms). Therefore, in the presence of KCNQ1-G229D, APD prolongation occurred more often at slower pacing rates.

There was no significant difference between the WT APDs between the prolongation models and other models in the population. However, the AP peak membrane voltage was

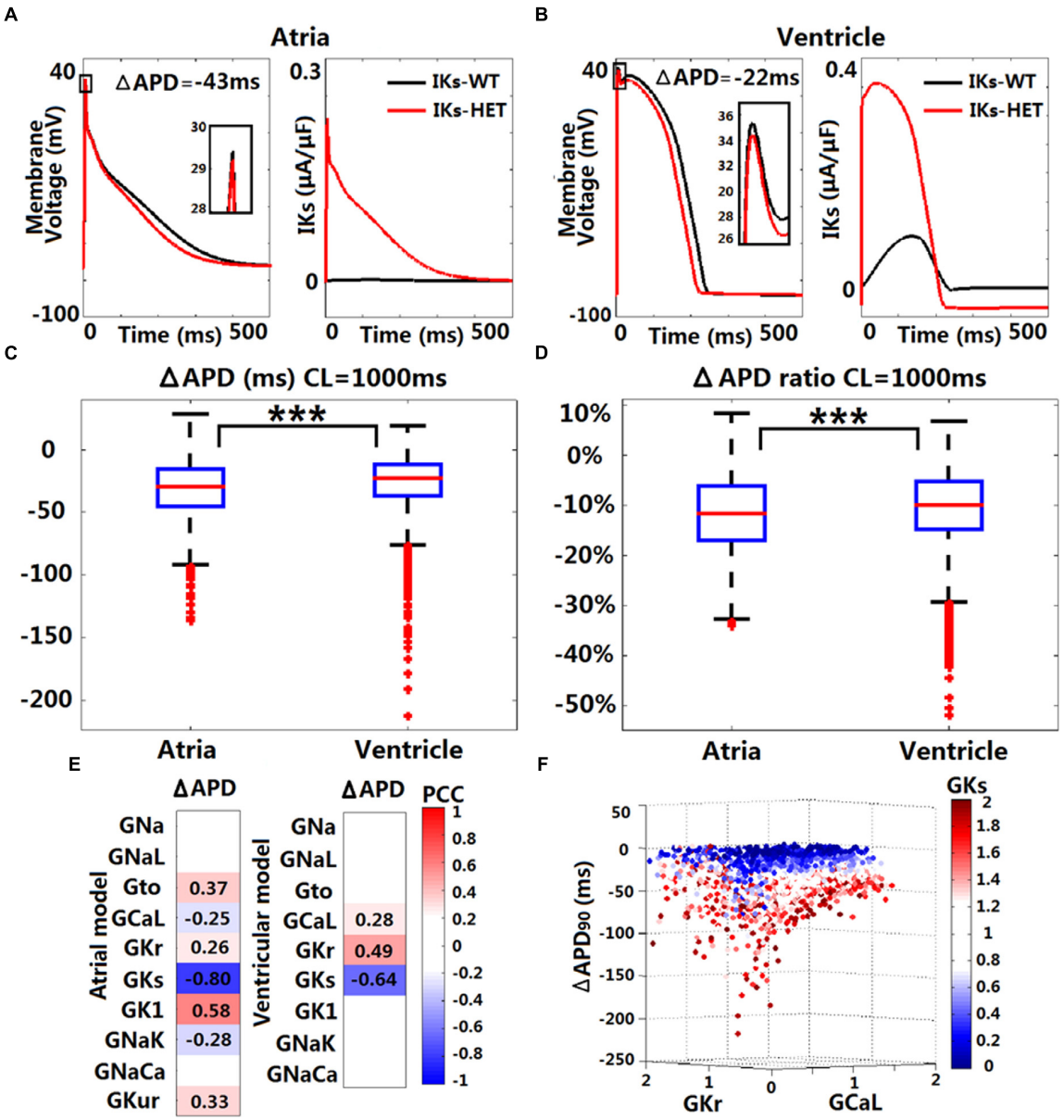

FIGURE 3 | *In silico* simulations of the effects of KCNQ1-G229D on human ventricular and atrial action potentials. The effect of the G229D mutation on membrane voltage (V_m, mV, insets showing peak upstroke) and I_{Ks} (μA/μF) in the Grandi human atrial cell model **(A)** and the ORd human ventricular epicardial cell model **(B)**. Comparison of absolute APD change (ΔAPD = APD-I_{Ks}-HET – APD-I_{Ks}-WT, **C**) and relative APD change (ΔAPD/APD-I_{Ks}-WT, **D)** after introducing I_{Ks}-HET between Grandi atrial population of models and ORd ventricular population of models at CL = 1,000 ms (***$P < 0.001$) (Wilcoxon rank-sum test). **(E)** Partial correlation analysis between ΔAPD at CL = 1,000 ms and current conductances in the population of atrial and ventricular models. The partial correlation coefficients (PCC) are indicated by the color scale, where red implies a strong positive correlation and blue implies a strong negative correlation. **(F)** Relationship between the conductances of I_{Kr}, I_{Ks}, and I_{CaL} and the ΔAPD in the ORd population. 0–2 represent the scaling factors for the baseline conductances in the ±100% range.

significantly reduced (**Figure 4B**) due to smaller baseline depolarization current conductances (G_{Na} and G_{CaL}) in the models displaying APD prolongation (**Figure 4C**). In addition, stronger baseline G_{Kr} was found in the models displaying APD prolongation at CL = 1,000 or 2,000 ms (**Figure 4C**). In the subgroup of models producing APD prolongation at CL = 1,000 ms, replacing our I_{Ks}/I_{Ks}-HET formulations with the I_{Ks}/I_{Ks}-HET formulations of Hasegawa et al. (2014) also generated consistent APD prolongation, supporting the robustness of these phenomena (**Supplementary Figure S6**).

To understand the ionic mechanisms underlying APD prolongation/shortening, we analyzed the change of individual currents induced by the presence of the G229D mutation. The biggest differences in ionic currents for both prolongation and shortening were the increase of I_{Ks} (**Figures 5A,B**, middle panels) and the secondary decrease of I_{Kr} (**Figures 5A,B**, right panels).

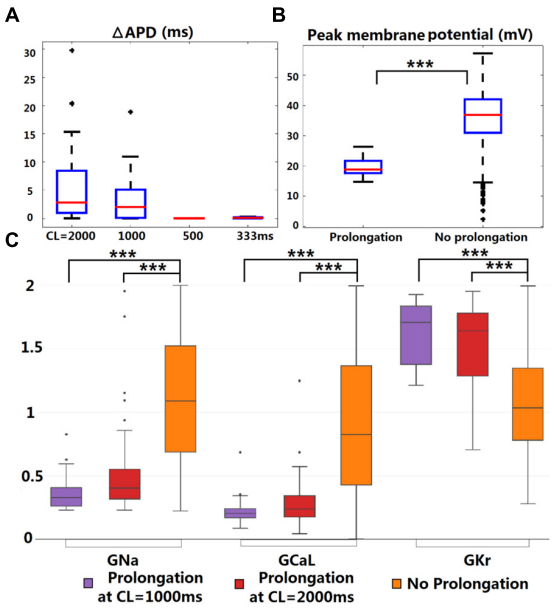

FIGURE 4 | KCNQ1-G229D can lead to ventricular APD prolongation at slow pacing rates. **(A)** APD prolongations under four pacing rates (ΔAPD = APD-I_{Ks}-HET – APD-I_{Ks}-WT). **(B)** Comparison of the WT peak membrane voltage between the models that showed or did not show APD prolongation under I_{Ks}-HET at CL = 1,000 ms. **(C)** Parameter comparison between models that showed APD prolongation at CL = 1,000 or 2,000 ms and those that did not show APD prolongation under I_{Ks}-HET. The *y*-axis represents the scaling factors in the ±100% range (0–2) to the original baseline ORd model current conductances (***$P < 0.001$) (Wilcoxon rank-sum test). Black points indicate extreme values that lie more than 1.5 times the interquartile range away from the top (the 75th percentile) or bottom (the 25th percentile) of the box.

We selected two representative ventricular cell models with similar AP upstroke but one displaying shortening and the other prolongation with I_{Ks}-HET. The presence of I_{Ks}-HET affected the AP upstroke and led to a smaller peak membrane voltage and a lower plateau in both models. The reduction in I_{Kr} magnitude after G229D introduction was likely due to the reduced phase 2 AP plateau (**Figures 5A,B**, left panels).

To verify whether this was model-specific, we conducted AP clamp simulations using different human I_{Kr} models. The I_{Kr} magnitude was consistently weaker under a smaller phase 2 AP plateau in all models tested (**Supplementary Figure S7**). For the human ventricular model displaying APD prolongation with I_{Ks}-HET, the decrease of I_{Kr} amplitude was slightly bigger than the increase of I_{Ks} amplitude under the I_{Ks}-HET condition (**Figure 5A**, middle and right panels). In contrast, in the human ventricular model displaying APD shortening, the augmentation of I_{Ks} was more significant than the inhibition of I_{Kr} (**Figure 5B**, middle and right panels).

Therefore, our explanation was that if the inhibition of I_{Kr} can overcome the augmentation of I_{Ks}, the presence of the G229D mutation could lead to an overall weaker repolarization, and therefore a prolonged APD. Importantly, the prolongation models tended to have stronger I_{Kr} (**Figure 4C**), which was crucial for I_{Kr} reduction to be dominant under I_{Ks}-HET. We also noticed that under slow pacing, the magnitude of I_{Ks} decreased, whereas I_{Kr} increased (**Supplementary Figure S8**), which explained the increased number of models with APD prolongation at slow pacing. Overall, these findings further highlight that in the presence of the G229D mutation, ventricular APD prolongation is more likely to occur during bradycardia, particularly for strong I_{Kr} models.

By Counteracting Action Potential Upstroke Dynamics KCNQ1-G229D Could Promote Tissue Conduction Abnormalities

As illustrated earlier, the G229D mutation can reduce peak AP membrane voltage. We hypothesized that I_{Ks}-HET by counteracting AP upstroke dynamics (**Figures 3A,B**, **5A,B**) could have important effects on the safety of conduction. In addition, we need to confirm whether the ionic mechanisms underlying APD prolongation in single cells hold true at the tissue level. Therefore, we investigated conduction and repolarization patterns in the presence of I_{Ks}-HET on the population of human ventricular one-dimensional (1D) fibers.

The original ventricular 1D fiber showed a shorter QT interval with the G229D mutation (**Figure 6A**). In the population of 1D fibers, both significant QT prolongation and QT shortening can be observed (**Figure 6B**). 36 I_{Ks}-HET fibers showed QT prolongation compared to the corresponding I_{Ks}-WT fibers. In the QT prolongation fibers, the AP upstroke was delayed at the end of the I_{Ks}-HET fiber (**Figure 6C**). In these cases, the QRS complex was wider, leading to a longer QT interval (**Figure 6C**, insert). 18 fibers developed depolarization abnormalities under I_{Ks}-HET, which meant no successful depolarization at the end of the fibers (**Figure 6D**), and the QT interval was also significantly affected (**Figure 6D**, insert). Similar results were obtained using transmural fibers (**Supplementary Figure S9**). By comparing the parameters of the different groups of fibers, we found that the conductances of I_{Na}, I_{CaL}, I_{Kr}, I_{Ks}, I_{K1}, I_{NaCa} were significantly different. In both QT prolongation and depolarization abnormalities, the baseline I_{Na} was weak (**Figure 6E**). Models exhibiting depolarization abnormalities also tended to have weak baseline I_{CaL}, I_{K1}, I_{NaCa} and relatively strong I_{Ks}, which explained the danger of G229D mutation presence in their conduction (**Figure 6E**). The fibers showing QT prolongation had the strongest baseline I_{Kr}, which was consistent with the results from the cellular simulations.

In silico Simulations Predict That KCNQ1-G229D Is Capable of Promoting SN Dysfunction by Perturbing Diastolic Depolarization

Sinus node dysfunction and bradycardia has been reported for carriers of different KCNQ1 gain-of-function mutations [S140G (Chen et al., 2003), V141M (Hong et al., 2005), R231C (Henrion et al., 2012), V241F (Ki et al., 2014), and F279I (Moreno et al., 2015)]. Even though SN dysfunction has not been associated

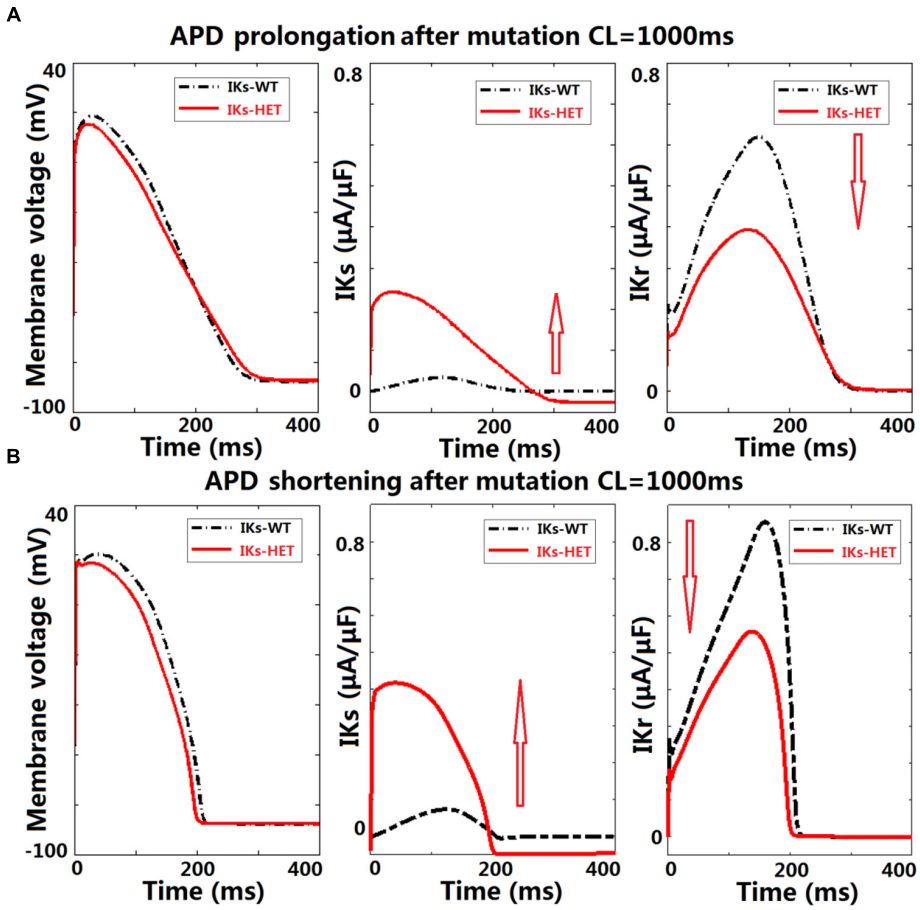

FIGURE 5 | KCNQ1-G229D can lead to ventricular APD prolongation by altering the interplay between I_{Kr} and I_{Ks}. Effects of KCNQ1-G229D mutation (I_{Ks}-HET) on I_{Kr} and I_{Ks} in representative models displaying **(A)** APD prolongation and **(B)** APD shortening, at CL = 1,000 ms. The arrows indicate the change of current magnitude after introducing G229D. In **(A)**, the decrease of I_{Kr} is more significant than the increase of I_{Ks}, while in **(B)** the opposite occurs.

with KCNQ1-G229D (Hasegawa et al., 2014) or in the mutation carriers reported here, the effects of V141M on channel gating (Hong et al., 2005) are similar to those induced by the G229D mutation [this study and (Hasegawa et al., 2014)]. Therefore, we investigated whether the G229D mutation can cause SN dysfunction in populations of sino-atrial node cells. In a recently published human SN model (Fabbri et al., 2017), the normal SN model had a stable heart rate (HR) around 73.7 beats per minute (bpm) (**Figure 7A**). Starting from the same initial condition, when introduced I_{Ks}-HET produced an increasingly stronger I_{Ks} and slower HR, and the sinus rhythm was terminated after 625 s (**Figure 7A**). Plugging the I_{Ks}-HET model developed by (Hasegawa et al., 2014) into the simulation was confirmatory, as this model also led to sinus rhythm termination after 135 s (**Supplementary Figure S10**).

Sinus node activity was related to the interplay between the calcium subsystem and membrane potential in agreement with (Lakatta et al., 2010). For successful spontaneous SN activation, a positive feedback loop between subsarcolemmal calcium (Ca_{sub}) and V_m was needed for the diastolic depolarization. I_{CaL} and I_{NaCa} provided the biggest depolarization current during the upstroke phase, and the net current excluding I_{CaL} and I_{NaCa} was always positive (**Supplementary Figures S11, S12**). The activation of I_{NaCa} was regulated by Ca_{sub}, and during diastolic depolarization, I_{CaL} provided the biggest contribution for the initial accumulation of Ca_{sub} (**Supplementary Figure S13**). During normal diastolic depolarization, the total net current was inward, leading to very slow/limited activation of I_{CaL}, accumulation of Ca_{sub} and enhancement of I_{NaCa} (**Figure 7B**, left columns). At the end of diastolic depolarization, the augmentation of I_{NaCa} was strong enough to result in a significant increase in V_m that further activated I_{CaL}, promoting faster depolarization in a positive feedback manner to initiate the upstroke phase (**Figure 7B**, left columns).

In the SN cell model I_{Ks}-HET produced a much stronger repolarization current to counteract the diastolic depolarization process. At the time of diastolic depolarization interruption (time = 628.5 s), I_{Ks} became so strong that the overall total current became outward. The membrane potential then started to decrease, along with the slow decay of I_{CaL}, Ca_{sub}, and I_{NaCa} activity (**Figure 7B**, right columns). Consequently, positive feedback during the depolarization phase was interrupted.

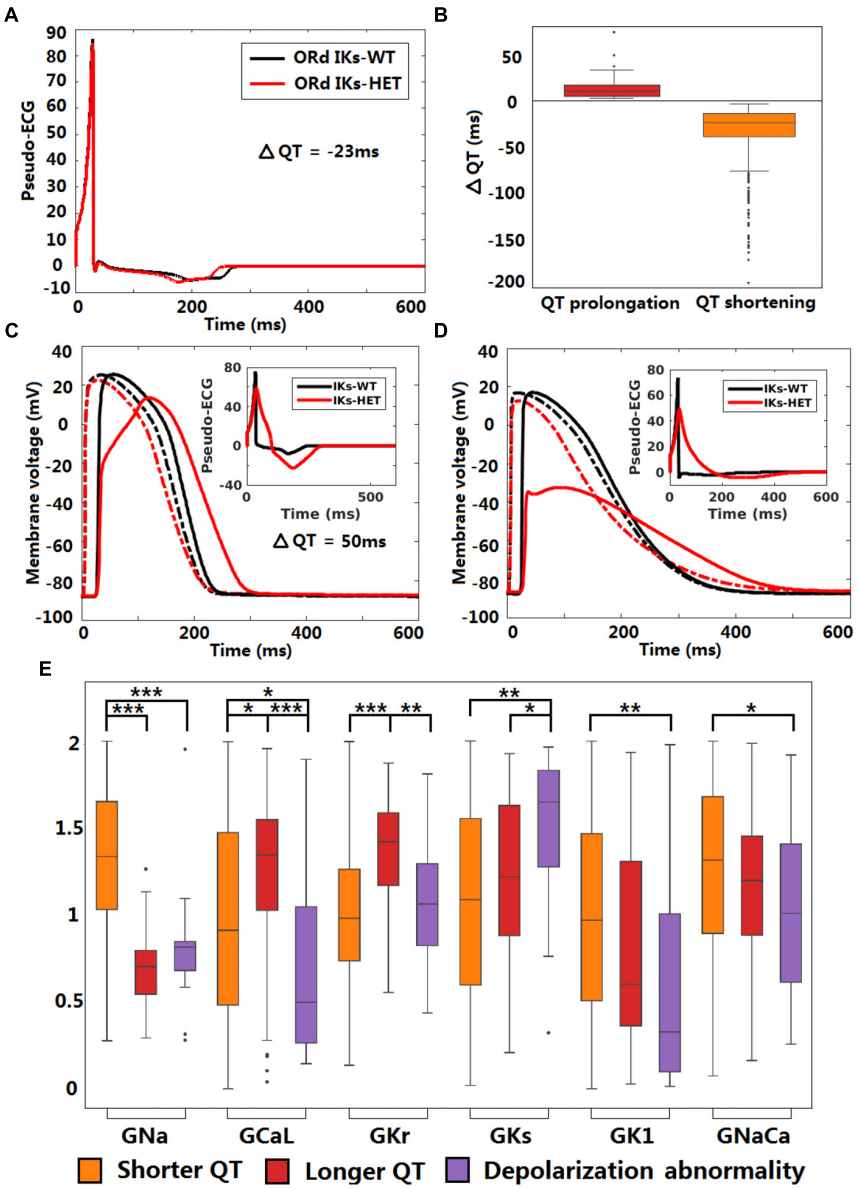

FIGURE 6 | KCNQ1-G229D can impair conduction safety by counteracting action potential upstroke. **(A)** Pseudo-ECG of the original ORd human homogeneous epicardial 1D fiber. **(B)** Longer and shorter QT intervals are possible in the presence of the G229D mutation (I_{Ks}-HET) in Pseudo-ECGs of the population of human epicardial 1D fiber. **(C)** APs of a fiber that showed slower conduction in the presence of the G229D mutation, with the corresponding pseudo-ECG as an insert. **(D)** APs of a fiber that showed a depolarization abnormality in the presence of the G229D mutation, with the corresponding pseudo-ECG as an insert. **(C,D)** There are 100 nodes in the whole fiber, and Node 20 (dashed lines) and Node 80 (solid lines) are at sites near the beginning and the end of the fiber. **(E)** Comparisons of ionic current conductances between the fibers that showed shorter QT, longer QT and depolarization abnormalities in the presence of G229D (***$P < 0.001$, **$P < 0.01$, *$P < 0.05$) (Wilcoxon rank-sum test). Black points indicate extreme values that lie more than 1.5 times the interquartile range away from the top (the 75th percentile) or bottom (the 25th percentile) of the box.

To understand why the carriers of KCNQ1-G229D described in our study and those reported by (Hasegawa et al., 2014) do not present with bradycardia, we used a population of human SN models to explore the effects of heterogeneity in ion channel expression. In the 1,046 human SN cell models, 168 models are robust to I_{Ks}-HET, 153 models became bradycardic, and the rest (725 models) displayed pacemaking failure. By comparing the parameters, we identified differences in I_{Ks}, I_{CaL}, I_{NaCa}, I_{NaK}, and I_{Kr} conductances between models displaying different phenotypes (**Figure 7C**). As expected, the Pacemaking failure group had the highest level of I_{Ks}-HET. A stronger I_{CaL} in the Robust and Bradycardia groups can counteract the changes caused by I_{Ks}-HET and enable safer spontaneous activation. In the Robust group, a stronger inward I_{NaCa} and a weaker outward I_{NaK} contributed to maintaining negative total current during diastolic depolarization. In addition, a stronger I_{Kr} in Robust and

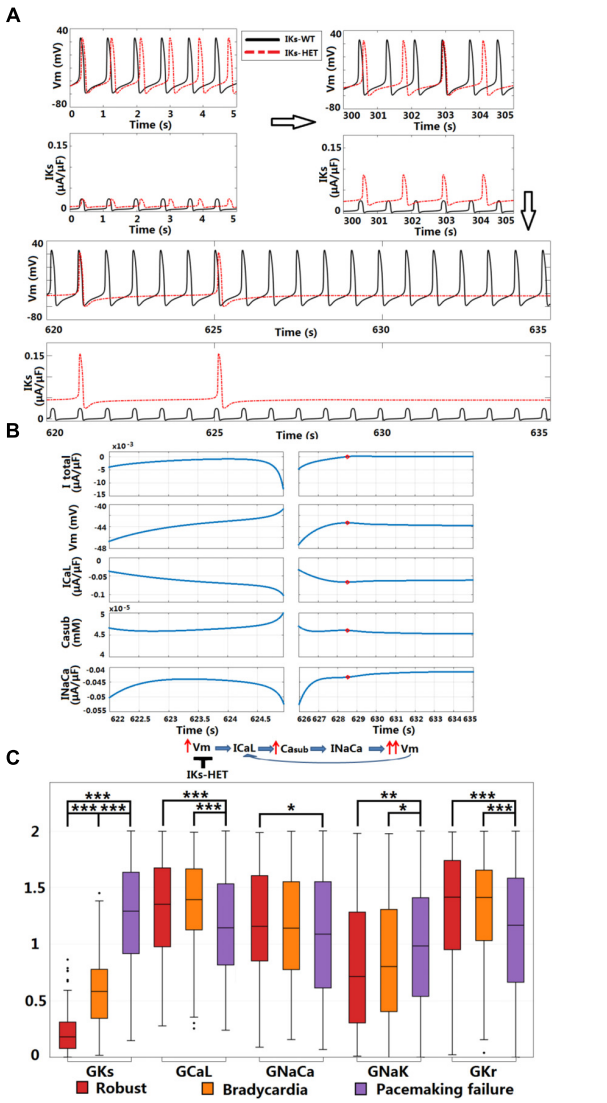

FIGURE 7 | KCNQ1-G229D can cause sinus node dysfunction. **(A)** I_{Ks}-HET presence results in a loss of sinus rhythm. **(B)** Comparison between the last spontaneous activated beat and the failing process under I_{Ks}-HET. The red circles in the right columns indicate the time = 628.5 s when diastolic depolarization was interrupted, and membrane potential started to decrease. **(C)** Parameter comparison between Robust, Bradycardia, and Pacemaking failure groups under I_{Ks}-HET (***$P < 0.001$, **$P < 0.01$, *$P < 0.05$) (Wilcoxon rank-sum test). Black points indicate extreme values that lie more than 1.5 times the interquartile range away from the top (the 75th percentile) or bottom (the 25th percentile) of the box.

Bradycardia groups can counteract the effect of high level I_{CaL}, preventing excessive APD prolongation (**Figure 7C**).

DISCUSSION

In this present study, we investigate the complex phenotypic implications of a gain-of-function mutation in I_{Ks} (KCNQ1-G229D) through a combination of computational modeling and simulation and patch clamp experimental characterization, as well as clinical presentation. We describe members of a family that carry KCNQ1-G229D and report that this mutation underlies a complex phenotype characterized by AF, borderline LQT and sudden death. Our clinical findings correlate well with those reported by Moreton et al. (2013) and Hasegawa et al. (2014). We explored the pathogenic role of this mutation using a combination of *in vitro* experiments and *in silico* simulations in human SN, atrial and ventricular models. In addition to providing further evidence supporting the role of G229D in promoting AF as shown in previous studies, we expand our knowledge of G229D and other gain-of-function KCNQ1 mutations in additional ways. Firstly, we present the first mechanistic investigation into why the G229D mutation (and perhaps other KCNQ1 gain-of function mutations) could be associated with a borderline LQT phenotype. Secondly, we demonstrate that the gain-of-function mutation could promote pro-arrhythmic conduction abnormalities by counteracting the AP depolarization phase and reducing conduction safety. This could be a critical mechanism of sudden cardiac death. Thirdly, we utilize populations of human SN models to provide detailed mechanistic predictions which highlight that KCNQ1-G229D could underlie SN dysfunction. Finally, our findings provide plausible reasons for observed phenotypic variability and insights for the clinical management of these patients.

A Potential Explanation for G229D Associated QT Prolongation

The mechanisms underlying the presence of borderline LQT in G229D carriers [(Moreton et al., 2013; Hasegawa et al., 2014) and this study] and other KCNQ1 gain-of-function mutations (particularly S140G) (Chen et al., 2003; Lundby et al., 2007; Bartos et al., 2011, 2013) are unclear. We used a population of human ventricular cell models to investigate the complex interactions between different currents in the presence of G229D. In addition to APD shortening produced by the standard ventricular model, a subset of the models in the population exhibited APD prolongation. We found that APD prolongation was caused by an interplay between a decrease in I_{Kr} activity and increase in I_{Ks} activity at slow pacing. Based on our simulations, the instantaneous current component produced by KCNQ1-G229D reduces the magnitude of the AP upstroke which leads to a smaller peak membrane voltage and a lower plateau. Consequently, the presence of a lower plateau acts to decrease the activity of I_{Kr} which, in turn, acts to prolong APD. In our fibers showing QT prolongation at the tissue level, I_{Kr} tended to be stronger, suggesting that the I_{Kr}/I_{Ks} interplay mechanism, originally identified in single cells, also holds true at the tissue level.

KCNQ1-G229D May Induce Defects in Conduction

The 1D fiber results also indicate that the presence of KCNQ1-G229D could impair myocardial conduction. Although QRS widening in fibers was not observed clinically in mutation carriers, whole ventricle simulations have shown that QRS width

is more sensitive to the activation pattern in the conduction system rather than myocardial propagation (Cardone-Noott et al., 2016). Therefore, local conduction abnormalities in the myocardium may still be present even with normal QRS width. Local or regional conduction abnormalities may also occur due to heterogeneous expression of KCNQ1/G229D throughout the ventricles (Liu and Antzelevitch, 1995; Viswanathan et al., 1999). Although the fiber simulations we used do not account for the full heterogeneity known to span the human ventricles, they do provide a rough approximation of tissue behavior. Despite these potential limitations, our findings emphasize that G229D could enhance regional differences in conduction and this could contribute to the substrate required for the formation of a lethal arrhythmia.

In silico Modeling Using Human Models Provides Explanations for SN and Atrial Dysfunction

Our human SN model simulations predict that the G229D mutation is likely to underlie SN dysfunction and that this could increase the risk of sinus arrest. By examining variations in ionic current density, our population of SN models may also provide plausible explanations as to why a dysfunctional SN phenotype was not seen by Hasegawa et al. (2014) or in the mutation carriers we report. Based on the mechanisms revealed in this study and those of Fabbri et al. (2017) and Whittaker et al. (2018), disturbed SN activity could be a general action of KCNQ1 gain-of-function mutations that alter channel gating in a similar fashion.

Mechanistically, the G229D mutation has been postulated to cause AF by promoting atrial APD shortening (Hasegawa et al., 2014) and two and three-dimensional tissue models have described that this mutation promotes the sustainment of re-entrant waves thereby increasing susceptibility to atrial arrhythmia (Zulfa et al., 2016). In our baseline and population of models, the G229D mutation results in atrial and ventricular AP shortening, but the average degree of shortening is less for ventricular than atrial APs, which agrees with the findings of Hasegawa et al. (2014) and implies a more prominent effect of the mutation on the human atria.

Clinical Implications for KCNQ1-G229D Carriers

KCNQ1-G229D presents in adults largely as AF, and Class I drugs such as flecainide and quinidine may be prescribed. Based on our simulation results, KCNQ1-G229D could impair conduction by counteracting AP upstroke, and class I sodium channel blockers could exacerbate this. Furthermore, our simulations predict that this mutation could underlie SN dysfunction which has been postulated to act as a substrate for the development of AF (Duhme et al., 2013). Indeed, a trend in disease progression from bradycardia in to persistent AF has been reported for patients that carry the KCNQ1 gain-of-function mutation V241F (Ki et al., 2014). As revealed by our SN simulations, I_{CaL} played a crucial role in the maintenance of normal sinus rhythm in the presence of the G229D mutation. Therefore, drugs with class IV calcium channel blocking actions could unravel bradycardia in G229D mutation carriers with normal sinus rhythm.

Our simulations showed that QT prolongation was primarily observed during bradycardia implying that the prevention of bradycardia to maintain sinus rhythm should be considered in the management of mutation carriers. The use of drugs with a negative chronotropic effect, such as beta-blockers, should therefore be reviewed and device implantation considered for KCNQ1 gain-of-function mutation carriers that present with bradycardia.

Another intriguing observation is that some G229D mutation carriers have died suddenly whilst sleeping [reported in this study and (Moreton et al., 2013)]. Sudden cardiac arrest during sleep has also been reported for a carrier of KCNQ1-R231H (Bartos et al., 2013). Unfortunately, we do not have the necessary clinical information to establish the precise mechanisms underlying these deaths. In LQT1, cardiac arrest normally occurs during exercise and sudden cardiac death during sleep is more a feature of LQT3 (Schwartz et al., 2001). Therefore, we can propose two possible mechanisms: sinus arrest without escape rhythms or a lethal arrhythmia caused by severe QT prolongation. It is worth noting that sinus arrest, due to SN dysfunction, is an unusual cause of death and SN disease in the absence of symptoms is not generally considered prognostically important. In view of these considerations we suspect that the most likely mechanism of sudden death in these patients is the promotion of a lethal arrhythmia by QT prolongation and/or conduction block.

Limitations of the Study

The effects of the G229D mutation on I_{Ks} channel function were modeled in a heterologous expression system. Therefore, it is possible that the expression and kinetics of the mutant channel complex could be distinct in cardiomyocytes. We were limited to this model because: (1) it is not possible to use mice or rats as a model as these species do not use I_{Ks} for cardiac repolarization in adult life (Nerbonne, 2014). (2) The generation of transgenic rabbit models of KCNQ1 mutations (Brunner et al., 2008), would be prohibitively expensive and the higher heart rate of this species would likely confound modeling the effects of the mutation on the SN. (3) The current utility of human induced pluripotent stem derived cardiomyocytes (hiPSC-CMs) for examining I_{Ks} function has been questioned and this may relate to their relative immaturity (Christ et al., 2015). We would also like to highlight that although we propose an explanation for the borderline LQT seen in carriers of the G229D mutation the observed APD prolongations in the population of models subset were relatively mild. This could relate to the potential differences between the function of the mutant channel complex in the heterologous expression system versus in cardiomyocytes or alternatively it could imply that other mechanisms contributing to QT prolongation exist. In the future, the validation of our *in silico* predictions in a physiological system is warranted. hiPSC-CM technology is rapidly advancing, and we hope that in time we will be able to use this model to study the effects of the G229D mutation in human cardiomyocytes that possess adult-like and chamber/region specific electrophysiological properties.

CONCLUSION

By using a combined *in vitro* and *in silico* approach we have explored how the KCNQ1 mutation G229D can underlie the reported phenotype of AF and borderline QT prolongation. In addition, our modeling results suggest that the G229D mutation can cause conduction abnormalities, and can underlie SN dysfunction. Importantly, our results suggest that for G229D mutation carriers (and perhaps for other KCNQ1 gain-of-function mutation carriers), the prescription of beta-blockers, class I sodium channel blockers and compounds with class IV calcium channel blocking properties should be used with caution.

DATA AVAILABILITY

The datasets generated for this study are available on request to the corresponding author.

AUTHOR CONTRIBUTIONS

XZ conducted the *in silico* simulations, took part in the design, analysis and interpretation of the modeling results. AB-O contributed to the design, interpretation, and discussion of the *in silico* results. RS, CK, CD, and DR were involved in collation of patient data and clinical interpretation. KB contributed to the design of the model fitting process. BR took part in the design, interpretation, discussion, and provided the funding for the modeling work. AT and SH conducted the *in vitro* experimentation, overviewed the project design, interpretation and discussion, and provided funding for the *in vitro* experiments. All authors contributed to writing the manuscript.

FUNDING

This work was supported by the British Heart Foundation (BHF) (FS/12/59/29756 to SH, RG/15/15/31742 to AT, FS/17/22/32644 to AB-O, and SP/15/9/31605, RG/15/6/31436, PG/14/59/31000, RG/14/1/30588, P47352/Centre for Regenerative Medicine to CD); the National Institute for Health Research Barts Biomedical Research Centre to AT and SH; Wellcome Trust (100246/Z/12/Z to BR and XZ); the National Centre for the Replacement, Refinement and Reduction of Animals in Research (NC/P001076/1 to AB-O, CRACK-IT. FULL PROPOSAL code 35911-259146., NC/K000225/1 to CD); Engineering and Physical Sciences Research Council Impact Acceleration Award (EP/K503769/1 to BR); the CompBioMed project (No. 675451 to BR); the Oxford BHF Centre of Research Excellence (RE/08/004/23915 and RE/13/1/30181 to BR); China Scholarship Council to XZ; BIRAX (04BX14CDLG to CD); Medical Research Council (MR/M017354/1 to CD); and Heart Research United Kingdom (TRP01/12 to CD).

ACKNOWLEDGMENTS

The authors would like to acknowledge the helpful discussions with Dr. Alan Fabbri. This work used the ARCHER UK National Supercomputing Service (http://www.archer.ac.uk).

SUPPLEMENTARY MATERIAL

The Supplementary Material for this article can be found online at: https://www.frontiersin.org/articles/10.3389/fphys.2019.00259/full#supplementary-material

REFERENCES

Adeniran, I., Whittaker, D. G., El Harchi, A., Hancox, J. C., and Zhang, H. (2017). 'In silico investigation of a KCNQ1 mutation associated with short QT syndrome'. *Sci. Rep.* 7:8469. doi: 10.1038/s41598-017-08367-2

Barhanin, J., Lesage, F., Guillemare, E., Fink, M., Lazdunski, M., and Romey, G. (1996). 'K(V)LQT1 and lsK (minK) proteins associate to form the I(Ks) cardiac potassium current'. *Nature* 384, 78–80. doi: 10.1038/384078a0

Bartos, D. C., Anderson, J. B., Bastiaenen, R., Johnson, J. N., Gollob, M. H., Tester, D. J., et al. (2013). 'A KCNQ1 mutation causes a high penetrance for familial atrial fibrillation'. *J. Cardiovasc. Electrophysiol.* 24, 562–569. doi: 10.1111/jce.12068

Bartos, D. C., Duchatelet, S., Burgess, D. E., Klug, D., Denjoy, I., Peat, R., et al. (2011). 'R231C mutation in KCNQ1 causes long QT syndrome type 1 and familial atrial fibrillation'. *Heart Rhythm* 8, 48–55. doi: 10.1016/j.hrthm.2010.09.010

Bazett, H. C. (1920). 'An analysis of the time-relations of electrocardiograms.'. *Heart J. Study Circ.* 7, 353–370.

Bellocq, C., van Ginneken, A. C., Bezzina, C. R., Alders, M., Escande, D., Mannens, M. M., et al. (2004). 'Mutation in the KCNQ1 gene leading to the short QT-interval syndrome'. *Circulation* 109, 2394–2397. doi: 10.1161/01.CIR.0000130409.72142.FE

Britton, O. J., Bueno-Orovio, A., Van Ammel, K., Lu, H. R., Towart, R., Gallacher, D. J., et al. (2013). 'Experimentally calibrated population of models predicts and explains intersubject variability in cardiac cellular electrophysiology'. *Proc. Natl. Acad. Sci. U.S.A.* 110, E2098–E2105. doi: 10.1073/pnas.1304382110

Brunner, M., Peng, X., Liu, G. X., Ren, X. Q., Ziv, O., Choi, B. R., et al. (2008). 'Mechanisms of cardiac arrhythmias and sudden death in transgenic rabbits with long QT syndrome'. *J. Clin. Invest.* 118, 2246–2259. doi: 10.1172/JCI33578

Cardone-Noott, L., Bueno-Orovio, A., Minchole, A., Zemzemi, N., and Rodriguez, B. (2016). 'Human ventricular activation sequence and the simulation of the electrocardiographic QRS complex and its variability in healthy and intraventricular block conditions'. *Europace* 18, iv4–iv15. doi: 10.1093/europace/euw346

Chen, Y. H., Xu, S. J., Bendahhou, S., Wang, X. L., Wang, Y., Xu, W. Y., et al. (2003). 'KCNQ1 gain-of-function mutation in familial atrial fibrillation'. *Science* 299, 251–254. doi: 10.1126/science.1077771

Christ, T., Horvath, A., and Eschenhagen, T. (2015). 'LQT1-phenotypes in hiPSC: are we measuring the right thing?'. *Proc. Natl. Acad. Sci. U.S.A.* 112:E1968. doi: 10.1073/pnas.1503347112

Das, S., Makino, S., Melman, Y. F., Shea, M. A., Goyal, S. B., Rosenzweig, A., et al. (2009). 'Mutation in the S3 segment of KCNQ1 results in familial lone atrial fibrillation'. *Heart Rhythm* 6, 1146–1153. doi: 10.1016/j.hrthm.2009.04.015

Duhme, N., Schweizer, P. A., Thomas, D., Becker, R., Schroter, J., Barends, T. R., et al. (2013). 'Altered HCN4 channel C-linker interaction is associated with familial tachycardia-bradycardia syndrome and atrial fibrillation'. *Eur. Heart J.* 34, 2768–2775. doi: 10.1093/eurheartj/ehs391

Fabbri, A., Fantini, M., Wilders, R., and Severi, S. (2017). 'Computational analysis of the human sinus node action potential: model development and effects of mutations'. *J. Physiol.* 595, 2365–2396. doi: 10.1113/JP273259

Gima, K., and Rudy, Y. (2002). 'Ionic current basis of electrocardiographic waveforms: a model study'. *Circ. Res.* 90, 889–896. doi: 10.1161/01.RES.0000016960.61087.86

Grandi, E., Pandit, S. V., Voigt, N., Workman, A. J., Dobrev, D., Jalife, J., et al. (2011). 'Human atrial action potential and Ca2+ model: sinus rhythm and chronic atrial fibrillation'. *Circ. Res.* 109, 1055–1066. doi: 10.1161/CIRCRESAHA.111.253955

Hancox, J. C., Kharche, S., El Harchi, A., Stott, J., Law, P., and Zhang, H. (2014). 'In silico investigation of a KCNQ1 mutation associated with familial atrial fibrillation'. *J. Electrocardiol.* 47, 158–165. doi: 10.1016/j.jelectrocard.2013.12.004

Harmer, S. C., Mohal, J. S., Royal, A. A., McKenna, W. J., Lambiase, P. D., and Tinker, A. (2014). 'Cellular mechanisms underlying the increased disease severity seen for patients with long QT syndrome caused by compound mutations in KCNQ1'. *Biochem. J.* 462, 133–142. doi: 10.1042/BJ20140425

Hasegawa, K., Ohno, S., Ashihara, T., Itoh, H., Ding, W. G., Toyoda, F., et al. (2014). 'A novel KCNQ1 missense mutation identified in a patient with juvenile-onset atrial fibrillation causes constitutively open IKs channels'. *Heart Rhythm* 11, 67–75. doi: 10.1016/j.hrthm.2013.09.073

Henrion, U., Zumhagen, S., Steinke, K., Strutz-Seebohm, N., Stallmeyer, B., Lang, F., et al. (2012). 'Overlapping cardiac phenotype associated with a familial mutation in the voltage sensor of the KCNQ1 channel'. *Cell Physiol. Biochem.* 29, 809–818. doi: 10.1159/000178470

Hong, K., Piper, D. R., Diaz-Valdecantos, A., Brugada, J., Oliva, A., Burashnikov, E., et al. (2005). 'De novo KCNQ1 mutation responsible for atrial fibrillation and short QT syndrome in utero'. *Cardiovasc. Res.* 68, 433–440. doi: 10.1016/j.cardiores.2005.06.023

Kharche, S., Adeniran, I., Stott, J., Law, P., Boyett, M. R., Hancox, J. C., et al. (2012). 'Pro-arrhythmogenic effects of the S140G KCNQ1 mutation in human atrial fibrillation - insights from modelling'. *J. Physiol.* 590, 4501–4514. doi: 10.1113/jphysiol.2012.229146

Ki, C. S., Jung, C. L., Kim, H. J., Baek, K. H., Park, S. J., On, Y. K., et al. (2014). 'A KCNQ1 mutation causes age-dependant bradycardia and persistent atrial fibrillation'. *Pflug. Arch.* 466, 529–540. doi: 10.1007/s00424-013-1337-6

Lakatta, E. G., Maltsev, V. A., and Vinogradova, T. M. (2010). 'A coupled SYSTEM of intracellular Ca2+ clocks and surface membrane voltage clocks controls the timekeeping mechanism of the heart's pacemaker'. *Circ. Res.* 106, 659–673. doi: 10.1161/CIRCRESAHA.109.206078

Liu, D. W., and Antzelevitch, C. (1995). 'Characteristics of the delayed rectifier current (IKr and IKs) in canine ventricular epicardial, midmyocardial, and endocardial myocytes. a weaker IKs contributes to the longer action potential of the M cell. *Circ. Res.* 76, 351–365. doi: 10.1161/01.RES.76.3.351

Lundby, A., Ravn, L. S., Svendsen, J. H., Olesen, S. P., and Schmitt, N. (2007). 'KCNQ1 mutation Q147R is associated with atrial fibrillation and prolonged QT interval'. *Heart Rhythm* 4, 1532–1541. doi: 10.1016/j.hrthm.2007.07.022

Maleckar, M. M., Greenstein, J. L., Giles, W. R., and Trayanova, N. A. (2009). 'K+ current changes account for the rate dependence of the action potential in the human atrial myocyte'. *Am. J. Physiol. Heart Circ. Physiol.* 297, H1398–H1410. doi: 10.1152/ajpheart.00411.2009

Moreno, C., Oliveras, A., de la Cruz, A., Bartolucci, C., Munoz, C., Salar, E., et al. (2015). 'A new KCNQ1 mutation at the S5 segment that impairs its association with KCNE1 is responsible for short QT syndrome'. *Cardiovasc. Res.* 107, 613–623. doi: 10.1093/cvr/cvv196

Moreton, N., Venetucci, L., Garratt, C. J., Newman, W., and Metcalfe, K. (2013). *'Atrial Fibrillation, Long QT Syndrome and Sudden Cardiac Death Found in an Extended Family With KCNQ1 C.686G > A (P.G229D).* Available at: http://www.genomicmedicine.org/wp-content/uploads/2014/01/Cardiovascular-Genetics-Symposium-Abstracts.pdf

Muszkiewicz, A., Britton, O. J., Gemmell, P., Passini, E., Sanchez, C., Zhou, X., et al. (2016). 'Variability in cardiac electrophysiology: using experimentally-calibrated populations of models to move beyond the single virtual physiological human paradigm'. *Prog. Biophys. Mol. Biol.* 120, 115–127. doi: 10.1016/j.pbiomolbio.2015.12.002

Muszkiewicz, A., Liu, X., Bueno-Orovio, A., Lawson, B. A. J., Burrage, K., Casadei, B., et al. (2018). 'From ionic to cellular variability in human atrial myocytes: an integrative computational and experimental study. *Am. J. Physiol. Heart Circ. Physiol.* 314, H895–H916. doi: 10.1152/ajpheart.00477.2017

Nerbonne, J. M. (2014). 'Mouse models of arrhythmogenic cardiovascular disease: challenges and opportunities'. *Curr. Opin. Pharmacol.* 15, 107–114. doi: 10.1016/j.coph.2014.02.003

O'Hara, T., Virag, L., Varro, A., and Rudy, Y. (2011). 'Simulation of the undiseased human cardiac ventricular action potential: model formulation and experimental validation'. *PLoS Comput. Biol.* 7:e1002061. doi: 10.1371/journal.pcbi.1002061

Passini, E., Minchole, A., Coppini, R., Cerbai, E., Rodriguez, B., Severi, S., et al. (2016). 'Mechanisms of pro-arrhythmic abnormalities in ventricular repolarisation and anti-arrhythmic therapies in human hypertrophic cardiomyopathy'. *J. Mol. Cell Cardiol.* 96, 72–81. doi: 10.1016/j.yjmcc.2015.09.003

Pitt-Francis, J., Pathmanathan, P., Bernabeu, M. O., Bordas, R., Cooper, J., Fletcher, A. G., et al. (2009). 'Chaste: a test-driven approach to software development for biological modelling'. *Comp. Phys. Commun.* 180, 2452–2471. doi: 10.1016/j.cpc.2009.07.019

Sanchez, C., Bueno-Orovio, A., Wettwer, E., Loose, S., Simon, J., Ravens, U., et al. (2014). 'Inter-subject variability in human atrial action potential in sinus rhythm versus chronic atrial fibrillation. *PLoS One* 9:e105897. doi: 10.1371/journal.pone.0105897

Sanguinetti, M. C., Curran, M. E., Zou, A., Shen, J., Spector, P. S., Atkinson, D. L., et al. (1996). 'Coassembly of K(V)LQT1 and minK (IsK) proteins to form cardiac I(Ks) potassium channel'. *Nature* 384, 80–83. doi: 10.1038/384080a0

Schwartz, P. J., Priori, S. G., Spazzolini, C., Moss, A. J., Vincent, G. M., Napolitano, C., et al. (2001). 'Genotype-phenotype correlation in the long-QT syndrome: gene-specific triggers for life-threatening arrhythmias'. *Circulation* 103, 89–95. doi: 10.1161/01.CIR.103.1.89

Thomas, A. M., Harmer, S. C., Khambra, T., and Tinker, A. (2011). 'Characterization of a binding site for anionic phospholipids on KCNQ1'. *J. Biol. Chem.* 286, 2088–2100. doi: 10.1074/jbc.M110.153551

Viswanathan, P. C., Shaw, R. M., and Rudy, Y. (1999). 'Effects of IKr and IKs heterogeneity on action potential duration and its rate dependence: a simulation study'. *Circulation* 99, 2466–2474. doi: 10.1161/01.CIR.99.18.2466

Wang, Q., Curran, M. E., Splawski, I., Burn, T. C., Millholland, J. M., VanRaay, T. J., et al. (1996). 'Positional cloning of a novel potassium channel gene: KVLQT1 mutations cause cardiac arrhythmias'. *Nat. Genet.* 12, 17–23. doi: 10.1038/ng0196-17

Whittaker, D. G., Colman, M. A., Ni, H., Hancox, J. C., and Zhang, H. (2018). 'Human atrial arrhythmogenesis and sinus bradycardia in KCNQ1-linked short QT syndrome: insights from computational modelling'. *Front. Physiol.* 9:1402. doi: 10.3389/fphys.2018.01402

Wu, Z. J., Huang, Y., Fu, Y. C., Zhao, X. J., Zhu, C., Zhang, Y., et al. (2015). 'Characterization of a chinese KCNQ1 mutation (R259H) that shortens repolarization and causes short QT syndrome 2'. *J. Geriatr. Cardiol.* 12, 394–401. doi: 10.11909/j.issn.1671-5411.2015.04.002

Zhou, X., Bueno-Orovio, A., Orini, M., Hanson, B., Hayward, M., Taggart, P., et al. (2016). 'In vivo and in silico investigation into mechanisms of frequency dependence of repolarization alternans in human ventricular cardiomyocytes'. *Circ. Res.* 118, 266–278. doi: 10.1161/CIRCRESAHA.115.307836

Zulfa, I., Shim, E. B., Song, K. S., and Lim, K. M. (2016). 'Computational simulations of the effects of the G229D KCNQ1 mutation on human atrial fibrillation'. *J. Physiol. Sci.* 66, 407–415. doi: 10.1007/s12576-016-0438-3

Conflict of Interest Statement: The authors declare that the research was conducted in the absence of any commercial or financial relationships that could be construed as a potential conflict of interest.

frontiers in Physiology

ORIGINAL RESEARCH
published: 22 March 2019
doi: 10.3389/fphys.2019.00237

In silico Optimization of Left Atrial Appendage Occluder Implantation Using Interactive and Modeling Tools

*Ainhoa M. Aguado[1], Andy L. Olivares[1], Carlos Yagüe[1], Etelvino Silva[2], Marta Nuñez-García[1], Álvaro Fernandez-Quilez[1], Jordi Mill[1], Ibai Genua[1], Dabit Arzamendi[2], Tom De Potter[3], Xavier Freixa[4] and Oscar Camara[1]**

[1] PhySense, Department of Information and Communication Technologies, Universitat Pompeu Fabra, Barcelona, Spain, [2] Division of Interventional Cardiology, Hospital de la Santa Creu i Sant Pau, Universitat Autònoma de Barcelona, Barcelona, Spain, [3] Arrhythmia Unit, Department of Cardiology, Cardiovascular Center, Aalst, Belgium, [4] Department of Cardiology, Hospital Clínic de Barcelona, Universitat de Barcelona, Barcelona, Spain

OPEN ACCESS

Edited by:
Javier Saiz,
Universitat Politècnica de València, Spain

Reviewed by:
Lucy T. Zhang,
Rensselaer Polytechnic Institute, United States
Joakim Sundnes,
Simula Research Laboratory, Norway

***Correspondence:**
Oscar Camara
oscar.camara@upf.edu

Specialty section:
This article was submitted to Computational Physiology and Medicine, a section of the journal Frontiers in Physiology

Received: *16 October 2018*
Accepted: *22 February 2019*
Published: *22 March 2019*

Citation:
Aguado AM, Olivares AL, Yagüe C, Silva E, Nuñez-García M, Fernandez-Quilez Á, Mill J, Genua I, Arzamendi D, De Potter T, Freixa X and Camara O (2019) In silico Optimization of Left Atrial Appendage Occluder Implantation Using Interactive and Modeling Tools. Front. Physiol. 10:237. doi: 10.3389/fphys.2019.00237

According to clinical studies, around one third of patients with atrial fibrillation (AF) will suffer a stroke during their lifetime. Between 70 and 90% of these strokes are caused by thrombus formed in the left atrial appendage. In patients with contraindications to oral anticoagulants, a left atrial appendage occluder (LAAO) is often implanted to prevent blood flow entering in the LAA. A limited range of LAAO devices is available, with different designs and sizes. Together with the heterogeneity of LAA morphology, these factors make LAAO success dependent on clinician's experience. A sub-optimal LAAO implantation can generate thrombi outside the device, eventually leading to stroke if not treated. The aim of this study was to develop clinician-friendly tools based on biophysical models to optimize LAAO device therapies. A web-based 3D interactive virtual implantation platform, so-called VIDAA, was created to select the most appropriate LAAO configurations (type of device, size, landing zone) for a given patient-specific LAA morphology. An initial LAAO configuration is proposed in VIDAA, automatically computed from LAA shape features (centreline, diameters). The most promising LAAO settings and LAA geometries were exported from VIDAA to build volumetric meshes and run Computational Fluid Dynamics (CFD) simulations to assess blood flow patterns after implantation. Risk of thrombus formation was estimated from the simulated hemodynamics with an index combining information from blood flow velocity and complexity. The combination of the VIDAA platform with *in silico* indices allowed to identify the LAAO configurations associated to a lower risk of thrombus formation; device positioning was key to the creation of regions with turbulent flows after implantation. Our results demonstrate the potential for optimizing LAAO therapy settings during pre-implant planning based on modeling tools and contribute to reduce the risk of thrombus formation after treatment.

Keywords: left atrial appendage occlusion, Computational Fluid Dynamics, *in silico* optimization of therapies, web-based implantation platform, atrial fibrillation

1. INTRODUCTION

Atrial Fibrillation (AF) is the most common cardiac arrhythmia diagnosed in clinical practice, affecting around 0.4–1% of the general population (Singh and Holmes, 2010). The atria beat irregularly during AF, which leads to ineffective blood flow pumping to the ventricles. The consequences of AF have been clearly established in multiple studies, being one of them the increased risk of stroke; one out of three ischemic strokes is related to AF (Boston Scientific, 2018). Between 70 and 90% of AF-related strokes originate from thrombus formed in a cavity of the left atrium, the left atrial appendage (LAA) (Wang et al., 2010; Lee et al., 2015). The LAA is a contractile reservoir and a decompression chamber, depending on the cardiac cycle phase (Fatkin et al., 1994; Al-Saady et al., 1999). It acts as a suction during ventricular systole and during diastole as a conduit. In addition, the LAA is characterized by its high morphological variability, in parameters such as size, height, smoothness or number of lobes. The different LAA morphologies are often classified into four categories: chicken wing, cauliflower, windsock and cactus (Di Biase et al., 2012). Left atrial motion irregularity due to AF causes a deceleration of blood flow and stasis, increasing the risk of thrombus formation in the LAA (Markl et al., 2016). The thrombus formed can then travel through the circulatory system to the brain, causing a cardioembolic stroke.

Oral anticoagulation (OAC) therapy is usually prescribed on those AF patients older than 65 years old (Morillo et al., 2017) to reduce the risk of thrombus formation. When OAC therapy is not appropriate, due to high risk of bleeding or because of patient's limitations, a physical LAA closure is performed with the implantation of a left atrial appendage occlusion (LAAO) device or surgery-based clipping (Le et al., 2014). LAAO devices are implanted percutaneously by a femoral vein approach under fluoroscopic and echocardiographic guidance. The most used LAAO devices available in the market (see **Figure 1**) are the Watchman (Boston Scientific, 2018) and the Amplatzer Amulet (Abbott, 2018), even if new promising devices such as the Lambre (Park et al., 2018) and the Wavecrest (Saw and Lempereur, 2014) are being proposed every year. In a LAAO procedure, the large intra-subject anatomical variation of the LAA influences the individual implantation. Therefore, biomedical images are acquired to have good anatomical knowledge of the cavity, before and during the intervention. In most clinical centers X-ray and transesophageal echocardiography (TEE) images are used to characterize the LAA morphology during the intervention to support decisions on device implantation. Other imaging modalities such as Computed Tomography (CT) (Chow et al., 2017) and 3D Rotational Angiography (3DRA) (De Potter et al., 2018) are also being explored in advanced hospitals to have higher-resolution structural information before and during the intervention, respectively. The ostium (interface betwen LA and LAA) dimensions and height/depth of the LAA cavity (Morillo et al., 2017) are critical LAA shape parameters to individualize the size of the implanted device and the landing zone (location where the device will be released). Appropriate sizing of the device, achieving a complete clinical closure, allows the procedure to be finished earlier since a second device is not required. A minimal leakage of jet blood flow entering into the LAA after device implantation is the standard criteria to define a successful closure (López-Mínguez et al., 2014). Unfortunately, LAA shape parameters are usually estimated from medical images with manual tools, being difficult to standardize criteria to objectively define them. Moreover, values of these parameters coming from different imaging modalities differ substantially due to their respective spatial resolution and limitations (López-Mínguez et al., 2014).

Beyond their morphology, studying LA and LAA hemodynamics is also important before and after LAAO treatment. The Virchow's triad defines blood hypercoagulability, hemodynamics changes and endothelial wall injury dysfunction as the three main players in thrombus formation (Chung and Lip, 2003). Left atrial appendage blood flow velocities below some threshold (<0.2 m/s) have been associated to the presence of thrombus in the LAA (Beigel et al., 2014). Unfortunately, most clinical studies (Beigel et al., 2014) involving the LAA, usually based on echocardiographic images, only report a single blood flow velocity value in one point in space (LAA ostium) and in time (end diastole), which constitutes an over-simplification of the complex hemodynamics in the LA and LAA. Detailed hemodynamics characterization is becoming possible these days with advanced 4D-flow magnetic resonance imaging technique, but there are few studies in the LA (Casas et al., 2017; Cibis et al., 2017a,b) and only one in the LAA (Markl et al., 2016). Some researchers (Zhang and Gay, 2008; Koizumi et al., 2015; Vedula et al., 2015; Otani et al., 2016; Olivares et al., 2017; Bosi et al., 2018; García-Isla et al., 2018) have developed biophysical modeling pipelines for a more detailed *in silico* analysis of LAA blood flow patterns with Computational Fluid Dynamics (CFD) simulations. However, none of these works studied the effect of implanting a LAAO device with different settings on atrial hemodynamics. In addition, as in the majority of biomedical applications, these biophysical models remain an engineering tool far from being used to support clinicians on their decisions.

Even if LAAO devices are generally becoming an accepted option when OAC therapy fails, it still exists controversy concerning the safety and the real clinical benefit of LAAO-based therapy. Although it seems to be effective, short- and long-term consequences are not fully known (Mandrola et al., 2018). As an example, a recent clinical trial (Fauchier et al., 2018) reported a high probability of getting a device-related thrombus (around 7%). Moreover, LAAO is recognized as a technically demanding procedure, requiring rigorous training and skills in order to reduce complications (Tzikas et al., 2016). However, there is a lack of advanced computational tools to provide a complete, objective and patient-specific characterization of LAA morphology and function to assist clinicians on the challenging LAAO device selection and planning steps. The aim of this work was to develop a clinician-friendly visualization tool to be combined with biophysical modeling for LAAO therapy optimization. A web-based 3D interactive virtual implantation platform, so-called VIDAA (Virtual Implantation and Device selection in left Atrial Appendages), was designed and implemented to

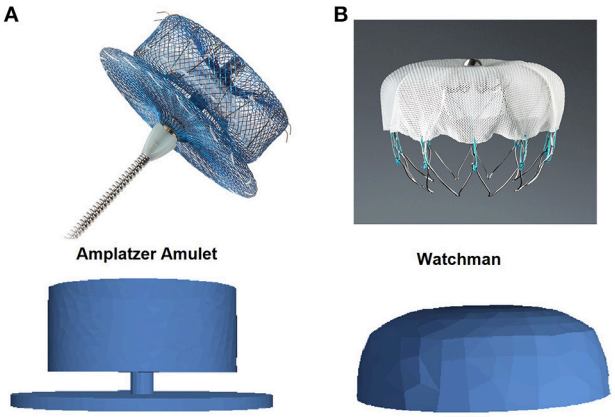

FIGURE 1 | Pictures (top) and Computational-Aided Design models (bottom) of left atrial appendage occlusion devices. **(A)** Amplatzer Amulet (Abbott, 2018); **(B)** Watchman (Boston Scientific, 2018).

jointly visualize the LA anatomy of an individual patient and different possible LAAO configurations. The VIDAA platform initially proposes LAAO setting parameters estimated after a morphological analysis of the LAA under study. The clinician later can interactively vary device parameters in VIDAA and export outside the platform the most promising configurations. Computational Fluid Dynamics (CFD) simulations were then run with a commercial solver for several LAAO configurations extracted from VIDAA to estimate their corresponding risk of thrombus formation after implantation. As a first proof of concept, the VIDAA platform was tested on retrospective data of four non-valvular AF patients that underwent a LAA closure.

2. MATERIALS AND METHODS

The computational workflow designed in this work (see **Figure 2**) is a planning tool that, together with computational modeling, provides enhanced individualized information to the clinician before the intervention. In all analyzed cases, surface meshes of the LA were reconstructed from binary masks obtained segmenting high-resolution 3D medical images (CT and 3DRA). In the next step, morphological indices characterizing patient-specific LAA shapes were automatically calculated. Based on these LAA shape-based indices, a range of optimal LAAO device parameters (size, position) were estimated. The optimal configuration for the two most popular devices (e.g., Watchman and Amplatzer Amulet) could then interactively be explored together with a 3D rendering of the LA in the web-based VIDAA platform. The clinician could manually modify several LAAO parameters to better understand the case under study and plan the intervention. Once a given LAAO configuration was considered appropriate by the clinician, the VIDAA platform exported all data (e.g., meshes and their spatial relationship) that will define the geometrical domain where CFD simulations were run outside VIDAA with a commercial software. Simulation results were post-processed to derive *in silico* hemodynamics indices estimating the risk of thrombus formation for a given LAA and device setting. The VIDAA platform in combination with CFD simulations then allowed the clinician to decide, prior to the intervention, which device configuration was safer, in terms of thrombus formation.

TABLE 1 | Patient and device information.

Patient	Medical image	CHAD2VASC	Device type	Device size (mm)
1	3DRA	3	Watchman	27
2	3DRA	3	Watchman	30
3	3DRA	6	Watchman	27
4	CT	5	Amplatzer Amulet	22

3DRA, 3D Rotational Angiography; CT, Computed Tomography; CHAD2VASC, clinical index characterizing the risk of thrombus formation.

2.1. Patient-Specific Imaging Data and Processing

Three-dimensional medical images were available for the four AF patients analyzed in this study: 3DRA images of three patients from OLV Hospital (Aalst, Belgium); and a CT image of one patient from Hospital Clínic de Barcelona (Spain). The OLV Hospital and Hospital Clínic de Barcelona ethical committees approved this study and written informed consent was obtained from every participant before the procedure. Watchman devices were implanted to patients at OLV Hospital while an Amplatzer Amulet was the choice at Hospital Clínic de Barcelona (see **Table 1**). All patients had persistent non-valvular atrial fibrillation with high risk of thrombus formation (e.g., CHAD2VASC > 2).

An Innova^{TM} monoplane fluoroscopy system (GE Healthcare, LLC, Waukesha,WI) was used at OLV Hospital to acquire the 3DRA images, with 0.23 or 0.45 mm pixel size for 512 or 256 isotropic voxels, respectively. Before and during the injection, the right ventricle was burst paced at a cycle length of 200 ms during end-expiratory apnea to interrupt the blood flow through the LA. All datasets were segmented by an experienced operator on the Advantage Workstation (GE Healthcare) using the Innova 3D software to reconstruct the LA, which is based on threshold and region-growing semi-automatic segmentation techniques. The CT image at Hospital Clínic de Barcelona was acquired using a Siemens^{TM} machine, synchronized with ECG and supplying 80 ml of contrast, having a volumetric pixel size of $0.33 \times 0.33 \times 0.40$ mm for an in-plane matrix of 512 pixels and 430 slices. The ITK-Snap[1] software (Yushkevich et al., 2006) was used to semi-automatically segment the LA in the CT image (also with region growing and threshold-based techniques, plus manual corrections). The LA binary masks from segmenting 3DRA and CT images were the basis to construct surface meshes with the Marching Cubes method for subsequent morphological analysis and simulations. A 2D plane was manually selected by the operator to define the ostium and the LAA in the LA 3D surface mesh.

[1]www.itksnap.org

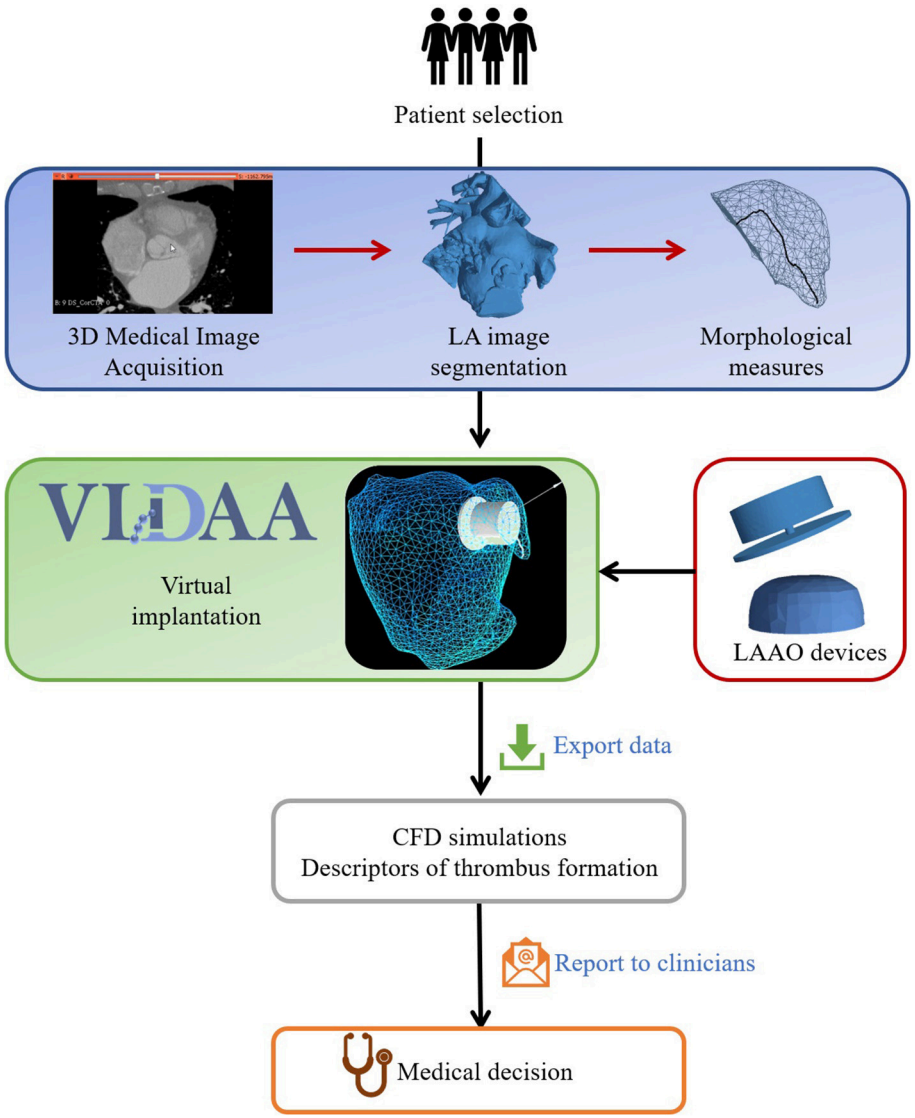

FIGURE 2 | Computational workflow to recommend optimal left atrial appendage occlusion (LAAO) settings for a selected patient. The first stage produces LAA morphological measures from LA segmentations obtained on three-dimensional medical images. Computational 3D renderings of LA/LAA geometries are then jointly visualized with morphological measures and Computer-Aided Design models of LAAO devices in the VIDAA platform. The VIDAA platform allows an interactive and individualized virtual implantation of LAAO devices, generating multiple configurations that can be exported for further processing. Computational-Fluid Dynamics (CFD) simulations run on the exported LAAO configurations provide hemodynamics descriptors to estimate the risk of thrombus formation for each case, which are finally reported to clinicians to support their decisions.

2.1.1. Left Atrial Appendage Morphological Parameters and Optimal Device Configuration

Two types of morphological parameters were automatically estimated from LAA surface meshes: ostium- and centreline-based parameters. The ostium area, perimeter and principal axes were computed directly from surface mesh elements labeled as ostium after the segmentation. The LAA centreline (see and example in **Figure 3**) was obtained following a marching algorithm (Genua et al., 2019), where its starting point (the furthest point of the LAA) and the centreline direction to the ostium were computed applying a heat transfer propagation simulation to the LAA volumetric mesh. Once the centreline was estimated, several transversal 2D planes, perpendicular to its main direction, were selected along its length to compute their maximal (D1) and minimal (D2) diameters.

The centreline-based parameters were used to automatically estimate the optimal LAAO configuration for the analyzed anatomy, as illustrated in **Figure 3**. Following criteria defined by our experienced clinicians, device (center) positioning was set at a geodesic distance along the centreline of 10 and 13 mm from the ostium for the Amplatzer Amulet and the Watchman, respectively. The diameters (D1, D2) of the transversal 2D plane

centered at the optimal device positioning were then computed. The initial orientation of the LAAO device was set perpendicular to the centreline. Based on empirical algorithms from clinicians and official device instructions, the most appropriate LAAO device sizes (three for the Amplatzer Amulet and two for the Watchman) were initially selected. For instance, optimal Amplatzer Amulet device sizes were established following the current clinical protocol at Hospital Clínic de Barcelona: 2–5 or 3–6 mm are usually added to the average mean diameter (between D1 and D2) if imaging data comes from CT or TEE, respectively. If the obtained size is smaller than D1, additional 2–5 mm are added. Finally, only devices ensuring at least a 10% of compression of original size after implantation were selected. Fulfilling the compression-based criteria increments the likelihood of getting the LAAO device attached to the wall for a successful closure, without creating too high stresses on the LAA. The optimal sizes for the Watchman device (see Table A.1 in **Appendix 1**) were selected based on D1, following official device instructions.

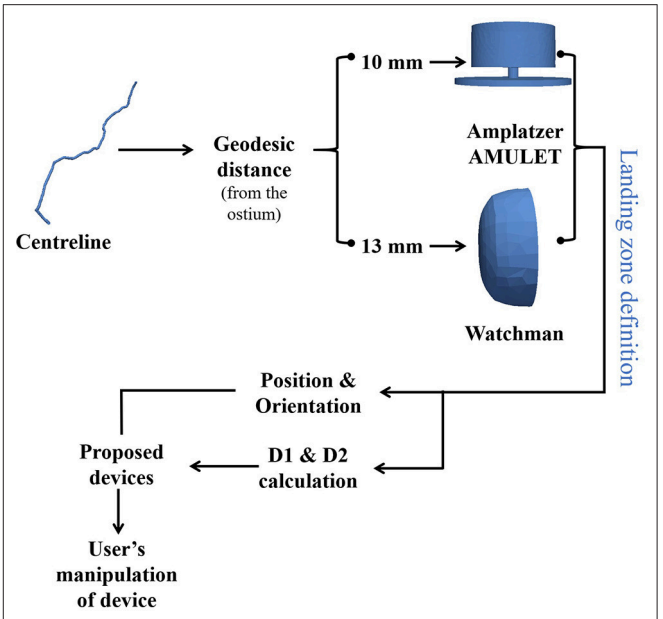

FIGURE 3 | Computational pipeline to obtain optimal left atrial appendage occlusion (LAAO) device configuration. Device positioning (e.g., landing zone) is initially estimated at a certain geodesic distance from the ostium following the LAA centreline (10 and 13 mm for the Amplatzer Amulet and Watchman, respectively). Device orientation is set perpendicular to the LAA centreline. LAAO size is based on the maximum diameters (D1 & D2) of a transversal 2D plane perpendicular to the centreline placed in the optimal positioning. The proposed LAAO devices are initially shown in the VIDAA platform with these settings (VIDAA-init), where the clinician can interactively manipulate all their parameters for a better fitting to the studied LAA morphology (VIDAA-end).

2.2. VIDAA: Virtual Implantation and Device Selection in Left Atrial Appendages

VIDAA is a web-based 3D interactive virtual implantation platform that allows clinicians to select the most appropriate LAAO configurations for a given patient. The main features of the VIDAA platform include: the joint 3D visualization of the LA/LAA surface meshes and the device models; different modes of mesh visualization and editing tools such as wireframe views or clipping, among others; transform controllers for user manipulation of the device such as translation, rotation and scaling; visualization of LAA morphological parameters such as the centreline, 2D transveral planes of the centreline and its diameters (D1, D2); visualization of the optimal LAA settings according to VIDAA such as device size and landing zone; manual modification of all LAAO settings; and export of a LAAO configuration for subsequent *in silico* hemodynamics study. **Figure 2** illustrates the different steps in the VIDAA workflow. A demonstration video of a proof-of-concept prototype of VIDAA is also available as **Supplementary Material** (**Appendix 2**).

Being a web-based platform, VIDAA is not linked to any software installation, operative system or browser, which facilitates its usage in a clinical environment. VIDAA was built using HTML5 programming language (JavaScript, scss), using different JavaScript libraries such as THREE.js and React.js. The first library, THREE.js, was used to visualize and interact with 3D objects (e.g., LA mesh) while React.js was used to separate into components the different modalities of the platform.

2.3. Hemodynamics Simulations

2.3.1. Mesh Processing Pipeline

To ensure convergence of hemodynamics simulations, LA meshes from medical image segmentations required several pre-processing phases (see **Figure 4**). First, a Taubin smoothing filter (with scale factors $\lambda = 0.6$, $\mu = -0.53$ and 10 iterations) was applied. Subsequently, cylinders representing the pulmonary veins (PV) and the mitral valve (MV) were manually inserted to the LA mesh using the Autodesk Meshmixer software[2] so that simulated flow was developed normal to the surface of the vessels. Volumetric meshes were built with a 3D Delaunay refinement algorithm available in the Gmsh software (default parameters) (Geuzaine and Remacle, 2009)[3] for the subsequent CFD simulations, resulting in the following number of tetrahedral elements for the four LA under study: Patient 1 = 597,550; Patient 2 = 961,015; Patient 3 = 330,091; Patient 4 = 200,951. The whole meshing pipeline was performed with the following Open-Source softwares: Gmsh, Autodesk MeshMixer, MeshLab[4] and Visual Computing Lab[5]. The reader is referred to García-Isla et al. (2018) for more details of the meshing pipeline.

The studied LAAO devices (see **Figure 1**) were built using a Computational-Aided Design (CAD) software[6] and following the on-line product manual and instructions from the companies (Abbott, 2018; Boston Scientific, 2018). Subsequently, several LAAO device configurations, including different size and positioning settings, were exported from the VIDAA platform.

[2]http://www.meshmixer.com/
[3]http://gmsh.info/
[4]http://www.meshlab.net/
[5]http://vcg.isti.cnr.it/
[6]Geometry-Design Modeler (Ansys 18.2)

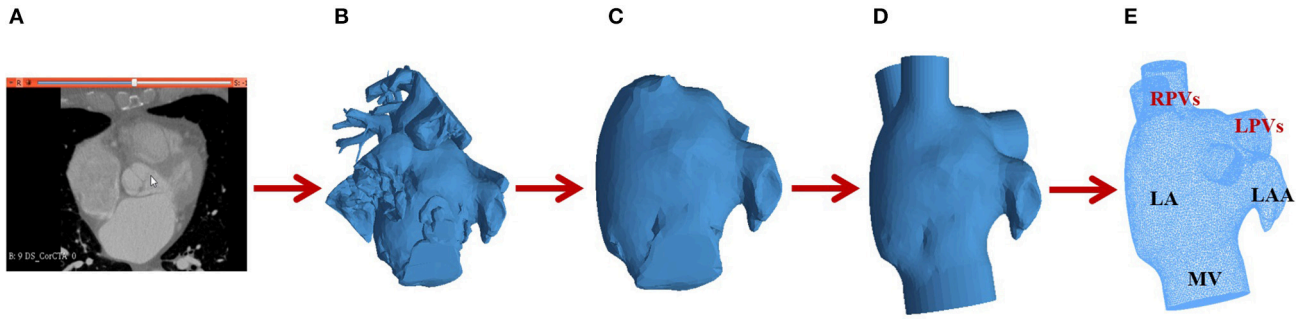

FIGURE 4 | Mesh processing pipeline for hemodynamics simulations: **(A)** Computed Tomography (CT) image; **(B)** Surface mesh after CT segmentation; **(C)** Removal of structures surrounding the left atrium (LA); **(D)** Insertion of cylinders for the pulmonary veins (PV); **(E)** Volumetric LA mesh with two right pulmonary veins (RPVs), two left pulmonary veins (LPVs), a mitral valve (MV) and the left atrial appendage (LAA).

Volumetric meshes for all configurations under study were obtained defining two surfaces in Gmsh: one for the LA and another for the implanted device.

2.3.2. Computational Fluid Dynamics

The CFD analysis was performed using ANSYS Fluent 18.2, in which blood was modeled as an incompressible Newtonian fluid (density of $\rho = 1{,}060$ kg/m^3; dynamic viscosity of $\mu = 0.0035$ Pa·s). Blood was simulated using the incompressible Navier-Stokes and continuity equations. Model dynamics was introduced with a sinusoidal function representing a heart cycle of a healthy patient (Fernandez-Perez et al., 2012; García-Isla et al., 2018). Boundary conditions at systole (first 0.40 s) were modeled with the PVs as velocity-inlets and the MV as a wall, to represent that the valve is closed during this cardiac phase (Fernandez-Perez et al., 2012). The opening of the MV in diastole (duration of 0.65 s) was modeled applying an outlet pressure of 8 mmHg (Nagueh et al., 2008) to the MV. All LA walls were modeled as rigid walls with no slip, representing the worst scenario in (persistent) AF, where the atrium barely contracts anymore. The LAAO device was also modeled as a wall to represent that no blood could go through it.

2.3.3. *In silico* Indices for Risk of Thrombus Formation

As in García-Isla et al. (2018), we estimated several *in silico* indices to characterize blood flow patterns derived from CFD simulations and identify pro-thrombotic regions in the LAA, usually where blood flow is complex and velocities are low (Achille et al., 2014). For the sake of simplicity, only the Endothelial Cell Activation Potential (ECAP) index is reported here since it combines the Time-Averaged Wall Shear Stress (TAWSS) with the Oscillatory Shear Index (OSI): low velocity (small TAWSS values) and high complex (large OSI values) blood flows will produce high ECAP values, thus indicating a region with a high risk of thrombus formation.

The equations to derive these indices are included in **Appendix 3**. For a qualitative analysis, the *in silico* indices were visualized (using ParaView 5.2.0) as colored maps superimposed on the 3D LA geometry, providing an intuitive way to detect regions with irregular blood flow. Furthermore, the distribution in the LAA of the ECAP index for different simulation scenarios was analyzed with histograms showing the percentage of nodes in different ECAP intervals.

2.3.4. Simulation Scenarios

In silico blood flow patterns were studied in different simulation scenarios to study the influence of the implanted device configuration. Four simulation scenarios were studied for each patient, resulting in a total number of 16 simulations:

- Without LAAO device (No LAAO).
- LAAO device with size and positioning derived from morphological analysis and criteria defined by experienced clinicians (see section 2.1.1); this is the default configuration shown in the VIDAA platform (VIDAA-init).
- LAAO device with VIDAA-init settings but with a 20% smaller size.
- LAAO device VIDAA-init settings but with a sub-optimal position and orientation (Misplaced).
- LAAO device after manipulation in VIDAA aiming at uniformly covering the union between the LA and LAA (VIDAA-end).

3. RESULTS

3.1. Blood Flow Velocity Patterns

Streamlines and velocity vector fields characterizing blood flow patterns in the LA/LAA for different simulation scenarios were analyzed. **Figure 5** shows simulation results for the four patients under study and the LAAO configurations described above, in diastole ($t = 0.55$ s, ventricular filling), when blood flow velocities in the LAA are higher. Videos of the hemodynamics simulations (blood flow velocity streamlines for the whole cardiac cycle) for all patients without a device and with the VIDAA-end settings are included as **Supplementary Material** (see **Appendix 2**).

At baseline (without an implanted LAAO device, No LAAO configuration, first row in **Figure 5**), blood flow is entering the LAA in all patients with relatively low velocities, in some cases with complex patterns (e.g., Patient 3) in secondary lobes. The device configuration proposed by the VIDAA platform (both

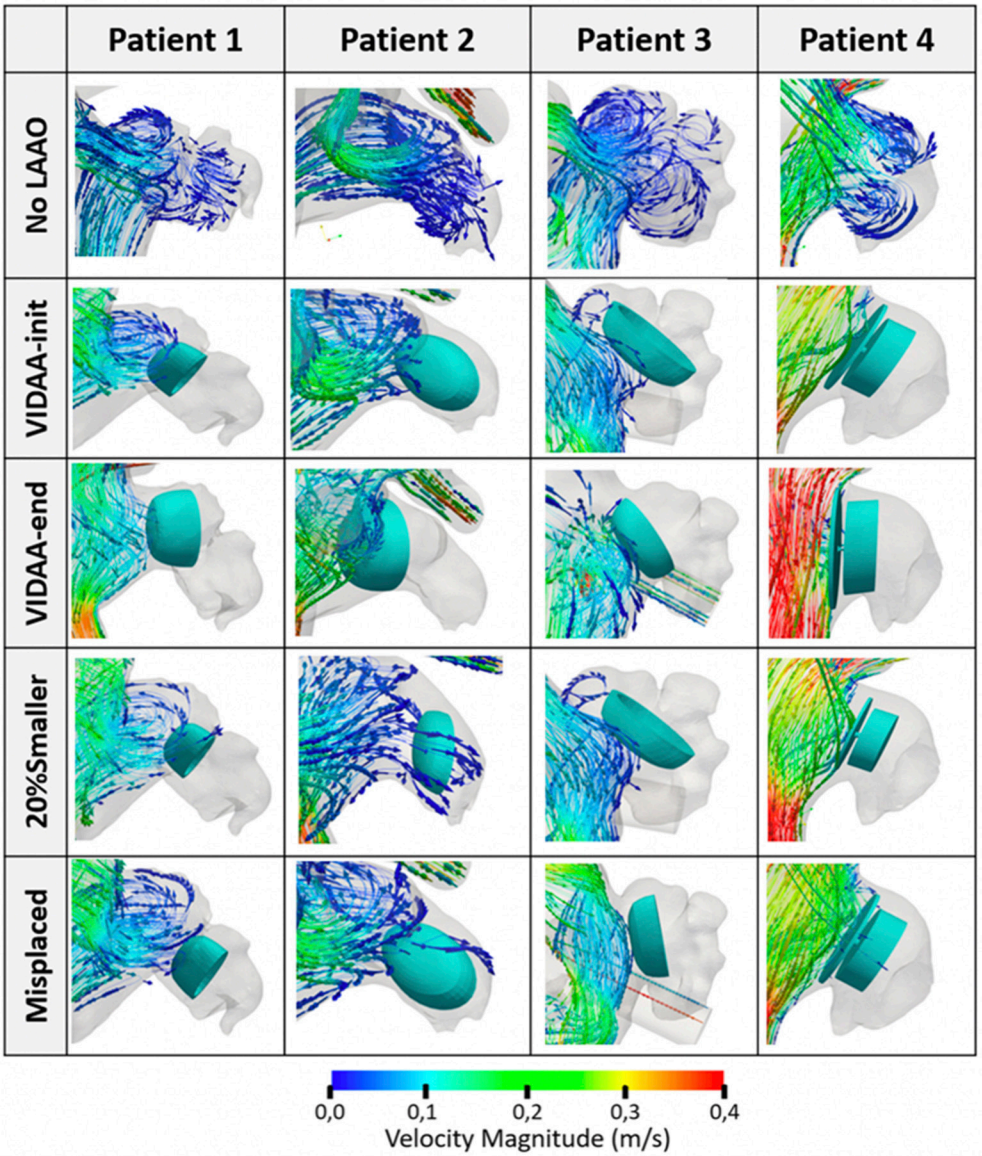

FIGURE 5 | Blood flow streamlines in the left atrial appendage (LAA) from hemodynamics simulations of the four patients under study. Snapshots capture the flow behavior in diastole, when higher velocities are present ($t = 0.55$ s). No LAAO: without device; VIDAA-init: device settings from morphological analysis and clinical recommendations; VIDAA-end: device settings after interactive manipulation in VIDAA; 20% smaller: device with a 20% smaller size than VIDAA-init; Misplaced: device with sub-optimal position and orientation.

VIDAA-init and VIDAA-end) achieved a perfect occlusion in Patient 1 (second and third row, first column, in **Figure 5**). On the other hand, blood flow was penetrating the LAA in the same case when decreasing the LAAO device size (20% Smaller scenario), showing a potential stagnation process, with low velocities, in the lateral part of the occluder (blue arrows next to the device; fourth row, first column, in **Figure 5**). All configurations have the device positioning deeper in the LAA than the VIDAA-end, creating a non-closed cavity between the ostium and the device where new complex blood flow loops appeared. Patient 2 presented a similar behavior to Patient 1 but with a more visible negative effect of reducing the size of the device, allowing more flow through the LAA (fourth row, second column, in **Figure 5**). On the other hand, Patient 3 (third column in **Figure 5**) showed a correct flow blockage in all device configurations. Finally, Patient 4 showed fast velocities and laminar flow in the LA cavity outside the implanted device for the VIDAA-end configuration (red streamlines in third row, fourth column in **Figure 5**), which was not achieved with the remaining settings.

Figure 6 depicts blood flow velocity curves over the whole cardiac cycle in a point outside the device (following the LAA centerline direction toward the main LA cavity) for all simulation scenarios in the four patients analyzed in this work. We can

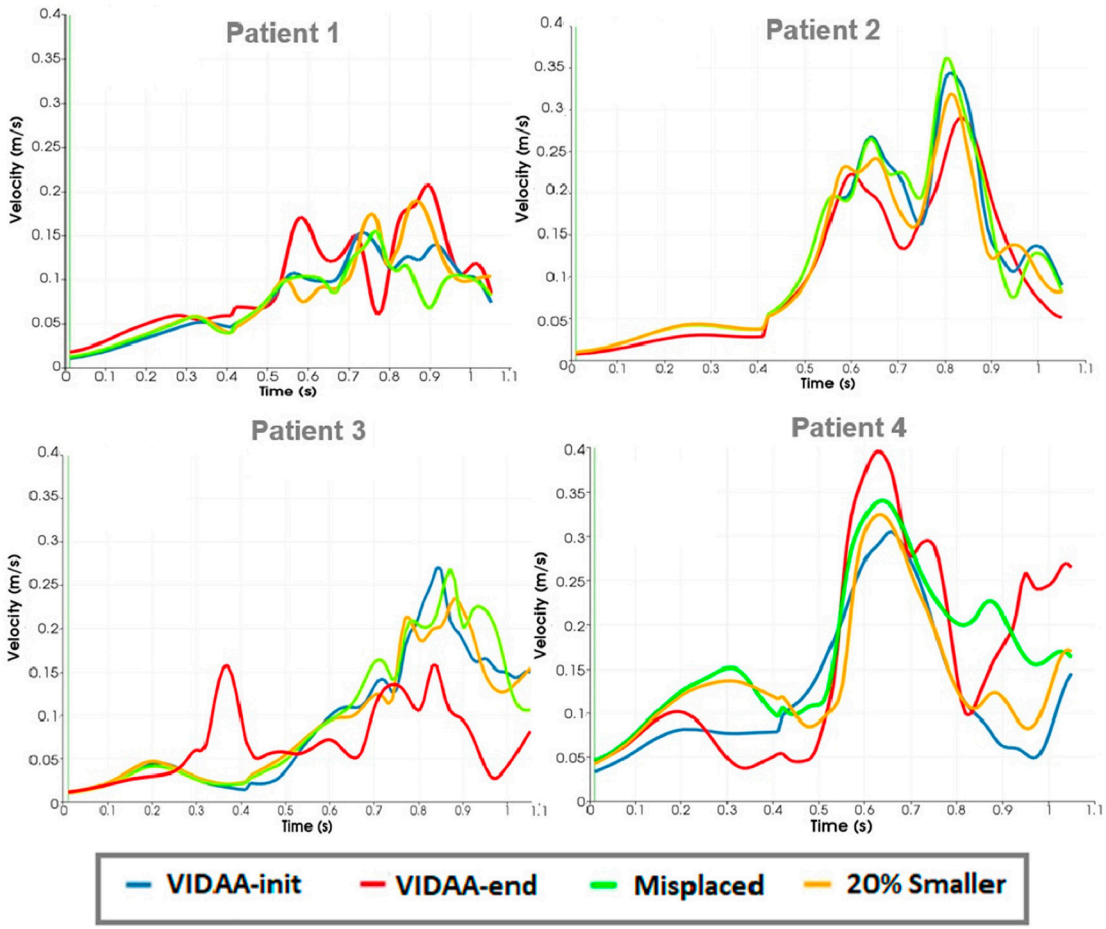

FIGURE 6 | Blood flow velocity curves over the whole cardiac cycle in a point outside the device in the left atrial cavity for all simulation scenarios in the four patients. VIDAA-init: device settings from morphological analysis and clinical recommendations; VIDAA-end: device settings after interactive manipulation in VIDAA; 20% smaller: device with a 20% smaller size than VIDAA-init; Misplaced: device with sub-optimal position and orientation.

appreciate that the VIDAA-end configuration (red curve in **Figure 6**) leads to velocity profiles with higher magnitudes in diastole for some cases (e.g., see Patient 4), suggesting faster flow circulation and thus less risk of thrombus formation due to device implantation. On the other hand, results are inconclusive for other patients (e.g., see Patient 3), exemplifying the difficulty of characterizing the 4D nature of blood flow patterns by observing 1D velocity profiles in an individual spatial point.

3.2. *In silico* Indices for Risk of Thrombus Formation

Figure 7 shows the ECAP distribution mapped as a colormap onto the LA/LAA geometries for all simulation scenarios in the patients under study. For LAAO scenarios (i.e., all except the No LAAO), the ECAP map is only displayed between the LAA ostium and the device to study the risk of thrombus formation outside the device. It can easily be observed at baseline (No LAAO configuration; first row in **Figure 7**) that higher values of ECAP (i.e., complex flows and low velocities; red-green areas in **Figure 7**), thus with a higher risk of thrombus formation, are located in several areas of the LAA depending on morphology complexity. For instance, Patient 4 is the case showing smaller ECAP values due to its smooth morphology and orientation with respect to the main LA cavity, leading to larger blood flow velocity magnitudes in most regions (except in its tip). More importantly, high ECAP areas appear more prominently in device configurations with incorrect LAAO settings (e.g., 20% smaller), whereas the VIDAA-end configuration seems to minimize the presence of these areas.

Figure 8 plots the histograms of ECAP intervals as percentages with respect to surface area for each patient and different LAAO scenarios. The ECAP maps were analyzed within the region between the device and the LAA ostium. For the four analyzed LAA geometries, the VIDAA-end settings resulted in the lower percentage of surface areas with higher ECAP values (>3). We can also observe that the VIDAA-init settings were not always adequate, sometimes even performing worse than the Misplaced and 20% smaller scenarios, illustrating the benefit of interactively manipulating the device settings in the VIDAA platform.

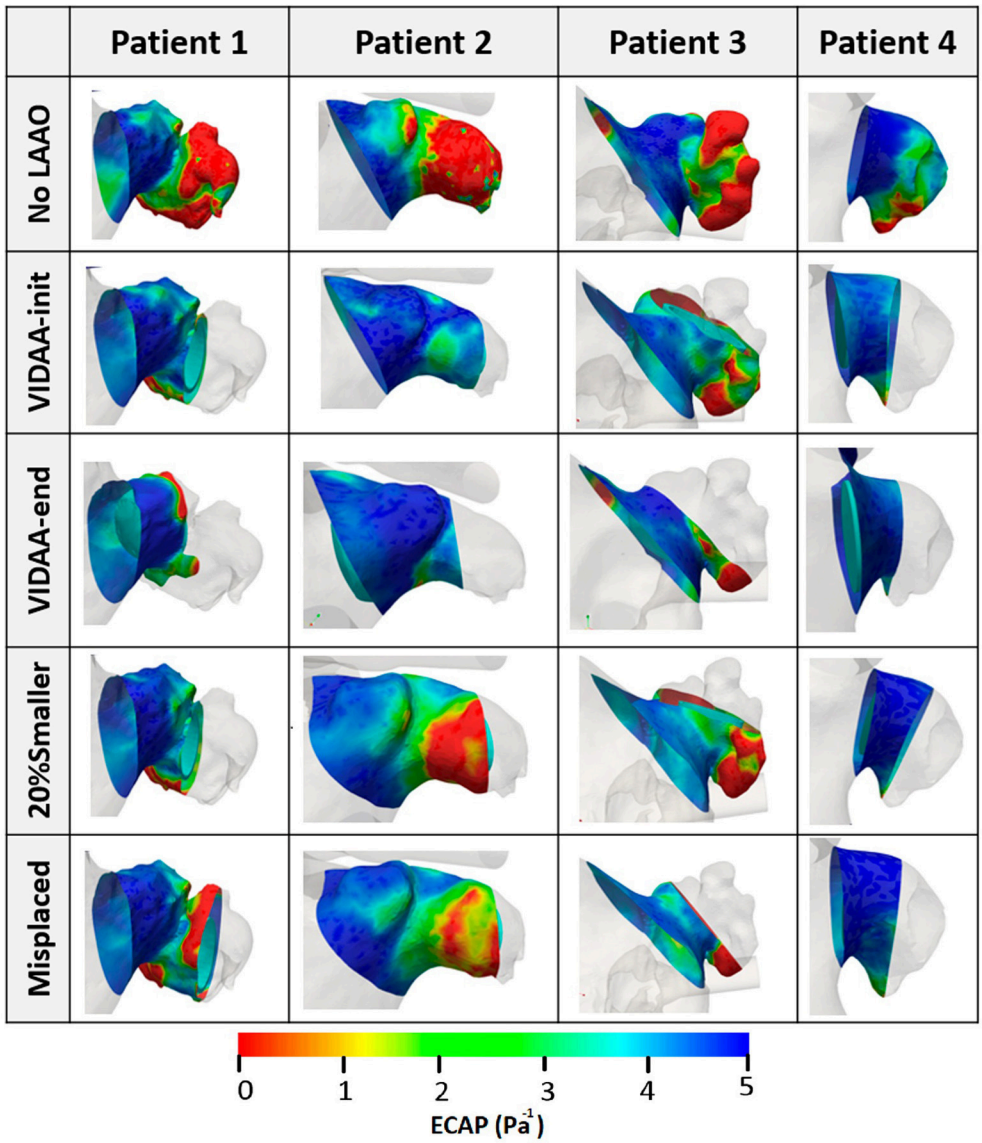

FIGURE 7 | Endothelial Cell Activation Potential (ECAP) distribution (Pa^{-1}) visualized as colored maps superimposed to the LA wall for the four patients under study. No LAAO: without device; VIDAA-init: device settings from morphological analysis and clinical recommendations; VIDAA-end: device settings after interactive manipulation in VIDAA; 20% smaller: device with a 20% smaller size than VIDAA-init; Misplaced: device with sub-optimal position and orientation.

4. DISCUSSION

In this study, different configurations of LAA occlusion devices were evaluated in four patient-specific left atria using advanced computational tools. A web-based platform, so-called VIDAA, was developed in which LAAO devices could be virtually implanted, interactively selecting the desired configuration for a given individual. Once a device configuration was chosen, it was exported out of the platform to built a computational domain where hemodynamics CFD-based simulations were run. The resulting blood flow simulations were post-processed to generate quantitative *in silico* indices (e.g., ECAP) to locally assess the risk of thrombus formation after device implantation, which is not currently possible with existing imaging modalities. Providing such information for different LAAO settings to the clinician would be quite beneficial for a better and faster planning of the intervention.

The implantation of LAAO devices is usually quite successful (around 95%, defined as small flow jets into the LAA after implantation), with peri-procedural complicate rates of approximately 5% (Grosset-Janin et al., 2015). Nevertheless, residual bleedings are not uncommon and the reduction of thrombus formation risk, even if superior to OAC-based therapy, could be improved (60–75% Grosset-Janin et al., 2015). Moreover, it is not well-known when patients can stop anti-coagulants after LAAO implantation, which can lead to

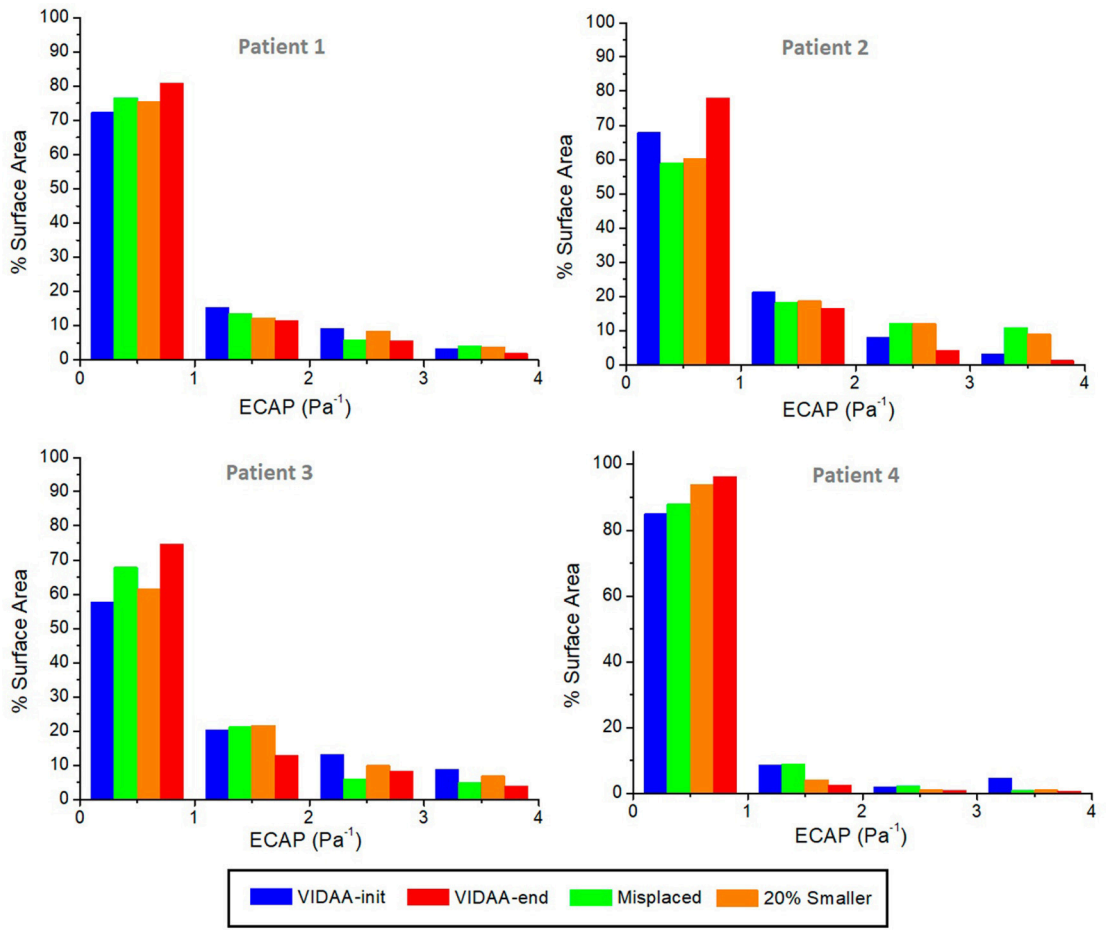

FIGURE 8 | Histograms of Endothelial Cell Activation Potential (ECAP) distribution (Pa^{-1}) as a percentage of surface area for each patient and different device scenarios. VIDAA-init: device settings from morphological analysis and clinical recommendations; VIDAA-end: device settings after interactive manipulation in VIDAA; 20% smaller: device with a 20% smaller size than VIDAA-init; Misplaced: device with sub-optimal position and orientation.

device-related thrombus formation (7% of cases in a recent study Fauchier et al., 2018). The development of advanced computational tools including 3D medical imaging, clinician-friendly interfaces and biophysical modeling to fully characterize the LAA 3D morphology, 4D blood flow patterns and virtually predict the individual risk of thrombus formation for different device settings, would contribute to the acceptance of LAAO therapies, properly assessing their cost-effectiveness and clinical benefit as well identifying their limitations, which is still under debate (Hu and Yogeswaran, 2015; Mandrola et al., 2018).

The obtained results confirm the relevance of an appropriate LAAO device configuration, personalized to each patient, to ensure a complete occlusion of the LAA cavity and minimize the creation of areas around the implanted device prone to thrombus formation (e.g., low velocities and complex flow). Consistently, LAAO settings obtained after device manipulation in the VIDAA platform (VIDAA-end) were the most appropriate, ensuring a complete blockage of the LAA cavity in all cases. On the contrary, other LAAO configurations, including the VIDAA initial configuration based on LAA morphological analysis and clinical recommendations (VIDAA-init), repeatedly created complex flow loops with low velocities around the device, incrementing the risk of thrombus formation post-intervention. However, the VIDAA-end positioning of the device may not be adequate if it leads to a blockage of the circumflex artery, which is located just outside the LAA ostium. Unfortunately, we did not have information about the circumflex artery exact location in the studied cases. In the future, this information will be obtained from CT images and added as an additional constraint in the VIDAA platform.

Device sizing and positioning are then crucial, assuming a good attachment to the LAA wall. Nowadays, the process for selecting the LAAO size and defining the landing zone where the device will be released is too subjective and prone to errors due to the lack of quantitative techniques and high-resolution 3D images. We have observed in our study that small changes in the selection of transversal 2D planes along the LAA centerline produced maximum diameters in the range of 22–31 mm in the same geometry. Similar variability can be found when using 2D-based or different medical imaging

modalities, as it was demonstrated in López-Mínguez et al. (2014), where LAAO dimensions were consistent from X-ray, echocardiography and CT images in only 23% of the cases. Therefore, a full 3D characterization of the LA/LAA geometry (i.e., dimensions, relative orientation) is required for an optimal device sizing/positioning and avoid generating areas between the implanted device and the atrial wall prone to thrombus formation. A reduced learning curve of the LAAO device implantation process and more comprehensive intervention planning has already been demonstrated by using CT images (Wang et al., 2016; Chow et al., 2017). Recently (De Potter et al., 2018), 3DRXA has also been proven an interesting alternative to echocardiographic images during the intervention.

The VIDAA platform has then been developed to allow the interactive 3D visualization of LA/LAA geometries and CAD models of the devices. The integration of VIDAA with hemodynamics simulations has been very helpful to identify areas with high risk of thrombus formation under certain LAAO configurations. The ECAP parameter, initially proposed by Achille et al. (2014) in an aortic aneurysm application, provided consistent results, with higher values in the LAA and showing its potential to estimate thrombogenesis. Overall, the VIDAA platform and biophysical models should provide a more complete way to analyze the relation between LAA shape, hemodynamics, device settings and thrombus formation to the clinicians prior to the intervention.

The presented methodology has several limitations that could be improved in the future. For instance, the 3D model construction, including image processing steps (e.g., segmentation, definition of ostium plane) and the meshing pipeline, is semi-automatic, which could lead to intra-operator inconsistencies. The obtained image processing results and corresponding 3D models were qualitatively evaluated by several observers for each case. However, even if developing a fully automatic image processing pipeline was out of the scope of this paper, left atrial segmentation techniques based on deep-learning algorithms are already becoming available (see recent Atrial Challenge at STACOM18 workshop[7]). Sensitivity analysis and convergence studies will also identify the most critical meshing pipeline parameters, such as the required mesh resolution, to obtain robust wall shear stress maps, which is critical to estimate reliable ECAP maps.

Moreover, several boundary conditions and modeling choices could be upgraded to achieve more realistic simulations. The assumption of rigid LA walls for a persistent AF patient is valid from a clinical point of view. Nevertheless, the LAA is quite a flexible structure and the mitral ring displacement is non-negligible to properly simulate LA reservoir, conduit and booster pump phases. Motion-based constraints could be imposed from patient-specific information, as in Otani et al. (2016) from CT images or similar. Moreover, boundary conditions such as the inlet velocity profile should be adapted to atrial fibrillation (i.e., absence of atrial contraction). More sophisticated numerical techniques such as Fluid-Structure interaction (between blood flow and LA wall), contact-based (between device and LA wall) or discrete particle models (for coagulation and thrombus formation Hathcock, 2006) may provide more realistic simulations, at the expense of increased computational costs and complexity. In addition, patient-specific blood flow boundary conditions (e.g., based on Doppler data), rather than the generic curves used in this study, would be required for an individualized assessment of hemodynamics.

The post-processing of CFD simulations has been one of the most critical steps in the developed modeling pipeline. For instance, the visualization of blood flow streamlines is highly dependent on the location of the seeds required to generate them. An incorrect seed placement can lead to misinterpretation of CFD simulations and wrong conclusions. To study LAA blood flow patterns in the LAA it is convenient to place seeds near the LAA ostium, according to our experience. Additionally, one needs to be cautious on using velocity 1D profiles and values evaluated in a single point in space as an estimation of blood flow pattern behavior. It is not obvious to select a point in which reliably comparing velocity profiles for different device configurations, as shown in **Figure 6**. This is also critical for the validation of simulation results with clinical data. We have performed initial visual comparisons between mitral valve and LAA velocity profiles from our simulations and from Doppler data of the studied patients, showing promising similarities. Nevertheless, a more exhaustive and quantitative validation with more complete Doppler or 4D-flow MRI data, ideally on several geometries and with different LAAO devices, is still missing. In addition, the analysis of a larger number of cases would allow identifying patients with thromboembolic history and compare their morphological and hemodynamics parameters given by VIDAA and biophysical models with patients without a thrombus.

5. CONCLUSIONS

The VIDAA platform was developed to perform virtual implantation of LAAO devices on patient-specific geometries in an interactive way. Its combination with biophysical models of hemodynamics and complete LAA shape 3D characterization offers clinicians unprecedented computational tools to select the optimal device settings prior to the intervention. Different LAAO device settings can be tested to minimize the areas prone to thrombus formation after device implantation, according to *in silico* indices derived from CFD simulation results. The LAAO configurations found after manipulation of device settings in the VIDAA platform were linked to a reduced risk of thrombus formation outside the implanted device, according to a qualitatively analysis of blood flow streamlines and ECAP maps. Future work will be focused on the evaluation of the VIDAA platform in a clinical environment, analyzing a larger number of LAA cases and exploring its use as an alternative to 3D printing for interventional planning, also in combination with immersive visualization interfaces.

[7]http://atriaseg2018.cardiacatlas.org/

DATA AVAILABILITY

Simulation data including solver configurations and results are available under request. A beta version of the VIDAA platform is available at the GitHub account of the BCN-Medtech research unit (https://github.com/bcnmedtech).

AUTHOR CONTRIBUTIONS

AA generated CFD models, processed and analyzed data, developed VIDAA platform, and wrote the paper. AO conceived the research and VIDAA platform, designed CFD models and analyzed data, wrote the paper. CY developed VIDAA platform, gave technical support on the web tools. ES provided clinical data from OLV and performed segmentation of 3DRA images. MN-G gave technical support on LA and LAA mesh processing. AF-Q computed LAA morphological measures and created database. JM gave technical support on reconstruction of CT images and CFD models. IG developed the algorithm for centreline extraction. TDP provided data from OLV and practical context. DA provided data from Hospital de la Santa Creu i Sant Pau of Barcelona and set specifications for VIDAA platform. XF provided data from Hospital Clínic de Barcelona and set specifications for VIDAA platform. OC oversaw the whole project, conceived the research, and wrote-revised the paper.

FUNDING

This work was supported by the Spanish Ministry of Economy and Competitiveness under the Maria de Maeztu Units of Excellence Programme (MDM-2015-0502) and the Retos I+D Programme (DPI2015-71640-R).

ACKNOWLEDGMENTS

We would like to thank Dr. Brugaletta from Hospital Clínic (Barcelona, Spain) for his support and additional information about LAAO-based therapies. We would like to give an special mention to the undergraduate students from Biomedical Engineering degree involved in the development of the first CFD models (E. Gonzalez, T. Orejon, J. Aviles, I. Sainz, A. Iribar, J. Pose and A. Serra). Also thank G. García for providing the code to obtain semi-automatically the numerical indices for risk of thrombus formation, and M. P. García for her help in the development of VIDAA platform.

SUPPLEMENTARY MATERIAL

The Supplementary Material for this article can be found online at: https://www.frontiersin.org/articles/10.3389/fphys.2019.00237/full#supplementary-material

REFERENCES

Abbott (2018). *AMPLATZER^{TM} Left Atrial Appendage Occluder*. Available online at: https://www.sjmglobal.com

Achille, P. D., Tellides, G., Figueroa, C. A., and Humphrey, J. D. (2014). A haemodynamic predictor of intraluminal thrombus formation in abdominal aortic aneurysms A haemodynamic predictor of intraluminal thrombus formation in abdominal aortic aneurysms. *Proc. R. Soc. A* 470:20140163. doi: 10.1098/rspa.2014.0163

Al-Saady, N. M., Obel, O. A., and Camm, A. J. (1999). Left atrial appendage: structure, function, and role in thromboembolism. *Heart* 82, 547–555. doi: 10.1136/hrt.82.5.547

Beigel, R., Wunderlich, N. C., Ho, S. Y., Arsanjani, R., and Siegel, R. J. (2014). The left atrial appendage: anatomy, function, and noninvasive evaluation. *JACC Cardiovasc. Imaging* 7, 1251–1265. doi: 10.1016/j.jcmg.2014.08.009

Bosi, G. M., Cook, A., Rai, R., Menezes, L. J., Schievano, S., Torii, R., et al. (2018). Computational fluid dynamic analysis of the left atrial appendage to predict thrombosis risk. *Front. Cardiovas. Med.* 5:34. doi: 10.3389/fcvm.2018.00034

Boston Scientific (2018). *WATCHMAN Left Atrial Appendage Closure Device*. Available online at: https://www.watchman.com

Casas, B., Lantz, J., Viola, F., Cedersund, G., Bolger, A. F., Carlhäll, C. J., et al. (2017). Bridging the gap between measurements and modelling: a cardiovascular functional avatar. *Sci. Rep.* 7, 1–15. doi: 10.1038/s41598-017-06339-0

Chow, D. H., Bieliauskas, G., Sawaya, F. J., Millan-Iturbe, O., Kofoed, K. F., Søndergaard, L., et al. (2017). A comparative study of different imaging modalities for successful percutaneous left atrial appendage closure. *Open Heart* 4:e000627. doi: 10.1136/openhrt-2017-000627

Chung, I., and Lip, G. Y. (2003). Virchow's triad revisited: blood constituents. *Pathophysiol. Haemost. Thromb.* 33, 449–454. doi: 10.1159/000083844

Cibis, M., Bustamante, M., Eriksson, J., Carlhäll, C. J., and Ebbers, T. (2017a). Creating hemodynamic atlases of cardiac 4D flow MRI. *J. Magn. Res. Imaging* 46, 1389–1399. doi: 10.1002/jmri.25691

Cibis, M., Lindahl, T. L., Ebbers, T., Karlsson, L. O., and Carlhäll, C. J. (2017b). Left atrial 4D blood flow dynamics and hemostasis following electrical cardioversion of atrial fibrillation. *Front. Physiol.* 8:1052. doi: 10.3389/fphys.2017.01052

De Potter, T., Chatzikyriakou, S., Silva, E., Camp, G., and Penicka, M. (2018). A pilot study for left atrial appendage occlusion guided by 3-Dimensional rotational angiography alone. *JACC Cardiovasc. Interv.* 11, 223–224. doi: 10.1016/j.jcin.2017.08.053

Di Biase, L., Santangeli, P., Anselmino, M., Mohanty, P., Salvetti, I., Gili, S., et al. (2012). Does the left atrial appendage morphology correlate with the risk of stroke in patients with atrial fibrillation? *J. Am. Coll. Cardiol.* 60, 531–538. doi: 10.1016/j.jacc.2012.04.032

Fatkin, D., Kelly, R. P., and Feneley, M. P. (1994). Relations between left atrial appendage blood flow velocity, spontaneous echocardiographic contrast and thromboembolic risk *in vivo*. *J. Am. Coll. Cardiol.* 23, 961–969. doi: 10.1016/0735-1097(94)90644-0

Fauchier, L., Cinaud, A., Brigadeau, F., Lepillier, A., Pierre, B., Abbey, S., et al. (2018). Device-related thrombosis after percutaneous left atrial appendage occlusion for atrial fibrillation. *J. Am. Coll. Cardiol.* 71, 1528–1536. doi: 10.1016/j.jacc.2018.01.076

Fernandez-Perez, G. C., Duarte, R., Corral de la Calle, M., Calatayud, J., and Sanchez Gonzalez, J. (2012). Analysis of left ventricular diastolic function using magnetic resonance imaging. *Radiologia* 54, 295–305. doi: 10.1016/j.rxeng.2011.09.003

García-Isla, G., Olivares, A. L., Silva, E., Nuñez-Garcia, M., Butakoff, C., Sanchez-Quintana, D., et al. (2018). Sensitivity analysis of geometrical parameters to study haemodynamics and thrombus formation in the left atrial appendage. *Int. J. Numer. Methods Biomed. Eng.* 34, 1–14. doi: 10.1002/cnm.3100

Genua I., Olivares, A. L., Silva, E., Mill, J., Fernández, Á., Aguado, A., et al. (2019). "Centreline-based shape descriptors of the left atrial appendage in relation with thrombus formation," in *Statistical Atlases and Computational Models of the Heart. Atrial Segmentation and LV Quantification Challenges, STACOM 2018*, *Lecture Notes in Computer Science*, Vol. 11395 (Granada), 200–208. doi: 10.1007/978-3-030-12029-0_22

Geuzaine, C., and Remacle, J.-F. (2009). Gmsh: a 3-d finite element mesh generator with built-in pre- and post-processing facilities. *Int. J. Numer. Methods Eng.* 79, 1309–1331. doi: 10.1002/nme.2579

Grosset-Janin, D., Barth, E., Bertrand, B., and Detante, O. (2015). Percutaneous left atrial appendage occlusion for stroke prevention in patients with atrial fibrillation and contraindication for anticoagulation. *Rev. Neurol. (Paris)* 171, 426–432. doi: 10.1016/j.neurol.2014.11.009

Hathcock, J. J. (2006). Flow effects on coagulation and thrombosis. *Arterioscler. Thromb. Vasc. Biol.* 26, 1729–1737. doi: 10.1161/01.ATV.0000229658.76797.30

Hu, T. Y., and Yogeswaran, V. (2015). Device-based approach to prevention of stroke in atrial fibrillation. *Innov. Cardiac Rhythm Manag.* 6, 2038–2050. doi: 10.19102/icrm.2015.060603

Koizumi, R., Funamoto, K., Hayase, T., Kanke, Y., Shibata, M., Shiraishi, Y., et al. (2015). Numerical analysis of hemodynamic changes in the left atrium due to atrial fibrillation. *J. Biomech.* 48, 472–478. doi: 10.1016/j.jbiomech.2014.12.025

Le, D. L., Khodjaev, S. D., and Morelli, R. L. (2014). Percutaneous methods of left atrial appendage exclusion: an alternative to the internist. *J. Commun. Hosp. Intern. Med. Perspect.* 4:0–5. doi: 10.3402/jchimp.v4.22719

Lee, J. M., Seo, J., Uhm, J.-S., Kim, Y. J., Lee, H.-J., Kim, J.-Y., et al. (2015). Why is left atrial appendage morphology related to strokes? an analysis of the flow velocity and orifice size of the left atrial appendage. *J. Cardiovasc. Electrophysiol.* 26, 922–927. doi: 10.1111/jce.12710

López-Mínguez, J., González-Fernández, R., Fernández-Vegas, C., Millán-Nuñez, V., Eugenia Fuentes-Cañamero, M., Manuel Nogales-Asensio, J., et al. (2014). Comparison of imaging techniques to assess appendage anatomy and measurements for left atrial appendage closure device selection. *J. Invasive Cardiol.* 26, 462–467.

Mandrola, J., Foy, A., and Naccarelli, G. (2018). Percutaneous left atrial appendage closure is not ready for routine clinical use. *Heart Rhythm.* 15, 298–301. doi: 10.1016/j.hrthm.2017.10.007

Markl, M., Lee, D. C., Furiasse, N., Carr, M., Foucar, C., Ng, J., et al. (2016). Atrial structure and function left atrial and left atrial appendage 4D blood flow dynamics in atrial fibrillation. *Circ. Cardiovasc. Imaging* 9:e004984. doi: 10.1161/CIRCIMAGING.116.004984

Morillo, C. A., Banerjee, A., Perel, P., Wood, D., and Jouven, X. (2017). Atrial fibrillation: the current epidemic. *J. Geriatr. Cardiol.* 14, 195–203. doi: 10.11909/j.issn.1671-5411.2017.03.011

Nagueh, S. F., Appleton, C. P., Gillebert, T. C., Marino, P. N., Oh, J. K., Smiseth, O. A., et al. (2008). Recommendations for the evaluation of left ventricular diastolic function by echocardiography. *Eur. J. Echocardiogr.* 10, 165–193. doi: 10.1093/ejechocard/jep007

Olivares, A. L., Silva, E., Nuñez-Garcia, M., Butakoff, C., Sánchez-quintana, D., Freixa, X., et al. (2017). *Functional Imaging and Modelling of the Heart*, Vol. 10263 of *Lecture Notes in Computer Science*. Cham: Springer International Publishing.

Otani, T., Al-Issa, A., Pourmorteza, A., McEigh, E., Wada, S., and Ashikaga, H. (2016). A computational framework for personalized blood flow analysis in the human left atrium. *Ann. Biomed. Eng.* 44, 3284–3294. doi: 10.1007/s10439-016-1590-x

Park, J. W., Sievert, H., Kleinecke, C., Vaskelyte, L., Schnupp, S., Sievert, K., et al. (2018). Left atrial appendage occlusion with lambre in atrial fibrillation: initial European experience. *Int. J. Cardiol.* 265, 97–102. doi: 10.1016/j.ijcard.2018.02.120

Saw, J., and Lempereur, M. (2014). Percutaneous left atrial appendage closure procedural techniques and outcomes. *JACC Cardiovasc Interv.* 7, 1205–1220. doi: 10.1016/j.jcin.2014.05.026

Singh, I. M., and Holmes, D. R. (2010). Left atrial appendage closure. *Curr. Cardiol. Rep.* 12, 413–421. doi: 10.1007/s11886-010-0122-9

Tzikas, A., Gafoor, S., Meerkin, D., Freixa, X., Cruz-Gonzalez, I., Lewalter, T., et al. (2016). Left atrial appendage occlusion with the AMPLATZER Amulet device: an expert consensus step-by-step approach. *EuroIntervention* 11, 1512–1521. doi: 10.4244/EIJV11I13A292

Vedula, V., George, R., Younes, L., and Mittal, R. (2015). Hemodynamics in the left atrium and its effect on ventricular flow patterns. *J. Biomech. Eng.* 137, 1–8. doi: 10.1115/1.4031487

Wang, D. D., Eng, M., Kupsky, D., Myers, E., Forbes, M., Rahman, M., et al. (2016). Application of 3-Dimensional computed tomographic image guidance to WATCHMAN implantation and impact onEarly operator learning curve: single-center experience. *JACC Cardiovasc. Interv.* 9, 2329–2340. doi: 10.1016/j.jcin.2016.07.038

Wang, Y., Di Biase, L., Horton, R. p., Nguyen, T., Morhanty, P., and Natale, A. (2010). Left atrial appendage studied by computed tomography to help planning for appendage closure device placement. *J. Cardiovasc. Electrophysiol.* 21, 973–982. doi: 10.1111/j.1540-8167.2010.01814.x

Yushkevich, P. A., Piven, J., Hazlett, H. C., Smith, R. G., Ho, S., Gee, J. C., et al. (2006). User-guided 3D active contour segmentation of anatomical structures: Significantly improved efficiency and reliability. *NeuroImage* 31, 1116–1128. doi: 10.1016/j.neuroimage.2006.01.015

Zhang, L. T., and Gay, M. (2008). Characterizing left atrial appendage functions in sinus rhythm and atrial fibrillation using computational models. *J. Biomech.* 41, 2515–2523. doi: 10.1016/j.jbiomech.2008.05.012

Conflict of Interest Statement: The authors declare that the research was conducted in the absence of any commercial or financial relationships that could be construed as a potential conflict of interest.

frontiers in Physiology

ORIGINAL RESEARCH
published: 03 April 2019
doi: 10.3389/fphys.2019.00337

Extended Bidomain Modeling of Defibrillation: Quantifying Virtual Electrode Strengths in Fibrotic Myocardium

Jean Bragard[1]*, *Aparna C. Sankarankutty*[2,3] and *Frank B. Sachse*[2,3]*

[1] Department of Physics and Applied Mathematics, University of Navarra, Pamplona, Spain, [2] Nora Eccles Harrison Cardiovascular Research and Training Institute, University of Utah, Salt Lake City, UT, United States, [3] Department of Biomedical Engineering, University of Utah, Salt Lake City, UT, United States

Defibrillation is a well-established therapy for atrial and ventricular arrhythmia. Here, we shed light on defibrillation in the fibrotic heart. Using the extended bidomain model of electrical conduction in cardiac tissue, we assessed the influence of fibrosis on the strength of virtual electrodes caused by extracellular electrical current. We created one-dimensional models of rabbit ventricular tissue with a central patch of fibrosis. The fibrosis was incorporated by altering volume fractions for extracellular, myocyte and fibroblast domains. In our prior work, we calculated these volume fractions from microscopic images at the infarct border zone of rabbit hearts. An average and a large degree of fibrosis were modeled. We simulated defibrillation by application of an extracellular current for a short duration (5 ms). We explored the effects of myocyte-fibroblast coupling, intra-fibroblast conductivity and patch length on the strength of the virtual electrodes present at the borders of the normal and fibrotic tissue. We discriminated between effects on myocyte and fibroblast membranes at both borders of the patch. Similarly, we studied defibrillation in two-dimensional models of fibrotic tissue. Square and disk-like patches of fibrotic tissue were embedded in control tissue. We quantified the influence of the geometry and fibrosis composition on virtual electrode strength. We compared the results obtained with a square and disk shape of the fibrotic patch with results from the one-dimensional simulations. Both, one- and two-dimensional simulations indicate that extracellular current application causes virtual electrodes at boundaries of fibrotic patches. A higher degree of fibrosis and larger patch size were associated with an increased strength of the virtual electrodes. Also, patch geometry affected the strength of the virtual electrodes. Our simulations suggest that increased fibroblast-myocyte coupling and intra-fibroblast conductivity reduce virtual electrode strength. However, experimental data to constrain these modeling parameters are limited and thus pinpointing the magnitude of the reduction will require further understanding of electrical coupling of fibroblasts in native cardiac tissues. We propose that the findings from our computational studies are important for development of patient-specific protocols for internal defibrillators.

Keywords: defibrillation, cardiac tissue, fibrosis, computational modeling, multidomain modeling

OPEN ACCESS

Edited by:
Javier Saiz,
Universitat Politècnica de València, Spain

Reviewed by:
Bradley John Roth,
Oakland University, United States
Edward Joseph Vigmond,
Université de Bordeaux, France

***Correspondence:**
Jean Bragard
jbragard@unav.es
Frank B. Sachse
frank.sachse@utah.edu

Specialty section:
This article was submitted to Computational Physiology and Medicine, a section of the journal Frontiers in Physiology

Received: *17 December 2018*
Accepted: *13 March 2019*
Published: *03 April 2019*

Citation:
Bragard J, Sankarankutty AC and Sachse FB (2019) Extended Bidomain Modeling of Defibrillation: Quantifying Virtual Electrode Strengths in Fibrotic Myocardium. Front. Physiol. 10:337. doi: 10.3389/fphys.2019.00337

INTRODUCTION

Several types of cardiac arrhythmias are treated with external or implanted defibrillators, which are devices for application of electrical current to a patient's thorax or heart (Al-Khatib et al., 2017). The electrical currents create an electrical field in the heart, which is determined by the location and geometry of the electrodes, the magnitude and waveform of the applied current, and the distribution, composition and electrical properties of tissues. Targets of defibrillation are constituents of cardiac muscle tissues, i.e., the myocytes. These cells respond to an extracellular electrical field caused by a defibrillator with changes of their transmembrane voltage. Modulated by the electrophysiological state of the myocytes, their transmembrane voltage will exhibit negative or positive shifts due to the electrical field. Thus, defibrillation might cause hyperpolarization and depolarization of myocytes. Also, defibrillation might trigger or modulate action potentials.

Several theories for mechanisms of defibrillation of the heart have been developed (Dosdall et al., 2010). The critical mass theory suggests that defibrillation success requires myocyte depolarization in a sufficient mass of tissue. The upper limit of vulnerability theory proposes the existence of a minimal electrical stimulus strength above which ventricular fibrillation cannot be induced even for stimuli occurring during the vulnerable period of the cardiac cycle. The sawtooth hypothesis and the syncytial heterogeneity hypothesis explains defibrillation effects on the transmembrane voltage of myocytes distally from the electrodes based on microscopic discontinuities of the intracellular space (Fishler, 1998). Similarly, the virtual electrode theory explains defibrillation effects based on structural heterogeneities such as endo- and epicardial surfaces as well as blood vessels. Virtual electrodes are thought to underlie local shifts of transmembrane voltages and thus trigger action potentials and elicit wave fronts that interfere with fibrillation. Recent work using computational modeling focused on understanding virtual electrodes caused by vessels (Connolly et al., 2017a,b) and related curvature of the surface of tissue heterogeneities to myocyte depolarization and initiation of wave fronts (Bittihn et al., 2012).

It is well-established that patients with myocardial fibrosis profit from defibrillator implantation (Iles et al., 2011), but it has also been reported that patients exhibit an increased mortality if they receive defibrillation shocks (Cevik et al., 2009). Several cardiac diseases including fibrosis are associated with discontinuity of the intracellular space and microstructural heterogeneity. For instance, myocardial infarction leads to scar regions with a decreased volume ratio of myocytes, but increased volume ratios of the extracellular space and fibroblasts. Also, our recent studies on a rabbit model of myocardial infarction revealed patches of fibrotic tissue interspersed within working myocardium distal from the scar (Seidel et al., 2017). Furthermore, several types of fibrosis of cardiac tissue are characterized by local increases of extracellular space and fibroblasts. Currently, our knowledge on defibrillation effects in fibrotic tissues is sparse and we do not even know if understanding these effects can help with parameterization of defibrillation protocols. Based on virtual electrode theory, it is conceivable that fibrotic tissue will exhibit substantial effects in response to defibrillation. However, experimental and computational studies on this subject have not been performed.

Here, we investigated the effects of defibrillation on transmembrane voltages in fibrotic tissues. We applied an extended bidomain model of electrical conduction in cardiac tissue. In contrast to the conventional bidomain model, which describes myocyte and extracellular domains only, the extended model comprises a description of a fibroblast domain. We performed simulations in one-dimensional (1D) and two-dimensional (2D) models of cardiac tissues with fibrotic patches of variable sizes, tissue composition and myocyte-fibroblast electrical coupling. We measured shifts of the myocyte membrane voltage caused by application of strong extracellular currents to assess the strength of virtual electrodes.

METHODS

Extended Bidomain Modeling of Cardiac Conduction

We utilized the extended bidomain model for computational simulations of defibrillation in 1D and 2D domains (Sachse et al., 2009). The model was developed based on the established bidomain model (Tung, 1978; Henriquez, 1993) and allows description of cardiac tissues comprising more than one cell species. The original extended bidomain model comprised two cell species, i.e., cardiac myocytes and fibroblasts. Intracellular domains for these two species together with the extracellular domain constitute three domains of interest.

The mathematical formulation of the extended bidomain model applies Kirchhoff's electrical current conservation law to myocardium (Plonsey and Barr, 2007). Here we followed the exposition in Sachse et al. (2009), which described the electrical dynamics of the myocardium in three "homogenized" continuous domains. In short, the expression of current conservation at any point in space mathematically translates into a Poisson equation for each of the three domains:

$$\nabla \cdot \left(\sigma_{myo} \nabla \phi_{myo}\right) = -f_{s,myo} + \beta_{myo,fib}\, I_{myo,fib} + \beta_{myo}\, I_{myo,e} \quad (1)$$

$$\nabla \cdot \left(\sigma_{fib} \nabla \phi_{fib}\right) = -f_{s,fib} - \beta_{myo,fib}\, I_{myo,fib} + \beta_{fib}\, I_{fib,e} \quad (2)$$

$$\nabla \cdot \left(\sigma_{e} \nabla \phi_{e}\right) = -f_{s,e} - \beta_{myo}\, I_{myo,e} - \beta_{fib}\, I_{fib,e} \quad (3)$$

where σ_{myo}, σ_{fib} and σ_e are the electrical conductivity tensors of the myocyte, fibroblast and extracellular domain, respectively, ϕ_{myo}, ϕ_{fib} , and ϕ_e are the intracellular potential of the myocyte, fibroblast and extracellular domain, respectively, and $f_{s,myo}$, $f_{s,fib}$, and $f_{s,e}$ (A/m^3), are the stimulus current source densities for the myocyte, fibroblast and extracellular domain, respectively. Membrane voltage of myocytes V_{myo} and fibroblasts V_{fib} was defined as the difference of their intracellular and extracellular potential. The number of myocytes per unit volume β_{myo} and fibroblasts per unit volume β_{fib} $(1/m^3)$ were defined as:

$$\beta_{myo} = \frac{Vol_{myo}}{Vol_{myo,single}} \quad (4)$$

$$\beta_{fib} = \frac{Vol_{fib}}{Vol_{fib,single}} \tag{5}$$

with the volume fraction of myocytes Vol_{myo} and fibroblasts Vol_{fib} (dimensionless) as well as the individual volume for a myocyte $Vol_{myo,single}$ and fibroblast $Vol_{fib,single}$ (m^3). Currents between the myocyte and extracellular, fibroblast and extracellular, and myocyte and fibroblast domains are identified by $I_{myo,e}$, $I_{fib,e}$, and $I_{myo,fib}$ (A), respectively.

The current between the myocyte and fibroblast domain was defined as:

$$I_{myo,fib} = \frac{\phi_{myo} - \phi_{fib}}{R_{myo,fib}} \tag{6}$$

where $R_{myo,fib}$ is the resistance of gap junction channels (Ω). We defined the effective volume density $\beta_{myo,fib}$ ($1/m^3$) of electrical connections between fibroblasts and myocytes as:

$$\beta_{myo,fib} = \frac{Vol_{fib}}{Vol_{fib,single}} \tag{7}$$

We assumed that the conductivity tensors (S/m) for each domain have a linear relationship with their respective volume fractions:

$$\sigma_{myo} = Vol_{myo}\,\overline{\sigma}_{myo} \tag{8}$$

$$\sigma_{fib} = Vol_{fib}\,\overline{\sigma}_{fib} \tag{9}$$

$$\sigma_{e} = Vol_{e}\,\overline{\sigma}_{e} \tag{10}$$

where the tensors $\overline{\sigma}_{myo}$, $\overline{\sigma}_{fib}$ and $\overline{\sigma}_{e}$ described conductivity for volume ratios of 100%. In the subsequently described simulations, we vary $\overline{\sigma}_{fib}$ over a wide range of conductivities. We note that the range of σ_{fib} is smaller, due to scaling by the fibroblast volume fraction.

We applied a mathematical model of a rabbit ventricular myocyte (Mahajan et al., 2008) and a cardiac fibroblast (Sachse et al., 2008) to calculate the currents $I_{myo,e}$ and $I_{fib,e}$, respectively. Temperature of the fibroblast model was set to the same temperature as the myocyte model (308 K). We applied a temperature coefficient (Q10) of 2 to adjust rate coefficients of the time- and voltage dependent outward current of the fibroblast model.

Implementation of Extended Bidomain Model

The extended bidomain model was implemented using the finite volume method and the programming language Fortran. The Portable, Extensible Toolkit for Scientific Computation (PETSc) (Balay et al., 2018) was used for parallelization and solving the Poisson equation. The myocyte (Cellml, 2008b) and fibroblast (Cellml, 2008a) models were implemented from CellML (Garny et al., 2008).

A simple forward Euler scheme with a fixed time step of 0.5 or 1 μs was applied to solve the time evolution of the model. The Poisson equation for the cellular domain was solved at each time step with a relative tolerance of 10^{-12}. We applied the GMRES method, a member of the iterative Krylov methods that are implemented in PETSc. We used the additive Schwarz preconditioner in order to speed up the convergence for the iterative solver. The internal number of iterations for the Poisson solver for the 2D simulations was in the range of 50–100. This constituted the main burden of the numerical calculation. We checked for current conservation at each link of the discretized domain up to this precision (no numerical artifact of creation or annihilation of currents). In order to validate our numerical implementation, we also checked that the change in grid size discretization does not affect the results. We have compiled measured parameters in **Tables S1–S3** to show that variation of spatial resolution in the range of 25–100 μm has only minor effects. We further evaluated this new implementation of the extended bidomain model using our prior implementation (Sachse et al., 2009; Seemann et al., 2010). Modifications of the prior implementation were performed to account for discontinuity in the material properties of the cardiac tissue at the interface between the control and fibrotic regions.

Setup of 1D Simulations

We created 1D models of normal rabbit ventricular myocardium with an embedded central fibrotic patch (**Figure 1A**). The model was discretized with a spatial resolution of 50 or 100 μm. The patch exhibited differences in volume fractions of extracellular space, myocytes and fibroblasts measured in our previous work of fibrotic tissue (Greiner et al., 2018). Two different types of patches representing average and large fibrosis were configured (**Table 1**). We varied $R_{myo,fib}$ and $\overline{\sigma}_{fib}$ in simulations. The simulations started with applying 9 depolarizing myocyte membrane currents at the location 32.5–33 mm of the domain with an amplitude of 20 $\mu A/cm^2$ and a duration of 5 ms at a frequency of 4 Hz. At 250 ms after the last stimulus, extracellular currents were applied at 1–1.5 mm and 32.5–33 mm of the domain with an amplitude of 0.7×10^5 and -0.7×10^5 A/m^3, respectively. These injected currents created a nearly uniform electric field between the two sites of magnitude $E = 0.546$ V/cm (**Figure S1**). This electric field, in turn, was responsible for the generation of the virtual electrodes at the left (referred as point 1) and right (point 2) boundary of the fibrotic patch.

In order to measure virtual electrode strengths, we monitored the difference in the membrane voltage of the myocytes V_{myo} and fibroblasts V_{fib} at patch boundaries during the application of extracellular current with respect to the membrane voltages before current application. V_{myo} was not a monotonic function of time during the current application (**Figure S2**). Therefore, we reported the largest absolute value (maintaining its sign) of the monitored difference during the current application as a measure of the local virtual electrode strength. In addition, we quantified space constants λ_{myo} and λ_{fib} by fitting the spatial profile of V_{myo} and V_{fib}, respectively, at and proximal to the boundaries of the patch.

Setup of 2D Simulations

We generated 2D models of normal rabbit ventricular myocardium with an embedded fibrotic patch of square and disk-like shapes (**Figures 1B,C**). The square side length and

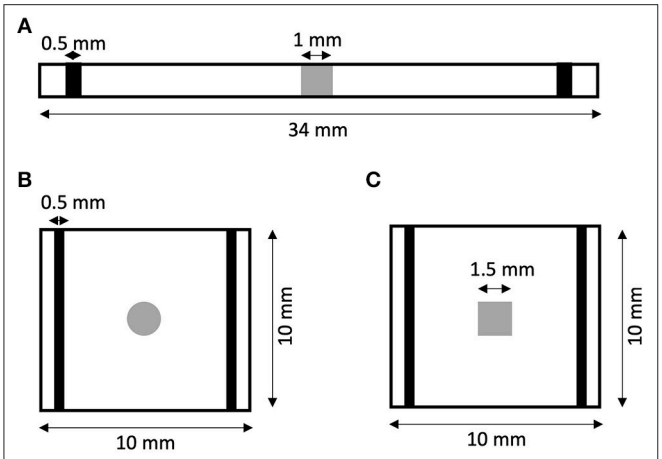

FIGURE 1 | Geometry of **(A)** 1D and **(B,C)** 2D models of rabbit ventricular tissue with central fibrotic patch. The sites of extracellular current application are marked in black. Fibrotic patches are shown in grey.

TABLE 1 | Parameters of extended bidomain model.

Parameter	Symbol	Region	Value
Extracellular volume fraction (%)	Vol_e	Control	32
		Average fibrosis	43
		Large fibrosis	60
Myocyte volume fraction (%)	Vol_{myo}	Control	65
		Average fibrosis	47
		Large fibrosis	20
Fibroblast volume fraction (%)	Vol_{fib}	Control	3
		Average fibrosis	10
		Large fibrosis	20
Extracellular conductivity (S/m)	$\overline{\sigma}_e$		1
Intra-myocyte conductivity (S/m)	$\overline{\sigma}_{myo}$		0.5
Intra-fibroblast conductivity (S/m)	$\overline{\sigma}_{fib}$		0, 0.1, 0.2, 0.5
Myocyte-fibroblast coupling resistance (MΩ)	$R_{myo,fib}$		1–10^6
Volume of single myocyte (pL)	$Vol_{myo,single}$		10.299
Volume of single fibroblast (pL)	$Vol_{fib,single}$		0.268
Membrane capacitance per unit area (μF/cm^2)			1
Myocyte surface to volume ratio (cm^{-1})			2,500
Fibroblast surface to volume ratio (cm^{-1})			16,800

the disk diameter were both set to 1.5 mm. We discretized the model with a spatial resolution of 50 μm in x and y direction. The computational domain was 1 cm x 1 cm in size. We applied four intracellular stimuli at 9–9.5 mm along the length and entire width with an amplitude of 20 μA/cm^2 for 5 ms at a frequency of 4 Hz. Two hundred and fifty milliseconds after the last stimulation, extracellular currents were applied at 0.5–1 mm and 9–9.5 mm along the length and throughout the width with an amplitude of 0.7×10^5 and -0.7×10^5 A/m^3, respectively. These injected currents created a nearly uniform electric field between the two electrodes of magnitude 0.530 V/cm.

Data Analysis

Effects of patch length W_p on ΔV_{myo} were analyzed using the fitting function:

$$\Delta V_{myo} = a\left(1 - e^{-\frac{W_p}{b}}\right) \tag{11}$$

with the parameters a and b. We used a different fitting function for ΔV_{fib}, because it was not always crossing the origin of axes:

$$\Delta V_{fib} = c - ae^{-\frac{W_p}{b}} \tag{12}$$

with the parameters a, b and c. We measured the fit quality using the adjusted R^2.

RESULTS

1D Simulations

We performed numerical simulations with the 1D extended bidomain model of control tissue with a central patch configured with parameters for average fibrosis (**Figure 1A**). The model was discretized with a spatial resolution of 100 μm. In **Figures 2A–C**, we present the results of a simulation of a propagating wave initiated by intracellular stimulation followed by application of extracellular current. The model parameters were $R_{myo,fib} = 4 \times 10^4$ MΩ and $\overline{\sigma}_{fib} = 0.1$ S/m. After scaling with the fibroblast volume fraction (Equation 9) in control tissue (3%) and patch (10%), σ_{fib} amounted to 0.003 and 0.01 S/m, respectively. In this case, the propagation of action potentials was only marginally affected by the fibrotic patch. Extracellular current altered ϕ_e as well as V_{myo} and V_{fib} at the application sites and the borders of the fibrotic patch.

We present the spatial distribution of ϕ_e, V_{myo}, and V_{fib} at the end ($t = 2.255$ s) of current application in **Figures 2D–F**, respectively. Due to current application, V_{myo} at the left border of the patch was increased from −84.95 mV before current application to −75.59 mV at the end of the current application. V_{fib} was reduced from −54.05 mV before current application to −58.97 mV at the end of the current application. At the right border of the patch V_{myo} was decreased from −85.00 to −93.44 mV. V_{fib} was increased from −54.21 to −51.18 mV. We determined the electric field for average and large fibrosis during the current application (**Figures S1A,B**, respectively). The spatial variation outside of the region for current application was small.

We applied the 1D model in a series of simulations varying $R_{myo,fib}$ and $\overline{\sigma}_{fib}$. Example simulated ϕ_e, V_{myo}, and V_{fib} are presented in **Figure S3**. Before current application, the biphasic relationship of V_{myo} with $R_{myo,fib}$ was nearly identical on both

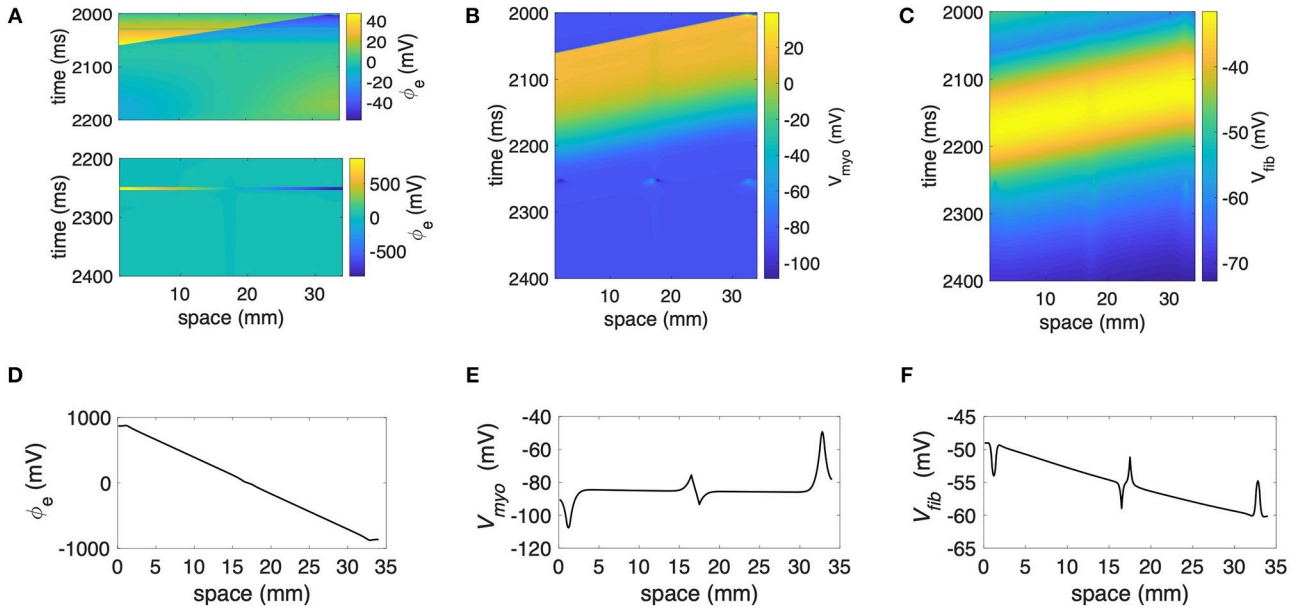

FIGURE 2 | Representative plots of **(A)** ϕ_e, **(B)** V_{myo}, and **(C)** V_{fib} for intracellular pacing and subsequent extracellular current application in the 1D model with the average fibrosis patch, $\overline{\sigma}_{fib}$ of 0.1 S/m and $R_{myo,fib}$ of 40 GΩ. Spatial distribution of **(D)** ϕ_e, **(E)** V_{myo}, and **(F)** V_{fib} at the end of application of extracellular currents. The extracellular current led to alterations of V_{myo} and V_{fib} not only at the application site, but also at the left and right border of the fibrotic patch.

boundaries of the patch (**Figures 3A,C**). Also, variation of $\overline{\sigma}_{fib}$ did not affect V_{myo}. After current application, the left border of the patch exhibited increased V_{myo}, measured as $\Delta V_{myo}^{(1)}$, dependent on $R_{myo,fib}$ and $\overline{\sigma}_{fib}$ (**Figure 3B**). At the right border of the patch, the reduction of V_{myo}, measured as $\Delta V_{myo}^{(2)}$, was dependent on $R_{myo,fib}$ and $\overline{\sigma}_{fib}$ (**Figure 3D**). At both borders of the patch, effects on V_{myo} were of similar magnitude for all $\overline{\sigma}_{fib}$ for large $R_{myo,fib}$.

We present corresponding measures on V_{fib} in **Figure 4**. The biphasic relationship of V_{fib} with $R_{myo,fib}$ before application of extracellular current (**Figures 4A,C**) was similar to the relationship of V_{myo} with $R_{myo,fib}$. For low $R_{myo,fib}$ (high myocyte-fibroblast coupling), V_{fib} was similar to the resting V_{myo} (**Figures 3A,C**). For high $R_{myo,fib}$ (low myocyte-fibroblast coupling), $V_{fib}$was close to the membrane voltage of isolated fibroblasts, i.e., ∼58 mV (Shibukawa et al., 2005; Sachse et al., 2008). Similar as myocytes, fibroblasts at the borders of the patch exhibit alterations of their membrane voltage, $\Delta V_{fib}^{(1)}$ and $\Delta V_{fib}^{(2)}$, dependent on $R_{myo,fib}$ and $\overline{\sigma}_{fib}$ in response to current application (**Figures 4B,D**). For low $R_{myo,fib}$, ΔV_{fib} was roughly similar to the ΔV_{myo} at both borders. In contrast, for high $R_{myo,fib}$, ΔV_{fib} exhibited a reverse sign vs. the corresponding ΔV_{myo} at both borders. This results in the discontinuity in ΔV_{fib} for $R_{myo,fib}$ of 100–1,000 MΩ (**Figures 4B,D**).

Using the same geometrical model and experimental protocol, we also performed simulations using a patch with large fibrosis (**Figures 5**, **6**). While the results were qualitatively similar as for the average case of fibrosis described above, we note important differences. In particular, the higher degree of fibrosis was associated with a higher magnitude of ΔV_{myo} and ΔV_{fib}. We observed conduction block for $R_{myo,fib}$ of 100–1,000 MΩ (**Figures 5A,C**). We confirmed that the magnitude ΔV_{myo} is a monotonously increasing function of the degree of fibrosis (**Figures 7A,B**). The parameter α described the variation between the low degree of fibrosis ($\alpha = 0$) to the high degree of fibrosis ($\alpha = 1$). In the range of settings that we have studied, the variation of ΔV_{myo} with α was roughly linear. Similarly, for low $R_{myo,fib}$ the magnitude ΔV_{fib} was a monotonously increasing function of α (**Figures 7C,D**). For high $R_{myo,fib}$, the magnitude ΔV_{fib} was approximately constant for α between 0 and 1.

We assessed the influence of patch length on virtual electrode strengths (**Figure 8**). The simulations were performed with a spatial resolution of 50 μm in order to explore smaller patch lengths. We present fit parameters of ΔV_{myo} and ΔV_{fib} in **Table 2**. The patch length was a major modulator of virtual electrode strengths. The larger the patch, the higher the effect on membrane voltages. However, there is a limit to this phenomenon, with the effect tapering off for longer patches. We assessed the length scale, which depends on the coupling between the myocyte and fibroblast domain through the coupling parameter $R_{myo,fib}$. For large $R_{myo,fib}$, the spatial length scales for the myocytes and fibroblasts correspond to their respective space constants λ_{myo} and λ_{fib}. In contrast, for low $R_{myo,fib}$ the spatial length scales were the same for the two species due to the coupling and settled at an intermediate value between λ_{myo} and λ_{fib}. Indeed, larger difference of the ΔV_{myo} and ΔV_{fib} were at the sub-millimeter scale (**Figure 8**), which is in agreement with the estimated values for of λ_{myo} and λ_{fib} (**Tables S1–S3**).

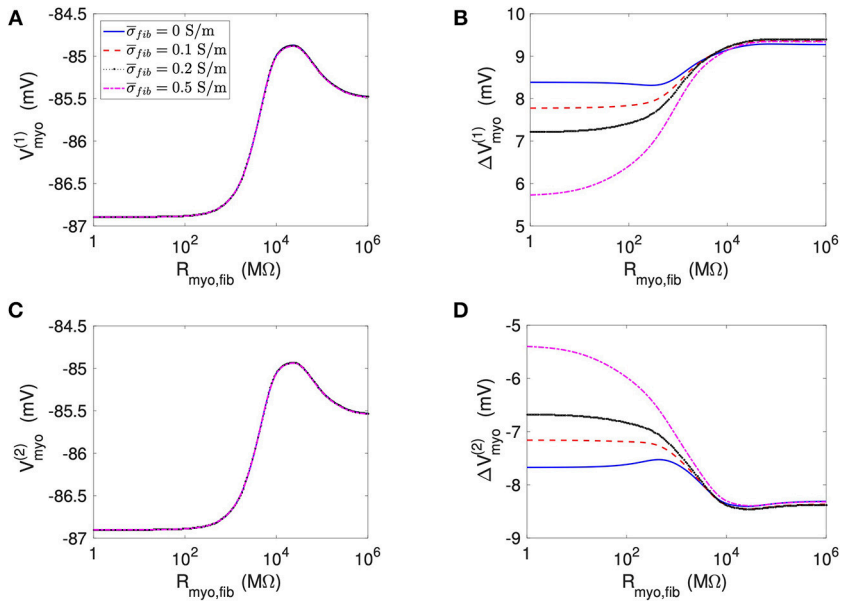

FIGURE 3 | Measurement of effects of extracellular current application on V_{myo} using the 1D model with the average fibrosis patch. Before application of extracellular currents, V_{myo} at the **(A)** left and **(C)** right border of the fibrotic patch was marginally affected by $R_{myo,fib}$ and $\overline{\sigma}_{fib}$. **(B)** At the end of current application, the left patch border exhibited a positive ΔV_{myo}. **(D)** In contrast, the right patch border exhibited a negative ΔV_{myo}.

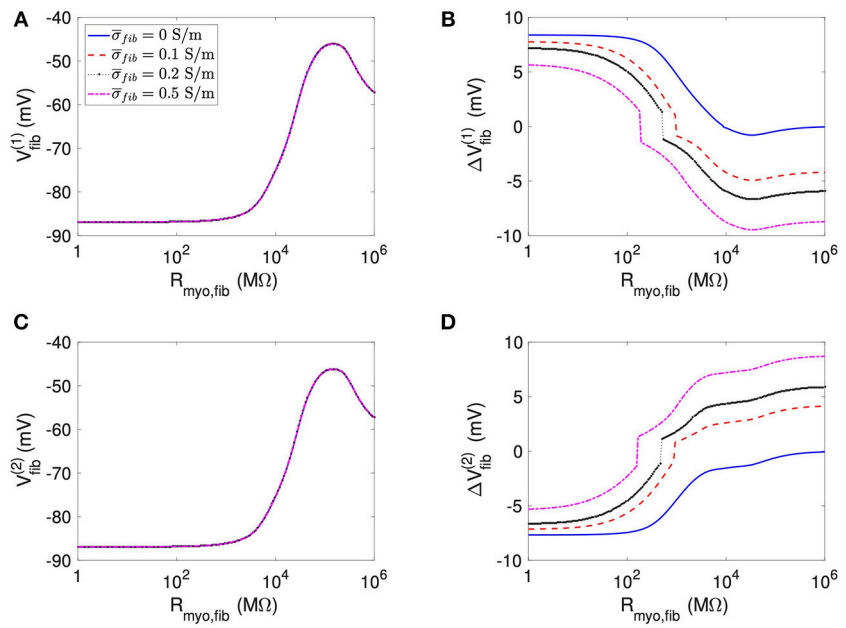

FIGURE 4 | Measurement of effects of extracellular current application on V_{fib} using the 1D model with the average fibrosis patch. Before application of extracellular currents, V_{fib} at the **(A)** left and **(C)** right border of the fibrotic patch was strongly affected by $R_{myo,fib}$ and $\overline{\sigma}_{fib}$. At the end of current application, the **(B)** left and **(D)** right border exhibited a ΔV_{fib} with magnitude and sign modulated by $R_{myo,fib}$ and $\overline{\sigma}_{fib}$.

2D Simulations

We investigated virtual electrodes in a 2D spatial domain of control tissue with central patches configured with parameters for average fibrosis (**Figures 1B,C**). Because we know from the 1D simulations that effects of the patch on ΔV_{myo} and ΔV_{fib} are larger at the millimeter than sub-millimeter scale, we set the patches (square and disk) to a size of 1.5 mm.

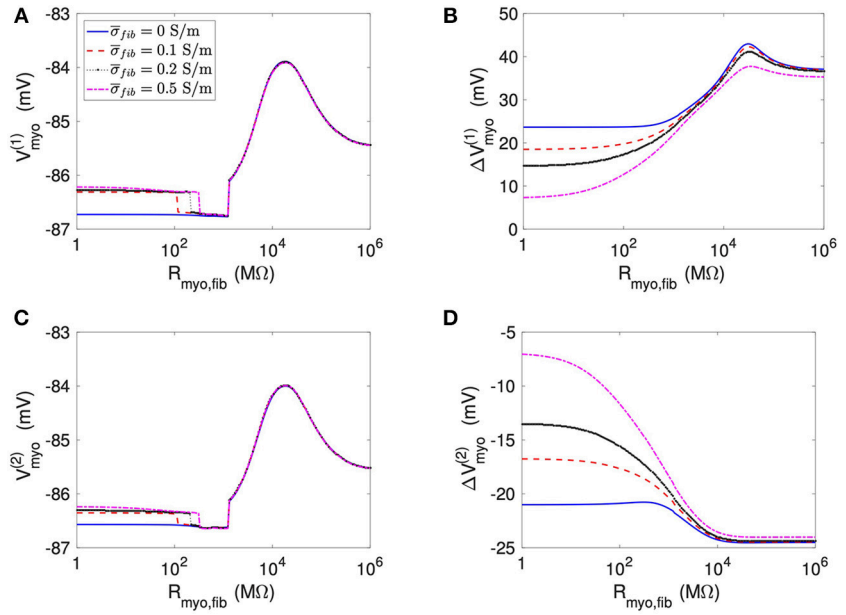

FIGURE 5 | Measurement of effects of extracellular current application on V_{myo} using the 1D model with the large fibrosis patch. Before application of extracellular currents, V_{myo} at the **(A)** left and **(C)** right border of the fibrotic patch was marginally affected by $R_{myo,fib}$ and $\overline{\sigma}_{fib}$. **(B)** At the end of current application, the left patch border exhibited a positive ΔV_{myo}. **(D)** In contrast, the right patch border exhibited a negative ΔV_{myo}.

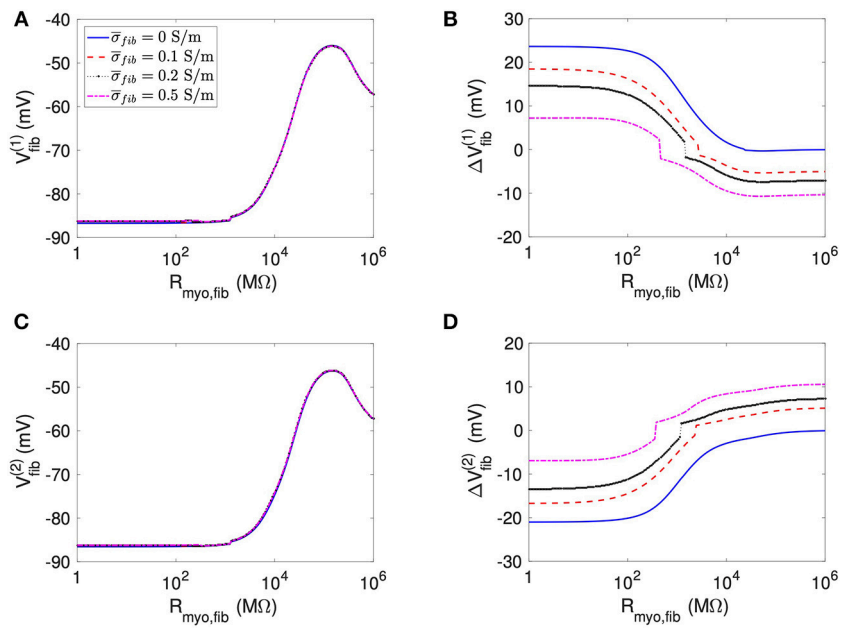

FIGURE 6 | Measurement of effects of extracellular current application on V_{fib} using the 1D model with the large fibrosis patch. Before application of extracellular currents, V_{fib} at the **(A)** left and **(C)** right border of the fibrotic patch was strongly affected by $R_{myo,fib}$ and $\overline{\sigma}_{fib}$. At the end of current application, the **(B)** left and **(D)** right border exhibited a ΔV_{fib} with magnitude and sign modulated by $R_{myo,fib}$ and $\overline{\sigma}_{fib}$.

Figure 9 displays the 3 main fields at the end of the extracellular current application in a model with a square-shaped patch, $\overline{\sigma}_{fib}$ of 0.1 S/m and $R_{myo,fib}$ of 1 GΩ. The injected currents at the electrode generated a fairly linear distribution for ϕ_e (**Figures 9A,D**), which implies a quasi-uniform electric field. Only close to the cathode (x≈9 mm) the field was distorted by a nascent wave initiated at the cathode location. Closer inspection revealed that the field is really uniform close to the patch

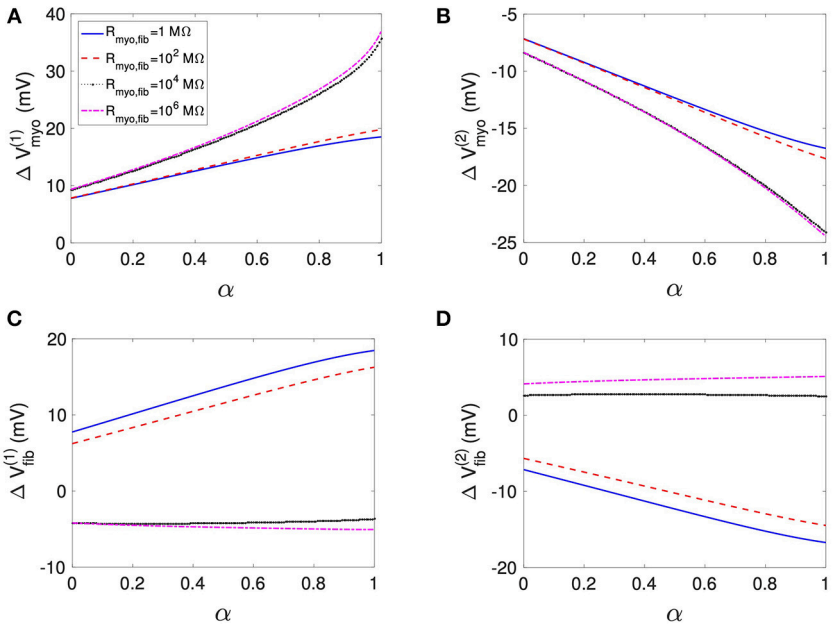

FIGURE 7 | Assessment of effects of extracellular current application on V_{myo} and V_{fib} simulated in 1D models with a patch of varying degrees of fibrosis. The degree of fibrosis ranged from average ($\alpha = 0$) to large ($\alpha = 1$). We also varied $R_{myo,fib}$. $\overline{\sigma}_{fib}$ was set to 0.1 S/m. The effects on the magnitude of ΔV_{myo} at the **(A)** left and **(B)** right boundary increased with the degree of fibrosis. Similarly, effects of ΔV_{fib} at the **(C)** left and **(D)** right boundary increased with the degree of fibrosis for small $R_{myo,fib}$. Marginal effects were present for larger $R_{myo,fib}$.

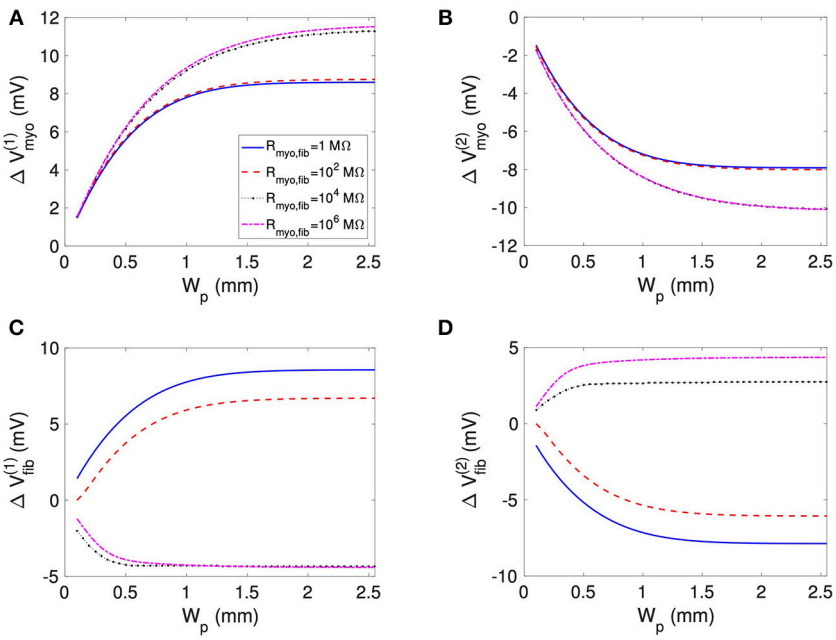

FIGURE 8 | Effects of patch length W_p on **(A,B)** V_{myo} and **(C,D)** V_{fib} at the boundary of the patch in response to application of the extracellular current. We varied $R_{myo,fib}$, but $\overline{\sigma}_{fib}$ was set on 0.1 S/m. For small W_p, V_{myo}, and V_{fib} were greatly reduced.

(**Figure 9D**). The corresponding spatial distribution of V_{myo} for the same time shows the virtual electrodes at the two edges of the square that are perpendicular to the applied field (**Figures 9B,E**). The edge corresponding to the small value of x exhibited a depolarization pattern (equivalent to point 1 in the 1D setting). On the contrary the other edge exhibited a hyperpolarization

TABLE 2 | Relationships of membrane voltage changes and W_p according to the fitting functions.

	$R_{myo,fib}$ (MΩ)	1	10^2	10^4	10^6
$\Delta V_{myo}^{(1)}$	a (mV)	8.778 (8.723, 8.833)	8.907 (8.862, 8.953)	11.65 (11.59, 11.71)	11.9 (11.84, 11.96)
	b (mm)	0.485 (0.473, 0.497)	0.4843 (0.4747, 0.494)	0.654 (0.6438,0.664)	0.6616 (0.651, 0.672)
	Adj. R^2	0.9965	0.9977	0.999	0.9989
$\Delta V_{myo}^{(2)}$	a (mV)	−8.049 (−8.087, −8.012)	−8.126 (−8.154, −8.097)	−10.24 (−10.25, −10.22)	−10.25 (−10.26, −10.23)
	b (mm)	0.4702 (0.4614, 0.479)	0.4671 (0.4606, 0.4737)	0.5756 (0.5725, 0.5787)	0.581 (0.578, 0.584)
	Adj. R^2	0.9979	0.9988	0.999	0.9999
$\Delta V_{fib}^{(1)}$	a (mV)	9.311 (9.171, 9.451)	8.965 (8.784, 9.146)	−4.682 (−4.902, −4.462)	−5.064 (−5.225, −4.903)
	b (mm)	0.447 (0.436, 0.4587)	0.455 (0.4396, 0.4709)	0.1521 (0.1454, 0.1588)	0.2181 (0.2103, 0.2259)
	c (mV)	8.677 (8.64, 8.714)	6.82 (6.771, 6.869)	−4.342 (−4.353, −4.33)	−4.374 (−4.389, −4.359)
	Adj. R^2	0.9985	0.9973	0.9944	0.9964
$\Delta V_{fib}^{(2)}$	a (mV)	−8.379 (−8.49, −8.26)	−8.106 (−8.265, −7.946)	3.136 (3.003, 3.269)	5.05 (4.887, 5.213)
	b (mm)	0.445 (0.435, 0.456)	0.454 (0.439, 0.4693)	0.1985 (0.1895, 0.2075)	0.2242 (0.216, 0.2324)
	c (mV)	−7.97 (−8.004, −7.94)	−6.17 (−6.213, −6.127)	2.728 (2.717, 2.738)	4.315 (4.299, 4.33)
	Adj. R^2	0.9988	0.9975	0.9941	0.9962

The values given in parentheses indicate a 95 % confidence interval for the parameter estimates.

pattern (equivalent to point 2 in the 1D setting). **Figures 9C,F** display the field for V_{fib}. In this example, $R_{myo,fib}$ was set to 1 GΩ, which is the value for which the coupling between the myocytes and the fibroblast cancels out the effect of the conductivity heterogeneities at the patch boundaries. According to the theory (see section Discussion), we expect to observe hyperpolarization for V_{fib} at point 1 and depolarization at point 2, which is the opposite of what happens to V_{myo}. However, the coupling term between the two domains caused that the V_{myo} is pulling the V_{fib} in the same direction. At the very edge of the patch (**Figure 9F**) the two effects cancel out.

We repeated the simulation using a disk-shaped patch with $R_{myo,fib} = 1$ TΩ, which represents negligible coupling between V_{fib} and V_{myo} (**Figure 10**). The simulation yielded a linear distribution for ϕ_e and the simulated electric field was almost identical as the field obtained with the square patch (**Figures 10A,D**). In **Figures 10B,E** we present the corresponding spatial distribution of V_{myo}. As before, we observed the two virtual electrodes at the edges of the patch. Due to the disk-shaped patch, the virtual electrodes were not so sharp and appeared diffuse also in the parallel direction of the electric field. **Figures 10C,F** confirmed that polarities of ΔV_{fib} are indeed opposite to the ΔV_{myo} at the patch boundary. Also, the spatial scale for the virtual electrode was much smaller than the virtual electrodes for the V_{myo} field, which agrees with the corresponding values for the space constants associated with the two fields.

Figure 11 and **Table S4** present quantitative measures for the virtual electrode strengths for the two patch geometries. We report the results for ΔV_{myo} and ΔV_{fib} at both locations of the patch boundaries as a function of $R_{myo,fib}$. We compared them with the corresponding values obtained for the 1D case. Using bidomain models it has been demonstrated that convex shape of boundaries leads to lower activation of the membrane (Entcheva et al., 1998, 1999; Pumir and Krinsky, 1999; Bittihn et al., 2012). This was confirmed in our simulation for ΔV_{myo} where the virtual electrode strengths were lower for the disk than for the square. However, the difference between the two geometries is rather minute. We measured an approximate 4% difference of ΔV_{myo} for low values of the $R_{myo,fib}$ and an approximate 5% difference for high values of the $R_{myo,fib}$. Also, ΔV_{myo} for the square-shaped were higher than for the disk-shaped patch, and close to the 1D patch geometry. ΔV_{fib} for the 1D and the two 2D geometries were similar (**Figures 11C,D**). For ΔV_{fib}, the influence of patch geometry was less pronounced.

DISCUSSION

Our computational study provided insights into the relationship between parameters of fibrotic patches and the strength of virtual electrodes caused by defibrillation. We applied the extended bidomain model to reflect that cardiac tissues comprise fibroblasts beyond myocytes. Our study showed that an increased degree of fibrosis and an increased size of the fibrotic patch cause an increased strength of virtual electrodes. Also, we found that the composition of tissue heterogeneities is a modulator

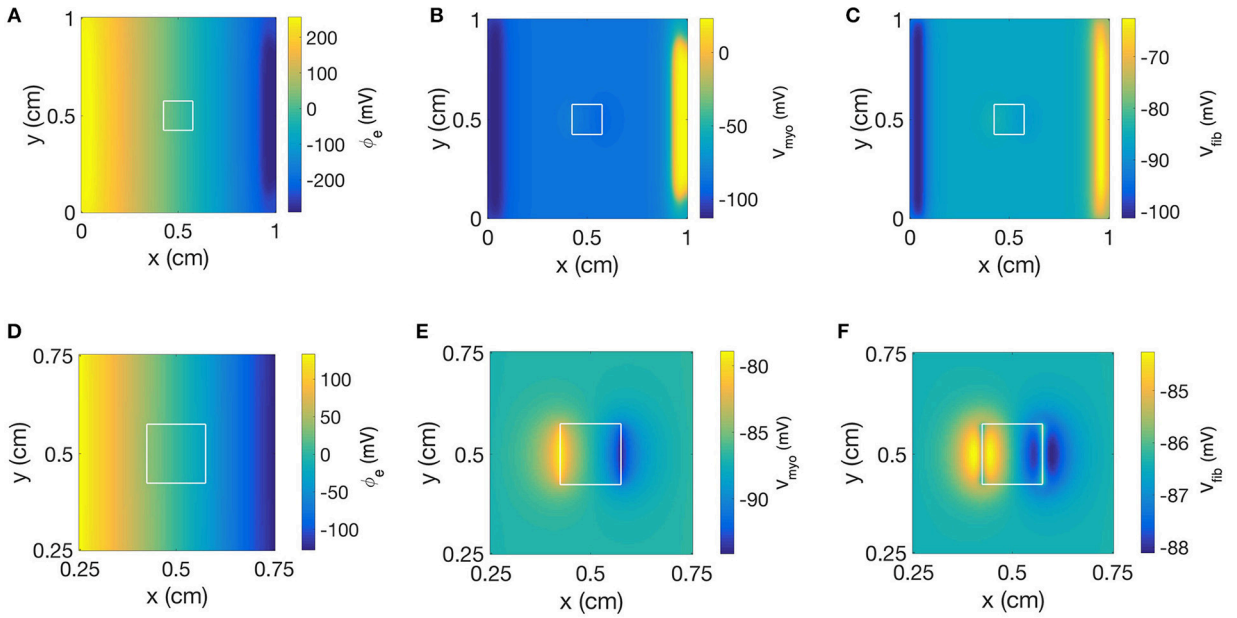

FIGURE 9 | Spatial distribution of **(A)** ϕ_e, **(B)** V_{myo}, and **(C)** V_{fib} at the end of extracellular current application in the 2D model with the square-shaped average fibrosis patch, $\overline{\sigma}_{fib}$ of 0.1 S/m and $R_{myo,fib}$ of 1 GΩ. Close-ups of the spatial distribution for **(D)** ϕ_e, **(E)** V_{myo}, and **(F)** V_{fib}. The extracellular current led to alterations of V_{myo} and V_{fib} not only at the application site, but also at the left and right border of the patch.

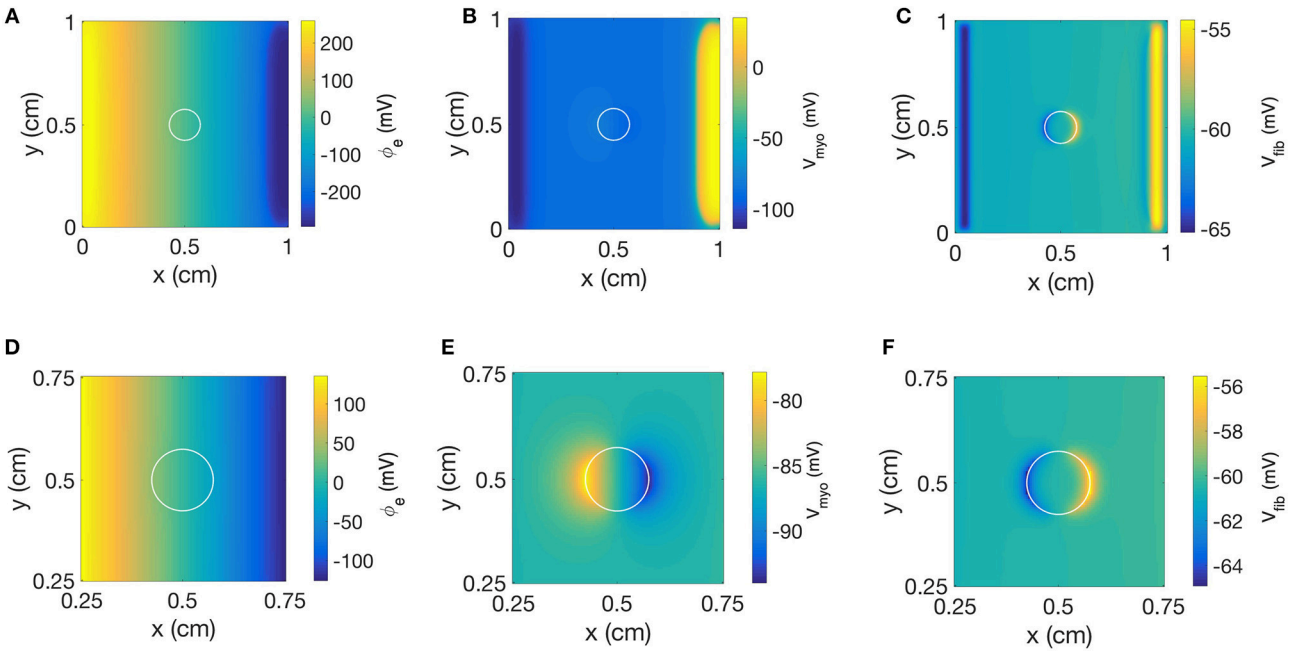

FIGURE 10 | Spatial distribution of **(A)** ϕ_e, **(B)** V_{myo}, and **(C)** V_{fib} at the end of extracellular current application in the 2D model with the disk-shaped average fibrosis patch, $\overline{\sigma}_{fib}$ of 0.1 S/m and $R_{myo,fib}$ of 1 TΩ. Close-ups of the spatial distribution for **(D)** ϕ_e, **(E)** V_{myo}, and **(F)** V_{fib} at the end of application of extracellular currents. The extracellular current led to alterations of V_{myo} and V_{fib} not only at the application site, but also at the left and right border of the patch.

of virtual electrode strength. Increased electrical coupling of myocytes with fibroblasts reduced the virtual electrode strength. Intra-fibroblast coupling reduced virtual electrodes in case of high myocyte-fibroblast coupling.

We explain our findings of depolarization and hyperpolarization of membranes during the application of the extracellular currents at the boundaries of the fibrotic patch based on reformulation of the equations for the extended

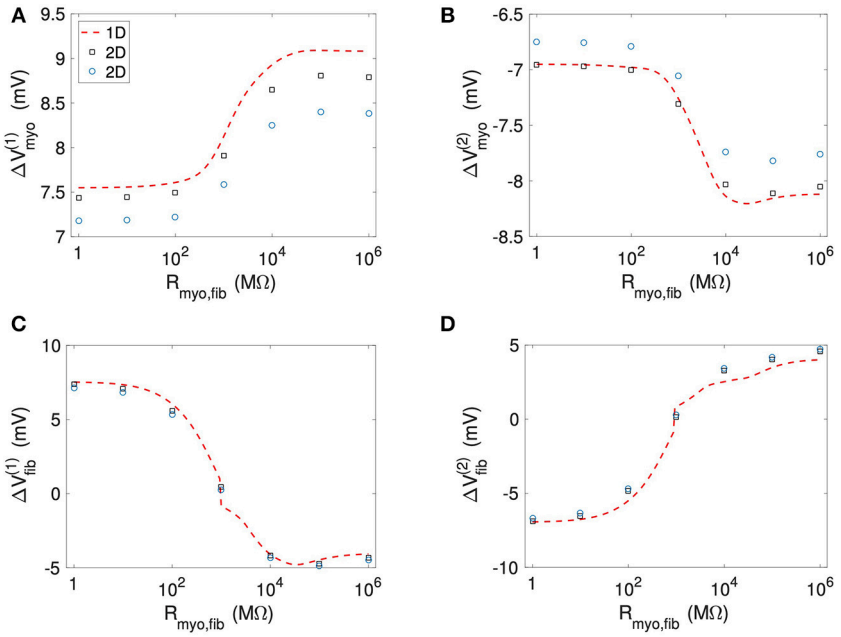

FIGURE 11 | Comparison of **(A,B)** V_{myo} and **(C,D)** V_{fib} from the 1D simulations and the 2D simulations with disk and square patch geometries. The square and circle symbols refer to the results for the respective square and disk patch geometry.

bidomain. The equations can be rewritten in the following simple form for numerical solution see Equations (17–20) in Sachse et al. (2009):

$$\frac{\partial V_{myo}}{\partial t} = \frac{1}{C_{myo}}\left(\nabla\cdot\left(\sigma_{myo}\nabla V_{myo}\right) + \nabla\cdot\left(\sigma_{myo}\nabla\phi_e\right) + \cdots\right) \tag{13}$$

$$\frac{\partial V_{fib}}{\partial t} = \frac{1}{C_{fib}}\left(\nabla\cdot\left(\sigma_{fib}\nabla V_{fib}\right) + \nabla\cdot\left(\sigma_{fib}\nabla\phi_e\right) + \cdots\right) \tag{14}$$

$$\nabla\cdot\left\{\left(\sigma_e + \sigma_{myo} + \sigma_{fib}\nabla\phi_e\right)\right\} = -f_e - \nabla\cdot\left(\sigma_{myo}\nabla V_{myo}\right) - \nabla\cdot\left(\sigma_{fib}\nabla V_{fib}\right) \tag{15}$$

with the injected current f_e due to extracellular current application, the myocyte membrane capacitance C_{myo} and the fibroblast membrane capacitance C_{fib}. Equations (13) and (14) are parabolic equations for the time evolution of the myocytes and fibroblast membrane voltage. Equation (15) is the Poisson equation for calculating the extracellular potential. In these equations, $\cdots$ indicates terms that are not of interest for our initial discussion and hence omitted.

During the current application, we injected positive charge at the electrode located at 1–1.5 mm and negative charge of the same magnitude at the electrode located at 32.5–33 mm of the extracellular domain. This current injection produced a rather uniform gradient of ϕ_e (**Figure 2**). This corresponds to a quasi-uniform E in the system (**Figure S1**):

$$E = -\nabla\phi_e \tag{16}$$

With our computational set-up, E is oriented in the same direction as the x-axis. E together with the discontinuity of the conductivity at the patch boundary is responsible for the initial changes of the membrane voltage during the current application. This can be shown by decomposing the second right hand term of Equation (13) into:

$$\frac{\partial V_{myo}}{\partial t} \propto -\left(\nabla\sigma_{myo}\right)\cdot E + \sigma_{myo}\nabla^2\phi_e \tag{17}$$

This represents the generalized activating function previously described to predict the distribution of virtual electrodes (Sobie et al., 1997). The crucial term in determining the direction of the membrane voltage change during the current application is the first right hand side term. If $\nabla\sigma_{myo}$ is oriented in the same direction as E one observes a decrease of V_{myo} (hyperpolarization). If $\nabla\sigma_{myo}$ points in the opposite direction of E, the current application leads to an increase of V_{myo} (depolarization). We extend this description for V_{fib} using a decomposition of the second right hand term of Equation (14):

$$\frac{\partial V_{fib}}{\partial t} \propto -\left(\nabla\sigma_{fib}\right)\cdot E + \sigma_{fib}\nabla^2\phi_e \tag{18}$$

In our setup, due to the variations of the volume fraction of the myocytes and fibroblasts, $\nabla\sigma_{myo}$ is pointing in the opposite direction of E at point 1 of the domain, which results in a depolarization of V_{myo}. On the contrary, $\nabla\sigma_{fib}$ at point 1 is aligned with E, which results in a hyperpolarization of V_{fib} at point 1.

However, this simple mechanistic explanation ignores the coupling term between the fibroblast and the myocyte domain.

The current $I_{myo,fib}$, which is determined by the parameter $R_{myo,fib}$ and the voltage between the domains, explains why in some cases, V_{fib} follows V_{myo}. In particular, at high coupling between myocyte and fibroblast domain (i.e., low values of $R_{myo,fib}$), V_{myo} is very similar to V_{fib}. Interestingly, at intermediate values of $R_{myo,fib}$, the simulations revealed a competition of the two antagonistic effects for V_{fib} (**Figures 4**, **6**). These two effects can even cancel each other out in a sort of tug of war situation, leaving V_{fib} at the patch boundary apparently unaffected by the application of the current (**Figure 9F**).

We note that the arguments presented here are valid in any spatial dimension. Based on the same arguments we also explain the mechanism behind the decrease of the virtual electrode strengths for large fibroblast-myocyte coupling. Our studies showed that due to heterogeneity of conductivity at the patch boundary, V_{fib} and V_{myo} tend to change in opposite directions. One membrane is depolarizing and the other one is hyperpolarizing, but the effect of the heterogeneities can be canceled out and even be inverted for V_{fib} because of current flow between the fibroblast and myocyte domain. This flow is lowering the effect of the conductivity heterogeneities and the virtual electrode strength. Theoretically, the current flow can go in either direction. If the fibroblast is the dominant constituent of the cardiac tissue at some heterogeneities, V_{fib} could pull V_{myo} to follow its electric depolarization or hyperpolarization. With the parameters applied in this study, myocytes were volume-wise dominant in the tissue. Thus, we did not observe such behavior.

For the 1D simulations, we reported extrema of the time evolution of ΔV_{fib} during the extracellular current application. In **Figures 4B,D**, the reported ΔV_{fib} is the largest absolute value (keeping its sign) of the monitored difference. These indicators exhibited a discontinuous behavior for intermediate values for the $R_{myo,fib}$ as exemplified in **Figures 4B,D**. The discontinuity is caused by the transition between dominant minima and maxima of V_{fib} as illustrated in **Figure S2B**. The transition occurred at decreased $R_{myo,fib}$, when increasing $\overline{\sigma}_{fib}$. This can be explained by the fact that the pull exerted by the myocytes on the fibroblasts diffuses faster when the diffusion is increased and is therefore less effective.

The 1D simulations for the large fibrosis revealed a complex behavior of V_{myo}. In **Figures 5A,C**, discontinuities occurred at intermediate values of $R_{myo,fib}$. This was caused by block of the propagating waves prior to the extracellular current application at the fibrotic patch, which modified the values of V_{myo}. Though this effect is important for the dynamics of the system, in the context of our study it did affect only marginally ΔV_{fib} and ΔV_{myo}.

In our 2D simulations, the influence of patch geometry on ΔV_{fib} was small (**Figures 11C,D**). This can be explained by the fact that the space constant for the fibroblast model is very small (computed previously around 0.15 mm) vs. the patch size of 1.5 mm. We refer the reader to Bittihn et al. (2012) for a more detailed description of the underlying mechanism.

A straightforward conclusion from our study is that fibrotic patches, similar as endo- and epicardial surfaces as well as blood vessels, constitute a potential site for wave initiation in response to defibrillation. This finding could help in parameterization of defibrillators. We suggest that further studies will lead to defibrillator protocols specifically for patients with known myocardial fibrosis to ensure defibrillation success. Also, based on our findings we propose that knowledge in the spatial distribution of fibrosis is valuable for optimization of positions for defibrillation electrodes. Potential clinical benefits of accounting for cardiac fibrosis are reduction in myocardial injury due to optimized defibrillation energy.

Prior studies on modeling of effects of fibrosis aimed at characterization of conduction and conduction defects as well as arrhythmogenesis and maintenance of arrhythmia in the atria and ventricles. Fibrosis was introduced in the models with various approaches including embedding of conduction barriers of various sizes and geometries, reduction of inter-myocyte coupling, regional replacement of myocytes with fibroblasts or myofibroblasts, and incorporation of myocyte-fibroblast coupling (Fishler, 1998; Fishler and Vepa, 1998; Mcdowell et al., 2012; Costa et al., 2014; Zeigler et al., 2016). Here, we applied the extended bidomain model to integrate various aspects of fibrotic remodeling.

A difficulty of applying the extended bidomain model is that we have only vague knowledge on parameters related to the fibroblast domain, in particular, the parameters $R_{myo,fib}$ and σ_{fib}. Quantitative measurements of these parameters have not been performed in normal and diseased myocardium (Kohl and Gourdie, 2014). However, a small number of *in vitro* measurements provided quantitative information to constrain these parameters. Beyond those, qualitative and indirect evidence suggests that etiologies and the progression of fibrotic remodeling affect the degree of myocyte-fibroblast and fibroblast-fibroblast electrical coupling in diseased myocardium. For these reasons, computational studies with the extended bidomain model and other computational modeling approaches commonly applied measurements from *in vitro* studies to justify parameter settings or varied parameters to reconstruct experimental findings. In this study, we chose to vary parameters within a wide range to go beyond the *in vitro* measurements and comprehensively explore potential effects of coupling.

We varied $R_{myo,fib}$ from 1 MΩ to 1 TΩ to describe strong and negligible electrical coupling, respectively, between fibroblasts and myocytes. The lower limit is close to the junctional resistance of a myocyte pair isolated from rabbit ventricular tissue (0.81 MΩ) (Kieval et al., 1992). The upper limit led to negligible currents between the fibroblast and myocyte domain, and effectively represents the case of electrical uncoupling of the domains. Experimental measurements on myocyte-fibroblast pairs in 24 h-old culture of neonatal rat hearts cells suggest that $R_{myo,fib}$ is variable and within a range of 125 MΩ and 3.23 GΩ (Rook et al., 1992). The variability was explained by the variable number of gap junction channels of the myocyte-fibroblast pairs. Prior modeling work applied measurements of gap junction channel conductances in the same preparation and assumed 10 to 30 gap junction channels per cell pair to vary $R_{myo,fib}$ from 1.11 to 3.33 GΩ for simulation of fibroblast effects in the sinoatrial node (Rook et al., 1989; Kohl et al., 1994). Assuming 0 to 75 gap junctions per cell pair, $R_{myo,fib}$ was varied from 0.44 to ∞ GΩ in a modeling study of fibroblast effects on conduction (Jacquemet and Henriquez, 2007). Based on the prior experimental and

computational studies, the lower $R_{myo,fib}$ limit (1 MΩ) in our studies appears small. We note that effects of $R_{myo,fib}$ between 1 and 10 MΩ on virtual electrodes were in general similar. This range represents the extreme case of strong myocyte-fibroblast coupling. Increasing the lower limit of the parameter range to e.g., 1 GΩ does not change our conclusions on the relationship between $R_{myo,fib}$ and virtual electrodes.

We varied $\overline{\sigma}_{fib}$ from 0 to 0.5 S/m to describe absence of electrical coupling and strong coupling, respectively, within the fibroblast domain. The lower limit represents the case of electrical uncoupling of fibroblasts. The upper limit is identical to our setting of σ_{myo}. Dependent on Vol_{fib} (Equation 9), this led to a range of σ_{fib} of 0 and up to 0.1 S/m in the region with high fibrosis with Vol_{fib} of 20%. An experimental framework for estimating σ_{fib} comprises measurements of junctional conductance in pairs of cultured rat cardiac cells. Conductances of fibroblast-fibroblasts pairs were in the range of 175 pS and 6 nS (Rook et al., 1992). Measurements of conductance in myocyte-myocyte pairs were up to 42 nS (Rook et al., 1990). Estimates of conductance based on gap-junctional area in myocyte pairs range between 0.9 and 216.6 nS. These measurements and estimates of conductance between cell pairs are not sufficient to determine σ_{fib} in normal and diseased myocardium. Further information on fibroblast geometry, gap junction distribution and cytosolic conductivity would be required to estimate σ_{fib} using computational approaches introduced by us previously (Bauer et al., 2013; Greiner et al., 2018). Considering that conductances of freshly isolated ventricular myocyte-myocyte pairs from control rabbit hearts were much higher (1.24 ± 0.25 μS) (Kieval et al., 1992), it is also unclear how the *in vitro* measurements relate to conductance in native myocardium. However, based on this information and the explored volume fractions, we argue that σ_{fib} cannot be larger than σ_{myo} even in the region of high fibrosis with identical volume fractions for the fibroblast and myocyte domain. In this region, our calculations (Equations 8, 9) using the maximal $\overline{\sigma}_{fib}$ (0.5 S/m) led to identical σ_{fib} and σ_{myo} (0.1 S/m). Prior modeling studies of electrical conduction in human atrial tissues applied σ_{fib} in the range of 0.02–0.1 S/m (Greisas and Zlochiver, 2016). Also, σ_{fib} was set to 0.06 S/m in a study on rabbit heart (Corrias et al., 2012). Based on these arguments and the prior work, we limited the exploration of σ_{fib} to values up to 0.1 S/m in our simulations. We note that this value is the maximum in our simulations and it is likely that smaller values in the explored range are more realistic. For small Vol_{fib} and thus sparse inter-fibroblast coupling, we point the reader at our simulations with σ_{fib} equal to zero.

We note that, despite the large flexibility of the extended bidomain model to describe tissue remodeling, the computational demands of the model are similar as for conventional bidomain models. A minor increase of computational demands is caused by the integration of the fibroblast domain.

We suggest that the extended bidomain model provides a more comprehensive framework for modeling of conduction in control and diseased tissue than the conventional bidomain model. While the additional parameters enable already more detailed parameterization, various refinements can be envisioned. For instance, an alternative method to define the effective volume density ($1/m^3$) of electrical connections between fibroblasts and myocytes is:

$$\beta_{myo,fib} = \beta^{(r)} \frac{Vol_{fib}}{Vol_{fib,single}} \tag{19}$$

Because the electrical coupling between the fibroblasts and myocytes is mainly unknown and potentially varies from one situation to another we can define a parameter, $\beta^{(r)}$ (dimensionless), for characterizing this coupling. A value of $\beta^{(r)} = 1$ corresponds to a situation where each of the fibroblasts has an electrical connection with the myocyte domain. A larger (smaller) value of $\beta^{(r)}$ allows changing this situation. For $\beta^{(r)} < 1$ not all the fibroblasts are coupled to a myocyte and conversely for $\beta^{(r)} > 1$ each fibroblast is coupled to more than one myocyte. Both, $R_{myo,fib}$ and $\beta^{(r)}$ are factors that contribute to the coupling between myocytes and fibroblasts and hence their effective influence can be combined in a single variable, $\beta^{(\text{fract})}$ defined as:

$$\beta^{(fract)} = \frac{\beta^{(r)}}{R_{myo,fib}} \tag{20}$$

Limitations

We acknowledge several limitations related to the presented work. The studies were performed in 1D and 2D domains with isotropic conductivities. We did not consider unequal anisotropy ratios of conductivities. We applied simple descriptions of fibrotic remodeling derived from a rabbit model of cardiac infarction. While fibrotic remodeling is known to be a multi-faceted process comprising e.g., activation of fibroblasts, their differentiation into myofibroblasts, and subcellular remodeling of structural und electrophysiological properties, we primarily considered increased volume ratios of cells and the extracellular space in our study. Also, we applied mathematical models of normal myocytes and fibroblasts, and did not adjust these models to account for fibrosis and associated remodeling.

A limitation of our work is related to incomplete understanding of myocyte-fibroblast and fibroblast-fibroblast coupling in the heart. As discussed above, experimental measurements exist only for *in vitro* models and it is difficult to apply these measurements for parameterization of models of fibrotic remodeling in native myocardium. Also, we applied a simple linear model for scaling of σ_{fib} by Vol_{fib} (Equation 9). Non-linear models might be more realistic. In particular, for small Vol_{fib}, it is likely that fibroblasts are not electrically coupled with other fibroblasts, which can be reflected by a model using piece-wise defined functions. We note the controversy on myocyte-fibroblast coupling and the contribution of fibroblasts in physiological and pathophysiological conduction (Kohl and Gourdie, 2014). Based on our simulations, myocyte-fibroblast coupling is a major determinant of virtual electrode strength. However, for the entire simulated range of myocyte-fibroblast coupling, boundaries of fibrotic patches were associated with virtual electrodes.

In our comparison of software for extended bidomain modeling, we confirmed that the new and our prior implementation yielded very similar results when simulating a homogenous tissue. Peak V_{myo} and V_{fib} differed only by 5.08% (13.98 vs. 13.3 mV) and 5.23% (13.69 vs. 13.03 mV), respectively. However, we noticed that the approach for discretization of the patch boundary affects the magnitude of the altered membrane voltages. Conventional finite difference discretization (Sachse, 2004) led to significant differences vs. the finite volume discretization used in our studies. We reduced differences to the finite volume method by implementation of a finite difference approximation based on Kirchhoff's law (Witwer et al., 1972). However, the appropriate modeling approach should be dictated by the spatial distribution of the structural remodeling. While our finite volume approach described structural remodeling as an abrupt change from control tissue to the fibrotic patch, a gradual approach might be more appropriate (Seidel et al., 2017).

A related limitation of our study is the geometry and size of patches explored in the 2D simulations. We focused on disk and square shaped patches with a single size. Larger effects of geometry are expected for smaller sizes, i.e., below the millimeter scale, but we leave this for a future exploration. Also, we suggest that microscopic imaging can provide insights into the detailed distribution of remodeling.

DATA AVAILABILITY

The datasets generated for this study are available on request to the corresponding author.

AUTHOR CONTRIBUTIONS

JB and FS designed the study. All authors developed software for this project, analyzed, and interpreted the data, drafted and critically revised the manuscript, and approved the version to be published.

FUNDING

JB acknowledges the support of a Fulbright Fellowship for his stay at the Nora Eccles Harrison Cardiovascular Research and Training Institute at the University of Utah and also partial support through a grant project by the Spanish Ministerio de Economía y Competitividad (MINECO) under number SAF2014-58286-C2-2-R. FS acknowledges financial support from the Nora Eccles Treadwell Foundation and the National Institutes of Health (R01 HL 135077 and R01 HL 132067).

ACKNOWLEDGMENTS

We thank Mr. Marcus Blackburn, Mr. Joachim Greiner, and Dr. Gunnar Seemann for their help and discussions. We also thank Mr. Haonan Yang and Mrs. Nancy Allen for technical support.

SUPPLEMENTARY MATERIAL

The Supplementary Material for this article can be found online at: https://www.frontiersin.org/articles/10.3389/fphys.2019.00337/full#supplementary-material

REFERENCES

Al-Khatib, S. M., Stevenson, W. G., Ackerman, M. J., Bryant, W. J., Callans, D. J., Curtis, A. B., et al. (2017). 2017 AHA/ACC/HRS Guideline for Management of Patients With Ventricular Arrhythmias and the Prevention of Sudden Cardiac Death: A Report of the American College of Cardiology/American Heart Association Task Force on Clinical Practice Guidelines and the Heart Rhythm Society. *Circulation* 138:e272–e391. doi: 10.1161/CIR.0000000000000549

Balay, S., Abhyankar, S., Adams, M. F., Brown, J., Brune, P., Buschelman, K., et al. (2018). *PETSc Users Manual*. Argonne National Laboratory.

Bauer, S., Edelmann, J. C., Seemann, G., Sachse, F. B., and Dossel, O. (2013). Estimating intracellular conductivity tensors from confocal microscopy of rabbit ventricular tissue. *Biomed. Tech.* 58(Suppl. 1). doi: 10.1515/bmt-2013-4333. Available online at: https://www.degruyter.com/view/j/bmte.2013.58.issue-s1-N/bmt-2013-4333/bmt-2013-4333.xml

Bittihn, P., Horning, M., and Luther, S. (2012). Negative curvature boundaries as wave emitting sites for the control of biological excitable media. *Phys. Rev. Lett.* 109:118106. doi: 10.1103/PhysRevLett.109.118106

Cellml (2008a). *Electrophysiological Modeling of Fibroblasts and Their Interaction with Myocytes [Online]*. Available online at: https://models.cellml.org/exposure/4e478093480e0d7e08a2f24177ec4906. (Accessed October 1, 2018).

Cellml (2008b). *A Rabbit Ventricular Action Potential Model Replicating Cardiac Dynamics at Rapid Heart Rates [Online]*. Available online at: https://models.cellml.org/exposure/a5586b72d07ce03fc40fc98ee846d7a5 (Accessed October 1, 2018).

Cevik, C., Perez-Verdia, A., and Nugent, K. (2009). Implantable cardioverter defibrillators and their role in heart failure progression. *Europace* 11, 710–715. doi: 10.1093/europace/eup091

Connolly, A., Vigmond, E., and Bishop, M. (2017a). Virtual electrodes around anatomical structures and their roles in defibrillation. *PLoS ONE* 12:e0173324. doi: 10.1371/journal.pone.0173324

Connolly, A. J., Vigmond, E., and Bishop, M. J. (2017b). Bidomain predictions of virtual electrode-induced make and break excitations around blood vessels. *Front Bioeng Biotechnol.* 5:18. doi: 10.3389/fbioe.2017.00018

Corrias, A., Pathmanathan, P., Gavaghan, D. J., and Buist, M. L. (2012). Modelling tissue electrophysiology with multiple cell types: applications of the extended bidomain framework. *Integr. Biol.* 4, 192–201. doi: 10.1039/c2ib00100d

Costa, C. M., Campos, F. O., Prassl, A. J., Dos Santos, R. W., Sanchez-Quintana, D., Ahammer, H., et al. (2014). An efficient finite element approach for modeling fibrotic clefts in the heart. *IEEE Trans. Biomed. Eng.* 61, 900–910. doi: 10.1109/TBME.2013.2292320

Dosdall, D. J., Fast, V. G., and Ideker, R. E. (2010). Mechanisms of defibrillation. *Annu. Rev. Biomed. Eng.* 12, 233–258. doi: 10.1146/annurev-bioeng-070909-105305

Entcheva, E., Eason, J., Efimov, I. R., Cheng, Y., Malkin, R., and Claydon, F. (1998). Virtual electrode effects in transvenous defibrillation-modulation by structure and interface: evidence from bidomain simulations and optical mapping. *J. Cardiovasc. Electrophysiol.* 9, 949–961. doi: 10.1111/j.1540-8167.1998.tb00135.x

Entcheva, E., Trayanova, N. A., and Claydon, F. J. (1999). Patterns of and mechanisms for shock-induced polarization in the heart: a bidomain analysis. *IEEE Trans. Biomed. Eng.* 46, 260–270. doi: 10.1109/10.748979

Fishler, M. G. (1998). Syncytial heterogeneity as a mechanism underlying cardiac far-field stimulation during defibrillation-level shocks. *J. Cardiovasc. Electrophysiol.* 9, 384–394. doi: 10.1111/j.1540-8167.1998.tb00926.x

Fishler, M. G., and Vepa, K. (1998). Spatiotemporal effects of syncytial heterogeneities on cardiac far-field excitations during monophasic and biphasic shocks. *J. Cardiovasc. Electrophysiol.* 9, 1310–1324. doi: 10.1111/j.1540-8167.1998.tb00107.x

Garny, A., Nickerson, D. P., Cooper, J., Weber Dos Santos, R., Miller, A. K., Mckeever, S., et al. (2008). CellML and associated tools and techniques. *Philos. Trans. A Math. Phys. Eng. Sci.* 366, 3017–3043. doi: 10.1098/rsta.2008.0094

Greiner, J., Sankarankutty, A. C., Seemann, G., Seidel, T., and Sachse, F. B. (2018). Confocal microscopy-based estimation of parameters for computational modeling of electrical conduction in the normal and infarcted heart. *Front. Physiol.* 9:239. doi: 10.3389/fphys.2018.00239

Greisas, A., and Zlochiver, S. (2016). The multi-domain fibroblast/myocyte coupling in the cardiac tissue: a theoretical study. *Cardiovasc. Eng. Technol.* 7, 290–304. doi: 10.1007/s13239-016-0266-x

Henriquez, C. S. (1993). Simulating the electrical behavior of cardiac tissue using the bidomain model. *Crit. Rev. Biomed. Eng.* 21, 1–77.

Iles, L., Pfluger, H., Lefkovits, L., Butler, M. J., Kistler, P. M., Kaye, D. M., et al. (2011). Myocardial fibrosis predicts appropriate device therapy in patients with implantable cardioverter-defibrillators for primary prevention of sudden cardiac death. *J. Am. Coll. Cardiol.* 57, 821–828. doi: 10.1016/j.jacc.2010.06.062

Jacquemet, V., and Henriquez, C. S. (2007). Modelling cardiac fibroblasts: interactions with myocytes and their impact on impulse propagation. *Europace* 9(Suppl. 6), vi29–37. doi: 10.1093/europace/eum207

Kieval, R. S., Spear, J. F., and Moore, E. N. (1992). Gap junctional conductance in ventricular myocyte pairs isolated from postischemic rabbit myocardium. *Circ. Res.* 71, 127–136. doi: 10.1161/01.RES.71.1.127

Kohl, P., and Gourdie, R. G. (2014). Fibroblast-myocyte electrotonic coupling: does it occur in native cardiac tissue? *J. Mol. Cell. Cardiol.* 70, 37–46. doi: 10.1016/j.yjmcc.2013.12.024

Kohl, P., Kamkin, A. G., Kiseleva, I. S., and Noble, D. (1994). Mechanosensitive fibroblasts in the sino-atrial node region of rat heart: interaction with cardiomyocytes and possible role. *Exp. Physiol.* 79, 943–956. doi: 10.1113/expphysiol.1994.sp003819

Mahajan, A., Shiferaw, Y., Sato, D., Baher, A., Olcese, R., Xie, L. H., et al. (2008). A rabbit ventricular action potential model replicating cardiac dynamics at rapid heart rates. *Biophys. J.* 94, 392–410. doi: 10.1529/biophysj.106.98160

Mcdowell, K. S., Vadakkumpadan, F., Blake, R., Blauer, J., Plank, G., Macleod, R. S., et al. (2012). Methodology for patient-specific modeling of atrial fibrosis as a substrate for atrial fibrillation. *J. Electrocardiol.* 45, 640–645. doi: 10.1016/j.jelectrocard.2012.08.005

Plonsey, R., and Barr, R. C. (2007). *Bioelectricity: A Quantitative Approach*. New York, NY: Springer.

Pumir, A., and Krinsky, V. (1999). Unpinning of a rotating wave in cardiac muscle by an electric field. *J. Theor. Biol.* 199, 311–319. doi: 10.1006/jtbi.1999.0957

Rook, M. B., De Jonge, B., Jongsma, H. J., and Masson-Pevet, M. A. (1990). Gap junction formation and functional interaction between neonatal rat cardiocytes in culture: a correlative physiological and ultrastructural study. *J. Membr. Biol.* 118, 179–192. doi: 10.1007/BF01868475

Rook, M. B., Jongsma, H. J., and De Jonge, B. (1989). Single channel currents of homo- and heterologous gap junctions between cardiac fibroblasts and myocytes. *Pflugers Arch.* 414, 95–98. doi: 10.1007/BF00585633

Rook, M. B., Van Ginneken, A. C., De Jonge, B., El Aoumari, A., Gros, D., and Jongsma, H. J. (1992). Differences in gap junction channels between cardiac myocytes, fibroblasts, and heterologous pairs. *Am. J. Physiol.* 263, C959–977. doi: 10.1152/ajpcell.1992.263.5.C959

Sachse, F. B. (2004). *Computational Cardiology: Modeling of Anatomy, Electrophysiology, and Mechanics*. Berlin; New York, NY: Springer. doi: 10.1007/b96841

Sachse, F. B., Moreno, A. P., and Abildskov, J. A. (2008). Electrophysiological modeling of fibroblasts and their interaction with myocytes. *Ann. Biomed. Eng.* 36, 41–56. doi: 10.1007/s10439-007-9405-8

Sachse, F. B., Moreno, A. P., Seemann, G., and Abildskov, J. A. (2009). A model of electrical conduction in cardiac tissue including fibroblasts. *Ann. Biomed. Eng.* 37, 874–889. doi: 10.1007/s10439-009-9667-4

Seemann, G., Sachse, F. B., Karl, M., Weiss, D. L., Heuveline, V., and Dössel, O. (2010). "Framework for modular, flexible and efficient solving the cardiac bidomain equation using PETSc," in *Progress in Industrial Mathematics at ECMI 2008*, eds A. D. Fitt, J. Norbury, H. Ockendon, and E. Wilson (Berlin; Heidelberg: Springer), 363–369. doi: 10.1007/978-3-642-12110-4_55

Seidel, T., Sankarankutty, A. C., and Sachse, F. B. (2017). Remodeling of the transverse tubular system after myocardial infarction in rabbit correlates with local fibrosis: a potential role of biomechanics. *Prog. Biophys. Mol. Biol.* 130, 302–314. doi: 10.1016/j.pbiomolbio.2017.07.006

Shibukawa, Y., Chilton, E. L., Maccannell, K. A., Clark, R. B., and Giles, W. R. (2005). K+ currents activated by depolarization in cardiac fibroblasts. *Biophys. J.* 88, 3924–3935. doi: 10.1529/biophysj.104.054429

Sobie, E. A., Susil, R. C., and Tung, L. (1997). A generalized activating function for predicting virtual electrodes in cardiac tissue. *Biophys. J.* 73, 1410–1423. doi: 10.1016/S0006-3495(97)78173-6

Tung, L. (1978). *A Bi-Domain Model for Describing Ischemic Myocardial d-c Potentials*. Ph.D. Thesis, MIT, Cambridge, MA.

Witwer, J. G., Trezek, G. J., and Jewett, D. L. (1972). The effect of media inhomogeneities upon intracranial electrical fields. *IEEE Trans. Biomed. Eng.* 19, 352–362. doi: 10.1109/TBME.1972.324138

Zeigler, A. C., Richardson, W. J., Holmes, J. W., and Saucerman, J. J. (2016). Computational modeling of cardiac fibroblasts and fibrosis. *J. Mol. Cell. Cardiol.* 93, 73–83. doi: 10.1016/j.yjmcc.2015.11.020

Conflict of Interest Statement: The authors declare that the research was conducted in the absence of any commercial or financial relationships that could be construed as a potential conflict of interest.

frontiers in Physiology

ORIGINAL RESEARCH
published: 15 May 2019
doi: 10.3389/fphys.2019.00580

Personalized Cardiac Computational Models: From Clinical Data to Simulation of Infarct-Related Ventricular Tachycardia

Alejandro Lopez-Perez[1]*, *Rafael Sebastian*[2], *M. Izquierdo*[3,4], *Ricardo Ruiz*[3,4], *Martin Bishop*[5] and *Jose M. Ferrero*[1]

[1] Center for Research and Innovation in Bioengineering (Ci2B), Universitat Politècnica de València, Valencia, Spain, [2] Computational Multiscale Simulation Lab (CoMMLab), Universitat de València, Valencia, Spain, [3] INCLIVA Health Research Institute, Valencia, Spain, [4] Arrhythmia Unit, Cardiology Department, Hospital Clínico Universitario de Valencia, Valencia, Spain, [5] Division of Imaging Sciences & Biomedical Engineering, Department of Biomedical Engineering, King's College London, London, United Kingdom

OPEN ACCESS

Edited by:
Olaf Doessel,
Karlsruhe Institute of Technology (KIT), Germany

Reviewed by:
Arun V. Holden,
University of Leeds, United Kingdom
Socrates Dokos,
University of New South Wales, Australia

***Correspondence:**
Alejandro Lopez-Perez
alopez@ci2b.upv.es

Specialty section:
This article was submitted to Computational Physiology and Medicine, a section of the journal Frontiers in Physiology

Received: 08 October 2018
Accepted: 25 April 2019
Published: 15 May 2019

Citation:
Lopez-Perez A, Sebastian R, Izquierdo M, Ruiz R, Bishop M and Ferrero JM (2019) Personalized Cardiac Computational Models: From Clinical Data to Simulation of Infarct-Related Ventricular Tachycardia. Front. Physiol. 10:580. doi: 10.3389/fphys.2019.00580

In the chronic stage of myocardial infarction, a significant number of patients develop life-threatening ventricular tachycardias (VT) due to the arrhythmogenic nature of the remodeled myocardium. Radiofrequency ablation (RFA) is a common procedure to isolate reentry pathways across the infarct scar that are responsible for VT. Unfortunately, this strategy show relatively low success rates; up to 50% of patients experience recurrent VT after the procedure. In the last decade, intensive research in the field of computational cardiac electrophysiology (EP) has demonstrated the ability of three-dimensional (3D) cardiac computational models to perform *in-silico* EP studies. However, the personalization and modeling of certain key components remain challenging, particularly in the case of the infarct border zone (BZ). In this study, we used a clinical dataset from a patient with a history of infarct-related VT to build an image-based 3D ventricular model aimed at computational simulation of cardiac EP, including detailed *patient-specific* cardiac anatomy and infarct scar geometry. We modeled the BZ in eight different ways by combining the presence or absence of electrical remodeling with four different levels of image-based patchy fibrosis (0, 10, 20, and 30%). A 3D torso model was also constructed to compute the ECG. *Patient-specific* sinus activation patterns were simulated and validated against the patient's ECG. Subsequently, the pacing protocol used to induce reentrant VTs in the EP laboratory was reproduced *in-silico*. The clinical VT was induced with different versions of the model and from different pacing points, thus identifying the slow conducting channel responsible for such VT. Finally, the real patient's ECG recorded during VT episodes was used to validate our simulation results and to assess different strategies to model the BZ. Our study showed that reduced conduction velocities and heterogeneity in action potential duration in the BZ are the main factors in promoting reentrant activity.

Either electrical remodeling or fibrosis in a degree of at least 30% in the BZ were required to initiate VT. Moreover, this proof-of-concept study confirms the feasibility of developing 3D computational models for cardiac EP able to reproduce cardiac activation in sinus rhythm and during VT, using exclusively non-invasive clinical data.

Keywords: myocardial infarction (MI), ventricular tachycardia (VT), border zone (BZ), electrical remodeling (ER), fibrosis, slow conducting channel (SCC), computational simulation, radiofrequency ablation (RFA)

INTRODUCTION

Cardiovascular disease is the leading cause of both morbidity and mortality worldwide, with ischemic heart disease being the most common cause among them (Nowbar et al., 2014; Abubakar et al., 2015). Months or even years after suffering from a myocardial infarction (MI), when the healing process is complete and the MI has reached the chronic stage (van den Borne et al., 2010; Daskalopoulos et al., 2012), a significant number of patients develop potentially lethal ventricular tachycardias (VT) due to the arrhythmogenic nature of remodeled tissue (Lazzara and Scherlag, 1984; de Bakker et al., 1993; Nguyen et al., 2014). Infarct-related VTs are commonly associated with the so-called *slow conducting channels* (SCC), also known as *isthmuses*, which are pathways composed of surviving myocytes across the infarct scar that are responsible for the initiation and maintenance of reentrant activity, usually leading to monomorphic VTs (de Bakker et al., 1988; Aliot et al., 2009). Moreover, SCC are closely related to the *border zone* (BZ) (also termed *gray zone* or *peri-infarct zone*), a region constituting the transition between infarct scar and healthy myocardium that comprises altered but still viable tissue surrounding the dense fibrotic scar (infarct scar) resulted from the healing of MI. Several studies have described the BZ as a region of slowed conduction composed of surviving but remodeled myocytes with infiltration of bundles of patchy fibrosis extending from the core of compact fibrosis (infarct scar), which results in a highly arrhythmogenic tissue (de Bakker et al., 1993; Rohr, 2012; Rutherford et al., 2012; Nguyen et al., 2014).

At present, cardiac delayed enhancement-MRI (DE-MRI) is commonly used to explore the infarcted area pre-operatively, since it enables *in-vivo* evaluation of the tissue damaged by MI (i.e., scar and BZ) due to the hyper-enhancement of the infarcted region in the images (Kim et al., 1999a; Fieno et al., 2000; Doltra et al., 2013). In fact, it is currently considered as the gold-standard test for *in-vivo* assessment of scar and myocardial viability after MI in clinical settings (Jamiel et al., 2017; Patel et al., 2017). Cardiac DE-MRI provides a substrate characterization after MI that has shown close correlation with histopathological analyzes (Kim et al., 1999a; Fieno et al., 2000; Wagner et al., 2003; Amado et al., 2004), allowing to differentiate between scar and BZ. The usefulness of MRI-based substrate characterization and SCCs delineation for planning and guiding ablation procedures aimed at infarct-related VTs has been tested in numerous studies (Ashikaga et al., 2007; Andreu et al., 2011, 2015, 2017; Perez-David et al., 2011; Wijnmaalen et al., 2011; Fernández-Armenta et al., 2013; Soto-Iglesias et al., 2016; Yamashita et al., 2016).

Radiofrequency ablation (RFA) is a common procedure to interrupt reentrant circuits through SCC responsible for VTs related to chronic MI (Stevenson et al., 1993; de Chillou et al., 2002; Wilber, 2008; Berruezo et al., 2015; Baldinger et al., 2016). As part of the electrophysiological (EP) study immediately prior to RFA in patients with infarct-related VT, interventional cardiologists try to induce the clinical VT originally undergone by the patient by means of pacing protocols applied at selected sites of myocardium. A positive induction of monomorphic VT is assumed as an evidence of the presence of at least one SCC responsible for the VT (Pedersen et al., 2014; Priori et al., 2015). In such a case, the SCC is ablated to block the propagation through the reentrant circuit, thus avoiding the reentry and, consequently, the VT. However, these procedures are invasive, risky and very time-consuming. Moreover, they show a relatively low success rate, as up to 50% of patients develop recurrent VT after the RFA procedure (Gerstenfeld, 2013; Yokokawa et al., 2013; Baldinger et al., 2016).

Electroanatomical mapping (EAM) systems (Ben-Haim et al., 1996; Gepstein et al., 1997), are commonly employed in the EP laboratory to guide RFA procedures aimed at assessing both atrial (Calkins et al., 2012) and ventricular arrhythmias (Aliot et al., 2009; Priori et al., 2015), due to its ability to integrate spatial 3D and EP information recorded by the catheter. In the case of infarct-related VTs, EAM systems are considered as a helpful tool to identify SCCs as RFA targets based on the abnormal features of electrograms (EGM) in such regions (Gardner et al., 1985; Bogun et al., 2005), especially when clinical VT is unmappable due to non-inducibility or hemodynamic instability (Marchlinski et al., 2000; Aliot et al., 2009; Priori et al., 2015).

In contrast to EAM systems, an alternative non-invasive approach for pre-operative characterization of target substrate and planning of RFA procedures is the use of 3D computational models able to simulate cardiac EP accurately. Such an approach has the potential to help physicians to better understand and predict the underlying mechanisms of a wide variety of cardiac disorders, as well as in therapy planning and management of those diseases (Vigmond et al., 2009; Smith et al., 2011; Trayanova et al., 2012, 2017; Krueger et al., 2013; Trayanova and Boyle, 2013; Lopez-Perez et al., 2015; Arevalo et al., 2016). Although such *in-silico* approaches show significant potential, a number of important questions related to the necessary level of detail required by the model remain unanswered. In particular, the specific manner in which the microscopic structural and functional remodeling, known to be present in the infarct BZ, is represented in these macroscopic clinical models, and the subsequent implications of these specific choices in the initiation

and the sustenance of reentrant VT events, has yet to be fully investigated. Related to this, the degree of model personalization necessary for accurate simulation of *patient-specific* VT episodes is also a matter of debate; for example, the requirement of only personalized anatomy (from images), or whether the inclusion of functional personalization (from ECG or EAM data, for instance) should also be an essential feature in model construction. Full exploration of these effects is often limited by clinical data availability.

The main goal of this project is to develop a pipeline for performing personalized *in-silico* EP studies able to aid electrophysiologists in surgical planning of RFA procedures aimed at infarct-related VTs. For this purpose, we first evaluate the feasibility of building image-based 3D *patient-specific* models of ventricles and torso of chronically infarcted patients, as well as the capability of such models to reproduce patients' cardiac EP during VT episodes by computational simulation, including simulated ECGs aiming to compare them with patients' clinical recordings. Here we present a feasibility case study, building computational 3D models of ventricles and torso that are exclusively based on non-invasive high-resolution clinical data. The ventricular model includes personalized and detailed 3D geometry of both cardiac anatomy and the heterogeneous remodeling resulting from the MI healing process (infarct scar and BZ), since both factors seem to be essential to identify SCCs as RFA targets by means of *in-silico* EP studies. Additionally, as part of the EP modeling associated with our pipeline, we explore the impact on VT inducibility and VT features of different modeling strategies for the BZ, in which we include electrical remodeling (ER) and structural remodeling in the form of different densities of image-based patchy fibrosis in order to assess the arrhythmogenic effects of those factors, both separately and in combination.

MATERIALS AND METHODS

Clinical Data

In this work, we used a set of clinical data from a 58-year-old male patient referred for a RFA procedure aimed at finishing a monomorphic VT related to a large chronic MI, which extended over seven out of the 17 segments of the left ventricle (LV) model of the American Heart Association (AHA). Myocardial regions that appear affected in the DE-MRI were basal and medial segments of both inferoseptal and inferolateral walls and all segments of the inferior wall (basal, mid, and apical), which correlates with an occlusion of the right coronary artery (Ortiz-Pérez et al., 2008). The patient suffered the acute MI 11 years before the clinical VT episode related to the MI. The clinical dataset includes: clinical high-resolution cardiac DE-MRI, whole thorax MRI, EAMs recorded via CARTO system (Biosense Webster, Inc., Diamond Bar, CA, USA) (Gepstein et al., 1997) and 12-lead ECG signals recorded during the RFA procedure both in sinus rhythm and during VT episodes induced by pacing. Importantly, all those data were not specifically generated for research purposes, but they were collected in a clinical environment as part of its daily routine.

Cardiac DE-MRI was acquired by a MRI scanner Magnetom Avanto 1.5T (Siemens Healthcare, Erlangen, Germany) using a phased-array body surface coil, about 15 min after the administration of the gadolinium-based contrast MultiHance (gadobenate dimeglumine, 529 mg/ml) (Bracco Diagnostics Inc., Monroe Township, New Jersey, USA). The acquisition was synchronized with both ECG (ECG-gated) and breathing (navigator-gated), imaging the heart at the end-diastolic phase of cardiac cycle (trigger delay = 685 ms, for a nominal R-R interval of 928 ms along the acquisition). The DE-MRI stack comprised 96 slices of 256 × 256 pixels encompassing the whole heart (ventricles and atria), with a pixel size of 1.4 × 1.4 mm and a slice thickness of 1.4 mm, thus resulting in isotropic voxel.

In vivo EP data were recorded by CARTO 3 system using the *NaviStar ThermoCool* ablation catheter with 3.5 mm saline-irrigated tip (Abdelwahab and Sapp, 2007). A pressure sensor placed at catheter tip ensured the proper contact between the catheter and the myocardial wall. A total of 847 points were registered: 315 from LV endocardium, 78 from right ventricle (RV) endocardium and 454 from epicardium.

Regarding the ethical considerations, the protocol was approved by the *Ethics Committee for Clinical Research of the Hospital Clinic Universitari de Valencia* (Valencia, Spain), which certifies that the present study was conducted in accordance with the recommendations gathered in the Declaration of Helsinki, originally adopted by the General Assembly of the World Medical Association in 1964, and in its subsequent revisions. Furthermore, the patient, who underwent the standard clinical protocol, gave written informed consent for the use of his anonymized clinical data in this study.

3D *Patient-Specific* Ventricular Model

Anatomical Model

We generated the 3D *patient-specific* bi-ventricular model by segmenting the short-axis slices from the cardiac DE-MRI using Seg3D software (Scientific Computing and Imaging Institute, University of Utah, USA) (Seg3D, 2013). We did it manually to perform a highly detailed segmentation of whole ventricles, including papillary muscles and main endocardial trabeculations (see **Figures 1A,B**). An expert radiologist in cardiac imaging checked all segmentations in order to ensure the fidelity of the 3D reconstruction of the *patient-specific* anatomy. From the segmented DE-MRI stack, we generated a surface model of ventricles that we carefully checked with Blender (Blender Foundation, Amsterdam, The Netherlands) to refine and correct defects in the mesh at the local level after applying a global smoothing. Then, using the surface model as a template, we performed a volume meshing with MeshGems-Hexa (Distene S.A.S., Bruyeres-le-Chatel, France), obtaining a hexahedra-based volume mesh comprised by 4 million nodes (vertices) and 3.71 million elements, with an average edge length of 0.4 mm.

To include the anisotropy of the cardiac muscle, we implemented Streeter's rule-based method (Streeter et al., 1969) modeled by the set of equations described in Sebastian et al. (2009), defining the helix (α_h) and transmural (α_t) angles (see **Figure 1D**) for every hexahedral mesh element, based on the apex-base relative distance and transmural depth of its position

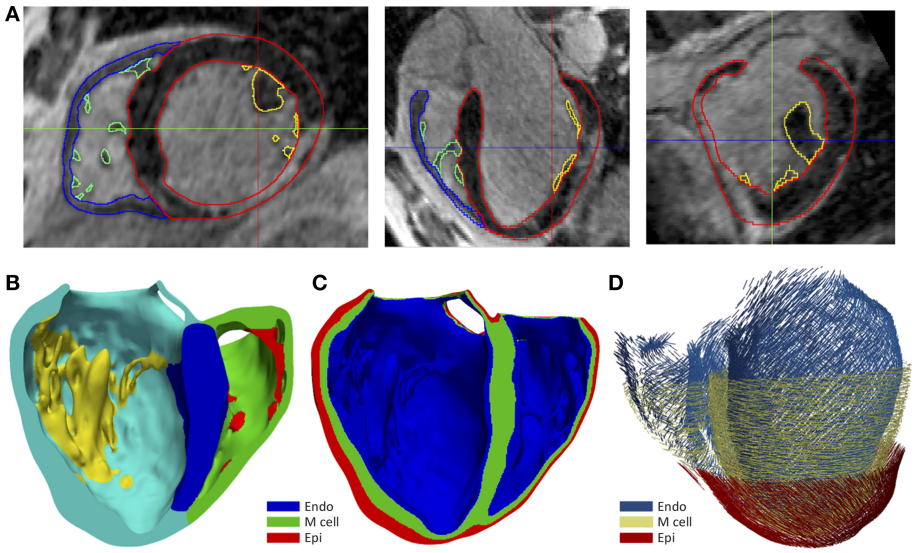

FIGURE 1 | (A) Manual segmentation process of cardiac DE-MRI performed with Seg3D, displaying three slices corresponding to the standard cardiac planes: short-axis (*left*), four-chamber plane (*center*) and long-axis showing the LV (*right*). (Note that in those views the LV appears on the right side and the RV on the left). Contours highlighted in distinct colors show: LV myocardium including the septum (*red*), RV myocardium (*blue*) and papillary muscles and endocardial trabeculations of LV (*yellow*) and RV (*green*). **(B)** Posterior view of a coronal cross-section (four-chamber plane) of the hexahedra-based FEM volume mesh of the 3D *patient-specific* ventricular model. Various cardiac regions are labeled with different colors: septum (*blue*), LV free wall (*cyan*), RV free wall (*green*) and papillary muscles and main endocardial trabeculations of LV (*yellow*) and RV (*red*). **(C)** Transmural heterogeneity of ventricular myocardium, showing the distribution of the three different kinds of ventricular myocytes: endo-, mid- (M cells), and epicardial cells. **(D)** Left antero-lateral view of the 3D ventricular model displaying a representation of cardiac fibers orientation at different wall depths (endocardium, mid-myocardium, and epicardium).

within the 3D model. We first applied this method to the whole LV myocardium (including septum) and then to RV free wall. In papillary muscles and endocardial trabeculations, fibers are known to be aligned parallel to the longitudinal axis of those anatomical structures (Greenbaum et al., 1981). In order to reproduce such configuration, we performed the topological skeletonization of the volume mesh to extract the medial axes of each one of those structures, what enabled to properly assign the fiber orientation within them. Finally, we performed a Gaussian smoothing with a 3D kernel to soften abrupt transitions in fibers direction between the myocardial wall and the papillary muscles and trabeculations, as well as at the RV free wall-septum junctions.

Infarct Scar and Border Zone

We generated 3D representations of the geometry of the infarct scar and BZ by segmenting the slices of the cardiac DE-MRI by means of a custom implementation of the so-called *standard deviation* (SD) *method* (Kim et al., 1999a). Briefly, we divided the segmented LV myocardium into two sub-regions (healthy and infarcted) (see **Figure 2A**), based on the pixel intensity levels (i.e., gray levels). Within the infarcted region, we classified every pixel as dense fibrotic scar (intensity levels higher than mean+3 × SD of healthy myocardium), BZ (levels between mean+2 × SD and mean+3 × SD) or healthy tissue (values under mean+2 × SD) (Kim et al., 1999a; Fieno et al., 2000; Kolipaka et al., 2005; Yan, 2006; Perez-David et al., 2011). Finally, we mapped the scar and BZ into the volume mesh of the 3D ventricular model, labeling every hexahedron in the 3D model as healthy, scar or BZ depending on its position relative to the surfaces representing the infarct scar and the whole MI (see **Figure 2B**).

In an attempt to reproduce the structural remodeling within the BZ (patchy fibrosis) based on our clinical data, we first mapped the intensity levels of the DE-MRI into the volume mesh of our 3D ventricular model (**Figure 3A**). Since the DE-MRI voxels (isotropic voxels with edge length of 1.4 mm) were larger than FEM mesh elements (hexahedra with average edge length of 0.4 mm), the intensity level corresponding to each DE-MRI voxel was assigned to several FEM elements that might comprise up to 64 hexahedra. We then generated different levels of fibrosis (10, 20, and 30%) within the BZ based on that information mapped from the DE-MRI (see **Figure 3**). Among the elements of the volume mesh previously labeled as BZ, we defined as fibrotic those ones associated with the highest intensity levels, in an amount depending on the desired fibrosis level. Thus, we labeled as fibrotic a percentage of elements belonging to the BZ that matched the specified level of patchy fibrosis.

As shown in **Figure 3**, our approach of image-based generation of different fibrosis levels within the BZ resulted in clusters of fibrotic tissue. This method produced a distribution that may be classified as patchy fibrosis, defined as a mixture of bundles of myocardial tissue and fibrotic tissue (de Jong et al., 2011).

CARTO Data Reannotation and Integration

Local activation times (LAT) annotations were automatically determined by the *Confidense* module of CARTO system. First, we discarded all points with peak-to-peak amplitude under

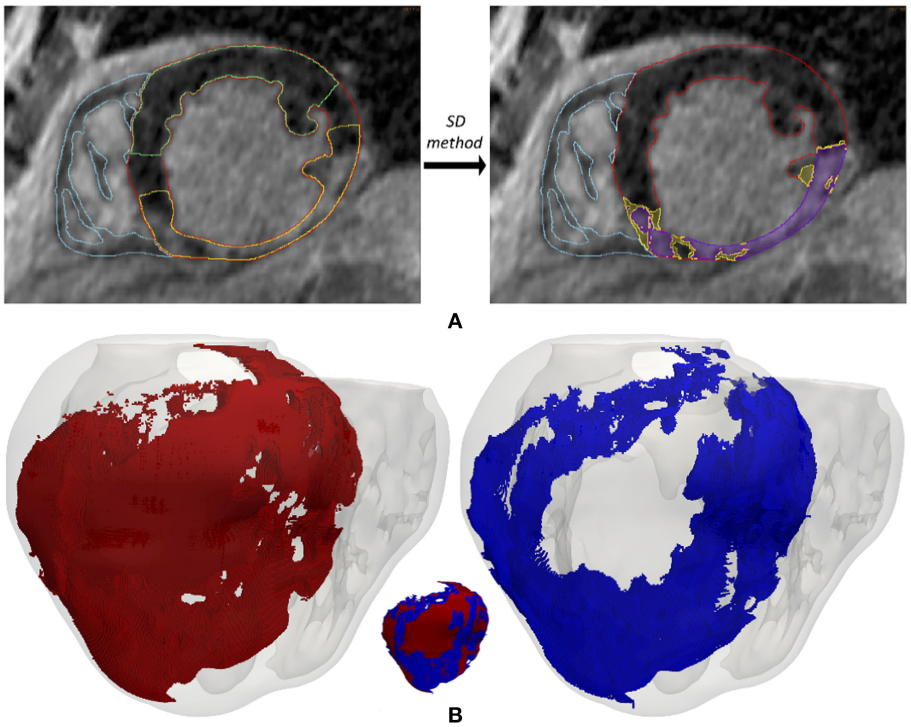

FIGURE 2 | (A) Segmentation process from short-axis DE-MRI slices of the heterogeneous remodeling caused by MI, including infarct scar and BZ. Left panel shows the first step that involves the manual delineation of remote ROI (region-of-interest) (*green*) and infarcted ROI (*yellow*) within the LV myocardium ROI (*red*), also displaying the RV myocardium ROI (*cyan*). Right panel shows the segmentation for infarct scar (*purple*) and BZ (*yellow*) resulting from the application within the infarcted ROI of thresholds determined by SD method from the remote ROI of each slice. **(B)** 3D representation of the MI reconstructed from DE-MRI images, showing posterior views of the 3D surface model of ventricles (rendered with transparency) along with those hexahedral elements of volume mesh labeled as infarct scar (*red*) and BZ (*blue*).

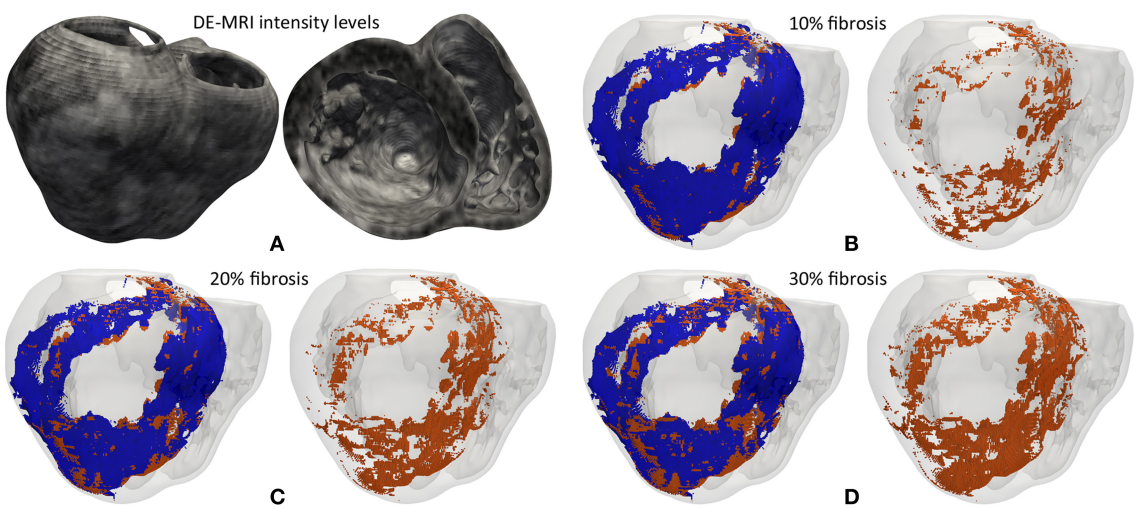

FIGURE 3 | (A) Gray intensity levels from DE-MRI mapped into the hexahedral volume mesh of the 3D ventricular model, showing a postero-basal view of the whole model (*left*) and a basal view of a cross-section in the short-axis plane (*right*). The next three panels show the 3D fibrosis distribution resulting from the introduction of several degrees of structural remodeling within the BZ: **(B)** 10%, **(C)** 20%, and **(D)** 30% patchy fibrosis. All those panels show a posterior view of the 3D surface model of ventricles (rendered with transparency) together with those hexahedral elements labeled as BZ (*blue*) and fibrosis (*orange*) extracted from the volume mesh of ventricular model. In each panel there is an image showing both the BZ and fibrosis (*left*) and another one only displaying the fibrotic elements (*right*).

0.5 mV in distal bipolar EGM (M1-M2), as they are considered as non-excitable tissue corresponding to the dense fibrotic scar (Marchlinski et al., 2000; Soejima et al., 2002). For the remaining EGMs, those acquired on healthy tissue were revised by a custom code for LAT re-annotation. We chose the deflection of distal bipolar signal closest to the point of maximum negative slope in distal unipolar signal as the activation time (Spach et al., 1979; Paul et al., 1990; Stevenson and Soejima, 2005), which showed good agreement with annotations determined by the *Confidense* module in most cases. However, such criterion is not reliable for points showing noisy and fragmented signals, typically located at the BZ surrounding the infarct scar (Aliot et al., 2009). In those cases, we placed LAT annotations manually under the close supervision of a well-trained electrophysiologist, who also reviewed LAT annotations for healthy EGMs. Furthermore, we discarded those points whose LAT value showed a poor spatio-temporal coherence with their closest neighbors. After this process, only 385 out of the 847 CARTO measurement points were preserved: 84 for LV endocardium, 49 for RV endocardium and 252 for epicardium.

We had three surfaces generated by the CARTO system, including both acquired and interpolated data: LV endocardium, RV endocardium and epicardium (**Figure 4A**). Epicardial mapping was performed by accessing pericardial space through percutaneous (non-surgical) transthoracic subxiphoid approach by means of puncture using an epidural needle (Brugada et al., 2003; Sosa and Scanavacca, 2005; Tedrow and Stevenson, 2009; Yamada, 2014), following the access procedure originally described by Sosa et al. (1996, 2000). We applied a rigid transformation using the ICP (iterative closest point) algorithm (Besl and McKay, 1992), to align those three CARTO surface meshes to our 3D *patient-specific* ventricular model. Then, we projected all measurement points from each CARTO mesh to the closest surface node of our ventricular model, in terms of Euclidean distance. Thus, we obtained all CARTO measurement points (those preserved after the checking process) mapped onto the external surface of our 3D bi-ventricular model (see **Figure 4B**). The earliest activated region was located on the septal region of the LV endocardium at mid-apical level and, the latest activated on the epicardial surface within the BZ near the scar.

3D Torso Model

The whole torso MRI stack was acquired in the coronal plane with a slice thickness of 10 mm. We roughly segmented the main organs (lungs, liver, heart) and structures (bones, body contour, blood pools, great vessels) using Seg3D software. The resolution of the torso MRI hampered a detailed reconstruction of some important structures, so we used the reconstructed parts of the model as landmarks to fit a detailed torso model previously developed (Ferrer et al., 2015) by means of a linear transformation. Next, we replaced the ventricles in the fitted detailed torso model by our *patient-specific* model and removed any intersections between our ventricular model and surrounding organs (see **Figure 5A**). Finally, we used TetGen (Si and Gärtner, 2005) to mesh the torso volume with tetrahedra, which resulted in 1.26 million nodes and 7.38 million elements organs (see **Figure 5B**). The average edge length was of 0.55 mm. Note that the problem of passive propagation of extracellular potentials, i.e., only diffusion without reaction component, does not require such a fine spatial resolution outside the heart domain (Prassl et al., 2009); for this reason, the mesh is highly refined only in the region of the ventricles, as shown in **Figure 5B**.

Electrophysiological Modeling

Healthy Myocardium

For healthy myocardium, we used the ten Tusscher model of human ventricular action potential (AP) (ten Tusscher and Panfilov, 2006), considering the transmural heterogeneity of the ventricular myocardium (Drouin et al., 1995; Antzelevitch et al., 1999). We defined three different transmural layers for endocardial, mid myocardial (M cells) and epicardial myocytes within the volume mesh of our ventricular model, spanning 17, 41, and 42% of ventricular wall thickness, respectively (see **Figure 1C**). These values were estimated from the data reported by several experimental studies (Sicouri and Antzelevitch, 1991; Sicouri et al., 1994; Yan et al., 1998).

In order to establish the conductivities that will define the conduction velocities (CV), we performed a set of test simulations on a 3D slab model ($20 \times 20 \times 6$ mm) composed of regular hexahedral elements (voxels) with an edge length of 0.4 mm, matching the average length in the ventricular model. As a result, we set the conductivity values to 0.24 S/m and 0.0456 S/m for longitudinal (σ_L) and transversal (σ_T) conductivity, respectively. This resulted in a CV of 0.68 m/s along the fiber direction and of 0.26 m/s in transverse direction. These values are consistent with the experimental measurements in human ventricles (Taggart et al., 2000).

Infarct Scar and Border Zone

We considered the infarct scar as a non-excitable tissue mainly composed of collagen, so we modeled it as an electrical insulator. To do so, we defined an internal boundary in our 3D model and imposed no-flux boundary condition at the interface between the scar and surrounding tissue, which mostly corresponded to the BZ.

To include the ER in the BZ, we modified the ten Tusscher model (ten Tusscher and Panfilov, 2006) by introducing reductions in the maximum conductance of certain ionic channels, as reported from several patch-clamp experiments with cells of epicardial BZs from canine hearts. According to those data, I_{Na} was reduced to 38% of its normal value (Pu and Boyden, 1997), I_{CaL} to 31% (Dun et al., 2004) and I_{Kr} and I_{Ks} to 30 and 20% (Jiang et al., 2000), respectively. At the tissue level, we reduced the conductivity parameters in the BZ to 0.05 S/m and 0.01 S/m for longitudinal (σ_L) and transversal (σ_T) conductivity, respectively. Importantly, we used the same conductivity values for the BZ for those versions of the model including fibrosis and ER and for those ones including only fibrosis in the BZ. Hence, we set reduced conductivities at tissue level for the BZ in all versions of the ventricular model regardless of whether or not it included ER at the ionic level. CVs measured on a 3D slab model using the remodeled version of ten Tusscher model were 0.17 m/s in the longitudinal direction and 0.065 m/s in the transverse directions, corresponding to a reduction of around 75% with respect to the

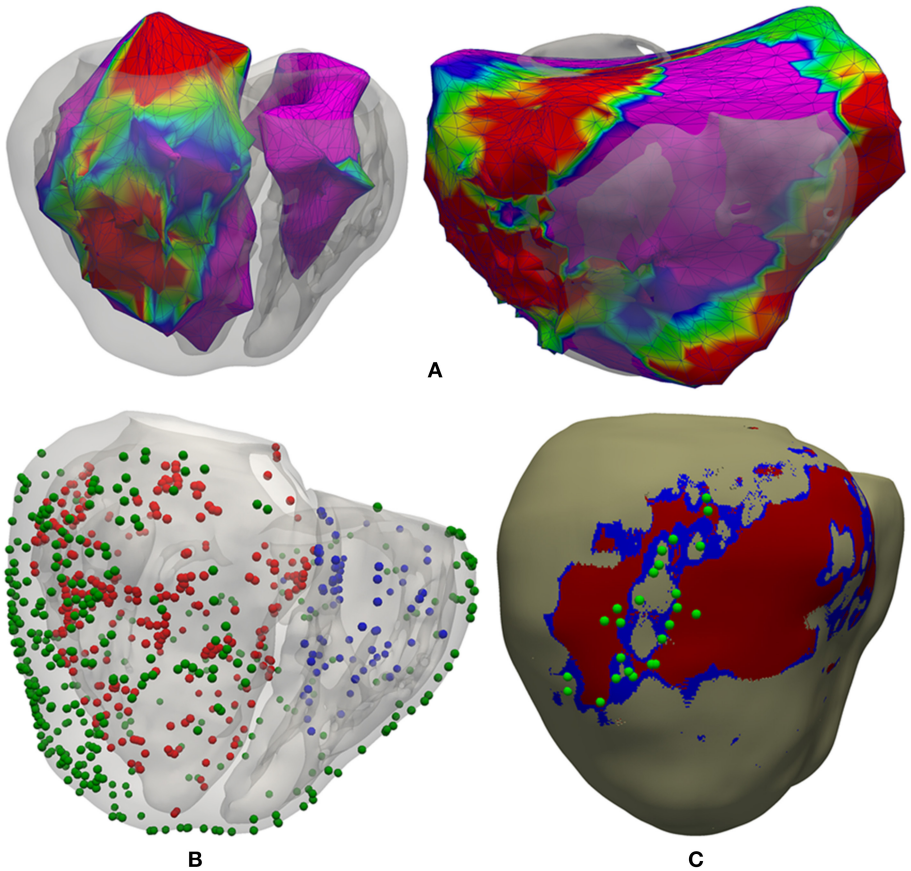

FIGURE 4 | Registration process between CARTO surface meshes and the 3D ventricular model. **(A)** Two posterior views of the 3D surface model of ventricles rendered with transparency, showing registered CARTO surfaces for both endocardia (*left*) and epicardium (*right*). **(B)** CARTO measurement points projected onto the 3D model with colored spheres representing CARTO points recorded from LV endocardium (*red*), RV endocardium (*blue*), and epicardium (*green*). **(C)** Postero-lateral view of the 3D ventricular model showing a possible epicardial SCC mainly composed of BZ (*blue*) intermingled with some thin patches of healthy tissue at epicardial level (*beige*) and completely surrounded by infarct scar (*red*), closely matching the location of projected CARTO points tagged during the RFA procedure as candidates to be part of a SCC (*green spheres*) according to the features of their EGMs.

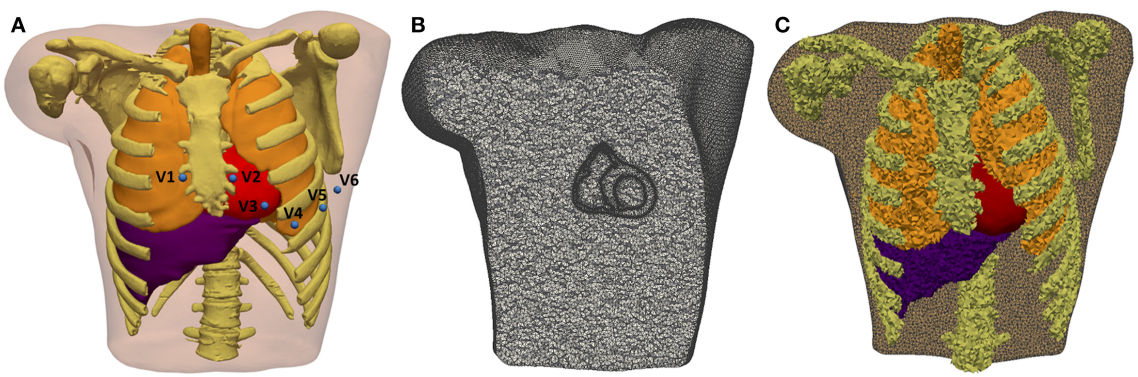

FIGURE 5 | 3D Torso model. **(A)** Anterior view of the torso model, showing the 3D surfaces that represents all organs and tissues included (bones, lungs, liver, ventricles, atria, and blood pools of four cardiac chambers). Blue spheres represent the location of virtual electrodes corresponding to precordial leads for ECG computation, placed in its standard positions. **(B)** Coronal cross-section of volume mesh of the 3D torso model, showing the edges of tetrahedral elements that are highly refined in the region of ventricles. **(C)** Labeled volume mesh. Different colors indicate to which organ or anatomical structure each tetrahedral element belongs as a result of the labeling process of volume mesh: lungs (*orange*), bones (*yellow*), liver (*purple*), and ventricles (*red*).

CVs in healthy tissue. Conductivities for BZ in combination with the original ten Tusscher model yielded CVs of 0.225 m/s and 0.09 m/s for longitudinal and transverse directions, respectively, which means a reduction of around 65%.

For fibrosis within the BZ, we used the MacCannell model for human ventricular fibroblast (MacCannell et al., 2007). At tissue level, we considered fibrotic tissue as isotropic and set its conductivity to 0.1 S/m; a reduction of 60% with respect to the longitudinal conductivity in healthy myocardium. Fibrotic tissue behaves as a passive conductor that only enables electrotonic conduction (passive propagation), rapidly leading to blocks due to the attenuation of propagated potentials. Since the conductivity value set for fibrosis affects the coupling between myocytes and fibroblasts, it defines the magnitude of the electrotonic load exerted by the fibroblasts over the adjacent myocytes (MacCannell et al., 2007), with fibroblasts acting as electrical sinks along plateau and repolarization phases, while behaving as electrical sources during resting state (Jacquemet, 2006; Miragoli et al., 2006; Xie et al., 2009; Rohr, 2012; Gomez et al., 2014; Trayanova et al., 2014; Mahoney et al., 2016; Zeigler et al., 2016). This electrotonic interaction between myocytes and fibroblasts can cause a considerable impact on electrical conduction at tissue and organ level depending on fibroblast density, as will be observed in our simulation results.

Electrical Modeling of the Torso

We automatically labeled every tetrahedral element of the volume mesh as belonging to a given organ. The 3D torso model included bones, lungs, liver, whole heart (ventricles and atria) and blood pools of all cardiac chambers organs (see **Figure 5C**). As in Ferrer et al. (2015), conductivity values assigned to different organs and tissues were taken from the literature (MacLeod et al., 1991; Gabriel et al., 1996; Klepfer et al., 1997; Bradley et al., 2000; Bressler and Ding, 2006). We considered isotropic propagation for all organs and tissues of our 3D torso model, except for the ventricular myocardium where we preserved the anisotropy imposed by the orientation of cardiac fibers. As in Klepfer et al. (1997), for the space not covered by any organ or anatomical structure we set a conductivity of 0.239 S/m calculated as the average of the conductivities for the other tissues, including the skeletal muscle that was not considered as a specific region in our torso model. Finally, to simulate ECG signals we defined virtual electrodes on the surface of torso model corresponding to the precordial leads, which were placed in their standard positions (see **Figure 5A**).

Computational Simulations

Simulations at the Organ Level

All simulations at the organ level were performed on eight different versions of our 3D *patient-specific* ventricular model, generated by combining the presence or absence of ER in the BZ with four different levels of image-based patchy fibrosis (0, 10, 20, and 30%), as detailed in **Table 1**. Thereby, we could independently assess the arrhythmogenic effect of the structural remodeling (fibrosis) and ER within the BZ, as well as the combination of both factors. We also performed some additional simulations with the model with ER and 10% fibrosis (model *#6*), aiming to study the effect of changing the conductivities within the BZ. We tested two new sets of values (0.12–0.03 S/m and 0.22–0.0485 S/m for longitudinal-transversal conductivities), which in combination with our remodeled version of the ten Tusscher model, respectively, resulted in CVs in the BZ reduced by 50 and 25% with respect to the CVs for healthy tissue.

To perform the simulations at the organ level, we used the software ELVIRA (Heidenreich et al., 2010), a FEM solver specifically developed for solving the anisotropic reaction-diffusion equation of the monodomain model for cardiac EP (Roth, 1988). For the numerical solution of our simulations, we applied the conjugate gradient method with an integration time step of 0.02 ms, using implicit integration for the parabolic partial differential equation of monodomain model and explicit integration with adaptive time stepping for the systems of ordinary differential equations associated with the ionic models.

Stabilization of myocyte-fibroblast coupling

Adjacent myocytes and fibroblasts are known to interact by coupling and signaling between them in both healthy and diseased myocardium (Kohl and Gourdie, 2014; Mahoney et al., 2016; Ongstad and Kohl, 2016). Electrotonic interaction induces changes in myocytes coupled to fibroblasts, such as elevation of resting potential (i.e., less negative) and APD shortening as a consequence of the effect of fibroblasts as electrical sinks (MacCannell et al., 2007; Zeigler et al., 2016). Thus, we needed to stabilize the myocyte-fibroblast electrotonic couplings as a first step in our simulation pipeline to let those interactions reach the steady state. For all models including any fibrosis level (10, 20, or 30%), first we performed a 1 s simulation without any stimulus. After an initial stabilization that caused a multi-foci ectopic-like activation, myocyte-fibroblast couplings remained stable in absence of stimulation (see **Video S1**), so the final state of those simulations would later serve as a starting point for the following ones in our simulation pipeline.

Simulation of the ECG

To obtain ECG signals on the body surface, we used an approximation of the bidomain model (Geselowitz and Miller, 1983) to compute the extracellular potentials across the torso volume. This approximation, described elsewhere (Keller et al., 2010) and recently used in other works (Ferrer-Albero et al., 2017; Martinez-Mateu et al., 2018), comprises several steps. First, transmembrane potentials, previously computed by simulation at the organ level using the solver ELVIRA as explained above, were interpolated from the ventricular model to the nodes of torso model corresponding to the ventricular myocardium. Then, solving the passive term (only diffusion) of the bidomain approach we obtained the extracellular potentials in the ventricles from the interpolated transmembrane voltages. Finally, applying Dirichlet boundary conditions at the ventricles-torso interface and Neumann-type conditions at the torso surface, the extracellular potentials were computed by using the FEM method to solve a Laplace equation over the volume mesh of 3D torso model. To obtain the numerical solution of the problem, we used the conjugate gradient method with the incomplete Cholesky decomposition as a pre-conditioner. (See

TABLE 1 | Different versions of the computational model of ventricles according to the kind of remodeling included in the BZ (ER and/or fibrosis) and results of *in-silico* VT inducibility tests performed with CVs in BZ reduced by 75% with respect to the healthy tissue.

Model version	Fibrosis in BZ (%)	ER in BZ	Pacing site		
			endo#1	***epi#1***	***epi#2***
#1	0	NO	no VT	no VT	no VT
#2	10		no VT	no VT	no VT
#3	20		no VT	no VT	no VT
#4	30		no VT	S3−290 ms 510 ms−117 bpm	no VT
#5	0	YES	no VT	S2−360 ms 506 ms−118 bpm	no VT
#6	10		S3−370 ms 526 ms−114 bpm	S2−360 ms 526 ms−114 bpm	no VT
#7	20		S3−370 ms 520 ms−115 bpm	S2−360 ms 520 ms−115 bpm	no VT
#8	30		no VT	no VT	no VT

In the cases of positive VT induction, we specify the premature stimulus (S2 or S3) responsible for the unidirectional block triggering the reentrant VT and its CI, as well as the BCL and heart rate associated with the VT.

Supplementary Material for more details about the method used to compute simulated ECGs).

RESULTS

3D Ventricular Model

As well as including *patient-specific* cardiac anatomy, our 3D ventricular model also integrated personalized geometry of heterogeneous remodeling caused by MI, differentiating between infarct scar and BZ that comprised 16 and 8.5% of the volume of LV myocardium, respectively. Importantly, 3D reconstruction of the MI remodeling from DE-MRI revealed the presence, at the epicardial level, of an isthmus mainly composed of BZ intermingled with several thin patches of healthy tissue that was surrounded by dense scar. Both the shape and features of this structure match the definition of a SCC representing a potential substrate for reentrant VT (de Bakker et al., 1988; Fernández-Armenta et al., 2013). Moreover, as observed in **Figure 4C**, integration of CARTO data onto the 3D model showed good agreement between the epicardial isthmus and a set of CARTO points labeled during the RFA procedure as candidates to be part of a SCC due to the characteristics of its bipolar EGMs (low voltage, fractionated and split signals, late and isolated potentials, etc.) (de Chillou et al., 2002; Bogun et al., 2005). The image-based *patient-specific* 3D model of infarcted ventricles developed in this work, as well as the 3D torso model, are both publicly available at http://commlab.uv.es/repository/.

Electrophysiological Modeling of the Border Zone

ER in the BZ, represented by our modified version of ten Tusscher model, resulted in a decrease of upstroke velocity and maximum amplitude of AP mainly caused by the downregulation of I_{Na}, as well as an increase in AP duration (APD) relative to the normal values due to the reduction of repolarizing potassium currents I_{Kr} and I_{Ks}. As observed in **Figure 6**, the main effect of the applied changes is the prolongation of the APD, which affects both a single isolated cell and a cell embedded in a 3D remodeled tissue in a similar degree. **Table S1** summarizes a quantitative analysis of the changes in several AP key biomarkers resulting from the modifications included in the ten Tusscher model for ER in the BZ, for both isolated and embedded cell.

Computational Simulations

Sinus Rhythm Simulation

We reproduced the patient's ECG in sinus rhythm using computational simulation, in order to test and validate our 3D *patient-specific* model. Since we had the endocardial EAMs for both ventricles, we used that information to generate a *patient-specific* stimulation sequence aiming to reproduce the patient's sinus activation pattern accurately. We used a total of 133 manually-checked endocardial CARTO points (84 for LV and 49 for RV) mapped onto the endocardial surfaces to create that personalized sinus stimulation sequence. We used those mapped points as stimulation sites, applying a stimulus at each one of them in the time instant given by the checked LAT value associated with the corresponding endocardial CARTO point. The endocardial CARTO point with the earliest LAT was the first stimulated site (at $t = 0$ ms) and the rest of points were sequentially stimulated until reaching the latest activated point (highest LAT value) according to recorded EAMs (see **Figure S1**). To perform these simulations of sinus rhythm, we took the final state of the stabilization step (myocyte-fibroblast coupling) as starting point ($t = 0$ ms). Then, we applied the CARTO-derived endocardial stimulation sequence to simulate six heartbeats at a basic cycle length (BCL) of 800 ms, thus matching the patient's heart rate in sinus rhythm (75 bpm) during the RFA procedure, which was measured from the ECG recordings included in CARTO data. Note that only the sixth beat was used to simulate the ECG signals in the 3D torso model for a single heartbeat in order to compare those signals to patient's recordings.

The activation map corresponding to sinus rhythm simulated with model *#6* (with ER and 10% fibrosis in BZ) is displayed **Figure 7**. As observed, most of the ventricular tissue is already activated in around 140 ms. However, certain regions of the BZ

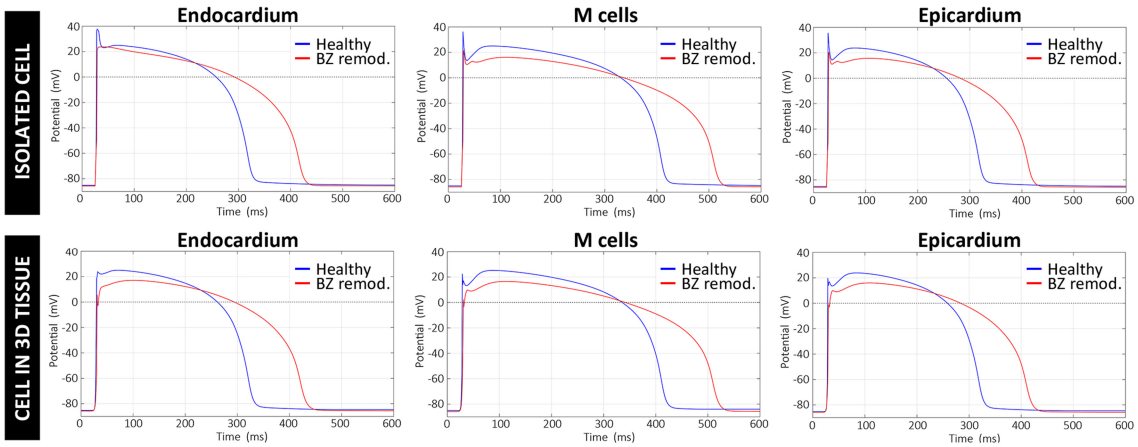

FIGURE 6 | Comparison between APs generated by the original version of ten Tusscher model (ten Tusscher and Panfilov, 2006), used in our simulations for healthy myocardium, and APs resulting from our modified version of such model for the remodeled BZ. Upper row shows APs from a simulation with a single isolated cell, after stabilizing the model at a BCL of 800 ms, while the lower row displays APs obtained for a cell embedded in a 3D tissue (i.e., surrounded by other cells and electrically coupled to them) exclusively composed of remodeled myocytes.

show a very late activation, especially the epicardial isthmus (see **Figure 7D**), where activation lasts up to 289 ms. Activation maps for this CARTO-derived sinus rhythm are very similar for all versions of the ventricular model. The only remarkable difference is the time that the tissue corresponding to the BZ takes to be fully activated, ranging from 243 ms for model *#1* (no ER and no fibrosis in BZ) to 296 ms for model *#8* (with ER and 30% fibrosis in BZ). Both factors slow down the activation of the BZ, with ER causing delays longer than fibrosis.

Figure 8 shows APD maps for four different versions of the ventricular model, depicting the repolarization dispersion (or APD heterogeneity) generated by both the ER and the presence of fibrosis in the BZ. The inclusion of ER in the BZ creates regions with longer APDs, while the presence of 10% image-based patchy fibrosis causes the opposite effect (APD shortening) in certain regions of the BZ. Thus, the combination of both factors increases the dispersion in the repolarization pattern, which may result in a higher arrhythmogenicity. For APD maps with 20% and 30% fibrosis in BZ, see **Figure S2**.

The comparison between the real and simulated ECG (at the precordial leads) for all versions of the ventricular model including ER in the BZ is shown in **Figure 9**. The inclusion or absence of ER in BZ did not have an important impact on the simulated ECG in sinus rhythm (see **Figure S3** for simulated ECGs with models without ER in BZ). Conversely, the presence of fibrosis in the BZ caused a deviation of the ST segment that matched that observed in the real ECG (see elevation in V1 and depression in V5 and V6, for instance). Furthermore, simulated QRS complex width and polarity was remarkably similar to the patient's one, with a signal correlation over 80%, except for V2 and V3 leads for which correlation was around 70%. The most important difference was the repolarization phase, since simulated ECGs showed a delayed T wave with respect to patient's one. Neither ER nor fibrosis in BZ appeared to have an important impact on repolarization, with only a slight effect on T wave magnitude depending on fibrosis level.

In-silico VT Induction

The final goal of our simulation pipeline was to reproduce the clinical VT *in-silico* in order to study its mechanisms and to identify reentry circuits responsible for the VT as ablation targets. Among CARTO points projected onto the 3D model, we chose two locations tagged as pacing sites in the actual procedure and replicated the same programmed electrical stimulation (PES) protocol applied by the electrophysiologists in the EP laboratory. First tested pacing site (*endo#1*) was located on the LV endocardium (**Figure 10**, green sphere), while the second one (*epi#1*) was on the LV posterior epicardial wall below the apical side of the MI (**Figure 10**, red sphere). Aiming to explore the influence of pacing location, we included an additional point (*epi#2*) located on the LV epicardial posterior wall, over the basal side of the MI (**Figure 10**, blue sphere).

Starting from the steady-state after the stabilization in sinus rhythm, we paced the ventricles from each pacing site (one at a time) with a train of six stimuli delivered with a BCL of 600 ms (S1 phase), followed by a single stimulus (S2 phase) coupled at 400 ms after the last S1. If it failed to induce VT, we reduced the S2 coupling interval (CI) in steps of 10 ms until reaching positive VT induction or propagation block at pacing site. In the latter case, when VT was non-inducible by a single S2 stimulus, we repeated the PES protocol adding another premature stimulus (S3 phase) after the S2 phase, with both S2 and S3 stimuli coupled at the same CI. We followed that protocol for the eight model versions (**Table 1**) and the three pacing sites (**Figure 10**). **Table 1** summarizes the results of all those *in-silico* tests of VT inducibility. Focusing on VT simulations at the organ level, such results show that our pipeline was able to replicate the outcomes of the VT inducibility tests performed in the EP laboratory. We achieved positive VT induction with several versions of the ventricular model from the two pacing sites (*endo#1* and *epi#1*) that succeeded in the real EP study. On the contrary, pacing site *epi#2* (not tested in the clinic) could not trigger VT on any model version.

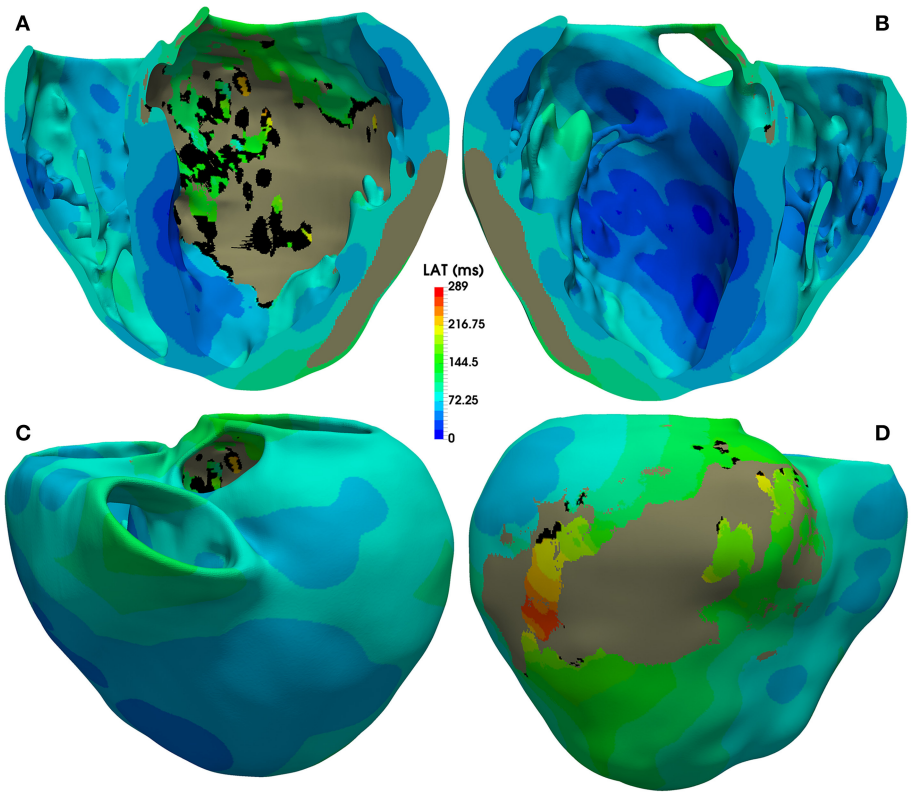

FIGURE 7 | Activation map for CARTO-derived sinus activation, corresponding to the sixth heartbeat simulated with the ventricular model with ER and 10% fibrosis in BZ (model #6). Top row shows an anterior **(A)** and a posterior **(B)** view of a coronal cross-section (four-chamber plane) of the ventricular model, showing the activation on the endocardial surfaces. Bottom row also displays anterior **(C)** and posterior **(D)** views of the whole model, showing the activation at epicardial level. Black regions correspond to not activated tissue (not depolarized) due to fibrosis accumulation. Gray region represents the infarct scar, modeled as non-conducting tissue.

Regardless the pacing site, all induced VTs showed a common mechanism characterized by a unidirectional block at the lower side (the most apical end) of the epicardial SCC previously described, consequently leading to reentry through its upper side (the most basal end). **Figures 11A–E** displays potential maps at different times, showing the propagation patterns generated by the S2 stimulus that gives rise to the unidirectional block and, subsequently, to the onset of the VT due to reentry. Such epicardial SCC enabled the perpetuation of the reentrant activity, showing a clockwise macroreentrant propagation pattern with the wavefront entering the SCC through its upper end and leaving it through the lower one (see **Figure 11F**), what triggered a self-sustained monomorphic VT with a BCL of 526 ms (114 bpm) on model *#6* (see **Video S2**).

In our model, the presence of ER in the BZ was necessary in three out of four configurations allowing positive VT induction (models *#5–7*). The only configuration providing positive VT induction without ER (model *#4*) required the highest fibrosis level (30%) in the BZ among tested ones, together with a CI for S2–S3 phases significantly shorter than that of cases including ER in BZ (see **Table 1**). Concerning pacing site *epi#2* that we added to those tested in the real EP study, the VT test was negative in all model versions, since the applied PES protocol never managed to induce unidirectional block at either of the ends of the epicardial SCC (see **Video S3**). Model *#8* was a special case, as it is the only configuration that always led to bidirectional block at the lower end of the epicardial SCC regardless both the pacing site and the CI for S2–S3 phases, blocking the propagation even in the S1 phase (see **Video S4**).

Figure 12 shows APD maps for three different versions of the ventricular model, exhibiting considerable repolarization dispersion caused by either ER or fibrosis in the BZ, as already observed in sinus activation (see **Figure 8** and **Figure S2**). Those maps, resulting from the propagation of the last stimulus of S1 phase, differ significantly between them, although sharing a common feature. All of them present regions of longer APDs (compared to the rest of BZ tissue) at both ends of the epicardial SCC that supports the reentrant activity. This effect seems more marked at the lower side of the SCC, where the unidirectional block that triggers the reentry occurs, especially in those models including ER in the BZ (**Figures 12B,C**). It is probably caused by a deeper impact of source-sink mismatches because of the narrower funnel shape of the lower end of the SCC compared to the upper one.

Following the premise of only including non-invasive clinical data in our pipeline, we obtained the simulated ECGs for all successful VT induction using the torso model in order to assess

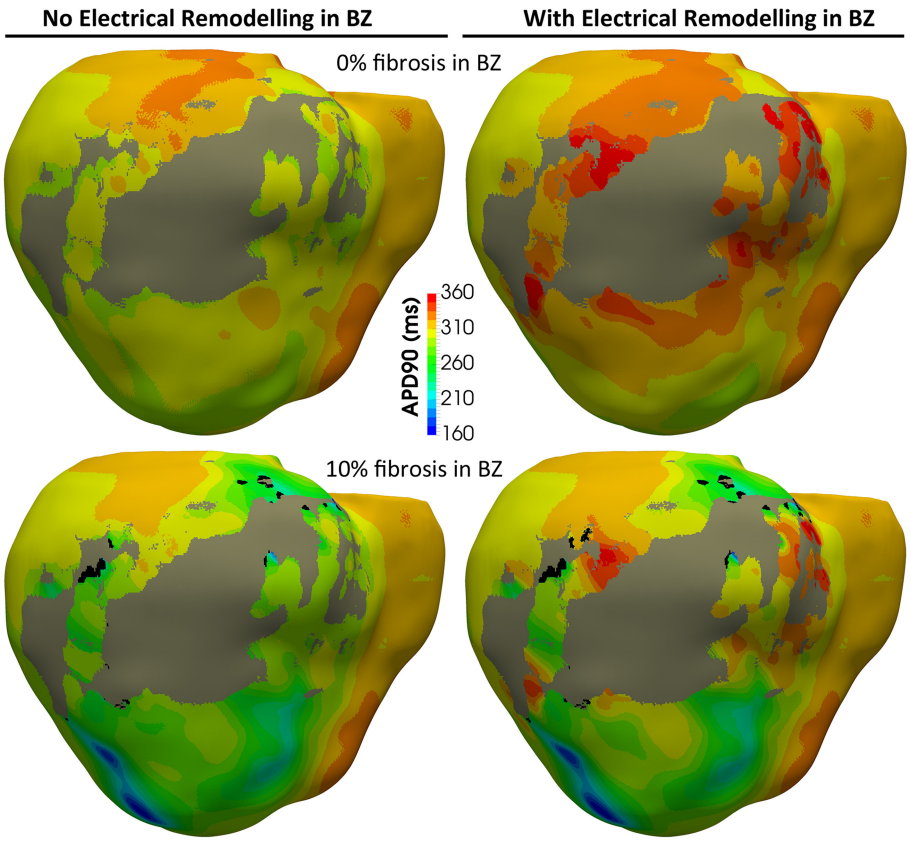

FIGURE 8 | APD maps showing the epicardial surface of the posterior wall of the ventricular model, exhibiting the differences in repolarization patterns during simulated sinus rhythm for the four versions of the model resulting from the combination of absence and presence of ER with no fibrosis and with 10% image-based patchy fibrosis in the BZ. Those maps correspond to the sixth heartbeat simulated from the CARTO-derived activation pattern at a BCL of 800 ms (75 bpm). As observed, both the ER and the presence of patchy fibrosis in the BZ affects the APDs in the BZ, creating repolarization dispersion around the infarct scar. (see **Supplementary Material** for APD maps with 20 and 30% fibrosis in the BZ).

the matching between the *in-silico* induced and the clinical VT by comparing both ECGs. The frequency of reentry around the scar was faster in the patient (BCL=340 ms, 175 bpm) than in the simulations (BCL = 506–526 ms, 114–118 bpm) (see **Table 1**), probably due to differences in CVs mainly in the BZ including the SCC. It is noteworthy that CVs, as well as APDs, were not personalized but based on population data. Aiming to compare the morphology of precordial leads, we removed the frequency variability by resampling a simulated ECG and overlapped it to the patient's ECG. **Figure 13** shows such comparison, where it is clearly appreciated that both morphologies present a high degree of correlation, with the simulated ECG following every signal deflection in the real signals in all precordial leads. Only lead V2 showed an enlarged amplitude in the simulated case in one of the sections of the signal. Hence, as in the case of sinus activation, V2 shows the most considerable differences with respect to the patient's ECG, along with V3 to a lesser extent. All configurations that managed to induce VT showed the same reentrant pattern depicted in **Figure 11F**, therefore resulting in highly similar ECGs, just revealing subtle differences in VT frequency, as observed in **Figure 13** and detailed in **Table 1**.

After analyzing our simulation results, given the significant difference in frequency between clinical and simulated VT (175 vs. 115 bpm), we chose model *#6* and pacing site *epi#1* to perform some additional tests aiming to study the influence of different CVs in the BZ on VT features and its related mechanisms. With CVs reduced by 25% with respect to healthy tissue, the result for VT induction was negative, since unidirectional block never happened (see **Video S5**), reaching propagation fail at pacing site at CI of 290 ms. In contrast, the test with CVs reduced by 50% resulted in a positive VT induction, triggered again by unidirectional block at the lower side of the epicardial SCC, due to S2–S3 stimuli with 320 ms for CI. Such interval is notably shorter than the successful CI in the case of CVs reduced in 75% (see **Table 1**), in which VT furthermore resulted from a single S2 stimulus. Regarding the simulated ECG, the morphology of the monomorphic VT did not exhibit significant variations. However, the acceleration of the reentrant activity due to increased CVs in the BZ led to a considerably shorter BCL

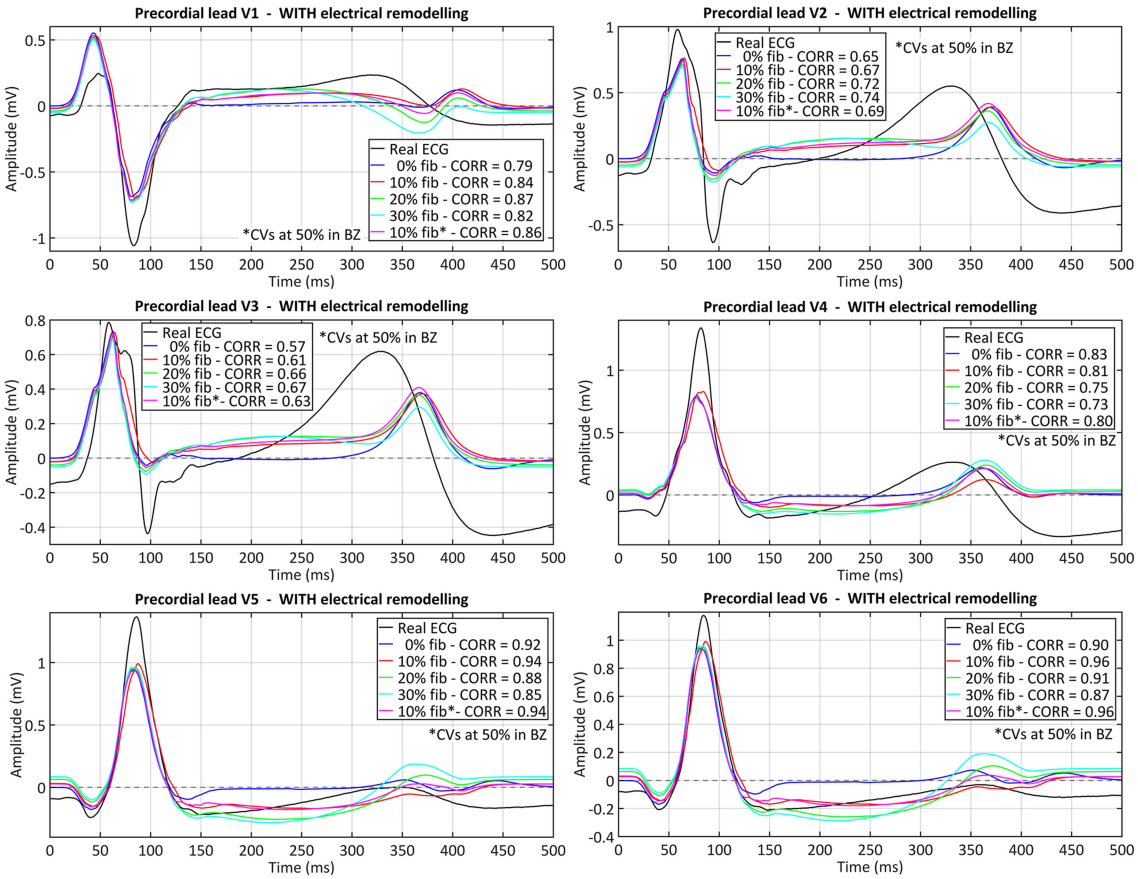

FIGURE 9 | Comparison between real and simulated ECG signals recorded at precordial leads in sinus rhythm. These plots display the ECG simulated with all model versions including ER (models *#5–8*), combined with the four tested levels of image-based patchy fibrosis in the BZ. The ECG for the model version with ER, 10% fibrosis and the CVs reduced by 50% in BZ (10% fib*), instead of 75%, is also represented. Correlation coefficients (CORR) are included in the plots legend. Those signals were obtained by propagating through the 3D torso model the sixth heartbeat simulated from the CARTO-derived sinus activation pattern at a BCL of 800 ms (75 bpm). (see **Supplementary Material** for simulated ECGs with model versions without ER in the BZ).

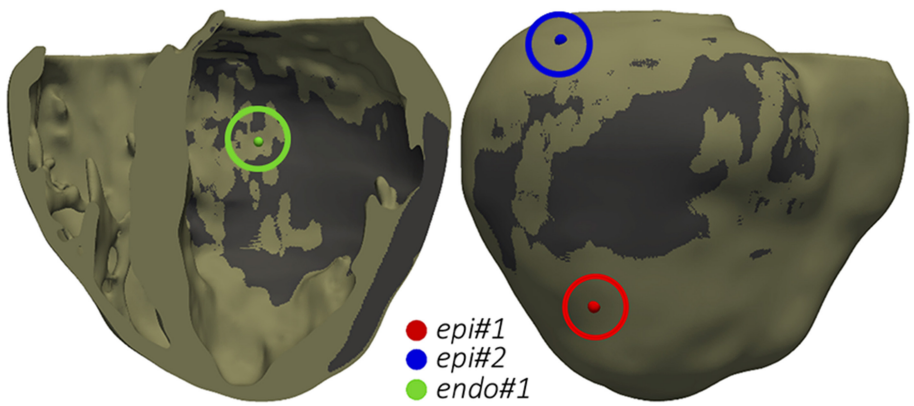

FIGURE 10 | Pacing sites for the application of PES protocols aiming to test VT inducibility by computational simulation. The dark gray region represents the infarct scar.

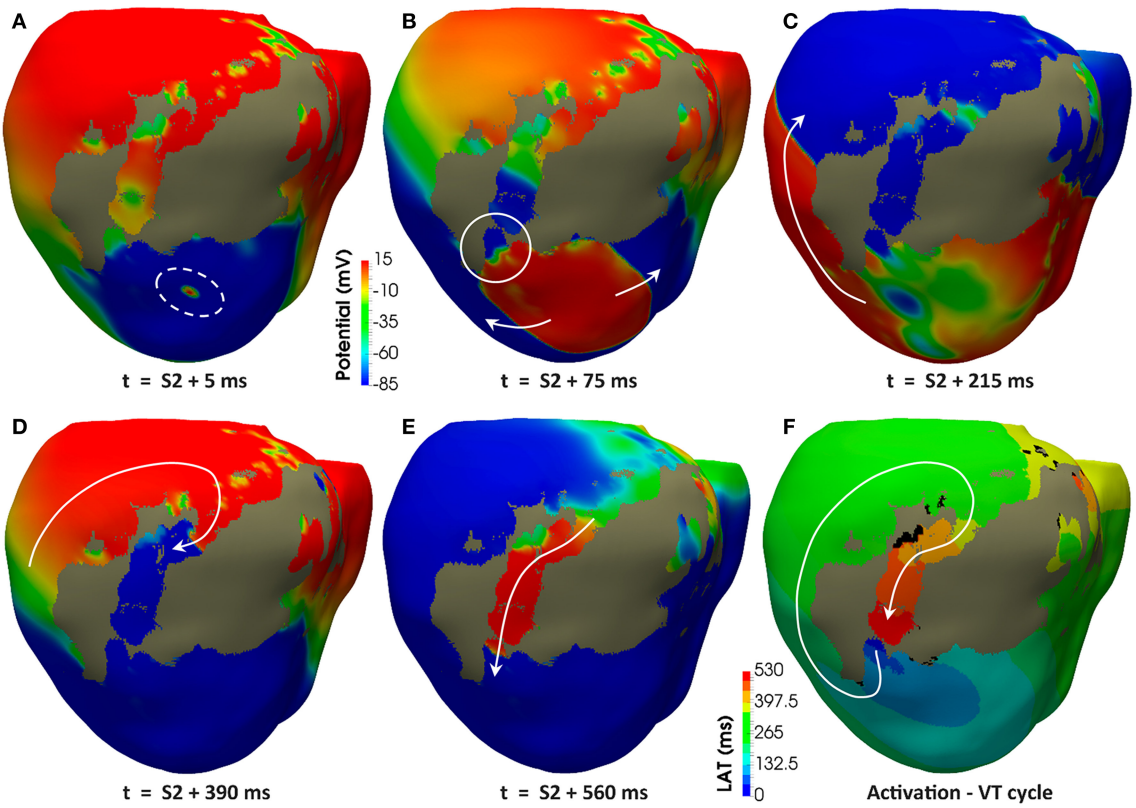

FIGURE 11 | Reentrant monomorphic VT induced *in-silico* by PES protocol. Posterior views of the 3D ventricular model displaying potential maps at different time instants of the PES protocol from pacing site *epi#1* leading to positive VT induction on the model *#6* (ER and 10% fibrosis in BZ). Non-excitable scar is represented in gray color. White arrows indicate direction of the depolarization wavefront. **(A)** Only one premature stimulus (S2) was delivered at a CI of 360 ms. **(B)** The wavefront generated by S2 stimulus causes a functional propagation block at the lower side of the epicardial isthmus (see white circle). **(C)** The wavefront continues propagating around the infarct scar, but not through the epicardial isthmus due to the functional block caused by S2 stimulus. **(D)** The wavefront reaches the upper side of the epicardial isthmus after propagating all around the infarct scar. **(E)** The wavefront enters through the upper side of the epicardial isthmus, propagating across the channel until leaving it through its lower side (unidirectional block) to propagate again around the scar, giving rise to a reentrant activity leading to a self-sustained monomorphic VT. **(F)** Activation map of a cycle of the induced VT, confirming that the epicardial isthmus constitutes a SCC acting as structural substrate for this infarct-related VT.

(425 ms, 141 bpm) (see **Figure 13**), closer to that of the clinical VT but still a 20% slower (175 vs. 141 bpm).

DISCUSSION

3D Modeling

In this study, we have built a detailed image-based 3D cardiac model that faithfully reproduces the *patient-specific* anatomy and function of the ventricles of a given subject (see **Figure 1**) from non-invasive clinical data, reaching a high level of anatomical detail. In contrast, fiber orientation and transmural EP heterogeneity were included based on population data. Unlike ours, most previous 3D ventricular models ignore papillary muscles and endocardial trabeculations, especially those based on *in-vivo* clinical images. Subtlety and high inter-subject variability of endocardial structures add difficulty to the already challenging task of segmenting *in-vivo* cardiac datasets. In our particular case, since the reentrant circuit is entirely confined at the epicardial level, neither papillary muscles nor trabeculations appear to have any impact on VT mechanisms. However, significant influence of some endocardial structures (e.g., moderator band in RV) on activation patterns has been observed both experimentally (Durrer et al., 1970) and by computational simulation (Bishop et al., 2010), as well as their potential role in the VT features (Kim et al., 1999b; Bogun et al., 2008; Walton et al., 2018). Further investigations with large cohorts of patients are required to assess the convenience of systematically including endocardial details in *patient-specific* models devoted to infarct-related VT simulations.

An essential element of our model was the anatomical and functional modeling of the infarcted region. We based our *patient-specific* anatomical MI model on cardiac DE-MRI (see **Figure 2**), which is the current gold-standard technique for *in-vivo* assessment of myocardial ischemic injury in clinical environments (Jamiel et al., 2017; Patel et al., 2017). Moreover, DE-MRI is a routine imaging technique recommended for infarcted patients referred for RFA procedures (Pedersen et al., 2014; Priori et al., 2015), so it satisfies our requisite of exclusively using non-invasive clinical data. DE-MRI enables

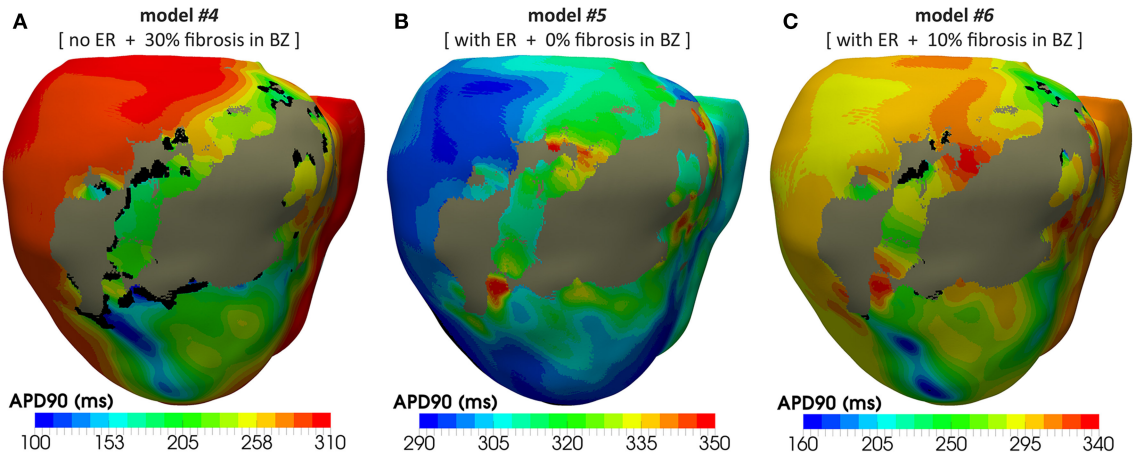

FIGURE 12 | APD maps resulting from the propagation of the last stimulus of the S1 phase triggered from pacing point *epi#1*. These maps correspond to three out of the four different versions of the ventricular model that enabled positive VT induction in *in-silico* tests: **(A)** model *#4* (no ER and 30% fibrosis), **(B)** model *#5* (with ER and 0% fibrosis), and **(C)** model *#6* (with ER and 10% fibrosis). All of them show repolarization dispersion in the BZ surrounding the infarct scar, with a region of longer APDs at both ends of the epicardial SCC, especially at the lower side where the unidirectional propagation block that triggers the reentrant activity occurs. Black regions correspond to not activated tissue due to fibrosis accumulation.

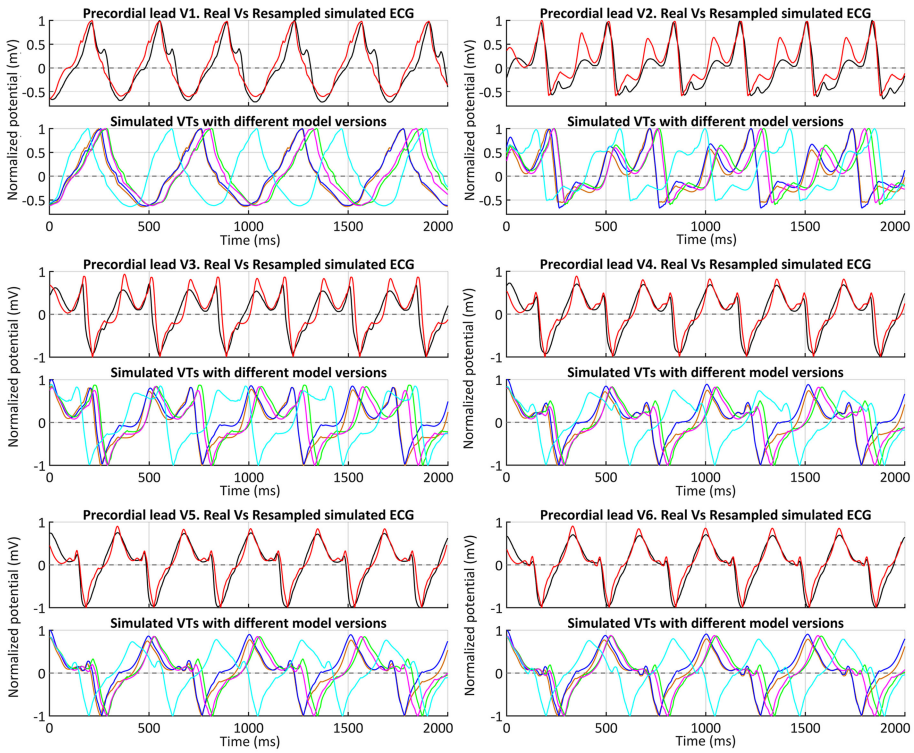

FIGURE 13 | ECGs during clinical VT. Comparison between real (*black*) and simulated ECGs with different model versions for *in-silico* induced VT. Simulated ECGs correspond to all model versions that enabled a positive VT induction: models *#4* (*orange*), *#5* (*blue*), *#6* (*green*) and *#7* (*magenta*). The ECG for model *#6* (ER and 10% fibrosis in BZ) with the CVs reduced by 50% (instead of 75%) is also represented (*cyan*). Together with the patient's ECG (*black*), a resampled version of the ECG obtained with model *#6* and CVs reduced by 75% in BZ is displayed (*red*) to ease a visual comparison of the waveform of both signals.

the segmentation of the MI differentiating between infarct scar and BZ, that is crucial in order to study infarct-related VT mechanisms by computational simulation (Ringenberg et al., 2014; Ukwatta et al., 2016). Nonetheless, the proper definition of both types of tissue from *in-vivo* clinical DE-MRI images remains controversial (especially for the BZ), something that

has given rise to a great variety of methods for this problem (Karim et al., 2016).

Electrophysiological Modeling

Although it is not a completely acellular tissue (Sun et al., 2002; Rog-Zielinska et al., 2016), the infarct scar is mainly composed of extracellular matrix (collagen) (Cleutjens et al., 1999; van den Borne et al., 2010; Daskalopoulos et al., 2012). However, there is no representation for the extracellular space in the monodomain model. In such a case, a passive model (cellular level) combined with a low conductivity (tissue level) could be used to account for a slight electrotonic load caused by the scar (Ringenberg et al., 2014; Deng et al., 2015). We performed some initial tests assigning the MacCannell model to the scar region, as done in McDowell et al. (2011). When we computed the ECG, the signals showed considerable distortion caused by strong gradients resulting from the presence of such a large region (the scar occupies the 16% of LV in our model) that practically remained at resting potential across the simulations. This unwanted "side effect" would be critical for this work, since simulating the ECG properly is a key goal in order to compare our results to a real patient's recordings. Hence, we decided to disregard the potential electrotonic effect of the scar and modeled it as an electrical insulator by imposing no-flux boundary condition, as done in many other studies (Relan et al., 2011; Rantner et al., 2012; Arevalo et al., 2013, 2016; Ashikaga et al., 2013).

A few simulation studies focused on infarct-related VTs have also included fibrosis within the BZ. Some authors have randomly included fibrosis, either diffuse fibrosis modeled as an electrically passive tissue in a 3D model of rabbit ventricles (McDowell et al., 2011) or as micro-regions (patches) of non-conducting scarred tissue in a 3D canine model (Arevalo et al., 2013). Similarly, a very recent work included randomly generated patterns of non-conducting fibrotic tissue within the BZ in a model of infarcted rabbit ventricles (Campos et al., 2018). Another study faithfully reproduced fibrosis distribution in the BZ by means of highly detailed 3D models of wedge samples resulting from the reconstruction of high-resolution histological sections of infarcted rat hearts, considering it as non-conducting dense fibrotic tissue (Rutherford et al., 2012).

The gadolinium-based contrast agent used in DE-MRI is not specific for fibrosis, so the hyper-enhancement is assumed to be caused by its distribution through the extracellular space (Moon et al., 2004; Mewton et al., 2011), which is expanded in fibrotic regions resulting from the healing of MI (Hein and Schaper, 2001; Daskalopoulos et al., 2012; Seidel et al., 2016). Experimental observations based on histological sections have witnessed the presence of fibrosis infiltrated within the BZ (de Bakker et al., 1988; Smith et al., 1991; Rutherford et al., 2012; Tschabrunn et al., 2016), mainly showing the appearance of patchy/interstitial fibrosis. Importantly, this is considered the most arrhythmogenic kind of structural remodeling. Patchy fibrosis increases the susceptibility to unidirectional blocks due to source-sink mismatches and slows down conduction because of propagation delays caused by the tortuous pathways that the wavefront has to take, also leading to EGM fragmentation due to impaired activation (de Bakker et al., 2005; de Jong et al., 2011; Nguyen et al., 2014; Dhanjal et al., 2017). According to histological observations, it is widely assumed that voxels showing intermediate intensity levels in DE-MRI images, usually classified as BZ, correspond to a mixture of myocytes and fibrotic tissue (Hsu et al., 2006; Schuleri et al., 2009; Varga-Szemes et al., 2016). Consequently, we assumed that voxels in the BZ showing the highest intensity levels in the images probably correspond to pieces of myocardium having a high percentage of fibrotic tissue. Here, the intensity level of each DE-MRI voxel was mapped into a cluster of hexahedral elements in the volume mesh of ventricular model. This, along with the fact that the brightest voxels in the BZ are usually surrounded by others with similar intensities, makes our image-based method to generate patches within the BZ (see **Figure 3**), resulting in a pattern of patchy fibrosis similar to that observed in histological examinations (Schuleri et al., 2009; Rutherford et al., 2012). Finally, we defined image-based fibrosis up to 30% of the BZ (represented by the MacCannell model), since larger levels generated fibrotic barriers completely blocking the electrical propagation inside the epicardial SCC responsible for the VT, as for instance in the case of model *#8* described above. A recent study used a similar approach to include realistic fibrosis patterns based on DE-MRI images, although in that case the aim was to assess the influence of several strategies of fibrosis modeling on atrial fibrillation dynamics using a 3D model of human left atrium (Roney et al., 2016).

Regarding myocyte-fibroblast coupling, there is experimental evidence of the existence of this kind of heterocellular coupling via gap junctions in the remodeled myocardium resulting from MI (Camelliti et al., 2004; Schwab et al., 2013; Mahoney et al., 2016), as well as by tunneling nanotubes (Quinn et al., 2016). However, there is a lack of experimental studies focused on the characterization of myocyte-fibroblast coupling in the BZ of chronic MIs in terms of density and distribution of functional gap junctions connecting both types of cells (Ongstad and Kohl, 2016). Hence, magnitude and anisotropy of the electrotonic load caused by myocyte-fibroblast coupling in the BZ remain undetermined. Finally, we decided to consider this influence by means of a fibroblast model (MacCannell et al., 2007) and a conductivity value set for fibrotic tissue that mainly affects the myocyte-fibroblast coupling within the BZ by modulating the electrotonic interaction between both cell types.

Besides fibrosis, we also considered the ER in the viable but altered myocardium corresponding to the BZ that surrounds the infarct scar. However, it must be noted that all changes affecting ionic channels considered for the BZ are based on experiments with cells harvested from epicardial BZ of canine hearts (Pu and Boyden, 1997; Jiang et al., 2000; Dun et al., 2004). As recently discussed elsewhere (Connolly and Bishop, 2016), it is unclear to what extent such data are representative of the ER in BZ of human hearts. The presence of epicardial collateral circulation in canine hearts, not present in humans, is known to influence the formation of the epicardial BZ in dogs (Ursell et al., 1985; Schaper et al., 1988), which could give rise to functional differences with respect to the surviving myocytes in human BZ. On the other hand, all of those experimental studies (Pu and Boyden, 1997; Jiang et al., 2000; Dun et al., 2004) were performed a few days

after the coronary occlusion, still in the healing phase of the MI rather than in its chronic stage (see Mendonca Costa et al., 2018 for a recent review). Nevertheless, these data have been widely used in previous studies (McDowell et al., 2011; Rantner et al., 2012; Arevalo et al., 2013; Ashikaga et al., 2013; Ringenberg et al., 2014; Deng et al., 2015; Hill et al., 2016) due to the lack of experimental data for ER in the BZ of chronically infarcted human hearts.

Our simulation results showed that VT inducibility was strongly related to slow conduction and APD heterogeneity in the BZ (including the SCC). Slow conduction in BZ is widely considered as a key factor in promoting reentry through SCC crossing the infarct scar, as it allows the working myocardium at the other side to recover its excitability before the arrival of the wavefront coming from the channel (Lazzara and Scherlag, 1984; de Bakker et al., 1993; Nguyen et al., 2014). However, the underlying mechanisms of this reduction in CVs still remain unclear, leading to a lack of consensus on the proper way to model it computationally. Some authors have reduced drastically only the transversal CV (McDowell et al., 2011; Deng et al., 2015). This approach could represent the severe reduction measured in gap junctional conductance in canine BZs only in the transverse direction (Yao et al., 2003) and/or the loss of side-to-side coupling between adjacent layers of myocytes due to the isolating effect of infiltrated fibrotic tissue (Spach and Boineau, 1997). Rutherford *et al.* managed to induce reentry in wedge models of infarcted myocardium due to the propagation delays exclusively caused by dense fibrosis (collagen) infiltrated within the BZ (Rutherford et al., 2012). Downregulation and lateralization of connexin 43 (i.e., gap junctions) have been also reported in the BZ (Smith et al., 1991; Severs et al., 2008). Downregulation of connexin 43 could result in an isotropic reduction of CV and its lateralization would exacerbate this effect in the longitudinal direction while keeping or even increasing transversal CV. Nonetheless, part of lateralized gap junctions of remodeled cardiomyocytes in the BZ are thought to be non-functional (Matsushita et al., 1999). Regarding tissue architecture, both DTI (diffusion tensor imaging) (Wu et al., 2006; Winklhofer et al., 2014) and histological preparations (Rutherford et al., 2012; Tschabrunn et al., 2016) have revealed fiber disarray within the BZ that consequently involves alterations in tissue anisotropy. Conversely, a recent study based on very high-resolution DTI observed good preservation of normal fiber orientation patterns in chronically infarcted regions of porcine and human hearts (Pashakhanloo et al., 2017). In conclusion, the slowed conduction in the BZ seems to derive from a complex combination of structural, electrical and gap junction remodeling that is not well-understood yet (de Bakker, 2017). In our case, aiming to reproduce macroscopically the global effect of all those combined factors affecting the propagation and promoting the reentrant activity, and in addition to the image-based patchy fibrosis, we imposed an isotropic reduction of CVs in the BZ as recently done by others (Ringenberg et al., 2014; Hill et al., 2016), testing reductions of 75, 50, and 25% for both longitudinal and transversal CVs with respect to the healthy myocardium.

Sinus Rhythm Simulation

Regarding the personalization of cardiac activation, other authors have exploited EAMs to personalize electrical propagation in simplified models by adapting the so-called apparent conductivities (Chinchapatnam et al., 2008; Relan et al., 2011; Chen et al., 2016). Since we excluded invasively recorded data from our pipeline, we just benefited from CARTO data to validate the full 3D model (ventricles-torso set) in sinus rhythm by means of the simulated ECG resulting from the activation pattern provided by endocardial EAMs. The main limitations of EAMs are the lack of accurate automatic tools to fit the data to a 3D model and to annotate LATs, especially in regions showing pathological EGMs due to the presence of fibrosis and scarred tissue. The myocardium affected by the MI (scar and BZ) is the most thoroughly mapped region aiming to find SCCs across the scar as potential substrates for reentry (Soejima et al., 2002; Baldinger et al., 2016; Pokorney et al., 2016). However, in that region most of EGMs show low amplitude and/or very fragmented signals (Gardner et al., 1985; Bogun et al., 2005; Aliot et al., 2009). That is why we had to exclude such a large amount of CARTO points: 462 points removed out of 847 included in the original CARTO data. In this regard, new multi-array catheters, such as *PentaRay* for CARTO system (Biosense Webster, Inc., Diamond Bar, CA, USA) or *IntellaMap Orion* for Rhythmia system (Boston Scientific, Marlborough, MA, USA) (Mantziari et al., 2015), are currently helping to acquire less noisy and much denser maps. Despite current limitations, including the uncertainty in LAT annotations, our whole-body level approach allowed obtaining ECGs in sinus rhythm where precordial leads showed a good signal correlation with real ECGs (between 80 and 96% for V1, V4, V5, and V6), as well as a similar R-wave progression (see **Figure 9**). This, along with the good agreement in QRS complex duration, indicates that chosen values for CVs in healthy myocardium and for conductivities of organs and structures in torso model are within a proper range. Moreover, the coincidence in T wave polarity between real and simulated ECGs (except for V1) suggests an appropriate definition of transmural layers, since transmural heterogeneity is known to have a great influence on the repolarization phase in organ-level simulations (Okada et al., 2011; Perotti et al., 2015). As observed in **Figure 9**, simulated signals for V2 and V3 are the leads that show most notable differences compared to real ECG, not only in the repolarization phase but also in QRS complex, as real ECG shows a prominent negative S wave that simulations could not properly reproduce. This might be partially caused by the fact that in the EP laboratory a pad for defibrillation shocks is usually fixed on the left side of patient's chest, forcing the relocation of V2 and (sometimes) V3 electrodes away from their standard positions. Hence, since we placed the virtual electrodes for simulated ECG on the standard position of precordial leads (see **Figure 5**), this is likely to be an important error source specifically affecting V2 and V3. Moreover, considering that V2 and V3 were also the most different signals obtained from simulated VTs compared to the real ECG (see **Figure 13**), it seems highly probable that V2 and V3 electrodes were not placed in its standard positions in the EP laboratory. In conclusion,

we consider this reproduction of the patient's ECG for sinus activation is an important step for the validation of our pipeline, even though it is usually omitted in other studies that also aim for planning of RFA interventions.

In-silico VT Induction

The results of our simulation pipeline for *in-silico* tests of VT inducibility suggest that, in the presence of a SCC with slowed conduction, a key factor to cause a unidirectional block able to trigger a reentrant VT is the repolarization dispersion due to APD heterogeneity, as observed in **Figure 12**. In models *#5–7* such APD heterogeneity (see **Figures 12B,C**) comes from the increased APD associated with the ER in the BZ (see **Figure 6**), even causing permanent blocks when combined with high fibrosis levels (model *#8*). Nevertheless, in model *#4*, the APD heterogeneity responsible for the unidirectional block is exclusively caused by the presence of patchy fibrosis within the BZ, which by contrast gives rise to patches of tissue with decreased APD because of myocyte-fibroblast interactions (**Figure 12A**). This explains the need of a shorter CI to induce VT in model *#4* compared to those versions including ER in the BZ (see **Table 1**). On the other hand, the complete failure of pacing site *epi#2*, along with the fact that models *#4* and *#5* allowed positive VT induction from *epi#1* but not from *endo#1*, gives evidence of the important influence of the location of pacing sites on the result of VT inducibility tests and even on the morphology of induced VTs. If PES protocol delivered from *epi#2* had been able to cause a unidirectional block at the upper end of the epicardial SCC, for instance, the morphology of the resulting monomorphic VT would have been different. In such a case, macroreentry would show a counterclockwise propagation pattern that, consequently, would alter the morphology of the ECG during the VT episode. Nonetheless, not only the location of pacing sites but also the geometry of the SCC seems to have an essential role in VT mechanisms, what might be the reason for which in our model propagation blocks occur at the lower side of the SCC but never at the upper one. In our case, the lower end of the SCC is narrower than the upper (see **Figure 11**), which makes it more prone to functional propagation blocks due to source-sink mismatches caused by abrupt changes in the geometry of excitable tissue (Connolly et al., 2015; Ciaccio et al., 2018). With respect to the tests performed with different conductivities, simulation results confirm the great impact of CVs in the BZ both on the initiation mechanisms and on the frequency of infarct-related reentrant VTs.

Therefore, according to our simulation results, derived from a unique MI geometry, the most influential factors in promoting reentrant infarct-related VTs are the reduction of CVs and APD heterogeneity (repolarization dispersion) in the BZ, either caused by ER (model *#5*) or by the presence of fibrosis (model *#4*), as well as by the combination of both kinds of remodeling (structural and ER) (models *#6–7*). However, our results suggest that arrhythmogenicity is more strongly correlated with ER than with fibrosis in the BZ. Only in one case (model *#4* paced from point *epi#1*) we managed to induce VT in the absence of ER, requiring a high fibrosis level (30%) to create an APD heterogeneity enough to promote a unidirectional propagation block (**Figure 12A**), in combination with a shorter CI for premature stimulus. This is in agreement with that observed in Arevalo et al. (2013) and recently discussed in Trayanova et al. (2017), whose authors concluded that the presence of fibrosis in the BZ is not a necessary element in order to predict reentrant circuits by means of cardiac computational models, as long as ER in BZ is considered. Focusing on model versions including ER (models *#5–8*), moderate levels of patchy fibrosis in the BZ are thought to facilitate the initiation of VTs, as in the case of models *#6* (10%) and *#7* (20%) paced from point *endo#1* (see **Video S6**). However, elevated levels appear to prevent from VT mechanisms, as observed in model *#8* (30%), where the formation of a permanent bidirectional block avoids the self-sustained reentry and, consequently, the VT. This matches the conclusions reached in McDowell et al. (2011), where the authors observed an increased risk of infarct-related VTs for intermediate levels of diffuse fibrosis randomly distributed within the BZ, as well as a protective role against VT derived from higher levels. Hence, our approach of image-based patchy fibrosis seems to have a similar impact on infarct-related VT mechanisms.

Although the morphology of the signals of simulated ECG is highly similar to that of clinical VT (only V2 and V3 show notable differences, probably due to inaccurate electrode location) (see **Figure 13**), the BCL of *in-silico* induced reentry is larger than the patient's one, thus resulting in a slower VT. We think it is due to differences in CVs in the BZ and, consequently, in the epicardial SCC supporting the reentry, where the model is likely to conduct slower than the real case. When we increased CVs in the BZ up to 75% with respect to healthy tissue (i.e., a reduction of 25%), we could not induce VT because premature stimuli (S2–S3) stopped propagating at a CI too short to produce the functional block at the SCC entrance. The faster the propagation, the shorter the CI needed to generate a wavefront able to reach the SCC entrance within the time window in which its tissue is vulnerable to functional blocks. On the other hand, in the simulated ECGs in sinus rhythm we observed a delayed repolarization with respect to the patient's ECG (**Figure 9**), something that suggests that APDs in our model are larger than the patient's ones. We did not include the personalization of any parameter relative to cardiac EP in the design of our pipeline. However, we hypothesize that the choice of an ionic model with a basal APD shorter than ten Tusscher's one probably might allow inducing a reentry with a shorter CI for premature stimuli in spite of relatively high CVs in the BZ, triggering a reentry with a shorter BCL and, thus, a faster VT. Hence, we believe that including in our pipeline a coarse personalization of the APD based on the features of patient's ECG in sinus rhythm, as well as for CVs in healthy myocardium, could improve the performance of our approach. Although there are a few precedents in this regard (Relan et al., 2011; Chen et al., 2016; Gillette et al., 2018), further studies should be conducted in order to test such hypothesis.

As in this work, the ability to reproduce infarct-related VTs by means of image-based human cardiac computational models has been demonstrated in a number of previous studies (Relan et al., 2011; Ashikaga et al., 2013; Ringenberg et al., 2014; Arevalo et al., 2016; Chen et al., 2016; Deng et al., 2016; Prakosa et al., 2018). Concerning the global performance of our particular approach,

we have been able to reproduce patient's ECG both in sinus rhythm and in clinical VT with good fidelity, considering that cardiac EP and myocardial architecture were not personalized. When PES protocols produce positive VT induction in the EP laboratory, electrophysiologists usually compare the resulting ECG to that registered during clinical VT episodes as a method to discern whether both VTs match or not, what helps in the process of choosing optimal ablation targets. Therefore, our pipeline completely based on non-invasive clinical data has the potential to replicate such process *in-silico*, such that it might become a helpful tool in therapy planning prior to RFA procedures aimed at finishing infarct-related VTs.

Limitations

The major limitation of our work derives from the fact that it relies on only one case. Thus, this work must be considered as a proof-of-concept study that shows promising, yet preliminary results. Hence, further studies including a larger number of patients should be conducted in order to improve and validate our pipeline, as well as to strengthen our conclusions.

Some features of the 3D ventricular model were not personalized. Myocardial architecture, for instance, was generated by means of a rule-based approach based on population data. The only alternative is the use of DTI (Hsu et al., 1998; Scollan et al., 1998; Holmes et al., 2000), although *in-vivo* cardiac DTI remains highly challenging because of the artifacts caused by cardiac motion. However, some studies have compared simulation results performed on 3D ventricular models using rule-based methods and *ex-vivo* DTI (Bishop et al., 2009; Bayer et al., 2012), finding only minor differences in electrical patterns at global level, what confirms the validity and robustness of rule-based approaches for simulations of cardiac EP.

Currently, the electrical propagation through ventricular myocardium is known to be characterized by three distinct conductivities in longitudinal, transverse (within myocardial sheets) and normal (along transmural direction) axes (Hooks, 2007; Caldwell et al., 2009). Recent computational studies have shown the impact on propagation patterns that might result from considering such full electrical anisotropy, both in simulations at organ level in healthy ventricles (Johnston et al., 2016) and in simplified models of cardiac tissue under diseased conditions (Johnston et al., 2018). Instead, we considered a unique conductivity for all directions perpendicular to myocyte longitudinal axis, as it has been commonly assumed in most of the 3D computational studies of cardiac EP so far. Hence, the incorporation of full anisotropy to the cardiac EP modeling of our pipeline might be one of the future improvements, as well as the study of its influence on infarct-related VT inducibility.

We did not incorporate the cardiac conduction system in our ventricular model, although it was not expected to have a significant impact on the infarct-related VT mechanisms that we aimed to study in this work. Considering the longer APD of Purkinje cells and the delay at the Purkinje-myocardial junctions, the kind of VTs simulated in this study could not have been mediated by the Purkinje system. In any case, currently there is no *in-vivo* imaging modality capable of providing information about the *patient-specific* geometry of Purkinje network. There are a few recent studies proposing approaches to infer models of conduction system from endocardial EAMs (Vergara et al., 2014; Palamara et al., 2015; Barber et al., 2017), yet it would break our requisite of only using non-invasive clinical data collected prior to the RFA procedure. Then, the only alternative would be to include a synthetic Purkinje model. Nevertheless, in such a case it would be impossible to assess to what extent the impact on simulation results of that artificial Purkinje network (if any) would be faithfully replicating the influence of the patient's conduction system in such scenario.

The poor quality of the anatomical whole-torso MRI hampered the construction of a *patient-specific* torso model, forcing us to reuse and adapt an existing one. However, given the results yielded for simulated ECGs, it does not appear to have been an important drawback, at least in this particular case.

CONCLUSIONS

Our 3D *patient-specific* model of the ventricles exclusively built from clinical data, in spite of avoiding the personalization of cardiac EP (based on population data), was able to reproduce the morphology of the clinical monomorphic VT suffered by the patient in the simulated ECGs. Furthermore, this allowed identification within the 3D model of the SCC responsible for the reentrant activity, matching the ablation target chosen by the experts in the RFA procedure that successfully eliminated VT inducibility in the patient. Hence, we have given a proof of the feasibility of developing 3D *patient-specific* computational models from clinical data aimed at simulation of the cardiac EP, with the potential to become a powerful tool for surgical planning. This approach could help to improve the currently low success rate of RFA procedures as well as to shorten surgery duration and, consequently, decrease the risk to the patient. It must be highlighted the great importance of the personalization of both cardiac anatomy and MI geometry from *in-vivo* high-resolution images to accurately locate reentry pathways as ablation targets by *in-silico* EP studies.

From the functional perspective, the computational modeling of the BZ remains a complex task due to the lack of experimental data from human hearts. In our study, the determinant aspects were the reduction of CVs and APD heterogeneity, which could be caused by ER in the BZ, a large amount of patchy fibrosis (30%) or a combination of both factors. The most arrhythmogenic versions of our ventricular model were those that combined the ER with intermediate fibrosis levels (10 and 20%) in the BZ. Such configurations generate an important repolarization dispersion (APD heterogeneity) around the infarct scar, especially in the vicinity of both terminal ends of the epicardial SCC, making the model more prone to the onset of reentrant activity due to functional unidirectional blocks in the channel.

Several challenging issues are still hampering the introduction of cardiac computational models as a common tool in clinical environments, such as the automatic and accurate reconstruction of *patient-specific* anatomy and infarct geometry from *in-vivo*

images, especially from MRI modalities. Another important drawback is the current high cost of 3D computational simulations of cardiac EP at organ and body levels, whose computational burden demands the use of high-performance computational resources and long computing times.

ETHICS STATEMENT

Regarding the ethical considerations, the protocol was approved by the Ethics Committee for Clinical Research of the Hospital Clinic Universitari de Valencia (Valencia, Spain), which certifies that the present study was conducted in accordance with the recommendations gathered in the Declaration of Helsinki, originally adopted by the General Assembly of the World Medical Association in 1964, and in its subsequent revisions. Furthermore, the patient, who underwent the standard clinical protocol, gave written informed consent for the use of his anonymized clinical data in this study.

AUTHOR CONTRIBUTIONS

AL-P, RS, MI, and JF jointly conceived this work and assessed the results. AL-P built the 3D models and performed the computational simulations for this work, all of this with the priceless help and close supervision from RS and JF. AL-P and RS wrote the manuscript. MI and RR collected and provided clinical data used in this work and gave valuable advice on the interpretation of electrophysiological data. MI checked the annotations of electrophysiological data and supervised this work, providing it with a clinical perspective. MB provided valuable advice on electrophysiological modeling issues, participated in the critical discussion of the results and contributed to the writing of the manuscript. All authors have read and approved the final version of the manuscript.

FUNDING

This work was partially supported by the Plan Estatal de Investigación Científica y Técnica y de Innovación 2013–2016 from the Ministerio de Economía, Industria y Competitividad of Spain (grant number DPI2016-75799-R) and AEI/FEDER, UE, and also by the Programa Estatal de Investigacion, Desarrollo e Innovacion Orientado a los Retos de la Sociedad from the Ministerio de Economia y Competitividad of Spain, and the European Commission (European Regional Development Funds—ERDF-FEDER) (award number TIN2014-59932-JIN). During this work, AL-P was financially supported by the Ministerio de Economía, Industria y Competitividad of Spain through the program Ayudas para contratos predoctorales para la formación de doctores (grant number BES-2013-064089).

ACKNOWLEDGMENTS

Authors are very grateful to María P. López-Lereu and José V. Monmeneu, from the Unit of Cardiac Imaging of ERESA (Valencia, Spain), for the acquisition of the cardiac MRI datasets that were used in this work.

SUPPLEMENTARY MATERIAL

The Supplementary Material for this article can be found online at: https://www.frontiersin.org/articles/10.3389/fphys.2019.00580/full#supplementary-material

REFERENCES

Abdelwahab, A., and Sapp, J. L. (2007). NaviStar ThermoCool catheter for ventricular tachycardia. *Expert Rev. Med. Devices* 4, 307–314. doi: 10.1586/17434440.4.3.307

Abubakar, I. I., Tillmann, T., and Banerjee, A. (2015). Global, regional, and national age–sex specific all-cause and cause-specific mortality for 240 causes of death, 1990–2013: a systematic analysis for the Global Burden of Disease Study 2013. *Lancet* 385, 117–171. doi: 10.1016/S0140-6736(14)61682-2

Aliot, E. M., Stevenson, W. G., Almendral-Garrote, J. M., Bogun, F., Calkins, C. H., Delacretaz, E., et al. (2009). EHRA/HRS expert consensus on catheter ablation of ventricular arrhythmias: developed in a partnership with the European Heart Rhythm Association (EHRA), a registered branch of the European Society of Cardiology (ESC), and the Heart Rhythm Society (HRS); i. *Europace* 11, 771–817. doi: 10.1093/europace/eup098

Amado, L. C., Gerber, B. L., Gupta, S. N., Rettmann, D. W., Szarf, G., Schock, R., et al. (2004). Accurate and objective infarct sizing by contrast-enhanced magnetic resonance imaging in a canine myocardial infarction model. *J. Am. Coll. Cardiol.* 44, 2383–2389. doi: 10.1016/j.jacc.2004.09.020

Andreu, D., Berruezo, A., Ortiz-Pérez, J. T., Silva, E., Mont, L., Borràs, R., et al. (2011). Integration of 3D electroanatomic maps and magnetic resonance scar characterization into the navigation system to guide ventricular tachycardia ablation. *Circ. Arrhythmia Electrophysiol.* 4, 674–683. doi: 10.1161/CIRCEP.111.961946

Andreu, D., Ortiz-Pérez, J. T., Fernández-Armenta, J., Guiu, E., Acosta, J., Prat-González, S., et al. (2015). 3D delayed-enhanced magnetic resonance sequences improve conducting channel delineation prior to ventricular tachycardia ablation. *EP Eur.* 17, 938–945. doi: 10.1093/europace/euu310

Andreu, D., Penela, D., Acosta, J., Fernández-Armenta, J., Perea, R. J., Soto-Iglesias, D., et al. (2017). Cardiac magnetic resonance–aided scar dechanneling: influence on acute and long-term outcomes. *Hear. Rhythm* 14, 1121–1128. doi: 10.1016/j.hrthm.2017.05.018

Antzelevitch, C., Shimizu, W., Yan, G. X., Sicouri, S., Weissenburger, J., Nesterenko, V. V., et al. (1999). The M cell: its contribution to the ECG and to normal and abnormal electrical function of the heart. *J. Cardiovasc. Electrophysiol.* 10, 1124–1152. doi: 10.1111/j.1540-8167.1999.tb00287.x

Arevalo, H., Plank, G., Helm, P., Halperin, H., and Trayanova, N. (2013). Tachycardia in post-infarction hearts: insights from 3D image-based ventricular models. *PLoS ONE* 8:e68872. doi: 10.1371/journal.pone.0068872

Arevalo, H. J., Vadakkumpadan, F., Guallar, E., Jebb, A., Malamas, P., Wu, K. C., et al. (2016). Arrhythmia risk stratification of patients after myocardial infarction using personalized heart models. *Nat. Commun.* 7:11437. doi: 10.1038/ncomms11437

Ashikaga, H., Arevalo, H., Vadakkumpadan, F., Blake, R. C., Bayer, J. D., Nazarian, S., et al. (2013). Feasibility of image-based simulation to estimate ablation target in human ventricular arrhythmia. *Hear. Rhythm* 10, 1109–1116. doi: 10.1016/j.hrthm.2013.04.015

Ashikaga, H., Sasano, T., Dong, J., Zviman, M. M., Evers, R., Hopenfeld, B., et al. (2007). Magnetic resonance based anatomical analysis of scar-related ventricular tachycardia: implications for catheter ablation. *Circ. Res.* 101, 939–947. doi: 10.1161/CIRCRESAHA.107.158980

Baldinger, S. H., Stevenson, W. G., and John, R. M. (2016). Ablation of ischemic ventricular tachycardia: evidence, techniques, results, and future directions. *Curr. Opin. Cardiol.* 31, 29–36. doi: 10.1097/HCO.0000000000000237

Barber, F., Lozano, M., García-Fernández, I., and Sebastián, R. (2017). Inverse estimation of terminal connections in the cardiac conduction system. *Math. Methods Appl.* Sci. 41, 2340–2349. doi: 10.1002/mma.4280

Bayer, J. D., Blake, R. C., Plank, G., and Trayanova, N. A. (2012). A novel rule-based algorithm for assigning myocardial fiber orientation to computational heart models. *Ann. Biomed. Eng.* 40, 2243–2254. doi: 10.1007/s10439-012-0593-5

Ben-Haim, S. A., Osadchy, D., Scnuster, I., Gepstein, L., Hayam, G., and Josephson, M. E. (1996). Nonfluoroscopic, *in vivo* navigation and mapping technology. *Nat. Med.* 2, 1393–1395. doi: 10.1038/nm1296-1393

Berruezo, A., Fernandez-Armenta, J., Andreu, D., Penela, D., Herczku, C., Evertz, R., et al. (2015). Scar dechanneling: new method for scar-related left ventricular tachycardia substrate ablation. *Circ. Arrhythmia Electrophysiol.* 8, 326–336. doi: 10.1161/CIRCEP.114.002386

Besl, P. J., and McKay, N. D. (1992). A method for registration of 3-D shapes. *IEEE Trans. Pattern Anal. Mach. Intell.* 14, 239–256. doi: 10.1109/34.121791

Bishop, M. J., Hales, P., Plank, G., Gavaghan, D. J., Scheider, J., and Grau, V. (2009). "Comparison of rule-based and DTMRI-derived fibre architecture in a whole rat ventricular computational model," in *Functional Imaging and Modeling of the Heart-FIMH 2009, LNCS 5528*, eds N. Ayache, H. Delingette, and M. Sermesant (Nice; Berlin; Heidelberg: Springer), 87–96.

Bishop, M. J., Plank, G., Burton, R. A. B., Schneider, J. E., Gavaghan, D. J., Grau, V., et al. (2010). Development of an anatomically detailed MRI-derived rabbit ventricular model and assessment of its impact on simulations of electrophysiological function. *Am. J. Physiol. Heart Circ. Physiol.* 298, H699–H718. doi: 10.1152/ajpheart.00606.2009

Bogun, F., Desjardins, B., Crawford, T., Good, E., Jongnarangsin, K., Oral, H., et al. (2008). Post-infarction ventricular arrhythmias originating in papillary muscles. *J. Am. Coll. Cardiol.* 51, 1794–1802. doi: 10.1016/j.jacc.2008.01.046

Bogun, F., Krishnan, S., Siddiqui, M., Good, E., Marine, J. E., Schuger, C., et al. (2005). Electrogram characteristics in postinfarction ventricular tachycardia: effect of infarct age. *J. Am. Coll. Cardiol.* 46, 667–674. doi: 10.1016/j.jacc.2005.01.064

Bradley, C. P., Pullan, A. J., and Hunter, P. J. (2000). Effects of material properties and geometry on electrocardiographic forward simulations. *Ann. Biomed. Eng.* 28, 721–741. doi: 10.1114/1.1289467

Bressler, S. L., and Ding, M. (2006). "Event-related potentials," in *Wiley Encyclopedia of Biomedical Engineering*, ed M. Akay (Hoboken, NJ: John Wiley and Sons, Inc.), 1–8.

Brugada, J., Berruezo, A., Cuesta, A., Osca, J., Chueca, E., Fosch, X., et al. (2003). Nonsurgical transthoracic epicardial radiofrequency ablation. *J. Am. Coll. Cardiol.* 41, 2036–2043. doi: 10.1016/S0735-1097(03)00398-X

Caldwell, B. J., Trew, M. L., Sands, G. B., Hooks, D. A., LeGrice, I. J., and Smaill, B. H. (2009). Three distinct directions of intramural activation reveal nonuniform side-to-side electrical coupling of ventricular myocytes. *Circ. Arrhythmia Electrophysiol.* 2, 433–440. doi: 10.1161/CIRCEP.108.830133

Calkins, H., Kuck, K. H., Cappato, R., Brugada, J., Camm, A. J., Chen, S.-A., et al. (2012). 2012 HRS/EHRA/ECAS expert consensus statement on catheter and surgical ablation of atrial fibrillation: recommendations for patient selection, procedural techniques, patient management and follow-up, definitions, endpoints, and research trial design. *Europace* 14, 528–606. doi: 10.1093/europace/eus027

Camelliti, P., Devlin, G. P., Matthews, K. G., Kohl, P., and Green, C. R. (2004). Spatially and temporally distinct expression of fibroblast connexins after sheep ventricular infarction. *Cardiovasc. Res.* 62, 415–425. doi: 10.1016/j.cardiores.2004.01.027

Campos, F. O., Shiferaw, Y., Weber dos Santos, R., Plank, G., and Bishop, M. J. (2018). Microscopic isthmuses and fibrosis within the border zone of infarcted hearts promote calcium-mediated ectopy and conduction block. *Front. Phys.* 6, 1–14. doi: 10.3389/fphy.2018.00057

Chen, Z., Cabrera-Lozoya, R., Relan, J., Sohal, M., Shetty, A., Karim, R., et al. (2016). Biophysical modeling predicts ventricular tachycardia inducibility and circuit morphology: a combined clinical validation and computer modeling approach. *J. Cardiovasc. Electrophysiol.* 27, 851–860. doi: 10.1111/jce.12991

Chinchapatnam, P., Rhode, K. S., Ginks, M., Rinaldi, C. A., Lambiase, P., Razavi, R., et al. (2008). Model-based imaging of cardiac apparent conductivity and local conduction velocity for diagnosis and planning of therapy. *IEEE Trans. Med. Imaging* 27, 1631–1642. doi: 10.1109/TMI.2008.2004644

Ciaccio, E. J., Coromilas, J., Wit, A. L., Peters, N. S., and Garan, H. (2018). Source-sink mismatch causing functional conduction block in re-entrant ventricular tachycardia. *JACC Clin. Electrophysiol.* 4, 1–16. doi: 10.1016/j.jacep.2017.08.019

Cleutjens, J. P., Blankesteijn, W. M., Daemen, M. J., and Smits, J. F. (1999). The infarcted myocardium: simply dead tissue, or a lively target for therapeutic interventions. *Cardiovasc. Res.* 44, 232–241. doi: 10.1016/S0008-6363(99)00212-6

Connolly, A., Trew, M. L., Smaill, B. H., Plank, G., and Bishop, M. J. (2015). Local gradients in electrotonic loading modulate the local effective refractory period: implications for arrhythmogenesis in the infarct border zone. *IEEE Trans. Biomed. Eng.* 62, 2251–2259. doi: 10.1109/TBME.2015.2421296

Connolly, A. J., and Bishop, M. J. (2016). Computational representations of myocardial infarct scars and implications for arrhythmogenesis. *Clin. Med. Insights Cardiol.* 10:27. doi: 10.4137/CMC.S39708

Daskalopoulos, E. P., Janssen, B. J., and Blankesteijn, W. M. (2012). Myofibroblasts in the infarct area: concepts and challenges. *Microsc. Microanal.* 18, 35–49. doi: 10.1017/S143192761101227X

de Bakker, J. M., van Capelle, F. J., Janse, M. J., Tasseron, S., Vermeulen, J. T., de Jonge, N., et al. (1993). Slow conduction in the infarcted human heart. "Zigzag" course of activation. *Circulation* 88, 915–926. doi: 10.1161/01.CIR.88.3.915

de Bakker, J. M., van Capelle, F. J., Janse, M. J., Wilde, A. A., Coronel, R., Becker, A. E., et al. (1988). Reentry as a cause of ventricular tachycardia in patients with chronic ischemic heart disease: electrophysiologic and anatomic correlation. *Circulation* 77, 589–606. doi: 10.1161/01.CIR.77.3.589

de Bakker, J. M. T. (2017). Do myofibroblasts represent a hidden factor for impaired conduction and tachyarrhythmia in post-myocardial infarction? *JACC Clin. Electrophysiol.* 3, 715–717. doi: 10.1016/j.jacep.2017.01.007

de Bakker, J. M. T., Stein, M., and van Rijen, H. V. M. (2005). Three-dimensional anatomic structure as substrate for ventricular tachycardia/ventricular fibrillation. *Hear. Rhythm* 2, 777–779. doi: 10.1016/j.hrthm.2005.03.022

de Chillou, C., Lacroix, D., Klug, D., Magnin-Poull, I., Marquié, C., Messier, M., et al. (2002). Isthmus characteristics of reentrant ventricular tachycardia after myocardial infarction. *Circulation* 105, 726–731. doi: 10.1161/hc0602.103675

de Jong, S., van Veen, T., B., van Rijen, H. V. M., and de Bakker, J. M. T. (2011). Fibrosis and cardiac arrhythmias. *J. Cardiovasc. Pharmacol.* 57, 630–638. doi: 10.1097/FJC.0b013e318207a35f

Deng, D., Arevalo, H., Pashakhanloo, F., Prakosa, A., Ashikaga, H., McVeigh, E., et al. (2015). Accuracy of prediction of infarct-related arrhythmic circuits from image-based models reconstructed from low and high resolution MRI. *Front. Physiol.* 6:282. doi: 10.3389/fphys.2015.00282

Deng, D., Arevalo, H. J., Prakosa, A., Callans, D. J., and Trayanova, N. A. (2016). A feasibility study of arrhythmia risk prediction in patients with myocardial infarction and preserved ejection fraction. *Europace* 18, iv60–iv66. doi: 10.1093/europace/euw351

Dhanjal, T. S., Lellouche, N., von Ruhland, C. J., Abehsira, G., Edwards, D. H., Dubois-Randé, J.-L., et al. (2017). Massive accumulation of myofibroblasts in the critical isthmus is associated with ventricular tachycardia inducibility in post-infarct swine heart. *JACC Clin. Electrophysiol.* 3, 703–714. doi: 10.1016/j.jacep.2016.11.010

Doltra, A., Amundsen, B., Gebker, R., Fleck, E., and Kelle, S. (2013). Emerging concepts for myocardial late gadolinium enhancement MRI. *Curr. Cardiol. Rev.* 9, 185–190. doi: 10.2174/1573403X113099990030

Drouin, E., Charpentier, F., Gauthier, C., Laurent, K., and Le Marec, H. (1995). Electrophysiologic characteristics of cells spanning the left ventricular wall of human heart: Evidence for presence of M cells. *J. Am. Coll. Cardiol.* 26, 185–192. doi: 10.1016/0735-1097(95)00167-X

Dun, W., Baba, S., Yagi, T., and Boyden, P. A. (2004). Dynamic remodeling of K+ and Ca2+ currents in cells that survived in the epicardial border zone of canine healed infarcted heart. *AJP Hear. Circ. Physiol.* 287, H1046–H1054. doi: 10.1152/ajpheart.00082.2004

Durrer, D., Van Dam, R. T., Freud, G. E., Janse, M. J., Meijler, F. L., and Arzbaecher, R. C. (1970). Total excitation of the isolated human heart. *Circulation* 41, 899–912. doi: 10.1161/01.CIR.41.6.899

Fernández-Armenta, J., Berruezo, A., Andreu, D., Camara, O., Silva, E., Serra, L., et al. (2013). Three-dimensional architecture of scar and conducting channels

based on high resolution ce-CMR: insights for ventricular tachycardia ablation. *Circ. Arrhythmia Electrophysiol.* 6, 528–537. doi: 10.1161/CIRCEP.113.000264

Ferrer, A., Sebastián, R., Sánchez-Quintana, D., Rodríguez, J. F., Godoy, E. J., Martínez, L., et al. (2015). Detailed anatomical and electrophysiological models of human atria and torso for the simulation of atrial activation. *PLoS ONE* 10:e0141573. doi: 10.1371/journal.pone.0141573

Ferrer-Albero, A., Godoy, E. J., Lozano, M., Martínez-Mateu, L., Atienza, F., Saiz, J., et al. (2017). Non-invasive localization of atrial ectopic beats by using simulated body surface P-wave integral maps. *PLoS ONE* 12:e0181263. doi: 10.1371/journal.pone.0181263

Fieno, D. S., Kim, R. J., Chen, E., Lomasney, J. W., Klocke, F. J., and Judd, R. M. (2000). Contrast-enhanced magnetic resonance imaging of myocardium at risk: distinction between reversible and irreversible injury throughout infarct healing. *J. Am. Coll. Cardiol.* 36, 1985–1991. doi: 10.1016/S0735-1097(00)00958-X

Gabriel, S., Lau, R. W., and Gabriel, C. (1996). The dielectric properties of biological tissues: II. Measurements in the frequency range 10 Hz to 20 GHz. *Phys. Med. Biol.* 41, 2251–2269. doi: 10.1088/0031-9155/41/11/002

Gardner, P. I., Ursell, P. C., Fenoglio, J. J., and Wit, A. L. (1985). Electrophysiologic and anatomic basis for fractionated electrograms recorded from healed myocardial infarcts. *Circulation* 72, 596–611. doi: 10.1161/01.CIR.72.3.596

Gepstein, L., Hayam, G., and Ben-Haim, S. A. (1997). A novel method for nonfluoroscopic catheter-based electroanatomical mapping of the heart : *in vitro* and *in vivo* accuracy results. *Circulation* 95, 1611–1622. doi: 10.1161/01.CIR.95.6.1611

Gerstenfeld, E. P. (2013). Recurrent ventricular tachycardia after catheter ablation in post-infarct cardiomyopathy. *J. Am. Coll. Cardiol.* 61, 74–76. doi: 10.1016/j.jacc.2012.07.057

Geselowitz, D. B., and Miller, W. T. (1983). A bidomain model for anisotropic cardiac muscle. *Ann. Biomed. Eng.* 11, 191–206. doi: 10.1007/BF02363286

Gillette, K., Prassl, A., Bayer, J., Vigmond, E., Neic, A., and Plank, G. (2018). Automatic generation of bi-ventricular models of cardiac electrophysiology for patient specific personalization using non-invasive recordings. *Comput. Cardiol.* 45, 2–5. doi: 10.22489/CinC.2018.265

Gomez, J. F., Cardona, K., Martinez, L., Saiz, J., and Trenor, B. (2014). Electrophysiological and structural remodeling in heart failure modulate arrhythmogenesis. 2D simulation study. *PLoS ONE* 9:e103273. doi: 10.1371/journal.pone.0103273

Greenbaum, R. A., Ho, S. Y., Gibson, D. G., Becker, A. E., and Anderson, R. H. (1981). Left ventricular fibre architecture in man. *Heart* 45, 248–263. doi: 10.1136/hrt.45.3.248

Heidenreich, E. A., Ferrero, J. M., Doblaré, M., and Rodríguez, J. F. (2010). Adaptive macro finite elements for the numerical solution of monodomain equations in cardiac electrophysiology. *Ann. Biomed. Eng.* 38, 2331–2345. doi: 10.1007/s10439-010-9997-2

Hein, S., and Schaper, J. (2001). The extracellular matrix in normal and diseased myocardium. *J. Nucl. Cardiol.* 8, 188–196. doi: 10.1067/mnc.2001.113331

Hill, Y. R., Child, N., Hanson, B., Wallman, M., Coronel, R., Plank, G., et al. (2016). Investigating a novel activation-repolarisation time metric to predict localised Vulnerability to reentry using computational modelling. *PLoS ONE* 11:e0149342. doi: 10.1371/journal.pone.0149342

Holmes, A. A., Scollan, D. F., and Winslow, R. L. (2000). Direct histological validation of diffusion tensor MRI in formaldehyde-fixed myocardium. *Magn. Reson. Med.* 44, 157–161. doi: 10.1002/1522-2594(200007)44:1<157::AID-MRM22>3.0.CO;2-F

Hooks, D. A (2007). Myocardial segment-specific model generation for simulating the electrical action of the heart. *Biomed. Eng. Online* 6:21. doi: 10.1186/1475-925X-6-21

Hsu, E. W., Muzikant, A. L., Matulevicius, S. A., Penland, R. C., and Henriquez, C. S. (1998). Magnetic resonance myocardial fiber-orientation mapping with direct histological correlation. *AJP Hear. Circ. Physiol.* 274, H1627–H1634.

Hsu, L.-Y., Natanzon, A., Kellman, P., Hirsch, G. A., Aletras, A. H., and Arai, A. E. (2006). Quantitative myocardial infarction on delayed enhancement MRI. Part I: animal validation of an automated feature analysis and combined thresholding infarct sizing algorithm. *J. Magn. Reson. Imaging* 23, 298–308. doi: 10.1002/jmri.20496

Jacquemet, V. (2006). Pacemaker activity resulting from the coupling with nonexcitable cells. *Phys. Rev. E* 74:011908. doi: 10.1103/PhysRevE.74.011908

Jamiel, A., Ebid, M., Ahmed, A. M., Ahmed, D., and Al-Mallah, M. H. (2017). The role of myocardial viability in contemporary cardiac practice. *Heart Fail. Rev.* 22, 401–413. doi: 10.1007/s10741-017-9626-3

Jiang, M., Cabo, C., Yao, J.-A., Boyden, P. A., and Tseng, G.-N. (2000). Delayed rectifier K currents have reduced amplitudes and altered kinetics in myocytes from infarcted canine ventricle. *Cardiovasc. Res.* 48, 34–43. doi: 10.1016/S0008-6363(00)00159-0

Johnston, B., Barnes, J., and Johnston, P. (2016). "The effect of conductivity values on activation times and defibrillation thresholds," in *2016 Computing in Cardiology Conference (CinC)* (Vancouver, BC), 10–13.

Johnston, B. M., Coveney, S., Chang, E. T. Y., Johnston, P. R., and Clayton, R. H. (2018). Quantifying the effect of uncertainty in input parameters in a simplified bidomain model of partial thickness ischaemia. *Med. Biol. Eng. Comput.* 56, 761–780. doi: 10.1007/s11517-017-1714-y

Karim, R., Bhagirath, P., Claus, P., James Housden, R., Chen, Z., Karimaghaloo, Z., et al. (2016). Evaluation of state-of-the-art segmentation algorithms for left ventricle infarct from late Gadolinium enhancement MR images. *Med. Image Anal.* 30, 95–107. doi: 10.1016/j.media.2016.01.004

Keller, D. U. J., Weber, F. M., Seemann, G., and Dössel, O. (2010). Ranking the influence of tissue conductivities on forward-calculated ECGs. *IEEE Trans. Biomed. Eng.* 57, 1568–1576. doi: 10.1109/TBME.2010.2046485

Kim, R. J., Fieno, D. S., Parrish, T. B., Harris, K., Chen, E. L., Simonetti, O., et al. (1999a). Relationship of MRI delayed contrast enhancement to irreversible injury, infarct age, and contractile function. *Circulation* 100, 1992–2002. doi: 10.1161/01.CIR.100.19.1992

Kim, Y.-H., Xie, F., Yashima, M., Wu, T.-J., Valderrabano, M., Lee, M.-H., et al. (1999b). Role of papillary muscle in the generation and maintenance of reentry during ventricular tachycardia and fibrillation in isolated swine right ventricle. *Circulation* 100, 1450–1459. doi: 10.1161/01.CIR.100.13.1450

Klepfer, R. N., Johnson, C. R., and Macleod, R. S. (1997). The effects of inhomogeneities and anisotropies on electrocardiographic fields: a 3-D finite-element study. *IEEE Trans. Biomed. Eng.* 44, 706–719. doi: 10.1109/10.605427

Kohl, P., and Gourdie, R. G. (2014). Fibroblast–myocyte electrotonic coupling: does it occur in native cardiac tissue? *J. Mol. Cell. Cardiol.* 70, 37–46. doi: 10.1016/j.yjmcc.2013.12.024

Kolipaka, A., Chatzimavroudis, G. P., White, R. D., O'Donnell, T. P., and Setser, R. M. (2005). Segmentation of non-viable myocardium in delayed enhancement magnetic resonance images. *Int. J. Cardiovasc. Imaging* 21, 303–311. doi: 10.1007/s10554-004-5806-z

Krueger, M. W., Schulze, W. H. W., Rhode, K. S., Razavi, R., Seemann, G., and Dössel, O. (2013). Towards personalized clinical *in-silico* modeling of atrial anatomy and electrophysiology. *Med. Biol. Eng. Comput.* 51, 1251–1260. doi: 10.1007/s11517-012-0970-0

Lazzara, R., and Scherlag, B. J. (1984). Electrophysiologic basis for arrhythmias in ischemic heart disease. *Am. J. Cardiol.* 53, B1–B7. doi: 10.1016/0002-9149(84)90493-4

Lopez-Perez, A., Sebastian, R., and Ferrero, J. M. (2015). Three-dimensional cardiac computational modelling: methods, features and applications. *Biomed. Eng. Online* 14:35. doi: 10.1186/s12938-015-0033-5

MacCannell, K. A., Bazzazi, H., Chilton, L., Shibukawa, Y., Clark, R. B., and Giles, W. R. (2007). A mathematical model of electrotonic interactions between ventricular myocytes and fibroblasts. *Biophys. J.* 92, 4121–4132. doi: 10.1529/biophysj.106.101410

MacLeod, R. S., Johnson, C. R., and Ershler, P. R. (1991). "Construction of an inhomogeneous model of the human torso for use in computational electrocardiography," in *Proceedings of the Annual Conference on Engineering in Medicine and Biology* (Publ by IEEE), 688–689. doi: 10.1109/IEMBS.1991.684145

Mahoney, V. M., Mezzano, V., and Morley, G. E. (2016). A review of the literature on cardiac electrical activity between fibroblasts and myocytes. *Prog. Biophys. Mol. Biol.* 120, 128–133. doi: 10.1016/j.pbiomolbio.2015.12.006

Mantziari, L., Butcher, C., Kontogeorgis, A., Panikker, S., Roy, K., Markides, V., et al. (2015). Utility of a novel rapid high-resolution mapping system in the catheter ablation of arrhythmias. *JACC Clin. Electrophysiol.* 1, 411–420. doi: 10.1016/j.jacep.2015.06.002

Marchlinski, F. E., Callans, D. J., Gottlieb, C. D., and Zado, E. (2000). Linear ablation lesions for control of unmappable ventricular tachycardia in patients

with ischemic and nonischemic cardiomyopathy. *Circulation* 101, 1288–1296. doi: 10.1161/01.CIR.101.11.1288

Martinez-Mateu, L., Romero, L., Ferrer-Albero, A., Sebastian, R., Rodríguez Matas, J. F., Jalife, J., et al. (2018). Factors affecting basket catheter detection of real and phantom rotors in the atria: a computational study. *PLOS Comput. Biol.* 14:e1006017. doi: 10.1371/journal.pcbi.1006017

Matsushita, T., Oyamada, M., Fujimoto, K., Yasuda, Y., Masuda, S., Wada, Y., et al. (1999). Remodeling of cell-cell and cell-extracellular matrix interactions at the border zone of rat myocardial infarcts. *Circ. Res.* 85, 1046–1055. doi: 10.1161/01.RES.85.11.1046

McDowell, K. S., Arevalo, H. J., Maleckar, M. M., and Trayanova, N. A. (2011). Susceptibility to arrhythmia in the infarcted heart depends on myofibroblast density. *Biophys. J.* 101, 1307–1315. doi: 10.1016/j.bpj.2011.08.009

Mendonca Costa, C., Plank, G., Rinaldi, C. A., Niederer, S. A., and Bishop, M. J. (2018). Modeling the electrophysiological properties of the infarct border zone. *Front. Physiol.* 9:356. doi: 10.3389/fphys.2018.00356

Mewton, N., Liu, C. Y., Croisille, P., Bluemke, D., and Lima, J. A. C. (2011). Assessment of myocardial fibrosis with cardiovascular magnetic resonance. *J. Am. Coll. Cardiol.* 57, 891–903. doi: 10.1016/j.jacc.2010.11.013

Miragoli, M., Gaudesius, G., and Rohr, S. (2006). Electrotonic modulation of cardiac impulse conduction by myofibroblasts. *Circ. Res.* 98, 801–810. doi: 10.1161/01.RES.0000214537.44195.a3

Moon, J. C., Reed, E., Sheppard, M. N., Elkington, A. G., Ho, S., Burke, M., et al. (2004). The histologic basis of late gadolinium enhancement cardiovascular magnetic resonance in hypertrophic cardiomyopathy. *J. Am. Coll. Cardiol.* 43, 2260–2264. doi: 10.1016/j.jacc.2004.03.035

Nguyen, T. P., Qu, Z., and Weiss, J. N. (2014). Cardiac fibrosis and arrhythmogenesis: the road to repair is paved with perils. *J. Mol. Cell. Cardiol.* 70, 83–91. doi: 10.1016/j.yjmcc.2013.10.018

Nowbar, A. N., Howard, J. P., Finegold, J. A., Asaria, P., and Francis, D. P. (2014). 2014 Global geographic analysis of mortality from ischaemic heart disease by country, age and income: Statistics from World Health Organisation and United Nations. *Int. J. Cardiol.* 174, 293–298. doi: 10.1016/j.ijcard.2014.04.096

Okada, J., Washio, T., Maehara, A., Momomura, S., Sugiura, S., and Hisada, T. (2011). Transmural and apicobasal gradients in repolarization contribute to T-wave genesis in human surface ECG. *Am. J. Physiol. Circ. Physiol.* 301, H200–H208. doi: 10.1152/ajpheart.01241.2010

Ongstad, E., and Kohl, P. (2016). Fibroblast–myocyte coupling in the heart: potential relevance for therapeutic interventions. *J. Mol. Cell. Cardiol.* 91, 238–246. doi: 10.1016/j.yjmcc.2016.01.010

Ortiz-Pérez, J. T., Rodríguez, J., Meyers, S. N., Lee, D. C., Davidson, C., and Wu, E. (2008). Correspondence between the 17-segment model and coronary arterial anatomy using contrast-enhanced cardiac magnetic resonance imaging. *JACC Cardiovasc. Imaging* 1, 282–293. doi: 10.1016/j.jcmg.2008.01.014

Palamara, S., Vergara, C., Faggiano, E., and Nobile, F. (2015). An effective algorithm for the generation of patient-specific Purkinje networks in computational electrocardiology. *J. Comput. Phys.* 283, 495–517. doi: 10.1016/j.jcp.2014.11.043

Pashakhanloo, F., Herzka, D. A., Mori, S., Zviman, M., Halperin, H., Gai, N., et al. (2017). Submillimeter diffusion tensor imaging and late gadolinium enhancement cardiovascular magnetic resonance of chronic myocardial infarction. *J. Cardiovasc. Magn. Reson.* 19:9. doi: 10.1186/s12968-016-0317-3

Patel, H., Mazur, W., Williams, K. A., and Kalra, D. K. (2017). Myocardial viability–State of the art: is it still relevant and how to best assess it with imaging? *Trends Cardiovasc. Med.* 28, 24–37. doi: 10.1016/j.tcm.2017.07.001

Paul, T., Moak, J. P., Morris, C., and Garson, A. (1990). Epicardial mapping: how to measure local activation? *Pacing Clin. Electrophysiol.* 13, 285–292. doi: 10.1111/j.1540-8159.1990.tb02042.x

Pedersen, C. T., Kay, G. N., Kalman, J., Borggrefe, M., Della-Bella, P., Dickfeld, T., et al. (2014). EHRA/HRS/APHRS expert consensus on ventricular arrhythmias. *Hear. Rhythm* 11, e166–e196. doi: 10.1016/j.hrthm.2014.07.024

Perez-David, E., Arenal, Á., Rubio-Guivernau, J. L., del Castillo, R., Atea, L., Arbelo, E., et al. (2011). Noninvasive identification of ventricular tachycardia-related conducting channels using contrast-enhanced magnetic resonance imaging in patients with chronic myocardial infarction. *J. Am. Coll. Cardiol.* 57, 184–194. doi: 10.1016/j.jacc.2010.07.043

Perotti, L. E., Krishnamoorthi, S., Borgstrom, N. P., Ennis, D. B., and Klug, W. S. (2015). Regional segmentation of ventricular models to achieve repolarization dispersion in cardiac electrophysiology modeling. *Int. J. Numer. Method. Biomed. Eng.* 31:e02718. doi: 10.1002/cnm.2718

Pokorney, S. D., Friedman, D. J., Calkins, H., Callans, D. J., Daoud, E. G., Della-Bella, P., et al. (2016). Catheter ablation of ventricular tachycardia: lessons learned from past clinical trials and implications for future clinical trials. *Hear. Rhythm* 13, 1748–1754. doi: 10.1016/j.hrthm.2016.04.001

Prakosa, A., Arevalo, H. J., Deng, D., Boyle, P. M., Nikolov, P. P., Ashikaga, H., et al. (2018). Personalized virtual-heart technology for guiding the ablation of infarct-related ventricular tachycardia. *Nat. Biomed. Eng.* 2, 732–740. doi: 10.1038/s41551-018-0282-2

Prassl, A. J., Kickinger, F., Ahammer, H., Grau, V., Schneider, J. E., Hofer, E., et al. (2009). Automatically generated, anatomically accurate meshes for cardiac electrophysiology problems. *IEEE Trans. Biomed. Eng.* 56, 1318–1330. doi: 10.1109/TBME.2009.2014243

Priori, S. G., Blomström-Lundqvist, C., Mazzanti, A., Blom, N., Borggrefe, M., Camm, J., et al. (2015). 2015 ESC Guidelines for the management of patients with ventricular arrhythmias and the prevention of sudden cardiac death. *Eur. Heart J.* 36, 2793–2867. doi: 10.1093/eurheartj/ehv316

Pu, J., and Boyden, P. A. (1997). Alterations of Na+ currents in myocytes from epicardial border zone of the infarcted heart : a possible ionic mechanism for reduced excitability and postrepolarization refractoriness. *Circ. Res.* 81, 110–119. doi: 10.1161/01.RES.81.1.110

Quinn, T. A., Camelliti, P., Rog-Zielinska, E. A., Siedlecka, U., Poggioli, T., O'Toole, E. T., et al. (2016). Electrotonic coupling of excitable and nonexcitable cells in the heart revealed by optogenetics. *Proc. Natl. Acad. Sci. U S A.* 113, 14852–14857. doi: 10.1073/pnas.1611184114

Rantner, L. J., Arevalo, H. J., Constantino, J. L., Efimov, I. R., Plank, G., and Trayanova, N. A. (2012). Three-dimensional mechanisms of increased vulnerability to electric shocks in myocardial infarction: altered virtual electrode polarizations and conduction delay in the peri-infarct zone. *J. Physiol.* 590, 4537–4551. doi: 10.1113/jphysiol.2012.229088

Relan, J., Chinchapatnam, P., Sermesant, M., Rhode, K., Ginks, M., Delingette, H., et al. (2011). Coupled personalization of cardiac electrophysiology models for prediction of ischaemic ventricular tachycardia. *Interface Focus* 1, 396–407. doi: 10.1098/rsfs.2010.0041

Ringenberg, J., Deo, M., Filgueiras-Rama, D., Pizarro, G., Ibañez, B., Peinado, R., et al. (2014). Effects of fibrosis morphology on reentrant ventricular tachycardia inducibility and simulation fidelity in patient-derived models. *Clin. Med. Insights. Cardiol.* 8, 1–13. doi: 10.4137/CMC.S15712

Rog-Zielinska, E. A., Norris, R. A., Kohl, P., and Markwald, R. (2016). The living scar – cardiac fibroblasts and the injured heart. *Trends Mol. Med.* 22, 99–114. doi: 10.1016/j.molmed.2015.12.006

Rohr, S. (2012). Arrhythmogenic implications of fibroblast-myocyte interactions. *Circ. Arrhythmia Electrophysiol.* 5, 442–452. doi: 10.1161/CIRCEP.110.957647

Roney, C. H., Bayer, J. D., Zahid, S., Meo, M., Boyle, P. M. J., Trayanova, N. A., et al. (2016). Modelling methodology of atrial fibrosis affects rotor dynamics and electrograms. *Europace* 18, 146–155. doi: 10.1093/europace/euw365

Roth, B. J. (1988). The electrical potential produced by a strand of cardiac muscle: a bidomain analysis. *Ann. Biomed. Eng.* 16, 609–637. doi: 10.1007/BF02368018

Rutherford, S. L., Trew, M. L., Sands, G. B., LeGrice, I. J., and Smaill, B. H. (2012). High-resolution 3-dimensional reconstruction of the infarct border zone: impact of structural remodeling on electrical activation. *Circ. Res.* 111, 301–311. doi: 10.1161/CIRCRESAHA.111.260943

Schaper, W., Görge, G., Winkler, B., and Schaper, J. (1988). The collateral circulation of the heart. *Prog. Cardiovasc. Dis.* 31, 57–77. doi: 10.1016/0033-0620(88)90011-4

Schuleri, K. H., Centola, M., George, R. T., Amado, L. C., Evers, K. S., Kitagawa, K., et al. (2009). Characterization of peri-infarct zone heterogeneity by contrast-enhanced multidetector computed tomography. *J. Am. Coll. Cardiol.* 53, 1699–1707. doi: 10.1016/j.jacc.2009.01.056

Schwab, B. C., Seemann, G., Lasher, R. A., Torres, N. S., Wulfers, E. M., Arp, M., et al. (2013). Quantitative analysis of cardiac tissue including fibroblasts using three-dimensional confocal microscopy and image reconstruction: towards a basis for electrophysiological modeling. *IEEE Trans. Med. Imaging* 32, 862–872. doi: 10.1109/TMI.2013.2240693

Scollan, D. F., Holmes, A., Winslow, R., and Forder, J. (1998). Histological validation of myocardial microstructure obtained from diffusion tensor magnetic resonance imaging. *AJP Hear. Circ. Physiol.* 275, H2308–H2318.

Sebastian, R., Zimmerman, V., Sukno, F., Bijnens, B. B., and Frangi, A. F. (2009). "Cardiac modelling for pathophysiology research and clinical applications. the need for an automated pipeline," in *World Congress on Medical Physics and Biomedical Engineering 2009*, eds O. Dössel and W. C. Schlegel (Berlin; Heidelberg: Springer-Verlag), 2207–2210.

Seg3D, C. (2013). *Volumetric Image Segmentation and Visualization*. Scientific Computing and Imaging Institute.

Seidel, T., Edelmann, J.-C., and Sachse, F. B. (2016). Analyzing remodeling of cardiac tissue: a comprehensive approach based on confocal microscopy and 3D reconstructions. *Ann. Biomed. Eng.* 44, 1436–1448. doi: 10.1007/s10439-015-1465-6

Severs, N. J., Bruce, A. F., Dupont, E., and Rothery, S. (2008). Remodelling of gap junctions and connexin expression in diseased myocardium. *Cardiovasc. Res.* 80, 9–19. doi: 10.1093/cvr/cvn133

Si, H., and Gärtner, K. (2005). "Meshing piecewise linear complexes by constrained delaunay tetrahedralizations," in *Proceedings of the 14th International Meshing Roundtable*, ed B. W. Hanks (Berlin; Heidelberg: Springer-Verlag), 147–163.

Sicouri, S., and Antzelevitch, C. (1991). A subpopulation of cells with unique electrophysiological properties in the deep subepicardium of the canine ventricle. *The M Cell. Circ. Res.* 68, 1729–1741. doi: 10.1161/01.RES.68.6.1729

Sicouri, S., Fish, J., and Antzelevitch, C. (1994). Distribution of M cells in the canine ventricle. *J. Cardiovasc. Electrophysiol.* 5, 824–837. doi: 10.1111/j.1540-8167.1994.tb01121.x

Smith, J. H., Green, C. R., Peters, N. S., Rothery, S., and Severs, N. J. (1991). Altered patterns of gap junction distribution in ischemic heart disease. An immunohistochemical study of human myocardium using laser scanning confocal microscopy. *Am. J. Pathol.* 139, 801–21.

Smith, N., de Vecchi, A., McCormick, M., Nordsletten, D., Camara, O., Frangi, A. F., et al. (2011). euHeart: personalized and integrated cardiac care using patient-specific cardiovascular modelling. *Interface Focus* 1, 349–364. doi: 10.1098/rsfs.2010.0048

Soejima, K., Stevenson, W. G., Maisel, W. H., Sapp, J. L., and Epstein, L. M. (2002). Electrically unexcitable scar mapping based on pacing threshold for identification of the reentry circuit isthmus: feasibility for guiding ventricular tachycardia ablation. *Circulation* 106, 1678–1683. doi: 10.1161/01.CIR.0000030187.39852.A7

Sosa, E., and Scanavacca, M. (2005). Epicardial mapping and ablation techniques to control ventricular tachycardia. *J. Cardiovasc. Electrophysiol.* 16, 449–452. doi: 10.1046/j.1540-8167.2005.40710.x

Sosa, E., Scanavacca, M., D'Avila, A., Oliveira, F., and Ramires, J. A. F. (2000). Nonsurgical transthoracic epicardial catheter ablation to treat recurrent ventricular tachycardia occurring late after myocardial infarction. *J. Am. Coll. Cardiol.* 35, 1442–1449. doi: 10.1016/S0735-1097(00)00606-9

Sosa, E., Scanavacca, M., D'Avila, A., and Pilleggi, F. (1996). A new technique to perform epicardial mapping in the electrophysiology laboratory. *J. Cardiovasc. Electrophysiol.* 7, 531–536. doi: 10.1111/j.1540-8167.1996.tb00559.x

Soto-Iglesias, D., Butakoff, C., Andreu, D., Fernández-Armenta, J., Berruezo, A., and Camara, O. (2016). Integration of electro-anatomical and imaging data of the left ventricle: an evaluation framework. *Med. Image Anal.* 32, 131–144. doi: 10.1016/j.media.2016.03.010

Spach, M. S., and Boineau, J. P. (1997). Microfibrosis produces electrical load variations due to loss of side-to-side cell connections: a major mechanism of structural heart disease arrhythmias. *Pacing Clin. Electrophysiol.* 20, 397–413. doi: 10.1111/j.1540-8159.1997.tb06199.x

Spach, M. S., Miller, W. T., Miller-Jones, E., Warren, R. B., and Barr, R. C. (1979). Extracellular potentials related to intracellular action potentials during impulse conduction in anisotropic canine cardiac muscle. *Circ. Res.* 45, 188–204. doi: 10.1161/01.RES.45.2.188

Stevenson, W. G., Khan, H., Sager, P., Saxon, L. A., Middlekauff, H. R., Natterson, P. D., et al. (1993). Identification of reentry circuit sites during catheter mapping and radiofrequency ablation of ventricular tachycardia late after myocardial infarction. *Circulation* 88, 1647–1670. doi: 10.1161/01.CIR.88.4.1647

Stevenson, W. G., and Soejima, K. (2005). Recording techniques for clinical electrophysiology. *J. Cardiovasc. Electrophysiol.* 16, 1017–1022. doi: 10.1111/j.1540-8167.2005.50155.x

Streeter, D. D., Spotnitz, H. M., Patel, D. P., Ross, J., and Sonnenblick, E. H. (1969). Fiber orientation in the canine left ventricle during diastole and systole. *Circ. Res.* 24, 339–347. doi: 10.1161/01.RES.24.3.339

Sun, Y., Kiani, M. F., Postlethwaite, A. E., and Weber, K. T. (2002). Infarct scar as living tissue. *Basic Res. Cardiol.* 97, 343–347. doi: 10.1007/s00395-002-0365-8

Taggart, P., Sutton, P. M., Opthof, T., Coronel, R., Trimlett, R., Pugsley, W., et al. (2000). Inhomogeneous transmural conduction during early ischaemia in patients with coronary artery disease. *J. Mol. Cell. Cardiol.* 32, 621–630. doi: 10.1006/jmcc.2000.1105

Tedrow, U., and Stevenson, W. G. (2009). Strategies for epicardial mapping and ablation of ventricular tachycardia. *J. Cardiovasc. Electrophysiol.* 20, 710–713. doi: 10.1111/j.1540-8167.2008.01427.x

ten Tusscher, K., and Panfilov, A. (2006). Alternans and spiral breakup in a human ventricular tissue model. *AJP Hear. Circ. Physiol.* 291, H1088–H1100. doi: 10.1152/ajpheart.00109.2006

Trayanova, N. a., and Boyle, P. M. (2013). Advances in modeling ventricular arrhythmias: from mechanisms to the clinic. *Wiley Interdiscip. Rev. Syst. Biol. Med.* 6, 209–224. doi: 10.1002/wsbm.1256

Trayanova, N. A., Boyle, P. M., Arevalo, H. J., and Zahid, S. (2014). Exploring susceptibility to atrial and ventricular arrhythmias resulting from remodeling of the passive electrical properties in the heart: a simulation approach. *Front. Physiol.* 5, 1–12. doi: 10.3389/fphys.2014.00435.

Trayanova, N. A., O'Hara, T., Bayer, J. D., Boyle, P. M., McDowell, K. S., Constantino, J., et al. (2012). Computational cardiology: how computer simulations could be used to develop new therapies and advance existing ones. *Europace* 14, v82–v89. doi: 10.1093/europace/eus277

Trayanova, N. A., Pashakhanloo, F., Wu, K. C., and Halperin, H. R. (2017). Imaging-Based Simulations for Predicting Sudden Death and Guiding Ventricular Tachycardia Ablation. *Circ. Arrhythmia Electrophysiol.* 10:435. doi: 10.1161/CIRCEP.117.004743

Tschabrunn, C. M., Roujol, S., Nezafat, R., Faulkner-Jones, B., Buxton, A. E., Josephson, M. E., et al. (2016). A swine model of infarct-related reentrant ventricular tachycardia: electroanatomic, magnetic resonance, and histopathological characterization. *Hear. Rhythm* 13, 262–273. doi: 10.1016/j.hrthm.2015.07.030

Ukwatta, E., Arevalo, H., Li, K., Yuan, J., Qiu, W., Malamas, P., et al. (2016). Myocardial infarct segmentation from magnetic resonance images for personalized modeling of cardiac electrophysiology. *IEEE Trans. Med. Imaging* 35, 1408–1419. doi: 10.1109/TMI.2015.2512711

Ursell, P. C., Gardner, P. I., Albala, A., Fenoglio, J. J., and Wit, a L. (1985). Structural and electrophysiological changes in the epicardial border zone of canine myocardial infarcts during infarct healing. *Circ. Res.* 56, 436–451. doi: 10.1161/01.RES.56.3.436

van den Borne, S. W. M., Diez, J., Blankesteijn, W. M., Verjans, J., Hofstra, L., and Narula, J. (2010). Myocardial remodeling after infarction: the role of myofibroblasts. *Nat. Rev. Cardiol.* 7, 30–37. doi: 10.1038/nrcardio.2009.199

Varga-Szemes, A., van der Geest, R. J., Schoepf, U. J., De Cecco, C. N., Tesche, C., Fuller, S. R., et al. (2016). MRI post-processing methods for myocardial infarct quantification. *Curr. Radiol. Rep.* 4:30. doi: 10.1007/s40134-016-0159-7

Vergara, C., Palamara, S., Catanzariti, D., Nobile, F., Faggiano, E., Pangrazzi, C., et al. (2014). Patient-specific generation of the Purkinje network driven by clinical measurements of a normal propagation. *Med. Biol. Eng. Comput.* 52, 813–826. doi: 10.1007/s11517-014-1183-5

Vigmond, E., Vadakkumpadan, F., Gurev, V., Arevalo, H., Deo, M., Plank, G., et al. (2009). Towards predictive modelling of the electrophysiology of the heart. *Exp. Physiol.* 94, 563–577. doi: 10.1113/expphysiol.2008.044073

Wagner, A., Mahrholdt, H., Holly, T. A., Elliott, M. D., Regenfus, M., Parker, M., et al. (2003). Contrast-enhanced MRI and routine single photon emission computed tomography (SPECT) perfusion imaging for detection of subendocardial myocardial infarcts: an imaging study. *Lancet* 361, 374–379. doi: 10.1016/S0140-6736(03)12389-6

Walton, R. D., Pashaei, A., Martinez, M. E., Constantin, M., Duchateau, J., Bear, L., et al. (2018). Compartmentalized structure of the moderator band provides a unique substrate for macroreentrant ventricular tachycardia. *Circ. Arrhythmia Electrophysiol.* 11:e005913. doi: 10.1161/CIRCEP.117.005913

Wijnmaalen, A. P., van der Geest, R. J., van Huls van Taxis, C. F. B., Siebelink, H.-M. J., Kroft, L. J. M., Bax, J. J., et al. (2011). Head-to-head comparison of contrast-enhanced magnetic resonance imaging and electroanatomical voltage

mapping to assess post-infarct scar characteristics in patients with ventricular tachycardias: real-time image integration and reversed registration. *Eur. Heart J.* 32, 104–114. doi: 10.1093/eurheartj/ehq345

Wilber, D. J. (2008). Catheter ablation of ventricular tachycardia: two decades of progress. *Hear. Rhythm* 5, S59–S63. doi: 10.1016/j.hrthm.2008.02.001

Winklhofer, S., Stoeck, C. T., Berger, N., Thali, M., Manka, R., Kozerke, S., et al. (2014). Post-mortem cardiac diffusion tensor imaging: detection of myocardial infarction and remodeling of myofiber architecture. *Eur. Radiol.* 24, 2810–2818. doi: 10.1007/s00330-014-3322-7

Wu, M.-T., Tseng, W.-Y. I., Su, M.-Y. M., Liu, C.-P., Chiou, K.-R., Wedeen, V. J., et al. (2006). Diffusion tensor magnetic resonance imaging mapping the fiber architecture remodeling in human myocardium after infarction: correlation with viability and wall motion. *Circulation* 114, 1036–1045. doi: 10.1161/CIRCULATIONAHA.105.545863

Xie, Y., Garfinkel, A., Camelliti, P., Kohl, P., Weiss, J. N., and Qu, Z. (2009). Effects of fibroblast-myocyte coupling on cardiac conduction and vulnerability to reentry: a computational study. *Hear. Rhythm* 6, 1641–1649. doi: 10.1016/j.hrthm.2009.08.003

Yamada, T. (2014). Catheter ablation of epicardial ventricular tachycardia. *J. Arrhythmia* 30, 262–271. doi: 10.1016/j.joa.2014.04.011

Yamashita, S., Sacher, F., Mahida, S., Berte, B., Lim, H. S., Komatsu, Y., et al. (2016). Image integration to guide catheter ablation in scar-related ventricular tachycardia. *J. Cardiovasc. Electrophysiol.* 27, 699–708. doi: 10.1111/jce.12963

Yan, A. T. (2006). Characterization of the peri-infarct zone by contrast-enhanced cardiac magnetic resonance imaging is a powerful predictor of post-myocardial infarction mortality. *Circulation* 114, 32–39. doi: 10.1161/CIRCULATIONAHA.106.613414

Yan, G.-X., Shimizu, W., and Antzelevitch, C. (1998). Characteristics and distribution of M cells in arterially perfused canine left ventricular wedge preparations. *Circulation* 98, 1921–1927. doi: 10.1161/01.CIR.98.18.1921

Yao, J.-A., Hussain, W., Patel, P., Peters, N. S., Boyden, P. A., and Wit, A. L. (2003). Remodeling of gap junctional channel function in epicardial border zone of healing canine infarcts. *Circ. Res.* 92, 437–443. doi: 10.1161/01.RES.0000059301.81035.06

Yokokawa, M., Desjardins, B., Crawford, T., Good, E., Morady, F., and Bogun, F. (2013). Reasons for recurrent ventricular tachycardia after catheter ablation of post-infarction ventricular tachycardia. *J. Am. Coll. Cardiol.* 61, 66–73. doi: 10.1016/j.jacc.2012.07.059

Zeigler, A. C., Richardson, W. J., Holmes, J. W., and Saucerman, J. J. (2016). Computational modeling of cardiac fibroblasts and fibrosis. *J. Mol. Cell. Cardiol.* 93, 73–83. doi: 10.1016/j.yjmcc.2015.11.020

Conflict of Interest Statement: The authors declare that the research was conducted in the absence of any commercial or financial relationships that could be construed as a potential conflict of interest.

NOMENCLATURE

2D	Two-dimensional
3D	Three-dimensional
AP	Action potential
APD	Action potential duration
BCL	Basic cycle length
SCC	Slow conducting channel
DE-MRI	Delayed enhancement-MRI
EAM	Electroanatomical map/mapping
ECG	Electrocardiogram
EGM	Electrogram
FEM	Finite-element method
LAT	Local activation time
LV	Left ventricle
MI	Myocardial infarction
RFA	Radiofrequency ablation
RV	Right ventricle
SD	Standard deviation
VT	Ventricular tachycardia
DTI	Diffusion tensor imaging
EP	Electrophysiology/electrophysiological

frontiers in Physiology

ORIGINAL RESEARCH
published: 24 May 2019
doi: 10.3389/fphys.2019.00628

Sensitivity of Ablation Targets Prediction to Electrophysiological Parameter Variability in Image-Based Computational Models of Ventricular Tachycardia in Post-infarction Patients

*Dongdong Deng[1,2], Adityo Prakosa[1], Julie Shade[1], Plamen Nikolov[1] and Natalia A. Trayanova[1]**

[1] Department of Biomedical Engineering, Johns Hopkins University, Baltimore, MD, United States, [2] School of Biomedical Engineering, Dalian University of Technology, Dalian, China

OPEN ACCESS

Edited by:
Olaf Doessel,
Karlsruhe Institute of Technology (KIT), Germany

Reviewed by:
Axel Loewe,
Karlsruhe Institute of Technology (KIT), Germany
Edward Joseph Vigmond,
Université de Bordeaux, France

***Correspondence:**
Natalia A. Trayanova
ntrayanova@jhu.edu

Specialty section:
This article was submitted to Computational Physiology and Medicine, a section of the journal Frontiers in Physiology

Received: 19 December 2018
Accepted: 03 May 2019
Published: 24 May 2019

Citation:
Deng D, Prakosa A, Shade J, Nikolov P and Trayanova NA (2019) Sensitivity of Ablation Targets Prediction to Electrophysiological Parameter Variability in Image-Based Computational Models of Ventricular Tachycardia in Post-infarction Patients. Front. Physiol. 10:628. doi: 10.3389/fphys.2019.00628

Ventricular tachycardia (VT), which could lead to sudden cardiac death, occurs frequently in patients with myocardial infarction. Computational modeling has emerged as a powerful platform for the non-invasive investigation of lethal heart rhythm disorders in post-infarction patients and for guiding patient VT ablation. However, it remains unclear how VT dynamics and predicted ablation targets are influenced by inter-patient variability in action potential duration (APD) and conduction velocity (CV). The goal of this study was to systematically assess the effect of changes in the electrophysiological parameters on the induced VTs and predicted ablation targets in personalized models of post-infarction hearts. Simulations were conducted in 5 patient-specific left ventricular models reconstructed from late gadolinium-enhanced magnetic resonance imaging scans. We comprehensively characterized all possible pre-ablation and post-ablation VTs in simulations conducted with either an "average human VT"-based electrophysiological representation (i.e., EP_{avg}) or with ±10% APD or CV (i.e., EP_{var}); additional simulations were also executed in some models for an extended range of these parameters. The results showed that: (1) a subset of reentries (76.2–100%, depending on EP parameter set) conducted with ±10% APD/CV was observed in approximately the same locations as reentries observed in EP_{avg} cases; (2) emergent VTs could be induced sometimes after ablation in EP_{avg} models, and these emergent VTs often corresponded to the pre-ablation reentries in simulations with EP_{var} parameter sets. These findings demonstrate that the VT ablation target uncertainty in patient-specific ventricular models with an average representation of VT-remodeled electrophysiology is relatively low and the ablation targets stable, as the localization of the induced VTs was primarily driven by the remodeled structural substrate. Thus, personalized ventricular modeling with an average representation of infarct-remodeled electrophysiology may uncover most targets for VT ablation.

Keywords: ventricular tachycardia, patient-specific modeling, ablation, uncertainty, LGE-MRI

INTRODUCTION

Ventricular tachycardia (VT), a life-threatening fast heart rhythm, occurs frequently in patients with myocardial infarction, and leading to sudden cardiac death. Although increased utilization of pre-procedural imaging (Fernandez-Armenta et al., 2013), high-density mapping (Anter et al., 2016), epicardial access (d'Avila et al., 2006), and more extensive ablation strategies (Di Biase et al., 2012; Jais et al., 2012) have all contributed to improved procedure outcome, a high efficacy of treatment for VT in the electrophysiology (EP) laboratory has not yet been achieved. At present, catheter ablation is the most effective method to eliminate VT, however, it only has modest success, 50–88% (Aliot et al., 2009). This is the result of limitations in current techniques for mapping the electrical functioning of the heart and identifying the targets for VT ablation.

Computational modeling has emerged as a powerful platform for the non-invasive investigation of lethal heart rhythm disorders and their treatment (Behradfar et al., 2014; Pathmanathan and Gray, 2014; Grandi and Maleckar, 2016; Loewe et al., 2018; Roney et al., 2018a,b); it has been used for risk stratification in patients with myocardial infarction (MI) (Vadakkumpadan et al., 2014; Arevalo et al., 2016; Deng et al., 2016) and prediction of reentry location (Ashikaga et al., 2013; Deng et al., 2015; Zahid et al., 2016). Computational technology has also been recently developed to guide patient ablation (the Virtual-heart Arrhythmia Ablation Targeting, or VAAT), and even used prospectively, as a prove of feasibility of the approach, in a small number of patients (Prakosa et al., 2018). In these models, the personalized element is limited to information that is extracted from non-invasive late gadolinium-enhanced magnetic resonance imaging (LGE-MRI) scans, which is the patient-specific ventricular geometry, and the spatial distribution of infarcted-remodeled tissue. Cell- and tissue scale EP in these models, while reflecting the fact that the substrate in VT patients involves EP ventricular remodeling (Dangman et al., 1982; Dun et al., 2004; Mendonca Costa et al., 2018), is derived from an average human set of EP parameters (i.e., EP_{avg}) to represent non-infarcted tissue and remodeled gray zone (GZ). Clearly, an ideal option would be to use personalized EP in each model, however acquisition of such information is invasive, in contrast to the VAAT approach, which offers a non-invasive prediction of the ablation targets. Thus, the ablation targets that are predicted to terminate VT in post-MI patients using the VAAT approach might have a level of uncertainty associated with the fact that pre-determined EP is used.

Similar issues had previously arisen in using patient-specific models of persistent atrial fibrillation (AF) in patients with fibrotic remodeling (Trayanova, 2014; Zahid et al., 2016; Deng et al., 2017; Hakim et al., 2018). As the intention is that such models be used in the future to predict the patient-specific targets for AF, in a series of papers we sought to assess the level of uncertainty in such predictions (Deng et al., 2017; Hakim et al., 2018). Research in these studies demonstrated that while not always the same ablation targets are predicted under the examined variable EP conditions (Deng et al., 2017), the majority of the targets that were not predicted under the average EP conditions manifested themselves upon repeating the pacing protocol post-ablation (Hakim et al., 2018).

While persistent AF in the fibrotic substrate and VT post-MI have very different arrhythmia dynamics, they both result from a combination of remodeled structural substrate interacting with a remodeled EP. Thus, in this study, we aimed to systematically assess the effect of changes in the electrophysiological parameter set on the induced VTs and predicted ablation targets in personalized models of post-MI patient hearts.

MATERIALS AND METHODS

Post-infarction Human Heart Models

For this retrospective study, we used data from 5 patients who were referred for catheter ablation of VT; their MRI data are used for model reconstruction. Details regarding patient information and model construction can be found in our previous publication (Prakosa et al., 2018). Briefly, the myocardium boundaries were semi-automatically segmented and regions of gray zone (GZ), core scar, and non-infarcted tissue were segmented from LGE-MRI by means of signal thresholding (Arevalo et al., 2016; Deng et al., 2016). Tetrahedral meshes were constructed directly from the segmented images using a previously described approach (Prassl et al., 2009), which uses the dual mesh of an octree applied directly to the segmented 3D image stacks. Fiber orientations in the mesh were assigned using a previously validated rule-based method (Bayer et al., 2012). In order to be able to conduct this research in a tractable manner, as it involves a very large number of simulations (see below), we conducted simulations in the left ventricle (LV) only in all these 5 models. The rationale for this choice is based on the fact that human infarcts resulting in VT are typically located in the LV (Cano et al., 2017; Martin et al., 2018); the LV was also the location where all the clinical VTs in these patients were sustained.

Modeling Cell- and Tissue-Scale Variability of Ventricle

Electrophysiology properties were assigned in the model as previously described (Prakosa et al., 2018). Briefly, the mathematical description of electrical conduction in cardiac tissue was based on the monodomain representation (Plank et al., 2008). Core scar was modeled as passive tissue. Non-infarcted tissue and GZ were assigned human ventricular myocyte action potential dynamics (ten Tusscher et al., 2004). The values of the non-infarcted tissue conductivities used in this study were 0.255 and 0.0775 S/m in the longitudinal and transverse directions, respectively. Tissue in the GZ region was characterized with a 90% decrease in transverse conductivity to reflect connexin-43 remodeling in the infarct border zone (Yao et al., 2003).

To establish baseline reentry dynamics in the absence of variability in the electrophysiological component of the infarcted substrate, we first conducted simulations under average human VT EP, as in previous studies (Arevalo et al., 2016; Deng et al., 2016). For brevity, these conditions are referred to as EP_{avg}. We then ran simulations in ventricular models with the same geometric structure and infarcted tissue distribution to

assess the effects of APD and CV variability. For simulations with APD variability, specific ionic currents were modified to achieve ±10% APD (**Figures 1A,B**), while minimally altering other AP properties, including resting membrane potential [V_m], AP amplitude, and restitution curve slope (**Figure 1C**). To simplify ionic current parameters selection process, I_{Kr} and I_{Ks} were modified simultaneously in 10% increments from −90 to 300%, and the current values that resulted in APD closest to the target APD (i.e., ±10% or ±20% APD) in each case were used in this study (**Table 1**). For simulations with CV variability, the longitudinal and transverse components of the conductivity tensor were modified to achieve ±10% CV. To avoid biasing effects from the complex infarcted structure in ventricular models, CV values were calibrated by simulating wavefront propagation following stimulation of the center point in a slab model (6 cm × 6 cm × 2.7 mm) with uniform fiber orientations, and conductivity tensor values were adjusted until the desired longitudinal and transverse CVs were observed. In both families of cases (i.e., $APD_{\pm 10\%}$ and $CV_{\pm 10\%}$ conditions), parameter changes required to achieve the desired emergent property were different for non-infarcted and GZ tissues. Complete details about these changes and the resulting variability in APD and CV are presented in **Tables 1**, **2**, respectively.

As experimental measurements (Britton et al., 2013) have shown that APD and CV could vary in a larger range, we conducted additional simulations in two models only (for computational tractability) with $APD_{\pm 20\%}$ and $CV_{\pm 25\%}$, and in one model, with a combination of $APD_{\pm 20\%}$ and $CV_{\pm 25\%}$. The parameter changes were listed in **Tables 1**, **2**. We chose $APD_{\pm 20\%}$ instead of $APD_{\pm 25\%}$ because $APD_{+25\%}$ resulted in longer APD

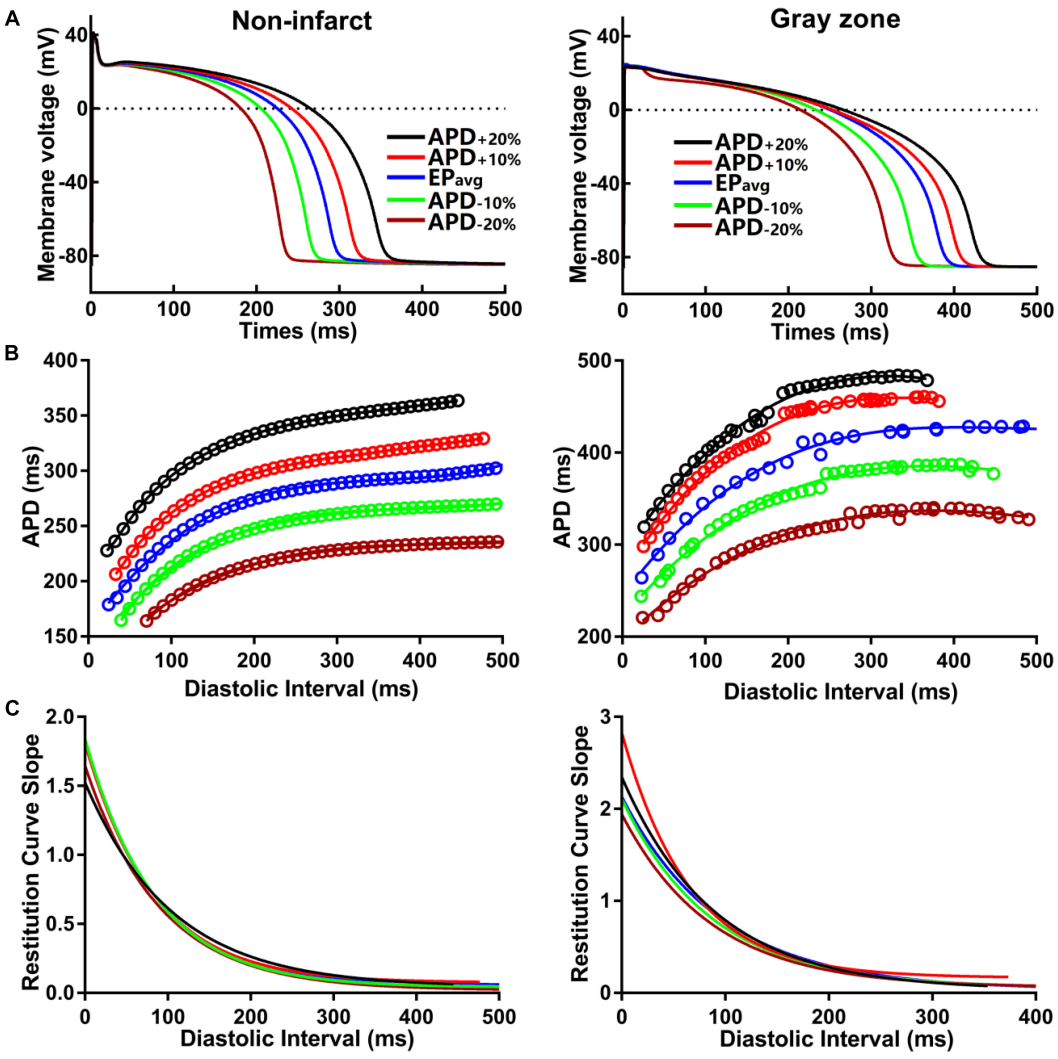

FIGURE 1 | (A) Action potential (AP) traces for simulated normal (non-infarcted) (left) and GZ (right) ventricular myocytes, paced to steady-state (1000 stimuli at basic CL = 600 ms) under average human VT electrophysiology (EP_{avg}) conditions, and with AP duration (APD_{90}) variability (±10% and ±20%). **(B)** APD restitution relationships for the respective cell types shown in A. Fit lines obtained via exponential regression. **(C)** Plots showing APD restitution curve slope values for different diastolic intervals.

TABLE 1 | Cell-scale electrophysiological model parameters modified to achieve ±10% and ±20% action potential duration (APD) in non-infarcted and GZ tissues.

		Parameters changed		APD_{target} (ms)	APD_{actual} (ms)	Percentage of APD changed	APA (mV)	V_{rest} (mV)
Non-infarcted	$APD_{-20\%}$	+80% I_{Kr}	+80% I_{Ks}	230.8	233.28	−20.8%	126.3	−84.8
	$APD_{-10\%}$	+30% I_{Kr}	+30% I_{Ks}	263.8	262.44	−9.5%	126.1	−84.8
	EP_{avg}	...	...	291.6	291.6	...	126.0	−84.7
	$APD_{+10\%}$	−20% I_{Kr}	−20% I_{Ks}	315.9	320.76	8.3%	126.0	−84.7
	$APD_{+20\%}$	−40% I_{Kr}	−40% I_{Ks}	348.5	349.92	19.5%	126.0	−84.6
Gray zone	$APD_{-20\%}$	+80% I_{Kr}	+80% I_{Ks}	309.7	306.24	−19.1%	110.1	−85.3
	$APD_{-10\%}$	+30% I_{Kr}	+30% I_{Ks}	348.1	344.52	−9.1%	109.9	−85.3
	EP_{avg}	...	...	382.8	382.8	...	109.9	−85.2
	$APD_{+10\%}$	−20% I_{Kr}	−20% I_{Ks}	409.4	421.08	7.0%	109.3	−85.2
	$APD_{+20\%}$	−30% I_{Kr}	−30% I_{Ks}	454.2	459.36	18.7%	108.7	−85.1

"..." indicates no change. EP_{avg}, average human VT electrophysiology; APA, action potential amplitude; V_{rest}, resting membrane potential; I_{Ks}, slow delayed rectifier potassium current; I_{Kr}, rapid delayed rectifier potassium current. APD_{90} was used to calculate APD. APD_{target}: The target APD (±10% or ±20% APD). APD_{actual}: It represents the actual value of APD (closest to the target) obtained by altering I_{Kr} and I_{Ks} simultaneously (see section "Materials and Methods).

TABLE 2 | Tissue-scale electrophysiological model parameters modified to achieve ±10% and ±25% longitudinal and transverse conduction velocities (CV_L and CV_T, respectively) in non-fibrotic and fibrotic atrial tissues.

		Parameters changed		CV_L (cm/s)	CV_T (cm/s)	CV_L:CV_T
Non-infarcted	$CV_{-25\%}$	−47.6% σ_{iL}	−47.6% σ_{iT}	41.1	26.2	1.57
	$CV_{-10\%}$	−22.2% σ_{iL}	−22.1% σ_{iT}	49.3	30.7	1.61
	EP_{avg}	...	...	54.8	33.5	1.63
	$CV_{+10\%}$	+28.5% σ_{iL}	+28.1% σ_{iT}	60.3	36.6	1.65
	$CV_{+25\%}$	+86.4% σ_{iL}	+86.5% σ_{iT}	68.5	41.3	1.66
Gray zone	$CV_{-25\%}$	−46.1% σ_{iL}	−46.1% σ_{iT}	32.6	15.3	2.13
	$CV_{-10\%}$	−21.4% σ_{iL}	−21.3% σ_{iT}	39.1	17.5	2.23
	EP_{avg}	...	...	43.4	18.8	2.42
	$CV_{+10\%}$	+25.6% σ_{iL}	+25.5% σ_{iT}	47.7	20.0	2.39
	$CV_{+25\%}$	+81.2% σ_{iL}	+81.4% σ_{iT}	54.6	21.9	2.49

"..." indicates no change. σ_{iL} and σ_{iT}, longitudinal and transverse conductivity tensor values; EP_{avg}, average human VT electrophysiology.

than the upper limit of APD in experimental measurements (364 ms vs. 340 ms) (Britton et al., 2013).

Stimulation Protocol

All simulations were performed using the software package CARP[1] on a parallel computing platform (Vigmond et al., 2003). A programmed electrical stimulation protocol similar to standard clinical stimulation protocols was performed to examine the arrhythmogenic propensity of the post-MI ventricular models (Cheng et al., 2013). All models were paced from 7 locations, optimized for maximum likelihood of VT induction, for 6 beats (S1) at a cycle length (CL) of 600 ms followed by a premature stimulus (S2) initially given at 90% of S1 CL. The timing between S1 and S2 was progressively shortened until reentry was induced. If reentry was not induced, a second premature stimulus (S3) was delivered after S2. If VT was still not induced, a third premature stimulus (S4) was delivered after S3. Three seconds of VT were simulated.

The smallest S1-S2 coupling interval was determined in the fowling way: Six stimulus of S1 (CL = 600 ms) were delivered; then S2 was given at 250 ms. If excitation was elicited, then we decreased S2 to 200 ms. If the excitation could propagate again, then we decreased S2 in 10 ms intervals until excitation could not be elicited. The S2 coupling interval was the last one that elicited excitation propagation. The same protocol was applied to determine the smallest S2-S3 and S3-S4 intervals. If reentry was induced after the S2 stimulus, then no addition stimulus was given.

Ablation Strategy

First, the reentrant circuit was identified in all models with EP_{avg} through analysis of the 3D reentrant wave propagation. *In silico* ablation was performed by rendering the tissue in the narrowest region of the reentrant circuit [typically a channel in the scar as in (Prakosa et al., 2018)] non-excitable. Each virtual ablation lesion was of radius in our simulation was 3.5 mm, which is similar to the clinical catheter size (Narayan et al., 2012). The VT induction protocol was then repeated to establish that VT was no longer inducible in the ablated LV substrate. If a new VT arose in the post-ablation model, then the new VT circuit was analyzed and additional ablation targets were determined and implemented in the model, and the pacing protocol was repeated until VT was no longer inducible.

[1]https://carpentry.medunigraz.at/carputils/

All simulations were then repeated in the family of models with EP_{var} ($APD_{\pm 10\%}$ and $CV_{\pm 10\%}$, 20 additional 3D LV models; 25 3D LV models in total for this study). For VTs induced in each of these models, if the reentry morphology was the same or similar to VT induced in the corresponding EP_{avg} model, the ablation lesion from the EP_{avg} model was applied to the same location in the EP_{var} model. By similar reentry morphology we refer to reentries that have the same wavefront conduction pathway, with the same critical conduction channels (or conduction isthmus), but could have different CL, and even different reentry direction. If VT in the EP_{var} model was terminated, the ablation lesions in EP_{var} and EP_{avg} models were considered "overlapping." If VT persisted in the EP_{var} model despite the ablation, then these two VTs were considered non-overlapping. Then ablation in the EP_{avg} model proceeded as described above. Finally, the number of ablation lesions was compared between EP_{avg} and EP_{var} models.

RESULTS

For simulations conducted under EP_{avg} conditions, rapid pacing induced sustained VTs in all 5 patient-specific ventricular models. **Table 3** summarized the results of simulations conducted in EP_{avg} models. A total of 16 distinct reentries were induced in five models under the EP_{avg} condition, and after ablation, only one new distinct reentry was induced. The average amount of ablated ventricular tissue under EP_{avg} condition was 0.92%. Before ablation, there were 2–4 different sustained VTs (3.2 ± 0.8) induced in each model, and the organizing centers of all 16 VTs perpetuated in distinct locations. Ablation, as described in Section "Materials and Methods," did not always render the remodeled substrate non-inducible for VT; in some cases, new VTs could arise. Specifically, after ablation, 4 patient models did not have emergent VTs, while 1 patient model had one emergent VT at a location different from those before ablation. The volume of the simulated ablation lesions that terminated the VTs, both original and emergent, in each model was $0.92 \pm 0.83\%$ of the total ventricular volume (min: 0.1%, max: 2.1%).

Comprehensive summary data for the VTs induced in simulations conducted in all 5 ventricular models under the 5 different $APD/CV_{\pm 10\%}$ conditions each (EP_{avg}, $APD_{\pm 10\%}$, and $CV_{\pm 10\%}$) are provided in **Table 4** and **Supplementary Tables S1–S4**. Of all 25 3D LV models used in this study, VT could be induced in 24. The only model in which VT could not be induced is that of patient 2 with $CV_{+10\%}$ parameters. In terms of the total number of VTs, 22 unique VTs were induced in the 24 inducible models. Eight of the VTs were induced under all five electrophysiological conditions; these were for patients 1, 3, 4, and 5. The activation maps of these 8 VTs are shown in **Figures 2** and **Supplementary Figures S1–S3**. The VT in model 2 that was induced under 4 of the 5 EP parameter sets (and not under the CV_{+10}) is shown in **Figure 3**. Of the 4 varied parameter sets ($APD_{\pm 10\%}$ and $CV_{\pm 10\%}$), $APD_{\pm 10\%}$, and $CV_{+10\%}$ resulted in less VTs, while $CV_{-10\%}$ resulted in more VTs compared with the EP_{avg} conditions.

TABLE 3 | Summary of results for simulations conducted in EP_{avg} models.

ID	# reentries pre-ablation	# reentries post-ablation	Extent of ablated tissue (%)
P01	4	1	1.3
P02	3	0	0.2
P03	2	0	0.1
P04	4	0	2.1
P05	3	0	0.9

There were 10 distinct reentries induced in models with the $APD_{+10\%}$ parameter set before ablation, and all of them corresponded to VTs under EP_{avg} conditions (**Table 4** and **Supplementary Table S1**). There were no emergent reentries after ablation under these electrophysiological conditions. For the $CV_{+10\%}$ parameter set (**Table 4** and **Supplementary Table S3**), there were 9 distinct VTs induced before ablation, and they all also matched the VTs in EP_{avg}. Under the $APD_{-10\%}$ conditions (**Table 4** and **Supplementary Table S2**), there were 11 distinct VTs before ablation, and 9 of them corresponded to those under EP_{avg} conditions. Only for patient 2 there was one emergent VT after ablation, which was different from any VT under EP_{avg} conditions before and after ablation (the blue lesion in Panel B of **Figure 3**). In patient 1, two reentries were new and different from any VT under EP_{avg} conditions before ablation, but one of them was induced under EP_{avg} conditions after ablation (Panel B in **Supplementary Figure S1**). Thus overall, for the $APD_{-10\%}$ parameter set, 10 out of 12 VTs had matching reentries under EP_{avg} conditions, while the remaining 2 VTs were new, and different from the reentries in EP_{avg}.

For the $CV_{-10\%}$ parameter set (**Table 4** and **Supplementary Table S4**), there were 20 distinct VTs induced before ablation, and 14 of them had corresponding reentries under EP_{avg} conditions. After ablation, there was only one emergent VT in patient 2 (Panel B in **Figure 3**), but 2 of the VTs induced before ablation were also induced under EP_{avg} conditions, so 16 out of 21 VTs in the $CV_{-10\%}$ parameter set models had matching VTs under EP_{avg} after ablation.

The results for one example model (patient 5) under all 5 EP parameter sets are shown in **Figure 2**. There were 3 distinct VTs induced under EP_{avg}, one located at the septum (**Figure 2C**, Morphology 1 in EP_{avg}), another one at the LV lateral wall (**Figure 2C**, Morphology 2 in EP_{avg}), and the third one located at the posterior wall (morphology not shown). For the $APD_{\pm 10\%}$ and $CV_{\pm 10\%}$ parameter sets, both resulted in two reentries being induced, which were located at the septum and the LV lateral wall. Under $CV_{-10\%}$ conditions, there were 5 distinct VTs induced, and 3 of them had matching reentries in EP_{avg} models (ablation lesions in Panel B of **Figure 2**).

For the 2 VTs induced under all 5 conditions, the morphology and location were very similar for across all models. For morphology 1 (first row in **Figure 2C**), the reentry was circular, with the only difference being the CL, which varied from 195 ms to 380 ms. After ablating the narrowest channel region in VT morphology 1, the reentry was terminated. After applying the ablation lesions from EP_{avg} to the other 4 conditions (light blue lesions on the left side of **Figure 2B**), and the reentry

TABLE 4 | Summary of simulation results regarding the number of VTs obtained for the EP_{avg} and EP_{var} ($APD_{\pm 10\%}$ and $CV_{\pm 10\%}$) models with the 5 patient-specific ventricular geometries.

		Total number of VTs	Number of VTs in EP_{avg} models	Percentage of VTs in EP_{var} models that were also present in EP_{avg} (%) models (%)
# of induced VTs in EP_{avg}	Pre- ablation	16	–	–
	Post-ablation	17	–	–
# of induced VTs in $APD_{+10\%}$	Pre- ablation	10	10	100
	Post-ablation	10	10	100
# of induced VTs in $APD_{-10\%}$	Pre- ablation	11	9	81.8
	Post-ablation	12	10	83.3
# of induced VTs in $CV_{+10\%}$	Pre- ablation	9	9	100
	Post-ablation	9	9	100
# of induced VTs in $CV_{-10\%}$	Pre- ablation	20	14	70
	Post-ablation	21	16	76.2
# of induced VTs in $APD_{+20\%}$*	Pre- ablation	3	3	100
	Post-ablation	3	3	100
# of induced VTs in $APD_{-20\%}$*	Pre- ablation	3	3	100
	Post-ablation	4	3	75
# of induced VTs in $CV_{+25\%}$*	Pre- ablation	3	3	100
	Post-ablation	3	3	100
# of induced VTs in $CV_{-25\%}$*	Pre- ablation	6	5	83.3
	Post-ablation	7	5	71.4
# of induced VTs in $APD_{+20\%}$ & $CV_{+25\%}$**	Pre- ablation	0	0	0
	Post-ablation	0	0	0
# of induced VTs in $APD_{-20\%}$ & $CV_{+25\%}$**	Pre- ablation	0	0	0
	Post-ablation	0	0	0
# of induced VTs in $APD_{+20\%}$ & $CV_{-25\%}$**	Pre- ablation	1	1	100
	Post-ablation	1	1	100
# of induced VTs in $APD_{-20\%}$ & $CV_{-25\%}$**	Pre- ablation	3	3	100
	Post-ablation	4	3	75

*"Number of VTs in EP_{avg} models" represents the number of reentry morphologies induced in each set of modified conditions with similar or same reentry morphologies induced under the EP_{avg} condition. The last column in **Table 4** is calculated as "Number of VTs in EPavg models"/" Total number of VTs", which represents how many reentry morphologies induced under each of the modified condition corresponded to the reentry morphologies induced under EP_{avg}. *, only 2 models were used with this EP parameter set; **, only 1 model was used with this EP parameter set.*

at that region was terminated in all 4 conditions too. For morphology 2, the reentry was circular in all 5 conditions, but the conduction pathway in $CV_{-10\%}$ condition showed differences. Under EP_{avg}, $APD_{\pm 10\%}$ and $CV_{+10\%}$ conditions, there was only one conduction pathway, but under the $CV_{-10\%}$ condition, the reentry had two condition pathways, one of which, the one close to posterior wall, was the same under the other 4 conditions. After ablating the narrowest channel region in morphology 2 in EP_{avg}, the reentry was terminated. Then applying the ablation lesion from EP_{avg} to the four other EP versions (light blue lesions on the right side of **Figure 2B**), the reentry under $APD_{\pm 10\%}$, and $CV_{+10\%}$ conditions was terminated. But applying the ablation lesions from EP_{avg} didn't terminate the reentry induced in $CV_{-10\%}$. After ablating the narrowest parts of both conducting pathways under $CV_{-10\%}$ conditions, reentry was terminated (the light blue and blue on the right-most side of $CV_{-10\%}$ in **Figure 2B**). The VTs induced at the posterior wall in EP_{avg} could not be induced under $APD_{\pm 10\%}$ and $CV_{+10\%}$ conditions; the ablation lesion for that reentry is shown in purple in the first 3 panels of **Figure 2B**. The 3 VTs induced in EP_{avg} were all induced in $CV_{-10\%}$ (light blue lesions in $CV_{-10\%}$ panel of **Figure 2B**), but there were 2 new VTs induced in $CV_{-10\%}$, of which the 2 ablation lesions are shown as blue in the $CV_{-10\%}$ panel in **Figure 2B**.

Figure 3 shows the results for another patient model (patient 2) for the 5 EP parameter sets. There were 3 VTs induced in EP_{avg}, with two of them being on the anterior wall, and the third on septum. For $CV_{+10\%}$, there was no reentry induced, and this is the only model variant of all 25 model variants in 5 the patients in which no reentry could be induced. Before ablation, the models with $APD_{\pm 10\%}$ parameters had only one reentry induced, on the anterior middle wall (**Figure 3C**), and this reentry is similar to the one induced in EP_{avg} (first panel in **Figure 3C**). In $CV_{-10\%}$, there were 3 VTs induced, and two of them had matching reentries in EP_{avg}. But the one on the middle anterior wall had minor differences compared to the corresponding one in EP_{avg}: it had 2 conduction pathways ($CV_{-10\%}$ panel in **Figure 3C**), with the pathway on the right matching the one in EP_{avg}, but the left side was a new pathway. Applying the lesions determined from EP_{avg}, the middle anterior wall VT could not be terminated in $CV_{-10\%}$ (light blue lesion in the $CV_{-10\%}$ panel of the first row

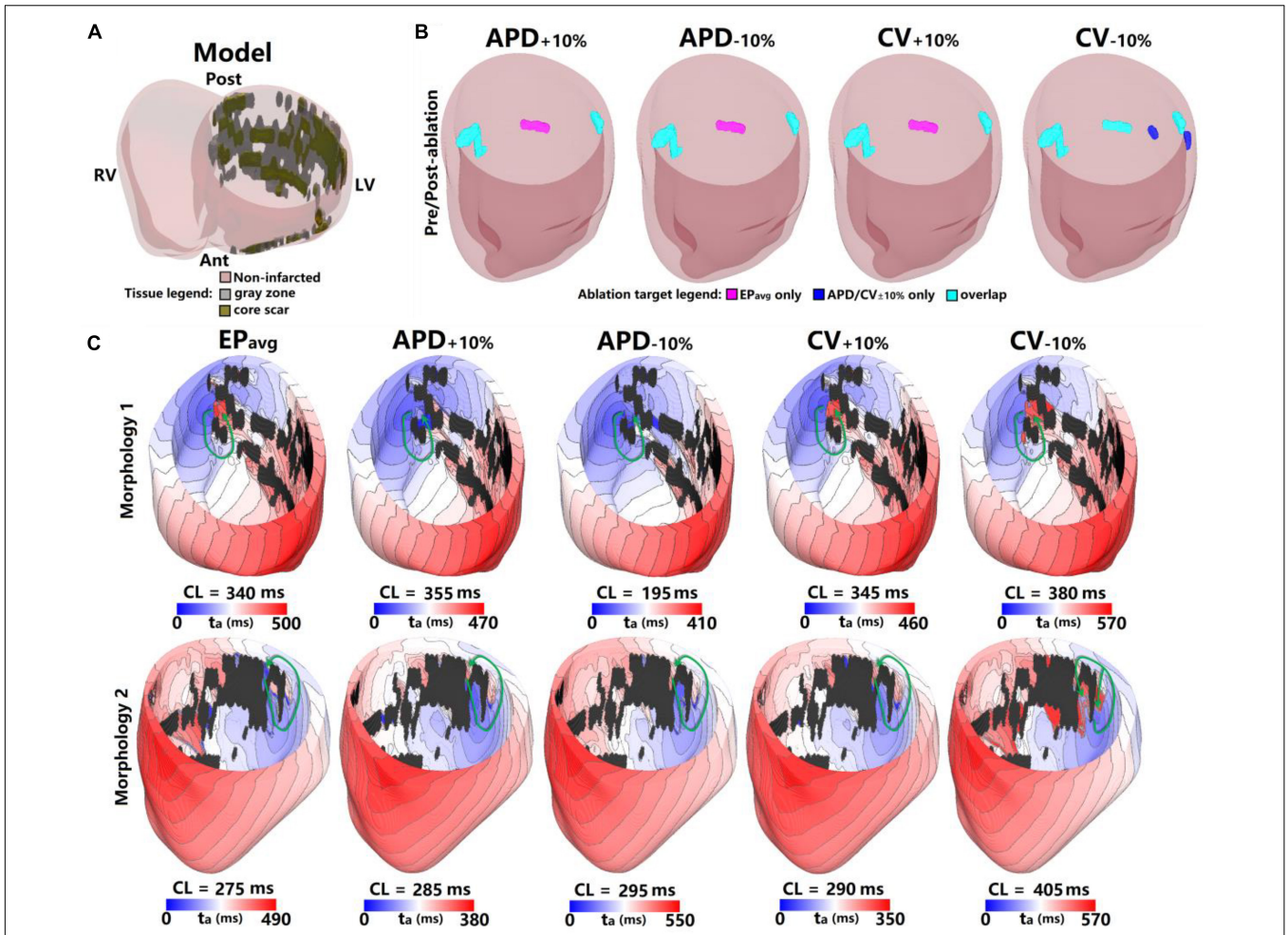

FIGURE 2 | Geometry and simulated activation maps and ablation lesions under average human VT EP_{avg} and variable APD/CV conditions for model 5. **(A)** Geometric model of the infarcted heart of patient model 5. **(B)** Ablation lesions for simulations with the 5 different parameter sets. **(C)** Highlighting two VT morphologies in which the same pacing sequence applied in the same model led to the initiation of VT driven by an RD in the same ventricular region, regardless of the variability in APD/CV. t_a, activation time. The black areas in panel C for all figures are core scar – there is no electrical activation there.

in **Figure 3B**), and an additional lesion had to be applied to narrowest portion of the left condition pathway in $CV_{-10\%}$ to terminate the reentry on the anterior middle wall (blue lesion in the $CV_{-10\%}$ panel of the first row in **Figure 3B**). After ablation, no reentry could be induced in EP_{avg} and $APD_{+10\%}$, but in $APD_{-10\%}$, a new VT emerged at the vicinity of the ablation lesion on the anterior wall; the condition pathway of this RD is very similar to the left side pathway of the VT induced in $CV_{-10\%}$. Applying the EP_{avg} ablation lesions to $CV_{-10\%}$ terminated the VT. In $CV_{-10\%}$ condition, after ablation, there was an emergent VT, which matched the VT on the left side of the anterior wall in EP_{avg}; applying the ablation lesion from EP_{avg} terminated the emergent reentry in $CV_{-10\%}$. Results of the study for the other 3 patients are shown in **Supplementary Figures S1–S3**. Vann diagrams summarizing the results of simulations for all above cases are presented in **Figure 4**.

Next, we present results of simulations with the additional EP parameter sets (from the extended parameter range) in the limited number of models, as described in Section "Materials and Methods." Results from simulations with model 2 are presented in **Figure 3**. Upon change of APD from +10% to +20% and from −10 to −20%, there was no difference in reentry morphology and reentry location. When changing CV from ±10 to ±25%, there was a difference between results for the $CV_{+10\%}$ and $CV_{+25\%}$ cases: no reentry was induced in $CV_{+10\%}$ simulations, and there was one reentry induced in $CV_{+25\%}$. There was no difference between the cases of $CV_{-10\%}$ and $CV_{-25\%}$. Results for model 3 and the same parameter range are presented in **Supplementary Figure S2**. For this model, there was no difference between results for the $APD_{\pm20\%}$ and $CV_{+25\%}$ conditions, but under the $CV_{-25\%}$ condition, one new reentry emerged (panel D of **Supplementary Figure S2**) that was not present for the other modified APD and CV cases. Thus, based on the simulation results for the 2 patients with $APD_{\pm20\%}$ and $CV_{\pm25\%}$, we conclude that APD changes within the range of ±20% had no additional effects on reentry location. Changing CV in the range

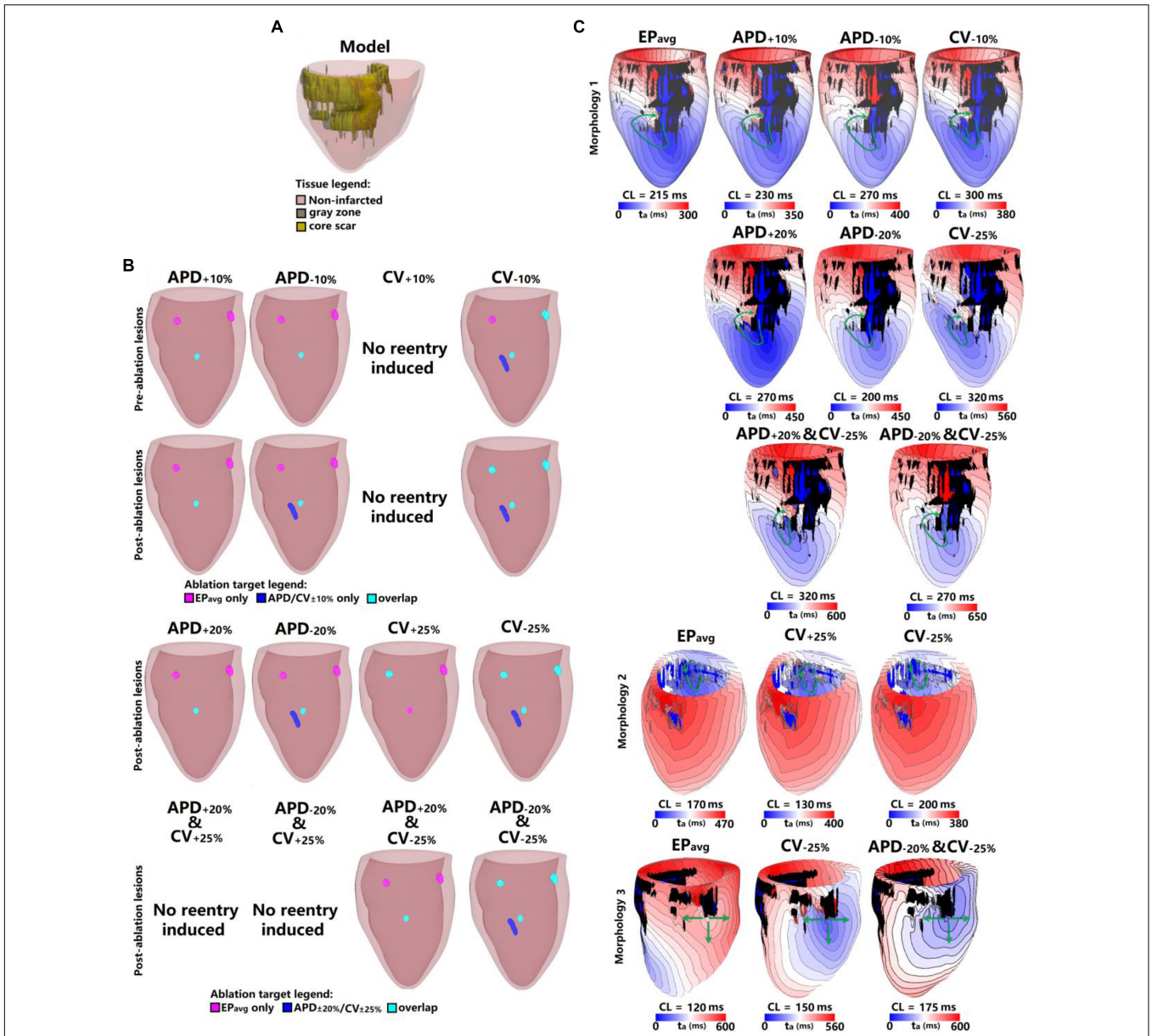

FIGURE 3 | Geometry and simulated activation maps and ablation lesions under average human VT EP_{avg} and variable APD/CV conditions for model 2. **(A)** Geometric model of the infarcted heart of patient model 2. **(B)** Ablation lesions for simulations for the 13 different parameter sets. **(C)** Highlighting one VT morphology in which the same pacing sequence applied in the same model led to the initiation of VT driven by an RD in the same ventricular region, regardless of the variability in APD/CV. t_a, activation time. The black areas in panel C for all figures represent core scar – there is no electrical activation there.

(±25%) resulted in changes in reentry location only when CV was at the boundaries of that range. A Venn diagram of these results is provided in **Figure 4**.

Finally we executed simulations in one model with a combination of parameter changes, as described in Section "Materials and Methods." Conducting simulations with model 2, the combinations of $APD_{+20\%}$ & $CV_{+25\%}$ and $APD_{-20\%}$ & $CV_{+25\%}$ conditions did not result in reentry. There were two reentries induced under the $APD_{+20\%}$ & $CV_{-25\%}$ condition, one of which corresponded to the reentry morphology in EP_{avg} (see **Figure 3**), and the other one was a new VT morphology with respect to the EP_{avg} case. There were four VT morphologies induced in the $APD_{-20\%}$ & $CV_{-25\%}$ condition, 3 of which corresponded to EP_{avg}, and one was new. The combined reduction/increase of CV and APD produced only one different VT morphology as compared to EP_{avg}. This VT morphology was the same as the ones induced for cases where only APD or only CV was changed. Thus we conclude, based on the simulations in model 2, that combined reduction/increase of CV and APD within the range of ±20%

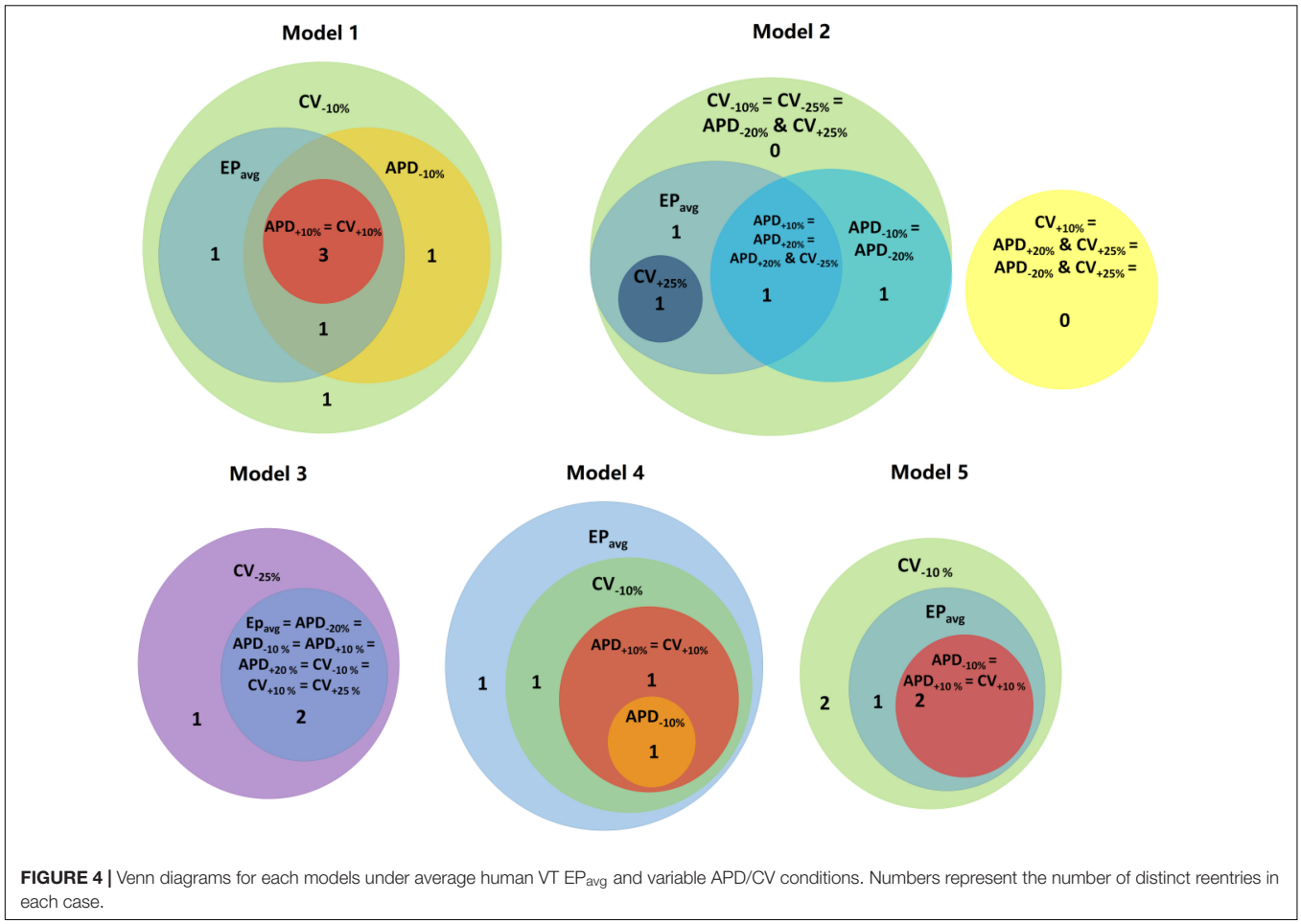

FIGURE 4 | Venn diagrams for each models under average human VT EP_{avg} and variable APD/CV conditions. Numbers represent the number of distinct reentries in each case.

or ±25% had no additional effects on VTs compared with only changing APD or CV.

DISCUSSION

In this study, we used computational models reconstructed from LGE-MRI scans of the infarcted ventricle of individuals with VT to assess the sensitivity of VT localization to variability in cell- and tissue-scale electrophysiological parameters. We showed that: (1) in simulations conducted with ±10% APD/CV, a subset of VTs (76.2–100%, depending on the EP parameter set) were observed in approximately the same locations as those in the EP_{avg} case; (2) EP_{avg} conditions resulted in more VTs (5–8) than in $APD_{\pm 10\%}$ and $CV_{+10\%}$, and in less reentries than in $CV_{-10\%}$; (3) Emergent VTs were induced sometimes post-ablation, and the emergent reentries often matched the pre-ablation VTs in models with other parameter sets. (4) Where the VTs were robust to APD/CV variability, there were differences, as expected, in macroscopic arrhythmia features such as CL and total activation time.

About 53% (9/17) of the reentries that occurred in EP_{avg} were also induced in all other four parameter set models (±10% APD/CV), and the remainder of reentries were induced in at least one of the four parameter set models. Interestingly, all the reentries induced in $APD_{+10\%}$ and $CV_{+10\%}$ models had matching reentries in the EP_{avg} models. The models with EP_{avg} were more inducible than the $APD_{+10\%}$ and $CV_{+10\%}$ models, as the wavelength in the former case was smaller, allowing for more space for the reentry to propagate and be sustained. While there were new VTs induced in models with $APD_{-10\%}$ and $CV_{-10\%}$, more than 76% of the VTs occurred also in models with EP_{avg}. The models with $APD_{-10\%}$ had a smaller number of induced VTs than the corresponding EP_{avg} models. A possible explanation for this finding is that APD in the EP_{avg} parameter set falls in the arrhythmogenesis susceptibility window of APD (Clayton and Holden, 2005), where there is a unidirectional block of electrical conduction through a VT-sustaining channel. Upon further reduction of APD, the VT channel conducts bi-directionally, resulting in a smaller number of included reentries.

In the additional simulations with the extended range of APD and CV and their combination, the results with the combined reduction/increase of CV and APD were very similar, in terms of reentry location, and pathway to those when varying APD or CV independently. Furthermore, $APD_{\pm 20\%}$ and $CV_{\pm 25\%}$ cases had similar outcomes to those with $APD_{\pm 10\%}$ and $CV_{\pm 10\%}$. Thus, simulating only ±10% APD or ±10% CV changes may be

sufficient in representing the results from simulations with larger electrophysiological parameters variations.

These findings present evidence that VT localization is fairly robust to electrophysiological variability, and that the distribution of the infarcted tissue (core scar and GZ) might play a dominant role in determining the location of infarct-related VTs. Our results suggest that EP_{avg} models identified most of the VT ablation targets that were consistently observed under different EP conditions. Nonetheless, there was a small subset of reentries that were observed only under EP_{avg} simulations. Furthermore, in some models, VTs only emerged upon APD and/or CV change, suggesting that there could be a small number of potential ablation targets that may not be revealed using the EP_{avg} parameter set. Furthermore, for reentries with the same morphology and location of the critical conduction isthmus (and thus the same ablation target) we observed differences in CL, total activation time and in rare cases, even direction of propagation. Finally, we demonstrated that majority of ablation targets that were not predicted under EP_{avg} conditions manifested themselves upon repeating the pacing protocol post-ablation, similar to the findings in modeling of ablation for persistent AF in patients with fibrotic remodeling (Hakim et al., 2018).

The results shown in this paper differ from our atrial sensitivity analysis study (Deng et al., 2017) because the mechanism of reentry in VT and AF are different. In the atrial models, there is only non-fibrotic and fibrotic tissue (both are excitable tissues, but fibrotic tissue has modified EP). In contrast, in the ventricular models, there is additionally a core scar. Thus reentries in the atrial models had a larger functional component and their morphologies and locations could be affected, by somewhat larger degree, by changes in APD or CV. In infarct-related VT, most of the reentries were anchored to core scar or included conduction through channels, consistent with published data (Martin et al., 2018).

Patient-specific computational modeling of VT has been proposed as a new approach to non-invasively predict personalized VT ablation targets in post-MI patients (Prakosa et al., 2018). The present study demonstrates that simulations conducted under EP_{avg} conditions identified most of VTs that were consistently observed under multiple different EP conditions. The uncertainty in the post-MI VT ablation targets under EP_{avg} is further mitigated by the design of the pipeline for determining the optimal set of targets [as in the VAAT approach (Prakosa et al., 2018)], where the protocol is repeated post-ablation with virtual targets incorporated, until the remodeled substrate is no longer capable of sustaining VT. This allows the protocol to reveal additional VTs under EP_{avg} that are not manifested following the initial pacing protocol prior to virtual ablation, but appear right away in simulations using models with different EP properties.

CONCLUSION

In conclusion, we showed that perturbing APD and CV by ±10% caused relatively small variation in VT localization. In a small number of cases, new reentries at locations distinct from those in EP_{avg} emerged when EP parameters changed. Most of those were revealed in EP_{avg} models when the simulation protocol for determining the ablation targets was repeated with the initial targets incorporated in the models. Overall, the localization of the induced VTs was primarily driven by the remodeled structural substrate. Thus, personalized ventricular modeling with an average representation of infarct-remodeled EP may uncover most targets for VT ablation.

LIMITATIONS

The first limitation is that we only considered a relatively limited subset of the parameter space of four discrete changes (±10% APD and ±10% CV). Considering the relatively low CV and long APD in GZ used in our model, further changes in these parameters will make these values fall out of the experimental range. Furthermore, we conducted a large number of simulations with 25 different 3D LV models. The sheer amount of computational time makes exploration of additional ranges of parameter values technically difficult. The second limitation in this study is that in order to achieve different APD values, we only changed I_{Kr} and I_{Ks} currents in our single cell models. We did not alter the Ca current as it would not only affect APD restitution, but would also have impact on other single cell properties and thus making the organ scale modeling too complicated to analyze. Furthermore, as the goal of this study was to provide a sensitivity analysis of ablation targeting, we did not explore the mechanisms of all the observed phenomena, including arrhythmogenesis arising from locally reduced APD. Finally, our model did not consider the influence of Purkinje system, the role of the right ventricle, and potential alterations in fiber orientation that cannot be captures by our patient-specific rule-based approach.

AUTHOR CONTRIBUTIONS

DD, AP, and PN performed the LGE-MRI scan segmentation and model creation. DD performed the simulations of VT in all models. DD, AP, and NT analyzed the data. DD, JS, and NT wrote the manuscript. All authors discussed the results and commented on the manuscript.

FUNDING

NT acknowledges support from NIH (Pioneer Award DP1-HL123271 and grants R01 HL126802 and U01 HL141074) and a grant from Foundation Leducq. DD acknowledges support from Dalian University of Technology [No. DUT18RC(3)068].

SUPPLEMENTARY MATERIAL

The Supplementary Material for this article can be found online at: https://www.frontiersin.org/articles/10.3389/fphys.2019.00628/full#supplementary-material

REFERENCES

Aliot, E. M., Stevenson, W. G., Almendral-Garrote, J. M., Bogun, F., Calkins, C. H., Delacretaz, E., et al. (2009). Registered Branch of the European Society of, C., Heart Rhythm, S., American College of, C., and American Heart, A. EHRA/HRS Expert Consensus on Catheter Ablation of Ventricular Arrhythmias: developed in a partnership with the European Heart Rhythm Association (EHRA), a Registered Branch of the European Society of Cardiology (ESC), and the Heart Rhythm Society (HRS); in collaboration with the American College of Cardiology (ACC) and the American Heart Association (AHA). *Heart Rhythm* 6, 886–933. doi: 10.1016/j.hrthm.2009.04.030

Anter, E., Tschabrunn, C. M., Buxton, A. E., and Josephson, M. E. (2016). High-resolution mapping of postinfarction reentrant ventricular tachycardia: electrophysiological characterization of the circuit. *Circulation* 134, 314–327. doi: 10.1161/CIRCULATIONAHA.116.021955

Arevalo, H. J., Vadakkumpadan, F., Guallar, E., Jebb, A., Malamas, P., Wu, K. C., et al. (2016). Arrhythmia risk stratification of patients after myocardial infarction using personalized heart models. *Nat. Commun.* 7:11437. doi: 10.1038/ncomms11437

Ashikaga, H., Arevalo, H., Vadakkumpadan, F., Blake, R. C., Bayer, J. D., Nazarian, S., et al. (2013). Feasibility of image-based simulation to estimate ablation target in human ventricular arrhythmia. *Heart Rhythm* 10, 1109–1116. doi: 10.1016/j.hrthm.2013.04.015

Bayer, J. D., Blake, R. C., Plank, G., and Trayanova, N. A. (2012). A novel rule-based algorithm for assigning myocardial fiber orientation to computational heart models. *Ann. Biomed. Eng.* 40, 2243–2254. doi: 10.1007/s10439-012-0593-5

Behradfar, E., Nygren, A., and Vigmond, E. J. (2014). The role of Purkinje-myocardial coupling during ventricular arrhythmia: a modeling study. *PLoS One* 9:e88000. doi: 10.1371/journal.pone.0088000

Britton, O. J., Bueno-Orovio, A., Van Ammel, K., Lu, H. R., Towart, R., Gallacher, D. J., et al. (2013). Experimentally calibrated population of models predicts and explains intersubject variability in cardiac cellular electrophysiology. *Proc. Natl. Acad. Sci. U.S.A.* 110, E2098–E2105. doi: 10.1073/pnas.1304382110

Cano, O., Plaza, D., Sauri, A., Osca, J., Alonso, P., Andres, A., et al. (2017). Utility of high density multielectrode mapping during ablation of scar-related ventricular tachycardia. *J. Cardiovasc. Electrophysiol.* 28, 1306–1315. doi: 10.1111/jce.13302

Cheng, A., Dalal, D., Butcher, B., Norgard, S., Zhang, Y. Y., Dickfeld, T., et al. (2013). Prospective observational study of implantable cardioverter-defibrillators in primary prevention of sudden cardiac death: study design and cohort description. *J. Am. Heart Assoc.* 2:e000083. doi: 10.1161/JAHA.112.000083

Clayton, R. H., and Holden, A. V. (2005). Dispersion of cardiac action potential duration and the initiation of re-entry: a computational study. *Biomed. Eng. Online* 4:11.

Dangman, K. H., Danilo, P., Hordof, A. J., Maryrabine, L., Reder, R. F., and Rosen, M. R. (1982). Electrophysiologic characteristics of human ventricular and purkinje-Fibers. *Circulation* 65, 362–368. doi: 10.1161/01.cir.65.2.362

d'Avila, A., Scanavacca, M., and Sosa, E. (2006). Transthoracic epicardial catheter ablation of ventricular tachycardia. *Heart Rhythm* 3, 1110–1111. doi: 10.1016/j.hrthm.2006.03.029

Deng, D., Arevalo, H. J., Prakosa, A., Callans, D. J., and Trayanova, N. A. (2016). A feasibility study of arrhythmia risk prediction in patients with myocardial infarction and preserved ejection fraction. *Europace* 18(Suppl. 4), iv60–iv66. doi: 10.1093/europace/euw351

Deng, D., Murphy, M. J., Hakim, J. B., Franceschi, W. H., Zahid, S., Pashakhanloo, F., et al. (2017). Sensitivity of reentrant driver localization to electrophysiological parameter variability in image-based computational models of persistent atrial fibrillation sustained by a fibrotic substrate. *Chaos* 27:093932. doi: 10.1063/1.5003340

Deng, D. D., Arevalo, H., Pashakhanloo, F., Prakosa, A., Ashikaga, H., McVeigh, E., et al. (2015). Accuracy of prediction of infarct-related arrhythmic circuits from image-based models reconstructed from low and high resolution MRI. *Front. Physiol.* 6:282. doi: 10.3389/fphys.2015.00282

Di Biase, L., Santangeli, P., Burkhardt, D. J., Bai, R., Mohanty, P., Carbucicchio, C., et al. (2012). Endo-epicardial homogenization of the scar versus limited substrate ablation for the treatment of electrical storms in patients with ischemic cardiomyopathy. *J. Am. Coll. Cardiol.* 60, 132–141. doi: 10.1016/j.jacc.2012.03.044

Dun, W., Baba, S. G., Yagi, T., and Boyden, A. (2004). Dynamic remodeling of K+ and Ca2+ currents in cells that survived in the epicardial border zone of canine healed infarcted heart. *Am. J. Physiol. Heart Circ. Physiol.* 287, H1046–H1054.

Fernandez-Armenta, J., Berruezo, A., Andreu, D., Camara, O., Silva, E., Serra, L., et al. (2013). Three-dimensional architecture of scar and conducting channels based on high resolution ce-cmr: insights for ventricular tachycardia ablation. *Circ. Arrhythm. Electrophysiol.* 6, 528–537. doi: 10.1161/CIRCEP.113.000264

Grandi, E., and Maleckar, M. M. (2016). Anti-arrhythmic strategies for atrial fibrillation: the role of computational modeling in discovery, development, and optimization. *Pharmacol. Ther.* 168, 126–142. doi: 10.1016/j.pharmthera.2016.09.012

Hakim, J. B., Murphy, M. J., Trayanova, N. A., and Boyle, M. (2018). Arrhythmia dynamics in computational models of the atria following virtual ablation of re-entrant drivers. *Europace* 20(Suppl. 3), iii45–iii54. doi: 10.1093/europace/euy234

Jais, P., Maury, P., Khairy, P., Sacher, F., Nault, I., Komatsu, Y., et al. (2012). Elimination of local abnormal ventricular activities: a new end point for substrate modification in patients with scar-related ventricular tachycardia. *Circulation* 125, 2184–2196. doi: 10.1161/CIRCULATIONAHA.111.043216

Loewe, A., Poremba, E., Oesterlein, T., Luik, A., Schmitt, C., Seemann, G., et al. (2018). Patient-specific identification of atrial flutter vulnerability-a computational approach to reveal latent reentry pathways. *Front. Physiol.* 9:1910. doi: 10.3389/fphys.2018.01910

Martin, R., Maury, P., Bisceglia, C., Wong, T., Estner, H., Meyer, C., et al. (2018). Characteristics of scar-related ventricular tachycardia circuits using ultra-high-density mapping: a multi-center study. *Circ. Arrhythm. Electrophysiol.* 11:e006569.

Mendonca Costa, C., Plank, G., Rinaldi, C. A., Niederer, S. A., and Bishop, M. J. (2018). Modeling the electrophysiological properties of the infarct border zone. *Front. Physiol.* 9:356. doi: 10.3389/fphys.2018.00356

Narayan, S. M., Krummen, D. E., Shivkumar, K., Clopton, P., Rappel, W. J., and Miller, J. M. (2012). Treatment of atrial fibrillation by the ablation of localized sources confirm (conventional ablation for atrial fibrillation with or without focal impulse and rotor modulation) trial. *JACC* 60, 628–636. doi: 10.1016/j.jacc.2012.05.022

Pathmanathan, P., and Gray, R. A. (2014). Verification of computational models of cardiac electro-physiology. *Int. J. Numer. Method Biomed. Eng.* 30, 525–544. doi: 10.1002/cnm.2615

Plank, G., Zhou, L., Greenstein, J. L., Cortassa, S., Winslow, R. L., O'Rourke, B., et al. (2008). From mitochondrial ion channels to arrhythmias in the heart: computational techniques to bridge the spatio-temporal scales. *Philos. Trans. A Math. Phys. Eng. Sci.* 366, 3381–3409. doi: 10.1098/rsta.2008.0112

Prakosa, A., Arevalo, H. J., Deng, D., Boyle, M., Nikolov, P., Ashikaga, H., et al. (2018). Personalized virtual-heart technology for guiding the ablation of infarct-related ventricular tachycardia. *Nat. Biomed. Eng.* 2, 732–740. doi: 10.1038/s41551-018-0282-2

Prassl, A. J., Kickinger, F., Ahammer, H., Grau, V., Schneider, J. E., Hofer, E., et al. (2009). Automatically generated, anatomically accurate meshes for cardiac electrophysiology problems. *IEEE Trans. Biomed. Eng.* 56, 1318–1330. doi: 10.1109/tbme.2009.2014243

Roney, C. H., Bayer, J. D., Cochet, H., Meo, M., Dubois, R., Jais, P., et al. (2018a). Variability in pulmonary vein electrophysiology and fibrosis determines arrhythmia susceptibility and dynamics. *PLoS Comput. Biol.* 14:e1006166. doi: 10.1371/journal.pcbi.1006166

Roney, C. H., Williams, S. E., Cochet, H., Mukherjee, R. K., O'Neill, L., Sim, I., et al. (2018b). Patient-specific simulations predict efficacy of ablation of interatrial connections for treatment of persistent atrial fibrillation. *Europace* 20(Suppl. 3), iii55–iii68. doi: 10.1093/europace/euy232

ten Tusscher, K. H. W. J., Noble, D., Noble, J., and Panfilov, A. V. (2004). A model for human ventricular tissue. *Am. J. Physiol. Heart Circ. Physiol.* 286, H1573–H1589.

Trayanova, N. A. (2014). Mathematical approaches to understanding and imaging atrial fibrillation significance for mechanisms and management. *Circ. Res.* 114, 1516–1531. doi: 10.1161/CIRCRESAHA.114.302240

Vadakkumpadan, F., Trayanova, N., and Wu, K. C. (2014). Image-based left ventricular shape analysis for sudden cardiac death risk stratification. *Heart Rhythm* 11, 1693–1700. doi: 10.1016/j.hrthm.2014.05.018

Vigmond, E. J., Hughes, M., Plank, G., and Leon, L. J. (2003). Computational tools for modeling electrical activity in cardiac tissue. *J. Electrocardiol.* 36(Suppl.), 69–74. doi: 10.1016/j.jelectrocard.2003.09.017

Yao, J. A., Hussain, W., Patel, P., Peters, N. S., Boyden, A., and Wit, A. L. (2003). Remodeling of gap junctional channel function in epicardial border zone of healing canine infarcts. *Circ. Res.* 92, 437–443. doi: 10.1161/01.res.0000059301.81035.06

Zahid, S., Cochet, H., Boyle, M., Schwarz, E. L., Whyte, K. N., Vigmond, E. J., et al. (2016). Patient-derived models link re-entrant driver localization in atrial fibrillation to fibrosis spatial pattern. *Cardiovasc. Res.* 110, 443–454. doi: 10.1093/cvr/cvw073

Conflict of Interest Statement: The authors declare that the research was conducted in the absence of any commercial or financial relationships that could be construed as a potential conflict of interest.

frontiers in Physiology

ORIGINAL RESEARCH
published: 04 July 2019
doi: 10.3389/fphys.2019.00847

Heterogeneous Effects of Fibroblast-Myocyte Coupling in Different Regions of the Human Atria Under Conditions of Atrial Fibrillation

*Jorge Sánchez, Juan F. Gomez, Laura Martinez-Mateu, Lucia Romero, Javier Saiz and Beatriz Trenor**

Centre for Research and Innovation in Bioengineering, Universitat Politècnica de València, Valencia, Spain

Background: Atrial fibrillation (AF), the most common cardiac arrhythmia, is characterized by alteration of the action potential (AP) propagation. Under persistent AF, myocytes undergo electrophysiological and structural remodeling, which involves fibroblast proliferation and differentiation, modifying the substrate for AP propagation. The aim of this study was to analyze the effects on the AP of fibroblast-myocyte coupling during AF and its propagation in different regions of the atria.

Methods: Isolated myocytes were coupled to different numbers of fibroblasts using the established AP models and tissue simulations were performed by randomly distributing fibroblasts. Fibroblast formulations were updated to match recent experimental data. Major ion current conductances of the myocyte model were modified to simulate AP heterogeneity in four different atrial regions (right atrium posterior wall, crista terminalis, left atrium posterior wall, and pulmonary vein) according to experimental and computational studies.

Results: The results of the coupled myocyte-fibroblast simulations suggest that a more depolarized membrane potential and higher fibroblast membrane capacitance have a greater impact on AP duration and myocyte maximum depolarization velocity. The number of coupled fibroblasts and the stimulation frequency are determining factors in altering myocyte AP. Strand simulations show that conduction velocity tends to homogenize in all regions, while the left atrium is more likely to be affected by fibroblast and AP propagation block is more likely to occur. The pulmonary vein is the most affected region, even at low fibroblast densities. In 2D sheets with randomly placed fibroblasts, wavebreaks are observed in the low density (10%) central fibrotic zone and when fibroblast density increases (40%) propagation in the fibrotic region is practically blocked. At densities of 10 and 20% the width of the vulnerable window increases with respect to control but is decreased at 40%.

Conclusion: Myocyte-fibroblast coupling characteristics heterogeneously affect AP propagation and features in the different atrial zones, and myocytes from the left atria are more sensitive to fibroblast coupling.

Keywords: atrial fibrillation, computer simulation, structural remodeling, myofibroblast, vulnerability

OPEN ACCESS

Edited by:
Natalia A. Trayanova, Johns Hopkins University, United States

Reviewed by:
Sanjay Ram Kharche, University of Western Ontario, Canada
Craig Henriquez, Duke University, United States
Oleg Aslanidi, King's College London, United Kingdom

***Correspondence:**
Beatriz Trenor
btrenor@eln.upv.es

Specialty section:
This article was submitted to Computational Physiology and Medicine, a section of the journal Frontiers in Physiology

Received: *16 December 2018*
Accepted: *19 June 2019*
Published: *04 July 2019*

Citation:
Sánchez J, Gomez JF, Martinez-Mateu L, Romero L, Saiz J and Trenor B (2019) Heterogeneous Effects of Fibroblast-Myocyte Coupling in Different Regions of the Human Atria Under Conditions of Atrial Fibrillation. Front. Physiol. 10:847. doi: 10.3389/fphys.2019.00847

INTRODUCTION

Atrial fibrillation (AF) is the most common cardiac arrhythmia and is becoming more prevalent with population aging (Iwasaki et al., 2011). In persistent atrial fibrillation (PeAF), lasting longer than 7 days (Kirchhof et al., 2016), spontaneous, pharmacological, or ablative resumption of sinus rhythm is infrequent with prompt recurrences or commonly failed cardioversions (Jalife and Kaur, 2015).

In PeAF, cardiac tissue experiences structural and electrical remodeling driven by changes of the extracellular matrix, fibroblast differentiation, fatty and inflammatory infiltration, and ion channel remodeling, among other alterations (Kirchhof et al., 2016). The heterogeneities in the atrial substrate cause fiber discontinuities and local conduction disturbances favoring re-entries (Nattel and Dobrev, 2017).

The atria have a complex anatomical structure, differences between the right and left atrium, and complex structures like the pulmonary vein or left and right appendages (Sanchez-Quintana et al., 2012; Ferrer et al., 2015). They all have their own electrophysiological characteristics, which determine specific action potential (AP) waveforms and conduction velocities (CV), which are crucial to AF pathophysiology.

Approximately 75% of the adult myocardium tissue volume is occupied by myocytes, accounting for only 30–40% of the total number of cells (Biernacka and Frangogiannis, 2011). Fibroblasts are considered as the predominant non-myocyte cell. They become active under inflammatory response and then differentiate into myofibroblasts (Chacar et al., 2017) by different pathways (e.g., oxidative stress, atrial dilatation, calcium overload, and inflammation), although the precise mechanisms have not yet been established (Jalife and Kaur, 2015). Myofibroblasts differ from fibroblasts in that they develop contractile proteins and exhibit a more depolarized resting membrane potential (Salvarani et al., 2017) and greater membrane capacitance (Sridhar et al., 2017). The differences in resting membrane potential and membrane capacitance between fibroblasts and myofibroblasts might have an important repercussion on the electrophysiology of coupled myocytes.

Recent experimental studies have shown that fibroblasts express voltage-dependent sodium channels allowing an inward current (I_{Na}) (Chatelier et al., 2012; Koivumäki et al., 2014a; Poulet et al., 2016). Although they are not electrically excitable they may affect the myocytes' electrophysiological properties (Gaudesius et al., 2003; Kohl et al., 2005; Miragoli et al., 2006). Several animal experimental models have shown that fibroblasts electrically couple to myocytes and alter their AP (Rook et al., 1992; Gaudesius et al., 2003; Burstein et al., 2007; Rohr, 2011; Jalife and Kaur, 2015; Jousset et al., 2016; Quinn et al., 2016). Kohl et al. (1994) found that fibroblasts reacted electrically with myocytes through gap junctions and this was later corroborated *in vitro* in several animal species (Gaudesius et al., 2003; Camelliti et al., 2004; Kohl et al., 2005). However, the extent of (*in vivo*) fibroblast-myocyte electrotonic coupling in native myocardium remains controversial (Kohl and Gourdie, 2014). Recently, a study by Quinn et al. (2016) showed the existence of tunneling nanotube connections between excitable and non-excitable cells (e.g., myofibroblasts) in cardiac scar border tissue at the border zone of the scar in mice hearts. Similarly, Burstein et al. (2007) observed fibroblasts proliferation and differentiation into myofibroblasts during AF *in vivo* canine hearts. Fibroblast proliferation has also been observed in human hearts (Krul et al., 2015; Fukumoto et al., 2016), in regions with altered conduction velocity, although electrical coupling has not been demonstrated.

Computational simulations of the cellular electrophysiology have become a powerful tool for studying the role that fibroblasts play in the atrial substrate (MacCannell et al., 2007; Maleckar et al., 2009; Koivumäki et al., 2014a). Their flexibility permits modifying the cellular electrophysiology and varying different characteristics to analyze the impact of electrotonic coupling with electrically remodeled myocytes in PeAF (McDowell et al., 2013; Morgan et al., 2014; Sridhar et al., 2017). MacCannell et al. (2007) formulated an active and a passive model for fibroblasts electrophysiology, considering a capacitance and an ohmic resistance in the first case and a capacitance and four ionic currents in the second case. The active model is more realistic and has a major impact on myocytes, this is why in the present study the active model is implemented. Simulations also offer the possibility of studying how fibroblasts can change arrhythmia dynamics by reducing CV and introducing heterogeneities in the atrial substrate (Tanaka et al., 2007; Saha et al., 2018).

The present simulation study analyzes the effects of fibroblast-myocyte coupling in PeAF in specific structurally and electrophysiologically remodeled atrial tissues and compares the effect of fibroblasts and myofibroblasts on myocyte AP features, tissue conduction velocity and vulnerability to re-entries.

MATERIALS AND METHODS

Myocyte Electrophysiological Models

The human atrial AP model proposed by Koivumäki et al. (2011) was used to simulate atrial APs. To reproduce the tissue electrophysiology of different anatomical atrial regions, we modified the conductance of five ionic currents: transient outward K^+ current (I_{to}), potassium rapid current (I_{Kr}), potassium slow current (I_{Ks}), time independent K^+ current (I_{K1}), and L-type Ca^{2+} current (I_{CaL}) as proposed in previous simulation studies (Krueger et al., 2012; Ferrer et al., 2015). The conductance values, shown in **Table 1**, were modified according to the experimental values to reproduce the AP waveform in all four regions: right atrium posterior wall (RA), crista terminalis (CT), left atrium posterior wall (LA), and the pulmonary vein (PV) areas.

Ionic Remodeling

Table 2 shows the values used to introduce AF electrical remodeling in all atrial regions by modifying ion channel conductances for I_{CaL}, I_{to}, I_{K1}, sustained outward K^+ current

TABLE 1 | Ionic conductance modifications.

Channel conductance	RA	LA	PV	CT
g_{to}	1.0	1.0	0.25	0.55
g_{Kr}	1.0	1.6	4.8	0.55
g_{CaL}	1.0	0.67	0.3	1.0
g_{K1}	1.0	1.0	0.7425	1.0
g_{Ks}	1.0	1.0	5.12	1.0

Relative values for each atrial region (right atrium -RA-, left atrium -LA-, pulmonary veins -PV- and crista terminalis -CT-) with respect to the maximum conductance of the potassium transient outward current (g_{to}), potassium rapid current (g_{Kr}), calcium L-type current (g_{CaL}), and potassium slow current (g_{Ks}) in the Koivumäki et al. (2011) model.

(I_{sus}), Na^+/Ca^{2+} exchanger (NCX), sarcoplasmic reticulum Ca^{2+} ATPase (SERCA) pump, and ryanodine receptors (RyR), and specific calcium handling parameters, such as phospholamban (PLB), sarcolipin (SLN), and the baseline phosphorylation (phos). Dilation was also modeled by increasing the length of the cell by a factor of 1.1 (see **Table 2**) as described in Koivumäki et al. (2014b).

Fibroblast Electrophysiological Model

Fibroblast electrophysiology was represented according to the Koivumäki et al. (2014a) model. Membrane sodium current was updated to match recent experimental results (Poulet et al., 2016) (see **Supplementary Table S1**). The uncoupled fibroblast resting membrane potential (RMP_f) was set to −45 or −26 mV, as suggested by experimental data (Poulet et al., 2016; Salvarani et al., 2017). These values were obtained by shifting the gating variable for the time dependent potassium current as in previous simulation studies (Maleckar et al., 2009; Morgan et al., 2016), and shown in **Supplementary Table S2**. The fibroblast membrane capacitance (C_{mf}) values were varied within experimental ranges (6.3 and 50.4 pF) (MacCannell et al., 2007; Xie et al., 2009; McArthur et al., 2015; Poulet et al., 2016; Sridhar et al., 2017). Following previous experimental and simulation studies, we set RMP_f to −45 mV and C_{mf} to 6.3 pF for atrial fibroblasts (MacCannell et al., 2007; Maleckar et al., 2009), and a more depolarized RMP_f of −26 mV and a C_{mf} of 50.4 pF for atrial myofibroblasts (Morgan et al., 2016; Poulet et al., 2016; Salvarani et al., 2017; Sridhar et al., 2017). The code is available and can be found at http://hdl.handle.net/10251/120395.

TABLE 2 | Atrial fibrillation electrical remodeling.

L_{cell}	g_{CaL}	g_{to}	g_{sus}	g_{K1}	K_{NaCa}	cpumps	PLB	SLN	phos	RyR
1.1	0.41	0.38	0.62	1.62	1.5	0.84	1.18	0.6	2	2

Based on experimental observations/prior computational works (Koivumäki et al., 2014b), to account for persistent atrial fibrillation remodeling the ionic and cellular parameters modified were: cell length (L_{cell}), conductance of calcium L-type current (g_{CaL}), conductance of potassium transient outward current (g_{to}), conductance of potassium sustained current (g_{sus}), conductance of potassium inward rectifier (g_{K1}), maximum conductance of Na+/Ca2+ exchanger (K_{NaCa}), conductance of sarcoplasmic reticulum Ca2+ ATPase (SERCA) pump (cpumps), phospholamban (PLB), sarcolipin (SLN), baseline phosphorylation (phos), and ryanodine receptors (RyR). The values indicate the factor by which the original values are multiplied.

Cellular Simulations (0D)

To compute the membrane potential in a cell, Equations (1, 2, and 3) were used:

$$C_{myo}\frac{dV_{myo}}{dt} + I_{ion-myo} + I_{gap} = 0 \quad (1)$$

$$C_{fib}\frac{dV_{fib}}{dt} + I_{ion-fib} - I_{gap} = 0 \quad (2)$$

$$I_{gap} = \sum_{i=0}^{n} G_{gap}\left(V_{myo} - V_{fib_i}\right) \quad (3)$$

where C_{myo} is the membrane capacitance of the myocyte, $I_{ion-myo}$ is the total ionic current flowing through ionic channels of the myocyte, V_{myo} is the membrane potential in the myocyte, C_{fib} is the membrane capacitance of the fibroblast, $I_{ion-fib}$ is the total ionic current flowing through ionic channels of the fibroblast, V_{fib} the membrane potential in the fibroblast, I_{gap} is the total ionic current flowing through the gap junction, n is the number of coupled fibroblasts to one myocyte and G_{gap} is the coupling conductance between myocyte and fibroblast. G_{gap} was set to 0.5 nS (Morgan et al., 2016), a value within the range of 0.3–8 nS measured in cultured myocyte-fibroblast experiments as used in previous simulation studies (MacCannell et al., 2007; Rook et al., 1992). The number of fibroblasts coupled to a single myocyte varied from 0 to 9 (Koivumäki et al., 2014a), as shown in **Supplementary Figure S1**.

Stabilization of the cellular model of each region was achieved after 1000 stimuli of 2 ms duration and an amplitude of twice the threshold value. After this number of stimuli, APD_{90} values and ion concentration ranges reached steady state. The basic cycle length (BCL) was 1 s, 250 ms, or 2 s.

The following features of the myocyte AP were measured: AP duration at 90% repolarization (APD_{90}), depolarization upstroke velocity measured as the maximum variation of the depolarization phase (dV/dt_{max}), and the RMP.

Strand and Tissue Simulations

The diffusion-reaction Eq. (4) of the monodomain formalism was used to simulate AP electrical propagation:

$$\nabla \cdot (D\nabla V) = C_m\frac{dV}{dt} + I_{ion} \quad (4)$$

where D is the diffusion tensor, C_m is the membrane capacitance, and I_{ion} stands for ionic currents through the membrane. Diffusion coefficients were adjusted for the different atrial regions to achieve physiological CVs along a strand of myocytes in this particular tissue.

Diffusion coefficients for myocytes (Dm) were calculated and adjusted to achieve physiological CVs, yielding a Dm of 3.84 cm^2/s in RA and LA (CV = 70 cm/s), a Dm of 6.384 cm^2/s in CT (CV = 100 cm/s), and a Dm of 4.081 cm^2/s in PV (CV = 80 cm/s). In PeAF, the diffusion coefficient was reduced by 50% to reproduce gap junction remodeling (Harrild and Hen, 2000; Ten Tusscher et al., 2004; Krogh-madsen et al., 2012; McDowell et al., 2012).

For one-dimensional simulations (1D), a strand with a space discretization of 100 μm was used for myocytes (Satoh et al., 1996; Courtemanche et al., 1998; Nygren et al., 1998; Sachse et al., 2008) and 10 μm for fibroblasts-myofibroblasts (Sachse et al., 2008; Xie et al., 2009; Brown et al., 2015). Fibroblasts-myofibroblasts were randomly distributed along the strand at different densities (10, 20, and 40%) using a uniform random probabilistic function. One hundred random distributions were generated for each density value (see **Supplementary Figure S3**). The strand was paced with a BCL of 1 s for 50 s. The first element of the strand was stimulated with an amplitude of twice its threshold. CV was measured in the 50th pulse. The diffusion coefficient for elements with fibroblasts was halved with respect to the myocyte elements (Vasquez et al., 2004; Gomez et al., 2014b; Morgan et al., 2016).

Two-dimensional (2D) meshes representing cardiac tissues for RA and LA were built with a central fibrotic region of 2 cm diameter with different randomly distributed myofibroblast densities. Ten random distributions were implemented for each density (see **Supplementary Figures S1**, **S3**). The tissue grid had 524 × 524 elements with a spatial resolution of 100 μm. An anisotropic ratio of 2.86:1 was considered in RA and LA (Ferrer et al., 2015).

To study the effect of myofibroblasts on vulnerability to reentry, reentrant activity was generated using cross-field stimulation protocol S1-S2. S1 stimuli consisted of 10 pulses applied to the left border of the computational mesh to stabilize the tissue and S2 was applied to the bottom left corner of the tissue.

In order to obtain the instantaneous location of the rotors, we used phase singularity (PS) detections (Sabir et al., 1974; Gray et al., 1998; Gomez et al., 2014a; Martinez-Mateu et al., 2018) first building phase maps based on the Hilbert transform (HT) of the APs (Warren et al., 2003; Yamazaki et al., 2012) (5) by computing the instantaneous phase θ (6), whose values ranged from -π to π radians:

$$\mathrm{HT}\left[V\left(\mathrm{t}\right)\right] = \frac{1}{\pi} \cdot \int_{-\infty}^{\infty} \frac{\mathrm{V}\left(\tau\right)}{\mathrm{t}-\tau} \cdot \mathrm{d}\tau \quad (5)$$

$$\theta = \tan^{-1}\left(\frac{\mathrm{HT}\left[\mathrm{V}\left(\mathrm{t}\right)\right]}{\mathrm{V}\left(\mathrm{t}\right)}\right) \quad (6)$$

where V is the membrane potential. Then PSs, where all phases converge (7), were computed to track the rotor trajectory:

$$\oint \nabla\theta dr = \pm 2\pi \quad (7)$$

Phase singularity detections were also used to assess heterogeneity degree in the tissue due to the inclusion of fibrotic regions.

Implementation

The differential equations of the cellular models were solved using the Rush-Larsen method for the gating variables and the forward Euler method for all other ordinary differential equations with a time step of 10 μs. The monodomain Eq. (4) was solved using the finite elements method with "no flux" boundary condition.

Simulations were implemented in C++ and CUDA languages. Computations were performed on an Intel(R) Xeon(R) CPU E5-2603v3 processor with an NVIDIA Tesla K40c graphic card (see **Supplementary Figure S2**).

RESULTS

Cellular Simulations

Figure 1 shows the APs obtained in cellular simulations with a BCL of 1000 ms under normal sinus rhythm (Panel A) and PeAF (Panel B) conditions, highlighting the differences in APD_{90} for each atrial region. Under physiological conditions, the APD_{90} was 236.4 ms for RA, 214 ms for LA, 176.1 ms for PV, and 292.8 ms for CT. However, under PeAF conditions APD_{90} was 165.5 ms, 139.8 ms, 120.8 ms, and 180.2 ms for the RA, LA, PV, and CT, respectively. APD_{90} decreased by 40% for RA, LA, and CT and by approximately 30% for PV with respect to normal conditions (see Panel C). In PaAF, in addition to APD shortening, RMP dropped from −75 to −79 mV, and dV/dt_{max} increased from 163 V/s to 168 V/s for RA, CT, and LA. RMP fell from −68 to −78 mV, and dV/dt_{max} rose from 157 V/s to 165 V/s for PV (see Panels E and D).

When fibroblasts were coupled to a single myocyte, we analyzed the effect of their electrophysiological characteristics (RMP_f and C_{mf}) on myocyte electrical behavior (see **Figure 2**). When the number of coupled fibroblasts increased, the myocyte RMP became more depolarized and moved closer to the value of RMP_f. A higher C_{mf} value seemed to further reduce myocyte APD when RMP_f was −45 mV.

Figure 3 shows the effect of myocyte fibroblast coupling at different BCLs. As can be seen in Panel A, at a BCL of 300 ms myocyte AP was barely affected by coupling 1 fibroblast. APD_{90} was very slightly reduced at both RMP_f values (purple and green traces in panel A), for all BCLs.

In panel B at higher C_{mf} the effect on APD_{90s} was similar to Panel A, except for the fact that an RMP_f of −26 mV, APD_{90} was slightly higher than for an RMP_f of −45 mV, for all BCLs. As the number of fibroblasts increased (Panels C–F), the effects changed with the electrical characteristics of the fibroblasts and the BCL. Panels C and D show that for a different RMP_f, APD_{90} changed with BCL. Longer APD_{90s} were obtained for BCLs of 500 ms and 1000 ms for a RMPf of −26 mV. In Panel D, for a BCL of 300 ms, APD alternans arose, and APD_{90} increased with higher BCL at an RMPf of −26 mV. When the number of coupled fibroblasts increased (Panels E and F), APD_{90} was reduced to 50 ms for −45 mV and all BCLs and to less than 40 ms for an RMP_f of −26 mV.

We also analyzed myocyte RMP and dV/dt_{max} (see **Figure 4**). Myocyte RMP (Panel B) changed similarly when C_{mf} increased for both RMP_f values (−26 mV and −45 mV). Increasing the number of fibroblasts moved the myocyte RMP closer to RMP_f. The most significant change was in the dV/dt_{max} (Panel A), which was much lower at an RMP_f of −26 mV than the reduction obtained at an RMPf of −45 mV. When fibroblasts couple to myocytes their RMP_f move closer to each other and more Na^+ channels are available,

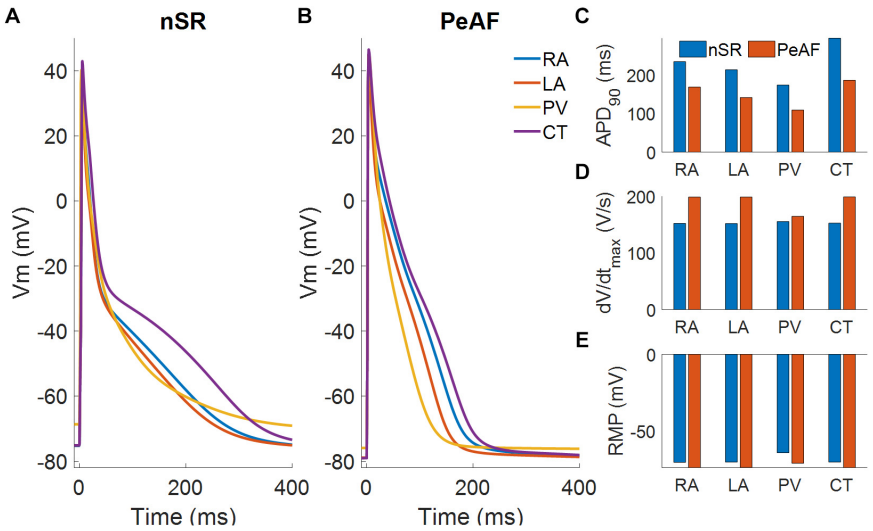

FIGURE 1 | Myocyte action potentials from four different regions of the atria: right atria (RA), left atria (LA), pulmonary vein (PV), and crista terminalis (CT). **(A)** Myocyte action potentials under normal sinus rhythm (nSR). **(B)** Myocyte action potentials under the effect of electrical remodeling during persistent atrial fibrillation (PeAF). **(C)** Myocyte action potential duration (APD_{90}) under nSR and PeAF. **(D)** Myocyte action potential maximum upstroke velocity (dV/dt_{max}) under nSR and PeAF. **(E)** Myocyte action potential resting membrane potential (RMP) under nSR and PeAF.

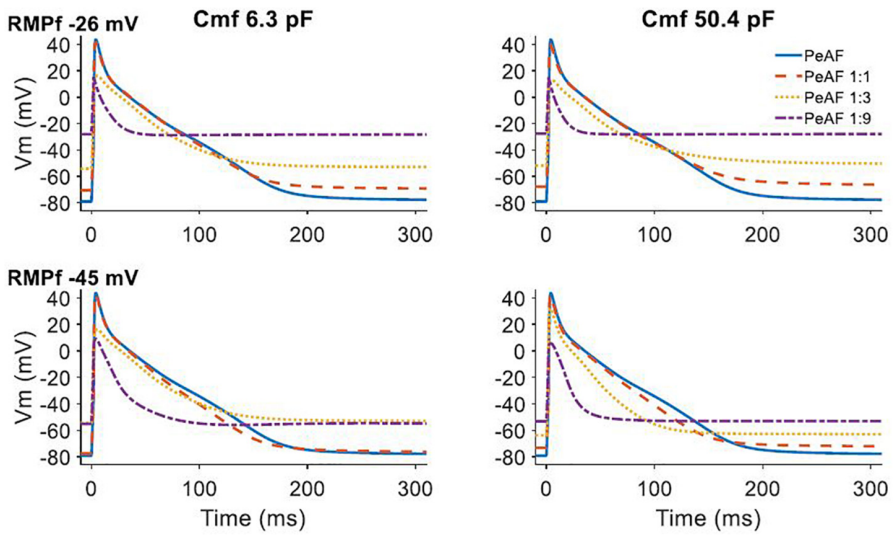

FIGURE 2 | Effect of fibroblast and myocyte coupling under persistent atrial fibrillation (PeAF) electrical remodeling in RA (baseline model). First and second rows show fibroblasts resting membrane potential (RMPf) of –26 and –45 mV, respectively, for a fibroblast membrane capacitance (Cmf) of 6.3 pF (first column) and 50.4 pF (second column). The different traces are action potentials of isolated myocytes under PeAF (blue), one myocyte under PeAF coupled to 1 fibroblast (1:1) (dashed orange), one myocyte under PeAF coupled to three fibroblasts (1:3) (dotted yellow), and one myocyte under PeAF coupled to nine fibroblasts (1:9) (dotted-dashed purple).

although myocyte Na^+ channel availability can be reduced due to a more depolarized RMP according to the number of coupled fibroblasts.

The experimental data agree with previous simulation studies in which fibroblasts presented an RMP of around −45 mV and a C_{mf} of 6.3 pF, while myofibroblasts have a more depolarized RMPf of −26 mV and a C_{mf} of 50.4 pF (Sridhar et al., 2017). In all the different atrial zones we analyzed the effects of coupling three fibroblasts or three myofibroblasts to a single myocyte (see **Figure 5**).

Panel A in **Figure 5** shows how APD_{90} was reduced when fibroblasts were coupled for all BCLs. When myofibroblasts were coupled, for a BCL of 300 ms APD alternans arose and for a BCL of 1000 ms APD_{90} increased. Panel B shows APD_{90s} in LA for different BCLs and similar fibroblast and myofibroblasts effects. The reduced APD_{90} in the PV case (Panel C) seems to be more

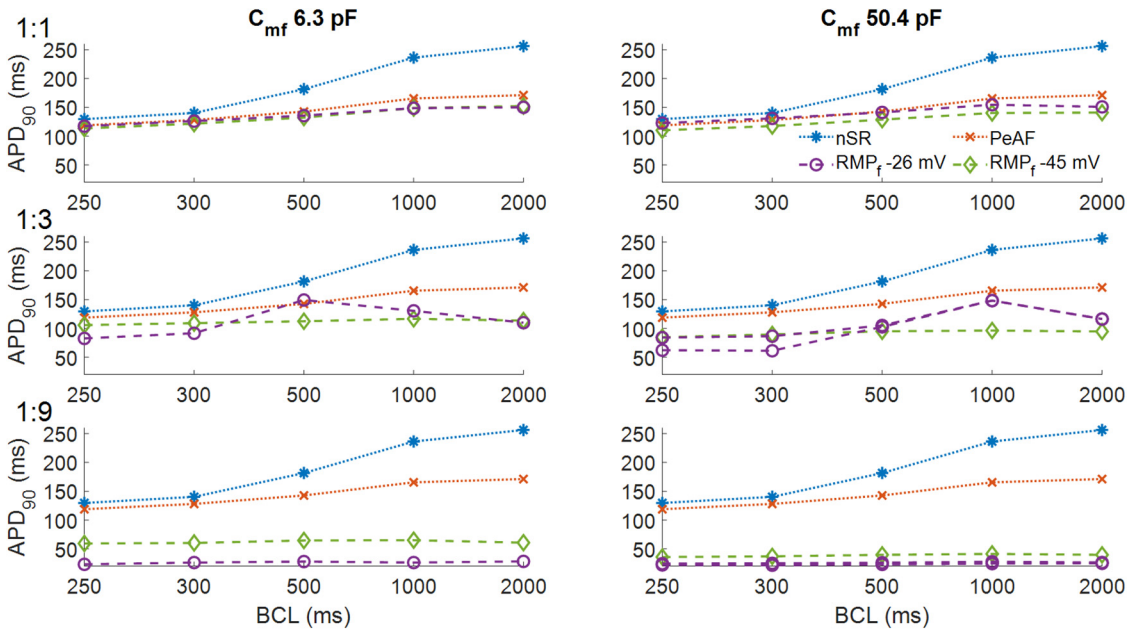

FIGURE 3 | Action potential durations of myocytes in normal sinus rhythm (nSR), under persistent atrial fibrillation electrical remodeling (PeAF) and after being coupled to fibroblasts with a resting membrane potential (RMPf) of –26 or –45 mV in RA (baseline model). In the first column the membrane capacitance of fibroblasts is 6.3 pF and in the second column 50.4 pF. One myocyte was coupled to one fibroblast (1:1) (first row), three fibroblasts (1:3) (second row), and nine fibroblasts (1:9) (third row).

pronounced in myofibroblast coupling. CT alternans also arose when myofibroblasts were coupled.

1D Strand Simulations

Conduction velocity in the atria changes locally according to the region's characteristics, as shown in **Figure 6**. During nSR and without fibroblasts, the RA has a CV of 70 cm/s, CT has a CV of 100 cm/s, LA has a CV of 70 cm/s, and PV has a CV of 80 cm/s (blue discontinuous lines) (Ferrer et al., 2015). AP propagation along the strand was affected by PeAF electrical remodeling (red discontinuous lines) and CVs dropped significantly. At higher fibroblast (yellow) or myofibroblasts (green) densities in the strand, CV dropped. Boxplot measurements of the CV are represented for the 100 random distributions of fibroblasts for each density (10, 20, and 40%). The region with the greatest differential effect on CV was the PV, depending on whether the distribution was with fibroblasts or myofibroblasts. PV also experienced conduction blocks in some of the random distributions (indicated by yellow asterisks). Conduction block was also seen in LA at a density of 40% in some distributions.

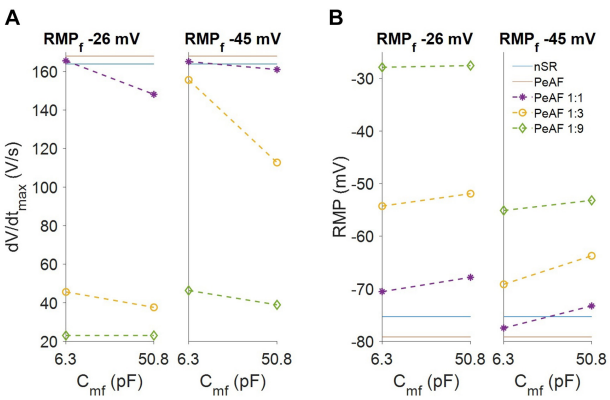

FIGURE 4 | Fibroblasts coupling effect on myocyte electrophysiology. **(A)** Myocyte maximum upstroke velocity (dV/dt_{max}). **(B)** Myocyte resting membrane potential (RMP). The levels for myocytes in normal sinus rhythm (nSR) and persistent atrial fibrillation (PeAF) conditions are given in blue and red, respectively. Discontinuous lines are myocytes in PeAF coupled to one fibroblast (1:1), 3 (1:3), or 9 (1:9).

2D Tissue Simulations

The 2D atrial tissue electrical activity in PeAF with different myofibroblast densities was analyzed to assess vulnerability to reentry. **Figure 7** shows snapshots of phase maps (taken at the same time). Re-entrant circuits can be seen in the RA (top panels) and in the LA (bottom panels) in PeAF remodeling and increasing levels of myofibroblast density from left to right (membrane potential snapshots can be seen in **Supplementary Figure S4**). In the absence of myofibroblasts a functional reentry was obtained in RA and LA. The tip of these rotors (**Figure 7**, first column), corresponding to the PS superimposed in white on the phase maps, describes a regular circular path, which agrees with the results obtained in previous simulation studies (Wilhelms et al., 2013). In LA, the rotor tip describes a smaller path due to the shorter wavelength caused by shorter

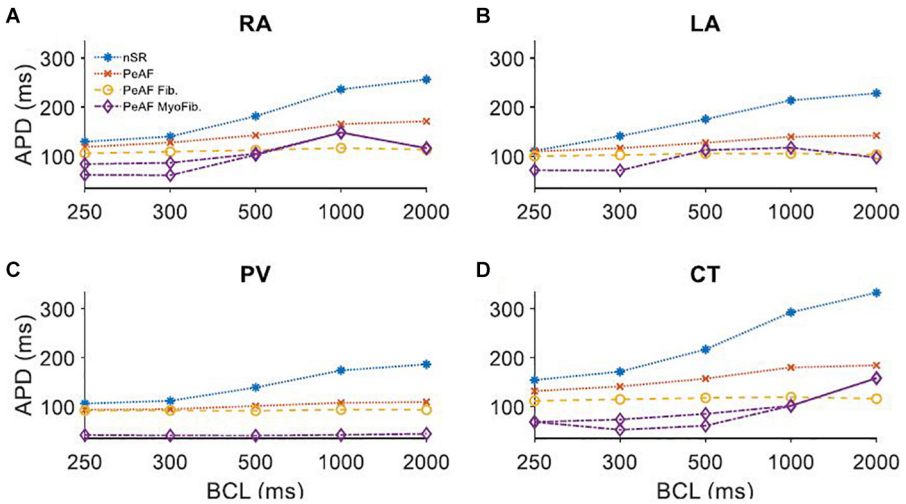

FIGURE 5 | Myocyte action potential duration (APD) of four different regions of the atria under persistent atrial fibrillation electrical remodeling (PeAF) coupled to three fibroblasts (Fib) or myofibroblasts (MyoFib) stimulated at different basic cycle lengths (BCLs). **(A)** Right atria (RA), **(B)** Left atria (LA), **(C)** Pulmonary vein (PV), and **(D)** Crista terminalis (CT).

LA ERP (Fernandez-Lozano et al., 2006; Krueger et al., 2012; Ferrer et al., 2015).

When myofibroblasts were present in the center of the tissue (see section "Materials and Methods"), the obstacle altered the reentrant activity. Small percentages of myofibroblasts (10–20%) allowed the wavefront to propagate through the fibrotic region, but the electrophysiological heterogeneities of myofibroblasts and myocytes caused wavebreaks, which were detected as PSs (quantified in **Supplementary Table S3**). However, propagation in the fibrotic region was practically blocked when myofibroblast density was raised to 40%, which produced an anatomical reentry surrounding the fibrotic obstacle. Since the wavefront did not propagate through the fibrotic region the number of wavebreaks was significantly reduced, as were the number of PSs detected (see **Supplementary Table S3**).

The myofibroblasts in the tissue increased reentry vulnerability, measured as the vulnerable window (VW), a time interval for which premature S2 stimulation generates a reentry (**Figure 8**). In the RA the vulnerable window in the absence of myofibroblasts was 37 ms. When myofibroblasts density was raised to 10%, the VW increased to 38 ± 0.0 ms. VW also increased (39 ± 0.63 ms) when density was raised to 20%, but at 40% VW dropped below the control value (35 ± 0.82 ms). Interestingly, LA was more sensitive to myofibroblasts with a larger VW than the RA. The LA VW in the absence of myofibroblasts was 40 ms. When myofibroblast density was raised to 10%, VW rose to 40 ± 0.0 ms, at 20% it increased to 40.5 ± 0.53 ms and at 40% it dropped to 38 ± 0.88 ms.

DISCUSSION

Computational modeling was used to investigate the effect of coupling fibroblasts and myofibroblasts to myocytes in four different regions of the atria during persistent AF. The study's major findings can be summarized as follows: (i) myocyte-fibroblast coupling heterogeneously shortens myocyte APD and depolarizes the myocyte resting membrane potential in the 4 different atrial regions These effects strongly depend on the fibroblast electrophysiology. (ii) Fibroblasts, and specially myofibroblasts, introduce heterogeneities in the atrial substrate which alter the propagation of the AP, slowing conduction velocity. (iii) Fibroblasts-myofibroblasts change the atrial substrate during PeAF, which alters the vulnerability to re-entries and the vulnerable window presents a biphasic behavior related to myofibroblast density. These results suggest that the heterogeneity of the atrial tissue in the presence of fibroblasts/myofibroblats promotes reentrant events and alters the dynamics of arrhythmogenic propagation.

Heterogeneous Effects of PeAF Remodeling and Electrical Coupling of Fibroblasts in Atrial Tissues

Atrial substrate is differently affected by PeAF remodeling and by the presence of fibroblasts, due to the electrophysiological heterogeneity of the different atrial regions. Our results from isolated single cells show differences in the RMP, dV/dt_{max}, and APD for the four different atrial regions (RA, LA, CT, and PV) in nSR and in PeAF. These differences are in agreement with the simulations carried out by Krueger et al. (2013), who reported the differential effects of AF remodeling in the different atrial regions. It has to be noted that in contrast to the Krueger study, our model presents a long-term stability in all regions in single-cell and tissue simulations and also considers the effect of fibroblast coupling. To our knowledge, this is the first simulation study including the three components (atrial heterogeneity, AF remodeling, and fibroblasts) using a detailed electrophysiological AP model for fibroblasts and focusing on the analysis of the different effects exerted by

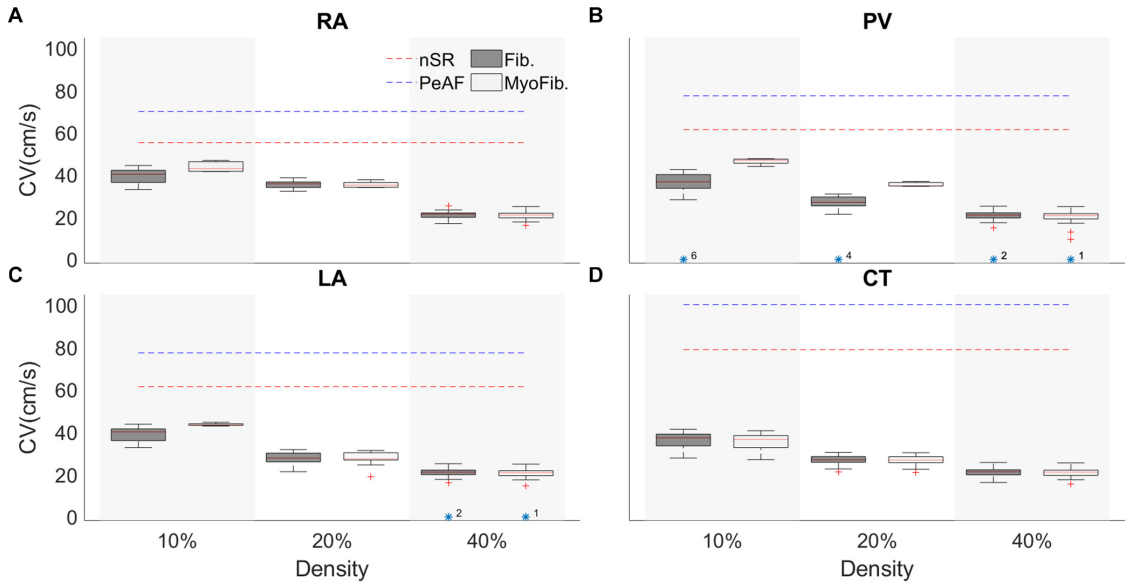

FIGURE 6 | Conduction velocity (CV) of a tissue strand in four different regions of the atria with random fibroblasts (Fib) or myofibroblast (MyoFib) distribution and different fibroblast densities. For each density 100 random configurations were simulated. CV measurements are represented in boxplots. **(A)** Right atria (RA). **(B)** Pulmonary vein (PV), **(C)** Left atria (LA), and **(D)** Crista terminalis (CT).

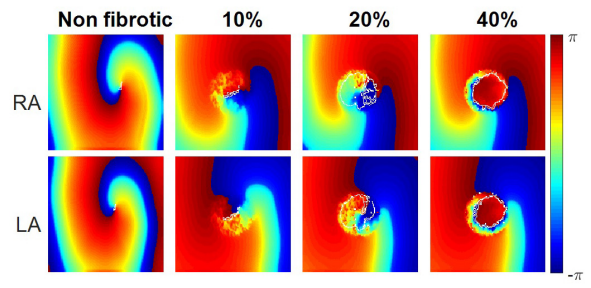

FIGURE 7 | Instantaneous phase maps and phase singularities (in white) for different densities of myofibroblasts (non-fibrotic, 10, 20, and 40%) in the right atria (RA) and left atria (LA) under conditions of persistent AF remodeling.

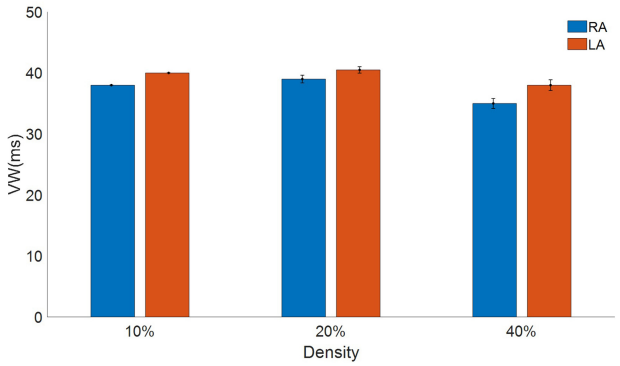

FIGURE 8 | Vulnerable window to reentry in atrial tissue with different densities of myofibroblasts indicated in percentage for the right atrial (RA) in blue and the left atrial (LA) in red subject to persistent atrial fibrillation remodeling.

fibrosis in the different atrial regions. A recent study by Roney et al. (2018) showed that high PS density in the PVs favored the effectiveness of PV isolation in ablation procedure. Their model also considered electrophysiological remodeling in AF, electrophysiological heterogeneities in different atrial regions, and fibrosis was simulated by changes in tissue conductivity. In a previous study (Roney et al., 2016), the same group modeled fibrosis by different methods and did not consider either electrophysiological heterogeneities in the atrial regions or AF remodeling to determine how different fibrosis models could affect rotor dynamics.

Different experimental studies show that atrial fibroblasts have a different electrophysiology from ventricular fibroblasts (MacCannell et al., 2007; Burstein and Nattel, 2008; Poulet et al., 2016; Salvarani et al., 2017). Morgan et al. (2016) found that fibroblast electrophysiology changes the dynamics of an arrhythmic process and provides relevant information on the effect of myocyte-fibroblast coupling in the atria. Our results indicate that RMPf, C_{mf}, and the number of coupled fibroblasts altered the behavior of myocytes AP, as was found in previous simulation studies (Maleckar et al., 2009; Koivumäki et al., 2014a; Sridhar et al., 2017). Furthermore, in the present study we found that introducing I_{Na} current into the fibroblast model had an interesting effect; due to the high RMP of isolated fibroblasts I_{Na} current was blocked but when fibroblasts were coupled with myocytes I_{Na} channels became available. Additionally, myocyte-fibroblast coupling led to a partial inactivation of the myocyte I_{Na} due to the higher RMP in the myocyte.

Fibroblast electrophysiology (RMPf and C_{mf}) changes myocyte AP characteristics (Jacquemet and Henriquez, 2008, 2009; Maleckar et al., 2009). Our simulation results also show that electrical coupling with myocytes increases atrial electrophysiological heterogeneity. Changes in the BCL altered the behavior of the coupled cells, with different responses in different regions. Interestingly, myofibroblast -myocyte coupling in regions with higher I_{K1} and I_{CaL} (RA and CT) exhibited more sensitivity to changes in frequency, while regions with smaller I_{K1} and I_{CaL} (PV) developed no AP for any of the BCLs. In contrast to McDowell et al. (2013), we defined different electric characteristics for the atrial myofibroblasts, which have a different effect on myocyte AP. Myofibroblasts act as the current source, raising the myocyte RMP (Jacquemet and Henriquez, 2007) according to the number of coupled myofibroblasts (Maleckar et al., 2009; Koivumäki et al., 2014a), thus leading to a partial inactivation of the myocyte I_{Na} current (see **Supplementary Figure S5**).

Heterogenous Effects of Fibrosis During PeAF in Atrial Tissues

Structural remodeling of the cardiac tissue contributes to reducing conduction velocity, delaying regional functional activations, and increasing structural heterogeneities, which are important factors for establishing a re-entrant driver or conduction block (Camelliti et al., 2005). Our results show that fibroblasts and myofibroblasts can alter the activation time in a 1D tissue strand, in agreement with different studies (Sachse et al., 2008; Xie et al., 2009). We implemented one hundred random configurations for different fibroblast/myofibroblast densities in the four atrial regions. Zhan et al. (2014) showed that fibroblasts can alter the CV and can lead to blocks in conduction with fibrosis densities of 40 and 45%, our results showed that a high density (40%) led to conduction blocks in the LA and that the PV was the most sensitive region to the presence of fibroblasts-myofibroblasts. Similarly, in an experimental study Miragoli et al. (2006) showed that myofibroblast proliferation changed the tissue conduction velocity and myocyte dV/dt_{max}. Our results showed a reduction in CV, in agreement with several other experimental and simulation studies that found that fibroblasts-myofibroblasts can establish an electric coupling with myocytes, reducing their dV/dt_{max} and activation time, reflected in reduced CV (Miragoli et al., 2006; Rohr, 2009; Xie et al., 2009; Yue et al., 2011). We also found a monotonic reduction in all four atrial regions.

Tanaka et al. (2007) have shown that local fibrosis distribution reduces CV in the different atrial regions, in agreement with our results, which showed a reduced CV with a tendency to homogenize in all four atrial regions. CV heterogeneity is responsible for giving the atria the characteristic activation times (Nguyen et al., 2012); if all the regions were to have a homogenous CV, this might induce the appropriate conditions for reentrant rhythms and conductions blocks (Gaspo et al., 1997). As the fast conduction systems' (CT) conduction velocity was significantly reduced, this may be an interesting mechanism for AF in the right atrium.

Vulnerability to Reentry During PeAF in Fibrotic Tissue

Structural remodeling and endo-epicardial dissociation alter the atrial substrate and could produce macroreentries and focal activity (Everett and Olgin, 2007; Verheule et al., 2014). When, we analyzed the propagation in different regions of the atria and at different myofibroblast densities, we found that a low myofibroblasts percentage increased the number of PSs due to the wavebreaks. However, at higher percentages, propagation through the fibrotic zone was blocked, the number of wavebreaks and PSs decreased, and an anatomical reentry was anchored around the fibrotic zone, in agreement with previous studies (McDowell et al., 2013; Roney et al., 2016). Several simulation studies have also shown that reentry dynamics is altered by heterogeneities of the AP in the cardiac tissue (Colman et al., 2014; Varela et al., 2016), the presence of fibroblasts (Ashihara et al., 2012; Gomez et al., 2014a; Morgan et al., 2016), and that PSs increase in the zones with fibroblasts (Saha et al., 2018).

Waks and Josephson (2014) demonstrated that the rotation dynamics depends on the atrial tissue (RA or LA) and its electrophysiological characteristics, as did we in the present study, in which vulnerability to reentries and the dynamics of the rotation depended on the atrial region. LA presented slightly higher VWs, due to its shorter APD.

Gomez et al. (2014b) showed that the density of fibroblasts had a biphasic impact on the ventricular vulnerable window for reentry, while our results showed the same VW biphasic behavior for the first time in atrial tissue. Krul et al. (2015) found that local fibrosis is associated with reentrant activity, comparable to our results at low fibroblast density (10%), which can be considered as a region of local diffuse fibrosis, presented higher tissue vulnerability and resulted in multiple wavebreaks. When myofibroblast density was raised (20%), tissue vulnerability to reentry rose and conduction blocks occurred. However, at higher densities (40%) the conduction blocks also occurred but VW dropped, as was found by Campos et al. (2018). This suggests that myocyte-fibroblast coupling in PeAF plays an important role in AF (Morgan et al., 2014), with different effects in different atrial regions.

Limitations

Several limitations must be considered when drawing conclusions from the present study. Firstly, we did not consider the effect of electrical remodeling due to cytokines like TGF-B, which have been reported during structural remodeling and are known to affect myocyte AP (Burstein and Nattel, 2008; Nattel et al., 2008; Zahid et al., 2016).

Secondly, as fibroblast electrophysiology and differentiation into myofibroblasts still remain unclear, the models we used should be considered as an approximation (Nattel, 2018). Myofibroblast electrophysiological characteristics are still not well understood. Furthermore, it is important to highlight that although animal models and *in vitro* experiments prove the existence of electrotonic coupling between myocytes and fibroblasts (Kohl et al., 2005; Miragoli et al., 2006; Grand et al., 2014; Salvarani et al., 2017), this has not been reported in humans

in vivo. However, human cardiac tissue with fibrosis presents altered electrical behavior (Krul et al., 2015; Fukumoto et al., 2016).

Thirdly, the pulmonary vein AP model was built on the basis of the reported experimental data for dogs and sheep APD_{90} and RMP. Electrophysiological data from human isolated myocytes from PV are still unavailable (Ehrlich et al., 2003).

Fourthly, while AF mechanisms are still unclear, there are different pathways by which reentrant drivers can be generated and maintained. Several studies have shown how non-myocyte cells like fibroblasts, macrophages (Hulsmans et al., 2017) and adipocytes (De Coster et al., 2018) alter the atrial substrate and promote arrhythmias. The effects of non-myocytes or endo-epicardial dissociation have not been considered in the present study, although these are factors which might alter the reentry dynamics and would be interesting to analyze in future studies (Verheule et al., 2014).

Fifthly, we are aware that fibrosis is a complex structure involving different actors such as collagen deposition, inflammatory cytokines and proteins which may alter the myocyte electrophysiology. There are different approaches to simulating the fibrotic regions such as non-conductive elements (Ten Tusscher et al., 2004), the paracrine effect changing the myocyte ion channel conductance (Zahid et al., 2016) and coupling to elements with a static RMP (Majumder et al., 2011) and using ionic models to describe the electrophysiology of fibroblasts (McDowell et al., 2013; Morgan et al., 2016; Saha et al., 2018).

Finally, we did not include the effect of different sizes or locations of fibrotic regions in the tissue. The fibrotic regions can in fact attract rotors (Roy et al., 2018), and future studies in this line would shed light into the mechanisms of chaotic rhythms when fibroblasts proliferate. Additionally, 3D simulations have shown how fibroblasts and non-conductive areas can modify the dynamics of the reentry (McDowell et al., 2013; Morgan et al., 2014). Zahid et al. (2016) introduced the paracrine effect, modifying myocyte electrophysiology in the fibrotic region in 3D simulations reducing the AP duration and the conductivity of the fibrotic region. We are also aware that 3D simulations include further structural details. The work by Ferrer et al. (2015), among others, presents a highly detailed atrial model. However, these simulations have a high computational cost while 2D simulations are computationally more efficient and provide a detailed insight into arrhythmia dynamics. Despite these limitations, we consider that our simulations represent a realistic heterogeneous PeAF remodeling (electrophysiological and structural) scenario in the different atrial regions and contribute a great deal to the understanding of AF mechanisms.

CONCLUSION

The results of the present simulation study show that fibroblast electrophysiology alters myocyte AP characteristics and leads to slower conduction velocity in atrial tissues affected by PeAF. These changes are heterogeneous within the different atrial regions.

Myocyte-fibroblast coupling creates a substrate in which the dynamics of arrhythmic reentries changes with the fibroblast density. By increasing the density of fibroblasts, reentries evolve from functional to anatomical around the obstacle formed by the fibrotic region. We also observed biphasic behavior of tissue vulnerability to reentries. Low myofibroblast densities (10 and 20%) increase the vulnerability to reentry, while a higher density (40%) reduces tissue vulnerability.

AUTHOR CONTRIBUTIONS

JoS, JaS, and BT contributed to the conception and design of the study. JG, LR, and LM-M contributed to the development of the model. JoS performed the computational simulations and JoS, JaS, and BT performed the analysis and interpretation of the results. All authors contributed to drafting of the manuscript and all revised, and approved the submitted version.

FUNDING

This work was supported by the "Plan Estatal de Investigación Científica y Técnica y de Innovación 2013–2016" from the Ministerio de Economía, Industria y Competitividad of Spain and Fondo Europeo de Desarrollo Regional (FEDER) DPI2016-75799-R (AEI/FEDER, UE), and by the Dirección General de Política Científica de la Generalitat Valenciana (PROMETEU 2016/088).

SUPPLEMENTARY MATERIAL

The Supplementary Material for this article can be found online at: https://www.frontiersin.org/articles/10.3389/fphys.2019.00847/full#supplementary-material

REFERENCES

Ashihara, T., Haraguchi, R., Nakazawa, K., Namba, T., Ikeda, T., Nakazawa, Y., et al. (2012). The role of fibroblasts in complex fractionated electrograms during persistent/permanent atrial fibrillation: implications for electrogram-based catheter ablation. *Circ. Res.* 110, 275–284. doi: 10.1161/CIRCRESAHA.111.255026

Biernacka, A., and Frangogiannis, N. G. (2011). Aging and cardiac fibrosis. *Aging Dis.* 2, 158–173. doi: 10.1016/j.bbi.2008.05.010

Brown, T. R., Krogh-Madsen, T., and Christini, D. J. (2015). Computational approaches to understanding the role of fibroblast-myocyte interactions in cardiac arrhythmogenesis. *Biomed. Res. Int.* 2015:465714. doi: 10.1155/2015/465714

Burstein, B., and Nattel, S. (2008). Atrial fibrosis: mechanisms and clinical relevance in atrial fibrillation. *J. Am. Coll. Cardiol.* 51, 802–809. doi: 10.1016/j.jacc.2007.09.064

Burstein, B., Qi, X. Y., Yeh, Y. H., Calderone, A., and Nattel, S. (2007). Atrial cardiomyocyte tachycardia alters cardiac fibroblast function: a novel

consideration in atrial remodeling. *Cardiovasc. Res.* 76, 442–452. doi: 10.1016/j.cardiores.2007.07.013

Camelliti, P., Borg, T. K., and Kohl, P. (2005). Structural and functional characterisation of cardiac fibroblasts. *Cardiovasc. Res.* 65, 40–51. doi: 10.1016/j.cardiores.2004.08.020

Camelliti, P., Devlin, G. P., Matthews, K. G., Kohl, P., and Green, C. R. (2004). Spatially and temporally distinct expression of fibroblast connexins after sheep ventricular infarction. *Cardiovasc. Res.* 62, 415–425. doi: 10.1016/j.cardiores.2004.01.027

Campos, F. O., Shiferaw, Y., Weber dos Santos, R., Plank, G., and Bishop, M. J. (2018). Microscopic isthmuses and fibrosis within the border zone of infarcted hearts promote calcium-mediated ectopy and conduction block. *Front. Phys.* 6:57. doi: 10.3389/fphy.2018.00057

Chacar, S., Farès, N., Bois, P., and Faivre, J.-F. (2017). Basic signaling in cardiac fibroblasts. *J. Cell. Physiol.* 232, 725–730. doi: 10.1002/jcp.25624

Chatelier, A., Mercier, A., Tremblier, B., Thériault, O., Moubarak, M., Benamer, N., et al. (2012). A distinct de novo expression of Na v 1.5 sodium channels in human atrial fibroblasts differentiated into myofibroblasts. *J. Physiol.* 590, 4307–4319. doi: 10.1113/jphysiol.2012.233593

Colman, M. A., Varela, M., Hancox, J. C., Zhang, H., and Aslanidi, O. V. (2014). Evolution and pharmacological modulation of the arrhythmogenic wave dynamics in canine pulmonary vein model. *Europace* 16, 416–423. doi: 10.1093/europace/eut349

Courtemanche, M., Ramirez, R. J., and Nattel, S. (1998). Ionic mechanisms underlying human atrial action potential properties: insights from a mathematical model. *Am. J. Physiol.* 275, H301–H321. doi: 10.1152/ajpheart.1998.275.1.H301

De Coster, T., Claus, P., Kazbanov, I. V., Haemers, P., Willems, R., Sipido, K. R., et al. (2018). Arrhythmogenicity of fibro-fatty infiltrations. *Sci. Rep.* 8, 2050. doi: 10.1038/s41598-018-20450-w

Ehrlich, J. R., Cha, T.-J., Zhang, L., Chartier, D., Melnyk, P., Hohnloser, S. H., et al. (2003). Cellular electrophysiology of canine pulmonary vein cardiomyocytes: action potential and ionic current properties. *J. Physiol.* 551, 801–813. doi: 10.1113/jphysiol.2003.046417

Everett, T. H., and Olgin, J. E. (2007). Atrial fibrosis and the mechanisms of atrial fibrillation. *Hear. Rhythm* 4, S24–S27. doi: 10.1016/j.hrthm.2006.12.040

Fernandez-Lozano, I., Toquero-Ramos, J., Escudero-Vela, C., Castedo-Mejuto, E., Escudier-Villa, J. M., and Alonso-Pulpon, L. (2006). [Left atrial posterior wall and pulmonary vein refractory periods are associated with atrial fibrillation inducibility in a swine model]. *Rev. Esp. Cardiol.* 59, 653–661.

Ferrer, A., Sebastián, R., Sánchez-Quintana, D., Rodríguez, J. F., Godoy, E. J., Martínez, L., et al. (2015). Detailed anatomical and electrophysiological models of human atria and torso for the simulation of atrial activation. *PLoS One* 10:e0141573. doi: 10.1371/journal.pone.0141573

Fukumoto, K., Habibi, M., Ipek, E. G., Zahid, S., Khurram, I. M., Zimmerman, S. L., et al. (2016). Association of left atrial local conduction velocity with late gadolinium enhancement on cardiac magnetic resonance in patients with atrial fibrillation. *Circ. Arrhythm. Electrophysiol.* 9:e002897. doi: 10.1161/CIRCEP.115.002897

Gaspo, R., Bosch, R. F., Talajic, M., and Nattel, S. (1997). Functional mechanisms underlying tachycardia-induced sustained atrial fibrillation in a chronic dog model. *Circulation* 96, 4027–4035. doi: 10.1161/01.CIR.96.11.4027

Gaudesius, G., Miragoli, M., Thomas, S. P., and Rohr, S. (2003). Coupling of cardiac electrical activity over extended distances by fibroblasts of cardiac origin. *Circ. Res.* 93, 421–428. doi: 10.1161/01.RES.0000089258.40661.0C

Gomez, J. F., Cardona, K., Martinez, L., Saiz, J., and Trenor, B. (2014a). Electrophysiological and structural remodeling in heart failure modulate arrhythmogenesis. 2D simulation study. *PLoS One* 10:e0117883. doi: 10.1371/journal.pone.0103273

Gomez, J. F., Cardona, K., Romero, L., Ferrero, J. M., and Trenor, B. (2014b). Electrophysiological and structural remodeling in heart failure modulate arrhythmogenesis. 1D simulation study. *PLoS One* 9:e106602. doi: 10.1371/journal.pone.0106602

Grand, T., Salvarani, N., Jousset, F., and Rohr, S. (2014). Aggravation of cardiac myofibroblast arrhythmogeneicity by mechanical stress. *Cardiovasc. Res.* 104, 489–500. doi: 10.1093/cvr/cvu227

Gray, R. A., Pertsov, A. M., and Jalife, J. (1998). Spatial and temporal organization during cardiac fibrillation. *Nature* 392, 75–78. doi: 10.1038/32164

Harrild, D. M., and Hen, C. S. (2000). A computer model of normal conduction in the human atria. *Circ. Res.* 87, e25–e36. doi: 10.1161/01.RES.87.7.e25

Hulsmans, M., Clauss, S., Xiao, L., Aguirre, A. D., King, K. R., Hanley, A., et al. (2017). Macrophages facilitate electrical conduction in the heart. *Cell* 169, 510.e20–522.e20. doi: 10.1016/j.cell.2017.03.050

Iwasaki, Y. K., Nishida, K., Kato, T., and Nattel, S. (2011). Atrial fibrillation pathophysiology: implications for management. *Circulation* 124, 2264–2274. doi: 10.1161/CIRCULATIONAHA.111.019893

Jacquemet, V., and Henriquez, C. S. (2007). Modelling cardiac fibroblasts: interactions with myocytes and their impact on impulse propagation. *Europace* 9(Suppl.6), vi29-vi37. doi: 10.1093/europace/eum207

Jacquemet, V., and Henriquez, C. S. (2008). Loading effect of fibroblast-myocyte coupling on resting potential, impulse propagation, and repolarization: insights from a microstructure model. *AJP Hear. Circ. Physiol.* 294, H2040–H2052. doi: 10.1152/ajpheart.01298.2007

Jacquemet, V., and Henriquez, C. S. (2009). Modulation of conduction velocity by nonmyocytes in the low coupling regime. *IEEE Trans. Biomed. Eng.* 56, 893–896. doi: 10.1109/TBME.2008.2006028

Jalife, J., and Kaur, K. (2015). Atrial remodeling, fibrosis, and atrial fibrillation. *Trends Cardiovasc. Med.* 25, 475–484. doi: 10.1016/j.tcm.2014.12.015

Jousset, F., Maguy, A., Rohr, S., and Kucera, J. P. (2016). Myofibroblasts electrotonically coupled to cardiomyocytes alter conduction: insights at the cellular level from a detailed in silico tissue structure model. *Front. Physiol.* 7:496. doi: 10.3389/fphys.2016.00496

Kirchhof, P., Benussi, S., Kotecha, D., Ahlsson, A., Atar, D., Casadei, B., et al. (2016). 2016 ESC guidelines for the management of atrial fibrillation developed in collaboration with EACTS. *Europace* 18, 1609–1678. doi: 10.1093/europace/euw295

Kohl, P., Camelliti, P., Burton, F. L., and Smith, G. L. (2005). Electrical coupling of fibroblasts and myocytes: relevance for cardiac propagation. *J. Electrocardiol.* 38, 45–50. doi: 10.1016/j.jelectrocard.2005.06.096

Kohl, P., and Gourdie, R. G. (2014). Fibroblast – myocyte electrotonic coupling: does it occur in native cardiac tissue? *J. Mol. Cell. Cardiol.* 70, 37–46. doi: 10.1016/j.yjmcc.2013.12.024

Kohl, P., Kamkin, A. G., Kiseleva, I. S., and Noble, D. (1994). Mechanosensitive fibroblasts in the sino-atrial node region of rat heart: interaction with cardiomyocytes and possible role. *Exp. Physiol.* 79, 943–956. doi: 10.1113/expphysiol.1994.sp003819

Koivumäki, J., Clark, R. B., Belke, D., Kondo, C., Fedak, P., Maleckar, M. M., et al. (2014a). Na+ current expression in human atrial myofibroblasts: identity and functional roles. *Front. Physiol.* 5:275. doi: 10.3389/fphys.2014.00275

Koivumäki, J. T., Seemann, G., Maleckar, M. M., and Tavi, P. (2014b). In silico screening of the key cellular remodeling targets in chronic atrial fibrillation. *PLoS Comput. Biol.* 10:e1003620. doi: 10.1371/journal.pcbi.1003620

Koivumäki, J. T., Korhonen, T., and Tavi, P. (2011). Impact of sarcoplasmic reticulum calcium release on calcium dynamics and action potential morphology in human atrial myocytes: a computational study. *PLoS Comput. Biol.* 7:e1001067. doi: 10.1371/journal.pcbi.1001067

Krogh-madsen, T., Abbott, G. W., and Christini, D. J. (2012). Effects of electrical and structural remodeling on atrial fibrillation maintenance?: a simulation study. *PLoS Comput. Biol.* 8:e1002390. doi: 10.1371/journal.pcbi.1002390

Krueger, M., Seemann, G., Rhode, K., Keller, D. U. J., Schilling, C., Arujuna, A., et al. (2012). Personalization of atrial anatomy and elelectophysiology as a basis for clinical modeling of radio-frequency-ablation of atrial fibrillation. *Med. Imaging IEEE Trans.* 32, 1–12. doi: 10.1109/TMI.2012.2201948

Krueger, M. W., Dorn, A., Keller, D. U. J., Holmqvist, F., Carlson, J., Platonov, P. G., et al. (2013). In-silico modeling of atrial repolarization in normal and atrial fibrillation remodeled state. *Med. Biol. Eng. Comput.* 51, 1105–1119. doi: 10.1007/s11517-013-1090-1

Krul, S. P. J., Berger, W. R., Smit, N. W., Van Amersfoorth, S. C. M., Driessen, A. H. G., Van Boven, W. J., et al. (2015). Atrial fibrosis and conduction slowing in the left atrial appendage of patients undergoing thoracoscopic surgical pulmonary vein isolation for atrial fibrillation. *Circ. Arrhythm. Electrophysiol.* 8, 288–295. doi: 10.1161/CIRCEP.114.001752

MacCannell, K. A., Bazzazi, H., Chilton, L., Shibukawa, Y., Clark, R. B., and Giles, W. R. (2007). A mathematical model of electrotonic interactions between ventricular myocytes and fibroblasts. *Biophys. J.* 92, 4121–4132. doi: 10.1529/biophysj.106.101410

Majumder, R., Nayak, A. R., and Pandit, R. (2011). Scroll-wave dynamics in human cardiac tissue: lessons from a mathematical model with inhomogeneities and fiber architecture. *PLoS One* 6:e18052. doi: 10.1371/journal.pone.0018052

Maleckar, M. M., Greenstein, J. L., Giles, W. R., and Trayanova, N. A. (2009). Electrotonic coupling between human atrial myocytes and fibroblasts alters myocyte excitability and repolarization. *Biophys. J.* 97, 2179–2190. doi: 10.1016/j.bpj.2009.07.054

Martinez-Mateu, L., Romero, L., Ferrer-Albero, A., Sebastian, R., Rodríguez Matas, J. F., Jalife, J., et al. (2018). Factors affecting basket catheter detection of real and phantom rotors in the atria: a computational study. *PLoS Comput. Biol.* 14:e1006017. doi: 10.1371/journal.pcbi.1006017

McArthur, L., Chilton, L., Smith, G. L., and Nicklin, S. A. (2015). Electrical consequences of cardiac myocyte: fibroblast coupling. *Biochem. Soc. Trans.* 43, 513–518. doi: 10.1042/BST20150035

McDowell, K. S., Vadakkumpadan, F., Blake, R., Blauer, J., Plank, G., MacLeod, R. S., et al. (2012). Methodology for patient-specific modeling of atrial fibrosis as a substrate for atrial fibrillation. *J. Electrocardiol.* 45, 640–645. doi: 10.1016/j.jelectrocard.2012.08.005

McDowell, K. S., Vadakkumpadan, F., Blake, R., Blauer, J., Plank, G., Macleod, R. S., et al. (2013). Mechanistic inquiry into the role of tissue remodeling in fibrotic lesions in human atrial fibrillation. *Biophys. J.* 104, 2764–2773. doi: 10.1016/j.bpj.2013.05.025

Miragoli, M., Gaudesius, G., and Rohr, S. (2006). Electrotonic modulation of cardiac impulse conduction by myofibroblasts. *Circ. Res.* 98, 801–810. doi: 10.1161/01.RES.0000214537.44195.a3

Morgan, R., Colman, M., Kruger, M., Seemann, G., Rhode, K., and Aslanidi, O. (2014). "Evaluating effects of fibrosis in atrial arrhythmogenesis using 3D computational modelling," in *Proceedings of the international conference on Computing in Cardiology 2014*, (Cambridge, MA), 765–768.

Morgan, R., Colman, M. A., Chubb, H., Seemann, G., and Aslanidi, O. V. (2016). Slow conduction in the border zones of patchy fibrosis stabilizes the drivers for atrial fibrillation: insights from multi-scale human atrial modeling. *Front. Physiol.* 7:474. doi: 10.3389/fphys.2016.00474

Nattel, S. (2018). Molecular and cellular mechanisms of atrial fibrosis in atrial fibrillation. *JACC Clin. Electrophysiol.* 3, 425–435. doi: 10.1016/j.jacep.2017.03.002

Nattel, S., Burstein, B., and Dobrev, D. (2008). Atrial remodeling and atrial fibrillation: mechanisms and implications. *Circ. Arrhythm. Electrophysiol.* 1, 62–73. doi: 10.1161/CIRCEP.107.754564

Nattel, S., and Dobrev, D. (2017). Controversies about atrial fibrillation mechanisms: aiming for order in chaos and whether it matters. *Circ. Res.* 120, 1396–1398. doi: 10.1161/CIRCRESAHA.116.310489

Nguyen, T. P., Xie, Y., Garfinkel, A., Qu, Z., and Weiss, J. N. (2012). Arrhythmogenic consequences of myofibroblastmyocyte coupling. *Cardiovasc. Res.* 93, 242–251. doi: 10.1093/cvr/cvr292

Nygren, A., Fiset, C., Firek, L., Clark, J. W., Lindblad, D. S., Clark, R. B., et al. (1998). Mathematical model of an adult human atrial cell: the role of K+ currents in repolarization. *Circ. Res.* 82, 63–81. doi: 10.1161/01.RES.82.1.63

Poulet, C., Künzel, S., Büttner, E., Lindner, D., Westermann, D., and Ravens, U. (2016). Altered physiological functions and ion currents in atrial fibroblasts from patients with chronic atrial fibrillation. *Physiol. Rep.* 4:e12681. doi: 10.14814/phy2.12681

Quinn, T. A., Camelliti, P., Rog-Zielinska, E. A., Siedlecka, U., Poggioli, T., O'Toole, E. T., et al. (2016). Electrotonic coupling of excitable and nonexcitable cells in the heart revealed by optogenetics. *Proc. Natl. Acad. Sci. U.S.A.* 113, 14852–14857. doi: 10.1073/pnas.1611184114

Rohr, S. (2009). Myofibroblasts in diseased hearts: new players in cardiac arrhythmias? *Hear. Rhythm* 6, 848–856. doi: 10.1016/j.hrthm.2009.02.038

Rohr, S. (2011). Cardiac fibroblasts in cell culture systems: myofibroblasts all along? *J. Cardiovasc. Pharmacol.* 57, 389–399. doi: 10.1097/FJC.0b013e3182137e17

Roney, C. H., Bayer, J. D., Cochet, H., Meo, M., Dubois, R., Jaïs, P., et al. (2018). Variability in pulmonary vein electrophysiology and fibrosis determines arrhythmia susceptibility and dynamics. *PLoS Comput. Biol.* 14:e1006166. doi: 10.1371/journal.pcbi.1006166

Roney, C. H., Bayer, J. D., Zahid, S., Meo, M., Boyle, P. M. J., Trayanova, N. A., et al. (2016). Modelling methodology of atrial fibrosis affects rotor dynamics and electrograms. *Europace* 18(Suppl. 4), iv146–iv155. doi: 10.1093/europace/euw365

Rook, M. B., Van Ginneken, A. C. G., de Jonge, B., el Aoumari, A., Gros, D., Jongsma, H. J., et al. (1992). Differences in gap junction channels between cardiac myocytes, fibroblasts, and heterologous pairs. *Am. J. Physiol.* 263, C959–C977. doi: 10.1152/ajpcell.1992.263.5.C959

Roy, A., Varela, M., and Aslanidi, O. (2018). Image-based computational evaluation of the effects of atrial wall thickness and fibrosis on re-entrant drivers for atrial fibrillation. *Front. Physiol.* 9:1352. doi: 10.3389/fphys.2018.01352

Sabir, M. A., Sosulski, F. W., and Finlayson, A. J. (1974). Chlorogenic acid-protein interactions in sunflower. *J. Agric. Food Chem.* 22, 575–578. doi: 10.1021/jf60194a052

Sachse, F. B., Moreno, A. P., and Abildskov, J. A. (2008). Electrophysiological modeling of fibroblasts and their interaction with myocytes. *Ann. Biomed. Eng.* 36, 41–56. doi: 10.1007/s10439-007-9405-8

Saha, M., Roney, C. H., Bayer, J. D., Meo, M., Cochet, H., Dubois, R., et al. (2018). Wavelength and fibrosis affect phase singularity locations during atrial fibrillation. *Front. Physiol.* 9:1207. doi: 10.3389/fphys.2018.01207

Salvarani, N., Maguy, A., De Simone, S. A., Miragoli, M., Jousset, F., and Rohr, S. (2017). TGF-β1(Transforming Growth Factor-β1) plays a pivotal role in cardiac myofibroblast arrhythmogenicity. *Circ. Arrhythm. Electrophysiol.* 10:e004567. doi: 10.1161/CIRCEP.116.004567

Sanchez-Quintana, D., Ramon Lopez-Mínguez, J., Pizarro, G., Murillo, M., and Angel Cabrera, J. (2012). Triggers and anatomical substrates in the genesis and perpetuation of atrial fibrillation. *Curr. Cardiol. Rev.* 8, 310–326. doi: 10.2174/157340312803760721

Satoh, H., Delbridge, L. M. D., Blatter, L. A., and Bers, D. M. (1996). Surface: volume relationship in cardiac myocytes studied with confocal microscopy and membrane capacitance measurements: species-dependence and developmental effects. *Biophys. J.* 70, 1494–1504. doi: 10.1016/S0006-3495(96)79711-4

Sridhar, S., Vandersickel, N., and Panfilov, A. V. (2017). Effect of myocyte-fibroblast coupling on the onset of pathological dynamics in a model of ventricular tissue. *Sci. Rep.* 7:40985. doi: 10.1038/srep40985

Tanaka, K., Zlochiver, S., Vikstrom, K. L., Yamazaki, M., Moreno, J., Klos, M., et al. (2007). Spatial distribution of fibrosis governs fibrillation wave dynamics in the posterior left atrium during heart failure. *Circ. Res.* 101, 839–847. doi: 10.1161/CIRCRESAHA.107.153858

Ten Tusscher, K., Noble, D., Noble, P. J., and Panfilov, A. V. (2004). A model for human ventricular tissue. *Am. J. Physiol. Circ. Physiol.* 286, H1573–H1589.

Varela, M., Colman, M. A., Hancox, J. C., and Aslanidi, O. V. (2016). Atrial heterogeneity generates re-entrant substrate during atrial fibrillation and anti-arrhythmic drug action: mechanistic insights from canine atrial models. *PLoS Comput. Biol.* 12:e1005245. doi: 10.1371/journal.pcbi.1005245

Vasquez, C., Moreno, A. P., and Berbari, E. J. (2004). Modeling fibroblast-mediated conduction in the ventricle. *Comput. Cardiol.* 2004, 349–352. doi: 10.1109/CIC.2004.1442944

Verheule, S., Eckstein, J., Linz, D., Maesen, B., Bidar, E., Gharaviri, A., et al. (2014). Role of endo-epicardial dissociation of electrical activity and transmural conduction in the development of persistent atrial fibrillation. *Prog. Biophys. Mol. Biol.* 115, 173–185. doi: 10.1016/j.pbiomolbio.2014.07.007

Waks, J. W., and Josephson, M. E. (2014). Mechanisms of atrial fibrillation – reentry, rotors and reality. *Arrhythm. Electrophysiol. Rev.* 3, 90–100. doi: 10.15420/aer.2014.3.2.90

Warren, M., Guha, P. K., Berenfeld, O., Zaitsev, A., Anumonwo, J. M. B., Dhamoon, A. S., et al. (2003). Blockade of the inward rectifying potassium current terminates ventricular fibrillation in the guinea pig heart. *J. Cardiovasc. Electrophysiol.* 14, 621–631. doi: 10.1046/j.1540-8167.2003.03006.x

Wilhelms, M., Hettmann, H., Maleckar, M. M., Koivumäki, J. T., Dössel, O., and Seemann, G. (2013). Benchmarking electrophysiological models of human atrial myocytes. *Front. Physiol.* 3:487. doi: 10.3389/fphys.2012.00487

Xie, Y., Garfinkel, A., Camelliti, P., Kohl, P., Weiss, J. N., and Qu, Z. (2009). Effects of fibroblast-myocyte coupling on cardiac conduction and vulnerability to reentry: a computational study. *Hear. Rhythm* 6, 1641–1649. doi: 10.1016/j.hrthm.2009.08.003

Yamazaki, M., Mironov, S., Taravant, C., Brec, J., Vaquero, L. M., Bandaru, K., et al. (2012). Heterogeneous atrial wall thickness and stretch promote scroll waves anchoring during atrial fibrillation. *Cardiovasc. Res.* 94, 48–57. doi: 10.1093/cvr/cvr357

Yue, L., Xie, J., and Nattel, S. (2011). Molecular determinants of cardiac fibroblast electrical function and therapeutic implications for atrial fibrillation. *Cardiovasc. Res.* 89, 744–753. doi: 10.1093/cvr/cvq329

Zahid, S., Cochet, H., Boyle, P. M., Schwarz, E. L., Whyte, K. N., Vigmond, E. J., et al. (2016). Patient-derived models link re-entrant driver localization in atrial fibrillation to fibrosis spatial pattern. *Cardiovasc. Res.* 110, 443–454. doi: 10.1093/cvr/cvw073

Zhan, H., Xia, L., Shou, G., Zang, Y., Liu, F., and Crozier, S. (2014). Fibroblast proliferation alters cardiac excitation conduction and contraction: a computational study. *J. Zhejiang Univ. Sci. B* 15, 225–242. doi: 10.1631/jzus.B1300156

Conflict of Interest Statement: The authors declare that the research was conducted in the absence of any commercial or financial relationships that could be construed as a potential conflict of interest.

frontiers in Physiology

ORIGINAL RESEARCH
published: 02 August 2019
doi: 10.3389/fphys.2019.00916

Mechanisms Underlying Interactions Between Low-Frequency Oscillations and Beat-to-Beat Variability of Celullar Ventricular Repolarization in Response to Sympathetic Stimulation: Implications for Arrhythmogenesis

David Adolfo Sampedro-Puente[1]*, *Jesus Fernandez-Bes*[1], *Bradley Porter*[2], *Stefan van Duijvenboden*[3], *Peter Taggart*[3] and *Esther Pueyo*[1,4]

[1] BSICOS Group, I3A, IIS Aragón, University of Zaragoza, Zaragoza, Spain, [2] Department of Imaging Sciences and Biomedical Engineering, Kings College London, London, United Kingdom, [3] Department of Cardiovascular Sciences, University College London, London, United Kingdom, [4] CIBER-BBN, Madrid, Spain

OPEN ACCESS

Edited by:
Javier Saiz,
Polytechnic University of Valencia, Spain

Reviewed by:
Arun V. Holden,
University of Leeds, United Kingdom
Jordi Heijman,
Maastricht University, Netherlands

***Correspondence:**
David Adolfo Sampedro-Puente
sampedro@unizar.es

Specialty section:
This article was submitted to Computational Physiology and Medicine, a section of the journal Frontiers in Physiology

Received: 16 December 2018
Accepted: 04 July 2019
Published: 02 August 2019

Citation:
Sampedro-Puente DA, Fernandez-Bes J, Porter B, van Duijvenboden S, Taggart P and Pueyo E (2019) Mechanisms Underlying Interactions Between Low-Frequency Oscillations and Beat-to-Beat Variability of Celullar Ventricular Repolarization in Response to Sympathetic Stimulation: Implications for Arrhythmogenesis. Front. Physiol. 10:916. doi: 10.3389/fphys.2019.00916

Background and Objectives: Enhanced beat-to-beat variability of ventricular repolarization (BVR) has been linked to arrhythmias and sudden cardiac death. Recent experimental studies on human left ventricular epicardial electrograms have shown that BVR closely interacts with low-frequency (LF) oscillations of activation recovery interval during sympathetic provocation. In this work human ventricular computational cell models are developed to reproduce the experimentally observed interactions between BVR and its LF oscillations, to assess underlying mechanisms and to establish a relationship with arrhythmic risk.

Materials and Methods: A set of human ventricular action potential (AP) models covering a range of experimental electrophysiological characteristics was constructed. These models incorporated stochasticity in major ionic currents as well as descriptions of β-adrenergic stimulation and mechanical effects to investigate the AP response to enhanced sympathetic activity. Statistical methods based on Automatic Relevance Determination and Canonical Correlation Analysis were developed to unravel individual and common factors contributing to BVR and LF patterning of APD in response to sympathetic provocation.

Results: Simulated results reproduced experimental evidences on the interactions between BVR and LF oscillations of AP duration (APD), with replication of the high inter-individual variability observed in both phenomena. I_{CaL}, I_{Kr} and I_{K1} currents were identified as common ionic modulators of the inter-individual differences in BVR and LF oscillatory behavior and were shown to be crucial in determining susceptibility to arrhythmogenic events.

Conclusions: The calibrated family of human ventricular cell models proposed in this study allows reproducing experimentally reported interactions between BVR and LF oscillations of APD. Ionic factors involving I_{CaL}, I_{Kr} and I_{K1} currents are found to underlie correlated increments in both phenomena in response to sympathetic provocation. A link to arrhythmogenesis is established for concomitantly elevated levels of BVR and its LF oscillations.

Keywords: low-frequency oscillations, beat-to-beat variability, cardiac cell models, beta-adrenergic stimulation, stochasticity, sympathetic provocation, arrhythmogenesis

1. BACKGROUND AND OBJECTIVES

Beat-to-beat variability of repolarization (BVR) is an inherent property of ventricular electrical function (Thomsen et al., 2006; Baumert et al., 2016). When enhanced, this temporal variability has been associated with arrhythmia vulnerability in patients with structural heart disease (Tereshchenko et al., 2009), drug-induced long QT syndrome (Hinterseer et al., 2008), heart failure (Hinterseer et al., 2010), and catecholaminergic polymorphic ventricular tachycardia (Paavola et al., 2015). A link between increased BVR and arrhythmogenesis has been established in a range of animal models as well (Thomsen et al., 2006; Gallacher et al., 2007; Wijers et al., 2018). Various approaches have been proposed in the literature to quantify BVR at the level of the body surface electrocadiogram (ECG), including measurements of QT interval variability (Baumert et al., 2016), T-wave alternans (Verrier et al., 2011), or T-wave morphology variations (Ramirez et al., 2017).

Recent studies have shown that BVR presents a clear low-frequency (LF) oscillatory pattern that can be quantified from the ECG by measuring LF oscillations of the T-wave vector, so-called Periodic Repolarization Dynamics (PRD) (Rizas et al., 2014, 2016). PRD has been shown to be unrelated to heart rate variability or respiratory activity and has been postulated to most likely reflect the effect of phasic sympathetic activity on the ventricular myocardium. Increases in PRD have been associated with destabilization of repolarization leading to ventricular arrhythmias and sudden cardiac death (Rizas et al., 2014, 2017). The described T-wave oscillations have been suggested to reflect oscillations of the ventricular action potential (AP) duration (APD) (Hanson et al., 2014; Rizas et al., 2016; Porter et al., 2018). In *in vivo* studies on heart failure patients, APD has been shown to indeed oscillate at the same LF range (Hanson et al., 2014). Additional studies have demonstrated that both LF oscillations of APD and BVR are significantly augmented in response to physiologically-induced increased sympathetic activity, with a close interaction between both observed increments (Porter et al., 2017, 2018).

The mechanisms underlying the interactions between BVR and LF patterning of APD in response to sympathetic provocation (SP) and its potential link to arrhythmogenesis remain to be investigated. Regarding BVR, a growing number of studies, both experimental and computational, have provided evidence on the role of ion channel stochasticity and Ca^{2+} cycling variations as underlying mechanisms of temporal variability at different scales, covering from isolated cells (Lemay et al., 2011; Pueyo et al., 2011, 2016a; Antoons et al., 2015; Kistamas et al., 2015; Nánási et al., 2017) to coupled cells / tissue (Zaniboni et al., 2000; Pueyo et al., 2011; Lemay et al., 2011; Magyar et al., 2015; Nánási et al., 2017) to whole heart (Yamabe et al., 2007; Baumert et al., 2016). Furthermore, the action of adrenergic stimulation in modulating those BVR mechanisms and facilitating arrhythmia initiation by the formation of afterdepolarizations and triggered activity has been reported in single cells (Johnson et al., 2010, 2013; Heijman et al., 2013; Szentandrássy et al., 2015; Hegyi et al., 2018) and in the whole heart (Gallacher et al., 2007). In respect of LF oscillations of APD, computational investigations in single cells have suggested that sympathetic nerve activity promotes their generation by both a direct β-adrenergic (βA) action and through the intermediary of mechano-electric feedback (Pueyo et al., 2016b). In the presence of disease-related conditions, like Ca^{2+} overload and reduced repolarization reserve (RRR), these oscillations have been shown to contribute to pro-arrhythmia (Pueyo et al., 2016b).

In the present study, which builds on the work published in Pueyo et al. (2016b), a set of stochastic human ventricular AP models are developed to reproduce the sympathetically-mediated interactions between BVR and LF patterning of APD observed experimentally, to investigate their underlying mechanisms and to establish a link to arrhythmic risk. The developed models are representative of a whole range of AP characteristics and include biophysically detailed descriptions of the electrophysiology, Ca^{2+} dynamics, βA signaling and mechanics of human ventricular cells in health and disease. Stochastic gating of ion channels are incorporated into major currents active during AP repolarization. An approach based on the Automatic Relevance Determination technique (MacKay, 1996) is adopted to unravel the major ionic contributors to augmented BVR and LF oscillations of APD in response to SP, with subsequent analysis of the involved mechanisms. The relationship between the unraveled mechanisms and arrhythmogenesis is established by a methodology grounded on Canonical Correlation Analysis (Hotelling, 1936).

2. MATERIALS AND METHODS

2.1. Human Data

Previously acquired human data has been described in detail elsewhere (Porter et al., 2018). Briefly, eleven heart failure patients with cardiac resynchronization therapy defibrillator

devices had activation recovery intervals (ARIs) recorded from left ventricular epicardial electrodes alongside simultaneous non-invasive blood pressure and respiratory recordings. Heart rate was clamped by right ventricular pacing. Recordings took place during resting conditions and following an autonomic stimulus (Valsalva maneuver). The study was approved by the West London Ethics Committee and conformed to the standards set by the Declaration of Helsinki (latest revision: 64th WMA General Assembly). Informed consent was obtained in writing from all subjects.

2.2. Stochastic Human Ventricular Models

2.2.1. Models of Electrophysiology

The ORd human ventricular epicardial cell model (O'Hara et al., 2011) served as a basis to construct a set of AP models covering a range of experimentally observed electrophysiological characteristics. Each AP model in the dataset, which represents a different virtual cell, was obtained by varying the ionic conductances of the following currents: rapid delayed rectifier K^+ current, I_{Kr}; slow delayed rectifier K^+ current, I_{Ks}; transient outward K^+ current, I_{to}; L-type Ca^{2+} current, I_{CaL}; inward rectifier K^+ current, I_{K1}; sodium current, I_{Na}; sodium-K^+ pump current, I_{NaK}; and sodium-Ca^{2+} exchanger current, I_{NaCa}. A total of 500 models were initially generated by sampling the nominal conductance values of the ORd model in the range ±100% using the Latin Hypercube Sampling method (McKay et al., 1979; Pueyo et al., 2016b).

Out of all the generated models, only those satisfying the calibration criteria shown in **Table 1** were retained. Such criteria were based on experimentally available human ventricular measures of steady-state AP characteristics taken from O'Hara et al. (2011), Guo et al. (2011), Britton et al. (2017), Jost et al. (2008), and Grandi et al. (2010). These characteristics included: $APD_{90|50}$, denoting 1 Hz steady-state APD at 90%|50% repolarization (expressed in ms); RMP, standing for resting membrane potential (in mV); V_{peak}, measuring peak membrane potential following stimulation (in mV); and ΔAPD_{90}, calculated as the percentage of change in APD_{90} with respect to baseline when selectively blocking I_{Ks}, I_{Kr} or I_{K1} currents (measured in ms). After applying the described calibration criteria, the initial set of 500 models was reduced to a set of 161 selected models. In addition, models leading to pro-arrhythmic events at baseline conditions were excluded because they did not allow quantification of BVR or LF oscillations of APD, thus resulting in a final population of 123 models. For each of those models, the parameters θ_{Ks}, θ_{Kr}, θ_{to}, θ_{CaL}, θ_{K1}, θ_{Na}, θ_{NaCa}, and θ_{NaK} were defined to take the values of the factors multiplying the nominal conductances of I_{Ks}, I_{Kr}, I_{to}, I_{CaL}, I_{K1}, I_{Na}, I_{NaK}, and I_{NaCa}, respectively, with respect to the original ORd model, i.e., $I_j = \theta_j I_{j,ORd}$, where $I_{j,ORd}$ represents current j in the ORd model, with j being one of the elements in the set {Ks, Kr, to, CaL, K1, Na, NaCa, NaK}.

Stochasticity was incorporated into the equations describing the ionic gating of four major currents active during AP repolarization, namely I_{Ks}, I_{Kr}, I_{to}, and I_{CaL}, following the approach described in Pueyo et al. (2011) For a gating variable x, the temporal evolution of the probability of this gate being open was calculated as in Equation (1), where the variance of the stochastic term introduced to formulate the Stochastic Differential Equation (SDE) describing ionic fluctuations was inversely proportional to the number of channels of each species. In Equation (1), x_∞ and τ_x represent the steady-state value of x and the time constant to reach that steady-state value, with x, x_∞ and τ_x being functions of voltage, while w is a Wiener process. The number of channels N associated with each species j were obtained for each virtual cell by multiplying the ionic factor θ_j of that cell by the corresponding number of channels in the ORd model, i.e., $N_j = \theta_j N_{j,ORd}$. Further details on estimation of channel numbers for the ORd model are presented in the **Supplementary Material** (section 1.1 and **Table S1**).

$$dx = \frac{x_\infty - x}{\tau_x}dt + \frac{\sqrt{x_\infty + (1-2x_\infty)x}}{\sqrt{\tau_x N}}dw. \quad (1)$$

TABLE 1 | Calibration criteria applied onto human ventricular cell models.

AP characteristic	Min. acceptable value	Max. acceptable value
Under baseline conditions (Guo et al., 2011; O'Hara et al., 2011 Britton et al., 2017)		
APD_{90} (ms)	178.1	442.7
APD_{50} (ms)	106.6	349.4
RMP (mV)	−94.4	−78.5
V_{peak} (mV)	7.3	–
Under 90% I_{Ks} block (O'Hara et al., 2011)		
ΔAPD_{90} (%)	−54.4	62
Under 70% I_{Kr} block (Grandi et al., 2010)		
ΔAPD_{90} (%)	34.25	91.94
Under 50% I_{K1} block (Jost et al., 2008)		
ΔAPD_{90} (%)	−5.26	14.86

2.2.2. Models of PKA Phosphorylation

βA stimulation (βAS) effects were modeled as in Pueyo et al. (2016b) by using a modified version of the Xie et al. (2013) model, with definition of graded and dynamic phosphorylation levels of cellular protein kinase A (PKA) substrates. This model was updated from the original βA signaling formulation proposed in Soltis and Saucerman (2010) to slow down the I_{Ks} phosphorylation and dephosphorylation rate constants to fit experimental observations. PKA-mediated phosphorylation of phospholemman (PLM) was accounted for by increasing the Na^+-K^+-ATPase (NKA) affinity for the intracellular Na^+ concentration, as in Xie et al. (2013). RyR phosphorylation was described in this study following the formulation proposed in Heijman et al. (2011).

2.2.3. Models of Electromechanical Coupling

An extended version of the Niederer model (Niederer et al., 2006), adjusted to human cell characteristics, as in Weise and Panfilov (2013) and Pueyo et al. (2016b), was used for the electromechanical coupling model. The current through stretch-activated channels (SACs), I_{SAC}, was introduced as in Pueyo et al. (2016b), with the total current obtained as the sum of the current through K^+-selective and non-specific cationic SACs. Further details can be found in the **Supplementary Material**.

2.2.4. Simulation of Baseline and Sympathetic Provocation

A 0.1 Hz periodic stepwise dose of the βA agonist isoproterenol (ISO) was simulated, in accordance with the pattern of muscle sympathetic nerve activity in humans (Pagani et al., 1997). For the first half of the simulated ISO period, the ISO dose was set to either 0.01 μM, for simulated baseline conditions, or 1 μM, for simulated SP, while it was 0 μM for the second half in both cases. Additionally, phasic changes in hemodynamic loading accompanying enhanced sympathetic activity were simulated at the same 0.1 Hz frequency by varying the stretch ratio following a sinusoidal waveform with a maximum change of 1% for baseline conditions and 10% for SP. Sympathetically induced changes in βAS and hemodynamic loading were considered to be in-phase with each other. A total of 640 beats (320 for baseline and 320 for SP) were simulated while pacing the cells at 1 Hz frequency. **Figure S1** illustrates simulation of βAS and stretch effects at baseline and in response to sympathetic provocation, while **Figure S2** illustrates the APD time series of a cell in the generated population in response to the simulated protocol. For comparison purposes, additional simulations were run under constant βAS and/or hemodynamic loading.

2.2.5. Simulation of Disease-Related Conditions

On top of simulating physiological conditions, models describing disease conditions were built by including representations of: Reduced Repolarization Reserve (RRR), defined by simultaneous blockades of I_{Kr} and I_{Ks} currents; and Ca^{2+} overload, defined by increases in the extracellular Ca^{2+} levels. In both cases, an approach like the one described in Pueyo et al. (2016b) was used. Mild disease conditions were simulated by a 1.5-fold increment in the extracellular Ca^{2+} concentration and 7.5% and 20% inhibitions of I_{Kr} and I_{Ks} currents, respectively. Moderate disease conditions were simulated by a 2.5-fold increment in the extracellular Ca^{2+} concentration and 22.5% and 60% inhibitions of I_{Kr} and I_{Ks} currents, respectively. Severe disease conditions were simulated by a 4-fold increment in the extracellular Ca^{2+} concentration, 30% and 80% inhibitions of I_{Kr} and I_{Ks} currents, respectively, and by additionally increasing the conductance of non-specific cationic SACs as described in Isenberg et al. (2003) ($G_{SAC,ns}$ changed from 0.006 nS/pF for physiological, mild and moderate disease conditions to 0.01 nS/pF for severe disease conditions). **Table S2** summarizes how physiological as well as mild, moderate and severe disease conditions were simulated in this study.

2.3. Measurements of Repolarization Variability

For each of the developed AP models, APD at 90% repolarization, denoted as APD in the following, was calculated for every beat of the stochastic realizations. A triangulation measure (T1) was calculated as the difference between APD at 90% and 50% repolarization. The last $L = 120$ beats of each condition (baseline and SP) were used for evaluation of measures describing BVR and LF oscillatory behavior. Averages of those measures over stochastic realizations were computed.

2.3.1. Beat-to-Beat Variability of Repolarization

The following BVR measures were evaluated:

- Standard deviation of APD over the last L beats:

$$m_{SD} = \sqrt{\frac{1}{L-1}\sum_{l=1}^{L}(\mathrm{APD}(l) - \overline{\mathrm{APD}})^2} \tag{2}$$

  where $\overline{\mathrm{APD}}$ is the average APD over those L beats.
- Normalized variance of APD over the last L beats:

$$m_{NSD} = \frac{m_{SD}^2}{\overline{\mathrm{APD}}^2}. \tag{3}$$

- Short-Term Variability (STV) of APD, defined as the average distance perpendicular to the identity line in the Poincaré plot, computed as the average over windows of $L_{win} = 30$ beats sliding every one beat along the last $L = 120$ simulated beats:

$$m_{STV} = \frac{1}{L - L_{win} + 1}\left(\sum_{l=1}^{L-L_{win}+1}\sum_{i=l}^{l+L_{win}-1}\frac{|\mathrm{APD}(i+1) - \mathrm{APD}(i)|}{(L_{win}-1)\sqrt{2}}\right). \tag{4}$$

- Normalized STV:

$$m_{NSTV} = \frac{m_{STV}^2}{\overline{\mathrm{APD}}^2}. \tag{5}$$

2.3.2. Low-Frequency Repolarization Variability

Spectral analysis was performed to compute LF variability measures following the methodology described in Porter et al. (2018). The APD time series of the last $L = 120$ beats, for either baseline or SP, was linearly detrended. Power Spectral Density (PSD) was estimated after fitting an autoregressive model to the detrended APD time series using the Yule-Walker method. The optimal order of the autoregressive model was chosen in the range between L/3 and L/2 to minimize Akike's Information Criterion, with a requisite on the residuals to pass a whiteness test. Two measures were extracted from the estimated PSD:

- LF power (m_{PLF}), calculated as the integral of the PSD over the [0.04, 0.15] Hz band.
- Normalized LF power (m_{NPLF}): LF power normalized by the total power in the [0.04, 0.5] Hz frequency band.

2.4. Contributors to BVR and LF Oscillations

Automatic Relevance Determination (ARD) was used to unravel individual and common factors, in the form of ionic conductance levels, contributing to BVR and LF oscillations of APD in response to SP. ARD is a Bayesian sparsity method, first proposed in the context of neural network models (MacKay, 1996), which has been successfully used to determine the relevance of various input features to given measures (see e.g., Rasmussen and Williams, 2006).

In a regression problem where an output variable (in this case, a BVR or LF oscillatory measure) is aimed to be predicted by several input variables (in this case, the conductances of ionic

currents), it commonly happens that some of the variables are irrelevant to the prediction. However, when a finite dataset is analyzed, random correlations between the irrelevant inputs and the output are always obtained, diminishing the capability of the techniques employed for the prediction. A method like ARD, able to infer which input variables are relevant and prune all the irrelevant ones, is advantageous. ARD works by adjusting multiple weight constants, one associated with each input, which are inferred from the data and automatically set to be large for the relevant features and small for the irrelevant ones. The fact that ARD renders a sparse set of explanatory variables makes its results more interpretable than for other correlation-based methods (see e.g., Gunn and Kandola, 2002 for the relation between sparsity and interpretability).

Each virtual cell n out of the N simulated models was considered as a data point determined by its $D = 8$ parameters (factors multiplying ionic conductances). Those factors were stacked in a row vector $\mathbf{x}^{(n)} = [\theta_{\mathrm{Ks}}^{(n)}, \theta_{\mathrm{Kr}}^{(n)}, \theta_{\mathrm{to}}^{(n)}, \theta_{\mathrm{CaL}}^{(n)}, \theta_{\mathrm{K1}}^{(n)}, \theta_{\mathrm{Na}}^{(n)}, \theta_{\mathrm{NaCa}}^{(n)}, \theta_{\mathrm{NaK}}^{(n)}]$, representing the feature vector of each data point. All data were stacked in the feature matrix $\mathbf{X}$, i.e., $\mathbf{X} = [\mathbf{x}^{(1)}; \cdots; \mathbf{x}^{(N)}]$. Hence an element of $\mathbf{X}$, denoted as $x_{n,i}$, was the value of the i-th conductance parameter of virtual cell n. In addition, we used $\mathbf{y}$ as a wildcard to denote the column vector with the values of the analyzed variability measure for the data points. Hence, the values in $\mathbf{y}$ can either correspond to a temporal BVR measure or a measure of the magnitude of APD LF oscillations: m_{SD}, m_{NSD}, m_{STV}, m_{NSTV}, m_{PLF} and m_{NPLF}. To simplify the training process of the algorithm, the values of $\mathbf{y}$ were standardized to zero mean and unit variance. Using this input-output definition we posed the following regression model.

$$y^{(n)} = f(\mathbf{x}^{(n)}) + r^{(n)} \tag{6}$$

where $r^{(n)}$ is additive random Gaussian noise with variance σ_r^2 and f is a function linking the inputs and the outputs. Typical choices for f include linear, polynomial or neural network functions, with the ones most extensively used by the Bayesian learning community being Gaussian Processes (Rasmussen and Williams, 2006), which represent a powerful and flexible non-parametric option:

$$f(\mathbf{x}^{(n)}) \sim \mathcal{GP}\left(m(\mathbf{x}^{(n)}), c(\mathbf{x}^{(n)}, \mathbf{x}^{(n')})\right) \tag{7}$$

where $m(\mathbf{x}^{(n)})$ is the mean function and $c(\mathbf{x}^{(n)}, \mathbf{x}^{(n')})$ is the covariance function between data points n and n'. In its simplest form, $m(\mathbf{x}^{(n)}) = 0$ and all the complexity of the model is captured by the covariance function. The covariance is commonly described by linear, polynomial or radial basis functions, or other more complicated functions (see e.g., Rasmussen and Williams, 2006). In this work, a linear function was used for the covariance:

$$c(\mathbf{x}^{(n)}, \mathbf{x}^{(n')}) = \sum_{i=1}^{D} \sigma_{d,i}^2 x_{n,i} x_{n',i}. \tag{8}$$

Considering this choice, $f(\mathbf{x}^{(n)})$ can be shown to define a set of linear functions with respect to $\mathbf{x}^{(n)}$, where directions (i.e., the different factors contained in each $\mathbf{x}^{(n)}$) are weighted according to $\sigma_{d,i}^2$.

ARD was applied to optimize type II Maximum Likelihood (ML-II) with respect to $\sigma_{d,i}^2$ and σ_r^2. Specifically, a quasi-Newton method (in the case of our implementation, L-BFGS, see e.g., Boyd and Vandenberghe, 2004) was used to find the values of the hyperparameters leading to maximization of the following function:

$$\begin{aligned}\mathcal{L}(\sigma_{d,1}^2, \cdots, \sigma_{d,8}^2, \sigma_r^2) &= \frac{1}{2}\log\det \mathbf{C_{ext}}(\sigma_{d,1}^2, \cdots, \sigma_{d,8}^2, \sigma_r^2) \\ &+ \frac{1}{2}\mathbf{y}^T \mathbf{C_{ext}}(\sigma_{d,1}^2, \cdots, \sigma_{d,8}^2, \sigma_r^2)^{-1}\mathbf{y} + \frac{N}{2}\log(2\pi)\end{aligned} \tag{9}$$

where $\mathbf{C_{ext}}(\sigma_{d,1}^2, \cdots, \sigma_{d,8}^2, \sigma_r^2) = \mathbf{C}(\sigma_{d,1}^2, \cdots, \sigma_{d,8}^2) + \sigma_r^2\mathbf{I}$, with $\mathbf{I}$ being the identity matrix and $\mathbf{C}(\sigma_{d,1}^2, \cdots, \sigma_{d,8}^2)$ being the matrix obtained by evaluating the covariance function $c(\mathbf{x}^{(n)}, \mathbf{x}^{(n')})$ for every pair of data points in $\mathbf{X}$. To avoid overfitting, ten-fold cross validation was applied. Results are presented after averaging the ten corresponding values for each $\sigma_{d,i}^2$. The higher the value of $\sigma_{d,i}^2$, the more relevant the i-th factor (input parameter) is for the prediction.

This methodology allows establishing which factors are more relevant to predict a given output measure (i.e., a BVR or LF oscillatory measure). In the following, these relevance values are presented as normalized values so that they add up to one to facilitate assessment of the relative relevance of each factor. Since relevance factors do no account for the sign of the contribution, that is, whether an increase in the BVR or LF oscillation measure corresponds to upregulation or downregulation of an ionic current, the Gaussian Process regression was interpreted as a linear regression where the covariance matrix is $\mathbf{C_{ext}}$ and the sign of each contribution was calculated as

$$\mathbf{s}_{\theta_i} = \mathrm{sign}((\mathbf{C_{ext}^{-1}X})^T\mathbf{y}) \tag{10}$$

where θ_i is each of the conductance parameters and T denotes matrix transposition.

Finally, to address the fact that a factor may only be relevant in association with another one, the same methodology was applied after removing one factor (ionic conductance) at a time. If after removing a specific factor, the relevance associated with another factor was found to be significantly changed, a tight relationship between the effects of the two factors was postulated and common mechanisms underlying such a relationship were explored.

This method is implemented in Python 3 using the GPy, Gaussian Process Toolbox (see Sheffield ML group, 2012) and is available in **Data Sheet 2** of the Supplementary Material (section 1.6).

2.5. Contributors to Arrhythmogenesis

Canonical Correlation Analysis (CCA) (Hotelling, 1936; Hardoon et al., 2004) was used to identify the ionic conductances with the largest contribution to the occurrence of arrhythmogenic events under simulated diseased conditions. This method has been widely used in several different applications (see e.g., Torres et al., 2007; Kaya et al., 2014; Zhu et al., 2014 for some representative examples).

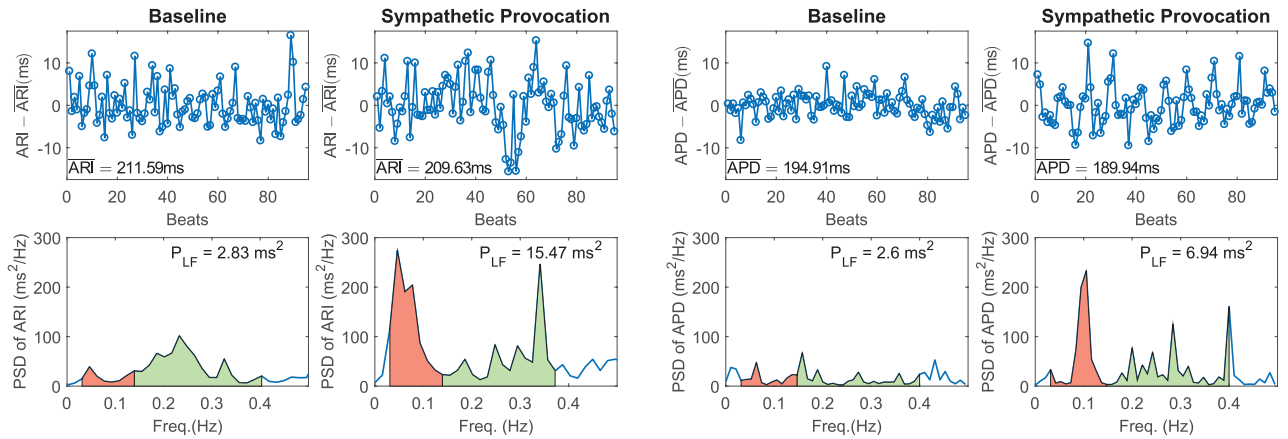

FIGURE 1 | (Left panel) Experimental zero-mean ARI series (ARI - $\overline{\text{ARI}}$) and corresponding spectra at rest (left) and following Valsalva maneuver (right). (Right panel) Simulated zero-mean APD series (APD - $\overline{\text{APD}}$) and corresponding spectra at baseline (left) and following sympathetic provocation (right). The LF region of the spectra is shadowed in red and the high frequency region in green.

Similarly to the description of ARD above, the data were stacked in the feature matrix $\mathbf{X}$, with $x_{n,i}$, being the value of the i-th factor for virtual cell n. A binary vector $\mathbf{z}$ of length N was generated, which contained a value of 1 in the positions corresponding to virtual cells for which pro-arrhythmic events were observed following SP and 0 otherwise.

Given $\mathbf{X}$ and $\mathbf{z}$, CCA was applied to compute the values of the *canonical variables* $\mathbf{w}_x$ and w_z such that:

$$(\mathbf{w}_x^*, w_z^*) = \arg\max_{\mathbf{w}_x, w_z} \text{corr}(\mathbf{X}\mathbf{w}_x, \mathbf{z}w_z) \tag{11}$$

with corr being the linear correlation between the projected versions of $\mathbf{X}$ and $\mathbf{z}$, i.e., $\mathbf{X}\mathbf{w}_x$, $\mathbf{z}w_z$. The elements of vector $\mathbf{w}_x^*$ represent the projection of ionic factors into a subspace common with $\mathbf{z}w_z^*$ and can be interpreted as the correlations of each of these factors with the presence of pro-arrhythmic events. Hence, the higher the value of an element in $\mathbf{w}_x^*$, the higher the relevance of such factor to the events in $\mathbf{z}$.

3. RESULTS

3.1. Sympathetic Provocation Increases BVR and LF Oscillations of APD

Figure 1 shows representative examples of zero-mean time series of experimental ARI (ARI - $\overline{\text{ARI}}$, with $\overline{\text{ARI}}$ denoting temporal mean of ARI, left panel) and simulated APD (APD - $\overline{\text{APD}}$, with $\overline{\text{APD}}$ denoting temporal mean of APD, right panel) and corresponding PSDs at baseline and following SP. In both experiments and simulations, a remarkable increase in BVR in response to SP can be clearly appreciated from the APD series. Also, the experimental and simulated spectra corresponding to SP show notably more marked peaks in the LF band as compared to baseline.

Of note, the peaks in the high frequency band present in the experimentally recorded data were not analyzed in this study, as vagal or respiratory effects were not included in our simulations for being out of the scope of the present study. The simulated results presented in this and the next sections correspond to simulation of mild disease conditions, since these are compared with experimental results obtained from heart failure patients (see section 2.1). Results for physiological conditions remained qualitatively unchanged with respect to those shown for mild disease conditions.

Figure 2 shows relative measures of BVR and LF oscillations at baseline and following SP for each individual of the experimental and simulated datasets (the cases shown in **Figure 1** are highlighted in blue). For the vast majority of individuals, m_{NSD} and m_{NPLF} increased in response to augmented sympathetic activity. Importantly, both the level of BVR and LF oscillations as well as the magnitude of change in response to SP presented a high degree of variation between individuals, as shown in **Figure 2**. As expected, the m_{NSD} values in the simulations were higher than in the experiments, as simulations correspond to single epicardial cells while experimental data is from left ventricular epicardial electrograms and, thus, includes the effects of intercellular coupling acting to mitigate cell-to-cell variability.

In both experiments and simulations, the sympathetically-mediated increases in BVR and LF oscillations were confirmed either when quantified in absolute terms by m_{SD}, m_{STV} and m_{PLF} or in relative terms by m_{NSD}, m_{NSTV} and m_{NPLF}.

3.2. There Is a Close Interaction Between BVR and LF Oscillations of APD, Particularly in Response to Sympathetic Provocation

Table 2 shows correlation values between measures of BVR and LF oscillations of APD, both calculated using absolute and normalized indices. As can be seen in **Table 2**, the LF power of APD, m_{PLF}, was highly correlated with BVR measured by the short-term variability of APD, m_{STV}, and, even to a larger extent, by the standard deviation of APD, m_{SD}. This observation held

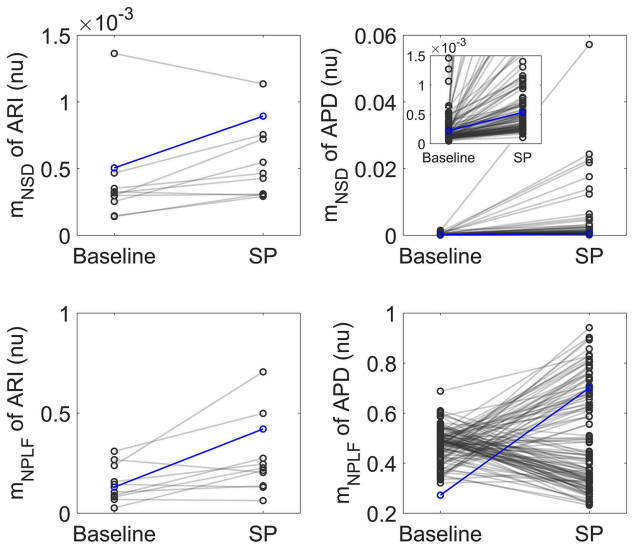

FIGURE 2 | Left: Normalized variance m_{NSD} (top) and Normalized LF power m_{NPLF} (bottom) at rest and following Valsalva maneuver calculated from experimental ARI series. Right: m_{NSD} (top) and m_{NPLF} (bottom) at baseline and following SP calculated from simulated APD series. The cases presented in **Figure 1** are highlighted in blue.

true when the correlation was evaluated both at baseline and in response to SP. The strong association found between BVR and LF oscillations of APD in our SP simulations was in line with the one measured experimentally, where the Spearman correlation coefficient between m_{PLF} and m_{SD} was 0.679.

When normalized measures were considered, **Table 2** shows that the correlation between the normalized LF power of APD, m_{NPLF}, and the normalized BVR measures, m_{NSTV} and m_{NSD}, was notably reduced. This highlights the relevance of absolute APD values in modulating the interactions between BVR and LF oscillations of APD. The reduction in correlation after considering normalized measures was particularly so for baseline conditions, while following SP there was still a high interaction between normalized BVR and LF oscillations of APD.

Figure S3 illustrates the simulated relationships between the absolute measures m_{PLF} and m_{SD} and between the relative measures m_{NPLF} and m_{NSD} at baseline and in response to SP.

Based on the fact that the two ways of evaluating BVR, i.e., by standard deviation and by short-term variability of APD, led to very similar outcomes in terms of the relationship with LF oscillations of APD, the results in the next sections will be shown for m_{STV} and its normalized counterpart m_{NSTV}. For APD oscillatory behavior, m_{PLF} and m_{NPLF} will be used.

3.3. K^+ and Ca^{2+} Current Densities Are Common Modulators of BVR and LF Oscillations of APD

Figure 3 illustrates the major contributors to the values of m_{STV}, m_{NSTV}, m_{PLF}, and m_{NPLF} found in our simulated population in response to SP. The sign of the relationship between the

TABLE 2 | Spearman correlation coefficients between simulated BVR and LF oscillation measures.

	Baseline		Sympathetic provocation	
	m_{PLF} (ms^2)	m_{NPLF} (nu)	m_{PLF} (ms^2)	m_{NPLF} (nu)
m_{SD} (ms)	0.9744	−0.1606	0.9439	0.5969
m_{NSD} (nu)	0.8528	−0.1602	0.8784	0.5721
m_{STV} (ms)	0.9096	−0.3381	0.8341	0.4054
m_{NSTV} (nu)	0.7646	−0.3530	0.7638	0.3868

contributing ionic current conductances and the evaluated BVR or LF oscillation measurements was negative in all relevant cases, meaning that downregulation of the ionic current density led to an increment in the analyzed measurement. Note that each bar in the graphs of **Figure 3** represents relative relevance with respect to the other evaluated factors, all adding up to one. According to the results in **Figure 3**, m_{STV} and m_{PLF} shared the same major contributors to their observed values following SP. Specifically, the three ionic conductances with the most relevant role in determining the values of m_{STV} and m_{PLF} were those of I_{Kr}, I_{K1}, and I_{CaL} currents. For the normalized measurements m_{NSTV} and m_{NPLF}, a substantial reduction in the relevance of I_{Kr} conductance was observed with respect to that quantified for the non-normalized measurements. I_{K1} and I_{CaL} current conductances remained as the two most relevant contributors to the values of m_{NSTV} and m_{NPLF} following SP.

To assess potential associations between ionic conductances in their contributions to the evaluated BVR and LF oscillations measures, the same ARD technique was applied after removing one ionic conductance at a time. For the majority of cases, the computed relevance levels were highly similar after such removals, meaning that there is no co-dependency in the contribution of the different ionic conductances. However, when I_{K1} conductance was removed from the analysis, the relevance of other repolarization currents, like I_{Kr} and I_{Ks}, in their contribution to m_{NSTV} was notably increased. This increment reveals common mechanisms in the contributions of all these repolarization currents to the m_{NSTV} values following SP.

Since the same ionic conductances were found to modulate BVR and LF oscillations of APD following SP, simulations were ran in which βAS and stretch were modeled as constant, with assigned values corresponding to the maximal effects in the above simulations. As can be seen in **Figure S4**, in those cases I_{Kr} and I_{K1} were still the major modulators of BVR whereas the contribution of I_{CaL} was drastically decreased. Thus, I_{CaL} modulation of BVR was mediated by the increment in the LF oscillations of APD, while the role of I_{Kr} and I_{K1} as modulators of BVR did not present such a strong dependence.

For healthy conditions, results were essentially the same as those shown in **Figure 3** for mild disease conditions, with only a slight decrease in the relevance of I_{NaCa} contribution to m_{PLF}. This is illustrated in **Figure S5**.

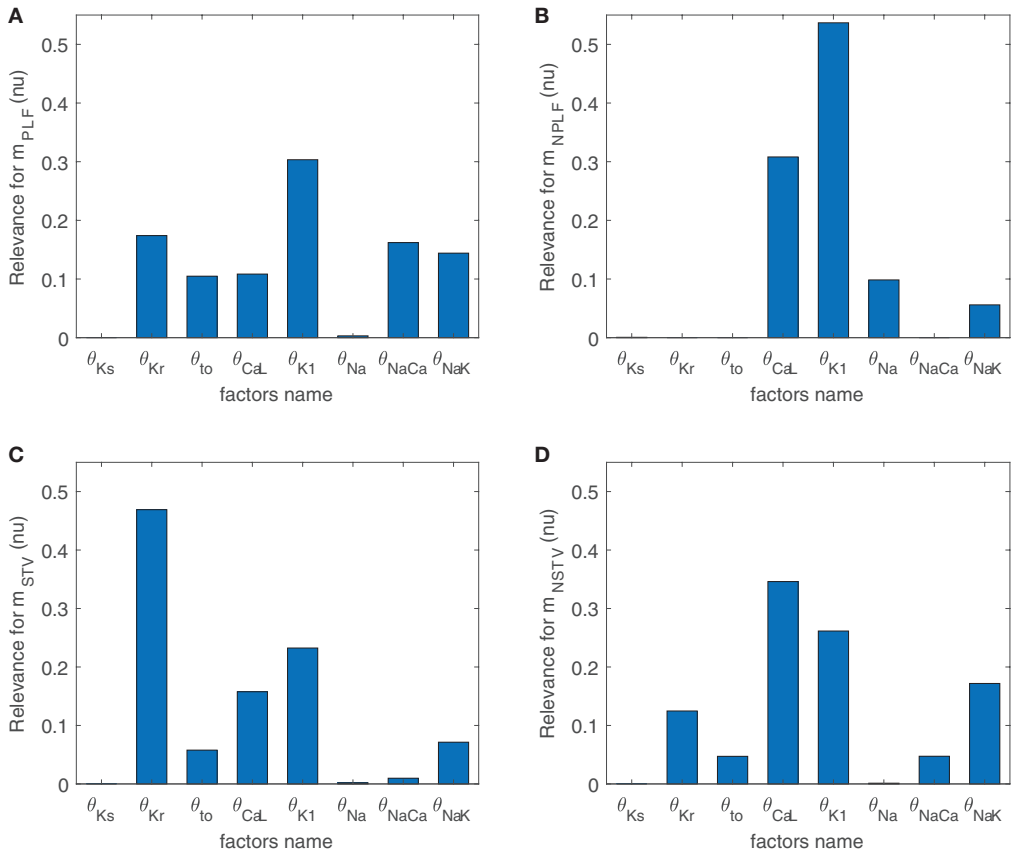

FIGURE 3 | Relevance of ionic current conductances to m_{PLF} **(A)**, m_{NPLF} **(B)**, m_{STV} **(C)** and m_{NSTV} **(D)**, calculated from simulated APD series under SP.

3.4. Modulation of BVR and LF Oscillations of APD by K^+ and Ca^{2+} Current Densities Is Explained by Their Effects on Ionic Gating Stochasticity, βAS, and Hemodynamic Loading

Before describing the mechanisms by which I_{Kr}, I_{K1}, and I_{CaL} current densities modulate BVR and LF oscillatory measures following SP, the differential effects of the two components associated with enhanced sympathetic activity, namely βAS and mechanical stretch, to such measures were analyzed. **Figure 4** illustrates the variations in BVR and LF oscillation measurements in the simulated population for different scenarios, including combined phasic βAS and mechanical stretch, only phasic βAS, only phasic mechanical stretch and only phasic mechanical stretch without SACs. Results showed that the largest contribution to LF oscillations, measured either by m_{PLF} or m_{NPLF}, was caused by phasic mechanical stretch, particularly when SACs were included in the models. Regarding BVR, both effects contributed to m_{STV} and m_{NSTV}, even if not in an additive manner and with the contribution of βAS being larger than that of mechanical stretch. Additional effects associated with stochastic ionic gating of currents active during AP repolarization added to the BVR values presented in **Figure 4**.

3.4.1. Mechanisms Underlying the Role of I_{K1} as a Modulator of BVR and LF Oscillations of APD

The role of I_{K1} current density as a modulator of APD oscillatory behavior following SP was only relevant when phasic mechanical stretch was simulated and particularly so when SACs were included in the models. The mechanism of action was as follows. Downregulation of I_{K1} increased resting membrane potential (**Figure 5A**) and this increment was associated with an enhancement of the total I_{SAC} current in the zenith of the oscillation, where phasic stretch reached maximal values (**Figures 5B,C**). These effects altered the AP shape at the end of the repolarization phase (**Figure 5D**) and this, in turn, had an impact on the calculated APD. In particular, the magnitude of the APD oscillations was amplified (**Figure 5E**), which led to increases in both m_{PLF} and m_{NPLF} (**Figure 5F**).

Furthermore, I_{K1} current density had an impact on modulating BVR following SP, especially when including the effects of SACs. Specifically, the above described alterations in AP morphology induced by I_{K1} downregulation, manifested as a slowing down of the final part of AP repolarization, rendered the AP more sensitive to the effects of stochastic ionic gating. This led to increased variability in APD values of consecutive beats, thus enlarging m_{STV} and m_{NSTV}.

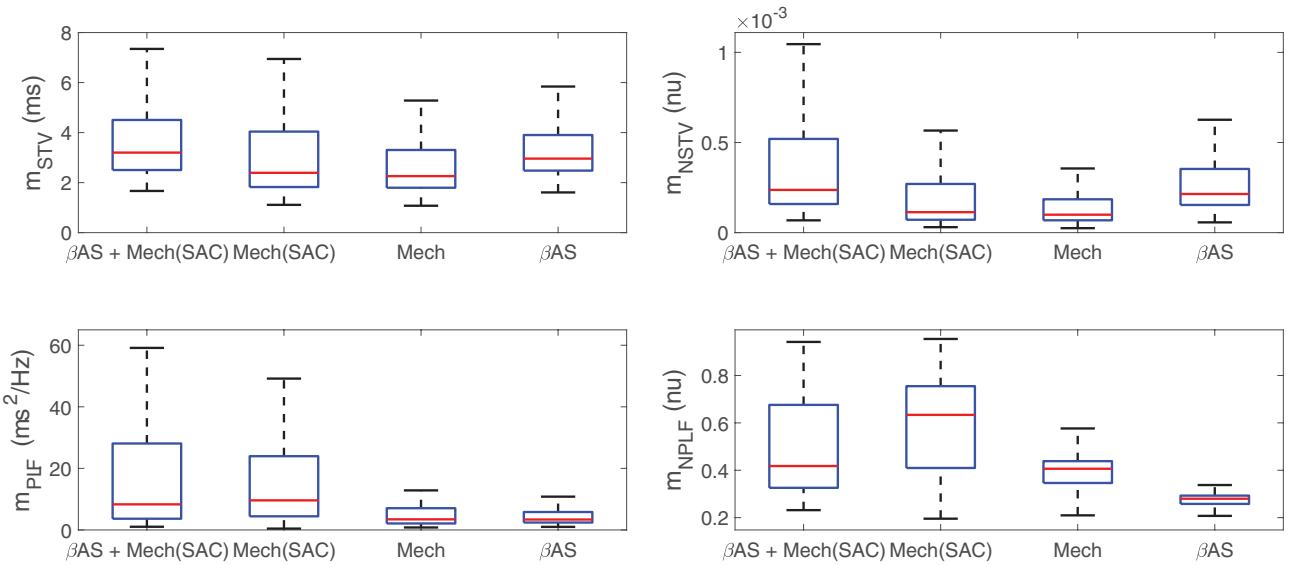

FIGURE 4 | Distributions of BVR and LF oscillation measurements for simulated scenarios including individual and combined βAS and mechanical stretch effects, with and without the contribution of SACs.

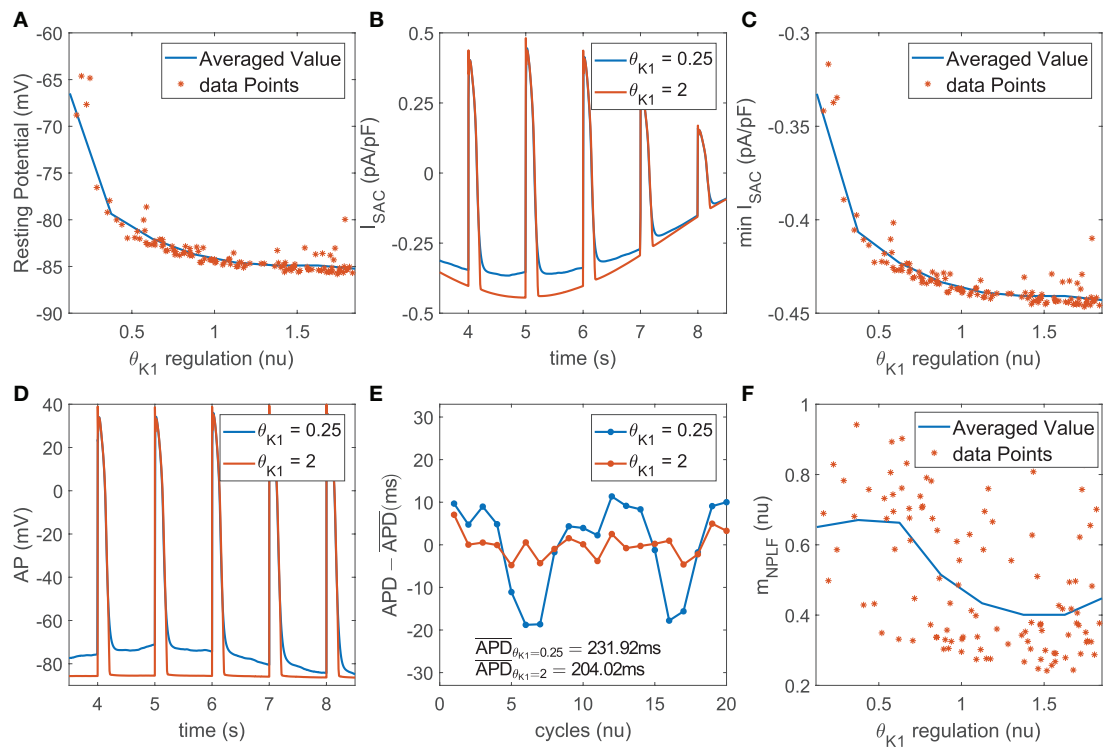

FIGURE 5 | (A) Resting membrane potential vs. I_{K1} current conductance in the population of virtual cells; **(B)** I_{SAC} current for two examples corresponding to upregulated and downregulated I_{K1} while keeping all the other currents at their default values in the ORd model; **(C)** Minimum I_{SAC} current value vs. I_{K1} current conductance in the population; **(D)** AP traces and **(E)** zero-mean APD series (APD - $\overline{\text{APD}}$) for the examples in **(B)**; **(F)** m_{NPLF} values vs. I_{K1} current conductance in the population.

3.4.2. Mechanisms Underlying the Role of I_{Kr} as a Modulator of BVR and LF Oscillations of APD

The impact of I_{Kr} current density on the magnitude of BVR and LF oscillations of APD was related to modulation of AP repolarization duration. This is evidenced by the fact that the contribution of I_{Kr} conductance was very relevant in the modulation of m_{PLF} and m_{STV} but was notably reduced for their normalized counterparts m_{NPLF} and m_{NSTV}.

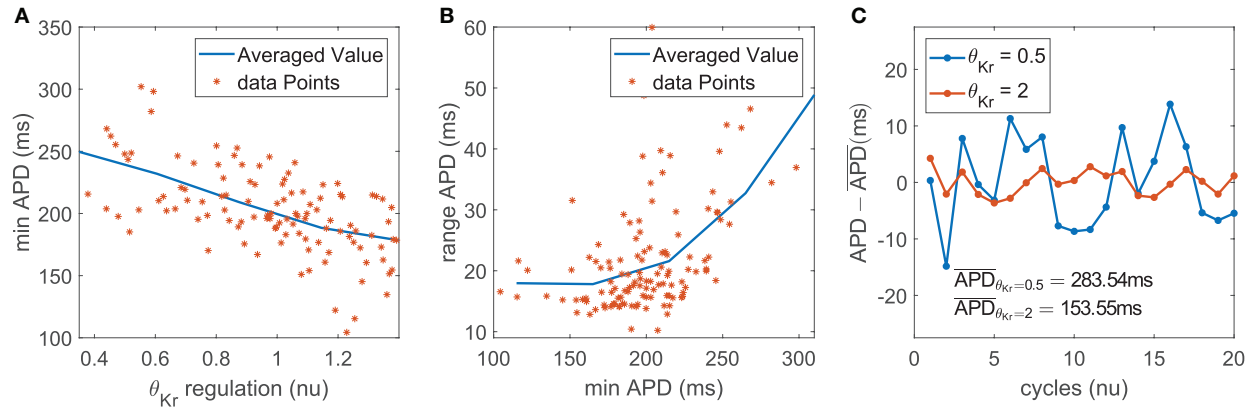

FIGURE 6 | (A) Minimum APD vs. I_{Kr} current conductance in the population of virtual cells; **(B)** APD range vs. minimum APD; **(C)** zero-mean APD series (APD - $\overline{APD}$) for two examples corresponding to downregulated and upregulated I_{Kr} while keeping all the other currents at their default values in the ORd model.

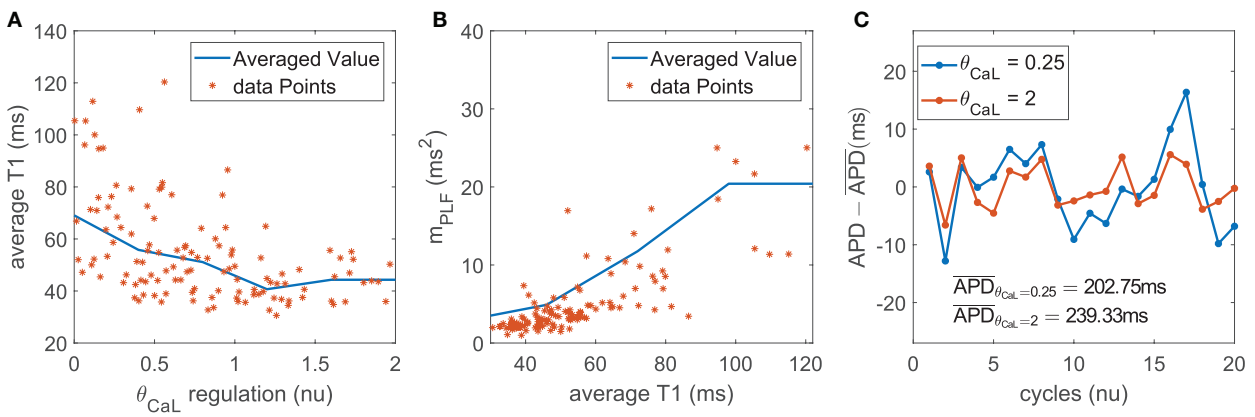

FIGURE 7 | (A) Average triangulation vs. I_{CaL} current conductance and **(B)** m_{PLF} values vs. average triangulation for the population of virtual cells; **(C)** zero-mean APD series (APD - $\overline{APD}$) for two examples corresponding to downregulated and updownregulated I_{CaL} while keeping all the other currents at their default values in the ORd model.

In the case of m_{PLF}, the mechanism of action was as follows. I_{Kr} downregulation led to AP prolongation, which in our simulations including phasic βAS and stretch could be seen as an increase in both the minimum and the average APD within each oscillation period (**Figure 6A**). The observed AP lengthening correlated with an increment in the magnitude of the APD oscillations, quantified by the APD range (**Figure 6B**). This was the result of amplified effects of βAS and stretch on the prolonged AP. In relation to the amplified oscillation amplitude, m_{PLF} was increased. Representative examples are shown in **Figure 6C**, where the case with longer APD induced by downregulated I_{Kr} was associated with larger LF oscillations.

In the case of m_{STV}, the lengthening of AP repolarization induced by I_{Kr} downregulation led to more accentuated temporal voltage variations. This occurred under phasic βAS, stretch and the combination of both effects associated with enhanced sympathetic activity.

3.4.3. Mechanisms Underlying the Role of I_{CaL} as a Modulator of BVR and LF Oscillations of APD

The contribution of I_{CaL} to BVR and LF oscillations was relevant under both simulated βAS and mechanical stretch, with an important role of SACs in explaining I_{CaL} modulation of APD oscillations.

I_{CaL} downregulation shortened the AP plateau, leading to more triangular APs (**Figure 7A**). This, in turn, magnified the effects of phasic βAS and accentuated the APD differences within each simulated oscillation period. This change produced an increase in the magnitude of LF oscillations of APD, associated with increments in both m_{PLF} and m_{NPLF} (**Figure 7B**). Representative examples of low and high BVR and LF oscillations of APD related to up- and downregulation of I_{CaL} current are presented in **Figure 7C**. In close correspondence with the above described mechanisms, the more triangular AP induced by I_{CaL} downregulation facilitated larger voltage fluctuations. This was seen as increased m_{STV} and m_{NSTV}.

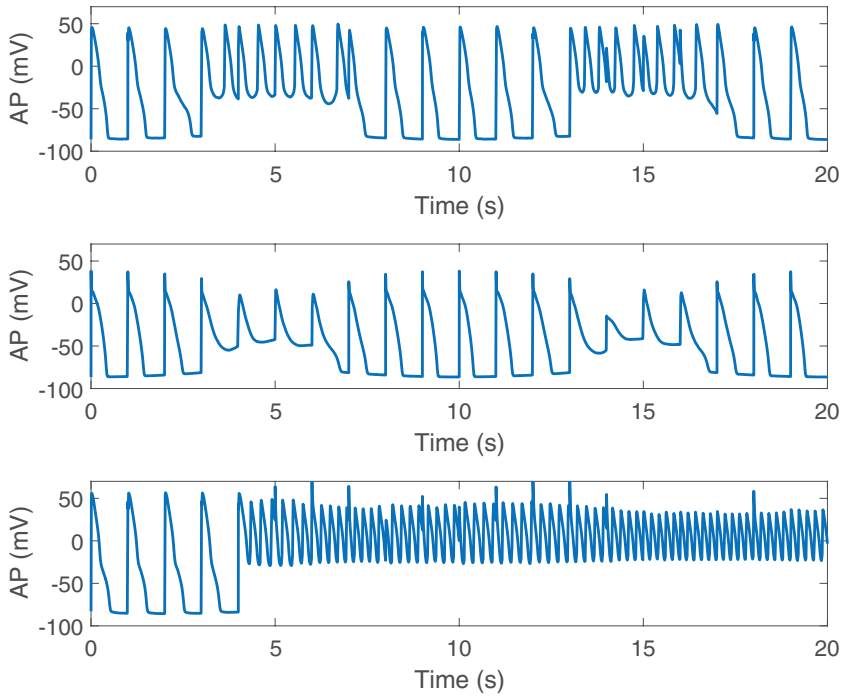

FIGURE 8 | Pro-arrhythmic events observed following SP in cells under simulated severe disease conditions.

Under simulated mechanical stretch on top of βAS, there was an additional change in the amplitude and duration of intracellular and subspace Ca^{2+} concentrations as well as in the I_{SAC} current. All these effects modified the AP repolarization morphology, enhancing the differences within each simulated oscillation period. As a consequence, m_{PLF} and m_{NPLF} were further increased and, correspondingly, m_{STV} and m_{NSTV} too.

3.5. Severe Disease Conditions Accentuate Both BVR and LF Oscillations of APD, Leading to Electrical Instabilities

Disease conditions simulated by Ca^{2+} overload and RRR had an impact on sympathetically-mediated BVR and LF oscillations of APD. Specifically, when severe disease conditions were simulated, including also an associated increase in the conductance of non-specific cationic SACs, pro-arrhythmic events could be observed. These occurred in 35% of the cases in our population and took the form of early afterdepolarizations (EADs), EAD bursts and spontaneous beats. Examples are presented in **Figure 8**.

For those cases where arrhythmogenic events were observed under severe disease conditions (denoted as subpopulation A), BVR and LF oscillations of APD were increasingly accentuated for higher levels of disease conditions, as illustrated in **Figure 9**. As can be noted from the figure, m_{NSTV} and m_{NPLF} took larger values for progressively higher levels of Ca^{2+} overload and RRR. Similarly occurred for the non-normalized indices m_{STV} and m_{PLF}. Those cases not presenting arrhythmogenic events under severe disease conditions (denoted as subpopulation NA) showed lower values of BVR and LF oscillation measures for both mild and moderated disease conditions. This can be appreciated in **Figure 9** as well.

The results of Canonical Correlation Analysis (CCA) performed to assess major contributors to pro-arrhythmic events under severe disease conditions are presented in **Figure 10**. According to these results, the ionic currents with a major involvement in pro-arrhythmicity were I_{Kr}, I_{CaL}, I_{K1}, and I_{NaK}, the first three being major modulators of BVR and LF oscillations of APD. The sign of the relationship between ionic conductances and pro-arrhythmicity was negative (i.e., current downregulation facilitating pro-arrhythmic events) in all cases except for I_{CaL}.

The role of I_{Kr}, I_{CaL}, and I_{K1} in contributing to pro-arrhythmicity is further illustrated in **Figure 11**, which shows the distribution of virtual cells as a function of their I_{Kr}, I_{CaL}, and I_{K1} conductances (θ_{Kr}, θ_{CaL}, and θ_{K1}, respectively). As can be appreciated, pro-arrhythmic cells were most commonly located in regions with low θ_{Kr} and θ_{K1}, thereby exemplifying how I_{Kr} and I_{K1} downregulation contribute to pro-arrhythmicity. The effect of I_{CaL} was only significant in the region where $\theta_{Kr} < 1$, implying that the role of I_{CaL} was dependent on I_{Kr} expression. The information needed to reproduce **Figure 11** is available in **Data Sheet 1** of the Supplementary Material (section 1.5).

4. DISCUSSION

A population of human ventricular stochastic AP models was built and shown to reproduce a range of responses in terms of BVR and LF oscillations of APD following enhanced sympathetic activity, as reported experimentally (Porter et al., 2018). The models included descriptions of electrophysiology, βA signaling,

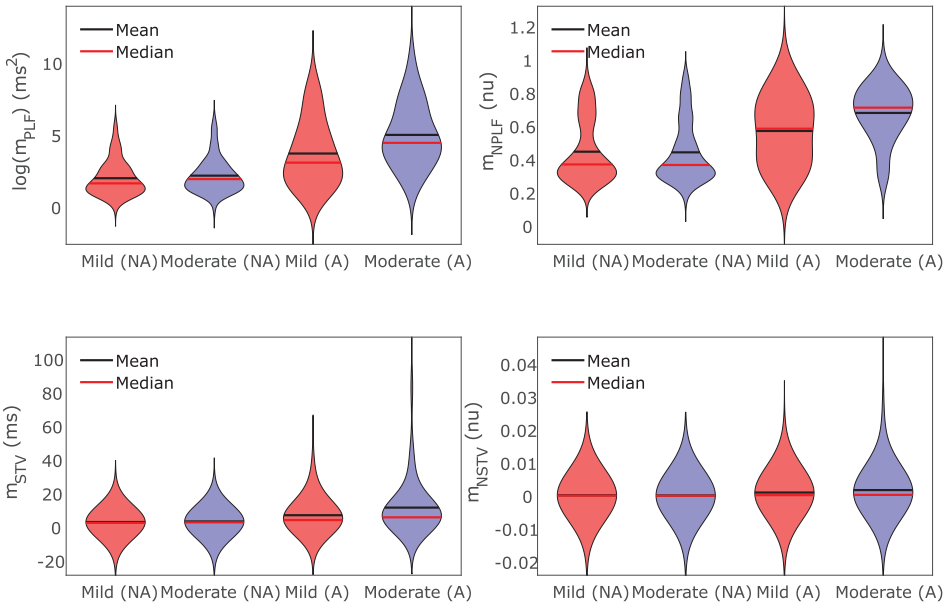

FIGURE 9 | Violin plots representing the distributions of $log(m_{PLF})$, m_{NPLF}, m_{STV}, and m_{NSTV} for mild and moderate disease conditions. The whole population of models is divided into two subpopulations: the set of cells presenting (denoted by A) and not presenting (denoted by NA) pro-arrhythmic events following SP under severe disease conditions.

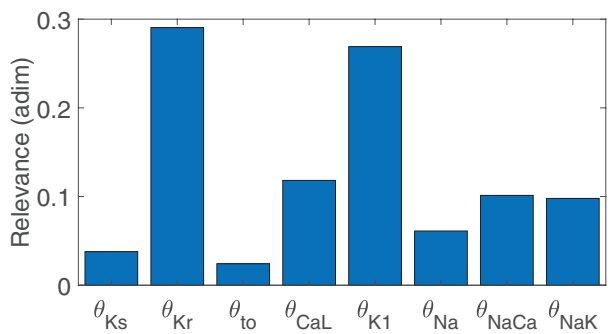

FIGURE 10 | Relevance of ionic current conductances to pro-arrhythmic events.

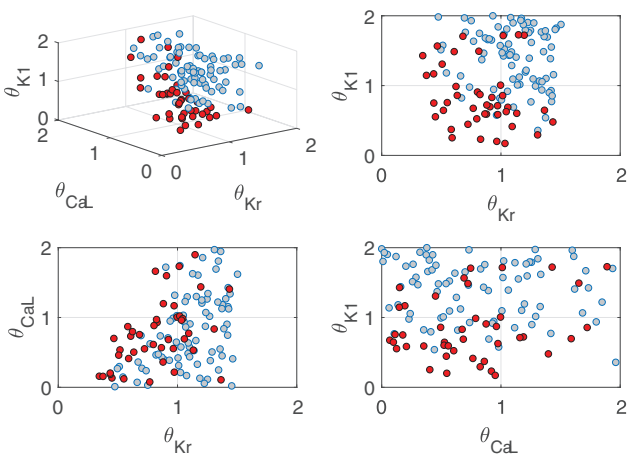

FIGURE 11 | Location of cells presenting (red) and not presenting (gray) pro-arrhythmic events under simulated severe disease conditions as a function of relevant ionic current conductance values.

mechanics and ionic gating stochasticity and served to investigate the interactions between the two investigated phenomena, namely temporal variability and LF oscillatory behavior of APD, following sympathetic provocation. Ionic mechanisms underlying inter-individual differences in those phenomena were ascertained and individual characteristics associated with concomitantly large beat-to-beat variability and LF oscillations of repolarization were established. These were linked to higher susceptibility to electrical instabilities in the presence of disease conditions like Ca^{2+} overload and RRR.

4.1. Relationship Between Sympathetically-Mediated BVR and LF Oscillations of APD in a Human Ventricular Population

Increases in LF oscillations of repolarization in response to enhanced sympathetic activity have been described at the level of the electrocardiographic T-wave and QT interval in humans and animals (Negoescu et al., 1997; Rizas et al., 2014, 2016) and at the level of the ventricular APD in ambulatory patients (Hanson et al., 2014; Porter et al., 2018). A direct effect related to enhanced activity of the sympathetic nerves innervating ventricular myocardium, rather than just an effect attributable to heart rate variability, has been proved (Negoescu et al., 1997; Rizas et al., 2014; Porter et al., 2018). In this study, phasic βAS and mechanical stretch were simulated in association with muscle sympathetic nerve activity patterns during enhanced sympathetic activity (Pagani et al., 1997). Pacing at a constant rate was applied to the models. In accordance with experimental observations,

increments in absolute and normalized LF power of APD have been overall measured in our population. Nevertheless, there is a high degree of inter-individual variability, with some individual cases showing no change or even a decrease in LF oscillations of APD in response to SP, which is in line with experimental reports as well.

Additionally, clinical and experimental studies have reported that enhanced sympathetic activity leads to increased BVR in patients with the long QT syndrome type 1 (Satomi et al., 2005) and animal models of this disease (Gallacher et al., 2007) as well as in heart failure patients (Porter et al., 2017). Our human ventricular AP models, by including stochastic expressions of ionic current gating, allowed investigation of BVR at baseline and in response to SP. In agreement with experimental evidences, most of the models in our diseased population have shown sympathetically-mediated increments in BVR. The increase in BVR in the referred experimental/clinical studies as well as in our simulations of disease could be explained by βAS effects under conditions of reduced IKs, which is indeed the case in our simulations and in long QT syndrome type 1 investigations and could also be the case in heart failure following previous reports suggesting downregulation of this current in failing hearts (Long et al., 2015). Also, mechanical effects associated with increased sympathetic activity could synergistically enhance BVR. Furthermore, in our simulations, a wide range of individual behaviors in terms of BVR patterns could be characterized following SP, in line with experimental data.

The interactions between BVR and LF oscillations of APD have been recently investigated in ambulatory patients with heart failure following a standard sympathetic provocation maneuver (Porter et al., 2018). In the present study, a strong correlation between BVR and LF oscillation measures has been measured as well by simulation of SP through phasic βAS and mechanical stretch in human ventricular myocytes. This holds true for physiological conditions and for disease conditions, simulated by Ca^{2+} overload and RRR, which are characteristic of diseased hearts like those of heart failure patients. In both simulations and experiments the variability measurements m_{SD}, m_{NSD}, m_{PLF} and m_{PLF} were quantified. In addition, the BVR measurement m_{STV}, which accounts for information on the APD variation between consecutive beats and has been extensively used for arrhythmic risk prediction (Thomsen et al., 2004; Hinterseer et al., 2010), was included in this study together with its APD-normalized version m_{NSTV}.

The strong correlation between m_{STV} and m_{PLF} found in simulations and experiments can be explained in light of our simulation outcomes. On the one hand, an increment in temporal APD variability associated with random ionic gating directly augments the LF power of APD, as it induces a rise in the power of APD at all frequencies. Although the measurement m_{NPLF} normalizes m_{PLF} by the total power, this marker turns out to be more insensitive to the amplitude of the LF oscillations of APD than m_{PLF}, while still indicative of the presence or absence of such oscillatory behavior. In the case of BVR, the normalized measurement m_{NSTV} has been quantified on top of m_{STV} to correct for the dependence on the APD. Even if the applied APD correction is able to reduce the correlation between APD and m_{NSTV} to a good extent, it does not abolish it completely. The very strong correlation between m_{PLF} and m_{STV}, both at baseline and following SP, dropped to very low correlation when m_{NPLF} and m_{NSTV} were evaluated at baseline. Following SP, the correlation between m_{NPLF} and m_{NSTV} was still remarkable, which can be explained by the fact that the presence of a marked LF oscillatory pattern directly impacts the temporal APD variability by increasing beat-to-beat APD differences.

4.2. Main Contributors to Increased BVR and LF Oscillations of APD Following Enhanced Sympathetic Activity

The tight relationship between BVR and LF oscillations of APD following enhanced sympathetic activity suggests there could be common modulators of both phenomena. By building a population of virtual cells representing a range of experimentally reported characteristics, in this study it was possible to elucidate the ionic current conductances with a major contribution to inter-individual differences in absolute (m_{STV} and m_{PLF}) and normalized (m_{NSTV} and m_{NPLF}) BVR and LF oscillation markers. For such elucidation, an approach based on the Automatic Relevance Determination (ARD) technique was developed. Similar approaches have been proposed in the context of magnetoencephalography (Nummenmaa et al., 2007) and wireless communications (Jacobs, 2012), among others, but to the best of our knowledge this is the first time an ARD-based technique is used to identify ionic modulators of cardiac electrophysiological phenomena.

In Pueyo et al. (2016b) the mechanisms underlying LF oscillations of ventricular APD were investigated by simulating phasic βAS and mechanical stretch in association with enhanced sympathetic activity. Differential I_{Ks} and I_{CaL} phosphorylation and dephosphorylation kinetics in response to βAS together with variations in Ca^{2+} cycling and SACs in response to stretch were found to synergistically underlie LF oscillatory behavior under SP. While that study provided meaningful insights into the bases for LF oscillations of ventricular repolarization, only an average cell was modeled, which did not allow investigation of inter-individual differences in LF oscillations of APD as in the present study. Also, the models of the population built here are stochastic, as opposed to the deterministic models employed in Pueyo et al. (2016b), thus allowing to quantify BVR at baseline and its change in response to SP. This is of major relevance for investigation of the interactions between BVR and LF oscillations of APD and of their modulators in a whole population.

Our results highlighted the relevance of I_{Kr}, I_{CaL}, and I_{K1} conductances in modulating inter-individual differences in both BVR and LF oscillatory pattern of APD under SP. Regarding I_{Kr}, its downregulation was shown to be a key factor for augmentation of m_{STV} and m_{PLF} but less important when considering their normalized counterparts m_{NSTV} and m_{NPLF}. Concerning LF oscillations of APD, there is little investigation in the literature into factors acting to modulate their magnitude. In Pueyo et al. (2016b), a reduction in the repolarization current was shown to amplify APD oscillatory behavior. Our results are in line with such observations. Considering the fact that m_{NPLF} does not

reflect the magnitude of the oscillations but mostly its presence or absence, this normalized marker was found not to be modulated by I_{Kr}. Regarding BVR, a variety of experimental, clinical and computational studies have addressed the role of ionic current conductances in modulating beat-to-beat temporal variability quantified by markers such as m_{STV} or m_{SD}. In accordance with the results presented in Pueyo et al. (2011) for baseline conditions and Heijman et al. (2013) for βAS, our study has shown I_{Kr} downregulation to act as a contributor of BVR magnification. Since such a contribution is to a large extent mediated by APD lengthening, it becomes importantly reduced when measured by markers that include APD normalization, such as m_{NSTV} or m_{NSD}.

Another very relevant current in the modulation of BVR and LF oscillatory behavior of APD was I_{CaL}. Although no previous studies in the literature have investigated the role of I_{CaL} as a modulator of LF oscillation amplitude, there have been a number of studies addressing its role as a modulator of BVR. In Lemay et al. (2011), I_{CaL} downregulation was shown to increase the random channel fluctuation effects in guinea pig models, which is in good agreement with our presented results. On top of the contribution of I_{CaL}, a role for I_{Ks} and persistent I_{Na} currents in enhancing BVR was also demonstrated in Lemay et al. (2011). We could not find such a role for those two currents, which could be due to differences between species [guinea pig in Lemay et al. (2011) and human in this study] and to the fact that this study investigated conditions of enhanced sympathetic activity rather than baseline conditions.

Regarding I_{K1} regulation, this is, to the best of our knowledge, the first study identifying its relevance to BVR and LF oscillations of APD. In our results, I_{K1} downregulation appears as a relevant contributor when SACs are incorporated into the models to simulate mechanical stretch changes associated with SP. Under donwregulated I_{K1}, SACs contribute to alter the AP shape during the last part of repolarization in a phasic manner, leading to increments in both BVR and LF oscillations.

As chronotropic effects of sympathetic provocation have been well documented in *in vivo* studies, computational simulations were additionally carried out while pacing the virtual cells at higher frequencies. The main ionic contributors I_{Kr}, I_{K1}, and I_{CaL} are confirmed to remain very relevant to explain inter-individual differences in BVR and LF oscillatory behavior in response to SP. Of note, the relevance of I_{NaK} in determining LF oscillations of APD increases when the analysis is performed for pacing frequencies above 1 Hz.

4.3. Pro-arrhythmic Events Associated With Increased BVR and LF Oscillations of APD Under Severe Disease Conditions

Ca^{2+} overload and RRR are properties commonly present in diseased hearts, like those of patients with heart failure, ischemic heart disease or post-myocardial infarction (Dhalla and Temsah, 2001; Sridhar et al., 2008; Varró and Baczkó, 2011; Guo et al., 2012; Nissen et al., 2012; Gorski et al., 2015). In this study, BVR and LF oscillations of APD have been found to become increasingly accentuated in response to disease progression. These results are in line with those reported in previous clinical, experimental and theoretical studies of the literature. In isolated myocytes and animal models of diseases like diabetes, heart failure or post-myocardial infarction, exaggerated temporal APD variability has been observed in association with Ca^{2+} overload and RRR (Maltsev et al., 2007; Sridhar et al., 2008; Wu et al., 2008; Meo et al., 2016). In the long QT syndrome type 1, involving loss of I_{Ks} function, elevated ventricular repolarization variability in response to βAS has been documented and mechanisms have been proposed based on animal models, isolated myocytes and computer simulation research (Gallacher et al., 2007; Johnson et al., 2010, 2013; Heijman et al., 2013). In chronic atrioventricular block dogs, where ventricular remodeling importantly compromises repolarization reserve, beat-to-beat APD variability has been found to be augmented with respect to healthy dogs (Stams et al., 2016); an observation also confirmed at the level of ventricular myocytes (Antoons et al., 2015). A mechanical challenge in the form of preload variability has been reported to be essential in that augmentation, with mechano-electrical feedback through stretch-activated channels (SACs) postulated as a major mechanism (Stams et al., 2016). In Pueyo et al. (2016b), the presence of disease conditions has been reported to lead to notably augmented LF oscillations of APD.

Under severe disease conditions, arrhythmogenic manifestations have been found to arise in individual cases of our population presenting large temporal repolarization variability, either quantified at the LF band (LF oscillations) or at all frequencies (BVR). These observations are in agreement with studies relating disproportionate APD fluctuations, particularly in response to enhanced sympathetic activity, and the generation of afterdepolarizations and arrhythmias. In Gallacher et al. (2007) the authors used an *in vivo* canine model of the long QT syndrome type 1 to demonstrate that βAS enhanced temporal and spatial variability of ventricular repolarization, which precipitated Torsades de Pointes (TdP) arrhythmias. The association between increased BVR and the onset of TdP arrhythmias has also been demonstrated in dogs with chronic atrioventricular block (Thomsen et al., 2006; Wijers et al., 2018). In ventricular myocytes and wedge preparations from human end-stage failing hearts, βAS has been shown to generate electrical abnormalities that result in EADs and delayed afterdepolarizations (DADs) (Veldkamp et al., 2001; Lang et al., 2016). Using a rabbit model mimicking electrophysiological and contractile alterations in human HF, βAS has been reported to be a key factor in inducing DADs and increasing the propensity for triggered arrhythmias (Pogwizd et al., 2001). At the level of the surface ECG, increased BVR and LF oscillations of repolarization have been shown to be risk predictors of ventricular arrhythmias and sudden cardiac death (Wu et al., 2008; Rizas et al., 2014, 2017; Baumert et al., 2016).

Provided the tight relationship between magnification of BVR and LF oscillations of APD and pro-arrhythmic risk, the existence of common modulators has been explored in the present study. Canonical Correlation Analysis has been proposed to identify ionic factors contributing to pro-arrhythmic risk following enhanced sympathetic activity. CCA revealed the important role

of I_{K1}, I_{Kr}, and I_{CaL} in the development of pro-arrhythmic events. These same factors are those primarily involved in modulation of sympathetically-mediated BVR and LF oscillations of APD. The role of I_{K1} in contributing to arrhythmogenesis has been reported in a rabbit model of heart failure, where the combination of upregulated I_{NaCa}, downregulated I_{K1} and residual βA responsiveness has been shown to increase the propensity for triggered arrhythmias (Pogwizd et al., 2001). In our study, the contribution of I_{K1} downregulation to pro-arrhythmicity in association with elevated temporal variability might have been more prominent if our population of stochastic AP models had been built based on an electrophysiological model more likely producing delayed afterdepolarizations under downregulated I_{K1}, and possibly upregulated I_{NaCa}, as compared to the ORd model. The role of I_{Kr} in arrhythmogenesis has been well established in a variety of previously published investigations. In Sridhar et al. (2008), the loss of repolarizing currents, including I_{Kr}, has been described to lead to increased BVR, repolarization instability and afterdepolarizations in myocytes from dogs susceptible to sudden cardiac death. In Pueyo et al. (2016b) reduced I_{Kr} and I_{Ks} have been reported to cause AP irregularities associated with enhanced LF oscillations of APD induced by sympathetic provocations. The implications of I_{Kr} inhibition in promoting ventricular arrhythmias associated with increased temporal APD dispersion has been further demonstrated in animal models of disease (Stams et al., 2016). On top of K^+ currents, the present work has identified I_{CaL} current as another relevant contributor to pro-arrhythmia associated with elevated BVR and LF oscillations of APD, even if conditioned to the presence of reduced I_{Kr}. In line with these results, increased I_{CaL} has been demonstrated to facilitate electrical abnormalities in the form of EADs in ventricular myocytes from human failing hearts (Veldkamp et al., 2001). The contribution of increased I_{CaL} to arrhythmogenesis during βAS has been also shown in Johnson et al. (2013) under reduced I_{Ks}.

In this study, other currents, like I_{Ks} and I_{NaL}, were found to have minor relevance as contributors to arrhythmogenesis in association with temporal dispersion of repolarization. This is contrast to previous studies showing major roles of I_{Ks} downregulation and I_{NaL} upregulation (Undrovinas et al., 2006; Gallacher et al., 2007; Maltsev et al., 2007; Wu et al., 2008; Johnson et al., 2010, 2013; Heijman et al., 2013). This discrepancy may be explained by differences between species, modeling characteristics and, importantly, investigated conditions, since this study has focused on the investigation of arrhythmic events occurring following enhanced sympathetic activity.

4.4. Limitations

The stochastic models built in this study included random gating descriptions for major ionic currents active during AP repolarization like I_{Ks}, I_{Kr}, I_{to}, and I_{CaL}, as in previous studies of the literature (Pueyo et al., 2016a; Tixier et al., 2017). Future studies could include stochasticity in other currents like I_{NaL}, whose contribution to BVR has been reported in canine ventricular models (Heijman et al., 2013).

In the present work the ORd ventricular AP model has been used, which was developed based on extensive undiseased human data. In this model the effect of varying the I_{Ks} current on AP is significantly smaller than in other human ventricular cell models, like the ten Tusscher-Panfilov model (ten Tusscher and Panfilov, 2006). The low relevance of I_{Ks} as an ionic modulator of BVR and LF oscillations of APD found in this work may have to do with it. In Pueyo et al. (2016b), which served as a starting point for the present work, several electrophysiological, mechanical and adrenergic signaling models were tested and only some quantitative differences could be found, while the conclusions remained qualitatively the same for all models. Nevertheless, the role of certain ionic currents in modulating inter-individual differences in BVR and LF oscillatory behavior, as investigated in this study, might still be different if another AP model were used as a basis. This should be addressed in future works.

Also in relation to the use of the ORd model as a basis for the development of the population of models in our study, it should be noted that other ventricular AP models with updated mechanisms of Ca^{2+} induced Ca^{2+} release could provide additional insight into the occurrence of spontaneous Ca^{2+} release and delayed afterdepolarizations in association with elevated BVR and LF oscillations of APD. Indeed, previous studies have been shown that Ca^{2+} handling abnormalities are a major driver of BVR during βAS (Johnson et al., 2013) and a link between Ca^{2+} handling and arrhythmia liability during increased sympathetic activity has been demonstrated, particularly in the setting of heart failure (Johnson and Antoons, 2018).

The population of human ventricular cells used in this work was generated by varying the conductances of eight ionic currents. Ionic parameters other than maximal current conductances might also represent relevant mechanisms underlying the interactions between BVR and LF oscillations of APD. In particular for the I_{CaL} current, previous studies have proved that modulation of other biophysical properties, like a reduction in the amplitude of the non-inactivating pedestal component of I_{CaL}, allows to effectively suppress EADs without blocking peak I_{CaL}, thus preserving excitation-contraction coupling (Madhvani et al., 2015). Future work could address the investigations of the present study by generating a population of virtual cells where biophysical ionic parameters other than maximal conductances were varied, which could eventually lead to findings that developed into more clinically useful therapeutic approaches.

The present study has focused on single cells, while the available experimental data on the interactions between BVR and LF oscillations of human APD are from *in vivo* measurements in ambulatory heart failure patients. Simulated results qualitatively reproduced the behavior observed in the experiments. Future work could include assessment of those interactions in tissue and whole-heart models. Nonetheless, cell-to-cell coupling has been shown to be remarkably reduced in heart failure and other disease conditions, which would render cell and tissue results close to each other.

Statistical approaches based on ARD and CCA have been used in this study. Future works could investigate generalization of these techniques to consider nonlinear relationships by using kernel functions, even if a larger number of simulations would be required to avoid overfitting.

5. CONCLUSIONS

Human ventricular models including descriptions of cell electrophysiology, ion channel stochasticity, β-adrenergic signaling and mechanical stretch were developed. These models reproduced experimentally reported interactions between beat-to-beat variability and low-frequency oscillations of repolarization in response to enhanced sympathetic activity. Ionic factors underlying correlated increments in both phenomena were investigated, which included downregulation of the inward and rapidly activating delayed rectifier K^+ currents and the L-type Ca^{2+} current. Concomitantly elevated levels of beat-to-beat repolarization variability and its low-frequency oscillations in diseased ventricles led to electrical instabilities and arrhythmogenic events. This investigation serves as a basis for future studies aiming at improving arrhythmic risk stratification and guiding the search for more efficient anti-arrhythmic therapies.

AUTHOR CONTRIBUTIONS

EP and PT devised the project, the main conceptual ideas and proof outline, and were responsible for overseeing the research and providing critical insight and recommendations regarding the focus, structure, and content of the paper. DS-P and JF-B performed computational simulations and analyzed the data results. BP and SvD contributed with technical details and analysis support. All authors participated in writing and proofreading throughout the publication process.

FUNDING

This work was supported by the European Research Council through grant ERC-2014-StG 638284, by MINECO (Spain) through project DPI2016-75458-R, by MULTITOOLS2HEART-ISCIII, by Gobierno de Aragón (Reference Group BSICoS T39-17R) cofunded by FEDER 2014-2020, by European Social Fund (EU) and Gobierno de Aragón through project LMP124_18 and a personal predoctoral grant to DS-P. Computations were performed by ICTS NANBIOSIS (HPC Unit at University of Zaragoza).

SUPPLEMENTARY MATERIAL

The Supplementary Material for this article can be found online at: https://www.frontiersin.org/articles/10.3389/fphys.2019.00916/full#supplementary-material

Data Sheet 1 | Population of virtual cells indicating the pro-arrhythmic models distribution (Figure-11-master.zip). This Data Sheet contains the ionic factors associated with each virtual cell, both for the group presenting and the group not presenting pro-arrhythmic events (as shown in **Figure 11**).

Data Sheet 2 | Automatic Relevance Determination (automatic-relevance-master.zip). This Data Sheet presents the Python code used to unravel individual and common factors, in form of ionic conductance levels, contributing to Beat-to-beat Variability of Repolarization and Low-Frequency Oscillations.

Data Sheet 3 | This document contains additional information about the stochastic ORd model and the stretch-activated channels and βAS formulation. In addition, details on the simulation of healthy and disease conditions are provided. Additional figures are included to facilitate understanding.

REFERENCES

Antoons, G., Johnson, D. M., Dries, E., Santiago, D. J., Ozdemir, S., Lenaerts, I., et al. (2015). Calcium release near L-type calcium channels promotes beat-to-beat variability in ventricular myocytes from the chronic AV block dog. *J. Mol. Cell. Cardiol.* 89, 326–334. doi: 10.1016/j.yjmcc.2015.10.008

Baumert, M., Porta, A., Vos, M. A., Malik, M., Couderc, J.-P., Laguna, P., et al. (2016). QT interval variability in body surface ECG: measurement, physiological basis, and clinical value: position statement and consensus guidance endorsed by the European Heart Rhythm Association jointly with the ESC Working Group on Cardiac Cellular Electrophysiology. *Europace* 18, 925–944. doi: 10.1093/europace/euv405

Boyd, S., and Vandenberghe, L. (2004). *Convex Optimization*. Cambridge: Cambridge University Press.

Britton, O. J., Bueno-Orovio, A., Virág, L., Varró, A., and Rodriguez, B. (2017). The electrogenic Na+/K+ pump is a key determinant of repolarization abnormality susceptibility in human ventricular cardiomyocytes: a population-based simulation study. *Front. Physiol.* 8:278. doi: 10.3389/fphys.2017.00278

Dhalla, N. S., and Temsah, R. M. (2001). Sarcoplasmic reticulum and cardiac oxidative stress: an emerging target for heart disease. *Emerging Ther. Targets* 5, 205–217. doi: 10.1517/14728222.5.2.205

Gallacher, D. J., Van de Water, A., van der Linde, H., Hermans, A. N., Lu, H. R., Towart, R., et al. (2007). *In vivo* mechanisms precipitating Torsades de Pointes in a canine model of drug-induced long-QT1 syndrome. *Cardiovas. Res.* 76, 247–256. doi: 10.1016/j.cardiores.2007.06.019

Gorski, P. A., Ceholski, D. K., and Hajjar, R. J. (2015). Altered myocardial calcium cycling and energetics in heart failure a rational approach for disease treatment. *Cell Metab.* 21, 183–194. doi: 10.1016/j.cmet.2015.01.005

Grandi, E., Pasqualini, F. S., and Bers, D. M. (2010). A novel computational model of the human ventricular action potential and Ca transient. *J. Mol. Cell. Cardiol.* 48, 112–121. doi: 10.1016/j.yjmcc.2009.09.019

Gunn, S. R., and Kandola, J. S. (2002). Structural modelling with sparse kernels. *Mach. Learn.* 48, 137–163. doi: 10.1023/A:1013903804720

Guo, D., Liu, Q., Liu, T., Elliott, G., Gingras, M., Kowey, P. R., et al. (2011). Electrophysiological properties of HBI-3000: a new antiarrhythmic agent with multiple-channel blocking properties in human ventricular myocytes. *J. Cardiovasc. Pharmacol.* 57, 79–85. doi: 10.1097/FJC.0b013e3181ffe8b3

Guo, X., Gao, X., Wang, Y., Peng, L., Zhu, Y., and Wang, S. (2012). Iks protects from ventricular arrhythmia during cardiac ischemia and reperfusion in rabbits by preserving the repolarization reserve. *PLoS ONE* 7:e31545. doi: 10.1371/journal.pone.0031545

Hanson, B., Child, N., Van Duijvenboden, S., Orini, M., Chen, Z., Coronel, R., et al. (2014). Oscillatory behavior of ventricular action potential duration in heart failure patients at respiratory rate and low frequency. *Front. Physiol.* 5:414. doi: 10.3389/fphys.2014.00414

Hardoon, D. R., Szedmak, S., and Shawe-Taylor, J. (2004). Canonical correlation analysis: an overview with application to learning methods. *Neural Comput.* 16, 2639–2664. doi: 10.1162/0899766042321814

Hegyi, B., Bányász, T., Izu, L. T., Belardinelli, L., Bers, D. M., and Chen-Izu, Y. (2018). β-adrenergic regulation of late Na^+ current during cardiac action potential is mediated by both PKA and CaMKII. *J. Mol. Cell. Cardiol.* 123, 168–179. doi: 10.1016/j.yjmcc.2018.09.006

Heijman, J., Volders, P. G., Westra, R. L., and Rudy, Y. (2011). Local control of β-adrenergic stimulation: effects on ventricular myocyte electrophysiology and Ca^2+-transient. *J. Mol. Cell. Cardiol.* 50, 863–871. doi: 10.1016/j.yjmcc.2011.02.007

Heijman, J., Zaza, A., Johnson, D. M., Rudy, Y., Peeters, R. L., Volders, P. G., et al. (2013). Determinants of beat-to-beat variability of repolarization duration in

the canine ventricular myocyte: a computational analysis. *PLoS Comput. Biol.* 9:e1003202. doi: 10.1371/journal.pcbi.1003202

Hinterseer, M., Beckmann, B.-M., Thomsen, M. B., Pfeufer, A., Ulbrich, M., Sinner, M. F., et al. (2010). Usefulness of short-term variability of qt intervals as a predictor for electrical remodeling and proarrhythmia in patients with nonischemic heart failure. *Am. J. Cardiol.* 106, 216–220. doi: 10.1016/j.amjcard.2010.02.033

Hinterseer, M., Thomsen, M. B., Beckmann, B.-M., Pfeufer, A., Schimpf, R., Wichmann, H.-E., et al. (2008). Beat-to-beat variability of QT intervals is increased in patients with drug-induced long-QT syndrome: a case control pilot study. *Eur. Heart J.* 29, 185–190. doi: 10.1093/eurheartj/ehm586

Hotelling, H. (1936). Relations between two sets of variates. *Biometrika* 28, 321–377. doi: 10.1093/biomet/28.3-4.321

Isenberg, G., Kazanski, V., Kondratev, D., Gallitelli, M. F., Kiseleva, I., and Kamkin, A. (2003). Differential effects of stretch and compression on membrane currents and $[Na^+]_c$ in ventricular myocytes. *Prog. Biophys. Mol. Biol.* 82, 43–56. doi: 10.1016/S0079-6107(03)00004-X

Jacobs, J. P. (2012). Bayesian support vector regression with automatic relevance determination kernel for modeling of antenna input characteristics. *IEEE Trans. Antennas Propag.* 60, 2114–2118. doi: 10.1109/TAP.2012.2186252

Johnson, D. M., and Antoons, G. (2018). Arrhythmogenic mechanisms in heart failure: linking β-adrenergic stimulation, stretch, and calcium. *Front. Physiol.* 9:1453. doi: 10.3389/fphys.2018.01453

Johnson, D. M., Heijman, J., Bode, E. F., Greensmith, D. J., van der Linde, H., Abi-Gerges, N., et al. (2013). Diastolic spontaneous calcium release from the sarcoplasmic reticulum increases beat-to-beat variability of repolarization in canine ventricular myocytes after β-adrenergic stimulation. *Circ. Res.* 112, 246–256. doi: 10.1161/CIRCRESAHA.112.275735

Johnson, D. M., Heijman, J., Pollard, C. E., Valentin, J.-P., Crijns, H. J., Abi-Gerges, N., et al. (2010). Iks restricts excessive beat-to-beat variability of repolarization during beta-adrenergic receptor stimulation. *J. Mol. Cel. Cardiol.* 48, 122–130. doi: 10.1016/j.yjmcc.2009.08.033

Jost, N., Varro, A., Szuts, V., Kovacs, P. P., Seprényi, G., Biliczki, P., et al. (2008). Molecular basis of repolarization reserve differences between dogs and man. *Circulation* 118:S342.

Kaya, H., Eyben, F., Salah, A. A., and Schuller, B. (2014). "Cca based feature selection with application to continuous depression recognition from acoustic speech features," in *2014 IEEE International Conference on Acoustics, Speech and Signal Processing (ICASSP)* (Florence: IEEE), 3729–3733. doi: 10.1109/ICASSP.2014.6854298

Kistamas, K., Szentandrassy, N., Hegyi, B., Vaczi, K., Ruzsnavszky, F., Horvath, B., et al. (2015). Changes in intracellular calcium concentration influence beat-to-beat variability of action potential duration in canine ventricular myocytes. *J. Physiol. Pharmacol.* 66, 73–81.

Lang, C. N., Menza, M., Jochem, S., Franke, G., Perez Feliz, S., Brunner, M., et al. (2016). Electro-mechanical dysfunction in long QT syndrome: role for arrhythmogenic risk prediction and modulation by sex and sex hormones. *Prog. Biophys. Mol. Biol.* 120, 255–269. doi: 10.1016/j.pbiomolbio.2015.12.010

Lemay, M., de Lange, E., and Kucera, J. P. (2011). Effects of stochastic channel gating and distribution on the cardiac action potential. *J. Theor. Biol.* 281, 84–96. doi: 10.1016/j.jtbi.2011.04.019

Long, V. P., Bonilla, I. M., Vargas-Pinto, P., Nishijima, Y., Sridhar, A., Li, C., et al. (2015). Heart failure duration progressively modulates the arrhythmia substrate through structural and electrical remodeling. *Life Sci.* 123, 61–71. doi: 10.1016/j.lfs.2014.12.024

MacKay, D. J. (1996). "Bayesian methods for Backpropagation networks," in *Models of Neural Networks III* (New York, NY: Springer), 211–254.

Madhvani, R. V., Angelini, M., Xie, Y., Pantazis, A., Suriany, S., Borgstrom, N. P. et al. (2015). Targeting the late component of the cardiac L-type Ca^{2+} current to suppress early afterdepolarizations. *J. Gen. Physiol.* 145, 395–404. doi: 10.1085/jgp.201411288

Magyar, J., Banyasz, T., Szentandrassy, N., potential, K., P Nanasi, P., and Satin, J. (2015). Role of gap junction channel in the development of beat-to-beat action potential repolarization variability and arrhythmias. *Curr. Pharm. Des.* 21, 1042–1052. doi: 10.2174/1381612820666141029102443

Maltsev, V. A., Silverman, N., Sabbah, H. N., and Undrovinas, A. I. (2007). Chronic heart failure slows late sodium current in human and canine ventricular myocytes: implications for repolarization variability. *Eur. J. Heart Fail.* 9, 219–227. doi: 10.1016/j.ejheart.2006.08.007

McKay, M. D., Beckman, R. J., and Conover, W. J. (1979). A comparison of three methods for selecting values of input variables in the analysis of output from a computer code. *Technometrics* 21:239. doi: 10.2307/1268522

Meo, M., Meste, O., Signore, S., Sorrentino, A., Cannata, A., Zhou, Y., et al. (2016). Reduction in Kv current enhances the temporal dispersion of the action potential in diabetic myocytes: insights from a novel repolarization algorithm. *J. Am. Heart Assoc.* 5:e003078. doi: 10.1161/JAHA.115.003078

Nánási, P. P., Magyar, J., Varró, A., and Ördög, B. (2017). Beat-to-beat variability of cardiac action potential duration: underlying mechanism and clinical implications. *Can. J. Physiol. Pharmacol.* 95, 1230–1235. doi: 10.1139/cjpp-2016-0597

Negoescu, R., Dinca-Panaitescu, S., Filcescu, V., Ionescu, D., and Wolf, S. (1997). Mental stress enhances the sympathetic fraction of QT variability in an RR-independent way. *Integr. Physiol. Behav. Sci.* 32, 220–227. doi: 10.1007/BF02688620

Niederer, S. A., Hunter, P. J., and Smith, N. P. (2006). A quantitative analysis of cardiac myocyte relaxation: a simulation study. *Biophys. J.* 90, 1697–1722. doi: 10.1529/biophysj.105.069534

Nissen, J. D., Thomsen, M. B., Bentzen, B. H., Diness, J. G., Diness, T. G., Jespersen, T., et al. (2012). Attenuated ventricular β-adrenergic response and reduced repolarization reserve in a rabbit model of chronic heart failure. *J. Cardiovasc. Pharmacol.* 59, 142–150. doi: 10.1097/FJC.0b013e318238727a

Nummenmaa, A., Auranen, T., Hämäläinen, M. S., Jääskeläinen, I. P., Sams, M., Vehtari, A., et al. (2007). Automatic relevance determination based hierarchical Bayesian MEG inversion in practice. *Neuroimage* 37, 876–889. doi: 10.1016/j.neuroimage.2007.04.021

O'Hara, T., Virág, L., Varró, A., and Rudy, Y. (2011). Simulation of the undiseased human cardiac ventricular action potential: model formulation and experimental validation. *PLoS Comput. Biol.* 7:e1002061. doi: 10.1371/journal.pcbi.1002061

Paavola, J., Väänänen, H., Larsson, K., Penttinen, K., Toivonen, L., Kontula, K., et al. (2015). Slowed depolarization and irregular repolarization in catecholaminergic polymorphic ventricular tachycardia: a study from cellular Ca^{2+} transients and action potentials to clinical monophasic action potentials and electrocardiography. *Eurospace* 18, 1599–1607. doi: 10.1093/europace/euv380

Pagani, M., Montano, N., Porta, A., Malliani, A., Abboud, F. M., Birkett, C., et al. (1997). Relationship between spectral components of cardiovascular variabilities and direct measures of muscle sympathetic nerve activity in humans. *Circulation* 95, 1441–1448. doi: 10.1161/01.CIR.95.6.1441

Pogwizd, S. M., Schlotthauer, K., Li, L., Yuan, W., and Bers, D. M. (2001). Arrhythmogenesis and contractile dysfunction in heart failure: roles of sodium-calcium exchange, inward rectifier potassium current, and residual β-adrenergic responsiveness. *Circ. Res.* 88, 1159–1167. doi: 10.1161/hh1101.091193

Porter, B., Bishop, M. J., Claridge, S., Behar, J., Sieniewicz, B. J., Webb, J., et al. (2017). Autonomic modulation in patients with heart failure increases beat-to-beat variability of ventricular action potential duration. *Front. Physiol.* 8:328. doi: 10.3389/fphys.2017.00328

Porter, B., Van Duijvenboden, S., Bishop, M. J., Orini, M., Claridge, S., Gould, J., et al. (2018). Beat-to-beat variability of ventricular action potential duration oscillates at low frequency during sympathetic provocation in humans. *Front. Physiol.* 9:147. doi: 10.3389/fphys.2018.00147

Pueyo, E., Corrias, A., Virág, L., Jost, N., Szél, T., Varró, A., et al. (2011). A multiscale investigation of repolarization variability and its role in cardiac arrhythmogenesis. *Biophys. J.* 101, 2892–2902. doi: 10.1016/j.bpj.2011.09.060

Pueyo, E., Dangerfield, C., Britton, O., Virág, L., Kistamás, K., Szentandrássy, N., et al. (2016a). Experimentally-based computational investigation into beat-to-beat variability in ventricular repolarization and its response to ionic current inhibition. *PLoS ONE* 11:e0151461. doi: 10.1371/journal.pone.0151461

Pueyo, E., Orini, M., Rodríguez, J. F., and Taggart, P. (2016b). Interactive effect of beta-adrenergic stimulation and mechanical stretch on low-frequency oscillations of ventricular action potential duration in humans. *J. Mol. Cell. Cardiol.* 97, 93–105. doi: 10.1016/j.yjmcc.2016.05.003

Ramirez, J., Orini, M., Tucker, J. D., Pueyo, E., and Laguna, P. (2017). Variability of ventricular repolarization dispersion quantified by time-warping the morphology of the T-waves. *IEEE Trans. Biomed. Eng.* 64, 1619–1630. doi: 10.1109/TBME.2016.2614899

Rasmussen, C. E. and Williams, C. K. (2006). *Gaussian Processes for Machine Learning* (Cambridge, MA: MIT Press).

Rizas, K. D., Hamm, W., Kääb, S., Schmidt, G., and Bauer, A. (2016). Periodic repolarisation dynamics: a natural probe of the ventricular response to sympathetic activation. *Arrhythm. Electrophysiol. Rev.* 5:31. doi: 10.15420/aer.2015:30:2

Rizas, K. D., McNitt, S., Hamm, W., Massberg, S., Kääb, S., Zareba, W., et al. (2017). Prediction of sudden and non-sudden cardiac death in post-infarction patients with reduced left ventricular ejection fraction by periodic repolarization dynamics: MADIT-II substudy. *Eur. Heart J.* 38, 2110–2118. doi: 10.1093/eurheartj/ehx161

Rizas, K. D., Nieminen, T., Barthel, P., Zürn, C. S., Kähönen, M., Viik, J., et al. (2014). Sympathetic activity–associated periodic repolarization dynamics predict mortality following myocardial infarction. *J. Clin. Invest.* 124, 1770–1780. doi: 10.1172/JCI70085

Satomi, K., Shimizu, W., Takaki, H., Suyama, K., Kurita, T., Aihara, N., et al. (2005). Response of beat-by-beat QT variability to sympathetic stimulation in the LQT1 form of congenital long QT syndrome. *Heart Rhythm* 2, 149–154. doi: 10.1016/j.hrthm.2004.11.010

Sheffield ML group (2012). *GPy: A Gaussian Process Framework in Python*. Available online at: http://github.com/SheffieldML/GPy

Soltis, A. R., and Saucerman, J. J. (2010). Synergy between CaMKII substrates and β-adrenergic signaling in regulation of cardiac myocyte Ca2+ handling. *Biophys. J.* 99, 2038–2047. doi: 10.1016/j.bpj.2010.08.016

Sridhar, A., Nishijima, Y., Terentyev, D., Terentyeva, R., Uelmen, R., Kukielka, M., et al. (2008). Repolarization abnormalities and afterdepolarizations in a canine model of sudden cardiac death. *Am. J. Physiol. Regul. Integr. Comp. Physiol.* 295, R1463–R1472. doi: 10.1152/ajpregu.90583.2008

Stams, T. R., Oosterhoff, P., Heijdel, A., Dunnink, A., Beekman, J. D., van der Nagel, R., et al. (2016). Beat-to-beat variability in preload unmasks latent risk of Torsade de Pointes in anesthetized chronic atrioventricular block dogs. *Circulation* 80, 1336–1345. doi: 10.1253/circj.CJ-15-1335

Szentandrássy, N., Kistamás, K., Hegyi, B., Horváth, B., Ruzsnavszky, F., Váczi, K., et al. (2015). Contribution of ion currents to beat-to-beat variability of action potential duration in canine ventricular myocytes. *Pfluegers Arch. Eur. J. Physiol.* 467, 1431–1443. doi: 10.1007/s00424-014-1581-4

ten Tusscher, K. H., and Panfilov, A. V. (2006). Alternans and spiral breakup in a human ventricular tissue model. *Am. J. Physiol. Heart Circ. Physiol.* 291, H1088–H1100. doi: 10.1152/ajpheart.00109.2006

Tereshchenko, L. G., Fetics, B. J., Domitrovich, P. P., Lindsay, B. D., and Berger, R. D. (2009). Prediction of ventricular tachyarrhythmias by intracardiac repolarization variability analysis. *Circ. Arrhyth. Electrophysiol.* 2:276. doi: 10.1161/CIRCEP.108.829440

Thomsen, M. B., Verduyn, S. C., Stengl, M., Beekman, J. D., de Pater, G., van Opstal, J., et al. (2004). Increased short-term variability of repolarization predicts d-sotalol–induced torsades de pointes in dogs. *Circulation* 110, 2453–2459. doi: 10.1161/01.CIR.0000145162.64183.C8

Thomsen, M. B., Volders, P. G., Beekman, J. D., Matz, J., and Vos, M. A. (2006). Beat-to-beat variability of repolarization determines proarrhythmic outcome in dogs susceptible to drug-induced Torsades de Pointes. *J. Am. Coll. Cardiol.* 48, 1268–1276. doi: 10.1016/j.jacc.2006.05.048

Tixier, E., Lombardi, D., Rodriguez, B., and Gerbeau, J.-F. (2017). Modelling variability in cardiac electrophysiology: a moment-matching approach. *J. R. Soc. Interface* 14:20170238. doi: 10.1098/rsif.2017.0238

Torres, D. A., Turnbull, D., Sriperumbudur, B. K., Barrington, L., and Lanckriet, G. R. (2007). "Finding musically meaningful words by sparse cca," in *Neural Information Processing Systems (NIPS) Workshop on Music, the Brain and Cognition* (Vancouver, BC).

Undrovinas, A. I., Belardinelli, L., Undrovinas, N. A., and Sabbah, H. N. (2006). Ranolazine improves abnormal repolarization and contraction in left ventricular myocytes of dogs with heart failure by inhibiting late sodium current. *J. Cardiovas. Electrophysiol.* 17, S169–S177. doi: 10.1111/j.1540-8167.2006.00401.x

Varró, A., and Baczkó, I. (2011). Cardiac ventricular repolarization reserve: a principle for understanding drug-related proarrhythmic risk. *Br. J. Pharmacol.* 164, 14–36. doi: 10.1111/j.1476-5381.2011.01367.x

Veldkamp, M. W., Verkerk, A. O., Van Ginneken, A. C., Baartscheer, A., Schumacher, C., de Jonge, N., et al. (2001). Norepinephrine induces action potential prolongation and early afterdepolarizations in ventricular myocytes isolated from human end-stage failing hearts. *Eur. Heart J.* 22, 955–963. doi: 10.1053/euhj.2000.2499

Verrier, R. L., Klingenheben, T., Malik, M., El-Sherif, N., Exner, D. V., Hohnloser, S. H., et al. (2011). Microvolt T-wave alternans: physiological basis, methods of measurement, and clinical utility consensus guideline by International Society for Holter and Noninvasive Electrocardiology. *J. Am. Coll. Cardiol.* 58, 1309–1324. doi: 10.1016/j.jacc.2011.06.029

Weise, L. D., and Panfilov, A. V. (2013). A discrete electromechanical model for human cardiac tissue: effects of stretch-activated currents and stretch conditions on restitution properties and spiral wave dynamics. *PLoS ONE* 8:e59317. doi: 10.1371/journal.pone.0059317

Wijers, S. C., Sprenkeler, D. J., Bossu, A., Dunnink, A., Beekman, J. D. M., Varkevisser, R., et al. (2018). Beat-to-beat variations in activation-recovery interval derived from the right ventricular electrogram can monitor arrhythmic risk under anesthetic and awake conditions in the canine chronic atrioventricular block model. *Heart Rhythm* 15, 442–448. doi: 10.1016/j.hrthm.2017.11.011

Wu, L., Guo, D., Li, H., Hackett, J., Yan, G.-X., Jiao, Z., et al. (2008). Role of late sodium current in modulating the proarrhythmic and antiarrhythmic effects of quinidine. *Heart Rhythm* 5, 1726–1734. doi: 10.1016/j.hrthm.2008.09.008

Xie, Y., Grandi, E., Puglisi, J. L., Sato, D., and Bers, D. M. (2013). β-adrenergic stimulation activates early afterdepolarizations transiently via kinetic mismatch of PKA targets. *J. Mol. Cell. Cardiol.* 58, 153–161. doi: 10.1016/j.yjmcc.2013.02.009

Yamabe, M., Sanyal, S. N., Miyamoto, S., Hadama, T., Isomoto, S., and Ono, K. (2007). Three different bradycardic agents, zatebradine, diltiazem and propranolol, distinctly modify heart rate variability and QT-interval variability. *Pharmacology* 80, 293–303. doi: 10.1159/000107103

Zaniboni, M., Pollard, A. E., Yang, L., and Spitzer, K. W. (2000). Beat-to-beat repolarization variability in ventricular myocytes and its suppression by electrical coupling. *Am. J. Physiol. Heart Circ. Physiol.* 278, H677–H687. doi: 10.1152/ajpheart.2000.278.3.H677

Zhu, X., Suk, H.-I., and Shen, D. (2014). "Multi-modality canonical feature selection for alzheimer's disease diagnosis," in *International Conference on Medical Image Computing and Computer-Assisted Intervention* (Boston, MA: Springer), 162–169.

Conflict of Interest Statement: The authors declare that the research was conducted in the absence of any commercial or financial relationships that could be construed as a potential conflict of interest.

frontiers in Physiology

ORIGINAL RESEARCH
published: 27 August 2019
doi: 10.3389/fphys.2019.01103

MRI-Based Computational Torso/Biventricular Multiscale Models to Investigate the Impact of Anatomical Variability on the ECG QRS Complex

Ana Mincholé[1†], Ernesto Zacur[2†], Rina Ariga[3], Vicente Grau[2‡] and Blanca Rodriguez[1‡]*

[1] Department of Computer Science, University of Oxford, Oxford, United Kingdom, [2] Institute of Biomedical Engineering (IBME), University of Oxford, Oxford, United Kingdom, [3] Division of Cardiovascular Medicine, Radcliffe Department of Medicine, University of Oxford, Oxford, United Kingdom

Aims: Patient-to-patient anatomical differences are an important source of variability in the electrocardiogram, and they may compromise the identification of pathological electrophysiological abnormalities. This study aims at quantifying the contribution of variability in ventricular and torso anatomies to differences in QRS complexes of the 12-lead ECG using computer simulations.

Methods: A computational pipeline is presented that enables computer simulations using human torso/biventricular anatomically based electrophysiological models from clinically standard magnetic resonance imaging (MRI). The ventricular model includes membrane kinetics represented by the biophysically detailed O'Hara Rudy model modified for tissue heterogeneity and includes fiber orientation based on the Streeter rule. A population of 265 torso/biventricular models was generated by combining ventricular and torso anatomies obtained from clinically standard MRIs, augmented with a statistical shape model of the body. 12-lead ECGs were simulated on the 265 human torso/biventricular electrophysiology models, and QRS morphology, duration and amplitude were quantified in each ECG lead for each of the human torso-biventricular models.

Results: QRS morphologies in limb leads are mainly determined by ventricular anatomy, while in the precordial leads, and especially V1 to V4, they are determined by heart position within the torso. Differences in ventricular orientation within the torso can explain morphological variability from monophasic to biphasic QRS complexes. QRS duration is mainly influenced by myocardial volume, while it is hardly affected by the torso anatomy or position. An average increase of 0.12 ± 0.05 ms in QRS duration is obtained for each cm^3 of myocardial volume across all the leads while it hardly changed due to changes in torso volume.

OPEN ACCESS

Edited by:
Javier Saiz,
Polytechnic University of Valencia, Spain

Reviewed by:
Arun V. Holden,
University of Leeds, United Kingdom
Gunnar Seemann,
University Heart Center Freiburg, Germany

****Correspondence:***
Ana Mincholé
ana.minchole@gmail.com

† These authors have contributed equally to this work as first authors

‡ These authors have contributed equally to this work as senior authors

Specialty section:
This article was submitted to Computational Physiology and Medicine, a section of the journal Frontiers in Physiology

Received: *08 March 2019*
Accepted: *08 August 2019*
Published: *27 August 2019*

Citation:
Mincholé A, Zacur E, Ariga R, Grau V and Rodriguez B (2019) MRI-Based Computational Torso/Biventricular Multiscale Models to Investigate the Impact of Anatomical Variability on the ECG QRS Complex. Front. Physiol. 10:1103. doi: 10.3389/fphys.2019.01103

Conclusion: Computer simulations using populations of human torso/biventricular models based on clinical MRI enable quantification of anatomical causes of variability in the QRS complex of the 12-lead ECG. The human models presented also pave the way toward their use as testbeds *in silico* clinical trials.

Keywords: clinical MRI-based torso/ventricular anatomical models, computer simulations, electrocardiogram, computational modeling, cardiac magnetic resonance imaging

INTRODUCTION

The electrocardiogram (ECG) is the most widely used clinical tool for evaluation of cardiac function. It records the electrical activity of the heart from electrodes positioned on the patient's torso, and the duration, amplitude, and morphology of ECG waveforms in the different leads are used for patients' diagnosis (Macfarlane and Lawrie, 2010).

Electrocardiogram features, and specifically its QRS complex, are affected not only by microstructural and physiological factors such as fiber orientation, Purkinje, myocardial conduction pathways and ionic currents (Boineau and Spach, 1968), but also by anatomical characteristics such as heart size and orientation, ventricular wall thickness, and body mass index (Hoekema et al., 1999, 2001; van Oosterom et al., 2000; Corlan et al., 2005). Quantitative information on the latter is, however, scarce. An experimental study showed large changes in QRS with varying heart locations, using one isolated perfused dog heart suspended in an electrolytic torso tank (MacLeod et al., 2000). Computer simulation studies are ideally placed to provide insight on the underlying basis of the ECG. Most of the previous computational studies focused on simulating the ECG using a single heart anatomy as (Keller et al., 2010; Zemzemi et al., 2013; Zemzemi and Rodriguez, 2015; Neic et al., 2017; Potse, 2018). More recently, a computational study using torso-biventricular anatomical models for five patients with heart failure showed that heart position and orientation strongly altered QRS amplitude, but only slightly, QRS duration (Nguyên et al., 2015). Sánchez et al. (2018) also provided insights into the key factors determining the ECG characteristics based on data for six heart failure patients. These studies highlight the potential of computer simulation studies using image-based models to shed light into the anatomical basis governing ECG variability and the QRS complex.

Whereas the dense volumetric information and high resolution of current CT scans is a clear advantage in the construction of cardiac anatomical models (Nazarian and Halperin, 2018) for ECG simulations, the radiation involved limits their use, for example in healthy subjects. The alternative of using magnetic resonance imaging (MRI) scans is very attractive as they provide good quality cardiac images safely and non-invasively. Clinical protocols, however, focus on the heart and therefore information on the torso is scarce. This is why previous studies have used MRI scans obtained using dedicated imaging protocols, not suitable for routine clinical practice (Potse et al., 2014; Sánchez et al., 2018). Methodological advances are therefore needed to exploit clinically standard MRI databases in computer simulations studies using image-based human torso/biventricular anatomical models.

The goal of this study is to conduct a computer simulation study using a population of 265 torso-ventricular anatomical models based on clinically standard MRI to dissect and quantify the individual contribution of ventricular and torso anatomy on QRS biomarkers in the 12-lead ECG. We hypothesize that QRS complexes in each of the standard 12-lead ECGs are affected differently by geometrical factors such as ventricular anatomy, heart orientation and location, or torso anatomy. To test this hypothesis, we develop a computational pipeline to conduct high-performance computing (HPC) electrophysiological simulations using biophysically detailed computational human models with ventricular and torso anatomies obtained from clinically standard cardiac MRI acquisitions. In a clinical scenario, the new insights could facilitate an improved discrimination in clinical ECG recordings between the contributions of patient's anatomical features and those arising from a cardiac condition or disease.

MATERIALS AND METHODS

Reconstruction of Ventricular and Torso Anatomical Meshes From Clinical MRI

In this study, a total of 265 combined torso-ventricles anatomical models were considered to quantify the effect of ventricular and torso volumes, and heart position and orientation on the QRS complex. Initially, as described in **Figure 1**, twenty-five human heart-torso models were generated by combining the bi-ventricular geometries (H1–H5) and torsos (T1–T5) (including corresponding heart orientations and positions) extracted from clinical MRI acquisition from 5 healthy subjects. The MRI datasets were selected to include ventricular end diastolic myocardial volumes between 75 and 170 cm^3 and torso volumes between 23 and 54 dm^3. Then, either rotation or translation was applied to each bi-ventricular model within each torso. 5° steps up to ($\pm$40° were considered both around the long axis (LA) and around the left-to-right-ventricle axis (LR) (Nguyên et al., 2015). Translation was considered in 1 cm steps up to ($\pm$4 cm either along the lateral or along cranio-caudal directions.

The MRI scans were obtained in five healthy subjects (three females and two males) with a range of ventricular end-diastolic myocardial volumes between 75 and 170 cm^3 and torso volumes between 23 and 54 dm^3, recruited at John Radcliffe Hospital, Oxford, United Kingdom. Subjects were non-smokers without cardiovascular disease, hypertension or diabetes, and no family history of cardiomyopathy or sudden cardiac death (SCD).

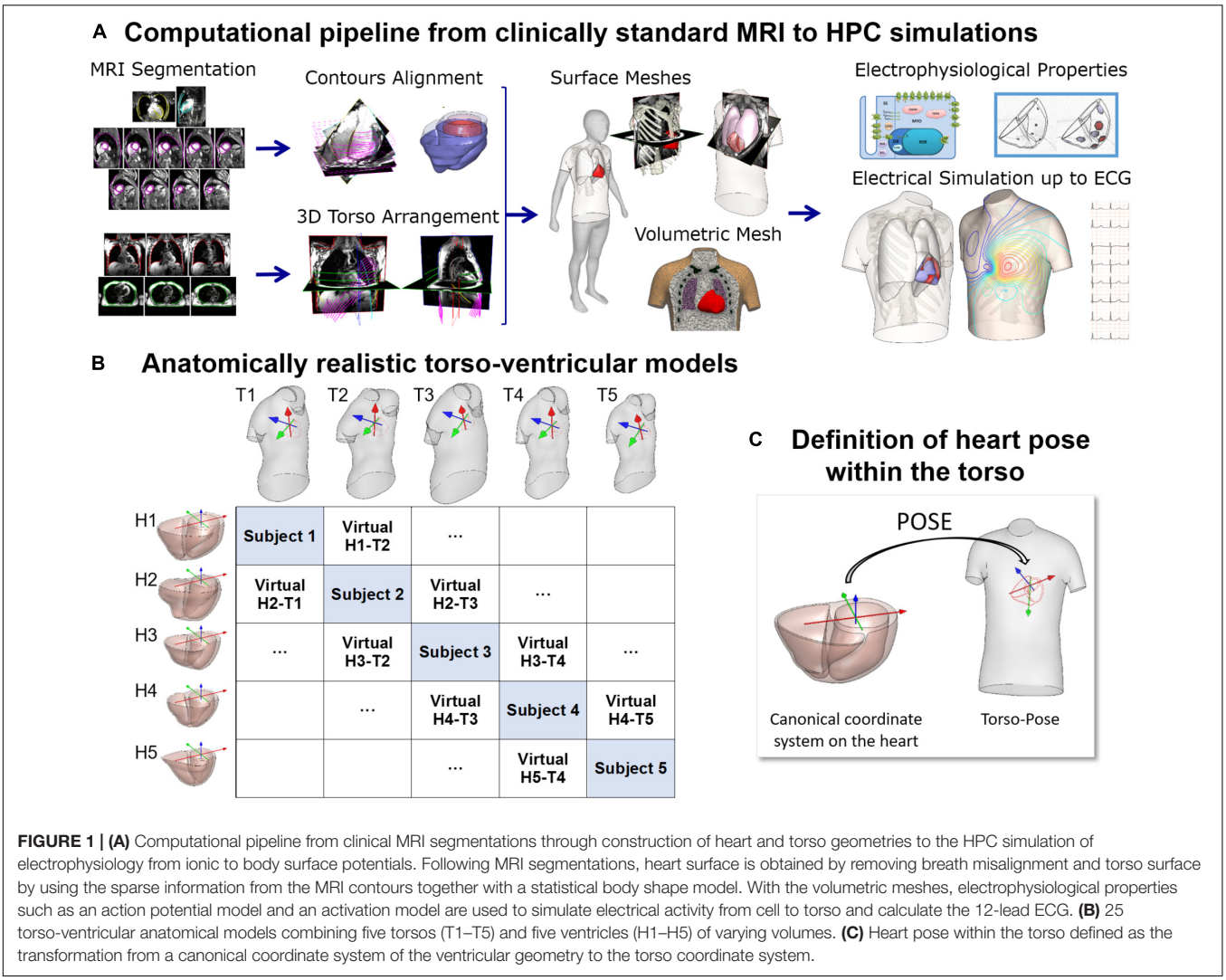

FIGURE 1 | (A) Computational pipeline from clinical MRI segmentations through construction of heart and torso geometries to the HPC simulation of electrophysiology from ionic to body surface potentials. Following MRI segmentations, heart surface is obtained by removing breath misalignment and torso surface by using the sparse information from the MRI contours together with a statistical body shape model. With the volumetric meshes, electrophysiological properties such as an action potential model and an activation model are used to simulate electrical activity from cell to torso and calculate the 12-lead ECG. **(B)** 25 torso-ventricular anatomical models combining five torsos (T1–T5) and five ventricles (H1–H5) of varying volumes. **(C)** Heart pose within the torso defined as the transformation from a canonical coordinate system of the ventricular geometry to the torso coordinate system.

Clinically standard cine cardiac MRI acquisition was performed for each subject, including long axis (LAX) and a stack of short axis (SAX) views. More specifically, for each subject, the data includes a 2 chamber LAX view, 4 chamber view, and a stack of SAX view from apex to base with 10 mm of separation between adjacent slices in the stack (8 mm slice thickness plus 2 mm gap). Image resolution ranges from 1.4 to 1.6 mm per pixel. An expert with several years of experience in cardiac MRI segmented the images at end-diastole including the following structures: left epicardium, left ventricle (LV) endocardium excluding the papillary muscles, and right ventricle (RV) endocardium (see **Figure 1A**, Segmentation). As the image resolution in standard MRI acquisitions does not allow to differentiate right ventricular epicardial and endocardial contours in the right ventricle, we synthesized right epicardial contours by a 3.5 mm offset from the endocardial contours (Prakash, 1978). Spatial misalignments in slice images and spatial discrepancies between the contours due to acquisitions at different breath holds were corrected by aligning intensity profiles of intersecting slices using a 3D rigid transformation for each image (Villard et al., 2017) (see **Figure 1A**, Contours alignment). Bi-ventricular geometries were built from the aligned contours using the end-diastole frames from the standard CINE acquisition as in Villard et al. (2018) and Zacur et al. (2017).

For the construction of the torso geometries, semi-automatic tools were developed and used to delineate the torso skin and lungs (Zacur et al., 2017). In brief, on each subject, the scout images (localizers), as well as, most of the MRI images (SAX and LAX images) with a large enough field of view were used and contoured. The sparse 3D geometrical information from the torso images is insufficient for the use of classical segmentation to surface methods such as isocontouring tools (**Figure 1A**, 3-Dimensional torso arrangement). Thus, we developed and applied a methodology to fit a statistical shape model of the human body to the skin contours (Zacur et al., 2017). The torso contours together with subject height, weight and gender information were used to reconstruct a body surface belonging to a learned class of plausible body shapes from the statistical shape model (Pishchulin et al., 2017; Zacur et al., 2017). The average discrepancy between MRI-based contours and model surface is

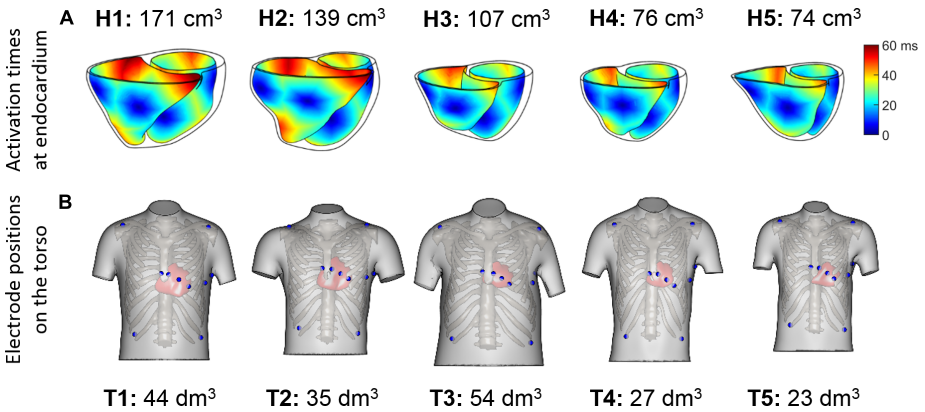

FIGURE 2 | (A) Endocardial activation maps for the five ventricular geometries. Information about ventricular volumes is also provided. **(B)** Homologous 12-lead electrode positions for the five virtualized subjects. Information about the torso volumes is provided.

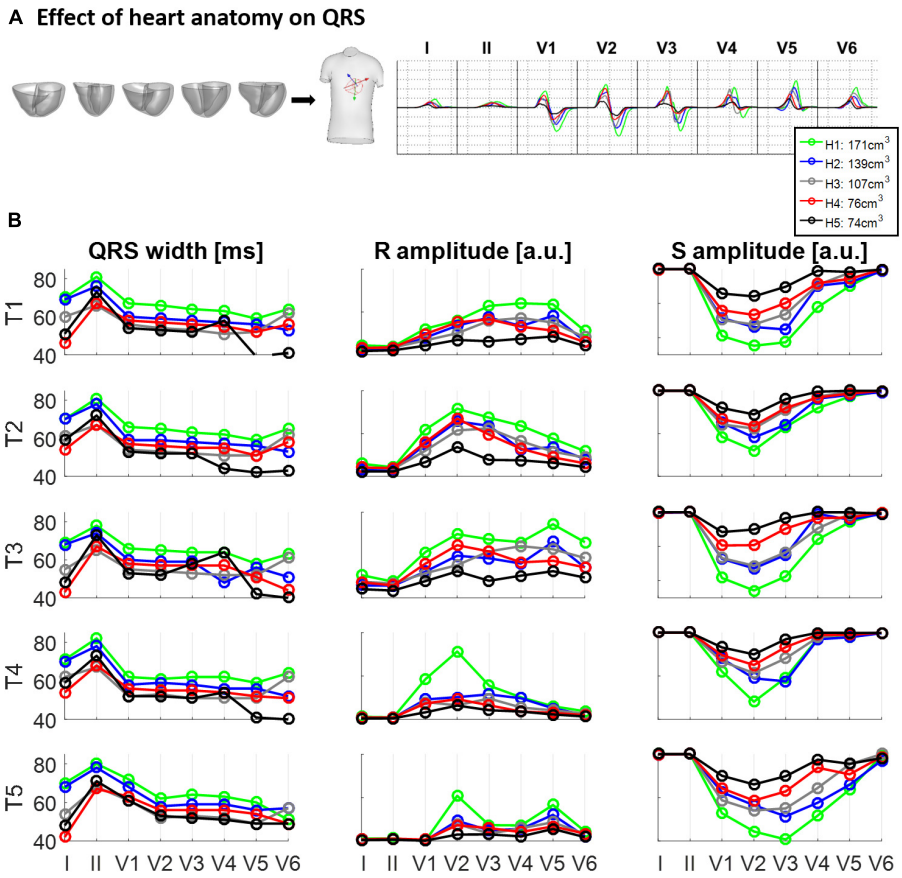

FIGURE 3 | Effect of ventricular geometry on QRS duration, and S and R wave amplitude. **(A)** Simulated QRS complexes obtained for five ventricular geometries placed in the torso-pose of Subject 3 (T3). **(B)** QRS duration (left), S and R amplitude (middle and right, respectively) obtained from simulations using the five ventricular geometries (H1 to H5) placed in each of the five torso-poses (T1 to T5). The term "a.u." stands for arbitrary units.

3 mm in terms of root mean square, being the 90th percentile 5 mm. A template-based approach was used to place other internal structures such as the lungs and the ribs (**Figure 1A**, Surface meshes). Full details about the procedure are provided in Zacur et al. (2017).

All surfaces were remeshed with different element sizes to ensure numerical convergence of the finite element software Chaste for electrophysiological simulations (Pitt-Francis et al., 2009; Dutta et al., 2016) as described in **Supplementary Material S1**. Finally, tetrahedral volumetric

meshes were constructed from these surfaces (see **Supplementary Material S1**). The surface and volumetric meshes can be downloaded from http://www.cs.ox.ac.uk/ccs/home.

Figure 1B shows the reconstructed ventricular geometries and, the torso geometries including their corresponding heart orientations and positions, constrained by chest boundaries. The generation of a new virtual torso-ventricular geometry requires the transformation of the ventricular geometry from a canonical reference frame to the position defined by the torso (pose, see **Figure 1C**). Hereinafter, torso-pose is defined as the torso geometry including the heart pose, which represents the coordinate system and location of the heart. This torso-pose linking is supported by physical constraints such as chest boundaries, since one specific torso anatomy does not allow any heart position (Engblom et al., 2005). Further information is found in **Supplementary Material S1**.

Electrophysiological Simulations

The anatomical torso-ventricular model combinations described above were used to compute 265 QRS complexes from computer simulations as follows. The propagation of the electrical activity in the human ventricles and torso was modeled using the fully coupled heart-torso bidomain equations and solved with the Chaste software (Pitt-Francis et al., 2009). Human ventricular membrane kinetics were simulated with a modified version of the O'Hara-Rudy action potential model (O'Hara et al., 2011) published in Dutta et al. (2017). Myocardial and torso conductivities, and, myocardial fiber structure were set as described in **Supplementary Material S2**. An anisotropic myocardial fiber architecture was implemented using the Streeter rule (Streeter et al., 1969). The three orthotropic intracellular and extracellular myocardial conductivities were set as in Cardone-Noott et al. (2016). Transmural, apex-to-base and interventricular cell electrophysiological heterogeneities were introduced based on experimental and clinical data and as described in **Supplementary Material S2**. The QRS complex is hardly affected by the electrophysiological heterogeneities included in our models as they mainly affect the repolarization properties and the T wave. However, they provide our computational pipeline with all the state of the art capabilities to extend the work to investigate variability in T wave morphology, as well as under disease and drug action.

Sinus rhythm was simulated using a phenomenological activation model with early endocardial activation initiated by root nodes and a fast endocardial layer representing a tightly packed endocardial Purkinje network (Cardone-Noott et al., 2016). In short, 7 root nodes are positioned in the ventricles on the endocardium: four in the LV (LV mid septum, LV anterior paraseptal, and two LV mid-posterior) and three in the RV (RV mid septum, two RV free wall), as shown in **Supplementary Material S2**. Simulated ventricular activation times for these models show the LV endocardial surfaces are fully activated within a range of 39 to 51 ms, and the latest moments of activation occurs in a range from 57 to 76 ms. This is in agreement with the *ex vivo* microelectrode recordings by Durrer et al. (1970) reporting around 45 ms in endocardial LV activation, and from 60 to 80 ms the latest moments of whole ventricular activation.

The aim of this study is to investigate, analyze and quantify the effect of anatomical/geometrical variability on the QRS complexes in an electrophysiological computer simulation framework. It is not to construct personalized electrophysiology models to replicate each of the patients' data. In order to isolate the effect of ventricular anatomy from differences in activation patterns, the endocardial speed was set to 120 cm/s in all models, and the locations of the root nodes were mapped to anatomically homologous locations from the geometry used in a previous study (Cardone-Noott et al., 2016). The coupled epicardial, RV and LV endocardial surfaces and ventricular insertion points from the original geometry (Cardone-Noott et al., 2016) were diffeomorphically registered to each ventricular geometry using a composition of approximated Thin-Plate Splines (TPS) deformations (Rohr et al., 2001). The deformation method was guided by an iterated closest point between the corresponding source and target surfaces/structures (left and right endo- and epicardial surfaces, atrio-ventricular planes, and anterior and posterior interventricular grooves). The successive deformations were performed by following an annealing process in the smoothness parameter of approximated TPS (Amberg et al., 2007). The resulting registered deformation was applied to the early activation sites from the original geometry resulting in the anatomically homologous locations that lead to similar activation sequences (see **Figure 2A**). The resulting deformations and the mapped activation sites were visually evaluated and approved by an expert cardiologist. This technique was used given its broad acceptance and success in the medical imaging and shape analysis field but the universal ventricular coordinates could represent an alternative (Bayer et al., 2018).

QRS complexes from the 12-lead ECGs were simulated by placing virtual electrodes in the standard 12-lead ECG positions for each torso. Since the statistical shape model used for reconstructing the torsos is based on anatomical correspondences, the virtual electrodes are located in anatomically homologous locations for all the torsos (see **Figure 2B**). These electrode positions correspond to analogous intercostal spaces for all subjects. Electrode coordinates are given for each of the torso geometries, and can be downloaded from http://www.cs.ox.ac.uk/ccs/home.

To simulate the QRS complex for 265 combinations of ventricular/torso positions and orientations while minimizing the number of expensive HPC simulations, extracellular potentials were computed from the ventricular potentials following the integral of dipole source density formulation (Gima and Rudy, 2002; Plonsey and Barr, 2007) as:

$$\phi(e) = \int_{\Omega} \left(-D \nabla V_m \cdot \left(\nabla \frac{1}{||r - e||} \right) \right) dr,$$

where $e = (e_x, e_y, e_z)$ are the electrode position coordinates, D is the diffusion tensor, and V_m is the membrane potential. The integral is calculated over the whole myocardium volume, Ω. Bidomain simulations coupled with the Poisson equation to propagate the electrical activity to the body surface were compared to the integration of dipole source density formulation for the torso propagation. The resulting QRS complexes were very similar as shown in **Supplementary Figure S3** from

Supplementary Material S2. The propagation model based on the integration of dipole source density formulation was chosen in order to simplify the numerical complexity of the computations and to avoid re-meshing the torso volume for each scenario in which the ventricular geometry was rotated, translated or permuted. Although this method does not allow the inclusion of tissue inhomogeneities in the torso, several studies suggest minimal differences in the resulting body surface potentials and the QRS complex when assuming homogeneous or inhomogeneous torso models (Ramanathan and Rudy, 2001; Geneser et al., 2008).

Quantification of QRS-Based Features and Descriptors

Clinically used features from the QRS, such as duration and amplitude, were extracted for each of the simulated 12-lead ECGs. QRS duration is calculated by using a relative threshold on the absolute value of the slopes of the ECG signal to identify QRS onset and offset as in Martínez et al. (2004). We compared the simulation results with those reported in the literature and also clinical ECG recordings from healthy volunteers, as part of a prospective study approved by the National Research Ethics Committee (REC ref 12/LO/1979). Informed written consent was obtained from each participant (Lyon et al., 2018a).

Furthermore, in order to quantify the effect of anatomical variability in QRS morphology, we proposed a similarity measure to quantify QRS morphological differences, invariant to QRS amplitude and duration. The new metric (PC*) is based on a continuous generalization of the Pearson coefficient (PC), which in order to ensure independence from QRS duration, includes the invariance to a uniform warping (time scaling) in time of the QRS complex. Therefore, PC* between two QRS complexes is 1 when these have the same morphology regardless of the amplitude or the duration.

Let f and g be two functions defined on the domains $\mathrm{dom}(f) = \left[t_0^f, t_1^f\right]$ and $\mathrm{dom}(g) = \left[t_0^g, t_1^g\right]$, respectively. Let's assume that $\mathrm{dom}(f) \cap \mathrm{dom}(g) \neq \emptyset$ and let's consider the combined domain $[t_0, t_1] = \mathrm{dom}(f) \cup \mathrm{dom}(g)$, where $t_0 = \min\left(t_0^f, t_0^g\right)$ and $t_1 = \max\left(t_1^f, t_1^g\right)$. On this combined domain, let $\tilde{f}$ be the replicated extension of the original function f,

$$\tilde{f} = \begin{cases} f(t) & \text{if } t \in \left[t_0^f, t_1^f\right] \\ f(t_0^f) & \text{if } t < t_0^f \\ f(t_1^f) & \text{if } t < t_1^f \end{cases}$$

and equivalently for $\tilde{g}$.

Our proposed generalized PC is given by

$$\mathrm{PC}_{f,g} = \frac{1}{t_1 - t_0} \int_{t_0}^{t_1} \frac{\tilde{f}(t) - \mu_{\tilde{f}}}{\sigma_{\tilde{f}}} \cdot \frac{\tilde{g}(t) - \mu_{\tilde{g}}}{\sigma_{\tilde{g}}}\, dt \qquad (1)$$

where $\mu_{\tilde{f}}$ and $\mu_{\tilde{g}}$ are means, and $\sigma_{\tilde{f}}$ and $\sigma_{\tilde{g}}$ are the standard deviations of the functions $\tilde{f}(t)$ and $\tilde{g}(t)$, respectively,

$$\mu_{\tilde{f}} = \frac{1}{t_1 - t_0} \int_{t_0}^{t_1} \tilde{f}(t) dt, \qquad \sigma_{\tilde{f}} = \sqrt{\frac{1}{t_1 - t_0} \int_{t_0}^{t_1} \left(\tilde{f}(t) - \mu_{\tilde{f}}\right)^2 dt}$$

and equivalently for $\mu_{\tilde{g}}$ and $\sigma_{\tilde{g}}$. The subtraction of the means $\mu_{\tilde{f}}$ and $\mu_{\tilde{g}}$ in Eq. (1) ensures the invariance of PC under changes in the baseline levels. Likewise, normalizations by $\sigma_{\tilde{f}}$ and $\sigma_{\tilde{g}}$, endow PC with invariance to scaling. The normalization by $(t_1 - t_0)$ allows independence from time units. Thus, PC values are within the [−1, 1] interval.

In order to ensure independence from QRS duration, we include the invariance to a uniform warping (time scaling) in time through the following similarity measurement PC*:

$$\mathrm{PC}^*_{f,g} = \max_{s \in \mathbb{R}^+} \mathrm{PC}_{f(\cdot), g(s\cdot)},$$

where $g(s\cdot)$ is a uniformly time-warped version of g. It is worth mentioning that since $\mathrm{dom}\left(g\left(s\cdot\right)\right) = 1/s \cdot \mathrm{dom}(g) = \left[t_0^g/s,\ t_1^g/s\right]$, the integral interval in Eq.(1) is updated accordingly, and the resulting PC* keeps having comparable values.

In the following, we will explain how to quantify a global similarity for a set of N functions $\left\{f_1(\cdot), f_2(\cdot), \cdots, f_N(\cdot)\right\}$. We propose to compute, the best time warping factors for the N functions simultaneously, in order to optimally align the set. Therefore, we search for

$$\{s_1, s_2, \ldots, s_N\} = \underset{s_1,\ldots,s_N \in \mathbb{R}^+}{\mathrm{argmax}} \min_{\substack{i=1\ldots N \\ j=i+1\ldots N}} \mathrm{PC}_{f_i(s_i\cdot), f_j(s_j\cdot)}$$

Once these optimal time warping factors have been computed, the global similarity for the functions $\left\{f_1(\cdot), f_2(\cdot), \cdots, f_N(\cdot)\right\}$ is given by

$$\mathrm{PC}^*_{f_1, f_2, \ldots f_N} = \max_{\substack{i=1\ldots N \\ j=i+1\ldots N}} \mathrm{PC}_{f_i(s_i\cdot), f_j(s_j\cdot)}$$

with this, the worst aligned pair defines the similarity of the whole set.

RESULTS

Effect of Ventricular Geometry on QRS Duration and Amplitude

Figure 3 illustrates the effect of different ventricular geometries within the same torso with corresponding heart position (hereinafter referred to as torso-pose) on QRS duration and amplitude. **Figure 3A** shows the QRS complexes obtained in leads I, II and V1–V6 for each of the five ventricles (H1–H5) placed in the torso-pose of Subject 3 (T3). **Figure 3B** shows QRS complex duration as well as S and R wave amplitude for all 25 torso-pose and ventricular combinations. For all torso-poses, QRS complexes decrease in amplitude and increase in duration

with an increase in myocardial volume (green versus black traces corresponding to the largest versus the smallest ventricular volumes, respectively). An average increase of 0.12 ± 0.05 ms in QRS duration for each cm^3 of myocardial volume across all the leads was found. Relationships between QRS durations and ventricular myocardial volumes for each of the leads is shown in **Supplementary Material S4**. **Supplementary Figure S4** shows the 12 lead QRS complexes of different ventricular geometries within the same torso-pose for each of the five subjects.

Effect of Torso-Heart Position on QRS Duration and Amplitude

Figure 4 shows the effect of different torso-poses on QRS duration and amplitude. **Figure 4A** shows as an example, the QRS complexes obtained for the ventricular geometry H3 when placed in all the torso-poses, and **Figure 4B** provides quantification of QRS duration and R and S wave amplitudes for the five ventricular geometries. QRS duration does not change substantially for different torso-poses, and this suggests that QRS duration is mainly determined by the ventricular geometry. Indeed, a slight increase in QRS duration of 0.01 ± 0.03 ms for dm^3 of torso volume across all leads is observed (further information regarding the relationship between QRS duration and torso volume can be found in **Supplementary Material S4**). However, both S and R wave amplitudes are mainly determined by torso volumes, with larger QRS amplitudes corresponding to smaller torso volumes. Exceptionally, QRS complexes in T4 with a torso volume of 27 dm^3 exhibit larger amplitudes in V1 to V3 compared to T5 (23 dm^3) that exhibit larger amplitudes in V4 to V6. For these two torsos with similar volumes, heart position plays an important role in QRS amplitude. By comparing the ventricular positions for T4 and T5 (see **Figure 2**), we observe that for T5, V5 and V6 electrode positions are closer to the ventricles resulting in larger QRS amplitudes, whilst V2 and V3 electrodes are further away, resulting in smaller amplitudes.

Effect of Ventricular Geometry and Torso-Pose on QRS Morphology

Figure 5A displays the similarity measurement computed from the modified Pearson correlation PC*, which measures differences in QRS morphology due to differences in ventricular geometry and torso-pose.

Results show that for limb leads (I, II, aVR, aVL and aVF), and V5, QRS morphology is more similar (and PC* higher) for fixed ventricular geometry (with varying torso-pose) than for fixed torso-pose (with varying ventricular geometry). Therefore, in these leads, the ventricular geometry mainly determines the QRS morphology.

On the contrary, for leads V1 to V4 and V6, QRS morphology is more similar (as shown by the higher PC* values) for fixed torso-poses than for fixed ventricular geometry. Thus, in these leads, QRS morphology is mostly determined by torso-pose rather than by ventricular geometry.

These results are further illustrated in **Figures 5B,C** for two representative leads, aVL and V1. Simulated QRS morphology is mostly determined by the ventricular geometry and torso-pose in leads aVL and V1, respectively. Simulated QRS complexes obtained with the same ventricular geometry are shown in the same row while those obtained with the same torso-pose are shown in the same column. The warped QRS complexes from which PC* is computed are shown in **Supplementary Material S5**.

Effect of Heart Orientation and Position on the QRS Morphology

Figures 6, **7** illustrate the results obtained from the 265 simulations conducted to evaluate the effect of rotation around the long axis and left-to-right ventricle directions and translation along the lateral and cranio-caudal directions of the ventricles within the torso in the QRS complex. **Figure 6** displays simulated QRS complexes obtained for a representative anatomical model (H3 within T3), whereas **Figure 7** shows quantification of the QRS morphology similarity metric (PC*) for all subject specific torso-ventricular geometries.

As shown in **Figures 6A**, **7A**, rotation along the long axis mainly affects the R and S amplitudes of leads V1 to V3. The amplitude of the R wave is larger when the LV faces the chest plane (orange traces) and decreases as the RV gets positioned between the LV and the chest (blue trace). The amplitude of the S wave also decreases in the precordial leads in ventricular positions where the RV faces the chest. Quantitative results regarding changes in QRS amplitudes with heart orientation and position can be found in **Supplementary Material S6**.

Figures 6B, **7B** show that rotation around the left-to-right ventricle axis severely affects the QRS morphology in leads II, and V1 to V5. More horizontal hearts (orange traces) result in larger R wave amplitudes in leads I, V1, and V6 while more vertical ones (blue traces) result in larger R and S wave amplitudes in leads V2 to V5.

Figures 6C, **7C** show that hearts located in more medial positions result in taller R and S waves in septal V1 to V3 leads while shorter R waves are observed in the precordial lateral leads V5 and V6. This is due to the closer ventricular location to V1 to V3 electrode positions and further from V5 and V6. On the other hand, hearts located in more lateral positions (toward the left-arm) displayed negatively deflected rS or even QS complexes in the septal V1 to V2 leads and larger R wave amplitudes in V5 to V6 (blue solid lines).

Figures 6D, **7D** show the effect of shifting the ventricles up along the cranio-caudal (superior-inferior) direction leads to larger R wave amplitudes in lead I, and longer R and S waves in V1 to V5 (blue lines). However, shifting the heart down leads to shorter R waves in leads I, V1 and V6 (orange line). The changes would be equivalent to changing the electrode position with respect to the ventricles.

Comparison to Clinical Data

Simulated ECGs obtained from our population of models exhibit QRS axis (computed from QRS complexes in leads I and III) ranging from 50° to 75° [normal range −30° to 90° as shown in Engblom et al. (2005)], QRS durations per lead from 45 to 80 ms [normal range including all leads 78 ± 8 ms as shown in van Oosterom et al. (2000)], and amplitudes from 0.5 to 3.5 mV [healthy: 2 ± 0.6 mV as shown in van Oosterom et al. (2000)].

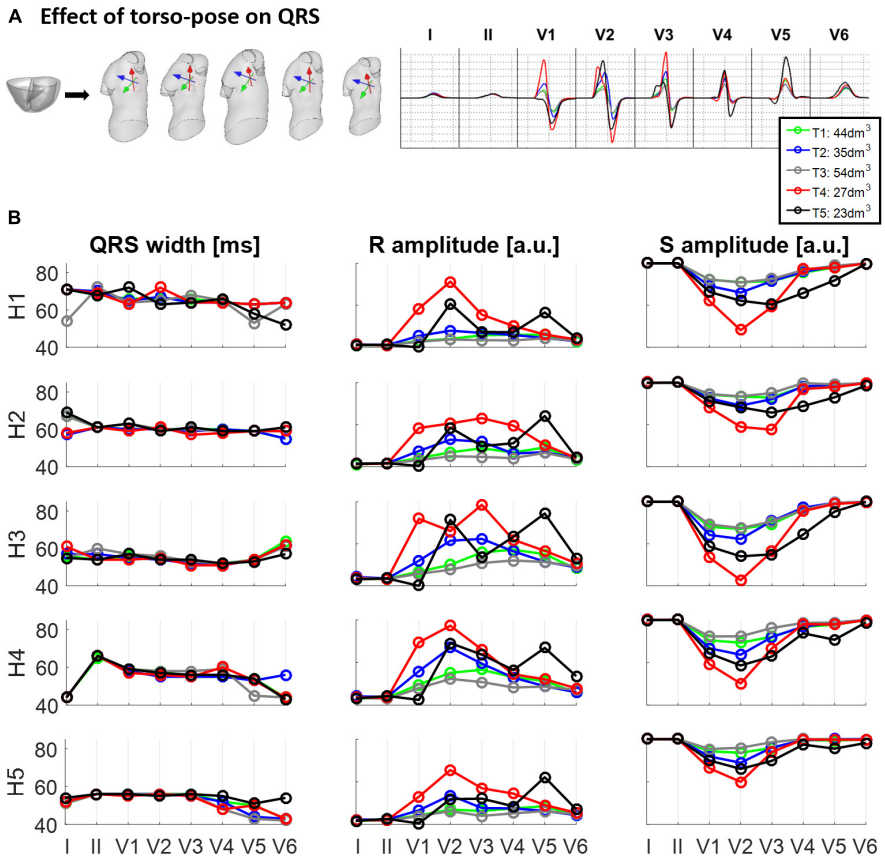

FIGURE 4 | Effect of torso-pose on QRS duration, and S and R wave amplitude. **(A)** Simulated QRS complexes obtained using the ventricular model from Subject 3 (H3) placed in the five different torsos-poses. **(B)** QRS duration (left), and S and R amplitudes (middle and right, respectively) from simulations using each of the five hearts (H1 to H5) placed in the different torso-poses (T1 to T5).

Thus, all these quantitative measurements are in agreement with clinical ECGs from healthy subjects (van Oosterom et al., 2000; Engblom et al., 2005; Stewart et al., 2011), supporting the credibility of the simulations.

Figure 8 shows a comparison of the variability exhibited in simulated and clinical 12 lead ECG QRS complexes. Simulated QRS complexes show variability in terms of morphology, especially in the precordial leads. The normal upright (positive) QRS complexes in both, lead I and lead aVF, result in a normal QRS axis. Furthermore, simulated QRS complexes show positive deflection with large, upright R wave in leads I, II, V4–V6 and a predominant negative deflection with a large, deep S wave in aVR, V1 and V2 (see **Figure 8A**). This is in agreement with the three clinical recordings shown in **Figure 8B**. Lead III in simulated ECGs shows biphasic QRS complexes with a negative deflection followed by a positive one as in the clinical recording of Subject 1 (**Figure 8B**). On the contrary, simulated lead aVL shows biphasic QRS complex with first a positive deflection followed by a negative one, as in clinical recordings of Subjects 1 and 3 (**Figure 8B**).

Precordial QRS complexes show R wave progression from V1 to V6, with an increasing R wave and a decreasing S wave when moving from V1 to V6. This progression is observed in both simulated (**Figure 8A**) and clinical ECGs (**Figure 8B**). QRS complexes in lead V1 show morphological variability from biphasic QRS complexes (positive-negative deflections) to downright QRS complexes (**Figure 8A**). This is in agreement with the variability in clinical recordings (**Figure 8B**).

DISCUSSION

The present study demonstrates the computational evaluation of the effect of heart-torso position and anatomy on the QRS complex using human torso/biventricular electrophysiology models derived from clinically standard MRI. The first contribution of the study is the computational pipeline to build the torso/biventricular anatomies initiating from standard clinical cardiac MRI augmented with a statistical shape model of the body (Zacur et al., 2017). This methodology enables exploiting clinical databases to evaluate the functional impact of MRI-extracted anatomical and structural features (Lyon et al., 2018b). Furthermore, human MRI-informed modeling and simulation based on this technology could accelerate the development of tailored pharmacological and electrical therapy

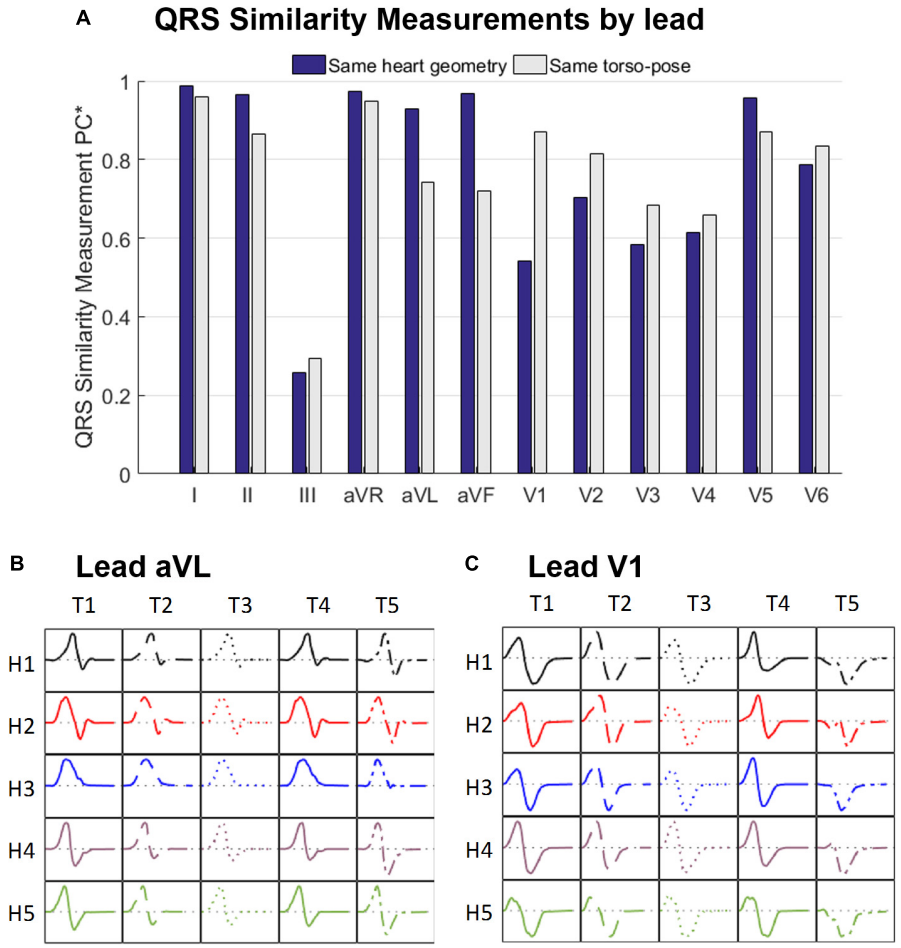

FIGURE 5 | (A) Similarity measurement (PC*) of the simulated QRS morphologies for fixed ventricular geometry (and varying torso-pose) (blue), and for fixed torso-pose (and varying ventricular geometry (gray). Panels **(B,C)** Simulated QRS morphologies obtained with the five ventricular geometries (H1 to H5) placed in the five torso-poses (T1 to T5) for leads aVL **(B)** and V1 **(C)**.

and the goal for precision care. Firstly, being able to reconstruct the patient's specific torso and ventricular model from standard cardiac MRI is a step forward to personalized computer modeling and simulation. The human models constructed have the biophysical detail required to enable future simulation studies into the response to disease and pharmacological treatment. Additionally, the simulation results demonstrate the influence of anatomical features on the QRS complex in healthy control conditions. This quantification of normal QRS complex variability is important to inform the evaluation of response to disease and treatment.

Analysis of the simulated QRSs yields the following findings: (i) QRS morphologies in limb leads I and II are mainly determined by the geometry of the ventricles whereas QRS morphologies in the precordial leads, and especially V1 to V4, are determined by the torso-pose. (ii) QRS duration is mainly influenced by myocardial volume while it is hardly affected by the torso geometry or heart position; (iii) QRS amplitude increases with large ventricular volumes and decreases with larger torso volumes. Quantification of the contribution of the individual heart structure, orientation and body habitus on the ECG is critical to aid the clinical interpretation of potential ECG abnormalities driven by disease or pharmacological treatment. In synergy with clinical databases, they could also drive the personalization of score metrics for risk stratification by discriminating in clinical recordings between the contribution of each patient's specific anatomy and those arising from their disease state.

Populations of Heart-Torso Electrophysiological Models From Standard Clinical MRI

In this paper, we present multiscale electrophysiological simulations using heart-torso anatomical models from standard cardiac MRI acquisitions (**Figure 1**). The generation of the subject-specific geometries is performed from standard cardiac MRI acquisitions allowing to be used directly on available clinical datasets. The scarce information of torso anatomy from standard cardiac MRI acquisitions makes the use of traditional

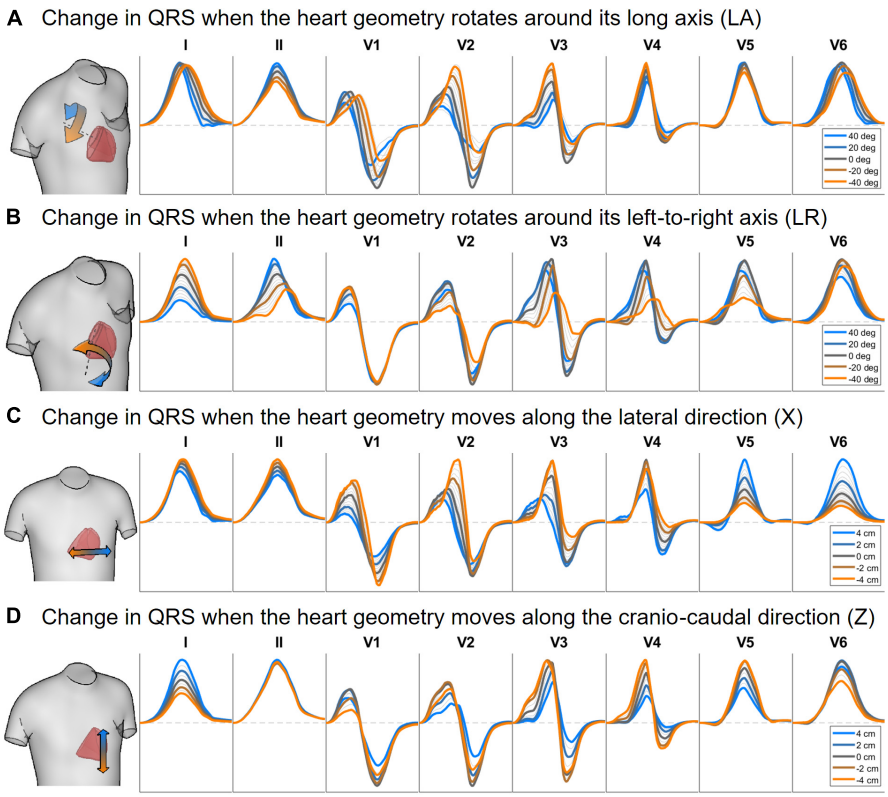

FIGURE 6 | Simulated QRS complex in leads I, II and V1 to V6 for different rotation angles around the long axis **(A)** and the left-to-right-ventricle direction **(B)**, and for different heart translations along the lateral **(C)** and cranio-caudal **(D)** directions. Gray lines correspond to intermediate results showing how the signals evolve from one colored state to another. The heart and torso geometries correspond to subject 3.

image-to-surface methods difficult and therefore, previous studies have required the use of dedicated imaging protocols (Potse et al., 2014). In the present pipeline, we make use of a statistical shape model together with the MRI information to accurately build the patient-specific torso geometry (Pishchulin et al., 2017; Zacur et al., 2017).

The comprehensive computational pipeline connects the outputs and inputs of different technologies, including the generation of torso-ventricular geometrical surfaces, the tetrahedralization into a multimaterial volumetric mesh, the generation of fiber orientations in the myocardium, the different input files to be used in the Chaste software to derive the fiber orientations and the endocardial layer for fast stimulation mimicking the Purkinje system, to assign different electrophysiological cell properties and finally to simulate the electrical activity and the 12-lead ECG. All files and torso-ventricular geometrical meshes are available for future studies.

In the evaluation of the role of anatomical features on the ECG, previous studies have typically performed perturbations to anatomical features (i.e., heart positioning and orientation) around a reference/original position to explore their individual effect (Corlan et al., 2005; Nguyên et al., 2015). In the present study, we sample the space of plausible anatomies and generate plausible instances by swapping ventricular anatomies together with torso-poses using their corresponding heart position and orientations (torso-poses) (see section "Reconstruction of Ventricular and Torso Anatomical Meshes From Clinical MRI"). This approach allows us to explore the role of ventricular anatomy on the QRS complex without the need to define a high dimensional parametrization of the ventricular shape. In particular, this population provides a generic open framework for further studies aimed to explore how anatomy and its variability influence the signature of the cardiac function in the ECG.

QRS Morphologies Are Determined by Ventricular Geometry in the Limb Leads and by Heart Orientation in Septal Leads

Ventricular geometry and not the torso-pose mainly determines the QRS morphology in the limb leads I and II, augmented leads, and V5 (see **Figure 5**). This finding may explain the weak correlation found in a number of studies between the anatomical heart orientation and the cardiac electrical axis (Dougherty, 1970; Horan, 1987; Engblom et al., 2005; Pellicori et al., 2015; Sathananthan et al., 2015). Cardiac electrical axis (Kashou and Kashou, 2018) is mainly estimated using the QRS complexes from leads I, II and aVF which, as shown in **Figures 5**, **7**, are more influenced by ventricular geometry than by heart orientation. Therefore,

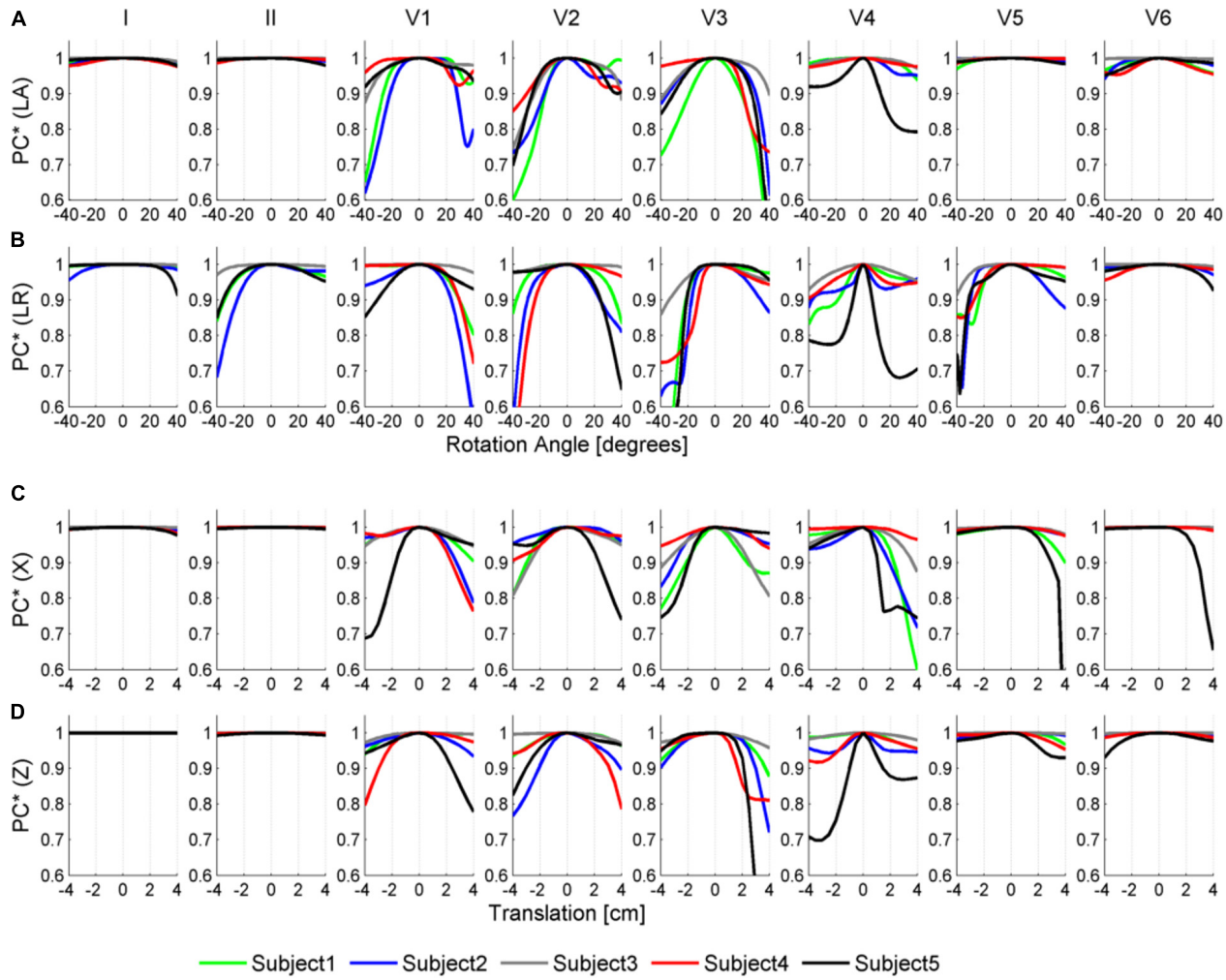

FIGURE 7 | Similarity measurement (PC*) for each lead (I, II, V1–V6) between the QRS at the original pose and the QRS when the heart is rotated along the long axis (LA) in panel **(A)**, the left-to-right-ventricles axis (LR) in panel **(B)**, and when translated in the lateral and cranio-caudal directions in panels **(C,D)**, respectively. Rotation angles range from –40° to 40° and translations range from –4 to 4 cm.

this results in a lower correlation between the electrical and anatomical axis.

On the other hand, QRS morphology in septal and anterior leads V1 to V4, III and V6 is mostly determined by the torso anatomy and its linked heart positioning. This could also result from changes in electrode position. The two different sources of variation, ventricular anatomy and torso-pose, affecting mainly limb/augmented leads and precordial leads, respectively, may have implications on the normal variability of QRS morphology in the different leads.

The proposed QRS similarity measurement is a global morphological measurement able to quantify differences in the QRS morphology due to the effect of anatomical variability. Unlike other studies proposing feature based differences as for example (Giffard-Roisin et al., 2017; Sánchez et al., 2018), we have measured differences in QRS morphology complementary and independent of QRS duration and amplitude. Our quantification allows a lead-wise evaluation of the influence of ventricular anatomy and torso-pose on the QRS morphology.

Importantly, the results on the contribution of the ventricular anatomy and the torso-pose on the QRS morphology of each of the leads do not depend on the endocardial and myocardial conduction (see **Supplementary Material S7**).

QRS Duration Depends Primarily on Ventricular Size and Is Hardly Affected by Heart Pose and Orientation

This study shows a positive correlation between ventricular volume and QRS duration (see **Figure 3**). Even if this finding is intuitive, little data exist on the influence of heart size and body weight on QRS duration. This correlation may have implications for the normal ranges of QRS duration and thus on the diagnosis of QRS prolongation. Most of the studies relating QRS duration and ventricular mass are in the context

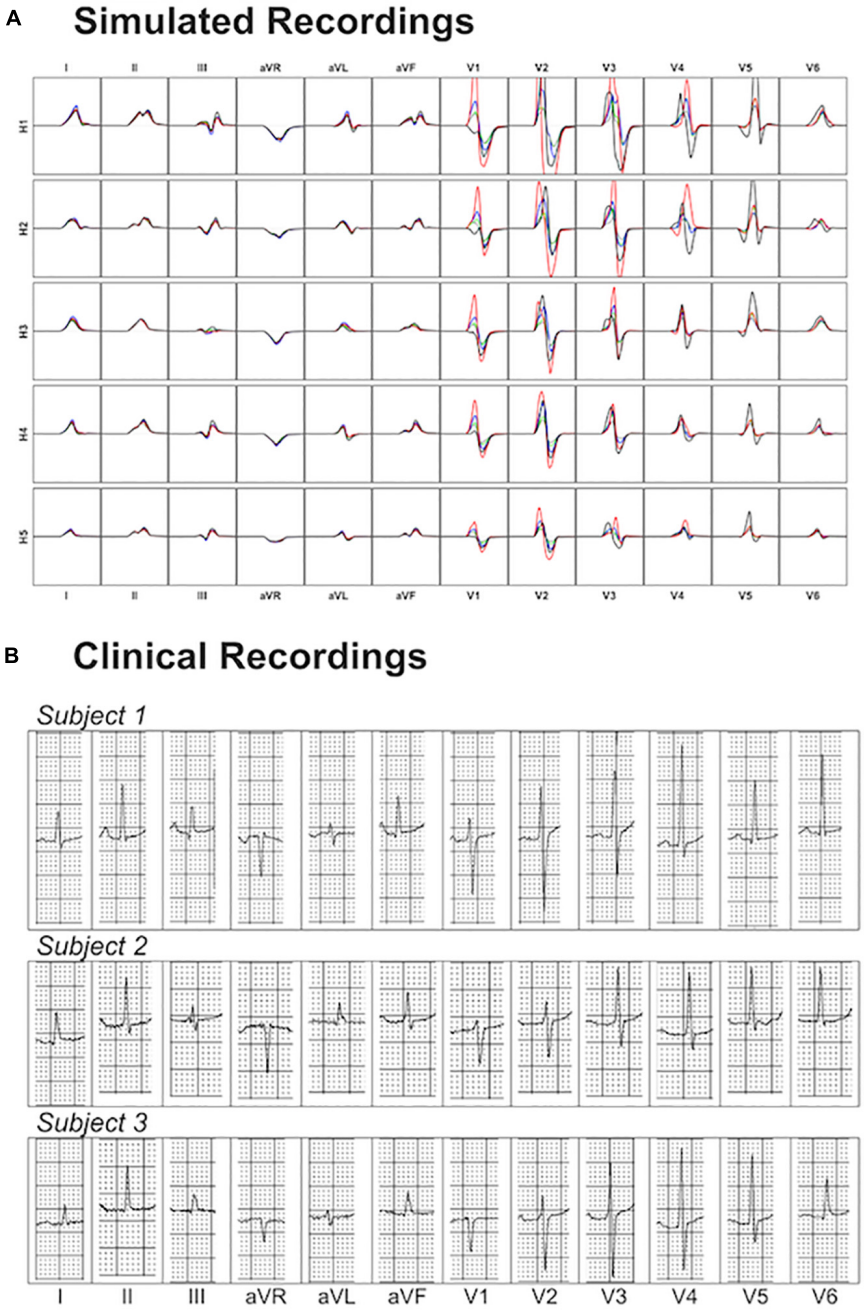

FIGURE 8 | Comparison between simulated and clinical 12-lead ECG recordings. Panel **(A)** shows the simulated 12-lead QRS complexes obtained using each of the ventricular models (H1–H5) placed in the five different torsos-poses. Panel **(B)** shows three exemplary clinical 12-lead ECG recordings from healthy subjects.

of patients at high cardiovascular risk (Stewart et al., 2011) and do not consider control subjects. Therefore, many factors may intervene for long QRS duration such as a reduced LV ejection fraction (Murkofsky et al., 1998) or ventricular dys-synchrony that are unrelated to LV hypertrophy (Oikarinen et al., 2004). On the contrary, we show that the torso-pose hardly modifies the QRS duration for any of the ventricular geometries (see **Figure 4**). This is in agreement with (Nguyên et al., 2015) that quantifies QRS duration differences from –6 to 10% in five heart failure patients.

Both Torso and Heart Geometrical Factors Have a Role in the QRS Amplitude

Ventricular and torso volumes are generally related since large body masses usually correspond to large hearts. Indeed, a recent

paper in the large-scale population-based study UK-Biobank showed that higher LV mass was associated with increasing body mass index (BMI) (Petersen et al., 2017), explaining the BMI 72% of the global LV mass variability. However, myocardial and torso volumes affect the QRS amplitude in opposite ways. While larger ventricular geometries result in larger R and S wave amplitudes due to the increase of excitable myocardial tissue (see **Figure 3**), larger torso volumes result in lower R and S wave amplitudes due to the larger distance between the ventricles and the electrodes (see **Figure 4**). These two opposite effects coexist and lead to an ascending-descending behavior of the R wave amplitude with BMI as observed in clinical data (Kurisu et al., 2015). More specifically, precordial lateral leads display a slight increase in R wave from underweight to normal weight subjects followed by an abrupt decrease in the R amplitude for obese subjects (Kurisu et al., 2015). Despite the role of heart and body sizes, heart diseases and clinical conditions also affect QRS amplitude. Low QRS amplitude has been associated to different clinical conditions such as large infarct sizes (Katragadda et al., 2017), or to an increased risk of mortality in individuals free of apparent cardiovascular diseases (Usoro et al., 2014), while increased QRS amplitude has been associated to diseases such as left ventricular hypertrophy. Our study provides digital evidence in agreement with those findings and allows a systematic analysis of the effect of both ventricular and torso volumes in QRS amplitude.

Heart Rotation and Position Mainly Affect QRS Morphology in Leads V1 to V4

The independent effect of heart position and orientation on QRS complex has also been investigated in the different heart-torso geometries showing slight differences in QRS duration with rotation around LA and LR axis directions and translation in the lateral and cranio-caudal directions (**Figures 6**, **7**). Large morphological and amplitude changes of QRS in V1 to V3 leads are observed with rotation around the LA direction, whereas V1 to V5 are mainly affected by rotation around LR direction. QRS morphologies in V1 to V4 are mainly affected by translation of the heart within the torso in the lateral and cranio-caudal directions. This is in agreement with studies reporting that variations in the magnitude of the electrocardiogram as observed through leads placed on the anterior thorax are dominated by the solid angle (van Oosterom et al., 2000). Small rotation angles in the range of $\pm 10^{\circ}$ could be considered as mimicking pose changes caused by respiration (McLeish et al., 2002; Shechter et al., 2004). These resulted in QRS morphological changes mainly in the anterior leads V3 and V4, with very minor scaling amplitudes in V1 to V4 (see **Supplementary Material S6**) in agreement with (Carey et al., 2016). Large changes in heart position and orientation lead to remarkable changes in QRS morphology and amplitude in agreement with body position changes that significantly affect the ECG (Mincholé et al., 2014).

LIMITATIONS AND FUTURE WORK

The QRS complex reflects the ventricular depolarization and its pattern is determined by the electrical activation sequence of the ventricles, as well as the geometric relationship between the heart and the body surface anatomy as shown in this study. The activation sequence is, in turn, related not only to ventricular geometry but also to Purkinje, myocardial conduction pathways, and, other tissue conductivities (Boineau and Spach, 1968; Keller et al., 2010). In this study, we focused on evaluating the role of anatomical ventricular/torso properties on the QRS complex. Further studies can evaluate the role of additional factors on the QRS complex such as for example variability in the Purkinje system (Wallman et al., 2014), myocardial conductivities, and disease conditions (Lyon et al., 2018b).

We have selected a wide range of ventricular and torso geometries with volumes from 75 to 170 cm^3, and from 23 to 54 dm^3, respectively. However, the total variability of control human geometries may not be represented by this dataset. The results showed in this study are not however, expected to change qualitatively with consideration of a larger dataset in healthy subjects. Considering disease conditions will include additional factors determining variability in QRS morphology (Lyon et al., 2018a,b).

We have tackled the reconstruction of the shape of the surface body by completing the sparse information obtained from the MRI with a statistical shape model of the body surface. The agreement of the reconstructed torso and the MRI contours is high (no more than few millimeters of discrepancy for all the cases). However, there are large areas where we have no information of the body shape and we rely on the shape plausibility provided by the statistical shape model. This may result in differences between the reconstructed torso and the real one, and, therefore, in differences in the simulated ECG. This is a limitation for the accuracy of the reconstruction pipeline, but does not invalidate the main message of the work, in which we evaluate scenarios with plausible anatomies without claiming personalization of the subjects.

The propagation of the electrical activity in the torso by means of the integration of dipole source density formulation is chosen in order to simplify the numerical complexity of the computations and to avoid re-meshing in each scenario. Although this method does not allow the inclusion of tissue inhomogeneities in the torso, previous studies (Ramanathan and Rudy, 2001; Geneser et al., 2008), and, our own evaluations (see **Supplementary Figure 3**) have suggested that differences in the QRS complex between homogeneous and heterogeneous torsos are minimal. The inclusion of vasculature close to the heart and all tissue inhomogeneities may result in differences in the QRS complex between homogeneous and heterogeneous torsos. For these inclusions, different numerical models should be chosen such as the coupled bidomain model by the finite element methods.

CONCLUSION

A population of 265 human torso-ventricular models is constructed based on clinical MRI using a computational pipeline for image analysis, construction of MRI-based anatomical models and HPC electrophysiological simulations. The technology

demonstrated here can further exploit clinical databases to evaluate the functional implications of MRI-extracted features (Lyon et al., 2018b). Analysis of ECG simulations demonstrates that ventricular anatomy mostly determines QRS morphology in limb leads I and II, whereas heart position within the torso determines QRS morphology in the precordial leads, and especially V1 to V4. QRS duration is mainly influenced by myocardial volume, whereas QRS amplitude increases with large ventricular volumes and decreases with larger torso volumes. The new insights provided here are expected to aid in the discrimination in clinical recordings between the contribution of each patient's specific anatomy and those arising from their disease state, and to contribute to accelerating the development of individualized score metrics for risk stratification, and therefore an improved tailoring of their pharmacological and electrical therapy.

DATA AVAILABILITY

The datasets generated for this study can be downloaded from http://www.cs.ox.ac.uk/ccs/home.

AUTHOR CONTRIBUTIONS

AM, EZ, VG, and BR contributed to the conception and design of the study. AM performed the electrophysiological simulations and ECG analysis. EZ performed the personalization of the geometrical models. RA acquired the MRI of the patients. AM and EZ worked on the analysis of the results and writing of the manuscript. All authors contributed to manuscript revision, and read and approved the submitted version.

FUNDING

AM and BR were supported by BR's Wellcome Trust Senior Research Fellowship in Basic Biomedical Sciences (100246/Z/12/Z). EZ and VG received funding by BHF Project Grant No. PG/16/75/32383 and the Marie Skłodowska-Curie Individual Fellowship from the H2020 EU Framework Program for Research and Innovation (Proposal No: 655020-DTI4micro-MSCA-IF-EF-ST). RA was supported by a BHF Clinical Research Training Fellowship (FS/12/32/29559). This project also received funding from the European Union's Horizon 2020 Research and Innovation Program under Grant Agreement No. 675451 (CompBioMed project).

ACKNOWLEDGMENTS

This work used the facilities of the UK National Supercomputing Service (Archer RAP and Archer Leadership Award e462), and the facilities of MareNostrum at Barcelona Supercomputing Center (BSC), Spain (PRACE project pr1efz00).

SUPPLEMENTARY MATERIAL

The Supplementary Material for this article can be found online at: https://www.frontiersin.org/articles/10.3389/fphys.2019.01103/full#supplementary-material

REFERENCES

Amberg, B., Romdhani, S., and Vetter, T. (2007). "Optimal step nonrigid ICP algorithms for surface registration," in *Proceedings of the 2007 IEEE Conference on Computer Vision and Pattern Recognition*, (Minneapolis, MN: IEEE), doi: 10.1109/CVPR.2007.383165

Bayer, J., Prassl, A. J., Pashaei, A., Gomez, J. F., Frontera, A., Neic, A., et al. (2018). Universal ventricular coordinates: a generic framework for describing position within the heart and transferring data. *Med. Image Anal.* 45, 83–93. doi: 10.1016/j.media.2018.01.005

Boineau, J. P., and Spach, M. S. (1968). The relationship between the electrocardiogram and the electrical activity of the heart. *J. Electrocardiol.* 1, 117–124. doi: 10.1016/S0022-0736(68)80014-7

Cardone-Noott, L., Bueno-Orovio, A., Mincholé, A., Zemzemi, N., and Rodriguez, B. (2016). Human ventricular activation sequence and the simulation of the electrocardiographic QRS complex and its variability in healthy and intraventricular block conditions. *Europace* 18, iv4–iv15. doi: 10.1093/europace/euw346

Carey, M. G., Al-Zaiti, S. S., Kozik, T. M., Schell-Chaple, H., and Pelter, M. M. (2016). QRS amplitude variation during monitoring. *Am. J. Crit. Care* 25, 97–98. doi: 10.4037/ajcc2016791

Corlan, A. D., Macleod, R. S., and De Ambroggi, L. (2005). The effect of intrathoracic heart position on electrocardiogram autocorrelation maps. *J. Electrocardiol.* 38, 87–94. doi: 10.1016/j.jelectrocard.2004.10.006

Dougherty, J. D. (1970). The relation of the frontal QRS axis to the anatomic position of the heart. *J. Electrocardiol.* 3, 267–284. doi: 10.1016/s0022-0736(70)80054-1

Durrer, D., van Dam, R. T., Freud, G. E., Janse, M. J., Meijler, F. L., and Arzbaecher, R. C. (1970). Total excitation of the isolated human heart. *Circulation* 41, 899–912. doi: 10.1161/01.CIR.41.6.899

Dutta, S., Mincholé, A., Quinn, T. A., and Rodriguez, B. (2017). Electrophysiological properties of computational human ventricular cell action potential models under acute ischemic conditions. *Prog. Biophys. Mol. Biol.* 129, 40–52. doi: 10.1016/j.pbiomolbio.2017.02.007

Dutta, S., Mincholé, A., Zacur, E., Quinn, T. A., Taggart, P., and Rodriguez, B. (2016). Early afterdepolarizations promote transmural reentry in ischemic human ventricles with reduced repolarization reserve. *Prog. Biophys. Mol. Biol.* 120, 236–248. doi: 10.1016/j.pbiomolbio.2016.01.008

Engblom, H., Foster, J. E., Martin, T. N., Groenning, B., Pahlm, O., Dargie, H. J., et al. (2005). The relationship between electrical axis by 12-lead electrocardiogram and anatomical axis of the heart by cardiac magnetic resonance in healthy subjects. *Am. Heart J.* 150, 507–512. doi: 10.1016/j.ahj.2004.10.041

Geneser, S. E., Kirby, R. M., and MacLeod, R. S. (2008). Application of stochastic finite element methods to study the sensitivity of ECG forward modeling to organ conductivity. *IEEE Trans. Biomed. Eng.* 55, 31–40. doi: 10.1109/TBME.2007.900563

Giffard-Roisin, S., Jackson, T., Fovargue, L., Lee, J., Delingette, H., Razavi, R., et al. (2017). Noninvasive personalization of a cardiac electrophysiology model from body surface potential mapping. *IEEE Trans. Biomed. Eng.* 64, 2206–2218. doi: 10.1109/TBME.2016.2629849

Gima, K., and Rudy, Y. (2002). Ionic current basis of electrocardiographic waveforms: a model study. *Circ. Res.* 90, 889–896. doi: 10.1161/01.res.0000016960.61087.86

Hoekema, R., Uijen, G. J., van Eming, L., and van Oosterom, A. (1999). Interindividual variability of multilead electrocardiographic recordings. Influence of heart position. *J. Electrocardiol.* 32, 137–148. doi: 10.1016/S0022-0736(99)90092-4

Hoekema, R., Uijen, G. J., and van Oosterom, A. (2001). Geometrical aspects of the interindividual variability of multilead ECG recordings. *IEEE Trans. Biomed. Eng.* 48, 551–559. doi: 10.1109/10.918594

Horan, L. G. (1987). Manifest orientation: the theoretical link between the anatomy of the heart and the clinical electrocardiogram. *J. Am. Coll. Cardiol.* 9, 1049–1056. doi: 10.1016/s0735-1097(87)80307-8

Kashou, A. H., and Kashou, H. E. (2018). *"Electrical axis (normal, right axis deviation, and left axis deviation)," in StatPearls, (Treasure Island (FL): StatPearls Publishing)*. Available at: http://www.ncbi.nlm.nih.gov/books/NBK470532/ (accessed September 12, 2018).

Katragadda, S., Alagesan, M., Rathakrishnan, S., Kaliyaperumal, D., and Mambatta, A. K. (2017). Correlation of reciprocal changes and QRS amplitude in ECG to left ventricular dysfunction, wall motion score and clinical outcome in first time St elevation myocardial infarction. *J. Clin. Diagn. Res.* 11, OC04–OC08. doi: 10.7860/JCDR/2017/26021.10155

Keller, D. U. J., Weber, F. M., Seemann, G., and Dössel, O. (2010). Ranking the influence of tissue conductivities on forward-calculated ECGs. *IEEE Trans. Biomed. Eng.* 57, 1568–1576. doi: 10.1109/TBME.2010.2046485

Kurisu, S., Ikenaga, H., Watanabe, N., Higaki, T., Shimonaga, T., Ishibashi, K., et al. (2015). Electrocardiographic characteristics in the underweight and obese in accordance with the world health organization classification. *IJC Metab. Endocr.* 9, 61–65. doi: 10.1016/j.ijcme.2015.10.006

Lyon, A., Ariga, R., Mincholé, A., Mahmod, M., Ormondroyd, E., Laguna, P., et al. (2018a). Distinct ECG phenotypes identified in hypertrophic cardiomyopathy using machine learning associate with arrhythmic risk markers. *Front. Physiol.* 9:213. doi: 10.3389/fphys.2018.00213

Lyon, A., Bueno-Orovio, A., Zacur, E., Ariga, R., Grau, V., Neubauer, S., et al. (2018b). Electrocardiogram phenotypes in hypertrophic cardiomyopathy caused by distinct mechanisms: apico-basal repolarization gradients vs. Purkinje-myocardial coupling abnormalities. *Europace* 20, iii102–iii112. doi: 10.1093/europace/euy226

Macfarlane, P. W., and Lawrie, T. D. V. (2010). "The normal electrocardiogram and vectorcardiogram," in *Comprehensive Electrocardiology*, eds P. W. Macfarlane, A. van Oosterom, O. Pahlm, P. Kligfield, M. Janse, and J. Camm (London: Springer), doi: 10.1007/978-1-84882-046-3-13

MacLeod, R. S., Ni, Q., Punske, B., Ershler, P. R., Yilmaz, B., and Taccardi, B. (2000). Effects of heart position on the body-surface electrocardiogram. *J. Electrocardiol.* 33(Suppl.), 229–237. doi: 10.1054/jelc.2000.20357

Martínez, J. P., Almeida, R., Olmos, S., Rocha, A. P., and Laguna, P. (2004). A wavelet-based ECG delineator: evaluation on standard databases. *IEEE Trans. Biomed. Eng.* 51, 570–581. doi: 10.1109/TBME.2003.821031

McLeish, K., Hill, D. L. G., Atkinson, D., Blackall, J. M., and Razavi, R. (2002). A study of the motion and deformation of the heart due to respiration. *IEEE Trans. Med. Imaging* 21, 1142–1150. doi: 10.1109/TMI.2002.804427

Mincholé, A., Sörnmo, L., and Laguna, P. (2014). Detection of body position changes from the ECG using a laplacian noise model. *Biomed. Signal Process. Control* 14, 189–196. doi: 10.1016/j.bspc.2014.08.002

Murkofsky, R. L., Dangas, G., Diamond, J. A., Mehta, D., Schaffer, A., and Ambrose, J. A. (1998). A prolonged QRS duration on surface electrocardiogram is a specific indicator of left ventricular dysfunction [see comment]. *J. Am. Coll. Cardiol.* 32, 476–482. doi: 10.1016/s0735-1097(98)00242-3

Nazarian, S., and Halperin, H. R. (2018). "Computed tomography and magnetic resonance imaging for electrophysiology," in *Cardiac Electrophysiology: From Cell to Bedside*, (Amsterdam: Elsevier), 601–607. doi: 10.1016/B978-0-323-44733-1.00063-8

Neic, A., Campos, F. O., Prassl, A. J., Niederer, S. A., Bishop, M. J., Vigmond, E. J., et al. (2017). Efficient computation of electrograms and ECGs in human whole heart simulations using a reaction-eikonal model. *J. Comput. Phys.* 346, 191–211. doi: 10.1016/j.jcp.2017.06.020

Nguyên, U. C., Potse, M., Regoli, F., Caputo, M. L., Conte, G., Murzilli, R., et al. (2015). An in-silico analysis of the effect of heart position and orientation on the ECG morphology and vectorcardiogram parameters in patients with heart failure and intraventricular conduction defects. *J. Electrocardiol.* 48, 617–625. doi: 10.1016/j.jelectrocard.2015.05.004

O'Hara, T., Virág, L., Varró, A., and Rudy, Y. (2011). Simulation of the undiseased human cardiac ventricular action potential: model formulation and experimental validation. *PLoS Comput. Biol.* 7:e1002061. doi: 10.1371/journal.pcbi.1002061

Oikarinen, L., Nieminen, M. S., Viitasalo, M., Toivonen, L., Jern, S., Dahlöf, B., et al. (2004). QRS duration and QT interval predict mortality in hypertensive patients with left ventricular hypertrophy: the losartan intervention for endpoint reduction in hypertension study. *Hypertension* 43, 1029–1034. doi: 10.1161/01.HYP.0000125230.46080.c6

Pellicori, P., Joseph, A. C., Zhang, J., Lukaschuk, E., Sherwi, N., Bourantas, C. V., et al. (2015). The relationship of QRS morphology with cardiac structure and function in patients with heart failure. *Clin. Res. Cardiol.* 104, 935–945. doi: 10.1007/s00392-015-0861-0

Petersen, S. E., Sanghvi, M. M., Aung, N., Cooper, J. A., Paiva, J. M., Zemrak, F., et al. (2017). The impact of cardiovascular risk factors on cardiac structure and function: insights from the UK Biobank imaging enhancement study. *PLoS One* 12:e0185114. doi: 10.1371/journal.pone.0185114

Pishchulin, L., Wuhrer, S., Helten, T., Theobalt, C., and Schiele, B. (2017). Building statistical shape spaces for 3D human modeling. *Pattern Recogn.* 67, 276–286. doi: 10.1016/j.patcog.2017.02.018

Pitt-Francis, J., Pathmanathan, P., Bernabeu, M. O., Bordas, R., Cooper, J., Fletcher, A. G., et al. (2009). Chaste: a test-driven approach to software development for biological modelling. *Comput. Phys. Commun.* 180, 2452–2471. doi: 10.1016/j.cpc.2009.07.019

Plonsey, R., and Barr, R. C. (2007). *Bioelectricity: A Quantitative Approach*, 3rd Edn. Berlin: Springer.

Potse, M. (2018). Scalable and accurate ECG simulation for reaction-diffusion models of the human heart. *Front. Physiol.* 9:370. doi: 10.3389/fphys.2018.00370

Potse, M., Krause, D., Kroon, W., Murzilli, R., Muzzarelli, S., Regoli, F., et al. (2014). Patient-specific modelling of cardiac electrophysiology in heart-failure patients. *Europace* 16, iv56–iv61. doi: 10.1093/europace/euu257

Prakash, R. (1978). Determination of right ventricular wall thickness in systole and diastole. Echocardiographic and necropsy correlation in 32 patients. *Br. Heart J.* 40, 1257–1261. doi: 10.1136/hrt.40.11.1257

Ramanathan, C., and Rudy, Y. (2001). Electrocardiographic imaging: i. effect of torso inhomogeneities on body surface electrocardiographic potentials. *J. Cardiovasc. Electrophysiol.* 12, 229–240. doi: 10.1046/j.1540-8167.2001.00229.x

Rohr, K., Stiehl, H. S., Sprengel, R., Buzug, T. M., Weese, J., and Kuhn, M. H. (2001). Landmark-based elastic registration using approximating thin-plate splines. *IEEE Trans. Med. Imaging* 20, 526–534. doi: 10.1109/42.929618

Sánchez, C., D'Ambrosio, G., Maffessanti, F., Caiani, E. G., Prinzen, F. W., Krause, R., et al. (2018). Sensitivity analysis of ventricular activation and electrocardiogram in tailored models of heart-failure patients. *Med. Biol. Eng. Comput.* 56, 491–504. doi: 10.1007/s11517-017-1696-99

Sathananthan, G., Zahid, S., Aggarwal, G., Chik, W., Friedman, D., and Thiagalingam, A. (2015). Cardiac orientation: is there a correlation between the anatomical and the electrical axis of the heart? *Br. J. Cardiol.* 22, doi: 10.5837/bjc.2015.016

Shechter, G., Ozturk, C., Resar, J. R., and McVeigh, E. R. (2004). Respiratory motion of the heart from free breathing coronary angiograms. *IEEE Trans. Med. Imaging* 23, 1046–1056. doi: 10.1109/TMI.2004.828676

Stewart, R. A., Young, A. A., Anderson, C., Teo, K. K., Jennings, G., and Cowan, B. R. (2011). Relationship between QRS duration and left ventricular mass and volume in patients at high cardiovascular risk. *Heart* 97, 1766–1770. doi: 10.1136/heartjnl-2011-300297

Streeter, D. D., Spotnitz, H. M., Patel, D. P., Ross, J., and Sonnenblick, E. H. (1969). Fiber orientation in the canine left ventricle during diastole and systole. *Circ. Res.* 24, 339–347. doi: 10.1161/01.res.24.3.339

Usoro, A. O., Bradford, N., Shah, A. J., and Soliman, E. Z. (2014). Risk of mortality in individuals with low QRS voltage and free of cardiovascular disease. *Am. J. Cardiol.* 113, 1514–1517. doi: 10.1016/j.amjcard.2014.02.006

van Oosterom, A., Hoekema, R., and Uijen, G. J. (2000). Geometrical factors affecting the interindividual variability of the ECG and the VCG. *J. Electrocardiol.* 33(Suppl.), 219–227. doi: 10.1054/jelc.2000.20356

Villard, B., Grau, V., and Zacur, E. (2018). Surface mesh reconstruction from cardiac mri contours. *J. Imaging* 4:16. doi: 10.3390/jimaging4010016

Villard, B., Zacur, E., Dall'Armellina, E., and Grau, V. (2017). "Correction of slice misalignment in multi-breath-hold cardiac MRI scans," in *Proceedings of the STACOM 2016: Statistical Atlases and Computational Models of the Heart. Imaging and Modelling Challenges (Lecture Notes in Computer Science). International Workshop on Statistical Atlases and Computational Models of the Heart*, (Athens: Springer), doi: 10.1007/978-3-319-52718-5-4

Wallman, M., Smith, N. P., and Rodriguez, B. (2014). Computational methods to reduce uncertainty in the estimation of cardiac conduction properties from electroanatomical recordings. *Med. Image Anal.* 18, 228–240. doi: 10.1016/j.media.2013.10.006

Zacur, E., Minchole, A., Villard, B., Carapella, V., Ariga, R., Rodriguez, B., et al. (2017). "MRI-based heart and torso personalization for computer modeling and simulation of cardiac electrophysiology," in *Proceedings of the Imaging for Patient-Customized Simulations and Systems for Point-of-Care Ultrasound Lecture Notes in Computer Science*, (Cham: Springer), 61–70. doi: 10.1007/978-3-319-67552-7-8

Zemzemi, N., Bernabeu, M. O., Saiz, J., Cooper, J., Pathmanathan, P., Mirams, G. R., et al. (2013). Computational assessment of drug-induced effects on the electrocardiogram: from ion channel to body surface potentials. *Br. J. Pharmacol.* 168, 718–733. doi: 10.1111/j.1476-5381.2012.02200.x

Zemzemi, N., and Rodriguez, B. (2015). Effects of L-type calcium channel and human ether-a-go-go related gene blockers on the electrical activity of the human heart: a simulation study. *Europace* 17, 326–333. doi: 10.1093/europace/euu122

Conflict of Interest Statement: The authors declare that the research was conducted in the absence of any commercial or financial relationships that could be construed as a potential conflict of interest.

frontiers in Physiology

ORIGINAL RESEARCH
published: 24 September 2019
doi: 10.3389/fphys.2019.01041

Interaction of the Mechano-Electrical Feedback With Passive Mechanical Models on a 3D Rat Left Ventricle: A Computational Study

Minh Tuấn Dương[1,2]*, *David Holz*[1], *Muhannad Alkassar*[3], *Sven Dittrich*[3] and *Sigrid Leyendecker*[1]

[1] Chair of Applied Dynamics, University of Erlangen-Nuremberg, Erlangen, Germany, [2] School of Mechanical Engineering, Hanoi University of Science and Technology, Hanoi, Vietnam, [3] Pediatric Cardiology, University of Erlangen-Nuremberg, Erlangen, Germany

OPEN ACCESS

Edited by:
Javier Saiz,
Polytechnic University of Valencia, Spain

Reviewed by:
Vicky Y. Wang,
The University of Auckland, New Zealand
Jeffrey Omens,
University of California, San Diego, United States
Simone Pezzuto,
Università della Svizzera italiana, Switzerland

***Correspondence:**
Minh Tuấn Dương
minh.tuan.duong@fau.de

Specialty section:
This article was submitted to Computational Physiology and Medicine, a section of the journal Frontiers in Physiology

Received: 01 September 2018
Accepted: 30 July 2019
Published: 24 September 2019

Citation:
Dương MT, Holz D, Alkassar M, Dittrich S and Leyendecker S (2019) Interaction of the Mechano-Electrical Feedback With Passive Mechanical Models on a 3D Rat Left Ventricle: A Computational Study. Front. Physiol. 10:1041. doi: 10.3389/fphys.2019.01041

In this paper, we are investigating the interaction between different passive material models and the mechano-electrical feedback (MEF) in cardiac modeling. Various types of passive mechanical laws (nearly incompressible/compressible, polynomial/exponential-type, transversally isotropic/orthotropic material models) are integrated in a fully coupled electromechanical model in order to study their specific influence on the overall MEF behavior. Our computational model is based on a three-dimensional (3D) geometry of a healthy rat left ventricle reconstructed from magnetic resonance imaging (MRI). The electromechanically coupled problem is solved using a fully implicit finite element-based approach. The effects of different passive material models on the MEF are studied with the help of numerical examples. It turns out that there is a significant difference between the behavior of the MEF for compressible and incompressible material models. Numerical results for the incompressible models exhibit that a change in the electrophysiology can be observed such that the transmembrane potential (TP) is unable to reach the resting state in the repolarization phase, and this leads to non-zero relaxation deformations. The most significant and strongest effects of the MEF on the rat cardiac muscle response are observed for the exponential passive material law.

Keywords: electromechanics, mechano-electrical feedback, passive mechanics, compressible, incompressible, exponential, polynomial, rat left ventricle

1. INTRODUCTION

Cardiovascular diseases remain the leading causes of death, e.g., 30% in the US and 45% in Europe (Wilkins et al., 2017), even though the cardiovascular system has been extensively studied. A great hope to reduce the mortality of cardiovascular diseases in the future lies in computational models. These models can be an effective tool to study and understand the cardiovascular system and related pathologies in a new fashion. This includes, e.g., the early recognition of heart failure, better understanding of the cardiac function under normal and pathological conditions (Trayanova, 2011; Gao et al., 2015), patient-specific diagnostics and treatments (Asner et al., 2017), as well as the development of cardiac devices (Baillargeon et al., 2015).

Computational models of the heart include an excitation-contraction coupling representing the physiological course of converting an electrical stimulus into an active muscle contraction. The electrical excitation, which induces depolarization and contraction of cardiac cells, is widely represented by the ionic Hodgkin-Huxley model for neurons (Hodgkin and Huxley, 1952). Based on the Hodgkin-Huxley description, a large number of models have been derived, which can be subdivided into physiological and phenomenological models. On the one hand, physiological models are used from cell to tissue level, for example drug testing of a cell drum compromising three different cardiac stem cells (Frotscher et al., 2016) as well as for drug investigations on a complete human heart (Costabal et al., 2018). On the other hand, phenomenological approaches like the Aliev-Panfilov model and the FitzHugh-Nagumo model are also widely used to model cardiac excitability, mostly at tissue level (Fitzhugh, 1961; Rogers and McCulloch, 1994; Aliev and Panfilov, 1996). Compared to physiological models, the phenomenological approach describes the TP evolution, using a significantly smaller number of internal variables, while still capturing the main characteristics of the cardiac electrophysiology. Thus, it is less complex, easier to implement, reduces computational costs (Cherubini et al., 2008) and is often used to investigate arrhythmia.

Apart from the excitation-induced contraction of cardiac cells, the depolarization and subsequently the contraction of cardiomyocytes can be also initiated through the stretch-induced opening of ion channels, commonly referred to as the mechano-electrical feedback (MEF) (Kohl et al., 1999; Keldermann et al., 2009). More specifically, the MEF is capable of modifying the electrophysiology (Kamkin et al., 2005) and might promote stretch-activated arrhythmias, which have been commonly identified as a result of electrical disorders in the cardiac muscle (Franz, 1996). Moreover, the MEF can shorten the action potential (AP) duration or shorten the time course of repolarization (Franz, 1996) and break up spiral waves (Panfilov et al., 2007). Furthermore, it has been shown that high strain and stretch rates can cause premature ventricular excitation (Franz et al., 1992; Hu and Sachs, 1997). In addition to the extensive investigations on humans, similar findings have been observed for arterial cardiomyocytes in rats (Kamkin et al., 2000). In particular, stretch can result in atrial fibrillation after ventricular infarction (Kamkin et al., 2000). Also in other mammals like rabbits, the MEF can give rise to spontaneous arrhythmia in an acute local ischemia (Jie et al., 2010). This phenomenon plays a key role in interpreting the interplay between the electrophysiology and mechanics of cardiomyocytes (Keldermann et al., 2007). In a comprehensive computational modeling approach for cardiac electromechanics, it is essential to account not only for the excitation-triggered contraction of cardiac myocytes but also for the stretch-activated excitation. To investigate the effect of the MEF, strongly coupled electromechanical models are used (Costabal et al., 2017). However, depending on each specific application with different imposed goals in heart research, weakly coupled problems are also considered and sequentially solved (Frotscher et al., 2016; Duong et al., 2018). On the other hand, decoupled or staggered approaches are suitable for one-way coupling formulation (Usyk et al., 2002; Nash and Panfilov, 2004; Baillargeon et al., 2014; Frotscher et al., 2016). While the effects of the MEF have been widely studied in experiments, the effects in connection with various computational models, especially different passive material models, remain relatively unclear. In this study, the MEF is investigated in combination with various types of passive mechanical laws (nearly incompressible/compressible, polynomial/exponential-type, transversally isotropic/orthotropic material models) in order to study their interaction with the MEF.

Specifically, we want to focus on the interaction of the passive mechanical model with the MEF and how different types of material laws (compressible, incompressible, polynomial, exponential, transversely isotropic, orthotropic) are influencing the overall MEF characteristics. We employ a transversely isotropic and nearly incompressible model, a transversely isotropic compressible model (Göktepe and Kuhl, 2010) and the orthotropic and nearly incompressible Holzapfel-Odgen model (Holzapfel and Ogden, 2009). Our study is based on a left ventricle of a rat heart, whose geometry is reconstructed from high resolution MRI at the University of Erlangen-Nuremberg (Duong et al., 2018). The phenomenological model of Aliev-Panfilov is used to represent the electrical excitation (Aliev and Panfilov, 1996). We investigate the variation in TP evolution and mechanical deformation due to the interaction between the passive mechanical models and the MEF.

2. METHODS

We briefly introduce the basic electromechanical model and numerical methods used to formulate and solve the boundary value problem of the contracting ventricle. More details on the kinematics and constitutive equations can be found in the **Appendix A**.

2.1. Governing Equations for Cardiac Electromechanics

The electromechanics of a left ventricle (LV) (see **Figure 1**) can be described by two primary field variables, placement $\boldsymbol{\varphi}(\boldsymbol{X}, t)$ and AP $\Phi(\boldsymbol{X}, t)$. Thus, two field equations, which govern the state of the material point $\boldsymbol{X}$ at time t, $t \in [t_0, t_f]$ (t_0 and t_f are the initial and final time, respectively), can be formulated. The mechanical field equation is the balance of linear momentum

$$\boldsymbol{0} = \mathrm{Div}[\mathbf{F} \cdot \mathbf{S}] + \boldsymbol{F}^{\varphi} \quad \text{in } \Omega_0, \tag{1}$$

where $\mathbf{F}$ is the deformation gradient, $\mathbf{S}$ is the second Piola-Kirchoff stress tensor and $\boldsymbol{F}^{\Phi}$ is the external mechanical body force. The other differential equation describes the spatiotemporal evolution of the AP Φ and can be written as

$$\dot{\Phi} = \mathrm{Div}[\boldsymbol{Q}] + F^{\Phi} \quad \text{in } \Omega_0. \tag{2}$$

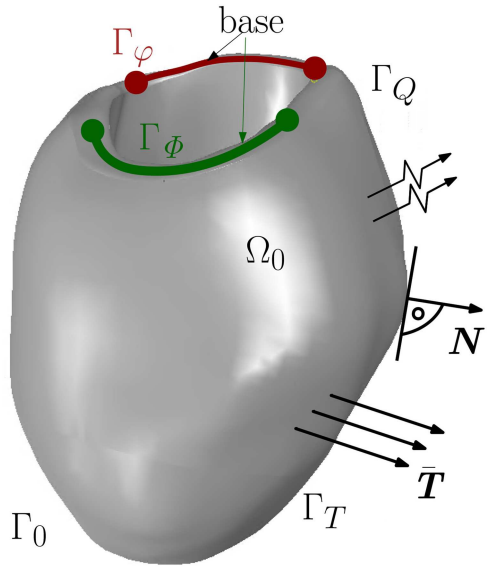

FIGURE 1 | Boundary surface Γ_0 decomposed into Γ_φ and Γ_T for the mechanical model and Γ_Φ and Γ_Q for the electrical model.

The non-linear current term F^Φ takes into account the electrical excitation, $\dot{\Phi}$ denotes the material time derivative of the AP field, Div[$\boldsymbol{Q}$] represents the diffusion of the AP, whereby $\boldsymbol{Q}$ describes the electrical flux vector. Together with the boundary conditions, the mechanical and electrical balance equations constitute an initial boundary value problem in the strong form for unknown placement and AP, $\{\boldsymbol{\varphi}(\boldsymbol{X},t), \Phi(\boldsymbol{X},t)\}$. The boundary conditions are Dirichlet and Neumann conditions as $\boldsymbol{\varphi}(\boldsymbol{X},t) = \bar{\boldsymbol{\varphi}}$ on Γ_φ, surface traction vector $\boldsymbol{T}(\boldsymbol{X},t) = \bar{\boldsymbol{T}}$ on Γ_T for all $t \in [t_0, t_f]$ and $\boldsymbol{\varphi}(\boldsymbol{X},t_0) = 0$ in Ω_0. For the electrical model, the boundary conditions are $\Phi(\boldsymbol{X},t_0) = \bar{\Phi}$ on Γ_Φ and $\boldsymbol{Q}(\boldsymbol{X},t)\cdot\boldsymbol{N} = \bar{Q}$ on Γ_Q with the unit normal vector $\boldsymbol{N}$ pointing outwards of surface Γ_Q (see **Figure 1**). By the Cauchy stress theorem, we get $\bar{\boldsymbol{T}} = \mathbf{F}\cdot\mathbf{S}\cdot\boldsymbol{N}$.

2.2. Mechanical Constitutive Models

By the active stress approach (see e.g., Smith et al., 2004; Göktepe and Kuhl, 2010; Pathmanathan et al., 2010), the stress response of cardiac muscles can be decomposed into a passive and an active part. While the passive part is only governed by the mechanical deformation, the active part takes into account the excitation-induced contraction. Hence, the total second Piola-Kirchhoff stress tensor $\mathbf{S}$ is written as

$$\mathbf{S} = \mathbf{S}^{pas}(\mathbf{C}) + \mathbf{S}^{act}(\boldsymbol{f}_0, \boldsymbol{s}_0, \Phi), \tag{3}$$

where $\mathbf{C}$ denotes the right Cauchy-Green deformation tensor, $\boldsymbol{f}_0$ the fiber direction and $\boldsymbol{s}_0$ the sheet direction in the material configuration. Now, three different models for the passive mechanical response are presented which are utilized to investigate their interaction with the MEF. From the strain energy function Ψ, which is used to describe the mechanics of soft tissues, the associated mechanical constitutive equation reads

$$\mathbf{S} = 2\frac{\partial\Psi}{\partial\mathbf{C}}. \tag{4}$$

All further derived quantities can be decomposed into their passive $(\square)^{pas}$ and active part $(\square)^{act}$.

Transversely Isotropic Compressible Model (TIC)

The first passive material model we are utilizing is a transversally isotropic compressible model, which is represented in the form of a polynomial function (see Göktepe and Kuhl, 2010). The passive material stress response is described by a modified neo-Hookean constitutive model in which the basic neo-Hookean model is extended by a transversely isotropic part taking into account the dependency of the material properties in the fiber direction $\boldsymbol{f}_0$ at each point $\boldsymbol{X}$ in the material configuration. The strain energy function can be written as

$$\Psi = \Psi_{iso} + \Psi_{ani} \tag{5}$$

$$\Psi_{iso} = \frac{\Lambda}{2}\ln^2 J + \frac{\mu}{2}\left(I_1 - 3 - 2\ln J\right) \tag{6}$$

$$\Psi_{ani} = \frac{1}{2}\vartheta\eta\left(I_{4f} - 1\right)^2 \tag{7}$$

in terms of the principal strain invariants of the symmetric right Cauchy-Green tensor $\mathbf{C}$ as $I_1 = tr(\mathbf{C})$, $\det(\mathbf{C}) = J^2$, and $I_{4f}(\mathbf{C}) = \boldsymbol{f}_0\cdot(\mathbf{C}\boldsymbol{f}_0)$, where the Jacobian J is defined as $J = \det(\mathbf{F})$. In Equation (5), the two constants Λ and μ in the isotropic part Ψ_{iso} are the Lamé parameters, and the passive stiffness of myofibers is denoted by η in the transversely isotropic (so-called anisotropic) part Ψ_{ani}.

Transversely Isotropic and Nearly Incompressible Model (TII)

The second polynomial-type model is basically derived from the above compressible modified neo-Hookean TIC model, but it is rewritten in a form such that it is transversely isotropic and nearly incompressible reading

$$\Psi = \Psi_{iso} + \Psi_{ani} + \Psi_{vol} \tag{8}$$

$$\Psi_{iso} = \frac{\mu}{2}\left(\bar{I}_1 - 3\right) \tag{9}$$

$$\Psi_{ani} = \frac{1}{2}\vartheta\eta\left(\bar{I}_{4f} - 1\right)^2 \tag{10}$$

in terms of the principal invariants of the isochoric Cauchy-Green tensor $\bar{\mathbf{C}} = \bar{\mathbf{F}}^T\bar{\mathbf{F}}$. The principal isochoric invariants of $\bar{\mathbf{C}}$ are defined as $\bar{I}_1(\bar{\mathbf{C}}) = tr(\bar{\mathbf{C}})$ and $\bar{I}_{4f}(\bar{\mathbf{C}}) = \boldsymbol{f}_0\cdot(\bar{\mathbf{C}}\boldsymbol{f}_0)$. Further, $\Psi_{vol} = \kappa(J-1)^2$ is the volumetric energy, where κ tunes the enforcement of incompressibility (we use κ=10^4 kPa). Similar as in TIC, the anisotropic part of the free energy function Ψ_{ani} only occurs if the fibers are under tension $\bar{\lambda} > 1$ with $\bar{\lambda} = \sqrt{\bar{I}_{4f}}$.

Orthotropic and Nearly Incompressible Model (HO)

The third considered model is an exponential-type strain energy function, the Holzapfel-Ogden model (see Holzapfel and Ogden, 2009). In the field of cardiac modeling, the HO model is one of the most suitable choices for describing the passive mechanical response of the myocardial tissues since it can capture the hyperelastic and orthotropic characteristics which have been found in experiments on porcine hearts (see Dokos et al., 2002). In contrast to the polynomial-type models TIC and TII, the HO is based on a strain energy function which is represented by exponentials. The orthotropy at each point $\boldsymbol{X}$ is characterized by a right-handed set of normalized basis vectors which are determined by the fiber direction $\boldsymbol{f}_0$, the sheet direction $\boldsymbol{s}_0$ and the orthogonal vector of the sheet plane $\boldsymbol{n}_0 = \boldsymbol{f}_0 \times \boldsymbol{s}_0$. By applying the incompressibility condition to the finite element setting, the HO model is, therefore, split into its isochoric term (in terms of the principal isochoric invariants) and a volumetric part Ψ_{vol} (as in TII). The strain energy function reads as

$$\Psi = \Psi_{iso} + \Psi_{ani} + \Psi_{vol}, \tag{11}$$

$$\Psi_{iso} = \frac{a}{2b}\exp[b(\bar{I}_1 - 3)], \tag{12}$$

$$\Psi_{ani} = \sum_{i=f,s} \frac{a_i}{2b_i}\left\{\exp\left[b_i(\bar{I}_{4i} - 1)^2\right] - 1\right\} + \frac{a_{fs}}{2b_{fs}}\left[\exp(b_{fs}\bar{I}^2_{8fs}) - 1\right], \tag{13}$$

where $i \in \{f, s\}$ and the variables a, b, a_f, b_f, a_s, b_s, a_{fs}, b_{fs} are material constants. While all a, a_f, a_s, a_{fs} parameters have the dimension of stress, all b, b_f, b_s, b_{fs} are dimensionless.

The active stress response is described in the **Appendix A.2**.

2.3. Electrophysiological Constitutive Models

The nonlinear current source term F^{Φ} controlling the AP in Equation (2) is split into two parts as

$$F^{\Phi} = F_e^{\Phi}(\Phi, r) + F_m^{\Phi}(\mathrm{C}, \Phi), \tag{14}$$

where F_e^{Φ} expresses the purely electrical part and F_m^{Φ} accounts for the MEF, i.e., a mechanically-induced excitation. The excitation-induced purely electrical part F_e^{Φ} characterizes the effective current, which is generated from the inward and outward flow of ions across the cardiac cell membrane. Meanwhile the stretch-induced mechano-electrical part F_m^{Φ} accounts for the opening of ion channels due to the mechanical deformation. By introducing the non-dimensional and normalized action potential Φ and the non-dimensional time $\bar{t}$, we derive the conversion forms as (Aliev and Panfilov, 1996)

$$\Phi = k_\phi \phi - \delta_\phi, \qquad t = k_t \bar{t}, \tag{15}$$

where k_ϕ and δ_ϕ relate the dimensionless action potential ϕ to the physical action potential Φ and k_t the dimensionless time $\bar{t}$ to the physical time t. Consequently, the purely electrical term F_e^{Φ} is modeled as

$$F_e^{\Phi}(\Phi, r) = \frac{k_\phi}{k_t} f_e^{\phi}(\phi, r),$$
$$f_e^{\phi}(\phi, r) = c\phi(\phi - \alpha)(1 - \phi) - r\phi + I, \tag{16}$$

where the coefficient α controls the oscillation threshold, c is a scaling parameter, I is an external stimulus and r is the recovery variable which controls the repolarization of the cardiac cell.

2.3.1. Potential Flux

The electrical constitutive equations are also formulated as functions of the deformation gradient and the AP, the material electrical flux reads

$$\boldsymbol{Q} = \mathbf{D} \cdot \nabla \Phi \tag{17}$$

with the conductivity tensor $\mathbf{D} = D_{iso}\mathbf{C}^{-1} + D_{ani}\boldsymbol{f}_0 \otimes \boldsymbol{f}_0/\lambda^2$, where $D_{iso} = Jd_{iso}$ and $D_{ani} = Jd_{ani}$. The parameter d_{iso} accounts for the isotropic and d_{ani} for the additional faster conduction along the fiber direction (Costabal et al., 2017).

2.4. Mechano-Electrical Feedback

As mentioned before, the electro-mechanical coupling plays an essential role in the cardiac function. A mechanical cell deformation induces electrical current generation. This behavior is observed due to stretch-induced opening of ion channels which induces AP generation. It can be described by the constitutive equation for the electrical source term F_m^{Φ} as

$$F_m^{\Phi}(\mathbf{C}, \Phi) = \frac{k_\phi}{k_t} f_m^{\phi}(\mathbf{C}, \phi),$$
$$f_m^{\phi}(\mathbf{C}, \phi) = \vartheta G_s (\lambda - 1)(\phi_s - \phi) \tag{18}$$

where G_s denotes the maximum conductance, ϕ is given in Equation (15), ϕ_s is the dimensionless reversal potential at which there is no net ion flux through the stretch-activated channels, ϑ is a switch function turning the feedback on for $\lambda > 1$ and off else. $\lambda = \sqrt{I_{4f}}$ (see Panfilov et al., 2005; Keldermann et al., 2007).

2.5. Excitation Stimulated by Deformation in a Plate

In this section, we refer to the benchmark problem performed on a plate using the compressible TIC model to study the effect of the MEF in which excitation wavefronts are observed caused by the deformation-induced excitation of cardiac tissue (Göktepe and Kuhl, 2010; Dal et al., 2013; Cansiz et al., 2015). The orthotropic conductivity is employed in the plate with $d_{iso} = 1.0$ mm^2 ms^{-}1 and $d_{ani} = 0.1$ mm^2 ms^{-}1, where according to section 2.3.1, the latter accounts for the additional conduction in fiber direction increased by 10% with respect to the other directions (Göktepe and Kuhl, 2009).

To illustrate the deformation-induced excitation in the plate, a mechanical load $p(t)$ is applied during $t \in [0, 10]$ ms as shown in **Figure 2A**. The plate with the dimensions of 100 × 100 × 12 mm is meshed by 21 × 21 × 2 eight-node brick elements. The fiber orientation $\boldsymbol{f}_0$ and the sheet plane direction $\boldsymbol{s}_0$ are defined

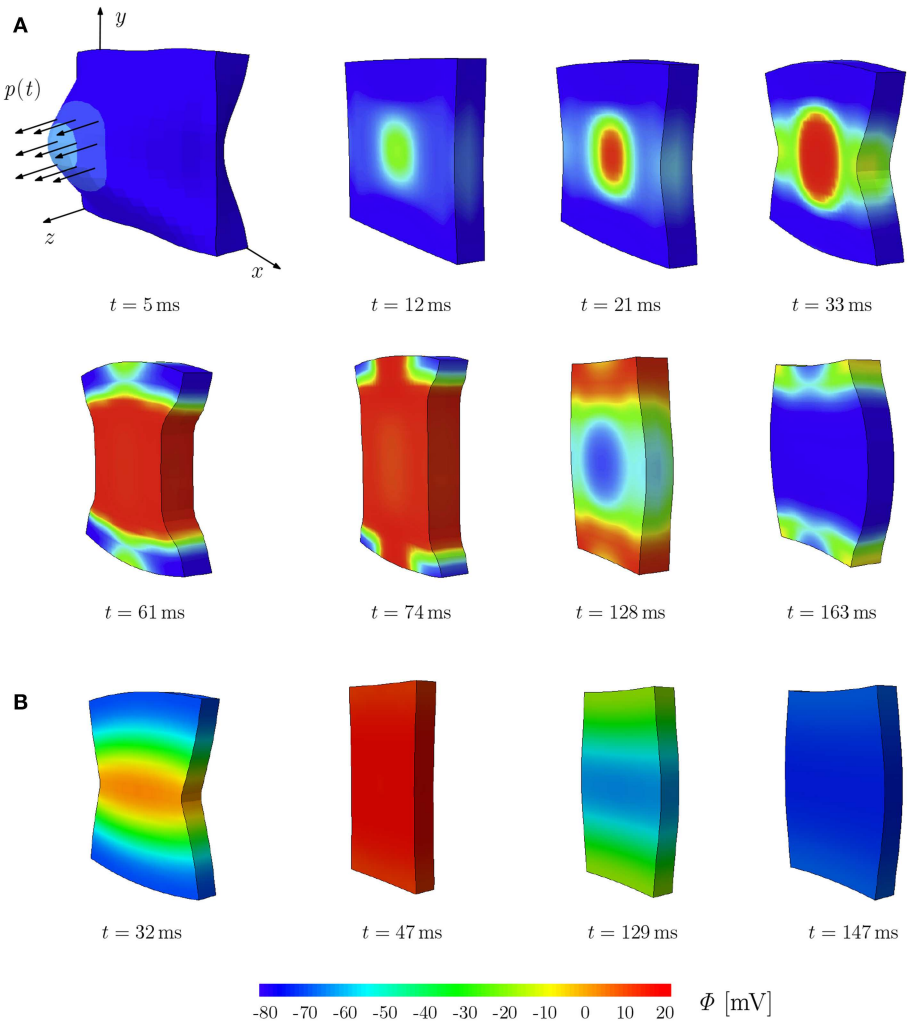

FIGURE 2 | Stretch-induced excitation in a plate; snapshots of the plate colored by the TP. **(A)** Plate of dimension 100 × 100 × 12 mm, $d_{iso} = 1.0$ mm^2 ms^{-}1 and $d_{ani} = 0.1$ mm^2/ms^{-1}. **(B)** Plate of dimension 10 × 10 × 1.2 mm, $d_{iso} = 0.1$ mm^2 ms^{-}1 and $d_{ani} = 0.3$ mm^2/ms^{-1}.

in x- and y-direction, respectively. The compressible model TIC is employed with parameters given in **Table A1**. The maximum conductance $G_s = 15$ is utilized to account for the MEF effect. Edge nodes of the plane in the middle at $z = 6$ mm are fixed in z-direction. Furthermore, the node at (0, 0, 0) is fixed in x- and y-directions and the node at (100, 0, 0) in y-direction. At the beginning of the simulation, the cellular TP in the plate is set to the resting value $\Phi = -80$ mV. To trigger the MEF, the nodes of a parallelepiped located in the center region of the plate with a dimension of 20 × 20 × 12 mm are subject to an impulsive cyclic loading $p(t)$ from $t = 0$ to $t = 10$ ms. It linearly reaches its maximum of 0.3 N at $t = 5$ ms and returns to 0 N at $t = 10$ ms.

This loading results in a stretched region in the middle of the plate and hence gives rise to a local depolarization, which then initiates an excitation wave traveling first elliptically (due to orthotropic conductivity, see $t = 12, 21$, and 33 ms) and then unidirectionally along the y-direction. At the same time, the plate shortens in the fiber direction x and elongates along the other directions orthogonal to the fibers ($t = 61$ and 74 ms). Since the model is compressible, the whole plate contracts and reduces its volume. The action potential impulse travels to the plate sides and the plate starts to repolarize with a lower potential wave starting in the middle as an elliptical shape ($t = 128$ and 163 ms). While repolarizing, the plate recovers the initial volume due to the relaxation phase of the cardiac muscles. This illustrates the change of TP due to the MEF, which will be discussed in more detail in the next section for different types of mechanical models. It is worth noting that for the TIC model, the applied mechanical load needs to be relatively large in order to cause a visible MEF effect. The same test is performed on a plate of the rat heart dimension (10 × 10 × 1.2 mm) with parameters used in the later simulations (see **Table A1**). We observed similar behavior; however due to the small dimension of the plate, complete depolarization is reached at $t = 47$ ms (**Figure 2B**).

2.6. Rat Heart Measurements

To generate a 3D left ventricle model of a rat using MRI data, we conducted several experiments on living and healthy rats. More importantly, we also confirm that the ethics committee (Tierschutzgesetz Regierung Unterfranken) approved our experimental protocol and procedures. Further, only the best measurement result was used to reconstruct the 3D rat left ventricle model in the diastolic phase.

3. RESULTS

In this section, we investigate the effect of different passive material laws in a strongly coupled electromechanical model of a 3D rat left ventricle.

3.1. Parameters of Cardiac Muscles of Rat Heart

The material parameters for our simulation are obtained by curve fitting to experimental data of a porcine heart by Dokos et al. (2002) (see **Figure 3**; using a scaling factor of 0.5 for rats). The resulting material parameters are displayed in **Table A1** (**Appendix A.5**). The parameters for the electrical and the active model originate partially from our parameter study and partially from work for healthy human hearts (Aliev and Panfilov, 1996; Göktepe and Kuhl, 2010; Baillargeon et al., 2015). We also use $k_T = 0.49$ kPa mV^{-1} in Equation (24), resulting in $T^{act}_{max} = 49$ kPa, which is sufficiently close to the maximum tension value of 45 kPa as obtained in rat experiments (see Niederer et al., 2009). The reversal potential ϕ_s in Equation (15) is set to 0.6, corresponding to -20 mV, which is in agreement with the physiological value by Kohl et al. (1999).

3.2. Rat Left Ventricle

In this section, the interaction of the three different passive material models with the MEF is investigated with regard to the influence of the maximum conductance with $G_s = 10$ and $G_s = 0$. For the electromechanical simulation, the parameters given in **Table A1** (**Appendix A.5**) are used. The base of the ventricle is mechanically fixed (see **Figure 1**). However, different boundary conditions (Baillargeon et al., 2015) can be applied such that the base of the ventricle can slightly translate or twist when it contracts and interacts with surrounding tissues, which greatly support and stabilize the whole heart. The mesh of the 3D solid left ventricle model is generated using 4-node tetrahedral elements based on a high resolution MRI from the Universitätsklinikum Erlangen-Nürnberg. The basic workflow from the MRI images to the finite element mesh can be seen in **Figure 4**.

The fiber and sheet orientations, which are crucially attributing to the mechanics and electrical conduction system, are assigned for the LV by interpolating the local fiber and sheet directions from the endocardial and epicardial surface such that the model can account for the transmural fiber and sheet directions (Vetter and McCulloch, 1998; Wong and Kuhl, 2014). Although the fiber angles on the endocardium and the epicardium vary largely between different rats (Chen et al., 2003; Hales et al., 2012; Mekkaoui et al., 2012), the fiber angles are chosen as $+80°$ on the endocardium and $-70°$ on the epicardium (see **Figure 5**).

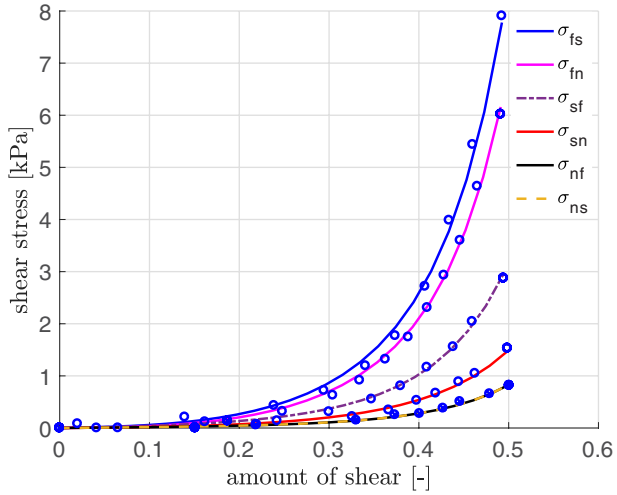

FIGURE 3 | Stress-strain relation with parameters fitted using simple shear data (modified for the rat heart) by Dokos et al. (2002).

For simplicity, we assume a chamber pressure of zero, no electrical flux on the boundary as well as zero surface traction. The computational mesh of the 3D LV consists of 49,769 tetrahedral elements corresponding to the global mesh size of 0.35 mm. Initially, all 10,237 nodes are set to the resting potential $\Phi_r = -80$ mV. Seven nodes at the base are used to trigger the depolarization in the surrounding cardiomyocytes. They are constrained at $\Phi = -20$ mV for a duration of 40 ms. Subsequently, we solve six fully coupled electromechanical problems for the three different passive material models with and without the MEF ($\text{TIC}_{G_s=10}$, $\text{TIC}_{G_s=0}$, $\text{TII}_{G_s=10}$, $\text{TII}_{G_s=0}$, $\text{HO}_{G_s=10}$, $\text{HO}_{G_s=0}$). We performed simulation on refined meshes up to a mesh size of 0.15 mm. The plot in **Figure 6** illustrates that neither the maximal, nor the residual TP show significant changes in regime of smaller meshes. In particular, the resting potential of -80 mV is not reached for all tested mesh sizes.

Figure 6 exemplarily shows the numerical result for the HO model with the MEF ($\text{HO}_{G_s=10}$)—the location of the stimulus can be seen at the base at $t = 2$ ms. From there, the electrical impulse propagates through the ventricle, see snapshots at $t = 60$ and 70 ms. The entire myocardium contracts at $t = 90$ ms when all ventricular cells are depolarized (in red). After the depolarization, the repolarization follows ($t = 120$, 150, 176, and 300 ms), but the ventricle is unable to return to the initial shape (light blue shadow) even for $t \geq 300$ ms. This behavior corresponds to a second peak in the AP curve for the HO model (peak 2 above -80 mV) after peak 1 (see **Figure 7**, right).

Moreover, the AP curve for the TII model with $G_s = 10$ in the repolarization phase reaches a minimum value of about -78.5 mV for $t \geq 300$ ms, while the AP curve for the TIC model is able to retrieve the resting potential of -80 mV (see **Figure 7**, right). The same characteristic behavior can

FIGURE 4 | Workflow from MRI images to the finite element mesh of the left ventricle. Left to right: MRI image-segmentation, NURBS model, finite element mesh.

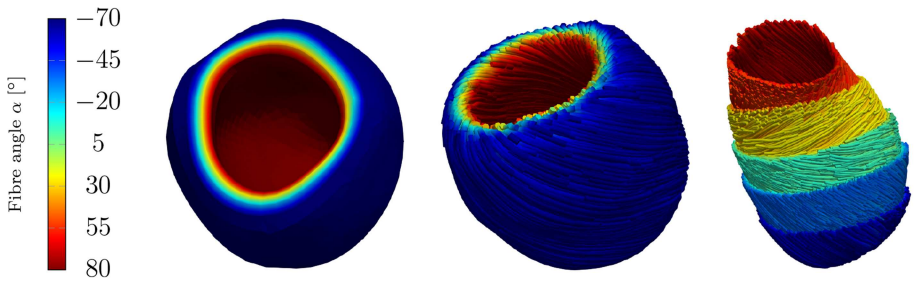

FIGURE 5 | Rat left ventricle with fiber orientations from −70° on the epicardium to +80° on the endocardium with respect to the circumferential direction; **(Left)**: the linear distribution of fiber angles in colors, **(Center)**: fibers (streamlines) on endocardium and epicardium, **(Right)**: fibers on different layers.

be observed by plotting the apex displacement u (**Figure 7**, right). On the contrary, **Figure 7** (left) exhibits no peak 2 in the AP and displacement curves for all three models without MEF ($TIC_{G_s=0}$, $TII_{G_s=0}$, $HO_{G_s=0}$). The LV consequently relaxes to its initial shape. The stretch-induced excitation changes the AP duration, leads to a delayed repolarization and thus the resting potential is reached more slowly. In **Figure 7** (left), the AP evolution profiles for the three models are very similar; however, the displacement predicted by the compressible TIC model is larger than the displacements predicted by the TII and HO models. Compared to the AP curves, the displacement of the apex starts before the depolarization. This is caused by the fact that the cardiac cells between the initiated nodes at the base and the considered node at the apex already depolarize and start to contract and hence cause the pre-displacement of the apex.

In summary, it can be stated that both incompressible models yield a different electrical and mechanical response (residual deformation and resting potential not reached at the end of the cardiac cycle) of the LV compared to the compressible TIC model. This raises the question, what exactly causes the difference in the results among the three passive mechanical models. On the one hand, the HO represents an orthotropic material law which is represented by exponentials, while the other two models are transversely isotropic and formulated in terms of polynomials. On the other hand, the HO and TII are both incompressible models, while TII is compressible. To study this more comprehensively, we extended the numerical investigations by performing a parameter study on the maximum conductance G_s, which is commonly known as the maximum stretch-activated ion channel conductance or the sensitivity of the electrical current to deformation. Note that diseased hearts can cause abnormal changes in the maximum conductance (Zhang et al., 2014). Thus, this value can be considered as a key variable to study the MEF effects.

We performed 18 simulations, which differ in the passive material model (TIC, TII, HO) and the maximum conductance (G_s = 0, 10, 20, 30, 40, and 50). Instead of performing a benchmark problem study using a simple cube, bar or beam, the effect is directly studied in a 3D LV model. The result of the AP evolution and the displacement are shown in **Figure 8**. The TIC model shows an almost independent behavior with respect to the strength of the MEF [see AP and displacement evolution **Figure 8** (top, left, and right)]. The polynomial, transversely isotropic and incompressible material law TII (middle, left, and right) and the exponential, orthotropic and incompressible material law HO (bottom, left, and right) exhibit a high sensitivity to the strength of the MEF. The observed characteristics in **Figure 7** (early depolarization, delay in the late repolarization phase, decrease of the maximum AP) are intensified with a higher maximum conductance.

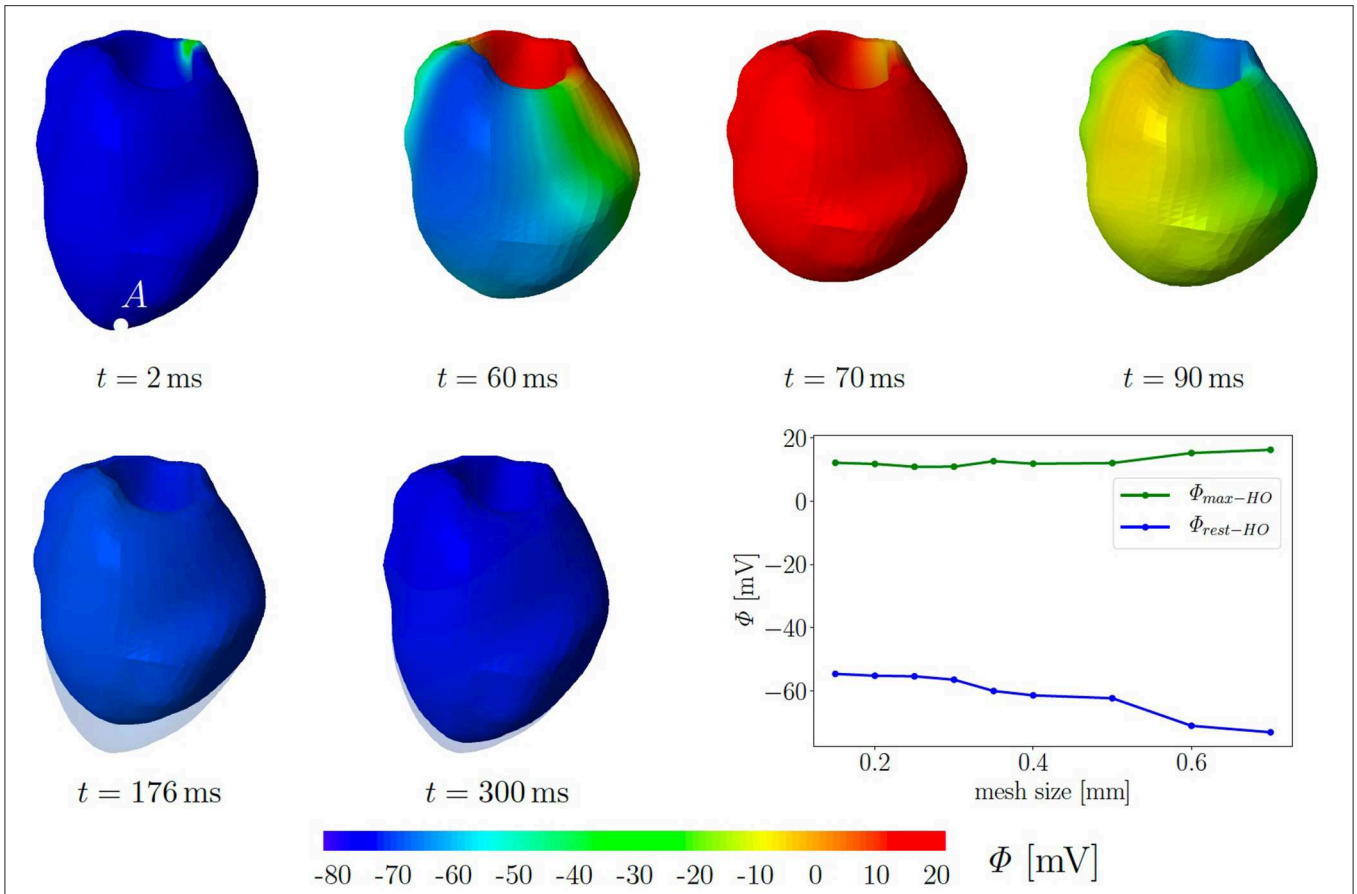

FIGURE 6 | Electromechanics in rat left ventricle with the HO model with MEF and $Gs = 10$. Material parameters are given in **Table A1**. Excitation by setting seven nodes at the base to $\Phi = -20$ mV for 40 ms. At the end of cardiac cycle (around $t = 300$ ms), the repolarised (resting) LV (blue) is unable to return to its initial shape (light blue region) since the MEF affects the AP and deformation of the LV. Plot at the right bottom shows the relation of maximal and residual potential versus the global mesh size (HO model with MEF and $G_S = 50$).

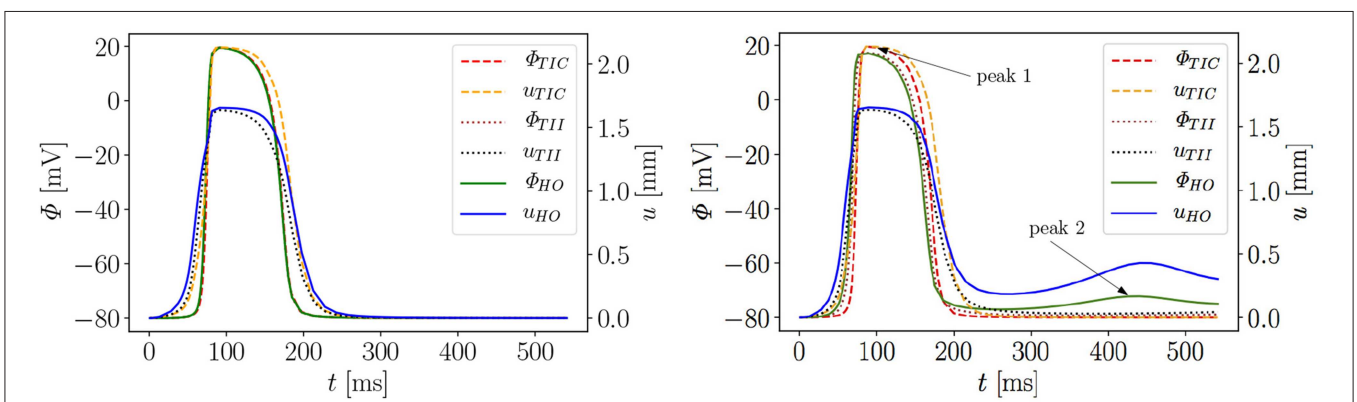

FIGURE 7 | Evolution of AP Φ and displacement u of apical node A in a rat left ventricle for three models, without MEF **(Left)** and with MEF using $G_S = 10$ **(Right)**.

4. DISCUSSION

As observed in the last section, the influence of the MEF on the overall electrophysiological and mechanical behavior significantly depends on the passive material model. In the following section, we want to discuss the differences and possible sources or causes. The main differences of the three different passive material models can be summarized as follows: (i)

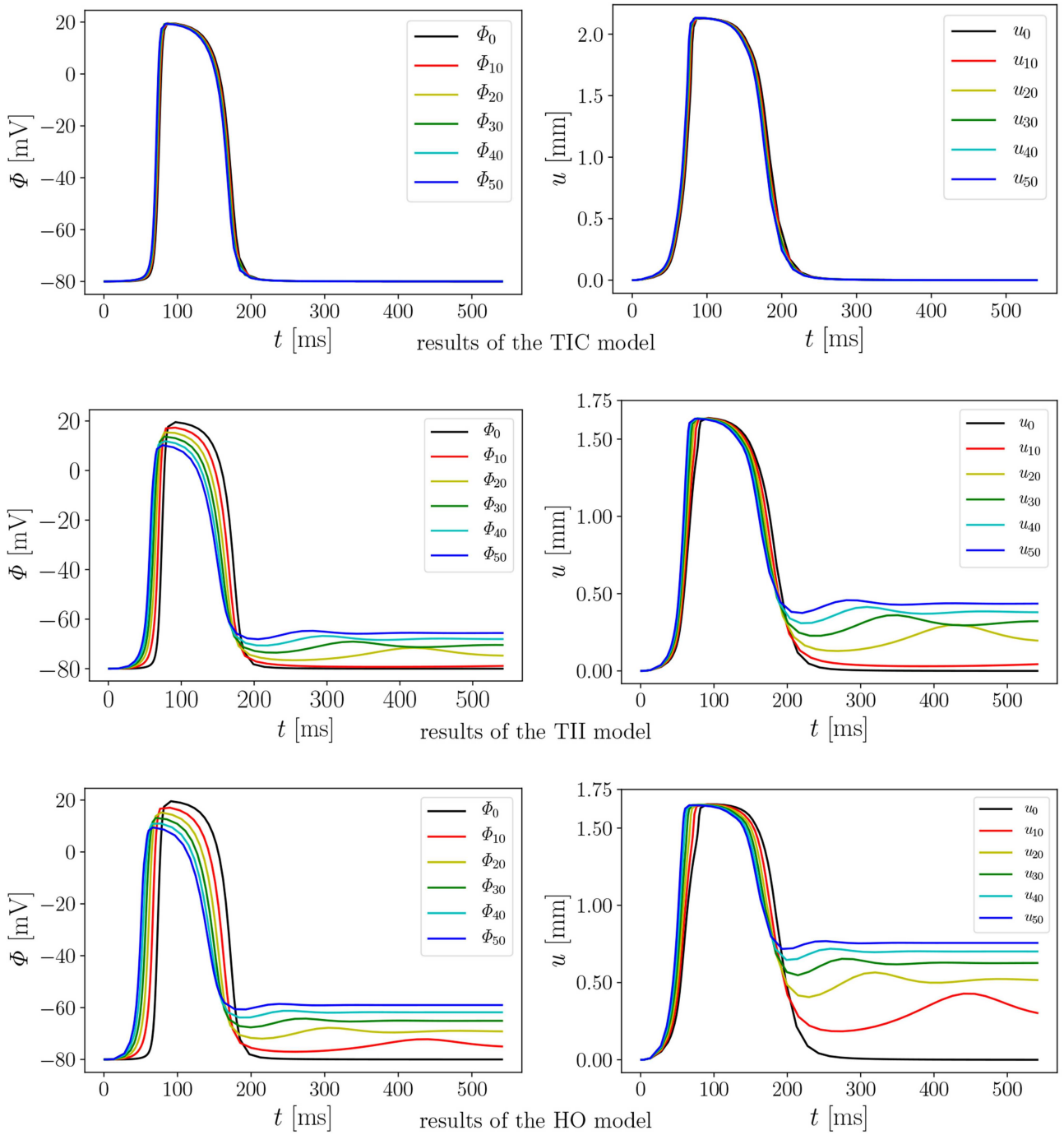

FIGURE 8 | Evolution of AP Φ **(Left)** and displacement u **(Right)** of node A with varying G_s in a rat left ventricle for the three material models.

compressible vs. incompressible, (ii) polynomial vs. exponential, (iii) orthotropic vs. transversely isotropic. Their respective results will be evaluated and compared here. Referring to the following explication, we introduce the notation: $\square_{max-a}$ and $\square_{rest-a}$ for values of the material a at peak 1 (e.g., the maximal value of the AP or displacement) and at peak 2 close to the resting potential −80 mV and zero deformation (see **Figure 7**, right), respectively. We define the difference of a value at $G_s = x$ to that at $G_s = 0$ as $\triangle \square^x_{i-a} = |\square_{i-a}(G_s = 0) - \square_{i-a}(G_s = x)|$, where $i \in \{max, rest\}$.

First we note that the MEF is capable of speeding up the electrical impulse propagating in the LV (**Figure 9**). For the compressible TIC model, it is clearly observed that the MEF has negligible effects on the electrophysiology and mechanics.

The largest change in time for the AP peak is $\triangle\, t^{50}_{max-TIC} = 5$ ms while there is no peak 2 and thus $\triangle\, t^{x}_{rest-TIC} = 0$ for all values $x \in \{0, 10, 20, 30, 40, 50\}$ (see also peak values in **Figure 9**). In contrast to that, we observe a significant effect of the MEF (or maximum conductance) for the incompressible models TII and HO. **Figure 8** indicates that for higher value of G_s, larger changes in AP and displacement curves can be observed. The largest changes in peak time for AP are $\triangle\, t^{50}_{max-TII} = 18$ ms and $\triangle\, t^{50}_{max-HO} = 23$ ms for the TII and HO models, respectively. The conduction velocity is apparently increased with G_s which is in good agreement with the findings in a study by Costabal et al. (2017). Similar observations have also been made in the numerical results by Amar et al. (2018), in which the AP was influenced by the MEF for different stretch levels for examples of a ventricle and a single cardiomyocyte.

Second, depending on the material model, the MEF influences AP Φ and displacement u in the late repolarization phase. For the compressible model TIC, no change in peak 2 for the AP and displacement curves ($\triangle\, \Phi^{x}_{rest-TIC} = 0$ mV and $\triangle\, u^{x}_{rest-TIC} = 0$ mm) for all values $x \in \{0, 10, 20, 30, 40, 50\}$ can be observed. At the same time, there are significant changes in peak 2, which can be observed in the curves for the TII and HO model. For example, the largest changes are introduced by $G_s = 50$ such as $\triangle\, \Phi^{50}_{rest-TII} = 16$ mV and $\triangle\, \Phi^{50}_{rest-HO} = 22$ mV, whereas $\triangle\, u^{50}_{rest-TII} = 0.45$ mm and $\triangle\, u^{50}_{rest-HO} = 0.79$ mm (see **Figure 10**, right). The maximum value of the AP Φ and displacement u for peak 1 for ($G_s = x$) for all values $x \in \{0, 10, 20, 30, 40, 50\}$ are depicted in **Figure 10** (left). While varying the maximum conductance G_s, the compressible model leads to an almost unchanged electrophysiology and mechanics, the nearly incompressible models show a stronger effect of the MEF on the electrophysiology (early depolarization, reduced maximum AP, increased conduction velocity, delayed repolarization) and consequently result in a significantly higher relaxation displacement of the LV.

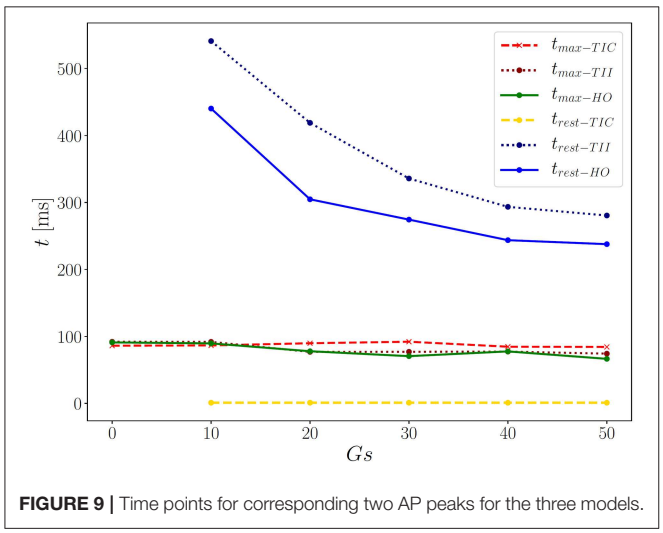

FIGURE 9 | Time points for corresponding two AP peaks for the three models.

Compressible vs. Incompressible

One important characteristic which influences the impact of the MEF on the overall model behavior is the level of compressibility. The compressible TIC model undergoes a significant volume change (compressible medium) during the active contraction phase, which in turn leads to a reduced overall strain/stretch. This is visualized in **Figure 11** showing the isotonic contraction of a cube for the three different material models.

As expected, when considering the volume ratio curves for the three models in isotonic contraction, the volume ratio during the time course of the cardiac cycle for the compressible TIC model decreases ineluctably, while the volume for the HO and TII models remains constant. By plotting the fiber stretch λ of the same apical node of the LV for the HO, TII and TIC model, we observe the fiber stretch $\lambda < 1$ (compression) for the TIC model and the fiber stretch $\lambda > 1$ for the HO and TII models (see **Figure 12**).

This leads to the fact that in this particular region, the MEF is active for the TII and HO models and inactive for the TIC model (see Equation 18, λ has to be >1 for the switch function ϑ to be non-zero). Furthermore, the fiber angles transmurally vary and thus the local change in fiber direction leads to an

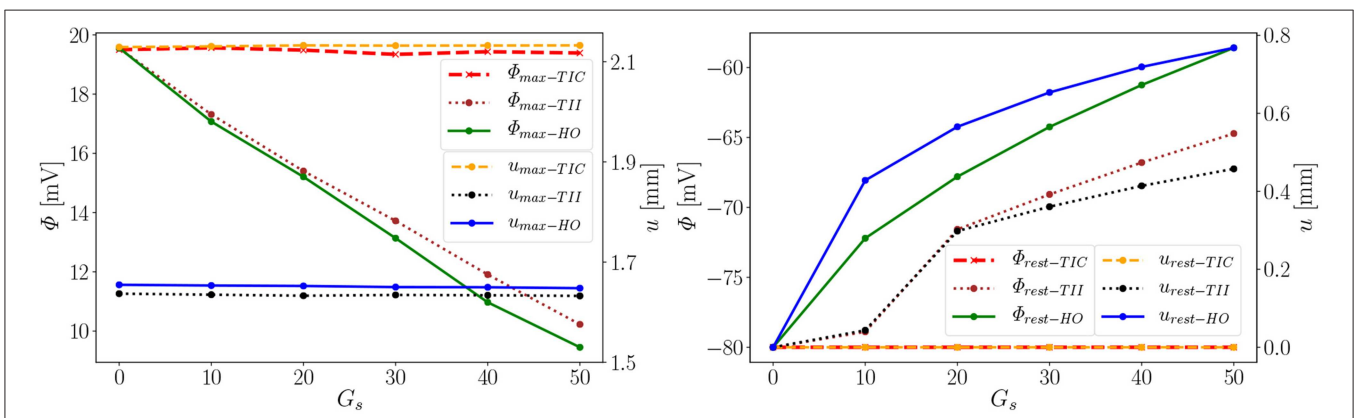

FIGURE 10 | Φ_{max} and u_{max} of peak 1 **(Left)**, Φ_{rest} and u_{rest} of peak 2 **(Right)** for the three models ($\Phi_{rest-TIC}$ curves invisible since $u_{rest-TIC}$ lies on top of it).

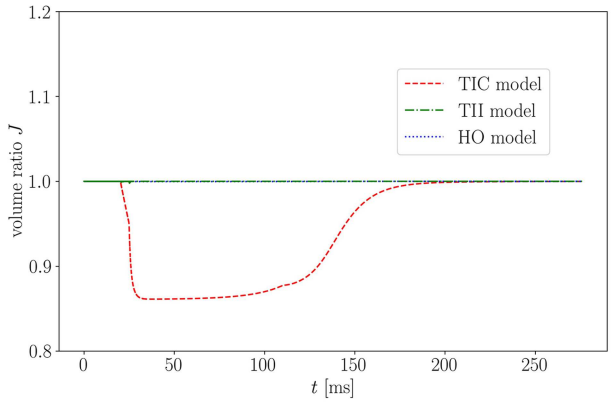

FIGURE 11 | Volume ratio J of isotonic contraction of a cube over time for the three models.

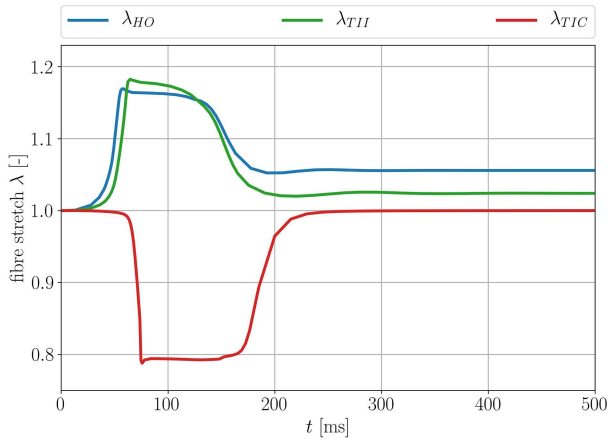

FIGURE 12 | Fiber stretch λ for an apical node for the three different passive material models.

increased fiber stretch through the wall (the expansion of the material in sheet and normal direction close to the boundaries leads to a fiber stretch in the middle layers; see **Figure 13**, left, center).

This behavior is characteristic for the incompressible TII and HO models. The TII model compensates this phenomenon due to the compressibility (volume change), and thus the expansion of the material in the sheet and normal direction is smaller, which finally induces no or insignificant stretches to the fibers in the middle layer (see **Figure 13**, right). For the TII and HO model, the high fiber stretch in the middle layers during the repolarization phase effectively causes a strong MEF current. In a real healthy rat left ventricle, the MEF effect might be caused by a strong mechanical stimulus when the AP reaches the threshold value. However, it is observed mainly in diseased cases (Kamkin et al., 2000). The MEF can alter the AP or shorten refractory periods in canine left ventricle and atrium, as reported in Franz (1996). Stretch-activated polarization and fibrillation can happen at a low stretch in a rat atrium after the infarction of the left ventricle (Kamkin et al., 2000). Moreover, it has been observed in our simulation of the LV as well as for cubes, plates and other 2D examples in Costabal et al. (2017), that the MEF is capable of altering the AP and increasing the conduction velocity. However, the phenomenon of the residual deformation (non-relaxed equilibrium between the AP generation and the fiber stretches in the late repolarization phase) is rather unrealistic in the healthy left ventricle simulation.

Polynomial vs. Exponential

In addition to the discussed differences due to the level of compressibility, the exponential and polynomial form of the passive material law plays a significant role concerning the overall MEF behavior. To clarify this, we performed the numerical tests for the HO and TII models with the same bulk modulus of $\kappa = 10^4$ kPa, which means that these models have the same level of compressibility. The compressibility value is reasonable in our simulations as it is only slightly larger compared to the *in vivo* measurements by Hassaballah et al. (2013). To compare the influence of the polynomial material law TII and the exponential material law HO, we evaluate the differences in **Figures 8**, **10**, **12**, **13**.

In the depolarization phase, the HO and TII models show an almost similar behavior concerning the AP and displacement curves even if the observed phenomenon is slightly more prominent for the HO model (see **Figures 10**, **8**, left). Nevertheless, in the late repolarization phase, the AP and displacement curves significantly differ between the HO and TII models (see **Figure 10**, right). It is worth noting that both models undergo a comparable maximum stretch level (see **Figure 13**, left, center). Thus the question arises regarding where the significant differences in the late repolarization come from.

Since the same bulk modulus is used, both models generate the same amount of active stress and result in relatively comparable displacements (see **Figure 13**, left, center). Therefore, the difference can only be explained by the fact that the HO model induces larger strain/stretch in the late repolarization phase and in turn produces a higher MEF current compared to the TII model. **Figure 12** exposes that the HO model has a steeper increase in the fiber stretch in the depolarization phase (which explains the faster depolarization compared to the TII model) and a slower change of the fiber stretch in the repolarization phase (which explains the higher stretch in the late repolarization phase). In other words, starting from the same deformation level during the contraction for the HO and TII models, the cardiac tissue relaxes in the repolarization phase, in which the exponential-type stress-strain relation of the HO model responds to the decreasing active fiber tension with a smaller change in fiber stretch compared to the TII model. Finally, this leads to a high MEF current in certain regions, which almost reached their resting potential.

Transversely Isotropic vs. Orthotropic

As we discussed in the previous paragraph, the main difference in the AP and displacement for the HO and TII models originate in the representation of the material law. Nevertheless,

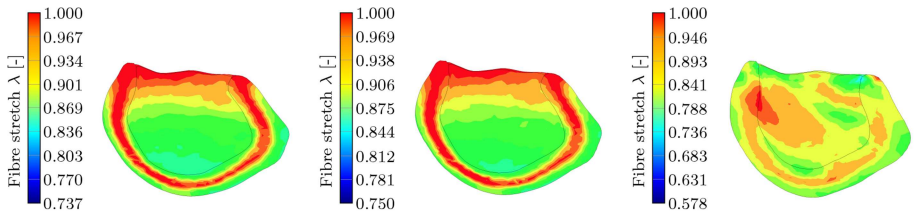

FIGURE 13 | Section view of the LV during the contraction phase at $t = 90$ ms for the three different passive material models. The snapshots show the transmural fiber stretch λ. The color code is limited to the maximum fiber stretch of 1 and thus all dark red regions show fiber stretch $\lambda \geq 1$. The maximum global fiber stretch for the three different models reads as: $\lambda_{HO}^{max} = 1.188$, $\lambda_{TII}^{max} = 1.204$, $\lambda_{TIC}^{max} = 1.024$. **(Left)**: transmural fiber stretch—HO, **(Middle)**: transmural fiber stretch—TII, **(Right)**: transmural fiber stretch—TIC.

the incompressibility condition with the associated stretches along the sheet and sheet normal direction at the boundaries [see **Figure 13** (left, center), fiber stretch $\lambda < 1$, and thus the compression in fiber direction has to be compensated by stretch in the sheet and sheet normal direction] leads to a stretch in fiber direction in the middle layers. As the fiber stretch λ depends on the material properties in sheet and sheet normal direction, there also exists a difference between a transversely isotropic and an orthotropic material law concerning the MEF behavior. To further investigate the difference, one would have to vary the passive material properties in sheet or sheet normal direction for the same material model (note that for the special case of transversal isotropy, the properties in sheet and sheet normal direction are the same) in order to eliminate the influence of the type of material model (polynomial and exponential). However, this goes beyond the scope of this study. In our case, the difference between the orthotropic material model HO and the transversely isotropic material model TII seems to be rather small as the overall fiber stretch levels are similar.

4.1. Limitations of the Work

In the following, we want to briefly discuss the limitations and assumptions for this study. Firstly, we ignore the possible influence of the right ventricle and other components which also contribute to the overall model behavior. Secondly, the electromechanical model uses several parameters, which are directly adapted or come from other studies on human and porcine hearts. Furthermore, the electrophysiological model is an obvious simplification of the actual electrophysiology of the heart. There exist different kinds of cardiac cells in the heart with different contractility and conductivity. In particular, the fast conducting Purkinje fibers need to be included in order to improve the choreographed depolarization and repolarization of the heart. However, the simple electrophysiological model is to be preferred for our application whereby a complex rat heart support system will be developed in order to compensate the function of the pathological heart. Further, more detailed experimental data, especially for rats, about the electrical and active model including the determination of the active muscle tension, transmembrane potential and maximum conductance, G_s are required. Measurements to identify the passive material parameters for rats would be desired to further improve the accuracy of the model. Moreover, the fixed base in the simulation model simplifies the actual support of the heart in the body (e.g., connective tissue, atria) and an advanced boundary condition should be applied for future studies. Further investigations are necessary to evaluate the influence of the specific morphology of the heart (different fiber distributions). Additionally, to more precisely describe the exact influence and differences of transversely isotropic and orthotropic material laws concerning the MEF behavior, a parameter study about the level of orthotropy is necessary.

5. CONCLUSION

In this paper, we focus on the interaction of passive mechanical models with the MEF and how different types of material laws (compressible, incompressible, polynomial, exponential, transversely isotropic, and orthotropic) influence the overall MEF characteristics. We employ a transversely isotropic and nearly incompressible model (TII), a transversely isotropic compressible model (TIC) (Göktepe and Kuhl, 2010) and the orthotropic and nearly incompressible Holzapfel-Odgen model (HO) (Holzapfel and Ogden, 2009). We investigate the variation in AP evolution and mechanical deformation due to the interaction between the passive mechanical models and the MEF.

The interaction between the passive models and the MEF is discussed through a computational study of a rat LV, whereby the following findings are obtained: (i) compressibility: the transversely isotropic material law (TIC) predicts a significantly smaller fiber stretch (compression almost everywhere in the LV) and thus leads to a nearly unrecognizable change in the overall MEF behavior (change in electrophysiology and mechanical contraction); additionally, for the incompressible models, we observe a residual deformation caused by a non-relaxed equilibrium; (ii) polynomial vs. exponential material laws: due to the exponential strain energy function, the HO model shows a faster temporal change of the fiber stretch in the depolarization phase (leading to a faster depolarization compared to the TII model; higher MEF current) and at the same time slower temporal change of the fiber stretch in the late repolarization phase; (iii) transversely isotropic vs. orthotropic: the incompressibility condition with the associated

stretches along the sheet and sheet normal direction on the boundaries [see **Figure 13** (left, center), fiber stretch $\lambda < 1$ and thus the compression in fiber direction has to be compensated by stretch in the sheet and sheet normal direction] leads to a stretch in fiber direction in the middle layers. As the fiber stretch λ depends on the material properties in the sheet and sheet normal direction, there also exists a difference in the electromechanical behavior and the MEF between a transversely isotropic and an orthotropic material law concerning the MEF behavior.

Obviously, the type of passive material model plays a key role in defining the MEF behavior in a fully coupled electromechanical model. It has to be further investigated which of the considered models reflect the cardiac tissue best concerning the overall MEF behavior.

ETHICS STATEMENT

The experimental protocol and procedures were approved by the ethics committee (Tierschutzgesetz Regierung Unterfranken).

AUTHOR CONTRIBUTIONS

MD mainly contributed to this paper concerning the manuscript, modeling, and simulation. DH contributed through the geometric and fiber modeling, simulation as well as the revision of the paper. MA, SD, and SL contributed through the conception and design of the study. MA provided the MRI data and the segmentation.

FUNDING

The authors thank the Klaus Tschira Stiftung grant 00.289.2016 for funding support.

ACKNOWLEDGMENTS

Denisa Martonova's support during the revision by carrying out further simulations and improving parts of the manuscript is gratefully acknowledged.

REFERENCES

Aliev, R. R., and Panfilov, A. V. (1996). A simple two-variable model of cardiac excitation. *Chaos Solitons Fract.* 7, 293–301. doi: 10.1016/0960-0779(95)00089-5

Amar, A., Zlochiver, S., and Barnea, O. (2018). Mechano-electric feedback effects in a three-dimensional (3D) model of the contracting cardiac ventricle. *PLoS ONE* 13:e0191238. doi: 10.1371/journal.pone.0191238

Asner, L., Hadjicharalambous, M., Chabiniok, R., Peressutti, D., Sammut, E., Wong, J., et al. (2017). Patient-specific modeling for left ventricular mechanics using data-driven boundary energies. *Comput. Methods Appl. Mech. Eng.* 314(Suppl. C), 269–295. doi: 10.1016/j.cma.2016.08.002

Baillargeon, B., Costa, I., Leach, J. R., Lee, L. C., Genet, M., Toutain, A., et al. (2015). Human cardiac function simulator for the optimal design of a novel annuloplasty ring with a sub-valvular element for correction of ischemic mitral regurgitation. *Cardiovasc. Eng. Technol.* 6, 105–116. doi: 10.1007/s13239-015-0216-z

Baillargeon, B., Rebelo, N., Fox, D. D., Taylor, R. L., and Kuhl, E. (2014). The living heart project: a robust and integrative simulator for human heart function. *Eur. J. Mech. A/Solids* 48, 38–47. doi: 10.1016/j.euromechsol.2014.04.001

Cansiz, B., Dal, H., and Kaliske, M. (2015). Fully coupled cardiac electromechanics with orthotropic viscoelastic effects. *Proc. IUTAM* 12(Suppl. C), 124–133. doi: 10.1016/j.piutam.2014.12.014

Chen, J., Song, S.-K., Liu, W., McLean, M., Allen, J. S., Tan, J., et al. (2003). Remodeling of cardiac fiber structure after infarction in rats quantified with diffusion tensor MRI. *Am. J. Physiol.* 285, H946–H954. doi: 10.1152/ajpheart.00889.2002

Cherubini, C., Filippi, S., Nardinocchi, P., and Teresi, L. (2008). An electromechanical model of cardiac tissue: constitutive issues and electrophysiological effects. *Progr. Biophys. Mol. Biol.* 97, 562–573. doi: 10.1016/j.pbiomolbio.2008.02.001

Costabal, F. S., Concha, F. A., Hurtado, D. E., and Kuhl, E. (2017). The importance of mechano-electrical feedback and inertia in cardiac electromechanics. *Comput. Methods Appl. Mech. Eng.* 320, 352–368. doi: 10.1016/j.cma.2017.03.015

Costabal, F. S., Hurtado, D. E., and Kuhl, E. (2016). Generating Purkinje networks in the human heart. *J. Biomech.* 49, 2455–2465. doi: 10.1016/j.jbiomech.2015.12.025

Costabal, F. S., Yao, J., and Kuhl, E. (2018). Predicting drug-induced arrhythmias by multiscale modeling. *Int. J. Numer. Methods Biomed. Eng.* 34:e2964. doi: 10.1002/cnm.2964

Dal, H., Göktepe, S., Kaliske, M., and Kuhl, E. (2013). A fully implicit finite element method for bidomain models of cardiac electromechanics. *Comput. Methods Appl. Mech. Eng.* 253, 323–336. doi: 10.1016/j.cma.2012.07.004

Dokos, S., Smaill, B. H., Young, A. a., and LeGrice, I. J. (2002). Shear properties of passive ventricular myocardium. *Am. J. Physiol. Heart Circul. Physiol.* 283, H2650–H2659. doi: 10.1152/ajpheart.00111.2002

Duong, M. T., Holz, D., Alkassar, M., Dittrich, S., and Leyendecker, S. (2018). Simulation of cardiac electromechanics of a rat left ventricle. *PAMM* 18:e201800326. doi: 10.1002/pamm.201800326

Fitzhugh, R. (1961). Impulses and physiological states in theoretical models of nerve induction. *Biophys. J.* 1, 455–466. doi: 10.1016/S0006-3495(61)86902-6

Franz, M. R. (1996). Mechano-electrical feedback in ventricular myocardium. *Cardiovasc. Res.* 32, 15–24. doi: 10.1016/S0008-6363(96)00074-0

Franz, M. R., Cima, R., Wang, D., Profitt, D., and Kurz, R. (1992). Electrophysiological effects of myocardial stretch and mechanical determinants of stretch-activated arrhythmias. *Circulation* 86, 968–978. doi: 10.1161/01.CIR.86.3.968

Frotscher, R., Muanghong, D., Dursun, G., Goßmann, M., Temiz-Artmann, A., and Staat, M. (2016). Sample-specific adaption of an improved electro-mechanical model of *in vitro* cardiac tissue. *J. Biomech.* 49, 2428–2435. doi: 10.1016/j.jbiomech.2016.01.039

Gao, H., Li, W. G., Cai, L., Berry, C., and Luo, X. Y. (2015). Parameter estimation in a Holzapfel-Ogden law for healthy myocardium. *J. Eng. Math.* 95, 231–248. doi: 10.1007/s10665-014-9740-3

Göktepe, S., and Kuhl, E. (2009). Computational modeling of cardiac electrophysiology: a novel finite element approach. *Int. J. Numer. Methods Eng.* 79, 156–178. doi: 10.1002/nme.2571

Göktepe, S., and Kuhl, E. (2010). Electromechanics of the heart: a unified approach to the strongly coupled excitation-contraction problem. *Comput. Mech.* 45, 227–243. doi: 10.1007/s00466-009-0434-z

Hales, P. W., Schneider, J. E., Burton, R. A. B., Wright, B. J., Bollensdorff, C., and Kohl, P. (2012). Histo-anatomical structure of the living isolated rat heart in two contraction states assessed by diffusion tensor MRI. *Progr. Biophys. Mol. Biol.* 110, 319–330. doi: 10.1016/j.pbiomolbio.2012.07.014

Hassaballah, A. I., Hassan, M. A., Mardi, A. N., and Hamdi, M. (2013). An inverse finite element method for determining the tissue compressibility of

human left ventricular wall during the cardiac cycle. *PLoS ONE* 8:e82703. doi: 10.1371/journal.pone.0082703

Hodgkin, A. L., and Huxley, A. F. (1952). A quantitative description of membrane current and its application to conduction and excitation in nerve. *J. Physiol.* 117, 500–544. doi: 10.1113/jphysiol.1952.sp004764

Holzapfel, G. A., and Ogden, R. W. (2009). Constitutive modelling of passive myocardium: a structurally based framework for material characterization. *R. Soc. Lond. Philos. Trans. A Math. Phys. Eng. Sci.* 367, 3445–3475. doi: 10.1098/rsta.2009.0091

Hu, H., and Sachs, F. (1997). Stretch-activated ion channels in the heart. *J. Mol. Cell. Cardiol.* 29, 1511–1523. doi: 10.1006/jmcc.1997.0392

Jie, X., Gurev, V., and Trayanova, N. (2010). Mechanisms of mechanically induced spontaneous arrhythmias in acute regional ischemia. *Circul. Res.* 106, 185–192. doi: 10.1161/CIRCRESAHA.109.210864

Kamkin, A., Kiseleva, I., Lozinsky, I., and Scholz, H. (2005). Electrical interaction of mechanosensitive fibroblasts and myocytes in the heart. *Basic Res. Cardiol.* 100, 337–345. doi: 10.1007/s00395-005-0529-4

Kamkin, A., Kiseleva, I., Wagner, K.-D., Leiterer, K. P., Theres, H., Scholz, H., et al. (2000). Mechano-electric feedback in right atrium after left ventricular infarction in rats. *J. Mol. Cell Cardiol.* 32, 465–477. doi: 10.1006/jmcc.1999.1091

Keldermann, R. H., Nash, M. P., and Panfilov, A. V. (2007). Pacemakers in a reaction-diffusion mechanics system. *J. Stat. Phys.* 128, 375–392. doi: 10.1007/s10955-006-9219-3

Keldermann, R. H., Nash, M. P., and Panfilov, A. V. (2009). Modeling cardiac mechano-electrical feedback using reaction-diffusion-mechanics systems. *Phys. D* 238, 1000–1007. doi: 10.1016/j.physd.2008.08.017

Kohl, P., Hunter, P., and Noble, D. (1999). Stretch-induced changes in heart rate and rhythm: clinical observations, experiments and mathematical models. *Progr. Biophys. Mol. Biol.* 71, 91–138. doi: 10.1016/S0079-6107(98)00038-8

Mekkaoui, C., Huang, S., Chen, H. H., Dai, G., Reese, T. G., Kostis, W. J., et al. (2012). Fiber architecture in remodeled myocardium revealed with a quantitative diffusion CMR tractography framework and histological validation. *J. Cardiovasc. Magn. Reson.* 14:70. doi: 10.1186/1532-429X-14-70

Nash, M. P., and Panfilov, A. V. (2004). Electromechanical model of excitable tissue to study reentrant cardiac arrhythmias. *Progr. Biophys. Mol. Biol.* 85, 501–522. doi: 10.1016/j.pbiomolbio.2004.01.016

Niederer, S. A., Ter Keurs, H. E. D. J., and Smith, N. P. (2009). Modelling and measuring electromechanical coupling in the rat heart. *Exp. Physiol.* 94, 529–540. doi: 10.1113/expphysiol.2008.045880

Panfilov, A. V., Keldermann, R. H., and Nash, M. P. (2005). Self-organized pacemakers in a coupled reaction-diffusion-mechanics system. *Phys. Rev. Lett.* 95:258104. doi: 10.1103/PhysRevLett.95.258104

Panfilov, A. V., Keldermann, R. H., and Nash, M. P. (2007). Drift and breakup of spiral waves in reaction-diffusion-mechanics systems. *Proc. Natl. Acad. Sci. U.S.A.* 104, 7922–7926. doi: 10.1073/pnas.0701895104

Pathmanathan, P., Chapman, S., Gavaghan, D., and Whiteley, J. (2010). Cardiac electromechanics: the effect of contraction model on the mathematical problem and accuracy of the numerical scheme. *Q. J. Mech. Appl. Math.* 63, 375–399. doi: 10.1093/qjmam/hbq014

Rogers, J. M., and McCulloch, A. D. (1994). A collocation-Galerkin finite element model of cardiac action potential propagation. *IEEE Trans. Biomed. Eng.* 41, 743–757. doi: 10.1109/10.310090

Smith, N., Nickerson, D., Crampin, E., and Hunter, P. (2004). Multiscale computational modelling of the heart. *Acta Numer.* 13, 371–431. doi: 10.1017/S0962492904000200

Trayanova, N. A. (2011). Whole-heart modeling. *Circul. Res.* 108, 113–128. doi: 10.1161/CIRCRESAHA.110.223610

Usyk, T. P., LeGrice, I. J., and McCulloch, A. D. (2002). Computational model of three-dimensional cardiac electromechanics. *Comput. Visual. Sci.* 4, 249–257. doi: 10.1007/s00791-002-0081-9

Vetter, F. J., and McCulloch, A. D. (1998). Three-dimensional analysis of regional cardiac function: a model of rabbit ventricular anatomy. *Progr. Biophys. Mol. Biol.* 69, 157–183. doi: 10.1016/S0079-6107(98)00006-6

Wilkins, E., Wilson, L., Wickramasinghe, K., Bhatnagar, P., Leal, J., Luengo-Fernandez, R., et al. (2017). *European Cardiovascular Disease Statistics 2017*. Brussels: European Heart Network.

Wong, J., and Kuhl, E. (2014). Generating fibre orientation maps in human heart models using Poisson interpolation. *Comput. Methods Biomech. Biomed. Eng.* 17, 1217–1226. doi: 10.1080/10255842.2012.739167

Zhang, Y., Wang, K., Yuan, Y., Sui, D., and Zhang, H. (2014). Effects of maximal sodium and potassium conductance on the stability of Hodgkin-Huxley model. *Comput. Math. Methods Med.* 2014:761907. doi: 10.1155/2014/761907

Conflict of Interest Statement: The authors declare that the research was conducted in the absence of any commercial or financial relationships that could be construed as a potential conflict of interest.

A. APPENDIX

A.1. Kinematics and Finite Element Approximation

The deformation gradient is defined as:

$$\mathbf{F} = \frac{\partial \boldsymbol{\varphi}(\boldsymbol{X},t)}{\partial \boldsymbol{X}} = \nabla \boldsymbol{\varphi}(\boldsymbol{X},t) \;\text{ with }\quad J = \det \mathbf{F} > 0, \tag{A1}$$

where the determinant of the deformation gradient J is also known as the volume ratio and has to be positive as the body is impenetrable. Further, the right Cauchy-Green tensor $\mathbf{C}$ can be introduced as $\mathbf{C} = \mathbf{F}^T\mathbf{F}$. To enforce the material incompressibility conditions ($J = 1$) in a framework of a finite element setting, the deformation gradient can be split into two parts $\mathbf{F} = (J^{1/3}\mathbf{I})\bar{\mathbf{F}}$, where $\mathbf{I}$ is the identity tensor. Specifically, $J^{1/3}\mathbf{I}$ describes purely volumetric deformation whereas $\bar{\mathbf{F}}$ denotes the purely isochoric deformation ($\bar{J} = det(\bar{\mathbf{F}}) = 1$).

Employing the Galerkin procedure, the residuals (2) and (1) are multiplied with the scalar- and vector-valued test functions $\delta\Phi$ and $\delta\boldsymbol{\varphi}$ which satisfy $\delta\Phi = 0$ on Γ_Φ and $\delta\boldsymbol{\varphi} = \boldsymbol{0}$ on $\Gamma_{\boldsymbol{\varphi}}$, respectively. These resulting expressions are further reformulated by using integration by parts and the Gauss theorem over the body Ω_0 such that the weak forms are obtained as:

$$\begin{aligned} &\int_{\Omega_0} \delta\Phi\,\dot{\Phi}\,\mathrm{d}V + \int_{\Omega_0} \nabla(\delta\Phi)\cdot\boldsymbol{Q}\,\mathrm{d}V \\ &-\int_{\Omega_0} \delta\Phi F^{\Phi}\,\mathrm{d}V - \int_{\Gamma_Q} \delta\Phi\,\bar{Q}\,\mathrm{d}a \doteq 0, \\ &\int_{\Omega_0} \nabla(\delta\boldsymbol{\varphi}) : [\mathbf{F}\cdot\mathbf{S}]\,\mathrm{d}V - \int_{\Omega_0} \delta\boldsymbol{\varphi}\cdot\boldsymbol{F}^{\varphi}\,\mathrm{d}V - \int_{\Gamma_T} \delta\boldsymbol{\varphi}\cdot\bar{\boldsymbol{T}}\,\mathrm{d}a \doteq 0\,. \end{aligned} \tag{A2}$$

Further, the Dirichlet boundary conditions prescribe the state of the respective surface points to be $\bar{\boldsymbol{\varphi}}$ and $\bar{\Phi}$. The Neumann boundary conditions prescribe the surface traction $\bar{\boldsymbol{T}}$ and the surface flux term $\bar{Q} = \boldsymbol{Q}\cdot\boldsymbol{N}$. $\boldsymbol{F}^{\Phi}$. All quantities of the boundary conditions are supposed to be given. In addition, in our problems $\bar{\boldsymbol{T}}$, $\bar{Q}$ and $\boldsymbol{F}^{\Phi}$ are independent of deformation and AP. In what follows, the notations are introduced: the material time derivative as $\{\dot{\square}\} = \mathrm{d}\{\square\}/\mathrm{d}t$ and the material divergence and gradient as $\mathrm{Div}\{\square\} = \partial\{\square\}/\partial\boldsymbol{X} : \mathbf{I}$ and $\nabla\{\square\} = \partial\{\square\}/\partial\boldsymbol{X}$. The equation of motion expresses the quasi-static force equilibrium and has to hold for all points $\boldsymbol{X}$ in Ω_0. In the following, we will review how to derive the main terms in the (A2).

A.2. Mechanical Constitutive Models

A.2.1. Transversely Isotropic Compressible Model (TIC)

The passive second Piola-Kirchhoff stress $\mathbf{S}^{pas}$ can be derived from the strain energy (5) as:

$$\begin{aligned} \mathbf{S}^{pas}(\mathbf{C}) &= 2\frac{\partial\Psi}{\partial\mathbf{C}} = \mathbf{S}_{iso}(\mathbf{C}) + \mathbf{S}_{ani}(\mathbf{C}), \\ \mathbf{S}_{iso}(\mathbf{C}) &= \left(\Lambda \ln J - \mu\right)\mathbf{C}^{-1} + \mu\mathbf{I}, \\ \mathbf{S}_{ani}(\mathbf{C}) &= +2\vartheta\,\eta(I_{4f} - 1)\boldsymbol{f}_0 \otimes \boldsymbol{f}_0. \end{aligned} \tag{A3}$$

A.2.2. Transversely Isotropic and Nearly Incompressible Model (TII)

The passive second Piola-Kirchhoff stress $\mathbf{S}^{pas}$ can be derived from (8) as follows:

$$\begin{aligned} \mathbf{S}^{pas}(\mathbf{C}) &= 2\frac{\partial\Psi}{\partial\mathbf{C}} = \mathbf{S}_{iso}(\mathbf{C}) + \mathbf{S}_{ani}(\mathbf{C}), \\ \mathbf{S}_{iso}(\mathbf{C}) &= \mu\left(J^{-2/3}\mathbf{I} - \frac{1}{3}\bar{I}_1\mathbf{C}^{-1}\right), \\ \mathbf{S}_{ani}(\mathbf{C}) &= 2\vartheta\,\eta(\bar{I}_{4f} - 1)\left(\boldsymbol{f}_0\otimes\boldsymbol{f}_0 - \frac{1}{3}\bar{I}_{4f}\mathbf{C}^{-1}\right). \end{aligned} \tag{A4}$$

A.2.3. Orthotropic and Nearly Incompressible Model (HO)

Based on (11), the passive second Piola-Kirchhoff stress is given as $\mathbf{S}^{pas} = \mathbf{S}_{iso} + \mathbf{S}_{ani}$, where

$$\begin{aligned} \mathbf{S}_{iso}(\mathbf{C}) &= a\exp\left[b(\bar{I}_1 - 3)\right]\left(J^{-2/3}\mathbf{I} - \tfrac{1}{3}\bar{I}_1\mathbf{C}^{-1}\right), \\ \mathbf{S}_{ani}(\mathbf{C}) &= \sum_{i=f,s} 2(\bar{I}_{4i} - 1)a_i\exp\left[b_i(\bar{I}_{4i} - 1)^2\right]\left(\boldsymbol{i}_0\otimes\boldsymbol{i}_0 - \frac{1}{3}\bar{I}_{4i}\mathbf{C}^{-1}\right) \\ &\quad + \bar{I}_{8fs}a_{fs}\exp\left(b_{fs}\bar{I}_{8fs}^2\right)\left[\left(\boldsymbol{f}_0\otimes\boldsymbol{s}_0 + \boldsymbol{s}_0\otimes\boldsymbol{f}_0\right) - \tfrac{2}{3}\bar{I}_{8fs}\mathbf{C}^{-1}\right]. \end{aligned} \tag{A5}$$

A.2.4. Transversely Isotropic Active Stress Response

Taking into account $\boldsymbol{f}_0$ only, the active second Piola-Kirchhoff stress is defined as follows:

$$\mathbf{S}^{act}(\boldsymbol{f}_0, \Phi) = T^{act}(\Phi)\boldsymbol{f}_0\otimes\boldsymbol{f}_0\,. \tag{A6}$$

The transversely isotropic characteristic is realized such that the magnitude of the active fiber tension $T^{act}(\Phi)$, which is driven by the AP, only has an effect along the material fiber orientation $\boldsymbol{f}_0$.

A.2.5. Orthotropic Active Stress Response

When both $\boldsymbol{f}_0$ and $\boldsymbol{s}_0$ are considered for active contraction, the stress is written as:

$$\mathbf{S}^{act}(\boldsymbol{f}_0, \boldsymbol{s}_0, \Phi) = T^{act}(\Phi)\left[\nu_{ff}\boldsymbol{f}_0\otimes\boldsymbol{f}_0 + \nu_{ss}\boldsymbol{s}_0\otimes\boldsymbol{s}_0\right], \tag{A7}$$

where ν_{ff} and ν_{ss} are weighting factors. Furthermore, $T^{act}(\Phi)$ is modeled via the evolution equation as $\dot{T}^{act} = T(\Phi, T^{act})$ in Nash and Panfilov (2004). According to the local ordinary differential equation of the active muscle traction, T^{act} can be treated as an internal variable and locally updated on the integration point level. The evolution equation for the muscle traction is herein used for both active tension models and reads:

$$\dot{T}^{act} = \epsilon(\Phi)\left[k_T\left(\Phi - \Phi_r\right) - T^{act}\right] \tag{A8}$$

with its sensitivity with respect to the action potential.

$$\frac{\partial\mathbf{S}^{act}}{\partial\Phi} = \partial_\Phi T^{act}(\Phi)\left[\nu_{ff}\boldsymbol{f}_0\otimes\boldsymbol{f}_0 + \nu_{ss}\boldsymbol{s}_0\otimes\boldsymbol{s}_0\right], \tag{A9}$$

where k_T specifies the saturated value of $T^{act}(\Phi)$, and Φ_r is the resting potential, where no new tension is evoked. Usually for

cardiac cells $\Phi_r = -80$mV, and $\epsilon(\Phi)$ represents the switch function which creates the typical cardiac cell performance via:

$$\epsilon(\Phi) = \epsilon_0 + (\epsilon_\infty - \epsilon_0) \exp\left[-\exp\left(-\xi\left(\Phi - \tilde{\Phi}\right)\right)\right]. \quad \text{(A10)}$$

The special behavior can be adjusted by the parameters ϵ_0 and ϵ_∞, which regulate the limitation values $\tilde{\Phi}$ denoting the phase shift and ξ controlling the transition rate from ϵ_0 to ϵ_∞. The impact of the active fiber tension on the active stress along the fiber direction and in sheet direction are controlled by ν_{ff} and ν_{ss}, respectively. Equation (A8) is approximately solved for the internal variable T^{act}. The temporal discretization of the time derivative reads $\dot{T}^{act} \approx \frac{T^{act} - T^{act}_n}{\Delta t}$. Here, T^{act} approximates the active fiber tension at time t_{n+1}, while T^{act}_n approximates the active fiber tension at t_n. Therefore, the residual is formed as follows:

$$R^T = T^{act} - T^{act}_n - \Delta t\, \epsilon(\Phi)\left[k_T\,(\Phi - \Phi_r) - T^{act}\right] \doteq 0. \quad \text{(A11)}$$

This equation can directly be solved for T^{act} by restructuring into

$$T^{act}(\Phi) = \frac{1}{1 + \Delta t\, \epsilon(\Phi)}\left[T^{act}_n + \Delta t\, \epsilon(\Phi)\left[k_T\,(\Phi - \Phi_r)\right]\right]. \quad \text{(A12)}$$

The sensitivity $\partial_\Phi T^{act}(\Phi)$ of the active stress to the transmembrane potential Φ in (A9) results from its derivation as:

$$\partial_\Phi T^{act}(\Phi) = \frac{\Delta t}{1 + \Delta t\, \epsilon(\Phi)}\left[\epsilon'(\Phi)\left[(k_T\,(\Phi - \Phi_r) - T^{act}\right] + \epsilon(\Phi) k_T\right] \quad \text{(A13)}$$

and the derivative of the switch function is calculated as:

$$\epsilon'(\Phi) = \frac{\partial \epsilon(\Phi)}{\partial \Phi} = \xi\left[\epsilon(\Phi) - \epsilon_0\right] \exp\left[-\xi\left(\Phi - \tilde{\Phi}\right)\right]. \quad \text{(A14)}$$

The sensitivities of potential flux $\mathrm{d_C}\boldsymbol{Q}$ and the stress tensor with respect to the deformation $\mathrm{d_C}\mathbf{S}$ can be evaluated as

$$\mathrm{d_C}\boldsymbol{Q} = \{D_{iso}\frac{1}{2}[\mathbf{C}^{-1} \bar{\otimes} \mathbf{C}^{-1}] + D_{ani} I_{4f}^{-2}(\boldsymbol{f}_0 \otimes \boldsymbol{f}_0) \otimes (\boldsymbol{f}_0 \otimes \boldsymbol{f}_0)\} \cdot \nabla \Phi. \quad \text{(A15)}$$

A.3. Electrophysiological Model

In (16), r is the recovery variable, whose evolution is governed by the local ordinary differential equation known as the Aliev-Panfilov (Aliev and Panfilov, 1996) model, which can capture all major characteristics of the cardiac electrophysiology.

$$\dot{r} = f^r = \left[\gamma + \frac{\mu_1 r}{\mu_2 + \phi}\right][-r - c\phi(\phi - \beta - 1)], \quad \text{(A16)}$$

where f^r is the source term for r and the variables μ_1, μ_2, β and γ are additional material parameters. While the coefficient term $[\gamma + \frac{\mu_1 r}{\mu_2 + \phi}]$ is a weighting factor, β controls the AP duration or effective refractory period (Costabal et al., 2016).

Considering the boundary value problem (A2), r can be also treated as an internal variable. In order to solve the internal evolution equation (29), the implicit Euler method is used. This requires a temporal discretization of the time derivative $\dot{r} \approx \frac{r - r_n}{\Delta t}$. Hence, the residual can be introduced as:

$$R^r = r - r_n - \Delta t f^r(\phi, r) \doteq 0. \quad \text{(A17)}$$

Using its linearization the local update equation for variable r can be achieved as:

$$r \leftarrow r - (\partial_r R^r)^{-1} R^r \quad \text{with} \quad \partial_r R^r = 1 + \Delta t\left[\gamma + \frac{\mu_1}{\mu_2 + \phi}[2r + c\phi(\phi - \beta - 1)]\right]. \quad \text{(A18)}$$

This is solved iteratively using the Newton-Raphson method.

In **Figure A1** (left), we carry out a parameter study to find the right parameter β for the rat electrophysiology and the curves show the AP Φ (solid) evolution displayed alongside the recovery variable r (dashed) over time t. Another way to derive the same electrophysiological behavior for the rat is to adapt the conversion coefficient of time k_t. The obtained parameter is then used to compute the normalized AP and the recovery variable, which are plotted over the normalized time $\bar{t}$ with initial values ($\phi = 0$, $r = 0$) in **Figure A1** (right). Roughly, the rat heart beats about four times faster than the human heart. To trigger the AP excitation, a stimulus I is required. As illustrated in **Figure A1** (right), the AP then increases steeply in the depolarization phase. After reaching its maximum value of 1.0, the repolarization follows and it smoothly returns to its resting potential $\phi_r = 0$. Apart from the non-pacemaker cells, there exist self-oscillating pacemaker cells, which can be modeled, e.g., by the FitzHugh-Nagumo model (Fitzhugh, 1961). In **Figure A2** (left), for the choice of $\beta = 0.55$, the phase plane of the two variables ϕ, r is shown with the steady state of equilibrium at $\phi = \dot{\phi} = r = \dot{r} = 0$ (red dot ●). Trajectories of nine starting points of the model (black dot ●) finally run into the stable equilibrium point. Four dashed nullclines, which are solutions of $\dot{\phi} = \bar{f}^\phi(\phi, r) = 0$ (red-dashed lines) and $\dot{r} = \bar{f}^r(\phi, r) = 0$ (green-dashed lines), pilot the solution trajectories of the model to the equilibrium point. This means that the parameters yield a stable model and the potential is only triggered by a stimulus. In **Figure A2** (right), the correlation between AP Φ and active fiber tension T^{act} computed using (16) is illustrated. The two curves are similar since their relation is linear.

A.4. Mechano-Electrical Feedback

For the electrical source term F^Φ_m, its tangent terms with respect to AP and deformation are:

$$\partial_\Phi F^\Phi_m = -\vartheta G_s\,(\lambda - 1), \quad \mathrm{d_C} F^\Phi = \tfrac{1}{2}\vartheta G_s\,(\Phi_s - \Phi)\,\lambda^{-1} \boldsymbol{f}_0 \otimes \boldsymbol{f}_0. \quad \text{(A19)}$$

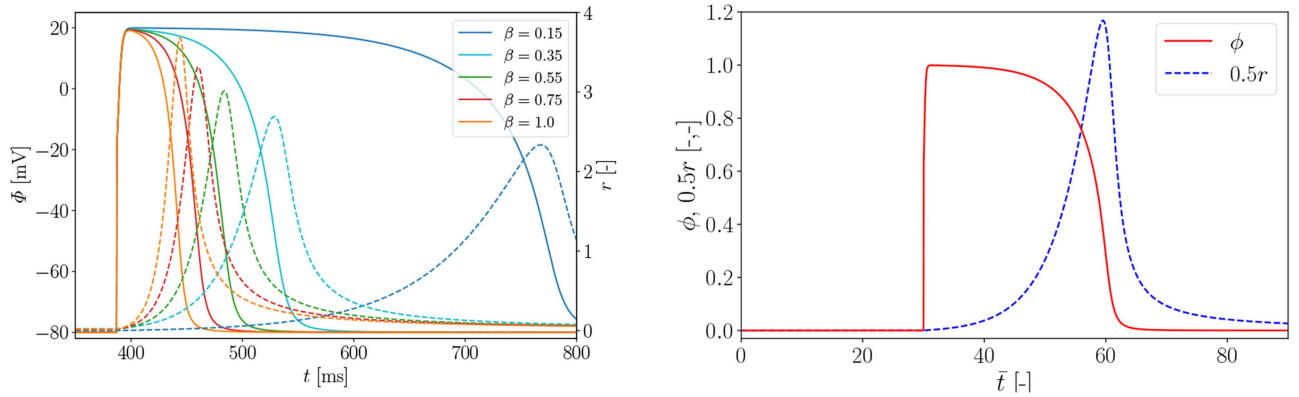

FIGURE A1 | Left: parameter study for rat electrophysiology AP (solid) and recovery variable (dashed); Right: evolution of normalized AP ϕ and recovery variable $0.5r$ over normalized time $\bar{t}$. Parameters $\alpha = 0.01$, $\gamma = 0.002$, $\beta = 0.55$, $c = 8$, $\mu_1 = 0.2$ and $\mu_2 = 0.3$ and an external excitation $I = 30$ at $\bar{t} = 30$ to trigger cardiac cells.

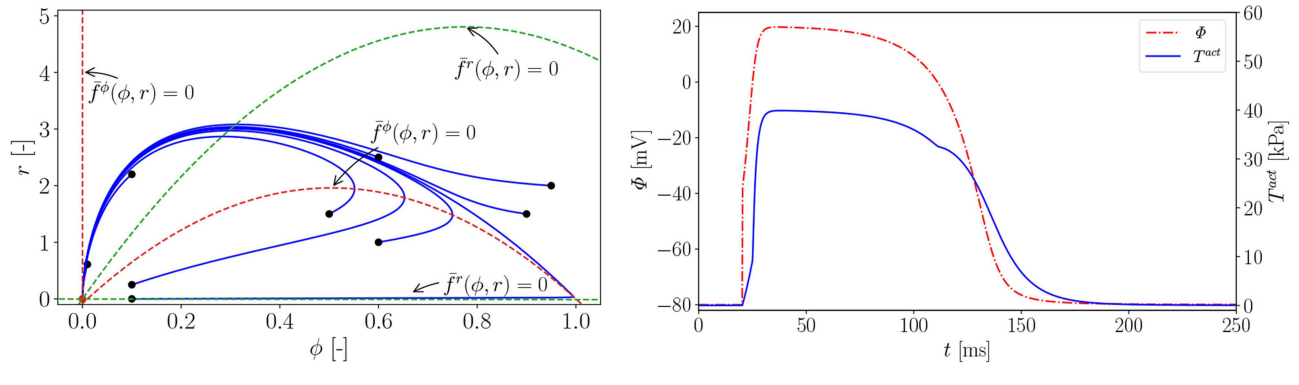

FIGURE A2 | Left: phase plane; the nullclines $\bar{f}^{r}$ and $\bar{f}^{\phi}$ (dashed lines) are functions of ϕ and $\bar{t}$ and guide all the solution trajectories (solid lines) to the equilibrium point from different starting points (•); Right: Active fiber tension T^{act} (Φ). Parameters: $\epsilon_0 = 0.1$ ms^{-1}, $\epsilon_\infty = 1.0$ ms^{-1}, $\tilde{\Phi} = 0.0$ mV, $\xi = 0.5$ mV^{-1}, $k_T = 0.40$ kPa and $\Phi_r = -80$ mV. Electrical characteristics as in **Figure A1**.

A.5. Material Parameters

TABLE A1 | Material parameters for simulation of rat cardiac muscles.

Mechanical	
Passive stress (TIC)	$\lambda = 0.5$ MPa, $\mu = 0.2$ MPa, $\eta = 0.1$ MPa (Göktepe and Kuhl, 2009)
Active stress	$k_T = 0.005$ MPa mV^{-1}, $\Phi_r = -80$ mV
Passive stress (TII)	$\mu = 0.5$ MPa, $\eta = 0.2$ MPa, κ=10^4 kPa (model fit)
Active stress	$k_T = 0.005$ MPa mV^{-1}, $\Phi_r = -80$ mV
Passive stress (HO)	$a = 0.144$ kPa, $b = 9.758$ [-], $a_f = 9.664$ kPa, (model fit)
	$b_f = 14.791$ [-], $a_s = 1.687$ kPa, $b_s = 7.336$ [-],
	$a_{fs} = 0.209$ kPa, $b_{fs} = 11.089$ [-], κ=10^{4}kPa
Active stress	$k_T = 0.49$ kPa mV^{-1}, $\Phi_r = -80$ mV, $\nu_{ff} = 1.0$, $\nu_{ss} = 0.0$ (Niederer et al., 2009)
Switch function	$\epsilon_0 = 0.1$ mV^{-1}, $\epsilon_\infty = 1.0$ mV^{-1} (Göktepe and Kuhl, 2010)
	$\xi = 1.0$ mV^{-1}, $\tilde{\Phi} = 0$ mV
Electrical	
Conduction	$d_{iso} = 0.1$ mm^2/mm^{-1}, $d_{ani} = 0.3$ mm^2/ms^{-1}
Excitation	$\alpha = 0.01$ [-], $\beta = 0.55$ [-], $c = 8$ [-] (parameter study)
	$\gamma = 0.002$ [-], $\mu_1 = 0.2$ [-], $\mu_2 = 0.3$ [-],
	$G_s = 10$ [-], $\phi_s = 0.6$ [-]
Conversion	$k_\phi = 100$ mV, $\delta_\phi = 80$ mV, $k_t = 12.9$ ms (Aliev and Panfilov, 1996)

Advantages of publishing in Frontiers

OPEN ACCESS
Articles are free to read for greatest visibility and readership

FAST PUBLICATION
Around 90 days from submission to decision

HIGH QUALITY PEER-REVIEW
Rigorous, collaborative, and constructive peer-review

TRANSPARENT PEER-REVIEW
Editors and reviewers acknowledged by name on published articles

Frontiers
Avenue du Tribunal-Fédéral 34
1005 Lausanne | Switzerland

Visit us: www.frontiersin.org
Contact us: info@frontiersin.org | +41 21 510 17 00

REPRODUCIBILITY OF RESEARCH
Support open data and methods to enhance research reproducibility

DIGITAL PUBLISHING
Articles designed for optimal readership across devices

FOLLOW US
@frontiersin

IMPACT METRICS
Advanced article metrics track visibility across digital media

EXTENSIVE PROMOTION
Marketing and promotion of impactful research

LOOP RESEARCH NETWORK
Our network increases your article's readership